Electromagnetic arc control for current interruption

Thesis submitted in accordance with the requirements of the University of Liverpool for the degree of Doctor in Philosophy by

Leonid Michael Shpanin

March 2006

ABSTRACT

A new approach for the control and interruption of a current carrying electrical arc using a magnetic field to contort the arc into a hitherto little investigated form is described. The essence of the approach is to use a magnetic field produced by a current through a coil to manipulate the arc outside rather than inside the coil. The interactions of the electrical arc in air, at atmospheric pressure with such a magnetic field have been investigated and shown to be capable of rapidly producing a stable azimuthal arc by the simple process of separating two contacts. Tests results have been obtained in air and in ablated PTFE. Preliminary investigations have been made in N_2 and SF_6 regarding the arc control and quenching capabilities of the approach. For such purposes, several different measurement techniques have been deployed which include current, voltage, high-speed and video photography, optical fibre probing, magnetic field probing and dielectric strength probing.

The results suggest that stable arc control and good arc quenching is achievable through the combined use of the azimuthal arc and self-pressurisation. There are preliminary indications that arc quenching similar to SF_6 maybe obtained with the use of air within the azimuthal arc unit and that dielectric recovery strengths similar to those achieved with other rotary arc interrupters may be achievable.

ACKNOWLEDGEMENTS

I would like to thank first my supervisors, Prof. G. Jones and Dr. J. Spencer, for their guidance, stimulating criticism and very helpful ideas, during the whole process of my work.

I would like to express my gratitude to Mr. J. Humphries, whom I am grateful for helping me both in deeds and in ideas during the numerous and prolonged hours we spent in the laboratory. His valuable assistance, as much as his moral support, helped this work to advance and to be achieved.

I would also like to express my many thanks to Mr. D. Turner, who has put in time and effort which has contributed to this research to a great extent, both in theory and in practice. I'm grateful for his help, as much as for his friendship.

Special thanks to Dr. D. Telfer, Dr. J. Yan and Dr. A. Deakin for their fruitful discussions and advice.

I am grateful to the members of workshop Ms. N. Telfer and Mr. R. Forde for their help with the machining of the devices.

To all members of the Centre for Intelligent Monitoring Systems at University of Liverpool, thanks for all the help and the encouragement, which made this work possible.

CONTENTS

CHAPTER 1 - INTRODUCTION

Over decades, circuit breaker technologies have been significantly advanced. The trend to further advance the technology continues with regard to several aspects including more advanced technologies, environmental considerations and cost reduction. From the second part of twenty century, sulphur hexafluoride gas (SF_6) has been used in circuit breakers because of its excellent arc-quenching action (Christophorou *et al*, 1997). The double pressure blast type circuit breakers (Ryan and Jones, 1989) have been superseded by a "puffer" type that has a number of advantages. However, a high-energy mechanism is required to operate these circuit breakers (Ali, 2001). The auto-expansion circuit breaker reduced the mechanism energy (Ali, 2001). Electromagnetically driven rotating arc circuit breakers (Ryan and Jones, 1989) are independent of pressurizing mechanism and contact erosion leading to extended circuit breaker life. However, there remain environmental concerns with the use of SF_6 in circuit breakers because of its potency as a greenhouse gas (Christophorou *et al*, 1997).

Circuit breaker diagnostics have an important role in the development of current interrupters. Early diagnostics consisted of a number of simple measurements of currents through and voltage across the circuit breaker (Ryan and Jones, 1989). During the interruption process a wide range of electrical, mechanical, aerodynamic, radiative and chemical diagnostic measurements are available for circuit breaker monitoring (Ryan and Jones, 1989). Under real operating conditions, the application of diagnostics becomes more complicated because of a number of reasons such as a size of the diagnostic devices, their shielding from the electromagnetic interference during switching (since many are based on electronic sensors) and the electrical insulation requirements of the circuit breaker to ground (Ryan and Jones, 1989). In contrast, the immunity of optical fibre sensors to electromagnetic interference and their intrinsic electrical insulation make them technically superior in many hostile environments (Medlock, 1989).

The above aspects present many technological challenges some of which have been addressed in the present thesis. As a result, it has been demonstrated that it is practicable to form a new arc configuration, which is azimuthal in nature and has potential for further technological developments. The objectives of the research were:

- To design and produce an experimental unit, which can demonstrate that an arc column can be rapidly transformed into a helical form simply during the opening of a contact gap.

- To test the experimental unit and provide evidence that the helical arc with azimuthal plasma flow around the arc column itself can be produced.

- To deploy the azimuthal arc form for use under alternating current conditions relevant to current interruption and current limiting applications.

- To incorporate the azimuthal arc in an interrupter geometry for enhancing PTFE ablation and self-pressurization.

- To explore the extent to which the azimuthal arc may be utilised in air without recourse to the use of SF_6 as an arc quenching gas.

This thesis describes the achievements of the above objectives.

Chapter 2 describes the background to the project. This begins with a description of general arc properties introducing some theoretical modelling, a review of circuit breaker technology and the development of circuit breaker diagnostics related to the work of previous authors.

The advantages of the rotary arc in a circuit breaker are considered, highlighting some key fundamental attributes of this arc form. The fundamental methods of arc rotation are described, based upon the work of previous authors.

Basic problems of current interruption are introduced with a brief discussion of the circuit breaking theory.

The final part of this chapter outlines the main parameters of circuit breaker diagnostics for monitoring the internal "health" of circuit breakers, which are described with a brief discussion.

Chapter 3 of the thesis discusses the design of a rotary arc-controlling

unit. It presents some new concepts of arc control that lead to the design principle for a unit for investigating the production and behavior of the electric arc under these conditions.

Details of the design method and the arc control unit are given. The extension of these considerations is made for the design of a possible arc-quenching device for current interruption. Components of the arc control unit are presented in detail and the assembly and construction of the experimental devices are described. The electromagnetic characteristics of the proposed arc interrupter unit are presented, highlighting the properties of the materials used in the design.

Theoretical calculations of magnetic fields external to the field-producing coil are presented in relation to the geometric form of the interrupter, which houses the coil. The chapter concludes with a consideration of assumptions made.

In **Chapter 4**, the experimental systems used in the project are described. The experimental test facility used in this work is presented (including a description of the experimental research laboratory at University of Liverpool (Department of Electrical Engineering and Electronics)) where by the electrical arcs were generated. The signal processing equipment in the research laboratory was adapted for use during the main series of experiments on the new arc units.

The methods for measuring current and voltage are described. This chapter is also devoted to the descriptions of diagnostic equipment used in research, e.g. for the measurement of magnetic field, gas dielectric strength, contact travel, arc shape, movement and decay which lead to improved understanding of the processes occurring during the arc control and current interruption tests.

The **chapter 5** is devoted to the experimental investigations and the results of the arc tests with the various arcing rigs constructed (reference non-rotary arc interrupter, arc control unit and prototype interrupter). **Chapter 5** is divided into two main parts - the first describes the experimental tests and the second the test results. The first part of this chapter describes the test strategy for each experiment, such as electrical, magnetic field, gas dielectric strength, PTFE ablation and optical observations for each of these test heads – reference interrupter, arc control model and prototype azimuthal interrupter. The second part, describes the experimental results obtained from these various tests. The experimental results of

the non-rotating arc interrupter (reference) present current and voltage interruption characteristics in which these results are used for design of the arc control unit. Results relevant to demonstrating the arc control are presented. The electrical, optical experimental results of the arc control unit are presented as the basis of further design development.

The final part of this chapter presents experimental results on the prototype azimuthal interrupter. Measurements for the variation of total magnetic field around the test head, obtained with a traditional search coil method are given. The results obtained from the main series of tests describe the control and extinction of ac-arcs in the various test heads. The test results presented demonstrate the current and voltage waveforms across the interrupter contacts, the optical fibre arc shape and movement measurements during both high current phase and post arcing, and the distribution of PTFE ablation. Experimental results are presented for arc quenching and dielectric strength recovery after current zero. The chapter concludes with a summary of the results obtained from the various tests (the range of experimental conditions and diagnostics used are presented in **chapter 6**).

Chapter 6 analyses the results obtained from the experimental tests described in **chapter 5**. The arc behaviour in the arc control unit and the azimuthal interrupter test heads are discussed, encompassing both quasi-dc and ac-arc conditions. Observations are made about the post arcing aerodynamic conditions in the different test units used. There is a comparison of theoretical calculations and practical measurements of the total magnetic field external to the coil. Comparisons are made between the results for the reference (non-rotary arc) and prototype interrupter units and the use of different arc quenching media. Recovery of dielectric strength is considered in the azimuthal arc interrupter. Empirical relationships for the breakdown voltage of dielectric strength and voltage extinction peak have also been considered in the prototype interrupter. The PTFE ablation distribution around the interrupter head is presented.

The **Chapter 7** summarizes the implication of the analyses presented in **chapter 6** and discusses its technological implications. The chapter produces an overview of fundamental knowledge generated by the research and suggests further research for the future.

CHAPTER 2 - REVIEW OF ELECTRIC ARCS AND CIRCUIT BREAKERS

This chapter gives a review of electric arcs and circuit breakers. It contains of a description of general arc properties including some theoretical modelling, and a review of circuit breaker technology and circuit breaker diagnostics, which are based upon the work of previous researchers. It also describes a different deployment of magnetic fields for controlling the electric arc in circuit breakers, highlighting some advantages of using this arc form. Fundamental problems of current interruption are presented with use of the circuit breaking theory. The chapter concludes with a consideration of basic parameters of circuit breaker diagnostics for investigating the internal "health" of circuit breakers.

2.1 INTRODUCTION

It has often been said that 99% of the matter in the universe is in the plasma state and that in this form it mainly exists as an ionized gas with the atoms dissociated into positive ions and negative electrons (Chen, 1984). This estimate is based upon the fact that stellar interiors, atmospheres, and much of the interstellar hydrogen are plasmas (Chen, 1984). The earliest work with plasma in the form of gas discharges was that of Langmuir, Tonks, and their collaborators in the 1920's (Bacon, 1976). However, the oldest known gas discharge of short duration was discovered by Davy about 1810 (Davy, 1840). When he connected two horizontal carbon rods to either terminal of a battery and later drew them apart, the current continued to flow, a gas discharge of extreme brilliance being set up. The discharge assumed the shape of an arc owing to the upward movement of the heated gas, and it is to this fact that the arc discharge owes its name. Electric arcs are encountered in a variety of situations in the field of electrical engineering. In some cases, arcs are unwelcome results of lightning strokes or insulation failures, but in many cases arcs were deliberately used, and their advantages exploited (Pansini and Smalling, 1992). In general, electrical arcs are created every time the contacts of a switch or circuit breaker are opened in order to either interrupt low or much higher current (Cobine, 1958). In high-voltage switches or circuit breaker, the arc is used as the conducting

element between the contacts that allows the current to continue to flow until the natural current zero of the ac current is reached, when the arc is extinguished. The electric arc is also used for heating purposes in arc furnaces (Mendis e*t al*, 1996) and arc welding equipments (Schupp e*t al* 2000). Overstress of the insulation system in an electric power network may lead to electrical flashover (Pansini and Smalling, 1992) and short-circuit of the system. At the location of the fault, the short circuit current will normally flow through an electric arc. Such a high-current arc may severely damage nearby equipment, and consequently the short circuit current will affect the whole network. It is a major task of the protection system to quickly de-energize the faulty part of the network.

2.2 ELECTRIC ARCS AND THEIR PROPERTIES

2.2.1 Arc channel

The arc channel (fig. 2.1) between two electrodes (anode and cathode) can be divided into an arc column, a cathode region and an anode region (Browne, 1984).

2.2.1.1 Column region

The temperature in the arc column is high typically ranging from 5000 K to 20000 K (Jones and Fang, 1980) and therefore the arc column is strongly ionized. There is a balance between the electrons and positive ion charges. Due to the strong ionization, a high current arc is a relatively good electrical conductor and conductivity of the arc plasma is sufficiently high.

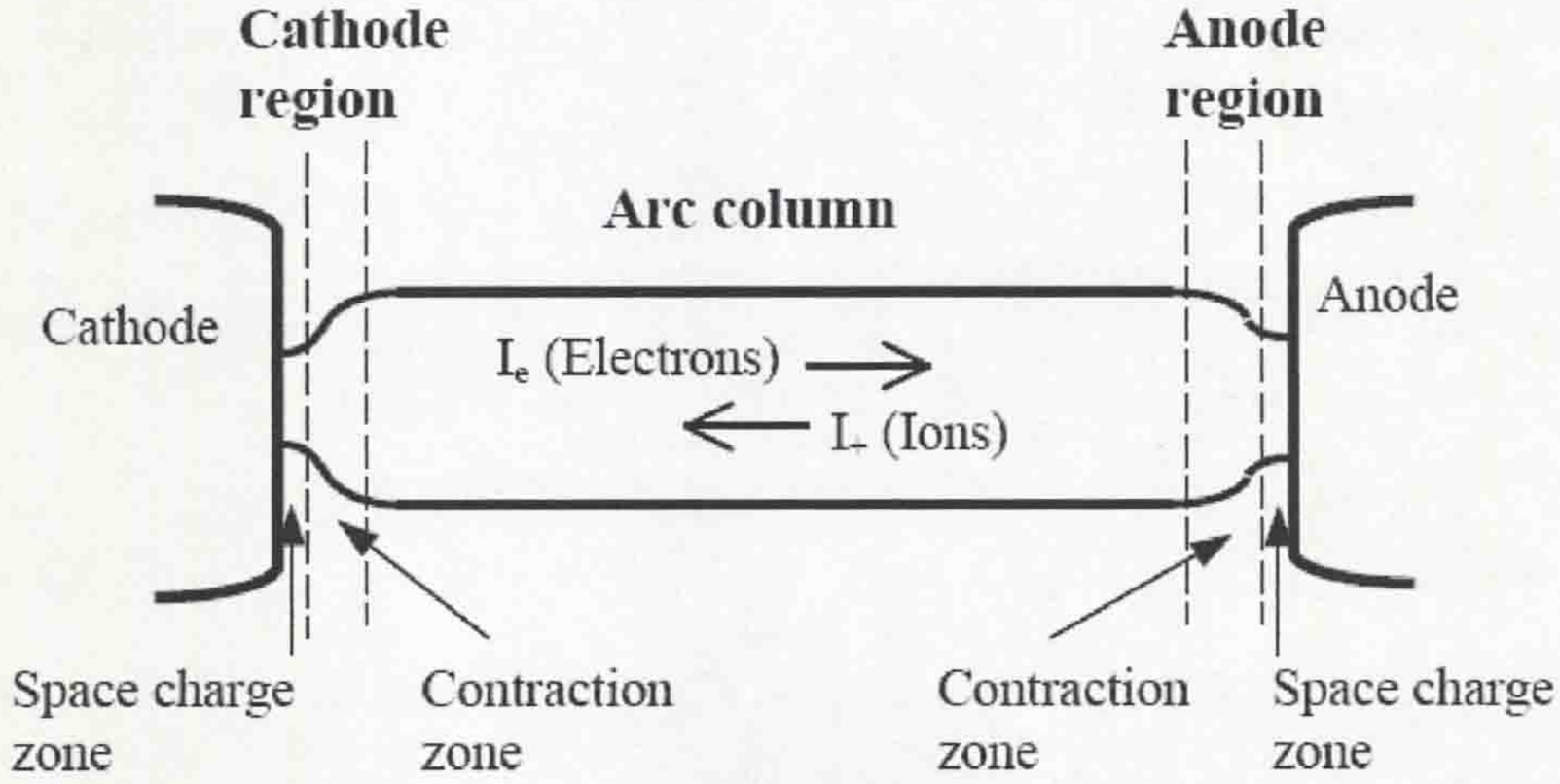

Figure 2.1 Regions of the arc channel (Browne, 1984)

The total arc voltage and voltage gradient along the arc column, depends on the current magnitude, the type of gas, and the pressure (Browne, 1984). When it is in thermal equilibrium (Cobine, 1958), the arc column adjusts itself in such a way that power supplied to the column (the ohmic heating) attains a minimum value. If there is a disturbance of this situation, which tends to increase the resistance of the arc, then the ohmic heating would increase, the temperature and/or diameter of the arc would increase, and automatically counteract the disturbance. If, on the other hand,

there is a disturbance that tends to increase the temperature or diameter of the arc, then the power losses would increase. Figure 2.2 shows a typical potential distribution along an arc channel (Browne, 1984).

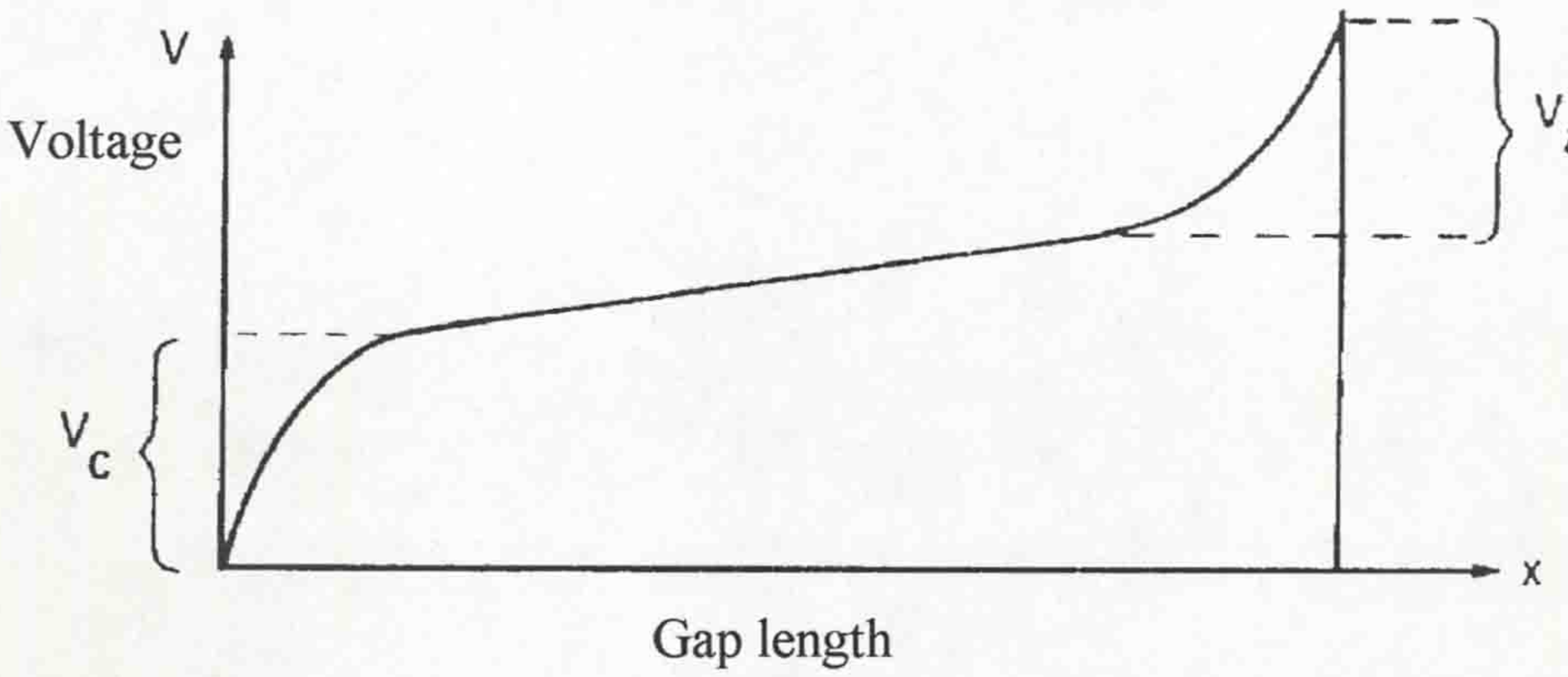

Figure 2.2 Typical potential distributions along an arc channel
V_c - Voltage: cathode region V_a - Voltage: anode region

2.2.1.2 Contact regions

The role of the cathode, and the surrounding cathode region, is to emit the current carrying electrons into the arc column (Browne, 1984). Some electrode materials have such a high boiling temperature that thermionic emission of electrons occurs well below the evaporation temperature. Such materials are carbon, tungsten and molybdenum (Browne, 1984). Other electrode materials have lower evaporation temperatures. In this case, the major emission mechanism will be field emission, where electrons will be emitted due to the high electric field strength close to the surface (Cobine, 1958). Copper is a typical example of such material. Close to the cathode, there will be an accumulation of positive ions, arriving from the arc column, which forms a space charge (Browne, 1984). Due to this space charge, there will be a high electric field strength close to the cathode surface (the cathode drop). This high field is essential for efficient (field) emission of electrons into the arc. The anode serves as a collector of electrons, arriving from the cathode (alternatively, it can be thermal ionization of gas). The electrons will arrive at high speed, and deliver all their energy to the anode (due to collision). The anode surface will therefore be kept at a high temperature. Close to the anode, there will be an area of positive ions, since they tend to drift away (Cobine, 1958). The surplus of electrons leads to high electric field strength close to the anode surface (the anode drop). Close to electrodes, the arc

diameter is often smaller than further away from the electrodes. This means that there will be a gradient in current density that lead to strong heating contacts in the surrounding medium (air, oil, vacuum or SF_6), and therefore also the gradient in internal pressure is produced (by electromagnetic compression due to the current density carrying within an arc channel). This pressure gradient will contribute to a transport of plasma and metal vapour from the electrodes into the arc column (Cobine, 1958).

2.2.2 Types of electric arc

The classification of the different types of electrical arcs is shown in figure 2.3 along with their subdivisions.

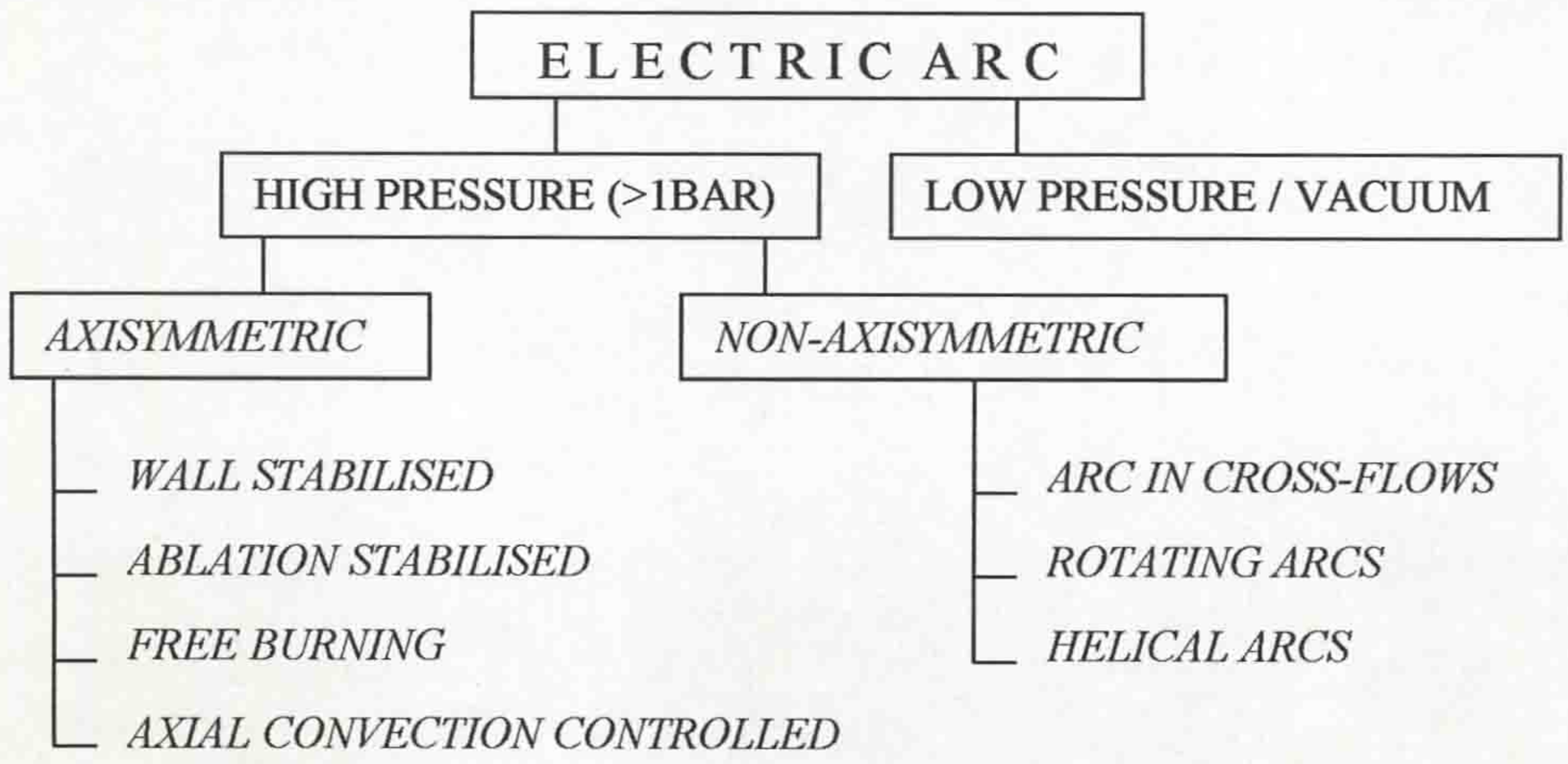

Figure 2.3 Electric arc classifications

Electric arcs can be divided into two fundamental classes: high-pressure arcs (>1bar) and vacuum (or low pressure) arcs with regard to current interruption applications successfully utilized at distribution level, while all transmission level circuit breakers involve interruption of a high-pressure arc (Jones, 1988). Such arcs can be further classified as axisymmetric or non-axisymmetric. The axial convection-controlled axisymmetric arc, used in two pressure circuit breakers, has found the most widespread use in circuit breaker technology and has received much theoretical investigation (Jones and Fang, 1980). This type of arc burns within a flow of high-speed gas coaxial with the arc column and arc boundary due to the entrainment of cool gas form by the flowed. Non-axisymmetric arcs, because of the nature of the

studies conducted into them, became known as cross-flow arcs. However, the rotating and helical arcs, which move under the action of Lorenz force produced by the cross arc current itself and an orthogonal electromagnetic field, are related to this class. This led to use this concept in present day rotary arc interrupters such as auto-puffer and self-pressurizing interrupters and development of rotating-arc and auto-expansion combined circuit breakers (Ali, 2001).

2.2.3 Arc modelling

The main concern of arc modelling is, to predict the electrical response of the arc through explicit or implicit knowledge of temporal thermal changes in the arc column (Ryan and Jones, 1989). Mathematical solutions of mass, momentum and energy conservation differential equations with Ohm's law and Maxwell's equations are sought simultaneously in axial, radial and time dimensions for axi-symmetric arcs. A number of additional phenomena during the arcing time complicate these e.g. nozzle ablation, radiation transport, turbulence and electrode melting processes (Fang, 1983). Therefore, there is a need to make some arc modelling simplifications, in which these models maybe used for accurate computations of parameters that could be measured in practice.

Mathematical solutions of arc models based on only a single ordinary differential equation were derived by Cassie, 1939, Mayr, 1943 and Browne, 1948. From the physical point of view, the Cassie model assumes that most loss of arc energy occurs by axial convection whereas the Mayr model considers that the radial contraction of the arc boundary dominates. These models are of only limited accuracy in predicting circuit breaker performance because they do not take sufficient account of the detailed physical processes occurring within arc column.

The numerical solutions of the model of the physical processes occurring in the arc column may be used as analytical tool by solving the governing arc equations. In addition, each model may be regarded as a special case of the boundary layer integral method (Cowley, 1974), which has been evaluated in further studies (e.g. Fang, 1983 and Tuma, 1980). This method describes the arc behaviour on the assumption of similarities between the radially integrated properties of various arc types. Thus, a detailed knowledge of the radial arc structure becomes redundant, once the scaling laws relating the various radial integrals have been established

(Ryan and Jones, 1989). The governing equations, describing the processes occurring during the arc interaction are used for arc modelling. In order to evaluate the accuracy of the solutions to these equations, the parameters appearing in the equations can be measured experimentally (e.g. temperature, current density, gas pressure, radiation loss, velocity and electric field strength). The effects of chemical reacting species upon the material properties of the plasma need to be taken into account in the governing equations. The conservation of momentum equation involves the magnetic field interactions that may be either external or produced by the arc current itself. Energy conservation concern must account for volumetric heat generation in the plasma via Ohm's low for resistive heat production (Heberlein *et al*, 1984). The radiation energy transport, which is usually important for high-power arcs complicates the arc analysis since it involves the whole volume of the discharge. The electromagnetic radiation from the plasma produces a major mechanism of energy dissipation occurring under many conditions. The equation for every component species in the plasma, e.g. electrons, ions, atoms and molecules, is described by the thermodynamic equation of state.

Mathematical arc modelling involves three dimensions (axial, radial, time). Therefore, simplifications of the general equations describing the arc at high-pressure may be presented in the following form (Jones and Fang, 1980):

Conservation of mass
$$\frac{\partial \rho}{\partial t} + \nabla.(\rho \mathbf{v}) = 0 \qquad (2.1)$$

Conservation of momentum
$$\rho \frac{d\mathbf{v}}{dt} = -\nabla p + \mathbf{j}x\mathbf{B} + \rho Fg + F(\eta) \qquad (2.2)$$

Conservation of energy
$$\frac{\partial}{\partial t}\left[\rho\left(\frac{1}{2}v^2 + e'\right)\right] + \nabla.\left[\rho\mathbf{v}\left(\frac{1}{2}v^2 + e'\right)\right] \qquad (2.3)$$
$$= \nabla.(K\nabla T) - \nabla.(p\mathbf{v}) - \nabla.(\mathbf{F}) + \phi + \mathbf{j}.\mathbf{E}$$

Maxwell's equations
$$\nabla x\mathbf{E} = -\frac{\partial \mathbf{B}}{\partial t} \qquad (2.4)$$
$$\nabla x\mathbf{B} = \mu_0 \mathbf{j} \qquad (2.5)$$

Simplified Ohm's law $\mathbf{j} = \sigma\mathbf{E}$ (2.6)

Equation of state $p = f(\rho, T)$ (2.7)

Radiation $\nabla.(\mathbf{F}) = 4\pi\int_0^\infty \kappa'_\nu(B_\nu - J_\nu)d\nu$ (2.8)

Where t is time, σ, ρ, η and K are the electrical conductivity, mass density, viscosity and thermal conductivity coefficient of the gas. T, **v** and p are the temperature, flow velocity and pressure of the gas. e' is the internal energy per unit mass, ϕ is the viscous friction heat dissipation function, **j** the current density, **E** is the electric field strength, $F(\eta)$ is the viscous stress and Fg is the sum of all other volume forces per unit mass. **F** is the radiation flux vector, defined by eqn.2.8, where κ_ν' is the effective spectral absorption coefficient, B_ν is the black-body spectral intensity, J_ν is the average spectral intensity and ν is the radiation frequency.

A complete solution of equations (2.1)-(2.8) in three dimensions is complicated and modelling for different types of arcs and operation conditions may require simplification.

Development of computer simulation program for quantitative understanding of the physical processes occurring in modern circuit breakers plays an important role. The use of computer simulation tools may significantly reduce the time for model calculations and for optimizing future circuit breaker designs (Yan, 1997 and Kweon, 2004).

2.2.3.1 Arc behaviour in a magnetic field

The current flow in the arc channel is associated with magnetic forces that lead to an internal overpressure in the arc channel, (Cullwick, 1966). This phenomenon is known as the "pinch effect", which is simplified shown in figure (fig. 2.4a).

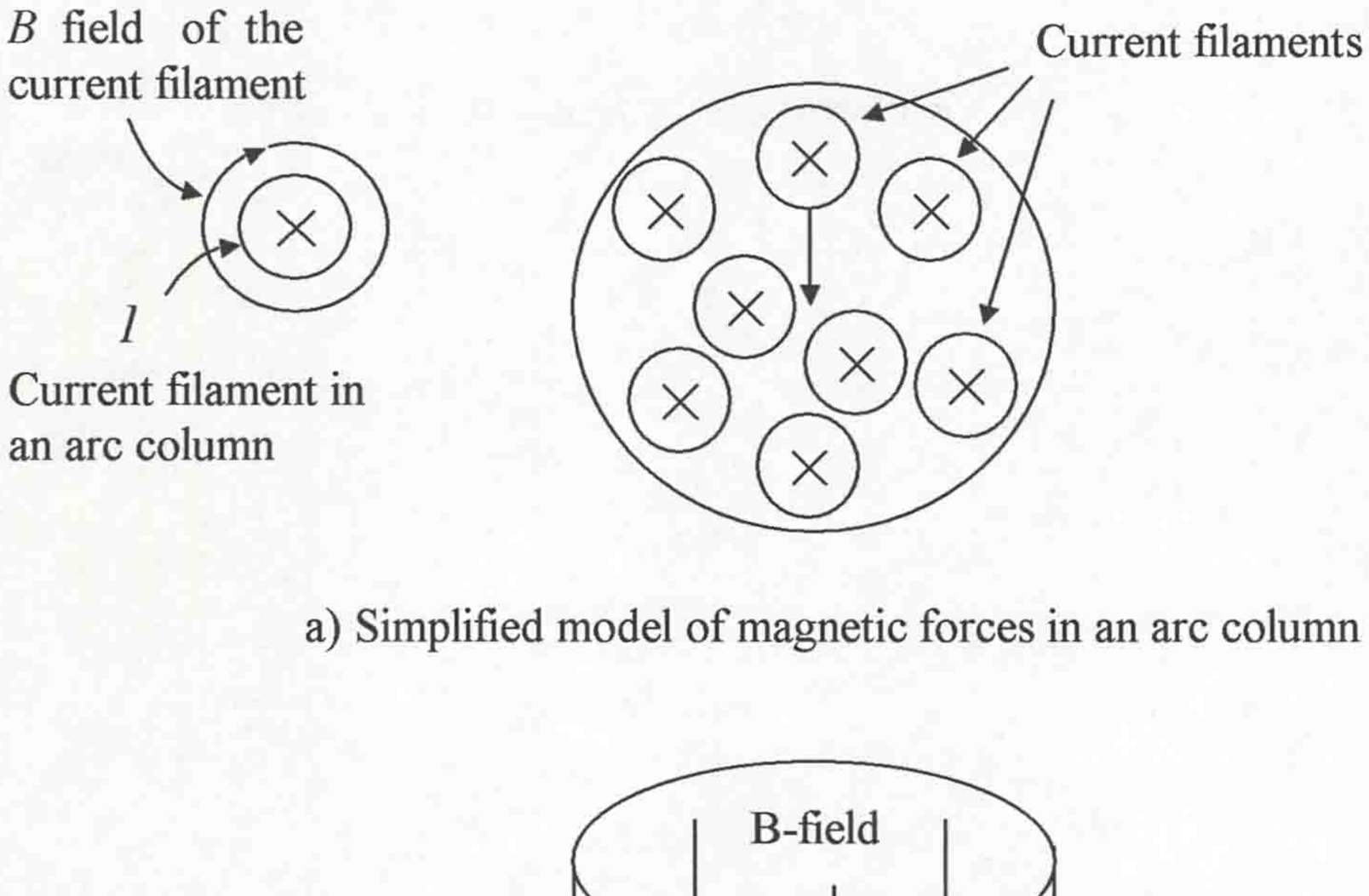

Figure 2.4 Behavior of the arc column with and without external magnetic field
(Where: I_+ - Ions, I_e - Electrons)

The total current in the column flowing through the arc can be presented as consisting of a number of parallel current filaments shown on figure 2.4a as circles with across. Each separate filament will be attracted to each of the others by a magnetic force. The resulting overall force on each filament will be directed towards the centre of the column. In the other words, the current that flows in the arc column, via interaction with the magnetic flux, will result in a mechanical force that is at each point of the column directed toward the centre. Thus, the arc current filaments are radially constrained (Chen, 1984).

The properties of plasma as the electrical arc are radically altered and controlled when it is placed in a strong magnetic field. The reason is that the motion of the charged plasma particles is affected by the magnetic field. In a strong magnetic field, the electrons and ions cannot move freely in the direction perpendicular to the line of force. The trajectory of each particle takes the form of a helix, which is parallel to the magnetic field, and as a consequence, its motion is highly directed (fig. 2.4b). Plasmas radially constrained by magnetic fields exhibit an internal pressure. The value of the internal pressure is directly related to the magnitude of the external magnetic flux density B and the current density J flowing through the arc column. In fact, without the external magnetic field this pressure would immediately reduce and would lead to the expansion of column, (Jones and Fang, 1980).

2.2.3.2 Arc shape and stability

An arc column of sufficient length can be controlled by the external magnetic field producing a Lorenz driving force on the arc. An arc column rotating between two concentric electrodes (fig. 2.5) has a complex convolute shape (Jones, 2001).

A simple model for a dc arc was proposed by Adams, 1963 for describing the behaviour of a rotary arc within a magnetic field and balanced by the aerodynamic drag force acting upon it. According to this theory the arc behaviour is governed by the following equation:

$$\frac{1}{2}\rho U^2 dC_D = Bi \qquad (2.9)$$

Where ρ - gas density

U - arc velocity at given radius

d - arc diameter

C_D - drag coefficient

B - magnetic flux density

i - arc current

The arc velocity (perpendicular for each arc element) is constant for a given Lorenz force (Bi) but has a different direction because of the convolute shape.

The shape of the arc column determined by the element of radial arc position (r) and angle (θ) with respect to the inner arc root (fig. 2.5).

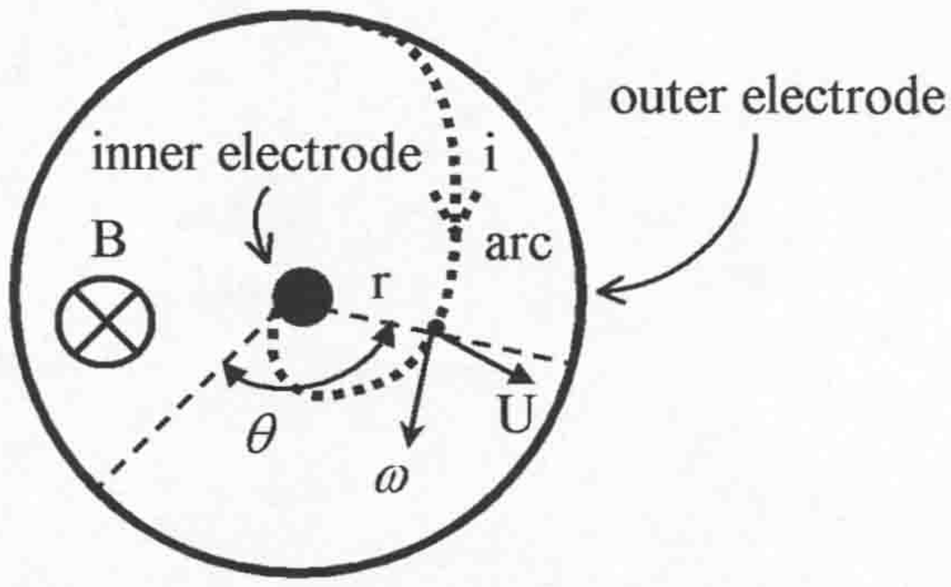

Figure 2.5 Arc shape between two concentric electrodes within an axial magnetic field

Estimation of the dc arc shape within the cross magnetic field is shown by Adams (1963) to be:

$$\theta = \sqrt{\frac{r^2}{c^2} - 1} - \cos^{-1}\frac{c}{r} \tag{2.10}$$

Where c is a constant, which defined by:

$$c = \frac{1}{\omega}\sqrt{\frac{Bi}{\frac{1}{2}\rho d\, C_D}} \tag{2.11}$$

and ω is the angular velocity of element of the rotary arc.

The shape of the arc column is independent of the absolute values of the electromagnetic and aerodynamic forces, since the constant c is the ratio of these forces. The experimental results (Adams, 1963) obtained during arcing achieved reasonable agreement with theoretical prediction of the arc shape. However, for sufficiently small arc gaps the predication of the arc shape becomes difficult because electrode phenomena becomes important and is neglected in the model.

During the arc rotation, the rotational symmetry of the arc column is significantly changed (Adams, 1963) leading to convection and momentum transport

between the surrounding gas and the arc column. Changes of the arc motion and its geometric shape lead this transport to be unstable becoming sufficiently stable when these components balanced. A stability criterion can be defined without detailed knowledge of the axial shape of the arc, the temperature distribution along the column and the mechanism of energy dissipation. For a balanced arc column, across which the magnetic field and a gas flow are imposed upon it, the stability criterion is (Schrade, 1973):

$$1+\beta-2\lambda^2-2\cos^2\alpha=0 \qquad (2.12)$$

Where

$\beta=\dfrac{P_\infty}{B_0/8\pi}$ - ratio compares the static pressure of the gas flow (P_∞) to the magnetic pressure ($B_0/8\pi$)

and

$\lambda=\dfrac{2i}{r_oB_o}$ - ratio of average self-magnetic field and external applied field

α - angle between the applied magnetic field and the radius of curvature vector (R) showing in figure 2.6

i - arc current

r_0 - arc radius

B_0 - applied (external) magnetic field

P_∞ - average static gas pressure

Equation (2.12) represents a different criterion of the arc stability. If the term on the left hand of equation (2.12) is positive, the arc is likely to be highly stable.

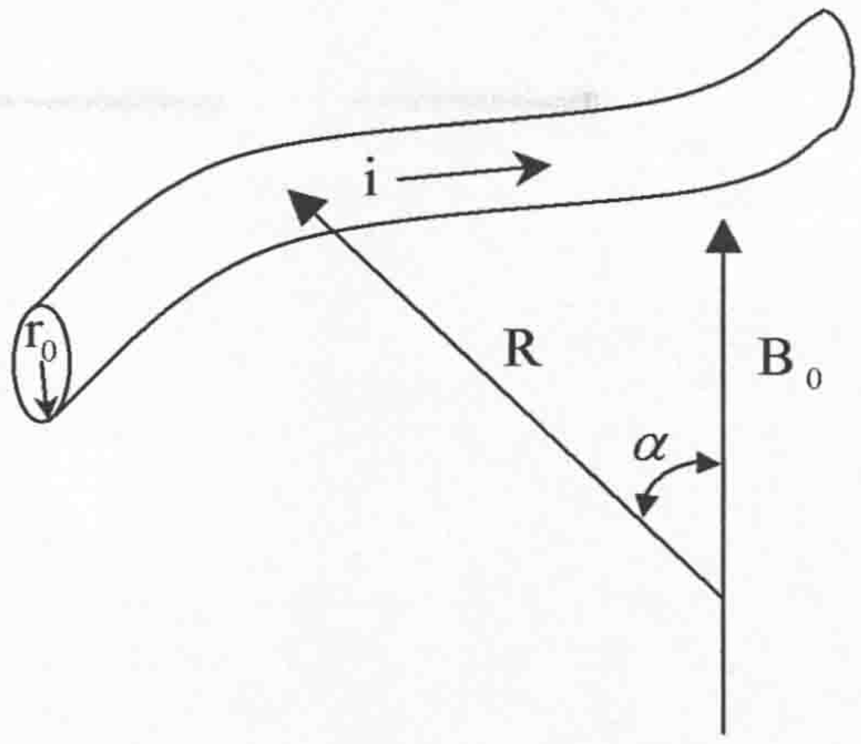

Figure 2.6 Parameters for describing the arc shape in an imposed magnetic field B_0

2.3 REVIEW OF CIRCUIT BREAKER TECHNOLOGY

2.3.1 Introduction to circuit breaking

The circuit breaker is a device, which breaks or interrupts the flow of current in a circuit. It is used for controlling and protecting the distribution and transmission of electrical power and is connected in series with the circuit it is expected to protect.

In high-voltage circuit breakers, the electric arc is used as part of the switching element because it can rapidly change from a good conductor to a good insulator when an alternating current reaches zero. The circuit breaker consists of: the interrupting medium (air, oil, vacuum or SF_6), the interrupter, insulators and the operating mechanism (Lythall, 1972 and Flurscheim, 1982). It has to be capable of successfully interrupting any level of current passing through its contacts from a few amperes to its rated full-short circuit current.

The basic function of ac-arc interruption is shown in figure 2.7. The contact separation and the ac-arc interruption process in figure 2.7 demonstrate a time interval with arcing between the contacts (anode and cathode), which extends for more than one ac half cycle. The main reason is that the circuit breaker often has still not reached conditions for the ac-arc to be extinguishable at the first current zero. At the second current zero, the ac-arc is extinguished.

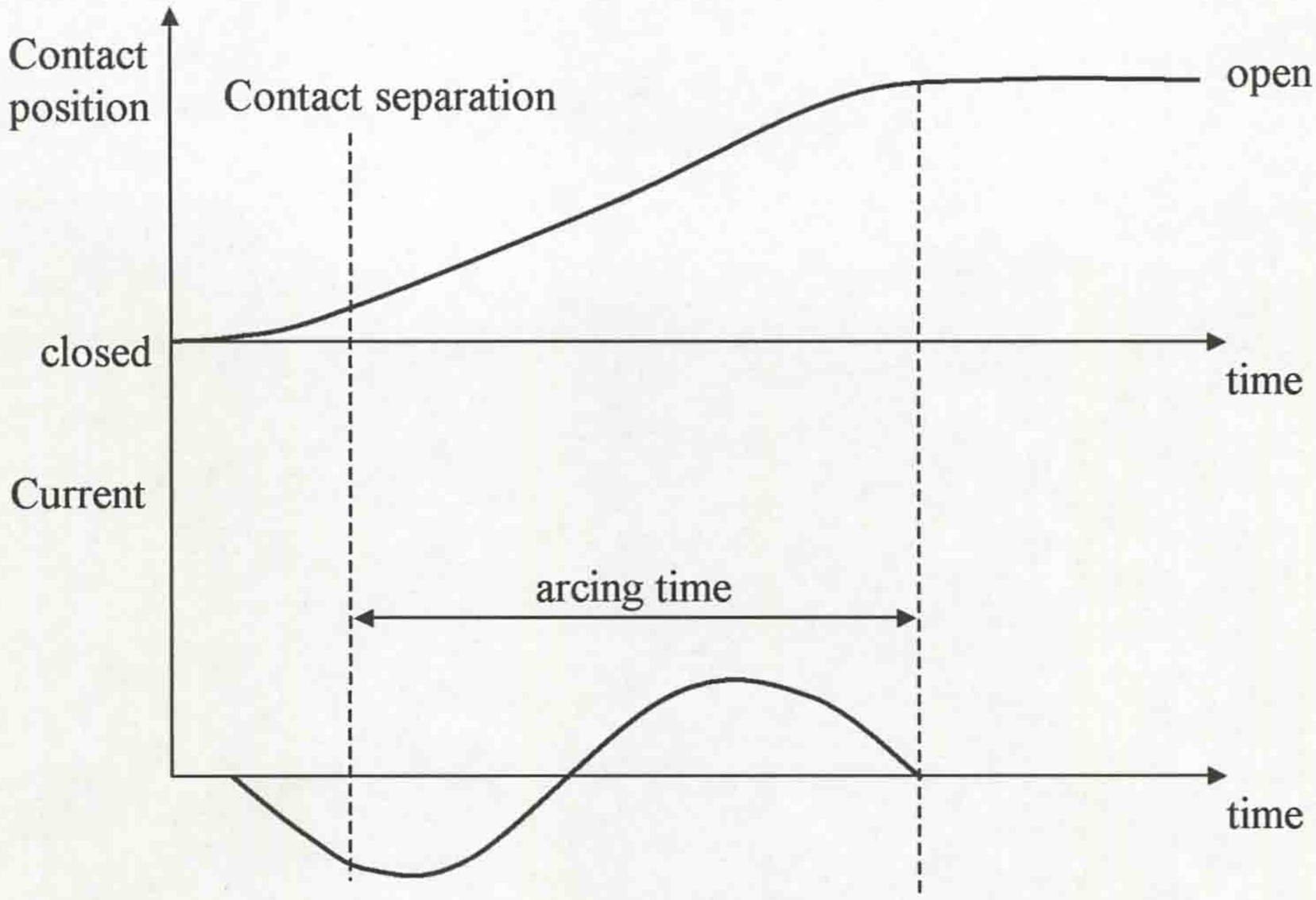

Figure 2.7 Interruption of an ac-arc at current zero in a circuit breaker

Two conditions need to be met for the successful ac-arc interruption (Cobine, 1958):

- At current zero, the ac-arc plasma needs to be cooled to become non-conducting
- The contact gap needs to withstand the recovery voltage that will appear between the contacts

In order to achieve arc extinction successfully, the E.H.V. circuit breaker designs use a nozzle around the arc between the separating contacts in order to produce a strong gas blast to control and extinguish the arc (fig. 2.8). At current zero, the arc plasma channel needs to be cooled to a sufficiently low temperature, to reduce the electrical conduction to low levels. However, some electrical conductivity will normally persist because of stored thermal energy of the arc (Lythall, 1972). This enables a "post arc current" to flow driven by a rising recovery voltage. The race between the energy removed from the arc by cooling and the energy input into the arc path by the post arc current are determined by the recovery voltage that will build up between the contacts immediately after current zero. The duration of this process is very short, a few microseconds (Lythall, 1972).

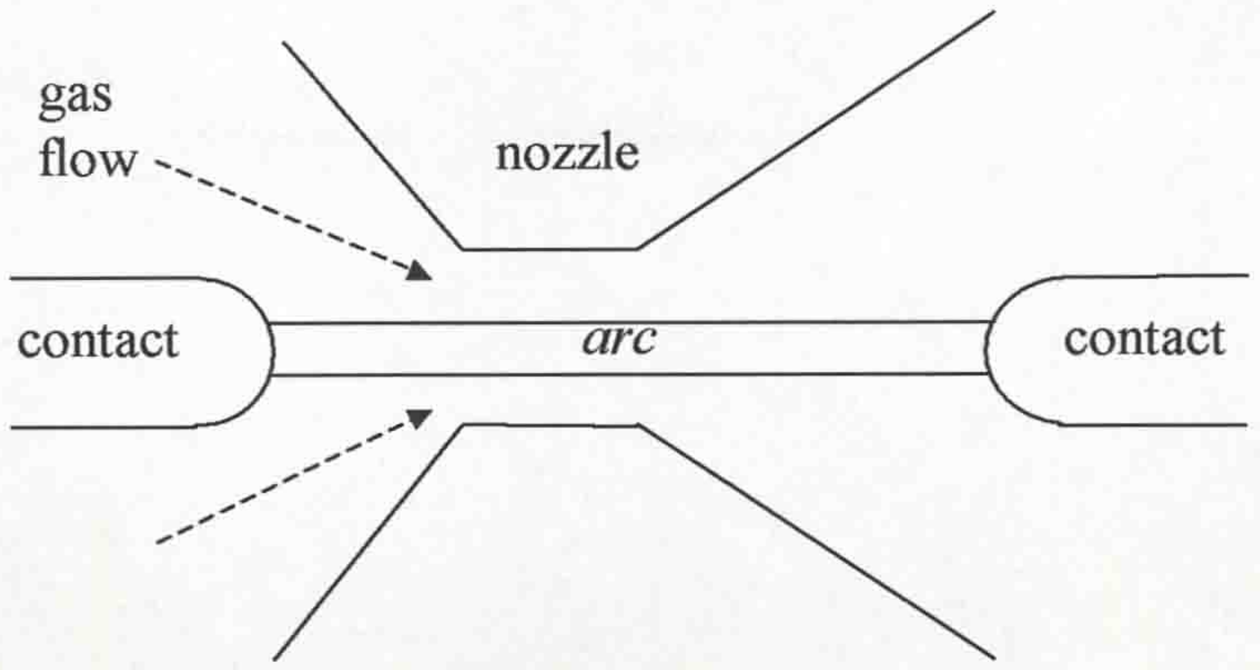

Figure 2.8 Circuit breaker arc in an axial gas flow nozzle

After this period, the contact gap withstands the voltage stress without electrical breakdown of the medium in which the arc was extinguished.

2.3.2 Circuit breaker early years

Early circuit breakers were quick-break knife switches (Dunsheath, 1962). However, the switch was not controlled and therefore the limitations of its compatibility necessitated further development to the new oil circuit breaker, which was most effective in comparison. The first oil circuit breaker relied upon the dissociation of oil molecules by the electric arc that generated hydrogen gas which consequently cooled and compressed the arc to extinction, (Flurscheim, 1982). However, this type of switch produced a large post-current leakage effect, which involved controlling the arc interruption. Consequently, there was a need to design a more controlled system of interruption using the oil circuit breaker as the basis. Two methods emerged. The first was the bulk oil current breaker (BOCB) in which its earth potential was the oil-containing tank. Pure oil was the medium between the live contact elements within the tank and between the contacts and the tank itself (Lythall, 1972). The second was the small volume circuit breaker (SVCB) in which the amount of oil and as a consequence the sizes of its contacts were much smaller than in the BOCB. The SVCB shape was a tube of insulating material situated between metal and caps. These caps were terminal points for the external circuit and therefore the tank was maintained at line potential. That structure was fixed on the insulator, which was isolated from earth. By the early 1970s most ac circuit breakers used oil (bulk or SVCB), air break and air blast interrupting techniques. Research

experiments on using air for the circuit breaker was already investigated before the 1920s. The dielectric properties of SF_6 (sulphur hexafluoride gas) were known at around 1940 (Cooper, 1940 and Nonken, 1941). However, only in about the 1950s was its use in circuit breakers began. Previous candidates as the interrupting the medium became obsolete and since the mid-1960s, vacuum (Lee *et al*, 1962) and SF_6 circuit breakers have been available worldwide.

2.3.2.1 Oil circuit breakers

The oil circuit breaker serves three purposes (Lythall, 1972):

- To insulate the life electrodes from earthed metal tank
- To provide an insulating barrier between the open electrodes after the arc is extinguished
- To produce hydrogen during the arcing period

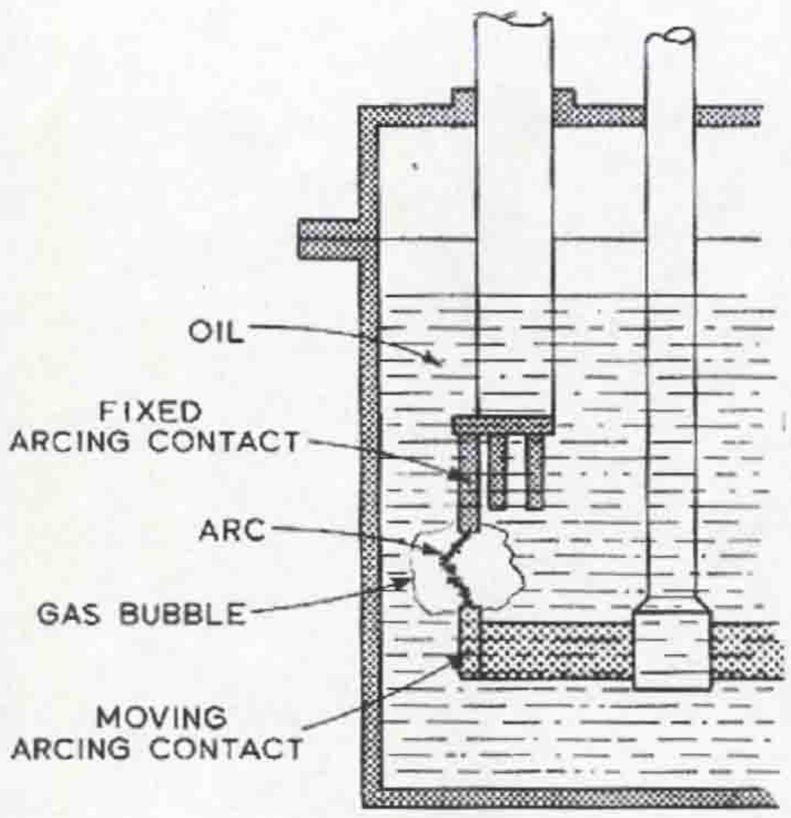

Figure 2.9 Plain-break bulk oil circuit breaker (Lythall, 1972)

Figure 2.9 shows how a bubble of gas surrounds the arc (Lythall, 1972). The thermal energy of the arc dissociated the oil in the electrode arcing area liberating a mixture of gases and vapours with hydrogen, which cooled and compressed the arc to extinction. However, the turbulence of the oil in the vicinity of the arc reduced the cooling action because there is the turbulent oil remained close to the arc. As a result, the arc tended to lengthen, producing relatively large post-arc leakage current (Lythall, 1972). Different devices, which enclosed the electrodes, arc, and gas bubble, achieved a number of improvements. One of these devices is shown in figure 2.10. The side-blast arc circuit breaker forced the arc by the blast of gas into the side

vents driven by the blast of hydrogen and oil vapour into the side vents of the breaker. This mechanism produced fresh-cool oil for the interrupter head that refilled the box-like enclosure. Many such forms using the same principles operation existed, eliminating the post arc leakage current.

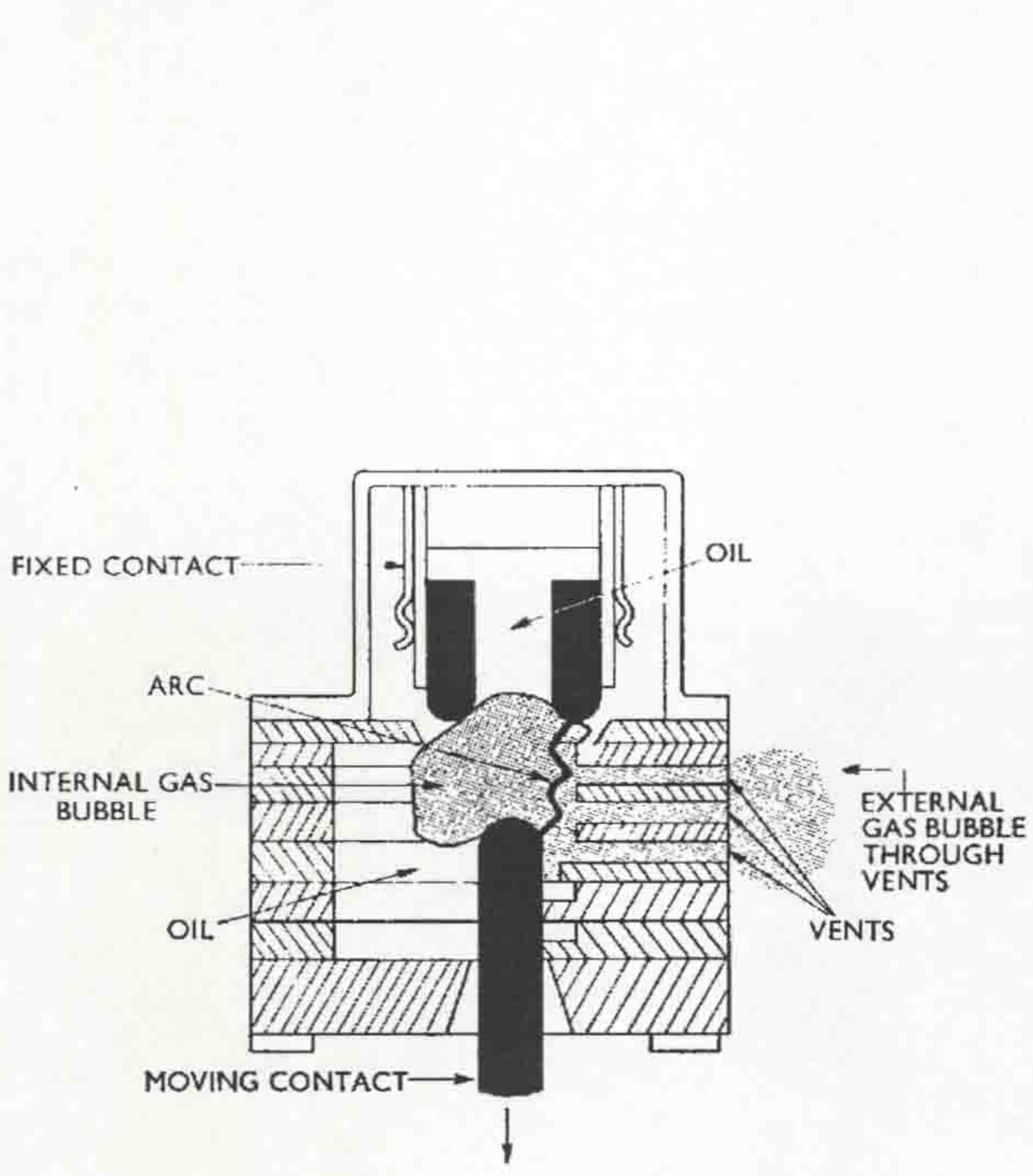

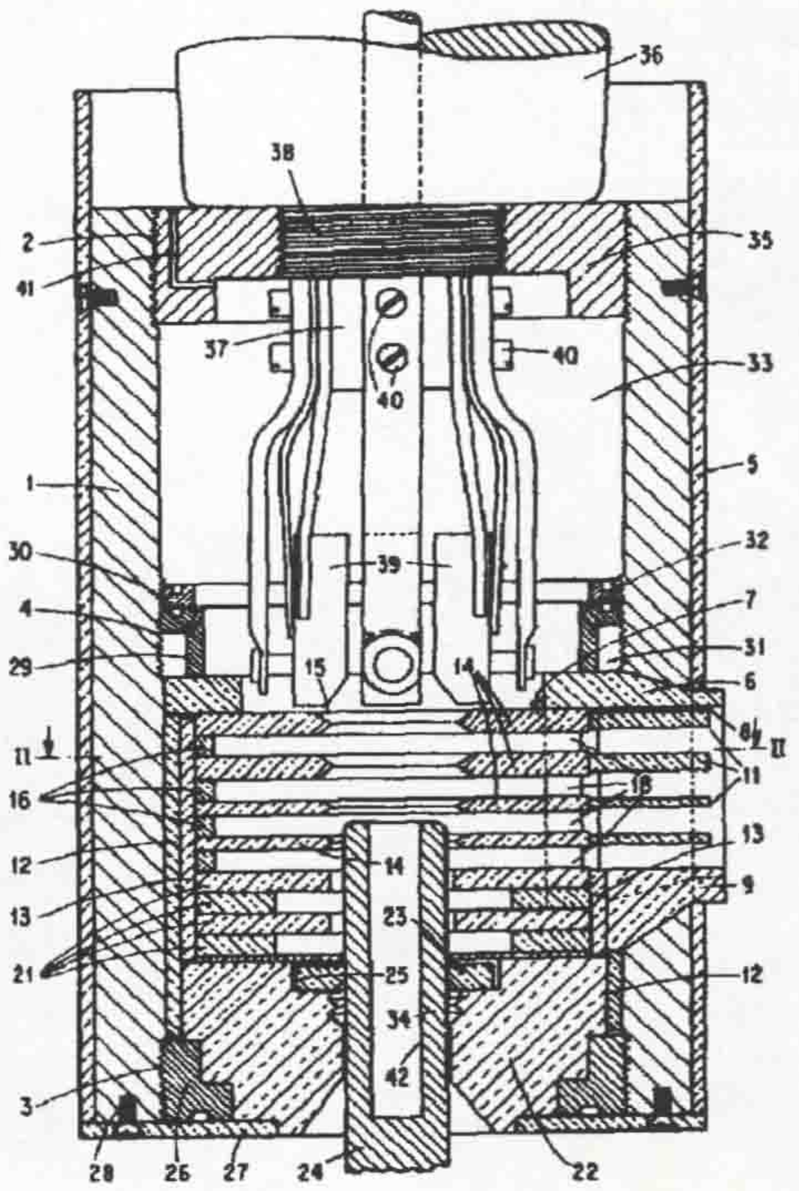

Figure 2.10 Side-blast oil circuit breaker (Flurscheim, 1982 and Lythall, 1972)

A number of devices were designed to maintain the voltage division in multi-breaker systems. Prince employed one of the successful multi-break circuit breaker designs in 1935. An 8-break 287kV 25MVA unit produced by the General Electric Company (USA) afforded a 3-cycle interruption under all condition of switching. These types of breakers still successful operate on a network up to 7000MVA fault capacity, (Flurscheim, 1982). Significant high cost of the powerful mechanisms required to drive the oil was one of the main drawbacks in using these breakers.

2.3.2.2 Air blast circuit breakers

Fundamental research into the air-blast type of breaker was carrying out by ERA (Whithey and Wedmore, 1927) in the 1920s (Lythall, 1972). In air-blast circuit breakers, the process of arc interruption is aided by an axial blast of air at high pressure (from a compressed air installation) admitted to the arcing chamber. In the

1940s, the development of high voltage air-blast circuit breakers followed two main directions. A metal axial blast nozzle was first one. Second direction was in the use of the insulated nozzle. The insulated nozzle in the air-blast breakers was operated at up to 110kV per break (Biermanns, 1938), when most manufactures used a metal nozzle operating at 35kV per break. Subsequent air-blast interrupters employed axial-blast principles, and as far as nozzle systems and internal pressurisation are concerned, provided an ability to obtain higher breaking capacities (Flurscheim, 1982).

2.3.2.3 Vacuum circuit breakers

A vacuum interrupter is based upon arcing in an evacuated enclosure forming a sealed for life ceramic bottle. It was first studied in the 1920s, (Sorenson and Mendenhall, 1926). In general, vacuum circuit breakers are safe and reliable, have low contact wear and as consequence requires low maintenance. However, metal vapour from the contacts may be formed so requiring the use of vapour condensation shield. In addition, magnetic drive of the arc is needed to lower contact erosion (Flurscheim, 1982). In the last few years, manufacturers have produced the vacuum bottle circuit breakers rated at 36 kV-50 kA, and 4000 A. However, the excellent insulating and interrupting characteristics of the vacuum interrupter also produce disadvantages in that there can be premature interruption of small inductive currents so generating excessive over voltages. Their magnitude depends on the surge impedance of the switched circuit (Flurscheim, 1982). The costs of implementing these effects is high so limiting the circuit breaker use up to a maximum voltage of 36 kV. As a result, the use of SF_6 (sulphur hexafluoride gas) circuit breakers has been preferred at higher voltage levels by switchgear manufacturers worldwide, (Flurscheim, 1982).

2.3.2.4 SF_6 circuit breakers

SF_6 gas has been successfully employed in the voltage engineering of circuit breakers up to 750 kV for the last 25 years. There is currently no single superior gas available to replace SF_6. The latest current interrupting designs have combined the excellent dielectric property of the gas with new techniques for arc interruption. For

instance, the single pressure puffer, the rotating-arc and the auto-expansion techniques are successfully employed worldwide (Ali, 2001). The method of a single pressure puffer-type interrupter is based on the principle of a bicycle pump. The SF_6 gas in the chamber is compressed by a movable cylinder against a stationary piston. The high-pressure gas is thereafter directed along the arc in the down-stream area of the nozzle to enhance the arc-extinguishing process. The compression and heating of SF_6 gas by the arc produce retarding forces, which act against the piston movement. A high-energy mechanism is required to overcome these forces and to support consistent opening characteristics for the circuit breaker. Puffer circuit breakers are now established worldwide for ratings up to 36 kV-50 kA and 4000 A (Ali, 2001). These circuit breakers have been improved and some designs work at slightly above atmospheric SF_6 gas pressures. These techniques helped to reduce a number of problems with gas-leak through seals and to reduce the energy requirement for the operating mechanism, and so minimizing their cost (Ali, 2001). The alternating-voltage withstand performance of SF_6 gas at 0.9 bar is comparable with that of insulating oil (Ali, 2001). For instance, 12 kV puffer circuit breaker designs are capable of interrupting circuits utilizing a pressure of only 0.6 bar (Ali, 2001). On the other hand, there are also issues relating to environmental aspects arising from the severe "greenhouse gas" properties of SF_6 (Christophorou *et al*, 1997). Pure SF_6 gas is chemically inert, non-explosive, odourless and non-toxic but it will not support life. It has a high thermal conductivity at high temperatures that enhances its cooling properties (Christophorou *et al*, 1997). In addition, it is a strong electronegative gas both at room temperatures and at temperatures well below ambient (Browne, 1984). This means that it forms negative ions by electron attachment to the neutral SF_6 molecule so making it effective for high-dielectric strength and good arc interruption. At temperature above 1000K, SF_6 gas dissociates. Re-association of the dissociation fragments form arc core temperatures of about 20000 K can produce a number of constituent gases including S_2F_{10}, which is highly toxic (Ali, 2001). However, these gases recombine rapidly as temperatures reduce and the dielectric strength of the gap can recover to its original level in microseconds. Re-evaluation of sulphur hexafluoride circuit breakers is constantly being reviewed by high voltage engineering companies worldwide in order to achieve a safer environment, (Ali, 2001). The environmental concern is a significant motivation toward improvement of SF_6 management or the use of alternatives. Pure

SF_6 has a grater ability to absorb infrared radiation then most other gases and it has a very long atmospheric lifetime. These properties make SF_6 a potent global warming gas that can affect directly the Global Warming Potential (GWP) of the planet, (Christophorou *et al*, 1997).

2.3.2.5 PTFE application in circuit breakers

PTFE (polymer consisting of recurring tetrafluorethylene monomer units) is used as an electrical insulating material (Sillars, 1973) e.g. for nozzles in high-voltage circuit breakers, transformer etc. PTFE is biologically inert. Therefore, it is used in many applications in biology, microbiology, medicine, and pharmacy and in the food industry. In addition, PTFE has very good electrical (high resistance) and dielectric properties at low electromagnetic frequencies. Pure PTFE is a white polymer in colour and is most commonly used because of its reasonable cost and ease of manufacture. When exposed to an electrical arc the rate of ablation of pure PTFE is relatively high but depends on the PTFE grain size, moulding or compacting pressure, special manufacturing procedures and the quality of machining and surface finish (Ali, 2001). It has also been observed that radiated energy from an electrical arc penetrates deep into the body of PTFE, producing carbon molecules. To overcome this, some manufacturers use coloured PTFE, which absorbs the radiated arc energy on the surface and prevents deep penetration (Ali, 2001). To ensure consistent performance with a reduced rate of ablation and long life, most manufacturers use filled PTFE for high short-circuit currents interruption (in the region of 63 kA and above). Filled PTFE is slightly more expensive than pure PTFE, but its consistent performance and extra-long life justify its use in high current interrupters. Its broad application at different temperature ranges and its ductility are other advantages of PTFE, (Ali, 2001).

2.3.3 Evaluation of circuit breakers

Most modern high-voltage circuit breakers use SF_6 gas because of its excellent arc-quenching properties supporting a good condition for the arc interruption despite some post-arc problems associated with its toxicity. The well-established techniques for arc interruption combination in SF_6 gas still make such circuit breakers powerful.

However, high-voltage switchgear companies constantly evaluate these devices in order to achieve the most effective technique for arc interruption, safe for the environment and consequently for cost reduction. There therefore follows descriptions of a number of modern puffer-type techniques for arc interruption that are successfully applied in the high-voltage circuit breakers. Moreover, new directions toward the use of rotating arc circuit breakers demonstrate a useful potential of such arc rotation for high-voltage switchgear.

2.3.3.1 Development of the puffer type circuit breakers

Early development of the puffer circuit breaker occurred in Europe and US. In 1930s, Delle, of France, had a load breaker of this type that used air as the arc-quenching medium (Noeske *et al*, 1983). The experiments in air showed that an air puffer circuit breaker is not effective for high-power interruption. One of the reasons is the relatively slow recovery speed of air. Second, the high sonic velocity of air makes the mass outflow through the nozzle so high that it is difficult to produce and maintain sufficiently high pressure in the puffer with reasonable piston speed. Therefore, the puffer breaker concept led a rather secluded life until it was revived when SF_6 gas was introduced as an arc-quenching medium, providing excellent dielectric property and current interruption speed. In 1960, SF_6 puffer breakers at 34.5 to 69kV were introduced (Browne, 1984). Thereafter two-pressure SF_6 breakers were developed. In the double pressure type breakers, high-pressure gas is stored in a high-pressure reservoir and is released when the interrupter contacts are separated. The danger that SF_6 arcing products may produce fluoric acid when water is available in either liquid or vapour form requires the gas to be dry (Christophorou *et al*, 1997). Moreover, the tendency of SF_6 to liquefy requires heating at the high pressure of a two-pressure breaker. In the puffer-type of circuit breaker the interruption pressure is produced by gas compression in the puffer cylinder during breaker opening. The compressed gas is directed to the arc through an insulated nozzle. As a result, the pressure in the chamber is increased and its duration is a critical variable for current interruption capability, (Christophorou *et al*, 1997). In contrast, in the two-pressure circuit breakers, heaters are required to avoid liquefaction of the SF_6 stored at high pressure. Different types of puffer interrupters are shown in figure 2.11 (Ryan and Jones, 1989). Figure 2.11a, shows a mono-flow

system that is the simplest type of breaker, utilising a unidirectional flow from the piston chamber. Types that are more effective have superseded this to reduce contact vapour in the arcing region. In the partial duo-blast interrupter (fig. 2.11 b), the main gas flow is through a large-diameter insulated (PTFE) nozzle occurring through both of the hollow electrodes. This subsidiary flows limit the entrainment of contact material into the main nozzle. The full duo-blast puffer utilises two conducting nozzles that operate as a main contacts also. Therefore, for this type of puffer the nozzles are conductors, (fig. 2.11c).

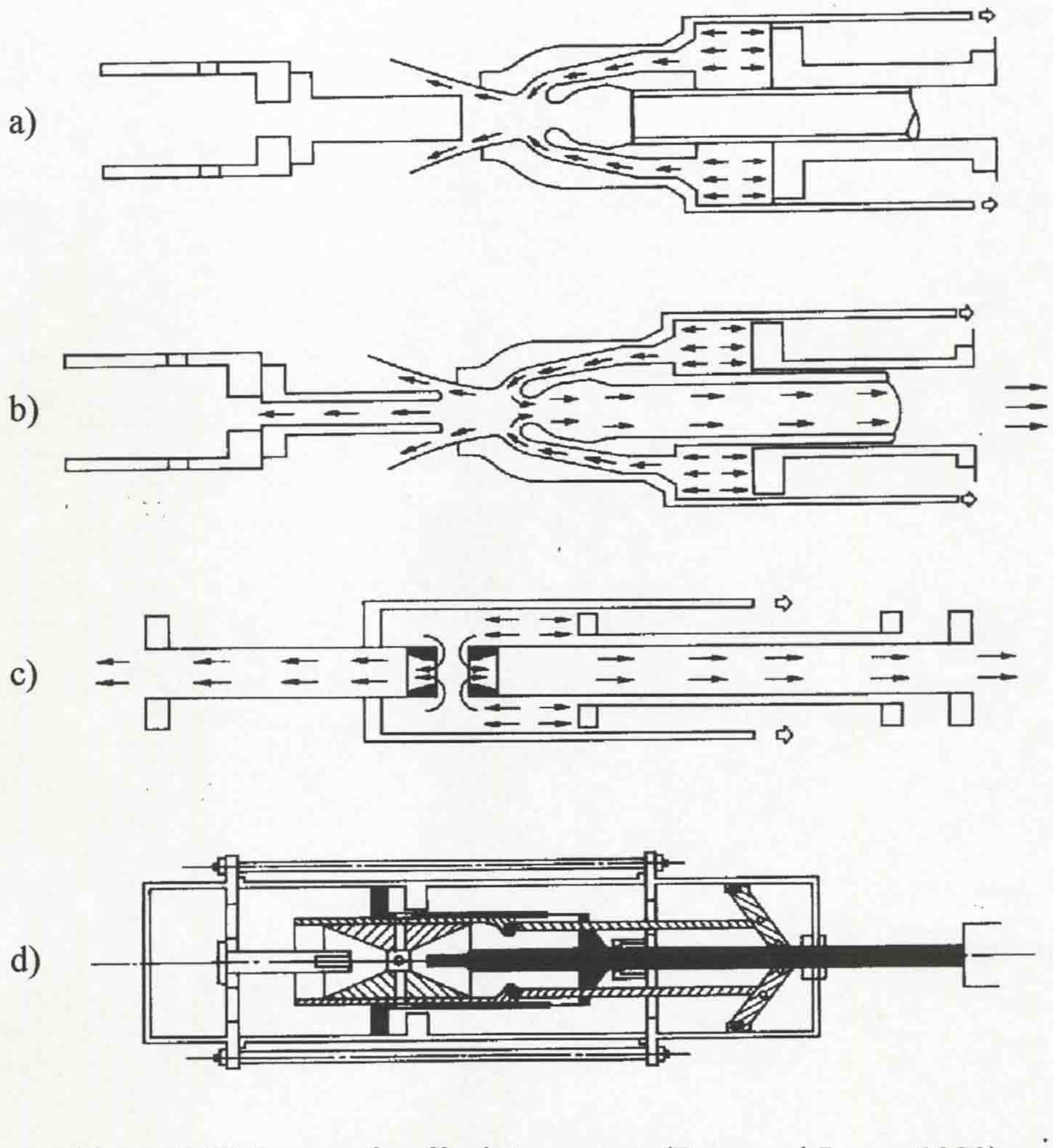

Figure 2.11 Types of puffer interrupters (Ryan and Jones, 1989)
a) Mono-flow b) Partial duo-blast
c) Full duo-blast (with conducting nuzzles) d) Full duo-blast (with insulating nuzzles)

The metal-vapour entrainment is limited by the bi-directional flow and may be regarded as two mono-flow breaks with two upstream contacts that reduce the metal vapour entrainment. The fourth type of interrupter is a full duo-blast interrupter with

insulating nozzles (fig. 2.11d), so that full advantage can be taken of optimised down-stream flow produced by detailed profiling of the nozzle and without interference by arc-root movement (Ryan and Jones, 1989).

The application of puffer type circuit breakers for medium and high-voltage interrupters are more attractive compared to lower-voltage system application. However, main drawback of these systems is the requirement for a powerful mechanism to overcome arc-induced pressurisation including nozzle blocking. Self-pressurising circuit breakers for medium-voltage application are more attractive, reducing demands of power mechanical drive.

2.3.3.2 Auto-expansion circuit breaker

The Auto-expansion circuit breaker, (fig. 2.12) is another interruption technique used on distribution circuit breakers. In fact, this is the third-generation of development of puffer-type interrupters for 170 kV-40kA circuit breakers, (Ali, 2001).

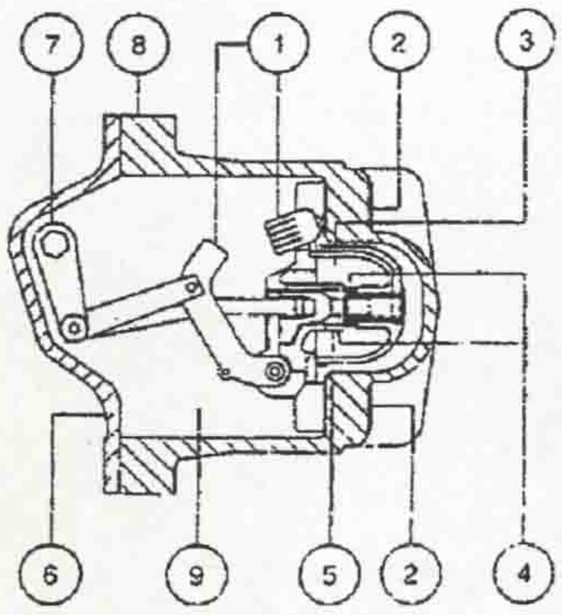

1 Main contacts
2 Terminals
3 Arcing chamber
4 Arcing contacts
5 Insulating nozzle
6 Cover
7 Control shaft
8 Case in epoxy resin
9 Expansion chamber

Figure 2.12 Auto-expansion circuit breaker (Ali, 2001)

The concept is to increase pressure in the expansion chamber via the power dissipated by the arc. By the pressure effect, which is generated in the chamber, causes strong turbulence in the gas forcing the gas out of the chamber across the arc as soon as the nozzle start to open. By this technique, it is possible to extinguish the arc, successfully.

The auto-expansion circuit breaker uses a low energy operating mechanism, operated up to 50 kA rating at 12 kV.

2.3.3.3 Rotating arc circuit breakers

The rotary arc circuit breaker is finding very useful for low and medium voltage circuit breakers since no piston drive mechanism is required, providing more simple contact separation mechanism and more effective use the electromagnetic and thermal arc's energy to assist in the interruption process (Ryan and Jones, 1989).

Rotating arc circuit breakers have some potential advantages over other forms of circuit breaker. For instance, the arc rotation enables quenching convection to be generated by driving the arc through the surrounding flow rather than vice versa. Another significant advantage in that, there is arc-induced pressure elevation in the volume within which the arc is rotated. This condition enhances the quenching of the electrical arc at current zero. Moreover, the rotation of the arc can reduce contact erosion due to the arc roots being continually moved also. This advantage leads to a longer contact life. Arc rotation is produced via Lorenz forces produced by the fault current flowing through a magnetic field (B-field) producing coil. In the rotary arc circuit breakers, the B-field is produced by a coil through which the arc current flows during the period between contact separation and arc extinction. Most arc-rotation circuit breakers use SF_6 gas because of its excellent dielectric properties. This technique has been used for SF_6 circuit breakers, which have a rating up to 40kA at 12 kV and requires an only low energy mechanism.

2.3.3.4 Fundamental methods of arc rotation for circuit breakers

An arc rotation technique for circuit interruption is based on two fundamental methods (Jones, 2001), (fig. 2.13). The arc can be rotated:

- Azimuthally
- Helically

Azimuthal arc rotation is usually controlled by the outer radial magnetic field of a coil (fig. 2.13a) while the helical arc is controlled by the inner axial magnetic field of a coil (fig. 2.13b). Techniques providing high-current arc control for extinguishing the arc at current zero involve rotating the arc electromagnetically (rotary arc circuit breakers). In both cases, the fault current through the coil and electrical arc **j** produce a strong axial magnetic field **B** into the coil that forces the arc to be driven by the Lorenz force **F**.

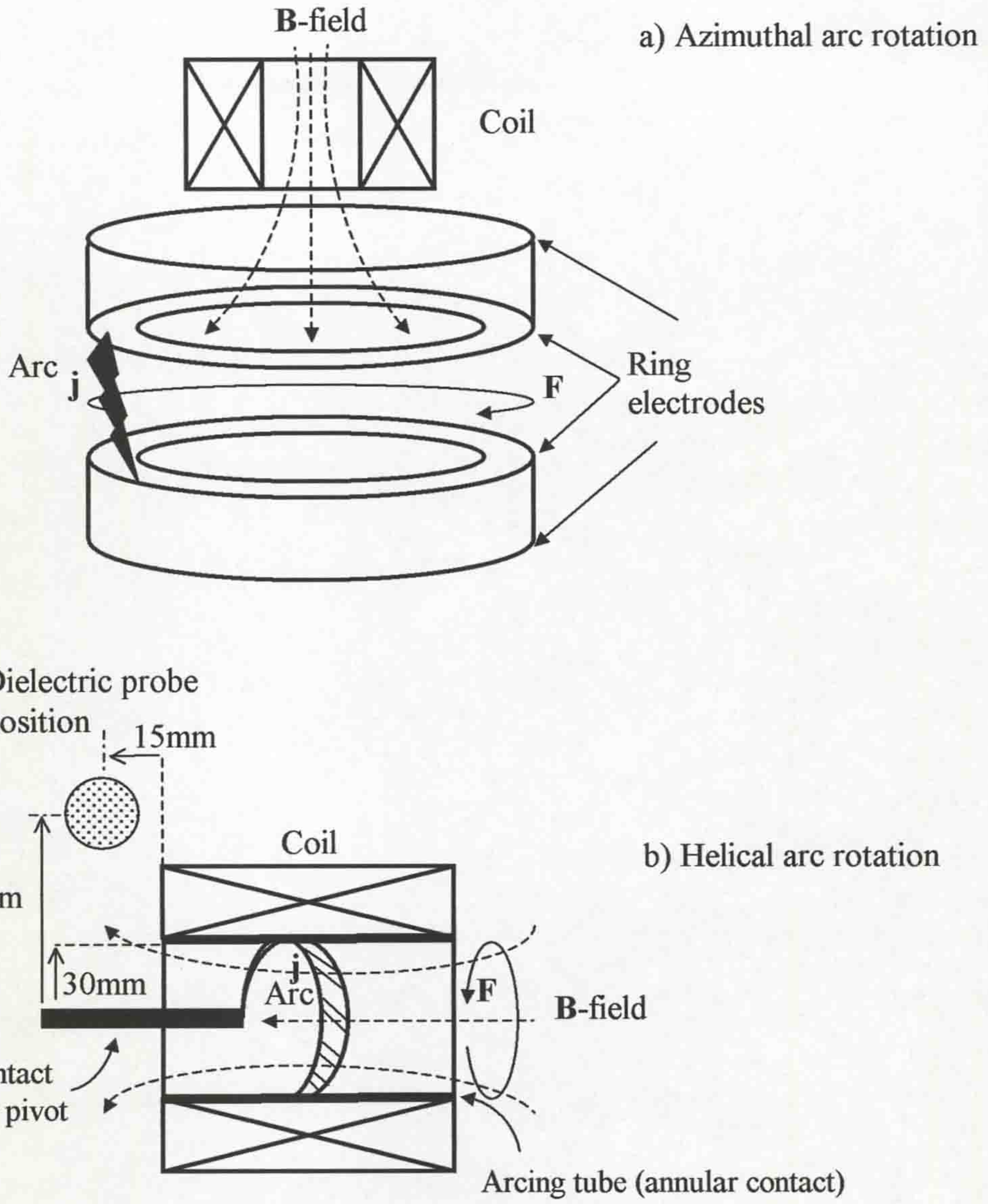

Figure 2.13 Base concepts of the arc rotation control (Jones, 2001), a) Azimuthal arc rotation, b) Helical arc rotation. (Identification of the dielectric probe position on figure 2.13b related to section 2.4.1.1 (Dielectric strength recovery measurements))

A general explanation of the arc motion in a B-field is shown in figure 2.14. The arc current **j** flowing through the coil produces the magnetic flux **B**. Its direction is continuous. On the other hand, the arc itself produces the magnetic field concentrated around itself. As a result, the B-fields of the arc and coil will be enhanced where the B-field direction of the coil is the same as the arc. It will be weakened where these are in opposition. The arc motion should be directed to the side where the magnetic fluxes of the arc and the coil are weakest (fig. 2.14). Both these magnetic fields provide a mechanism for greater interaction between the arc current and the magnetic field of the coil. The strength of their interaction is determined by the Lorenz force

jx**B**. By this force, the arc can be moved in one direction or it can be rotated around the contact bar, (fig. 2.14).

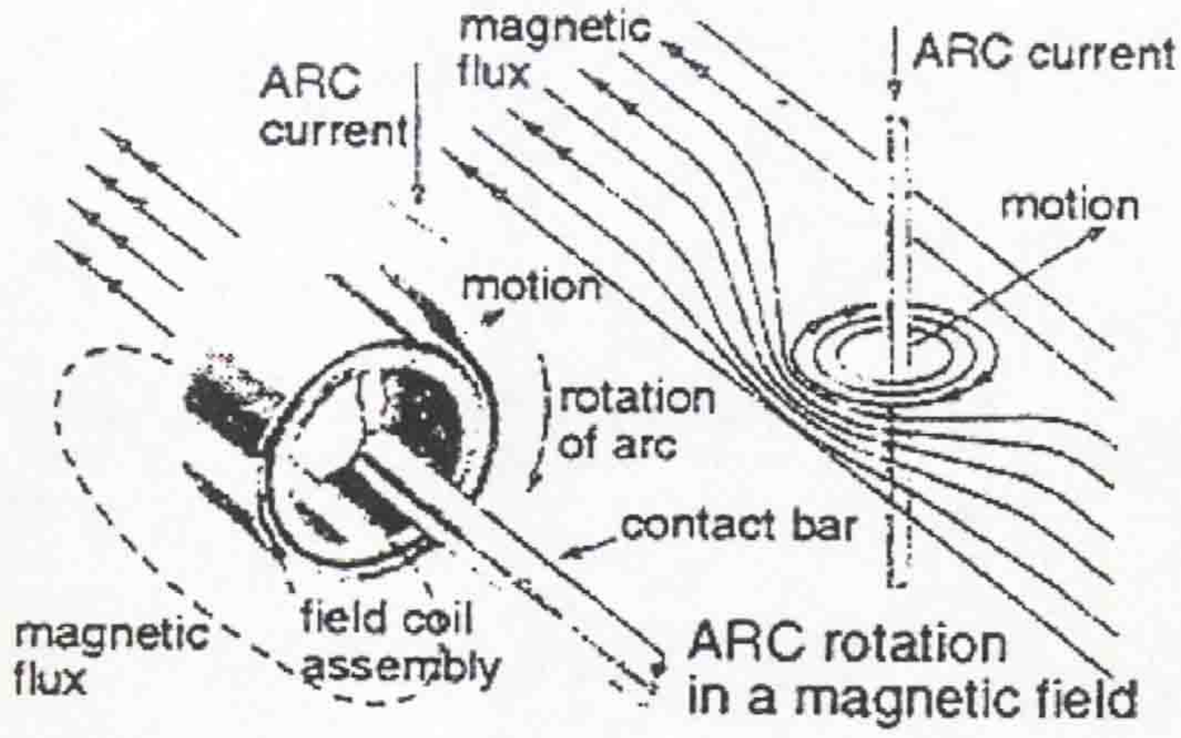

Figure 2.14 Arc motion in a magnetic field (Ali, 2001)

Thus, unlike the puffer-type interrupters, which utilise superimposed axisymmetric flows the rotary arc interrupters are non-axisymmetric and the arc, rather than the surrounding gas suffers most movement to generate an effective cross-flow (Ryan and Jones, 1989).

Two different types of geometries are commercially available. The first (fig. 2.15) uses two angular contacts (B,C) where the arc along two electrodes is rotating by magnetic field producing by coil (A). The second geometry involves rotating the arc between a rod and an annular electrode that also serves as a yoke to support the magnetic field producing coil (fig. 2.16).

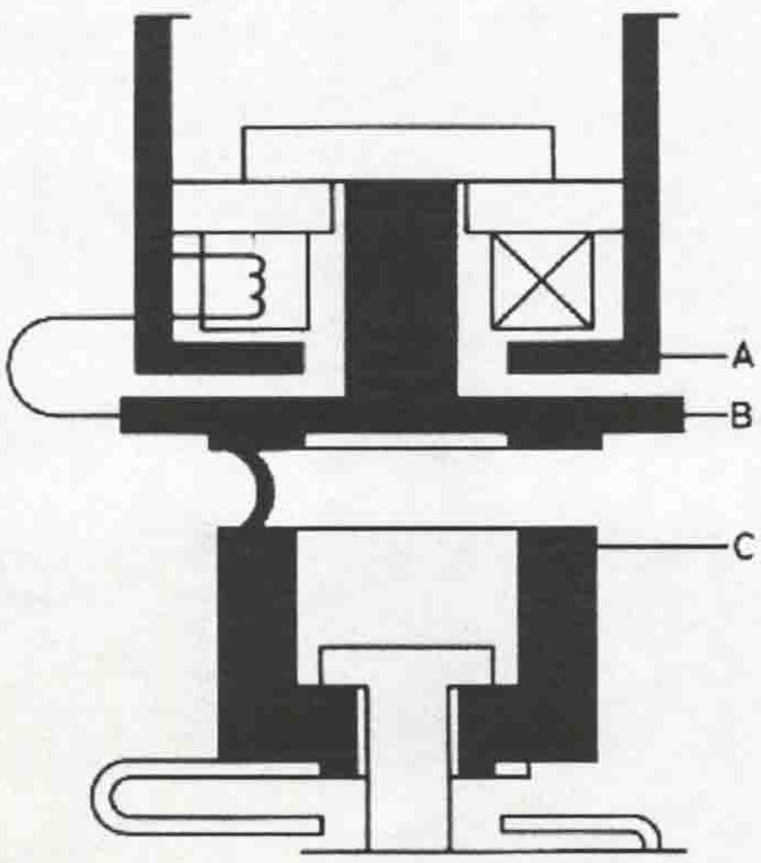

Figure 2.15 Rotary arc circuit breaker, Ring contacts
(Duplay and Hennebert, (1983). Merlin-Gerin)

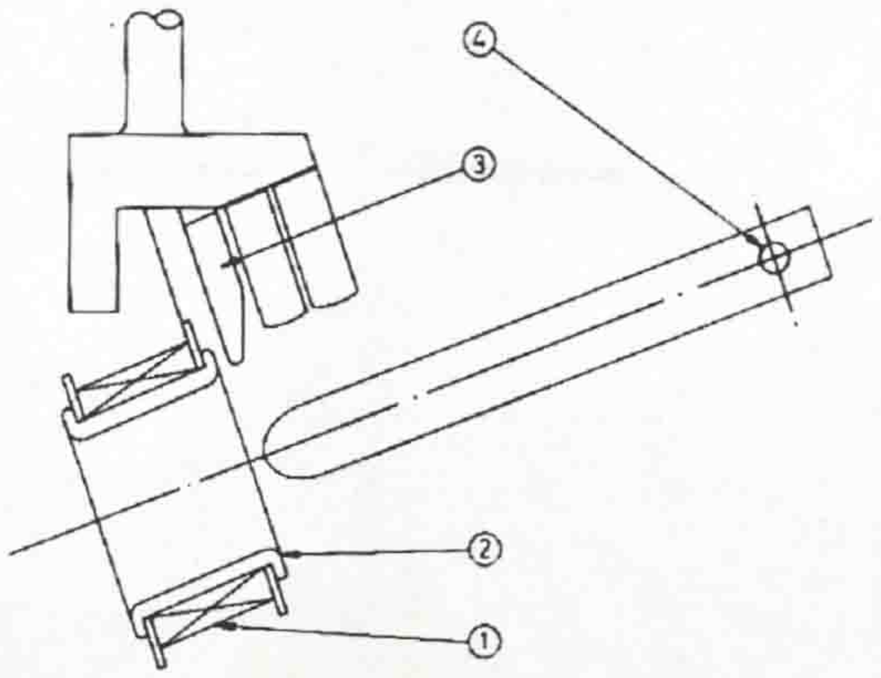

1 Magnetic field coil 3 Fixed arcing contact
2 Arcing tube 4 Contact bar pivot

Figure 2.16 Helical arc (12kV rotary-arc circuit breaker (Parry, 1984))

The advantage of this type of arc rotation is in forming the arc in the area of maximal magnetic flux density and encouraging helical penetration of the arc into the coil. First design (fig. 2.15) does not necessarily involve arc transfer during electrode separation because the arc is situated far from the coil. Both types of rotary arc circuit breakers unfortunately have low-fault current limitations, since the electromagnetic driving force decreases with fault current. On the other hand, increasing the number of coil turns to produce a stronger magnetic field can overcome this problem. However, at the higher values of fault current, there is a limitation of mechanical strength of the coil resulting from the high magnetic forces occurring. These difficulties have been successfully overcome by optimization of the devices, an example of which is shown in figure 2.17.

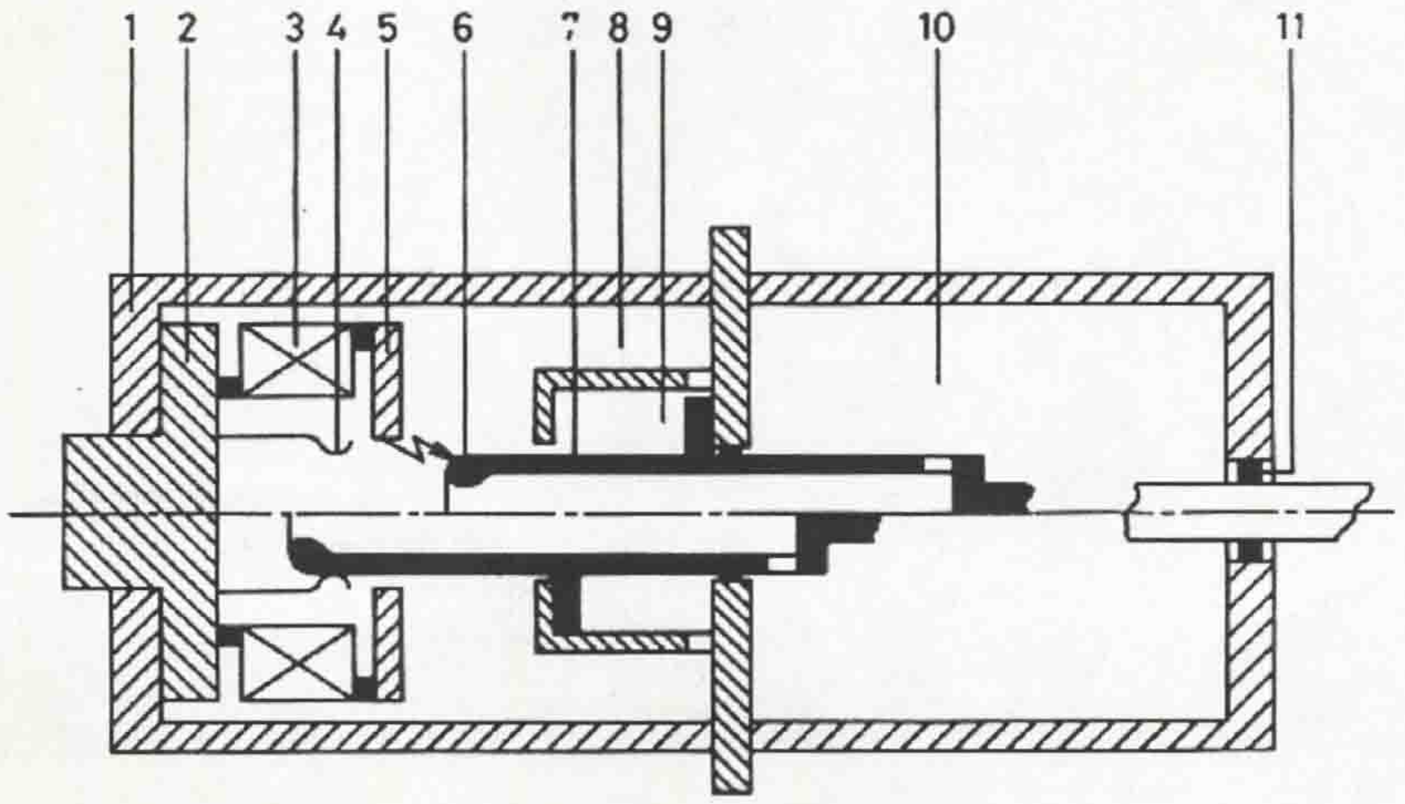

Figure 2.17 Hybrid circuit breakers (Brown Bovery type, Jakob *et al* 1985)
Down of centre-line: breaker contact is closed; up, open.

1 Tubular extinction chamber, 2 Fixed contact, 3 Cylindrical coil, 4 Contact fingers,

5 Annular electrode, 6 Nozzle, 7 Moving contact, 8 Pressurised space,

9 Auxiliary blast facility, 10 Exhaust space, 11 Seal against atmosphere.

Hybrid interrupters use more efficient arc-induced heating and pressurization for low fault current interruption. They operate by auxiliary piston action improving the process of current interruption. The advantages of rotary arc self-pressurising circuit breakers for low to medium-voltage levels are increasingly attractive compared to the puffer-type circuit breakers since no piston drive mechanism is required so simplifying the contact separation mechanism.

2.3.3.5 Rotating-arc and auto-expansion combined circuit breaker

The design that has demonstrated a useful application of the rotating arc is the SF_6 rotating-arc and auto-expansion combined methods, (fig. 2.18) which has produced circuit breaker design for rating up to 72.5 kV, (Ali, 2001). The arc current flowing through the coil (4) produces the magnetic field for the arc rotation between the fixed (2) and moving (3) arcing contacts within the expansion cylinder (1). This method enhances the pressurization process within the chamber providing pressure reduction in the circuit breakers before arcing, reduces contact erosion etc.

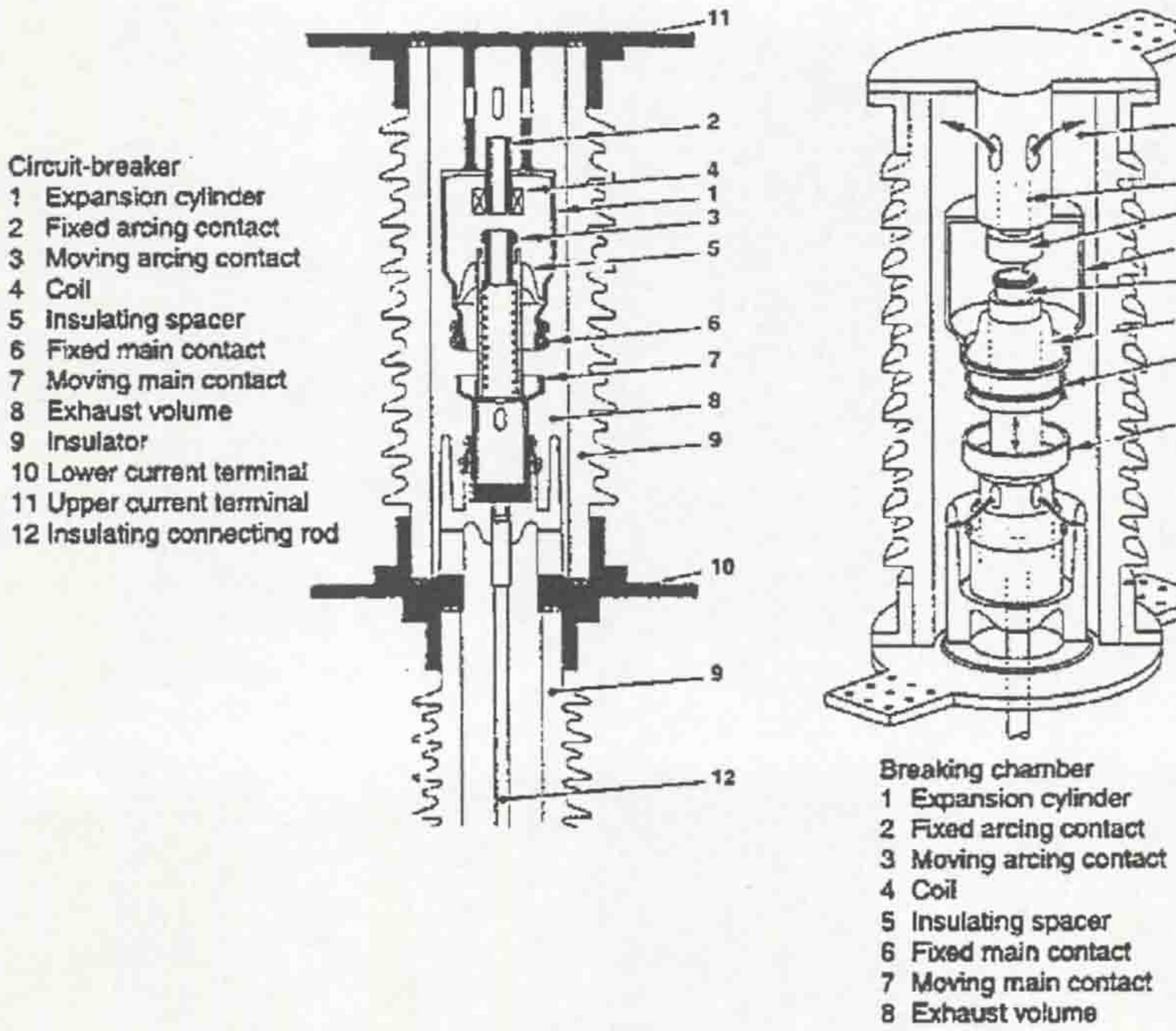

a) SB6-72 circuit breaker pole unit b) Schematic view of breaking chamber

Figure 2.18 SF_6 rotating arc and auto-expansion combined circuit breaker (Ali, 2001)

2.3.3.6 Development of rotating arc circuit breakers

The evaluation of rotating the arc in circuit breakers has been widely pursued worldwide in order partly to avoid the expensive mechanisms required with puffer circuit breakers, contact erosion, etc. As with puffer interrupters, rotary arc circuit breakers are more efficient at high currents. At low currents, current chopping phenomena (whereby the arc is prematurely extinguished) are observed with both puffer and vacuum interrupters, (Ennis *et al*, 1994). In addition, at low current the arc is not rapidly rotated as at high current and therefore the arc cooling is gentler regarding to the arc interruption as "soft". In fact, it will be less able to interrupt high frequency arcs in the circuit interruption (typically a few 100kHz), such as reactor or capacitor switching. Therefore, more research should be done for solving the problems mentioned above to advance the rotating arc interrupters.

2.3.4 Arc-circuit interactions

2.3.4.1 The arc as a current interrupting element

The electrical arc has the capability to act as a rapidly changing resistor during when conducting an ac current. At the current zero of the ac wave, the arc conductance rapidly decreases and therefore prevents the arc from re-ignition. Consequently, an electric ac-arc is simpler to interrupt compared to a dc-arc. In the ac-arc, the current is reduced to zero once each half cycle so that deionising processes may operate on the hot plasma of the arc column. In the case of the dc-arc, there are no natural currents zeroes where an arc may extinguish. Therefore, there is a need to force the dc-arc to become unstable (Nakao *et al*, 2001). One method is encourage the dc-arc resistance to increase so much that the corresponding arc voltage will approach the supply voltage of the network and consequently force the current towards zero. However, such methods are usually used for relatively low voltages. Another method is to simulate the artificial current zero by means of a current oscillation forced on the quasi-dc current. This method is more realistic for high-voltage dc current interruption. However, the extinction of an ac-arc is easier than that of a dc-arc of the same power. The variation of the ac current leads to dynamic changes in the arc properties. Therefore, the arc temperature will still be

high when the current reaches zero. At current zero, the electrical power input (V_i) to the arc is zero so that need is only to remove the stored thermal energy. However, there is a possibility that the alternating current may fail to be interrupted after current zero for either of two reasons (Cobine, 1958):

- Thermal re-ignition

  If the remnant arc column is still ionised after current zero and the cathode emits a sufficient amount of electrons right immediately after current zero.

- Dielectric re-ignition

  If the remnant arc column at current zero is so cold that it is only weakly ionised, it contains only space charges. The voltage that appears between the electrodes may then stimulate a flashover and a new arc will be established.

2.3.4.2 Voltage characteristic during interruption

The voltage required to re-ignite the arc is consequently higher then the arc burning voltage, and the process of re-ignition may be considered a race between the de-ionization process in the gap and the increasing recovery voltage determined by the external circuit. At this point, it is necessary to distinguish clearly between short and long arcs, (Cobine, 1958). For short arcs, the phenomena at the electrodes of the normal arc consume a considerable part of the total voltage, and during re-ignition the regions near the electrodes become very important. For long arcs, the voltage drops at the electrodes are relatively small compared with the voltage required to sustain the column, in which regions the de-ionization phenomena are complicated.

2.3.4.3 Rate of rise of recovery voltage (RRRV)

Once the arc current has ceased to flow, the voltage across the arc gap may increase rapidly in response to the current interruption. The rate of rise of recovery voltage (RRRV) is therefore important in determining whether the arc re-ignites. The situation is depicted in figure 2.19. The higher the frequency of the transient voltage, across the arc contacts the higher the average gradient of the voltage rise from zero to its first peak with respect to time. The RRRV across the arc gap is therefore given by the straight line shown in figure 2.19.

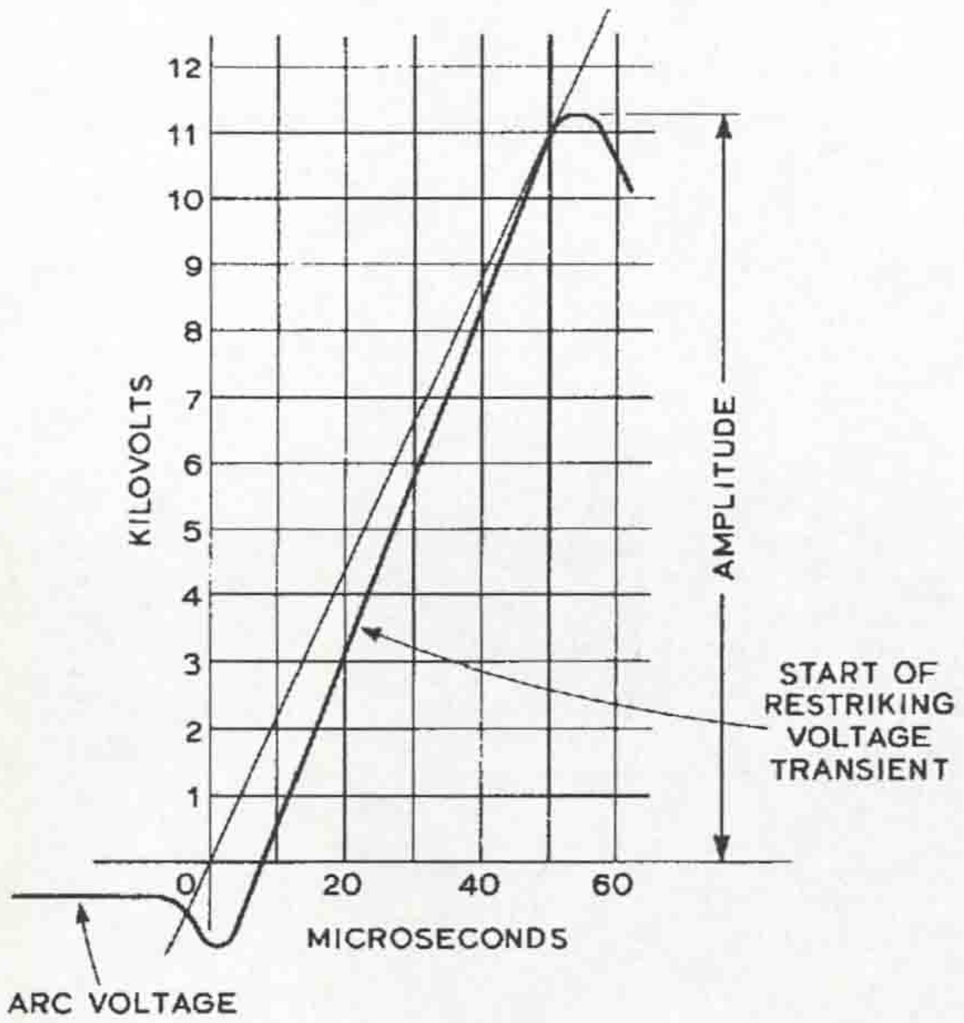

Figure 2.19 Determination of rate of rise of recovery voltage (RRRV), (Lythall, 1972)

In practice the RRRV across an arc gap is directly related to the current decay rate before current zero. Therefore, this relationship measures severity of conditions imposed on an arc gap at different current interruption levels.

2.3.4.4 Recovery strength of the contact gap

The recovery strength is characterized by the properties of the contact gap after arc extinction. By varying the recovery voltage, the recovery strength of the gap may be changed and is considered as a function of the time after which the arc is extinguished (fig. 2.20).

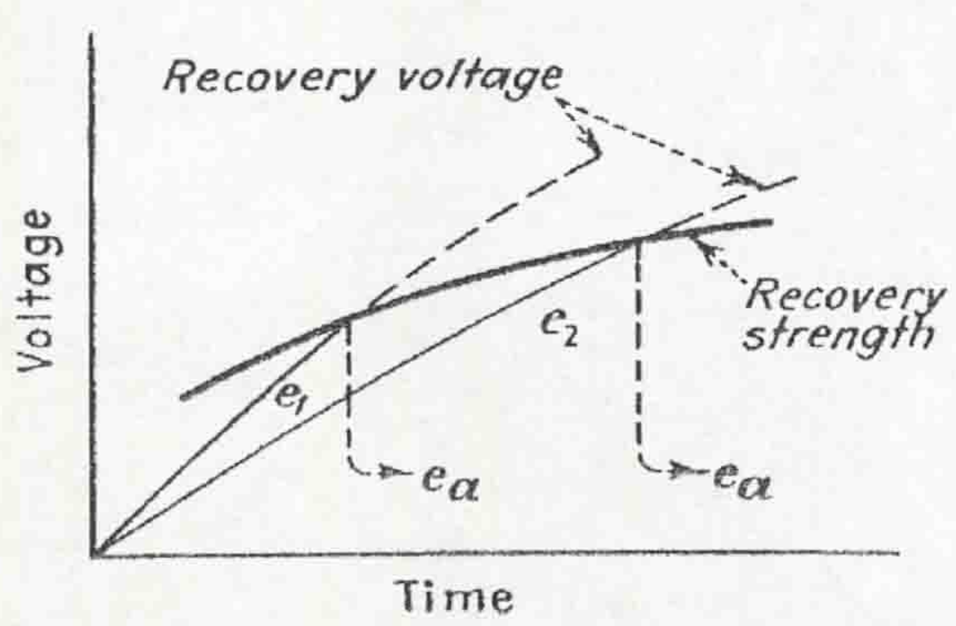

Figure 2.20 Determination of recovery strength curve for arc gap (Cobine, 1958).

The typical recovery voltage curves (e_1 and e_2) that are shown in figure 2.20 demonstrate some relationship with the recovery strength curve for the arc gap (e_a is the arc burning voltage). Each point of such a recovery strength curve depends on the nature of the recovery voltage. This means that a greater voltage would be expected at a given time if the recovery voltage had the form of a pulse occurring at that instant, than if the recovery voltage increases uniformly with time and was adding ionizing energy to the gap during the entire elapsed time after arc extinction, (Cobine, 1958). The complex problems of what happens in the period of just before to just after current zero is shown in figure 2.21, (Lythall, 1972).

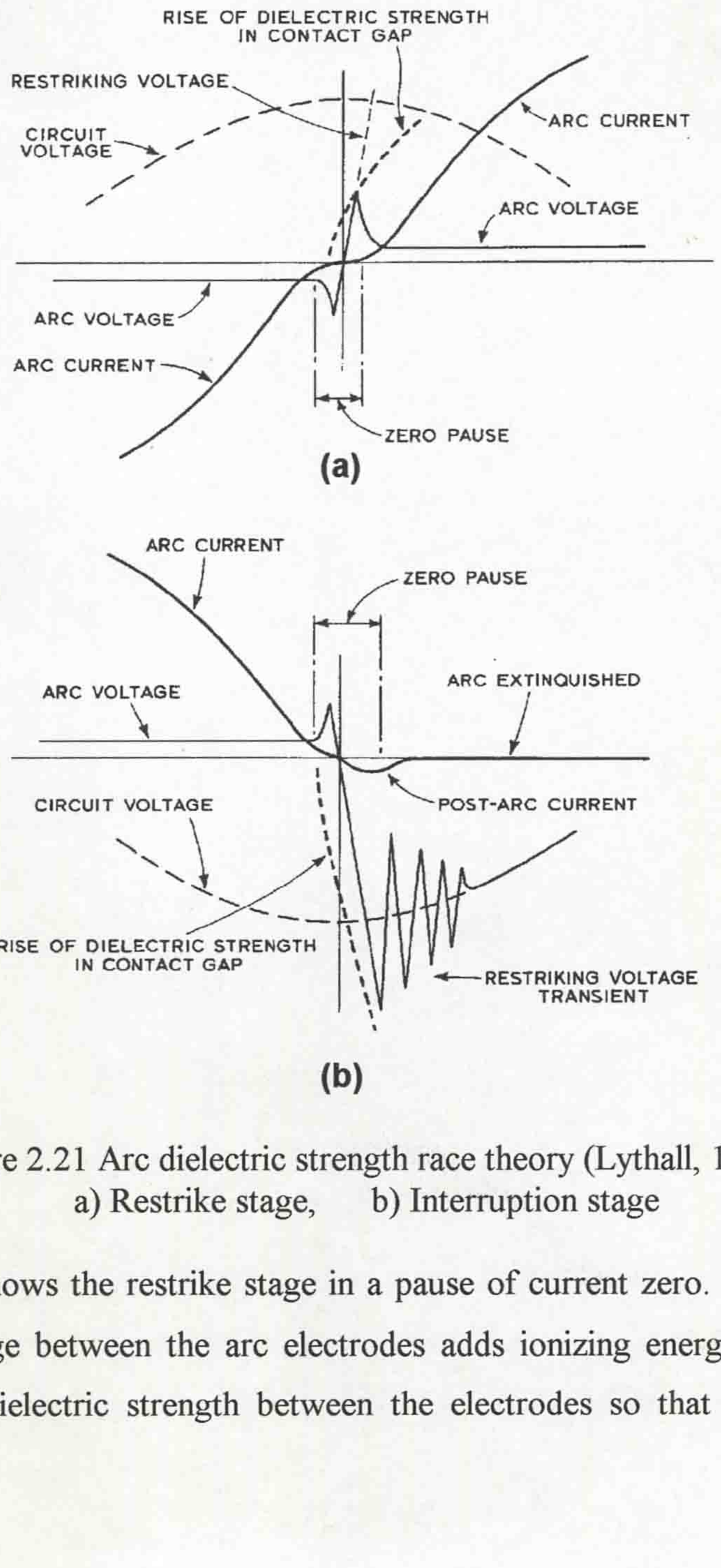

Figure 2.21 Arc dielectric strength race theory (Lythall, 1972)
a) Restrike stage, b) Interruption stage

Figure 2.21a, shows the restrike stage in a pause of current zero. The rapidly rising restriking voltage between the arc electrodes adds ionizing energy to the gap that decreases the dielectric strength between the electrodes so that the recovers less

rapidly than the rate of rise of the voltage. Consequently, when the recovery voltage and the dielectric strength curves interact the arc re-ignites to conduct the second half cycle. Figure 2.21b, shows the current interruption stage when the arc current is interrupted at current zero. In this case, the dielectric strength between the electrodes gap rapidly increases compared. At the instant of arc extinction, some post arc conductivity is observed, so that current flows in response to the restriking voltage transient. This current known, as post arc current, is indicated in figure 2.21b. An example of theoretical model of the arc dielectric strength at current zero known as the energy balance theory was produced by Cassie, (Cassie, 1939). At an actual current zero, where theoretically no current is flowing, there is clearly no power input to the gap. If post arc conductivity continues for a short while in the gap and then ceases so that the current again becomes zero, the power input is again zero. In between these two instants however, there is a flow of current and the power input will pass through a maximum. Clearly, if the maximum power input exceeds the power loss from the arc column by a sufficient amount, the column will heat, its conductivity will increase and a full arc will reform (Lythall, 1972).

2.3.4.5 Restrike voltage as a function of power

The instantaneous value of restrike voltage peak, occurring across the arc gap at current zero, is affected by the fault current and the power factor of the connected network. The amplitude of the restrike voltage depends on the magnitude of the normal frequency voltage at current zero, (i.e. on the power factor). A typical case is the fault current produced by a natural fault to earth on a system that is earthed at the supply neutral of a three-phase supply (Flurscheim, 1982). In such a case, a transient doubling of the voltage peak can be reached being $2\sqrt{2}$ times the phase voltage (Flurscheim, 1982). For a three-phase fault, one phase will clear before the other two and the restriking voltage in this phase will reach a peak of $1.5 \times 2\sqrt{2}$ times the phase voltage (Flurscheim, 1982). Typical examples of a restriking voltage and restriking voltage transient are shown on figure 2.21. The frequency of the transient recovery voltage depends on the inductance and capacitance of the supply and the load sides of the circuit breaker each given by (Flurscheim, 1982):

$$f = \frac{1}{2\pi\sqrt{LC}} \tag{2.13}$$

For the load side, L is the inductance and C is the capacitance of the load and connecting network up to the point of the fault. The electrical resistance in the circuit, such as the connecting cables or overhead line has two effects improving the power factor and dampening the oscillation of the restriking voltage transient, so reducing the severity of duty during arc interruption, (Lythall, 1972).

2.3.4.6 Influence of gas pressure on arcing

The total pressure P in an arc plasma can rise considerably above the original neutral gas pressure due to ionization (Von Engel, 1983). By Dalton's law the total pressure of the gas in the chamber at the time of its ionisation is:

$$P = p_{\text{gas}} + p_{\text{ion}} + p_{\text{electron}} \tag{2.14}$$

In thermal equilibrium, the number of positive ions and secondary electrons produced equally the number of ions recombining with free electrons. Pressure transients produced during arcing may arise due to a number of effects in the circuit breakers, which are associated with the formation of the heated (but electrically non conducting) gas surrounding the arc column and obeys the gas laws (Jones, 1984). Although such pressure increases are advantages in puffer-type and electromagnetic arc rotation (rotary arc) circuit breakers, there can also be disadvantages. For example aerodynamic resonance (within the interrupter) can occur during the arcing, which is likely at peak current, and can disturb the gas-flow trough the nozzle. In the other words, at peak current a pressure elevation is produced owing to the accumulation of mass within the nozzle but which cannot be transported through the nozzle. This phenomenon can produce instabilities of the arc column itself, (Leclerc *et al*, 1980). Additional pressure increases can also be produced by ablation of the nozzle wall by the arc leading to injection of additional mass into the nozzle volume, which demands an additional mass-transport capability.

Clearly pressurization effects during arc quenching are complex, but can be beneficial for assisting arc extinction.

2.4 CIRCUIT BREAKER DIAGNOSTICS

High-voltage circuit breakers and gas-insulated components are constantly evaluated by electrical, dielectric and mechanical testing systems, which need to meet specifications as stipulated by existing standards (IEC, ANSI) and any additional requirements of the end user (Ryan and Jones, 1989). This section describes diagnostic methods for circuit breaker investigations and their application.

2.4.1 Instrumentation and diagnostics

A survey of major measurement techniques used for circuit breaker diagnostics is introduced. Although a knowledge of the overall voltage across a circuit breaker terminal and current flowing through the breaker are sufficient to indicate whether a circuit breaker has successfully interrupted a fault, there are a number of additional diagnostic techniques, which can be applied to yield more details. Diagnostic information is essential for effective circuit breaker design and evaluation, and which can improve the current interruption capabilities.

Measurements in the research laboratory have usually been made on models of the circuit breaker so that sometimes it is difficult to extrapolate the results to commercial interrupters. The problem of monitoring high voltage equipment live without prejudicing the system's electrical insulation is a basic requirement for circuit breaker diagnostics. Optical fibre sensing techniques is one method, which provides the essential isolation for the circuit breakers diagnostic devices. A wide rang of parameters have been measured in commercial circuit breakers utilizing optical instrumentation and which provide the basis for condition monitoring system (Ali *et al*, 1985 and Henderson *et al*, 1993). This section describes some of the main diagnostic methods, which are capable of providing test information about interrupters. The monitored parameters are divided into five groups:

- Electrical
- Mechanical
- Aerodynamic
- Radiative
- Chemical

including information on how each parameter has been measured (Jones, 1988).

2.4.1.1 Electrical measurements

Two types of electrical measurable parameters can be distinguished. These are the overall and the localised (Jones, 1988). The overall parameters enable an immediate performance assessment to be made in an industrial environment. These parameters consist of the overall voltage across the circuit breaker terminals and the total current flowing through the circuit breaker. Low-ohmic resistance shunts (current shunt) have been used for the total arc current measurement, (Schwab, 1972). For measuring post-arc currents of a few amperes, a high shunt resistance is advantageous (to give good signal/noise ratio) and a rapid rise time (to follow current change during re-ignition), (Ryan and Jones, 1989). Overall-arc voltages can be measured by using a tailored R-C voltage divider system known as a commercial high-voltage probe (Schwab, 1972), such as Tektronix Model P6015, 1000:1. The principle of H.V. probe operation is based on the compensated RC-arm resistive voltage divider (connected in series). The divider's attenuation factor is the ratio of the voltage to be divided and the measuring signal. The current and voltage measurements enable the total power dissipated by the arc to be calculated and the effective electrical resistance of the arc. During the research or design phase, more local measurements (localised parameters) may be used, such as spatial variations of the electric field strength, plasma temperatures, species concentrations, and current density within the arc column (Ryan and Jones, 1989). Measurement of localised parameters is needed to provide an insight into detailed arc behaviour leading to an understanding of processes occurring in the arc column, and assisting in interrupter development. Local electric arc properties can usually be measured in research laboratories and are intermediate between the overall electrical measurements and these other basic property measurements. The electrical cross-section of the arc column at different axial location (Dhar *et al*, 1979), the spatial voltage variation in the plasma (Chapman, 1977) etc. are examples of such local measurements. A recently designed optical method for high ac voltage measurement (Francisco *et al*, 2004) sufficiently improved the quality of electrical measurements and has advantages over conventional techniques, such as freedom from electromagnetic interference, size reduction and electrical isolation. The method uses a sensor, which

is based on a double pass configuration of light through a photo refractive crystal in which the properties (conductivity) within specialized optical crystal are changed by high voltage impulses. During the operation of a gas circuit breaker, the hot gas generated by the arc at the arcing time (current fault interruption) leads to the dielectric strength of the gas being decreased (Okamoto *et al*, 1991). This phenomenon is important for current interruption process investigations in gas circuit breakers, including the post arc dielectric strength. The rotary arc gas circuit breaker provides a number of advantages for current interruption compared with other circuit breaker types (**section 2.3**). The dielectric strength tests on a rotary arc circuit breaker are important for characterizing the environmental condition in the breaker chamber during arcing and post arcing. Ennis (1996) and Mori (2005) used a dielectric probe system to monitor the dielectric strength of SF_6, at 3bar after ac-arc interruption (Ennis, 1996) in a rotary arc distribution circuit breaker (**section 2.3.3.4**, fig. 2.16) and atmospheric pressures (Mori, 2005) in an experimental rotary arc interrupter (without the inner PTFE rod, **section 4.1.5.1**, fig. 4.4). The operation of the experimental breakers involved rotating the arc azimuthally between a contact bar pivot and an arcing tube (fig. 2.16, Ennis (1996) and fig.4.4, Mori (2005)). The ac-arc current of 4.48kA and a magnetic field of 1.07T generated Lorenz forces of 4794N/m for the arc motion (Ennis, 1996). Alternatively, ac-arc of 9.5kA, a B-field of 0.408T generated Lorenz forces of 3876N/m for arc motion in Mori's tests (2005). The position of the dielectric probe is shown in figure 2.13b (Ennis, 1996) and figure 4.4 (Mori, 2005). The probe was fixed to the test head at the end of the annular contact isolated from both the test head and the gap. The probe was situated 50mm from an axis of the contact bar and 15mm from the end of the arcing tube (having a coil winding, Ennis 1996). The probe position in Mori's tests was similar to the Ennis experiments. However, a coil winding was fixed around the fibre tube (fig. 4.4). The principle of operation of the dielectric probe is based upon the circuit shown on figure 4.20, **section 4.2.6.2** in which the dielectric strength at different media is monitored via the breakdown voltage across the spark plug contacts. The dielectric probe (RC-integrating circuit) together with the high-voltage (HV) source produces repetitive HV discharge pulses through the spark plug monitoring pre-arcing, during arcing and post arcing. Examples of dielectric strength measurements on the electromagnetically rotated arc breakers after ac-arc interruption are shown in figure 2.22. These are results obtained in SF_6 by both Ennis

(1996) (3bar) and Mori (2005) (atmospheric pressure) for two different heads. Both sets of results show similar dielectric recovery trends. The ratio of breakdown voltage (across the dielectric probe) after the arc extinction slowly recovered to the pre-arcing ratio of breakdown voltage (~1) and is fully recovered after around 58ms.

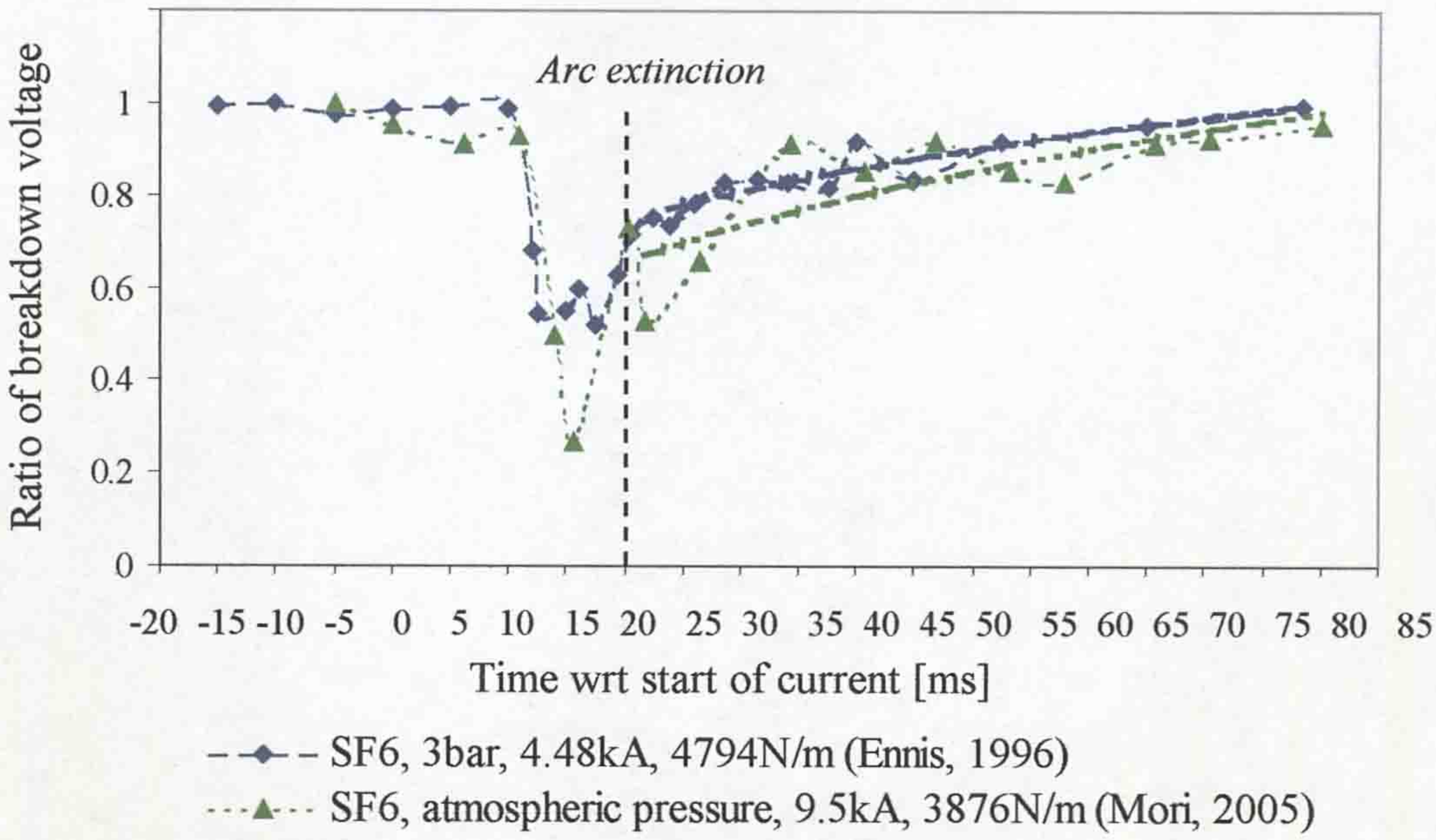

Figure 2.22 Response of dielectric probe to ac-arc of 4.48kA (Ennis, 1996) without PTFE arrangement and ac-arc of 9.5kA (Mori, 2005) with PTFE

The results shown in fig. 2.22 yield the following approximate empirical relationship for times greater then about 40ms after arc initiation, (Mori, 2005) is:

$$\frac{V_B^{(t)}}{V_{B_0}} \cong 1 - K_1(1+\alpha_1 B)^{m_1} d^{n_1} i_p^{-l_1} \exp[-\frac{t}{\{\tau(B,d,i_p)\}}] \qquad (2.15)$$

Where,

$V_B^{(t)}$ is the breakdown voltage at different time scale

V_{B_0} is the pre arc breakdown voltage

B is the magnetic field [T]

i_p is a peak current [A]

d is a PTFE hollow diameter [m], (outer PTFE cylinder (fig. 4.4))

K_1, α_1, m_1, n_1, and l_1 are constants determined from the tests having values $3.3\times10^{-6}, 1.6, 1.1, 0.3$, and 1.2 respectively, for Mori (2005) operating conditions

$\tau(B, d, i_p)$ represents a dielectric recovery time constant, which is a function of B, d, i_p also derived from the experimental tests. The curve corresponding to these constants was compared with the experimental data on figure 2.22, where the value of $\tau(B, d, i_p)$ was 70 for the curve, respectively (Mori, 2005).

The implication of (2.15) is that an increase in peak current i_p reduces the breakdown voltage substantially. Moreover, for a given fault current, larger magnetic fields and diameters lead to substantial lowering of breakdown voltage that can be as low as 70% of pre arc breakdown voltage even 200ms after arc extinction respectively (Mori, 2005).

Magnetic field measurements usually relate to the rotary arc circuit breakers where the magnetic field of the coil, which is usually fixed inside of the interrupter, produces Lorenz forces for the arc motion. The magnetic flux density measurement is based on the method utilized an initially calibrated search coil, under ac conditions within a long solenoid (Spencer, 1987 and Ennis, 1996). The magnetic field generated by exited coil is measured using a small short coil (search coil), where the B field lines passing through the search coil produce an instantaneous changing voltage across the search coil that is directly monitored using an oscilloscope. This voltage (after integration) presents a value of the magnetic field. The radial B_x and axial B_z magnetic field components of the coil (**Appendix III**) put together the total B field ($\sqrt{B_x^2 + B_z^2}$). The technique of magnetic flux measurement is presented in **section 4.2.4** in detail. The general shape of the B field distribution due to a coil is presented in **Appendix III** in which the effect of non-uniform distribution of the current flowing trough the coil using a wide strip (foil) and having a cylindrical shape of winding is described.

2.4.1.2 Mechanical-drive measurements

Monitoring the movement of the mechanical drive of the piston and contacts of a puffer type circuit breaker can yield accurate measurements of the contact travel (Ryan and Jones, 1989). In the early years, the mechanical-drive diagnostic used potentiometric measurements via a mechanical link to the slider of the potentiometer. However, the size of the device and the linkages with the other end of a drive rod

would lead to some defective link being undetected. More recently, mechanical-drive diagnostics have been made to measure the contact movement directly.

A miniature travel recorder (Ryan and Jones, 1989) that can be mounted directly on the contact stalk within the circuit breaker has been developed for monitoring the moving contact directly without interference from linkages, (fig. 2.23). This unit consisted of a coded wheel rotated by the linear movement of the travel contact (fig. 2.23a).

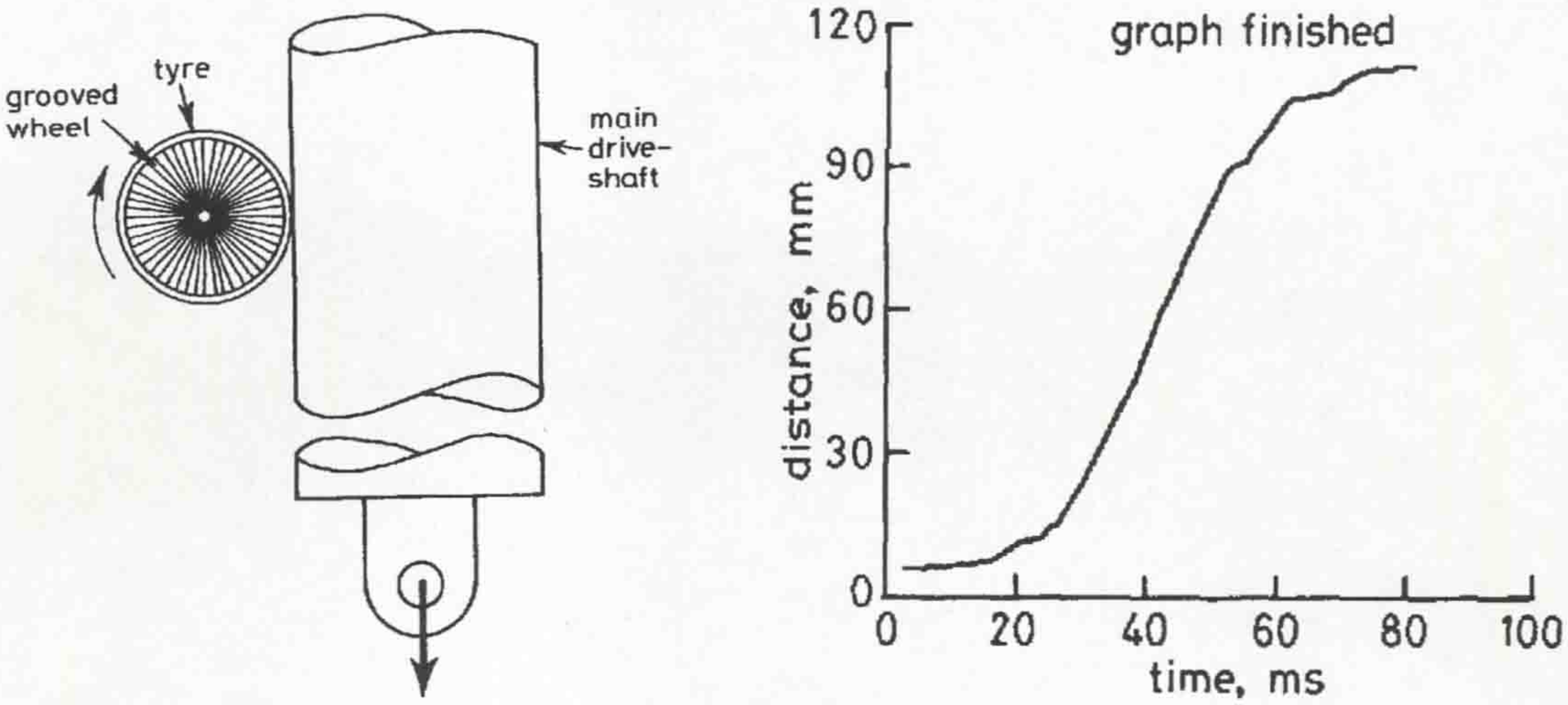

a) Transducer schematic b) Typical travel record

Figure 2.23 Schematic of optical rotary travel recorder (Shimmin, 1986)

The rotation of the wheel was measured optically, using the input and output light signals transmitted to the signal processing system via optical fiber transmission. A typical example of the travel record is shown in figure 2.23b.

2.4.1.3 Aerodynamic measurements

Aerodynamic flow measurements in a circuit breaker provides information about the gas flow, which is important for arc control and quenching. Pressure is considered as a main parameter, which is increasingly being used to monitor flow conditions in puffer type circuit breakers. A number of different types of transducers maybe used for observing the aerodynamic conditions inside the breakers. Piezoelectric and piezoresistive transducers have been used on puffer type circuit breakers to define the axial pressure distribution inside the circuit breaker, (Tominaga *et al*, 1980 and Shimmin, 1986).

A typical pressure transient result is shown on figure 2.24. This shows how the piston pressure can be changed from cold-flow (no arcing) to an arcing interaction time, using such transducers.

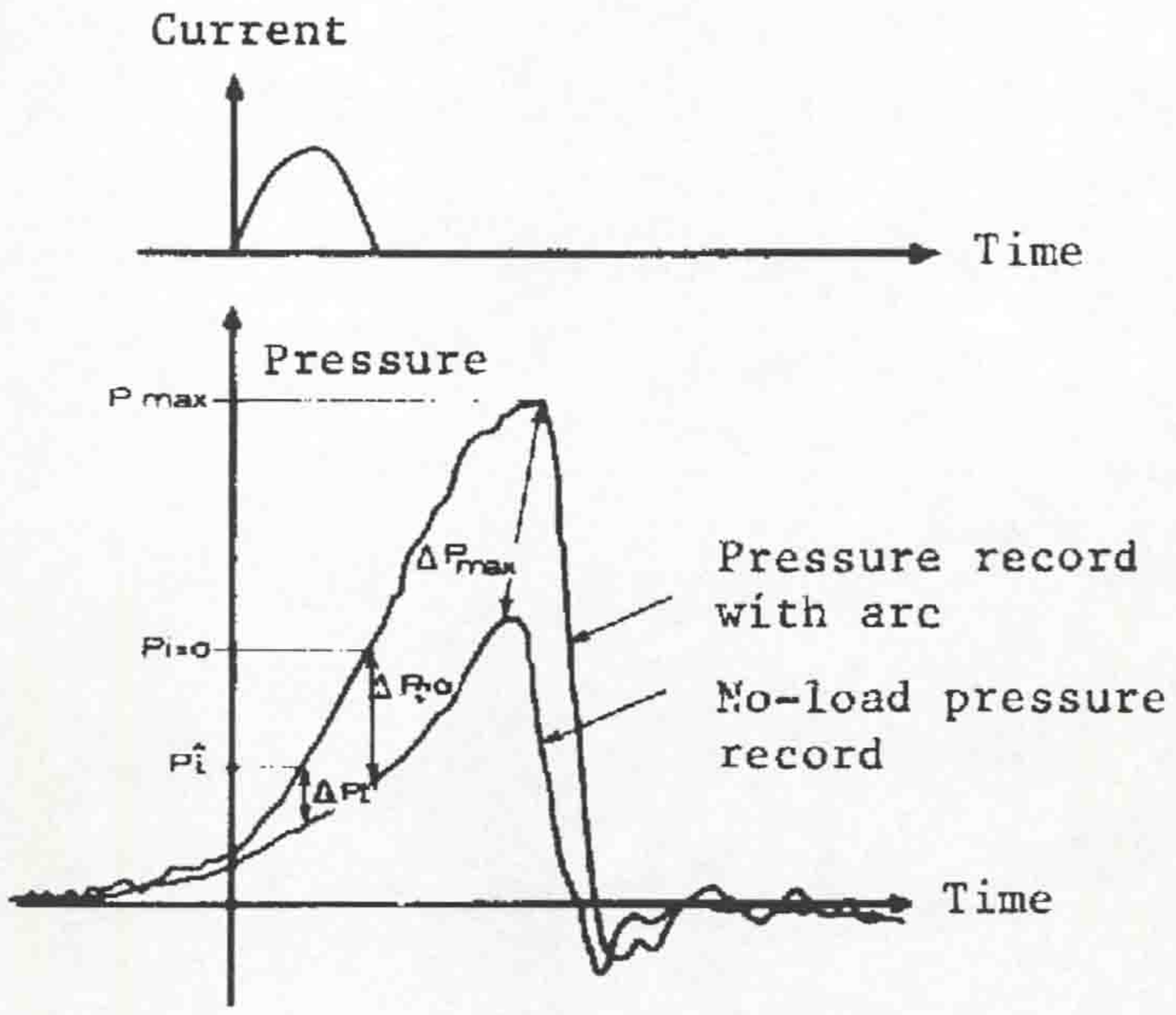

Fig. 2.24 Measurements of puffer piston pressure (Shimmin, 1986)

The electrical type transducers need to be protected electrically and thermally from the arc discharge, using interconnecting tubes. One problem in using electrical pressure transducers is the need to provide electromagnetic shielding from the arc which leads to the use of inter connecting tubes and hence more difficult measurement compensation schemes. More direct measurements of plasma and gas-flow velocities in the circuit breakers have been obtained using laser Doppler velocimetry (Todorovic and Jones, 1985).

2.4.1.4 Radiation measurements

Analysis of the radiation emitted by an arc discharge provides an attractive means for non-invasive measurements, (Ryan and Jones, 1989). The simplest form of radiation measurement is high-speed photography, enabling the spatial extent of the plasma to be determined. Such methods have been utilized for investigating nozzle blocking by electric arc, arc behavior and arc location at current zero, including post arcing time, (Lewis *et al*, 1985). The influence of nozzle material, e.g. through ablation is difficult to assure with such investigations because of nozzle material is

not sufficiently transparent. Therefore, rapid-response photomultipliers and narrow-band optical filters are used via narrow gaps in the nozzle wall to measure the total radiation reaching the nozzle wall, including the temperature of the ablated nozzle material, (Jones *et al.*, 1986). Spectroscopic techniques can provide information not only about the plasma properties, such as temperature and electron density, but also about contacts and nozzle material entrainment and vapour jetting, (Ryan and Jones, 1989). Investigation of the arc column following high-peak arc currents of ~ 53kA show that the temperature, as well as cross-section, of the arc column is sufficiently increased at current zero to reduce the interrupting capability, (Lewis *et al*, 1985). The spectroscopic techniques have been restricted to the research laboratory. However, the use of optical fibre techniques has enabled spectroscopic and radiation measurements to be made in commercial circuit breakers during testing at industrial short-circuit test stations. Figure 2.25 shows typical example of such system used in commercial 420kV, 63kA SF_6 puffer circuit breaker, (Ali *et al*, 1985).

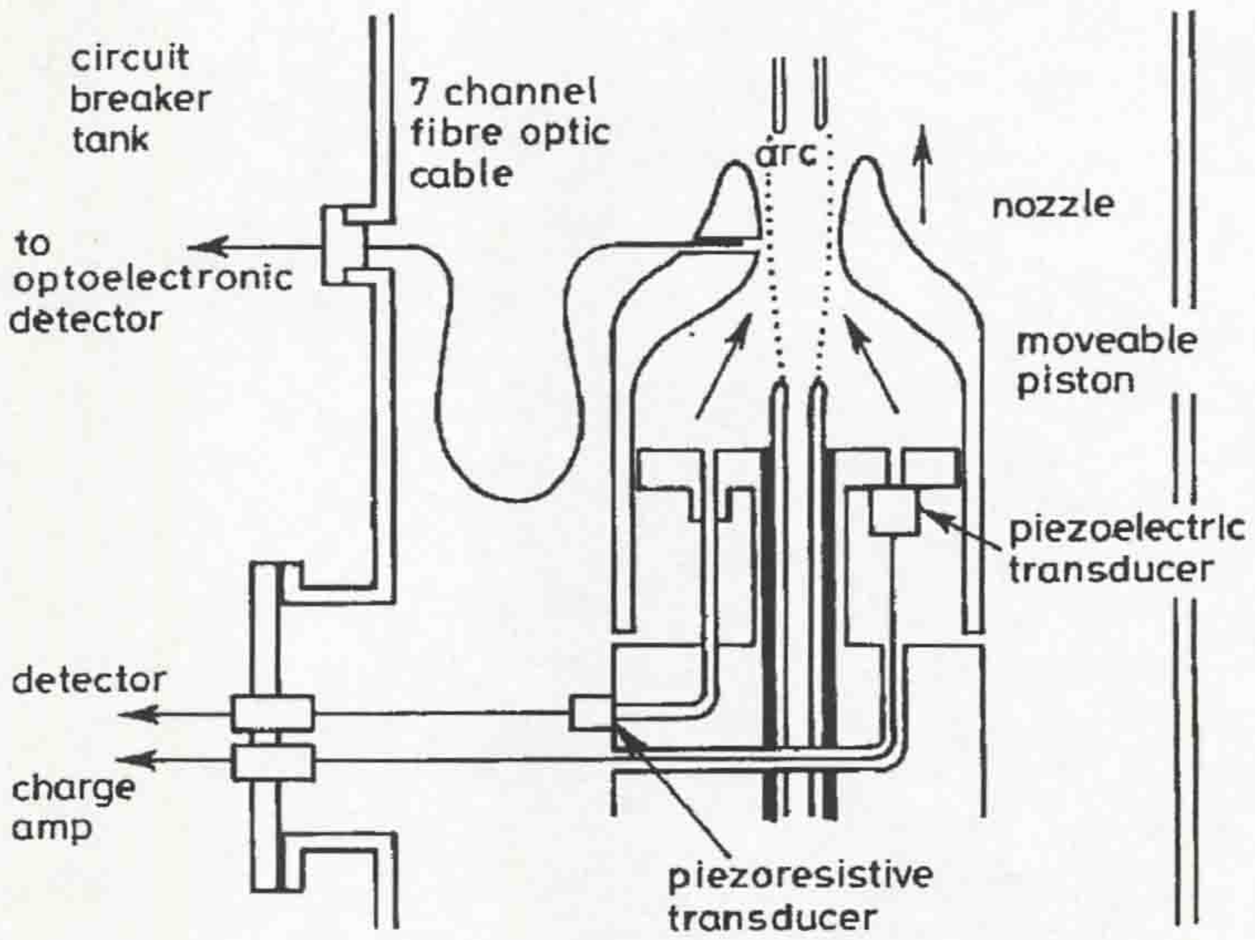

Figure 2.25 Optical fibres position in commercial 420kV; 63kA puffer circuit breaker tests (Ali *et al*, 1985)

2.4.1.5 Chemical measurements

During arc interaction in a circuit breaker decomposition products of SF_6 are produced and can be monitored off-line by gas chromatography, (Sauers *et al*, 1984). From a practical point of view, the formation of CF_4 (the carbon which was produced

by the thermal influence of the polymeric nozzle) can indicate the arc energy dissipated in a circuit breaker and consequently the nozzle conditions (Belmadini *et al*, 1991 and Ruegsegger *et al*, 1985). Unfortunately, these methods are too difficult to use for on-site testing. Therefore, simpler techniques have been proposed which rely upon chemical reactions involving different decomposed species, (Ryan and Jones, 1989). Tominaga *et al*, (1981) report the use of a simple sensor for contamination product concentration monitoring, utilizing colour changing indicators for use on site. Optical fibres systems have a potential of monitoring decomposition products. These systems can accurately quantify colour "chromatically" (Jones *et al*, 1987) and consequently are capable of analyzing the colour indicators mentioned above. Monitoring of SF_6 decomposition products is currently being investigated, but there only few reports have been reported in the literature.

2.5 SUMMARY

The development of the circuit breaker technology during the last 25 years is a result of increased use of SF_6 gas and vacuum as major quenching media for arc interruption. Different switchgear manufacturers have employed various circuit breaker technologies such as the puffer, self-pressurizing and rotary-arc types. Amongst factors, which are increasingly being evaluated are cost (particularly associated with operating mechanisms, encapsulations etc.) and environmental compatibility (with SF_6 being a greenhouse gas). Consequently, the quest for new circuit breaker technology is needed environmentally safe and cost effective.

This thesis therefore explores a new way in which high-pressure arc might be controlled and extinguished as a basis for possible future circuit interrupting means as new forms of either interrupters or current limiters. The approaches used involve the use of new forms of electromagnetic arc control and the production of an advantageous arc-quenching medium through the ablation of solid material confining the arc. As part of the exploration use is made of measurement and diagnostic techniques of the form reviewed in **section 2.4**. An particular use is made of current and voltage measurement techniques, high speed photography and video methods, optical fibre monitoring of arc position and movement, magnetic field probing and post arcing dielectric strength of the arc heated gas. Results from these measurements are used to evaluate the usefulness of various arc-controlling mechanisms used.

CHAPTER 3 - DESIGN AND MODELLING OF A NOVEL INTERRUPTER

3.1 DESIGN OF THE METHOD FOR ARC CONTROL

3.1.1 New concept of arc control

The control of electric arcs at atmospheric pressures is important for the operation of many devices such as plasma torches, arc heaters etc. Some equipment utilizes a combination of electromagnetic fields and high temperature insulation materials in order to provide suitable conditions for long duration arc control. Most of these use the same arc-rotating technique utilizing different gases to increase their effectiveness. This chapter introduces a new design principle for controlling the electric arc, which is different from previous designs. The basis of previous methods is to produce passive electrical arc rotation inside a coil producing magnetic field for control. In contrast to these previous techniques, the arc is wrapped around the outside of the coil and is electromagnetically attracted to it. The coil produces a strong magnetic field, which interacts with the convoluted arc creating Lorenz forces for producing arc movement. This design also uses a polymeric material for enhancing this interaction. The experimental test rig for producing the magnetic field and arc is shown in figure 3.1, and is built to demonstrate the arc control feasibility.

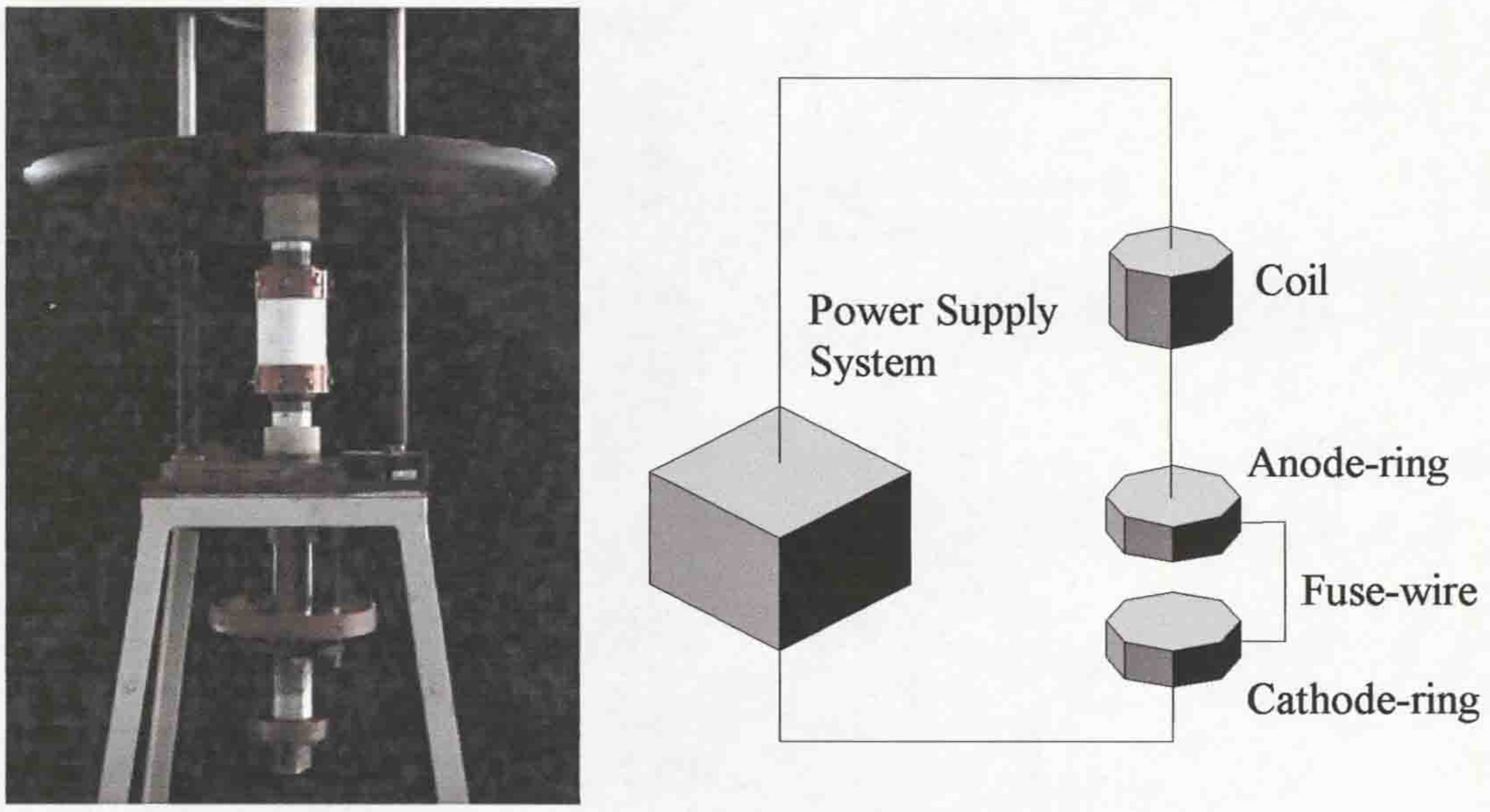

Figure 3.1 Experimental apparatus assembly

An open rig is chosen for monitoring the behaviour of the arc rotation in detail under the following conditions: air, atmospheric pressure. Ring-electrodes are situated at a fixed distance from each other. The coil is connected in series with the electrodes and situated inside a white PTFE cylinder. A fuse wire is linearly connected between the two electrodes enabling the electric arc to be ignited between them. The concept for controlling the arc is shown in figure 3.2. The inner coil produces an outer strong magnetic field around the PTFE cylinder. As a result, different Lorenz force directions are created producing two main field components for controlling the arc. The first is the radial component of the magnetic field producing two opposite directions of the Lorenz forces F at the top and bottom of the coil, (B_T, B_B, fig. 3.2).

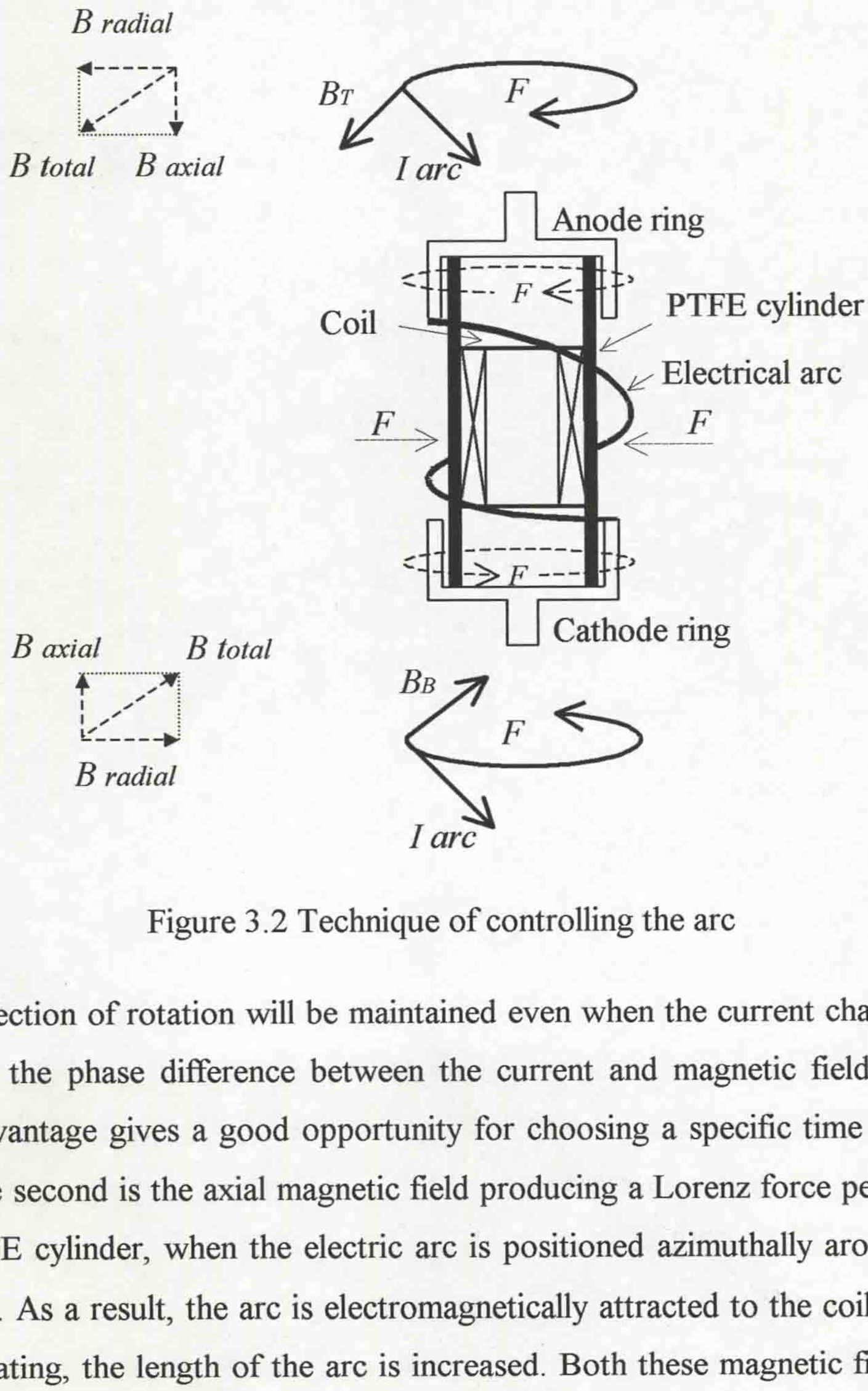

Figure 3.2 Technique of controlling the arc

This direction of rotation will be maintained even when the current changes direction because the phase difference between the current and magnetic field is near zero. This advantage gives a good opportunity for choosing a specific time to control the arc. The second is the axial magnetic field producing a Lorenz force perpendicular to the PTFE cylinder, when the electric arc is positioned azimuthally around the PTFE cylinder. As a result, the arc is electromagnetically attracted to the coil. As the arc is also rotating, the length of the arc is increased. Both these magnetic fields provide a

mechanism for greater interaction between the rotating arc and the PTFE cylinder. Furthermore, through ablation, the thermal energy of the arc is reduced and therefore the duration of the arc may be reduced. Figure 3.1 and figure 3.2 show the electrodes position that have constant fixed gap, with the coil situated inside the PTFE cylinder at the same distance from each of the electrodes.

3.1.2 Arc control model

The experimental model for arc control is shown in figure 3.3. The dimension of the device is depended on the coil size calculated in the **section 3.1.3**. The gap between the electrodes was derived by experiments in **section 5.2.1.3**. The experimental model consists from two electrodes (anode and cathode), white PTFE cylinder and the coil fixed inside this cylinder. The model is fixed on the

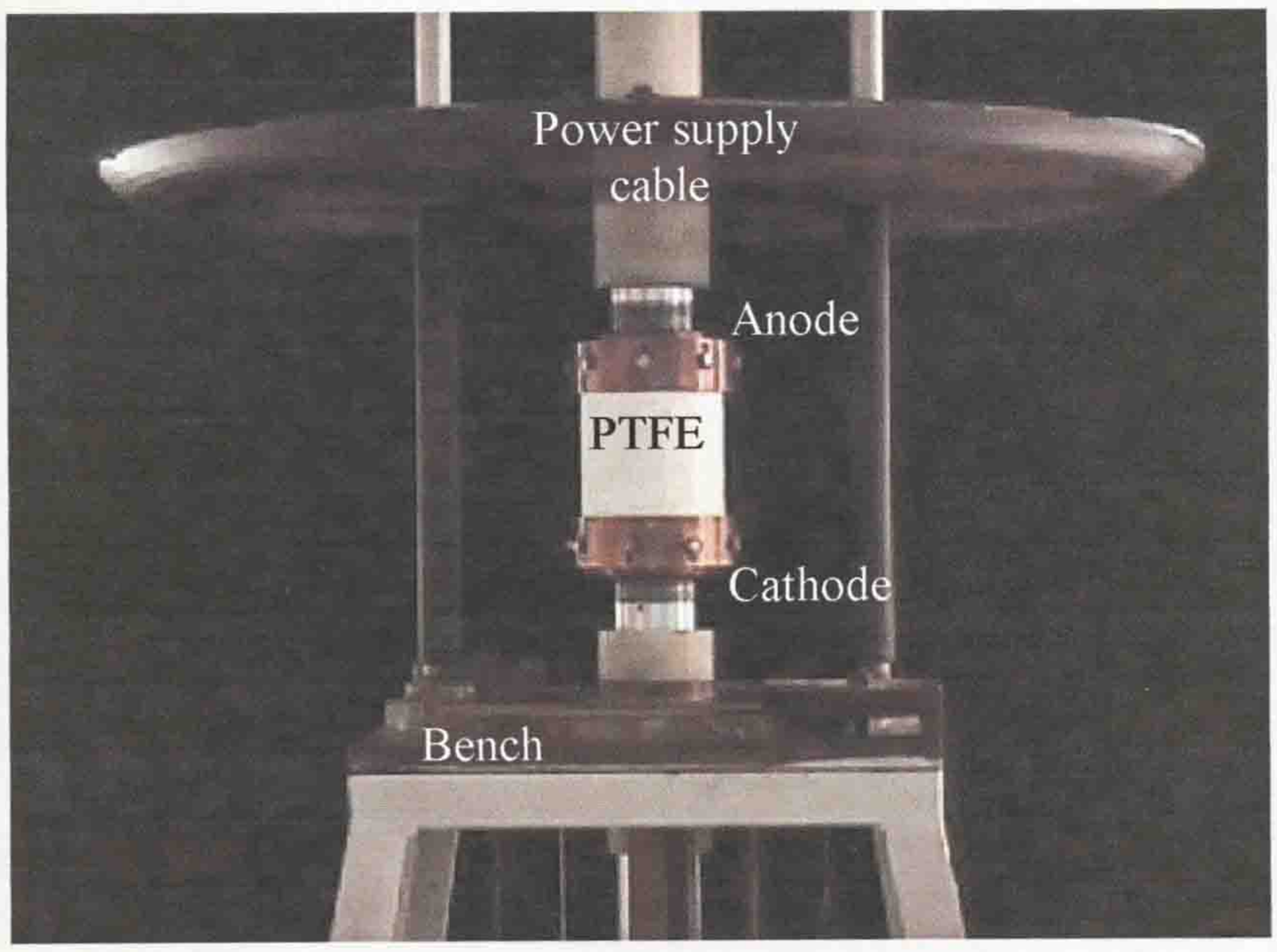

Figure 3.3 Experimental model

bench, which is insulated from the electrodes and ground. This construction supports comfortable access to the model during the tests. The big insulating lid situated on the top of the model protects the power supply cable and the high voltage probe from any mechanical damages, which may involve the electrical measurements during the experiments. The high electrical insulation between the power supply cable and anode-electrode prevents any electrical shorting between them during the high current and voltage tests.

3.1.3 Components calculation of the model

This section describes the magnetic induction calculation technique for the air-core structure. The main goal of this design is to develop and to calculate the universal high-current miniature coil that may be operated in the model for the arc control demonstration and in the current interrupter operation. The measured inductance and resistance of the coil maybe compared with these calculations in order to extract the coil voltage from the total voltage to give the arc voltage across the model terminal (**section 4.2.3.1**). All results have been converted to MKS units with inductance in Henries and all dimensions in metres. The coil size is depended on a number of points, which are discussed during model development. The circular planar (foil-type winding) coil has increasing application in the rotary arc circuit breakers (Ennis, 1996) and this type of the coil will be used in this design.

A number of methods are used for calculation of the inductance of a circular coil with rectangular cross section any desired proportions. The Grover method (Grover, 1946) is one of the methods used for a round planar circular coil calculation. The shape of the coil is shown in figure 3.4.

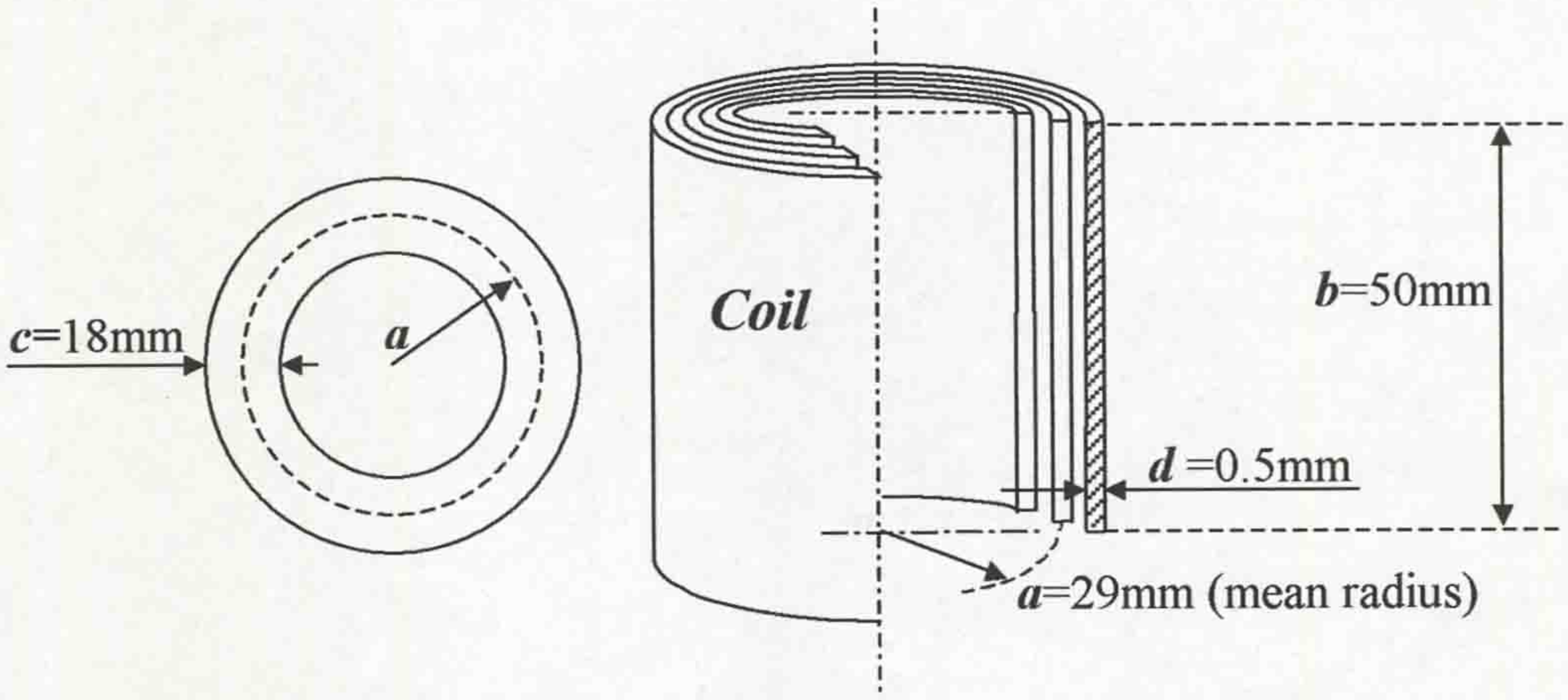

a) Top view b) Cross sectional view

Figure 3.4 Round planar (foil-type) coil with rectangular cross section

Using the Grover method, the coil inductance is:

$$L = 0.001 a_{cm} N^2 P' = 0.001 \times 2.9 \times 16^2 \times (26.2) \times (0.41) \approx 8, [\mu H] \qquad (3.1)$$

Where P' is a unitless constant considered as the product of two factors (P and F). The first (P) is a function of $c/2a$ and applies to a coil of zero axial dimension,

(obtained from Tab. 26 Grover, 1946). The second, due to separating the turns in the axial direction, (F) is c/b takes into account the reduction of inductance, (obtained from Tab. 25 Grover, 1946). Where a, is a mean coil radius. The number

$$\frac{c}{2a}=0.31 \Rightarrow P \approx 26.2 \text{ and } \frac{c}{b}=0.36 \Rightarrow F \approx 0.41 \qquad (3.2)$$

of turns of the coil is 16 and it is marked as N. From preliminary arc test investigations (**section 5.2.1**), the optimal length of the coil was about 50 mm, (**section 5.2.1.3**). N, inner 40mm and outer 76mm diameters of the coil (mean coil diameter/radii are 58mm/29mm) produce the optimal magnitudes of the magnetic field around the model (**section 3.4**). The length (strip) of the coil is calculated as,

$$l \approx 2\pi \times a \times N \approx 2\pi \times 0.029 \times 16 \approx 2.913,[m] \qquad (3.3)$$

As a result the coil resistance is:

$$R_{coil} = \rho_{copper} \times \frac{l}{A} = 1.7 \times 10^{-8} \times \frac{2.913}{25 \times 10^{-6}} \approx 0.198 \times 10^{-2} \approx 1.98,[m\Omega] \qquad (3.4)$$

Where ρ_{copper} , [Ω x m] - Copper resistively (Guru *at al*, 2004).

$A = d \times b = 0.5 \times 50 = 25,[mm^2] = 25 \times 10^{-6},[m^2]$ is a cross-section of a wide strip of the coil, (fig. 3.4b). The same type of tinned copper strip (cross-section) was used in the previous rotary arc circuit breaker tests (Spencer, 1987) up to 18kA.

3.1.4 Components

The components of the experimental model are shown in figure 3.5. The arc

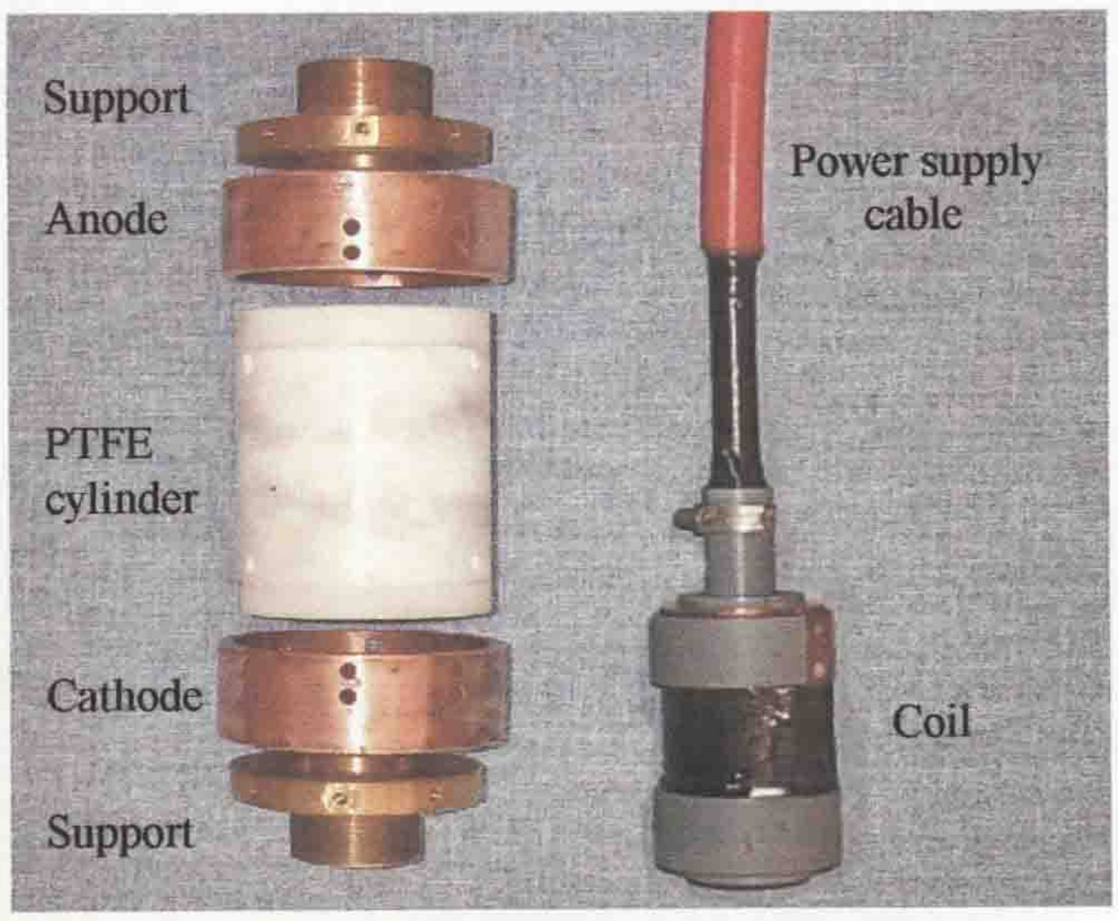

Figure 3.5 Components of the testing model

control test head (**Appendix IV**) consists of the power supply cable, coil, anode, supports, cathode, PTFE cylinder, and the experimental bench. The experimental bench (fig. 3.3) consists of a number of additional details, which are designed for the tests. However, their descriptions are ignored. The shape and dimension of the details are chosen experimentally. For example, the thickness of the PTFE cylinder was chosen from a visual inspection of the cylinder after a number of high-current tests.

3.1.5 Assembly structure

This section describes the assembly of the model as shown in figure 3.6. The positions of different sub-assemblies shown on figure 3.6 are identified by a colour-scale. The power supply cable passing through the anode is connected to the coil and the anode in series. The coil, fixed inside the PTFE cylinder, is protected from the electrical arc during the arcing tests. The electrodes position in figure 3.6 show that the anode and cathode are fixed at the same distance from the coil.

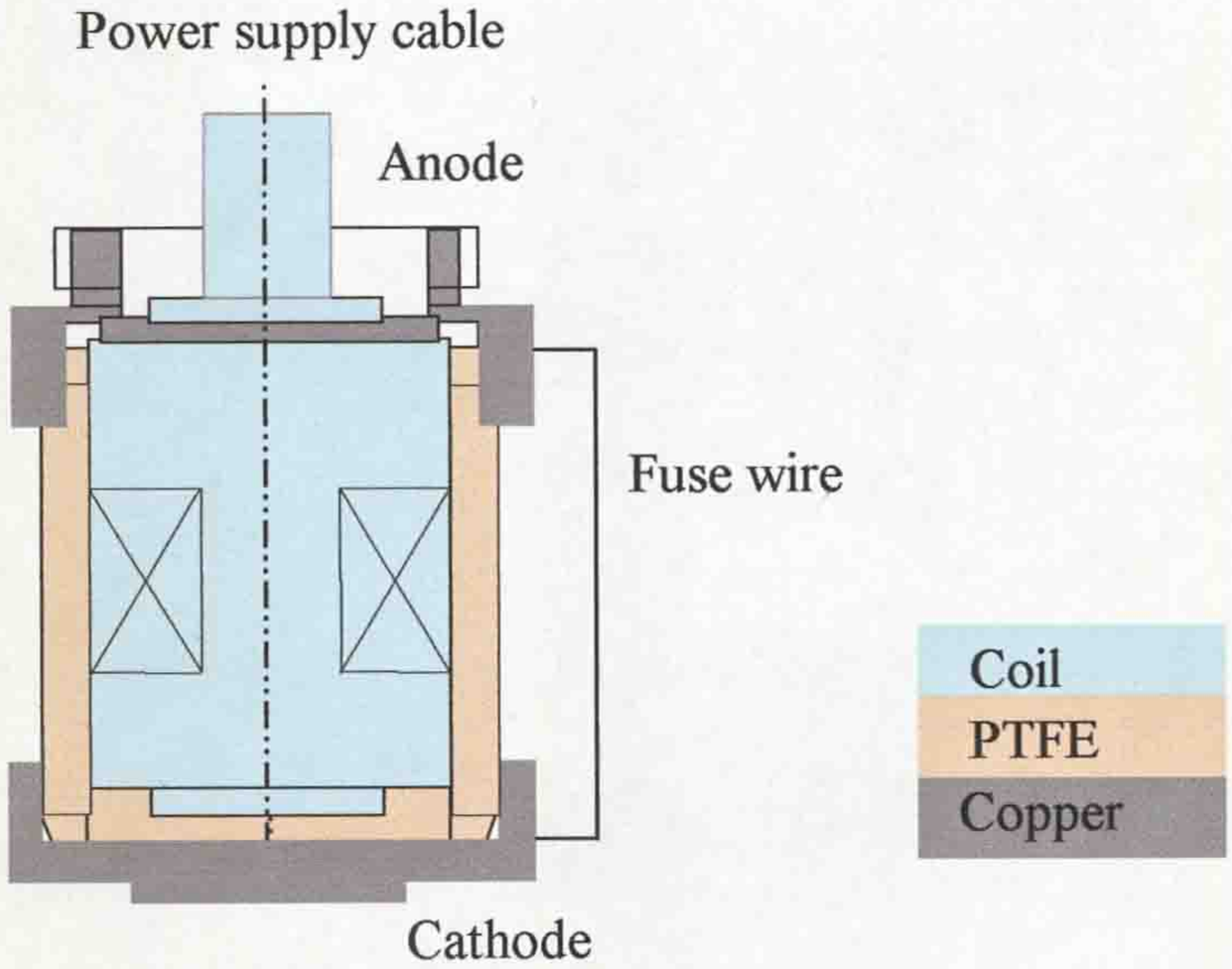

Figure 3.6 Model assembly

In order to ignite the arc between the anode and cathode, during the arcing test, a fuse wire is connected between the electrodes. During the measurement of spatial variation magnetic field around the model, (**section 5.2.3.1**) the anode should be connected by a short cable to the earth of the power supply system and the position of this cable should be as far as possible from the measurement coil, to reduce any electromagnetic fields interference.

3.2 INTERRUPTER HEAD DESIGN

The fundamental process of current interruption has hitherto involved the contraction of the arc plasma during the extinction process as a base for circuit breakers development worldwide. A new fundamental aspect of the present ac arc interruption technique is that the ac arc may be successfully interrupted using an opposite technique (i.e. expansion the arc during the arc extinction). A main goal of this project is to design a rotary arc interrupter model that could operate competitively in this different mode.

3.2.1 Objective

Evaluation of the rotary arc circuit breakers is constantly made by the high voltage (HV) engineering companies worldwide in order to achieve:

- Cost and space reductions
- Improved arc interruption techniques
- Evaluated SF_6 management or use of alternatives
- Increase the fault current ratings and dielectric strength after current zero
- Longer contact life
- Low energy and reliable circuit breaker operating mechanisms
- Ultimately maintenance free and sealed for life circuit breaker

One of the main requirements of the rotary arc circuit breakers is the need to shorten time of arc spinning. From the previous methods of the arc rotations (**section 2.3.3.4**), the arc is spun through the action of Lorenz force produced by the fault current flowing through a B field, producing coil, (fig. 2.14). However, because the B field distribution is not uniform at the centre and at the ends of the coil, the Lorenz forces do not act on the arc with the same forces. This effect produces a non-stable helical arc rotation that influences to the circuit breaker interruption characteristics. In contrast, the arc rotation may be made more stable using a new technique of arc control (**section 3.1.1**). In the previous techniques, the initial conditions of the arc rotation are not effective. This means that at the time of contact separation the direction of arc current and azimuthal lines of the inner magnetic field of the coil are almost parallel to each other, (fig. 2.13, fig. 2.17). In fact, this condition reduces the instantaneous arc rotation. A number of the requirements mentioned above by HV

engineering companies should be achieved utilizing the new technique of arc control for the novel interrupter head design.

3.2.2 Principle of operation

This section describes the operation of the rotary arc interrupter head, (fig. 3.7). The coil, connected in series with the anode and cathode, is situated inside the PTFE cylinder. The movable rod (cathode) of the experimental breaker changes its position in relation to the anode during the ac arc interruption. The contact travel record characterizes the movable rod operation of the breaker and this relationship is obtained experimentally, (**section 4.2.5.3**). The Lorenz forces operating in the circuit breaker is depend on the electrodes position in relation to the coil situated inside of the PTFE cylinder. Figure 3.7 shows the Lorenz forces directions acting on the arc with a dc arc of 4ms duration and an ac-half cycle of 10ms. The colour-scale identifies the position of different materials in the figure. In the contact closed state, (fig.3.7a) the dc current flowing through the coil and the electrodes produces a low level of magnetic field around the coil. After a couple of milliseconds, contact separation occurs and the main half cycle sinusoidal current commences to flow through the coil and the arc. At the arc discharge state, (fig. 3.7b) the Lorenz forces act upon the arc forcing it around the PTFE cylinder. The total magnetic field of the coil is increased, becoming almost maximal while the ac current is at its peak value. In fact, the arc is maximal rotated around the PTFE cylinder until the cathode is level with the centre of the coil. Moreover, the arc length is increased gradually until the movable cathode is level with the centre of the coil. When the movable cathode is situated half way along the coil, the Lorenz forces begin to act on the arc in such a way as to draw it toward the PTFE cylinder radially. The reason is that radial B field of the coil is low outside the coil especially at the centre of the coil, while the outer axial coil B field is larger at the same point. On the other hand, the current direction in the coil and the arc is of the same polarity and consequently the arc is electromagnetically attracted to the coil. As a result, the electric arc is rapidly wrapped around the PTFE cylinder increasing its length. In the interruption state, (fig. 3.7c) the electrode positions correspond to the end of the first half cycle. In this state, coil B- field acting on the arc creates different Lorenz force directions at the top and bottom of the coil, which forces the arc to be wrapped around the PTFE cylinder.

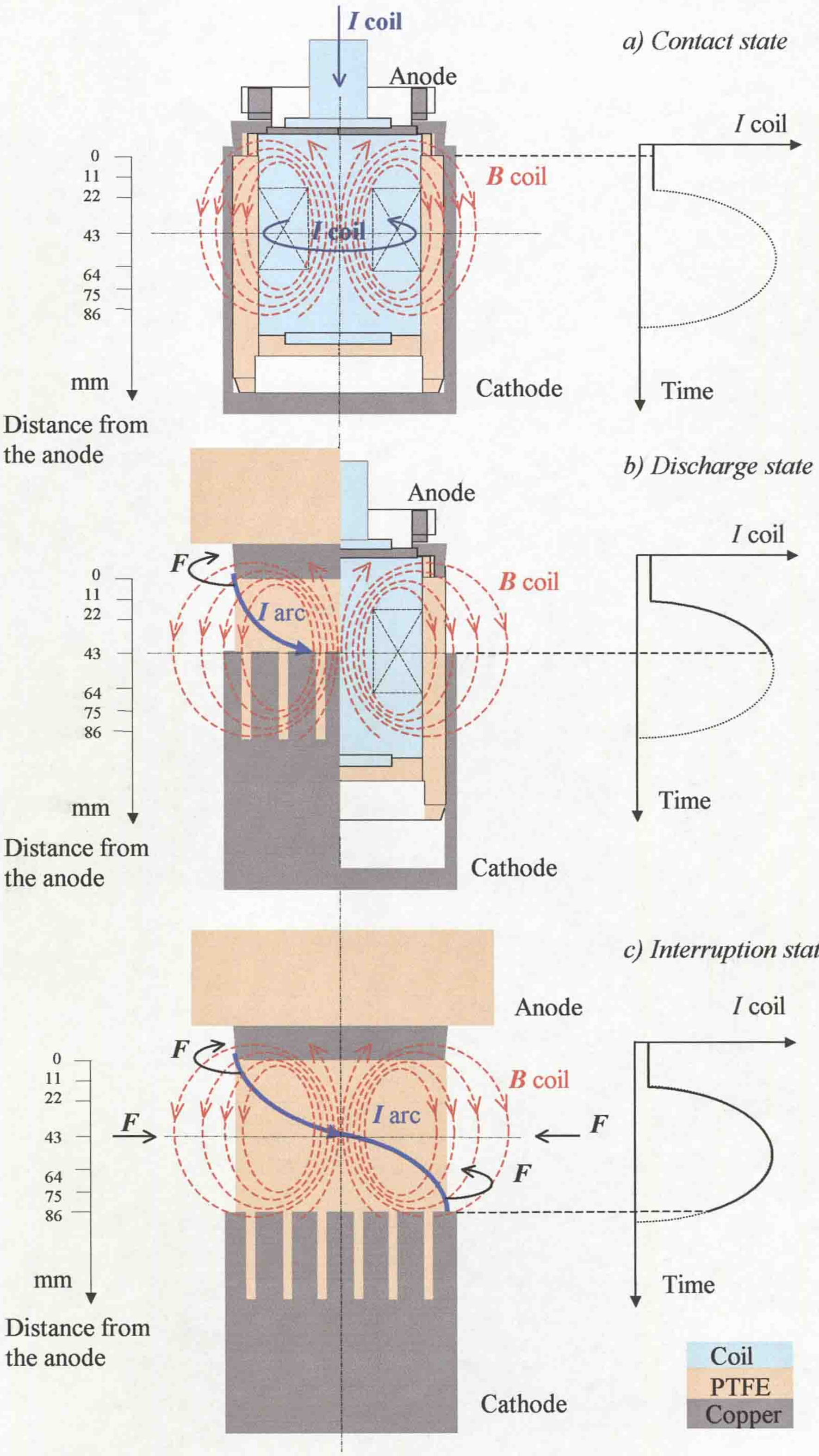

Figure 3.7 Current interrupter head operation

At the same time, the Lorenz forces will be forcing the arc onto the cylinder surface. The thermal energy of the arc could reduce through ablation of the PTFE material, and therefore the duration of the arc may be reduced. Theoretically, the arc should be wrapped around the cylinder and may be interrupted at current zero.

3.2.3 Model of the interrupter head

Design and development of the rotary arc interrupter head model is introduced. The main goal of the current interrupter head design is to find the optimal geometry of the devise in which the PTFE material could be ablated maximally, utilizing spatially varying cross magnetic fields around the model. The ac fault current ratings of this model are assumed to be up to 15-18kA. The geometric shape of the devise is based on the cylindrical shape supporting a good aerodynamic shape during the arc interaction. Figure 3.8 shows the current interrupter head assembly. The coil situated inside of the white PTFE cylinder produces the outer magnetic field for controlling the electric arc. The spatial variation of outer B-field around the coil should depend on the distance from the coil to the measurement point. In addition, magnetic field produced by the coil decreases with distance. Consequently, the thickness of the PTFE cylinder around the coil should limit the value of the B-field acting on the arc and as a result reduce the Lorenz forces, which control and hold the arc around the PTFE cylinder before current zero. In fact, the thickness of PTFE cylinder should be as small as practically possible in order to increase the magnetic flux acting on the arc. However, too severe an ablation of PTFE cylinder could destroy the coil if its thickness was too small. Therefore, this dimension would need to be optimized. The position of the anode relative to the coil can improve the initial conditions for arc rotation. The anode-ring needs to be situated close to the maximal B-field distribution producing the coil, i.e. the magnetic field produced by the coil should pass through the arc current orthogonally in the area near to the anode and cathode, (fig. 3.7b,c). This would provide a maximal Lorenz force at the edge of the anode during the entire period of ac arc interruption. The anode-ring has a little sloping shape. The cathode-ring has finger-contacts operated by the movable rod. The mechanical contact between the anode and the cathode reduces any mechanical stress at the time of contact mating. The white PTFE ring situated at the top of the current interrupter has two purposes. First, it protects the Aluminium interface tube

from the arc plasma. In fact, the aluminium melting temperature is less than that of copper and therefore heating of the aluminium can produce additional ionization detrimental to the ac-arc extinction at current zero. Second, the PTFE material could produce more ablation by the burning arc during the arc rotation, (fig. 3.8).

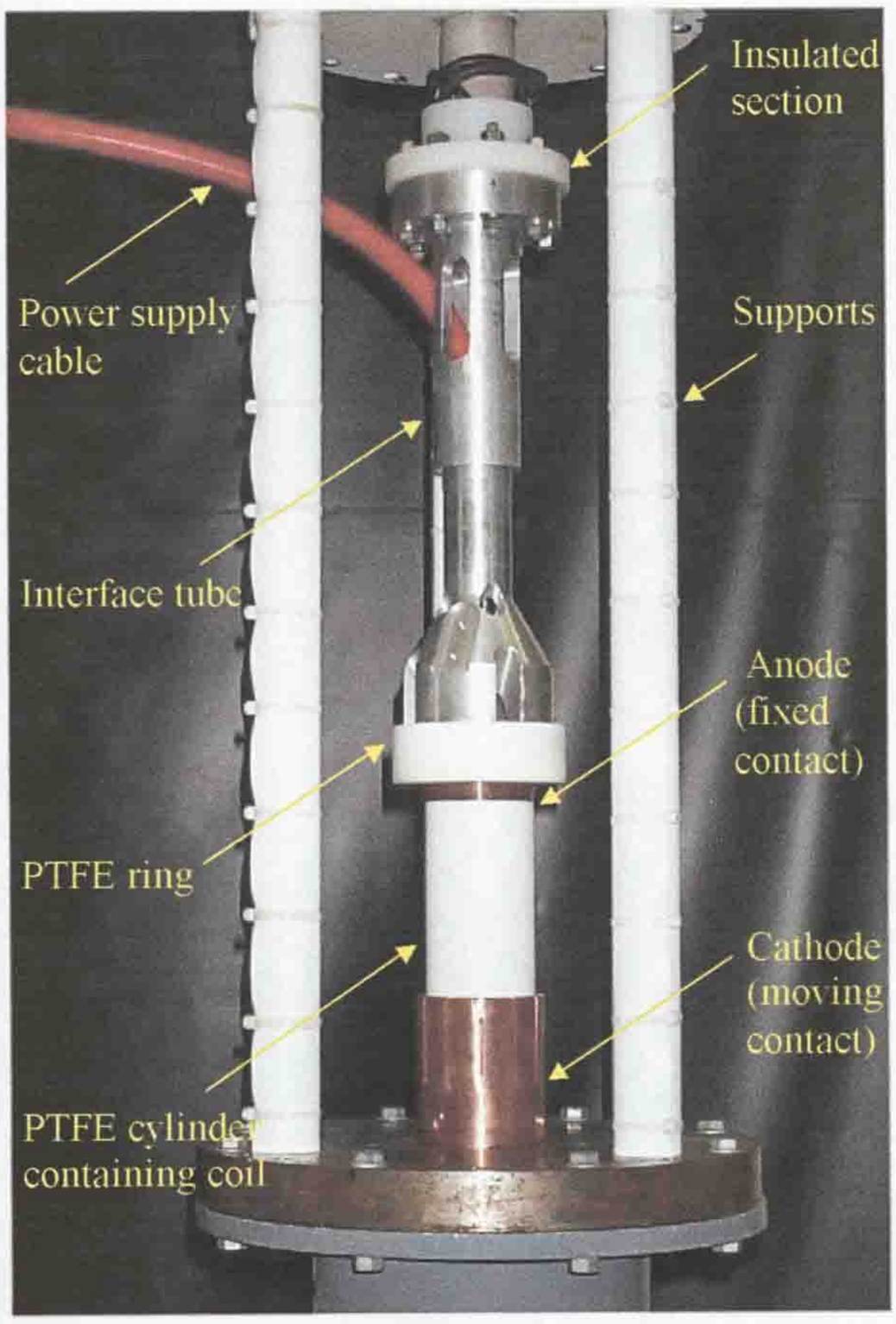

Figure 3.8 The current interrupter head assembling

From the mechanical point of view, the PTFE cylinder directs the cathode towards the anode providing direct movement (i.e. without a stress contact travel) of the cathode at the time of electrodes mating. Three insulated steel columns, wrapped within the white PTFE material, support the current interrupter head, which are fixed on the metal base of the hydraulic system. The hydraulic system supports the vertical movement of the travel rod that is connected to the cathode. The instantaneous acceleration of the movable rod is depends on the weight of the cathode. As a result, the holes, which are observed on the cathode, reduce the total weight of the cathode to alleviate the mechanical load on the hydraulic system via the movable rod (fig. 3.9). The power supply unit is connected through the red cable (fig. 3.8), carries the main current to the experimental circuit breaker head. The Aluminium interface tube is connected with an insulated section that is used to electrically isolate the current

interrupter head from the chamber (fig. 3.8). Photographs of the electrodes positions at various times during interrupter operation are shown in figure 3.9. In the mated contact state, (fig. 3.9a) the electrodes are connected. In this position, the finger-contact of the cathode makes good electrical contact with the anode. In the arc discharge state, the electrodes are separated (fig. 3.9b) and an electrical arc is ignited between the electrodes. It interacts with the spatially variable cross magnetic fields produced by the coil. In the interruption state, the ac-arc should be extinguished at current zero, (fig. 3.9c).

a) Contacts closed *b) Contacts partially open* *c) Contacts fully open*

Figure 3.9 Electrodes position of the interrupter head

The experimental model operating in air, at atmospheric pressure provides good access for external visual observation during the series of tests to be performed.

3.2.4 Components

An explored view of the components of the experimental current interruption test head (**Appendix V**) is shown in figure 3.10. The Aluminium anode-holder is connected with an insulated section (fig. 3.8), which is used to electrically isolate the current interrupter head from the chamber. The Aluminium collar is used for adjusting the anode-interface that ensures good contact between the anode and the cathode. The PTFE ring was used to protect the anode-interface from the electric arc. The copper anode is connected with the anode-interface thought the PTFE ring. The PTFE cylinder is connected with the anode inside which the coil is fixed. The copper movable rod and cathode are connected together in conjunction with the

PTFE cylinder and the anode. The power supply system produces a main current, which is connected to the power supply cable and the coil in series.

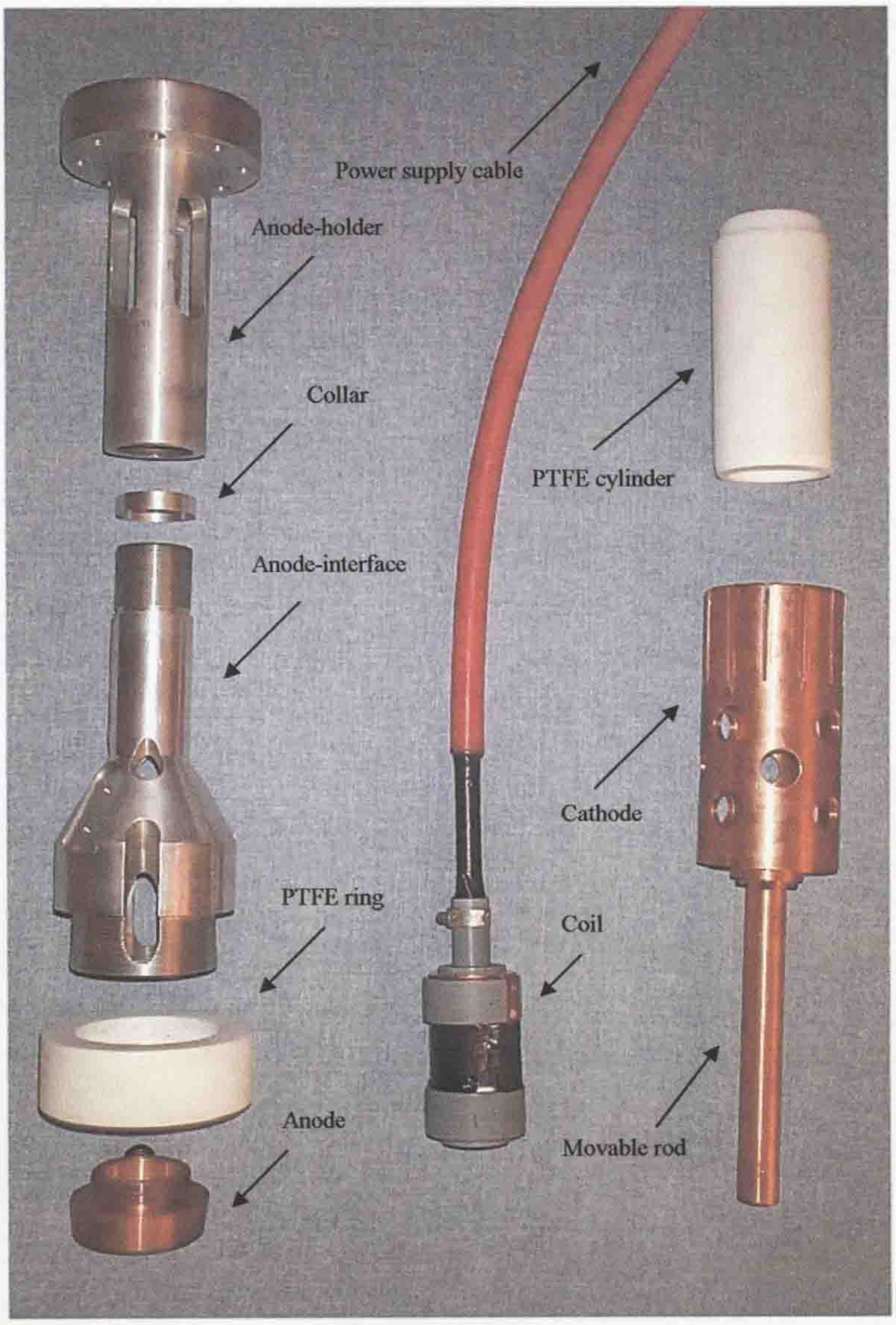

Figure 3.10 Interrupter head components

3.2.5 Assembled unit

This section shows details of the components, which are assembled to form of the rotary arc interrupter and which is shown in figure 3.11. The scale of the drawing is 4:1 and the colour-scale in the figure corresponds to the different materials used in the experimental model. The function of each part is as previously discussed in **section 3.2.4**. However, the function of the outer PTFE cylinder, which

is shown in the figure 3.11 has been described in **section 3.3** where the novel rotary arc interrupter design is presented.

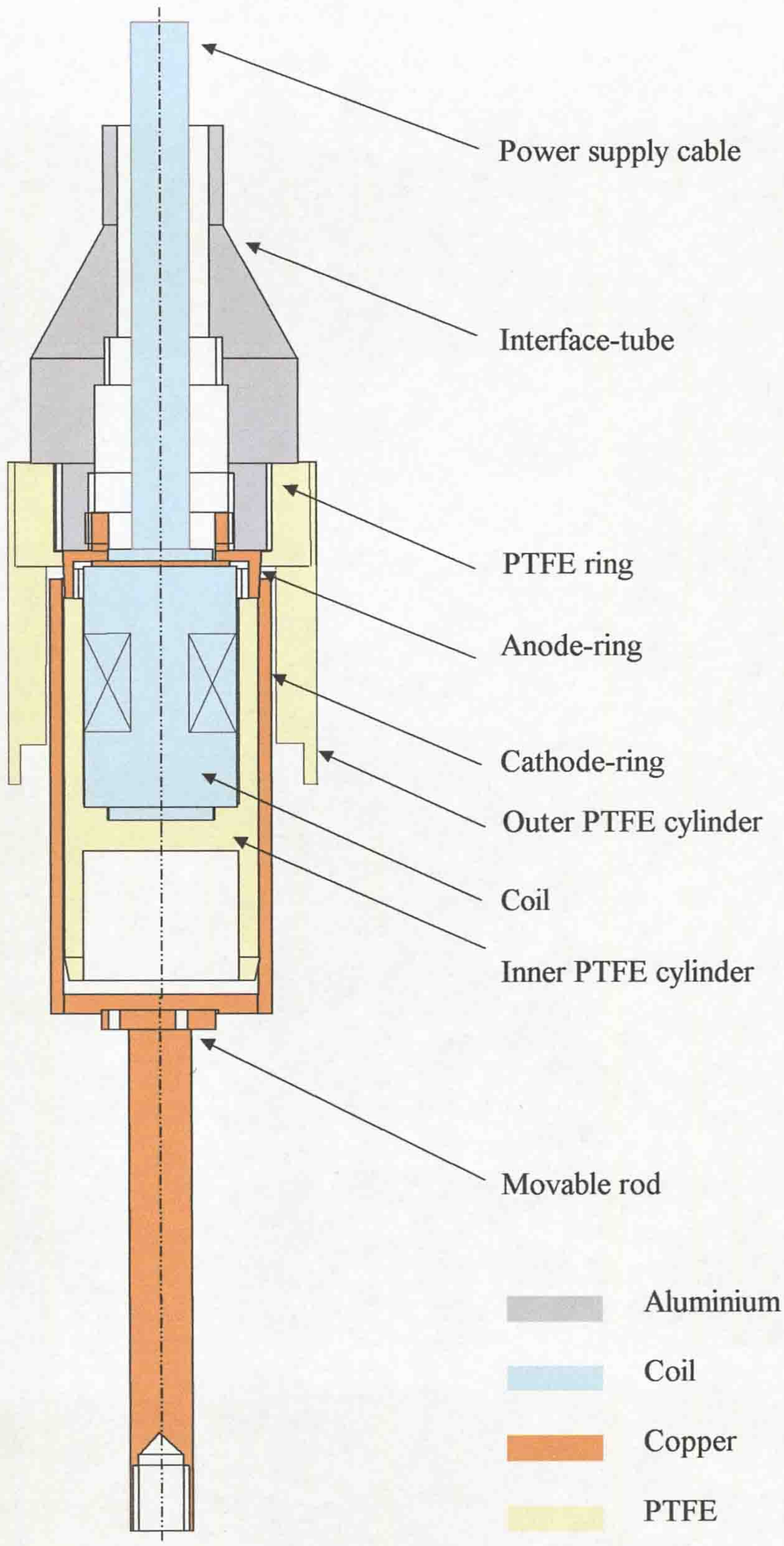

Figure 3.11 Interrupter assembly

3.3 EVALUATION OF THE INTERRUPTER HEAD DESIGN

The prototype rotary arc interrupter design is presented, which is an evaluation of the interrupter head design (**section 3.2**). Philosophy of the interrupter design is described, providing a base concept of the recently designed technology.

3.3.1 Philosophy of the new rotary arc interrupter

A major objective of this project is to design a new rotary arc interrupter, in which the technique of the arc interruption will be more effective providing the requirements that are mentioned above (**section 3.2.1**) in removing the need to use SF_6 as the quenching medium and in reducing maintenance requirements.

3.3.2 Principle of operation

The principle operation of the prototype rotary arc interrupter is based on the rotary arc interrupter head design, which has been tested in air, at atmospheric pressure, and at different fault current ratings. The geometric shape of the interrupter head uses as a base of the prototype rotary arc interrupter (**section 3.2**). The principle operation of both designs is based on the use of the rotary arc operating by the spatial variation of a magnetic field produced by a coil. Optical external observations for the interrupter head operation determined the base concept of the prototype interrupter operation. In order to increase the effectiveness of the operation of the interrupter head, the outer PTFE cylinder was designed and to be fixed around the interrupter head (fig. 3.11). The geometry of the outer PTFE cylinder was designed using the results obtained from the interrupter head optical observation (high-speed photographs) utilizing dc and ac arcing tests, which are presented in the **section 5.2.3.5**. Analyzing the arc behaviour close to current zero, the optimal shape of the outer PTFE cylinder was made in the shape of a nozzle. This provides a number of additional effects to support good conditions for arc extinction at current zero. The nozzle shape of the outer PTFE cylinder may provide a good aerodynamic characteristic of the interrupter immediately after current zero, improving the dielectric strength recovery conditions inside the breaker. Moreover, the inner and outer PTFE cylinders may provide additional arc extinction effects by increasing the

PTFE ablation. Finally, the outer PTFE cylinder electrically insulates the interrupter head from making electrical contact with the outer metal chamber that could be used as a gas container in future experimental work for investigating different arc extinction media.

3.3.3 Prototype of the rotary arc interrupter

Figure 3.12 shows the prototype rotary arc interrupter assembly in air,

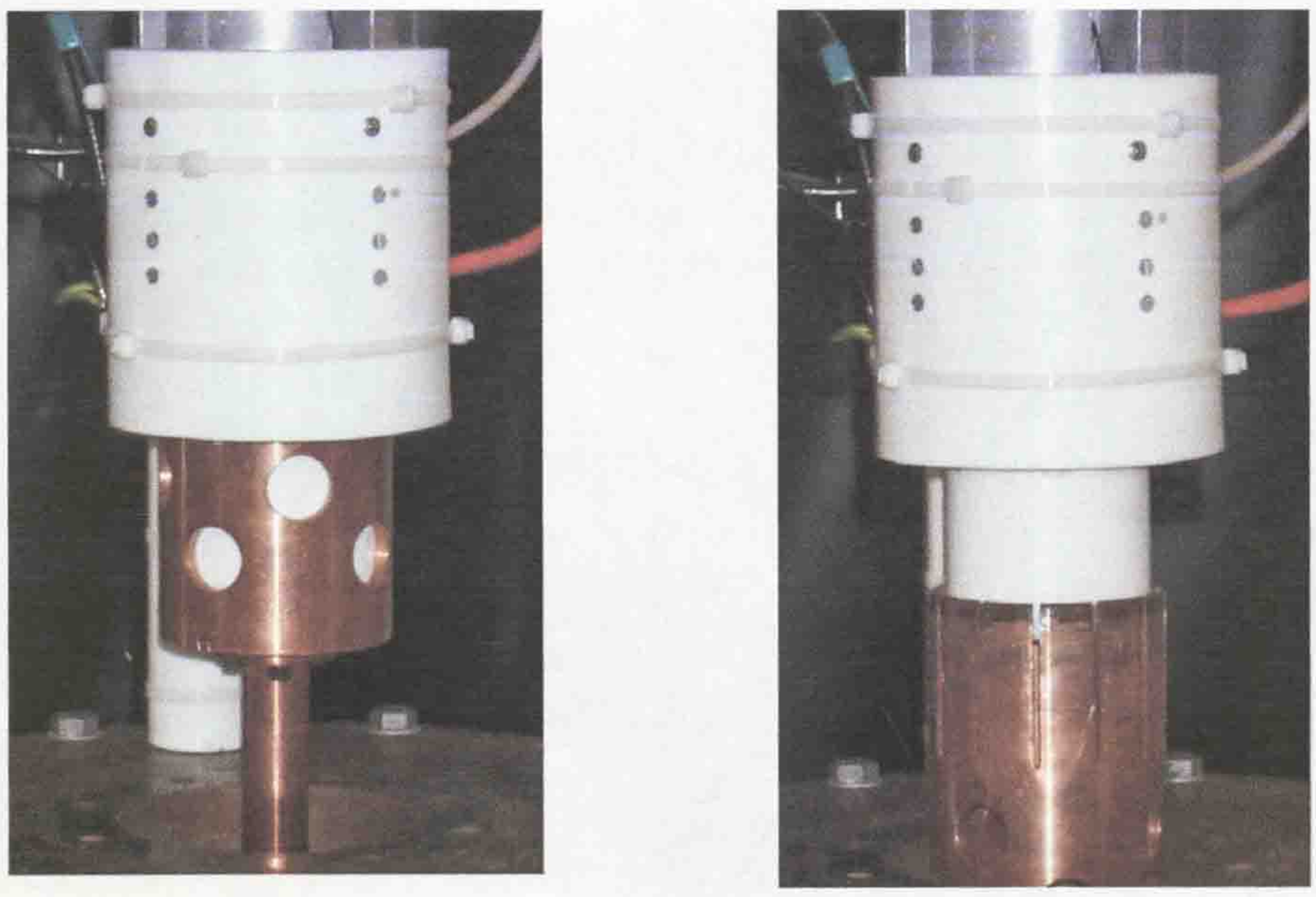

a) Contacts closed b) Contacts open

Figure 3.12 Prototype rotary arc interrupter assembly

at atmospheric pressure (open rig). The position of the cathode indicates the stage of the interrupter operation. The contact stage (fig. 3.12a) indicates that the anode and cathode are electrically connected. The Interruption stage (fig.3.12b) demonstrates that the electrodes are disconnected while the electrical arc is extinguished.

3.3.4 Assembly

The structure of the prototype rotary arc interrupter is shown in figure 3.11 at approximately ¼ size. A colour-scale in figure 3.11 distinguishes the different materials used in the interrupter head and the purpose of each part has already been

described in the **section 3.2.4** except for the outer PTFE cylinder (**Appendix V**). Two different effects are observed with and without outer PTFE cylinder. The outer PTFE cylinder determinates the gas flow direction at current zero. Moreover, two different volumes between the inner and outer PTFE cylinders are designed (at the top and bottom of the coil), providing a difference in pressures at current zero. The rotary arc causes the pressure between the PTFE cylinders to increase. The maximum gas flow should occur when the cathode is level with the bottom of the outer PTFE cylinder.

3.4 THEORETICAL MODELLING OF THE MAGNETIC FIELD PRODUCING COIL

The geometric structure of the interrupter units designed for the present investigations have been shown on figures 3.6 and 3.11. These will now be described in term of their electromagnetic characteristics. A colour-scale is used in figures 3.6 and 3.11 to distinguish between the different materials used in these devices. With regard to the B field producing coil the winding were made of a thin, wide copper strip having rectangular cross-section (fig. 3.4). This leads to a non-uniform current distribution in the circular (air-core) cylindrical coil (**Appendix III**). The position of the coil is sufficiently far from any other conducting material in which there could be induced currents. In addition, no ferromagnetic material was used in the designed structures. Potential induced current is ignored in this calculation. However, a validity of this assumption will be checked from the experimental results (fig. 4.16). Low frequency B field calculations have been used for the estimation of the B field external to the coil. These calculations were made rather then using software packages such as "Opera-2d" because the non-uniform distribution of current in the coil winding is difficult to accommodate in such software packages. The method becomes available for B field calculations for possible future coil designs.

3.4.1 Derivation of the theoretical model

The calculation of the magnetic field produced by a coil in free space for relatively slow time-varying currents is described. The Biot-Savart law (Johnk, 1988), relating magnetic field to current, quantifies the B field at a point in space due

to an element of current flow. Another approach for determining the magnetic field is to use an auxiliary potential field, in this case a vector. In fact, any B field has the solenoidal property, that is:

$$\nabla \times B = 0 \tag{3.5}$$

The divergenceless property (3.5) specifies that the B flux lines are always closed so that B may be expressed in terms of an auxiliary vector function A by means of the curl relation (Johnk, 1988):

$$B = \nabla \times A \tag{3.6}$$

The function A defined by (3.6) is called the vector magnetic potential field. Identification of the vector magnetic potential in free space produced by a circular loop carrying current is given in figure 3.13. This shown that the element of current Idl' at a typical source point P' produces at any fixed field point P a vector contribution dA parallel to the element Idl'. In addition, the magnitude of its influence at P is inversely proportional to the distance r from the loop (as a source). This is valid provided $r>>a$. This approximation provides a significant simplification for calculating a magnetic field at any point in space.

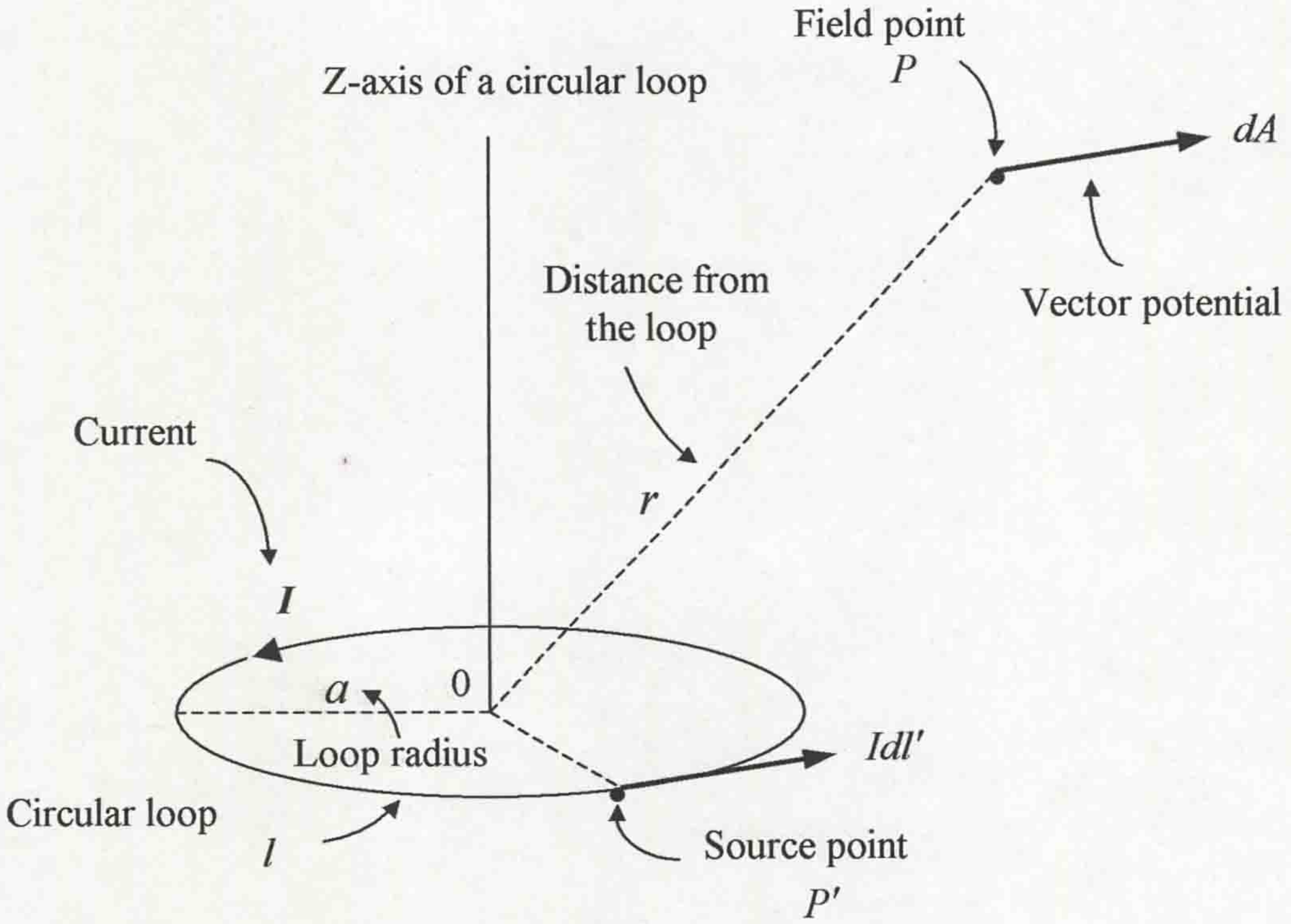

Figure 3.13 Circular loop carrying a current I, producing magnetic field at point P

The magnetic field of a single turn coil (fig. 3.14) can be given in terms of the vector magnetic potential at P (Johnk, 1988) by

$$B = curl\ A = \nabla \times A \tag{3.7}$$

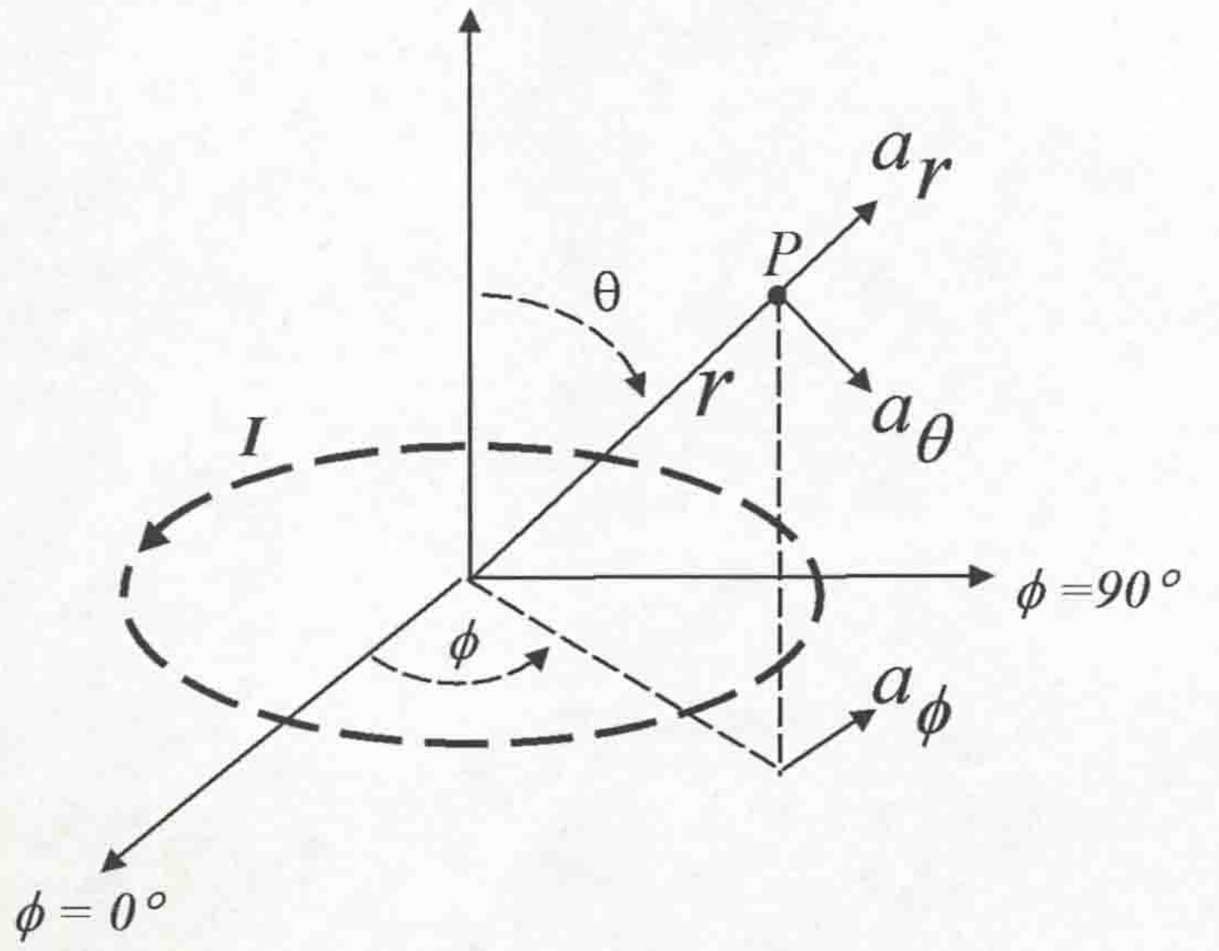

Figure 3.14 Circular loop, showing the spherical coordinate geometry adopted for finding the magnetic field at P

The curl in spherical coordinates (Portis, 1978) is

$$curl\ A = \nabla \times A = \frac{1}{r\sin\theta}\left[\frac{\partial}{\partial\theta}\left(A_\phi \sin\theta\right) - \frac{\partial}{\partial\phi}A_\theta\right]a_r +$$
$$+\frac{1}{r}\left[\frac{1}{\sin\theta}\frac{\partial}{\partial\phi}A_r - \frac{\partial}{\partial r}\left(rA_\phi\right)\right]a_\theta + \tag{3.8}$$
$$+\frac{1}{r}\left[\frac{\partial}{\partial r}\left(rA_\theta\right) - \frac{\partial}{\partial\theta}A_r\right]a_\phi$$

Where θ is the vertical angle, ϕ is the azimuthal angle

$a_r; a_\theta; a_\phi$ are the unit vectors,

$A_r; A_\theta; A_\phi$ are the vector potential magnitudes along r, θ, ϕ

Thus for the simple circular current which is shown in figures 3.13 and 3.14 the lines of A are also circles, concentric with the current loop ($A_r = A_\theta = 0$)

$A_\phi = \frac{\mu m}{4\pi r^2}\sin\theta$ - Vector potential is present along ϕ and the magnetic field in free

space for an elemental circular loop is generated (Johnk, 1988). The vector magnetic potential field at P is:

$$A = 0 \times a_r + 0 \times a_\theta + \frac{\mu m}{4\pi r^2} \sin\theta \times a_\phi \tag{3.9}$$

Where m is a magnetic dipole $m = \pi a^2 I$, and

a radius of the turn

I current

Then

$$B_r = \frac{1}{r\sin\theta}\left[\frac{\partial}{\partial\theta}\frac{\mu m}{4\pi r^2}\sin\theta - 0\right] = \frac{\mu m}{4\pi r^3 \sin\theta}\frac{\partial}{\partial\theta}\sin^2\theta = \tag{3.10}$$

$$= \frac{\mu m}{4\pi r^3 \sin\theta} 2\sin\theta\cos\theta = \frac{\mu m}{2\pi r^3}\cos\theta$$

and

$$B_\theta = \frac{1}{r}\left[\frac{1}{\sin\theta}\times 0 - \frac{\partial}{\partial r}\frac{r\mu m}{4\pi r^2}\sin\theta\right] = \frac{1}{r}\left[-\frac{\mu m}{4\pi}\sin\theta\frac{\partial}{\partial r}\frac{1}{r}\right] = \frac{\mu m}{4\pi r^3}\sin\theta \tag{3.11}$$

Finally $B_\phi = 0$ (3.12)

The total magnetic field at a point field external to a coil will be calculated as the assumption of a uniform current density in a turn and by considering the field due to a single elemental turn and integrating over the radius and length of the coil. The coil is assumed to be composed of a series of radial sections each of the form shown on figure 3.15. The total magnetic field may be determined by summing the fields due to each of the elemental coils.

If the thickness of a single turn is *dz*, length of the coil is *h*, the number of turns N and the total current is I then the current density is $J=NI/h(a_2 - a_1)$. Where a_1 and a_2 are the inner and outer radii of the turn. For the radial element *da* (fig. 3.15) at a radius a the current is:

$$I' = Jdadz \tag{3.13}$$

and

$$m' = \pi a^2 I' = \pi J dz a^2 da \tag{3.14}$$

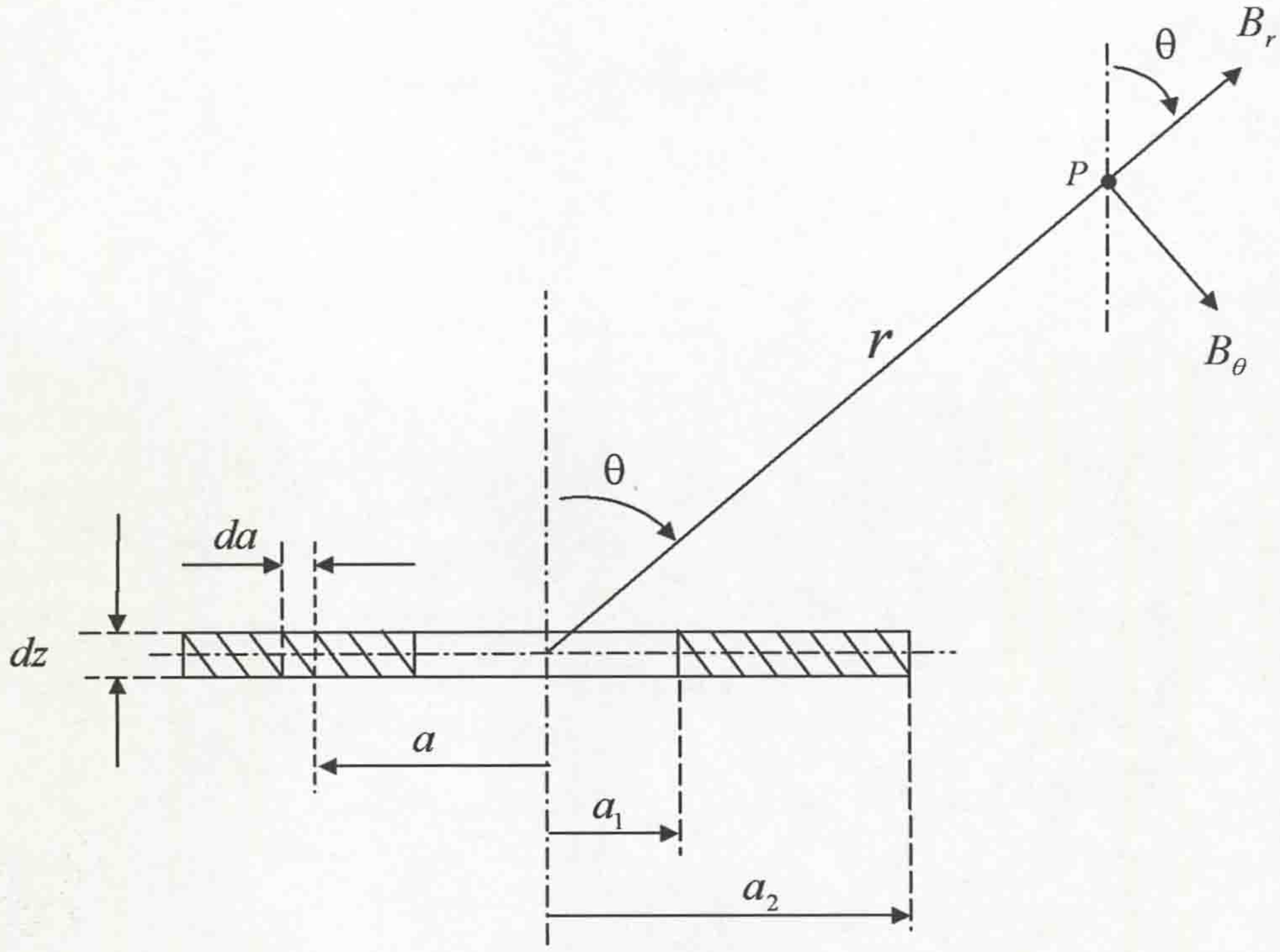

Figure 3.15 B field due to a radial element of thickness *dz* of a solenoid

Thus for the element *da* the components of B using equations (3.10) and (3.11) are

$$\Delta B_r = \frac{\mu m'}{2\pi r^3}\cos\theta = \frac{\pi J\mu}{2\pi r^3}\cos\theta dz a^2 da \tag{3.15}$$

and

$$\Delta B_\theta = \frac{\mu m'}{4\pi r^3}\sin\theta = \frac{\pi J\mu}{4\pi r^3}\sin\theta dz a^2 da \tag{3.16}$$

For the entire radial element (fig. 3.15) the components of B are

$$B_r = \int_{a_1}^{a_2}\frac{\mu\cos\theta}{2\pi r^3}\pi J dz a^2 da = \frac{\mu\cos\theta}{2r^3}dz \times \frac{NI}{h(a_2-a_1)} \times \frac{\left(a_2^3-a_1^3\right)}{3} = \tag{3.17}$$

$$= \frac{\mu\cos\theta}{6r^3 h} NI dz\,(a_2^2 + a_1 a_2 + a_1^2)$$

and

$$B_\theta = \int_{a_1}^{a_2}\frac{\mu\sin\theta}{4\pi r^3}\pi J dz a^2 da = \frac{\mu\sin\theta}{4r^3}dz \times \frac{NI}{h(a_2-a_1)} \times \frac{\left(a_2^3-a_1^3\right)}{3} = \tag{3.18}$$

$$= \frac{\mu\sin\theta}{12r^3 h} NI dz\,(a_2^2 + a_1 a_2 + a_1^2)$$

3.4.2 Preliminary magnetic field evaluations

The equations (**section 3.4.1**), which give the magnetic field for one layer, may be used to determine the B field for a planar circular coil. In order to compare the measured and calculated magnetic flux densities it is necessary to determined the flux densities with respect to a rectangular (cartesian) coordinate system i.e. B_x and B_z. Where B_x is the component along the coil radius and B_z the component along the coil axis. Derivation of expressions for B_x and B_z is given in **Appendix II**. These expressions being as follows:

$$B_z = \frac{\mu NI(a_2^2 + a_1 a_2 + a_1^2)}{6h} \times \times \int_0^h \left\{ \frac{(z_0^2 - 2z_0 z + z^2)}{\left[z_0^2 - 2z_0 z + z^2 + {x_0}^2\right]^{\frac{5}{2}}} - \frac{x_0^2}{2\left[z_0^2 - 2z_0 z + z^2 + {x_0}^2\right]^{\frac{5}{2}}} \right\} dz \tag{3.19}$$

and

$$B_x = \frac{\mu NI(a_2^2 + a_1 a_2 + a_1^2)}{4h} \times \times \int_0^h \left\{ \frac{x_0(z_0 - z)}{\left[z_0^2 - 2z_0 z + z^2 + {x_0}^2\right]^{\frac{5}{2}}} \right\} dz \tag{3.20}$$

Where a_1, a_2 are the inner and outer radii of the coil, h is the length of the coil, x_0, z_0 are the Cartesian coordinates of the point at which the field is B_x, B_z, the origin of the Cartesian coordinates being on the axis of the coil at an end. In general, possible so recourse needs to be made to numerical integration using software packages such as MathCAD. The total value of the B field in Tesla at a point $P(x_o,z_o)$ is:

$$B = \sqrt{\left(B_x^2 + B_z^2\right)} \tag{3.21}$$

The orientation of the total B field relative to B_x and B_z is given by:

$$\phi = \text{atan}\left(\frac{B_z}{B_x}\right) \text{[Radian]}, \quad \text{Where: Radian x } (180°/\pi) \Leftrightarrow \text{degree} \tag{3.22}$$

Thus the total field at any point (x,z) external to the solenoid can be calculated using the analytical solution presented above (Turner, 2005).

Figure 3.16 shows the geometric layout of the coil, arc anode, PTFE cylinder and 16 points at which the magnetic field was calculated.

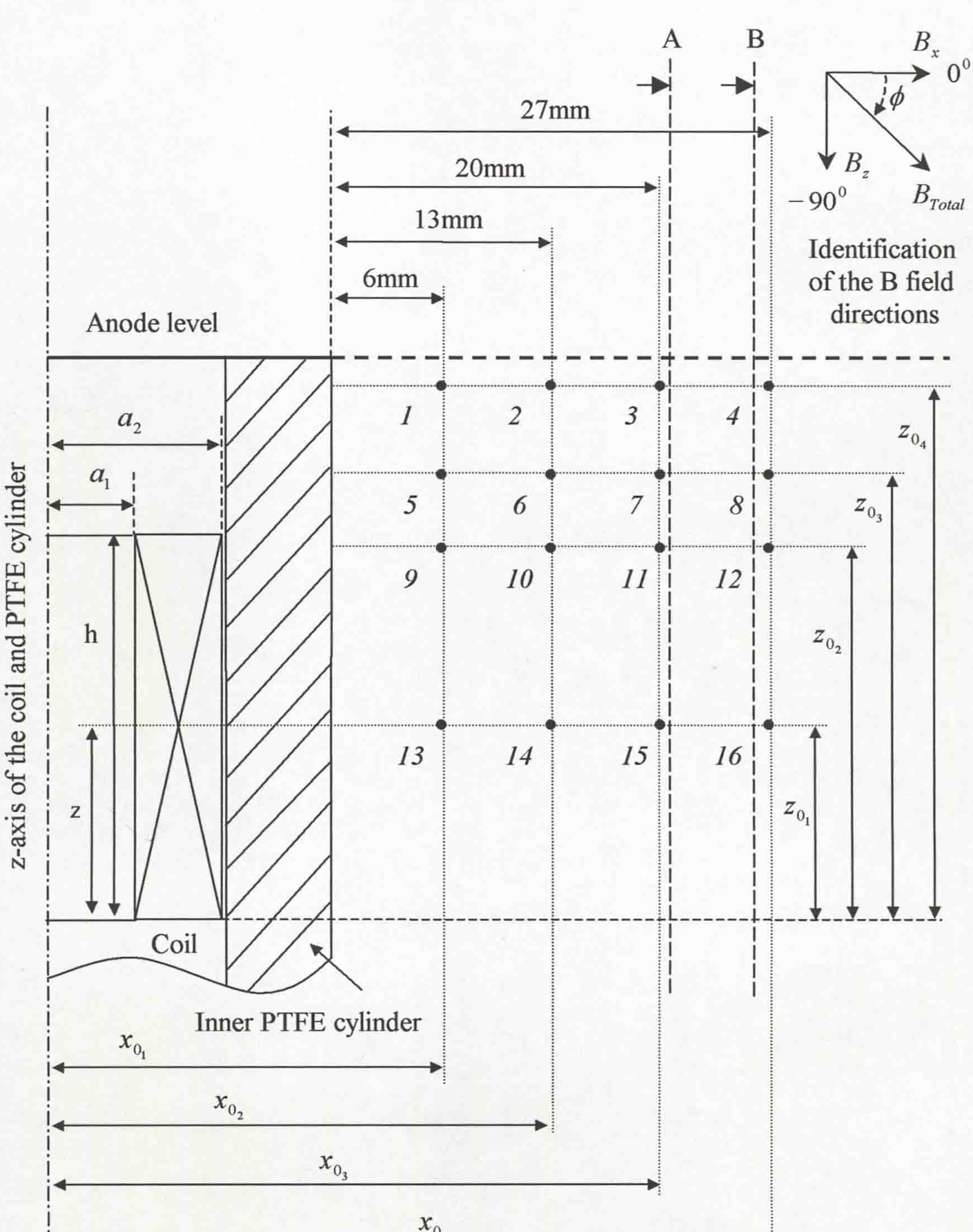

Figure 3.16 Coil geometry showing the arc anode, inner PTFE cylinder and 16 points at which the magnetic field was calculated

Where the parameters utilizing in the analytical solution relevant to the designs are given in Table 3.1. The nearest point at which practical measurements could be made external to PTFE cylinder was for the x coordinate (fig. 3.16) $x_{0_1} = 0.056\text{m}$ (6mm from the cylinder). The nearest axial position to the anode was at $z_{0_4} = 0.068\text{m}$ (~0mm from the anode).

The results of computed B field values (Tables 3.3, 3.4, and 3.5) are given at the positions represented on Table 3.2 under the certain conditions (Tab. 3.1). On the Table 3.2, the position of the measurements is given in term of the distance from the PTFE cylinder (rather than x_0) and the position from the anode (rather than z_0).

Parameter	Value	Unit	Meaning
μ	$4\pi \times 10^{-7}$	H/m	Permeability in free space (vacuum)
h	0.05	m	Length of the coil
z	from 0 to h	m	Height of an individual layer
I	5.3	kA	Peak ac current
N	16		Number of turns
a_1	0.020	m	Inner radius
a_2	0.038	m	Outer radius

Table 3.1 Coil operational parameters

		x_0	x_{0_1}	x_{0_2}	x_{0_3}	x_{0_4}
		m	0.056	0.063	0.070	0.077
z_0	m	mm	6	13	20	27
z_{0_1}	0.025	43	***13***	***14***	***15***	***16***
z_{0_2}	0.046	22	***9***	***10***	***11***	***12***
z_{0_3}	0.053	11	***5***	***6***	***7***	***8***
z_{0_4}	0.068	0	***1***	***2***	***3***	***4***
			Points			

Table 3.2 Coordinates of measurement points

In addition, the positions of the inner and outer PTFE cylinders (A) of the prototype rotary arc interrupter are shown in figure 3.16. The initial gap between these surfaces was designed about 20mm (A) (fig. 3.11). However, after ablation of the both cylinders this space might be increased up to 27mm (B) (fig. 3.16). Therefore, the

theoretical calculation of the total magnetic field produced by the coil was extended up to 27mm (distance from the inner to outer PTFE cylinders).

Tab. 3.3, Tab. 3.4 and Tab. 3.5 show the peak values of B_x, B_z and B_{Total} fields produced at each designated point by a peak current of 5.3kA. These results indicate a maximum B_z field and a zero B_x field half way along the coil (i.e. the total field is axial). The negative values of the axial B fields (Tab. 3.4) show field's direction. Tab. 3.6 shows the orientation of the B field *(ϕ)* at each of these points.

Distance from the Anode, *mm*	B, mT Distance from the cylinder *6mm*	B, mT Distance from the cylinder *13mm*	B, mT Distance from the cylinder *20mm*	B, mT Distance from the cylinder *27mm*
0	89.37	67.01	50.91	39.17
11	93.32	66.89	48.98	36.55
22	78.31	54.44	38.84	28.34
43	0	0	0	0

Table 3.3 Outer radial B_x field

Distance from the Anode, *mm*	B, mT Distance from the cylinder *6mm*	B, mT Distance from the cylinder *13mm*	B, mT Distance from the cylinder *20mm*	B, mT Distance from the cylinder *27mm*
0	-5.10	-9.89	-11.79	-12.17
11	-33.66	-30.28	-26.54	-22.98
22	-66.35	-52.17	-41.57	-33.52
43	-100.2	-74.26	-56.31	-43.58

Table 3.4 Outer axial B_z field

Distance from the Anode, *mm*	B, mT Distance from the cylinder *6mm*	B, mT Distance from the cylinder *13mm*	B, mT Distance from the cylinder *20mm*	B, mT Distance from the cylinder *27mm*
0	89.51	67.73	52.25	41.02
11	99.21	73.41	55.70	43.17
22	102.63	75.40	56.88	43.89
43	100.2	74.26	56.31	43.58

Table 3.5 Outer total B field

Distance from the Anode, *mm*	Degree Distance from the cylinder *6mm*	Degree Distance from the cylinder *13mm*	Degree Distance from the cylinder *20mm*	Degree Distance from the cylinder *27mm*
0	-3.3°	-8.4°	-13.0°	-17.3°
11	-19.8°	-24.3°	-28.4°	-32.1°
22	-40.3°	-43.8°	-46.9°	-49.8°
43	-90°	-90°	-90°	-90°

Table 3.6 Angle ϕ of the total B field

Figures 3.17a (Tab. 3.3), b (Tab. 3.4) and c (Tab. 3.5) show the spatial distribution of B_x, B_z and B_{Total} fields at various axial *r* positions (0-43mm) and radiuses of (6-27mm) refer to the grid shown on figure 3.16 at which calculations were made.

It was found that maximum value of external total magnetic field (~100mT, 6mm from the PTFE cylinder) occurred at the centre of the coil (r≈43mm) and minimum value (~90mT, 6mm from the PTFE cylinder) occurred at the level of anode (r≈0mm), (e.g. peak values for outer total magnetic field at the centre of the coil is greater then those at the end (level of anode)). The same regularity occurred at different distances (13mm, 20mm and 27mm) from the cylinder.

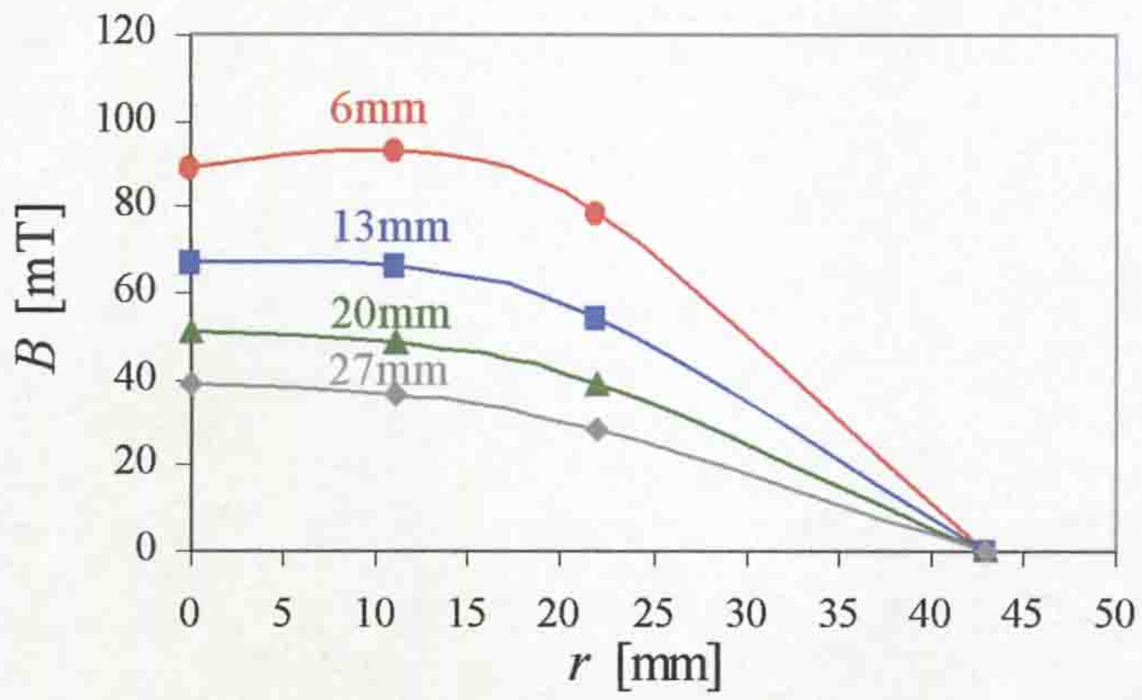

a) Radial B_x field component vs radius with axial (r) position as parameter (Tab. 3.3)

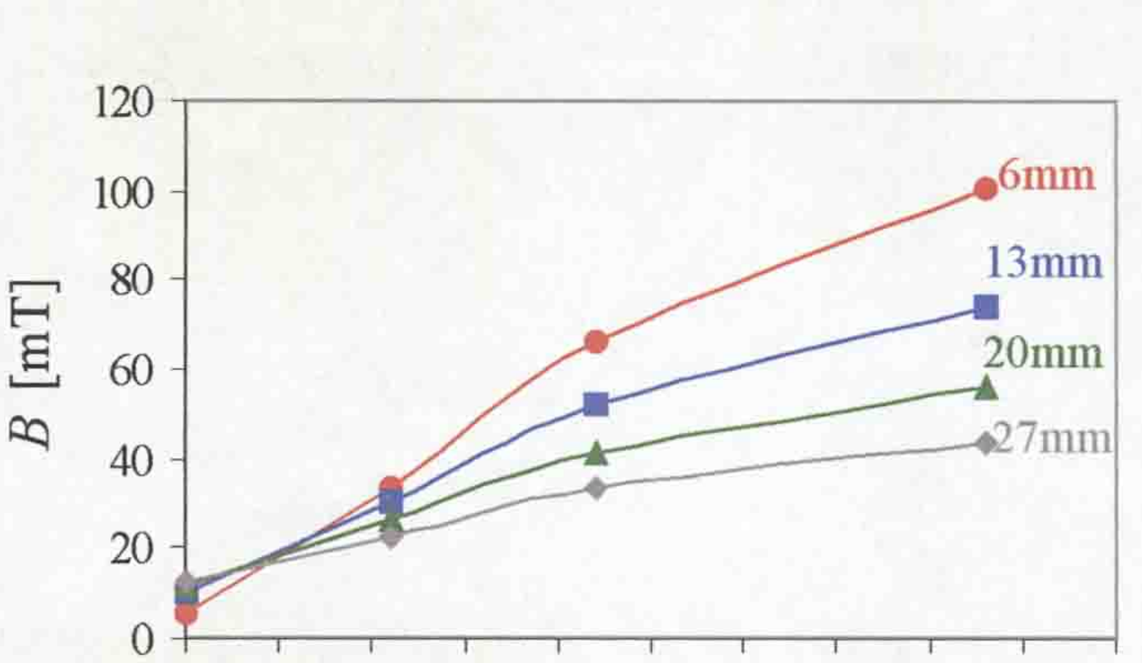

b) Axial B_z field component vs radius with axial (r) position as parameter (Tab. 3.4)

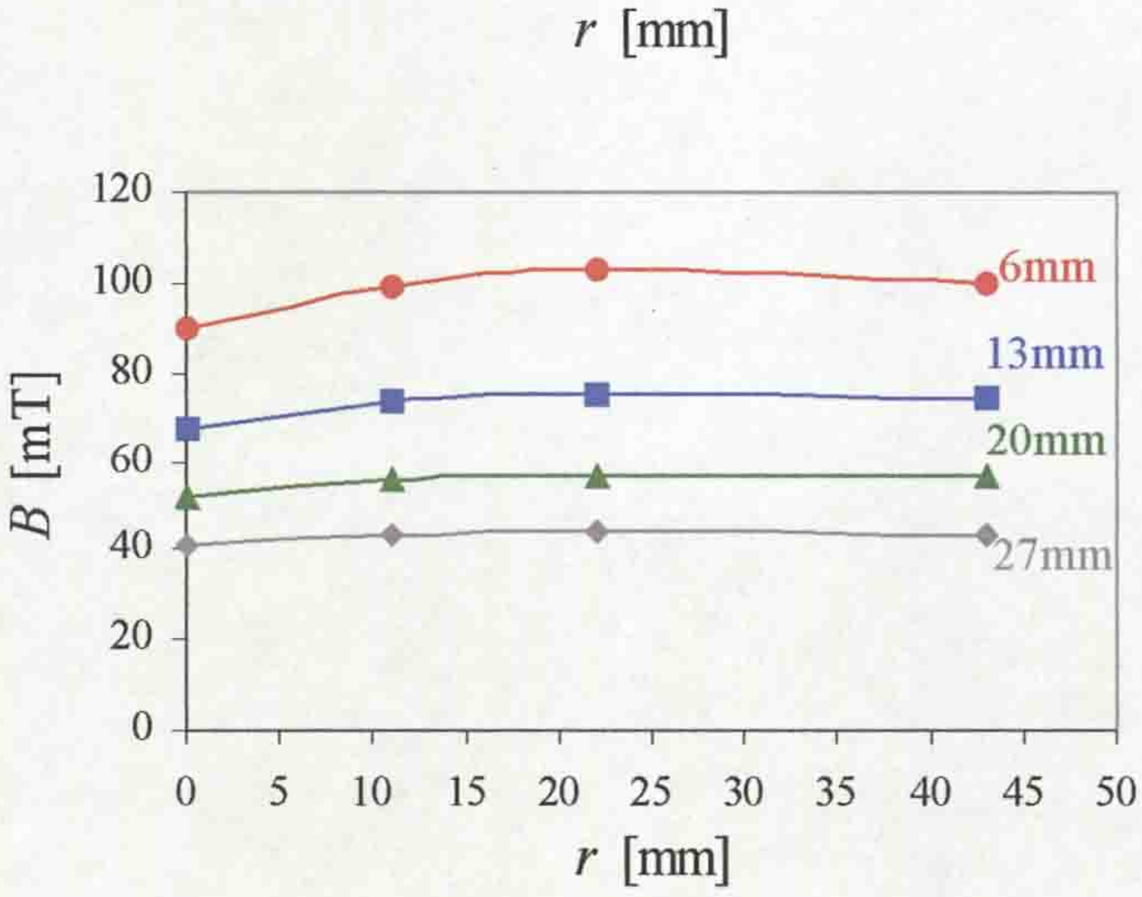

c) Total B_{Total} field component vs radius with axial (r) position as parameter (Tab. 3.5)

Figure 3.17 Magnetic field components at various axial positions

3.5 SUMMARY

In order to avoid expensive mechanisms required for circuit breaker operation a new concept for arc control is proposed based upon a novel form of rotary arc. Moreover, controlling and containing such an arc presents many technological challenges and has important implications commercially.

The new concept of the arc control (**section 3.1**) involves the deployment of magnetic fields for controlling the arc plasma. This showed enable substantially convoluted and produce an azimuthal plasma flow around to arc column itself. Consideration of the design of the model circuit breaker is made.

A novel rotary arc interrupter head is proposed (**section 3.2**), which yields a new design of a prototype rotary arc interrupter (**section 3.3**).

Finally, the theoretical modelling of the magnetic field producing coil (**section 3.4**) has been designed, which will be compared with experimentally measured values of the magnetic field, producing coil.

CHAPTER 4 - THE EXPERIMENTAL SYSTEMS

This section describes the experimental test facility and diagnostic measurements used for providing effective research for the design development of the units described in the **chapter 3**. Optical, electrical, mechanical-drive, dielectric strength, video tests etc. were used to determine the strategy of the design development during the project.

4.1 EXPERIMENTAL TEST FACILITY

4.1.1 Power supply unit

Electric arcs generated in the experimental research laboratory at the University of Liverpool, Department of Electrical Engineering and Electronics. The power supply system, situated in the research laboratory, consisted of a capacitor bank, ignitrons switch unit and a central control unit, (fig. 4.1). The capacitor bank consisted of 192 capacitors. Each capacitor has a capacitance of 185μF and a maximum charging voltage of 6.3kV. The total capacitance of the bank was 35mF, giving a maximal stored energy of 695kJ. For simulation of a sinusoidal current around 50Hz, there was a coil of heavy cable having an inductance ~206μH, which resonates with the capacitor bank. This arrangement gave an un-damped frequency that was slightly changed by the loading present in the circuit. The ignitrons switch unit produced a quasi-dc and an alternative current (two half cycles) controlled by a central unit, supplying a maximal current up to 60kA.

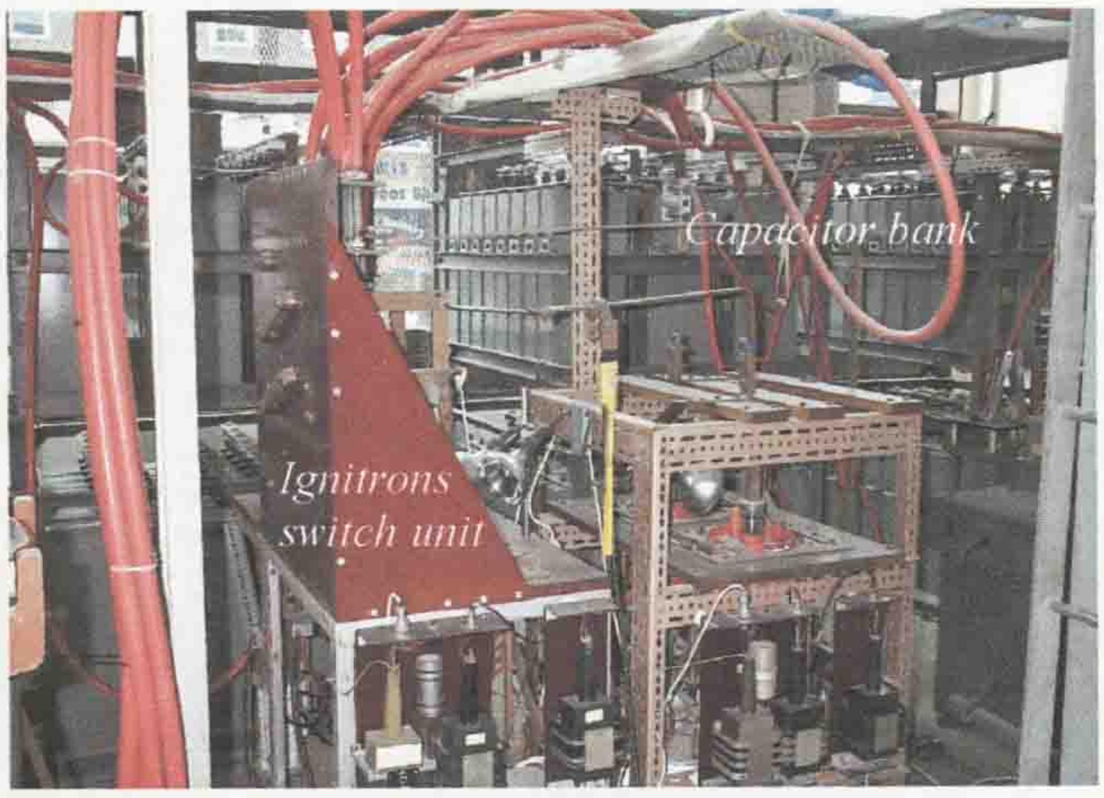

Figure 4.1 Power supply system

4.1.2 Vacuum and gas systems

The vacuum and gas systems shown in figure 4.2 are operated for the safe handling of SF_6 and N_2 gases in the chamber of the circuit breaker. The process of changing the gas involves the following procedure. The vacuum system (fig. 4.2) extracts the used gas after a number of arcing tests to a special container. Thereafter a new gas is filled into the circuit breaker by the gas filling system (fig. 4.2). The operating pressure of the circuit breaker is up to 3bar (pressure gauge), (1bar =0.9869 atmosphere). The gas handling system is used to support these conditions in the experimental circuit breakers.

Fig. 4.2 Gas handling system

4.1.3 Synthetic test circuit

The synthetic test circuit, providing the currents and voltages for the experimental test investigations is shown in figure 4.3. The power supply system (**section 4.1.1**) produces the dc and ac main currents (through ignitrons IG1, IG2 for electric arcs) generation from the capacitor (35mF) via the inductance (~206μH). Ignitron IG3 was required for dumping any residual energy, stored on the capacitors, to experimental earth at the end of the test.

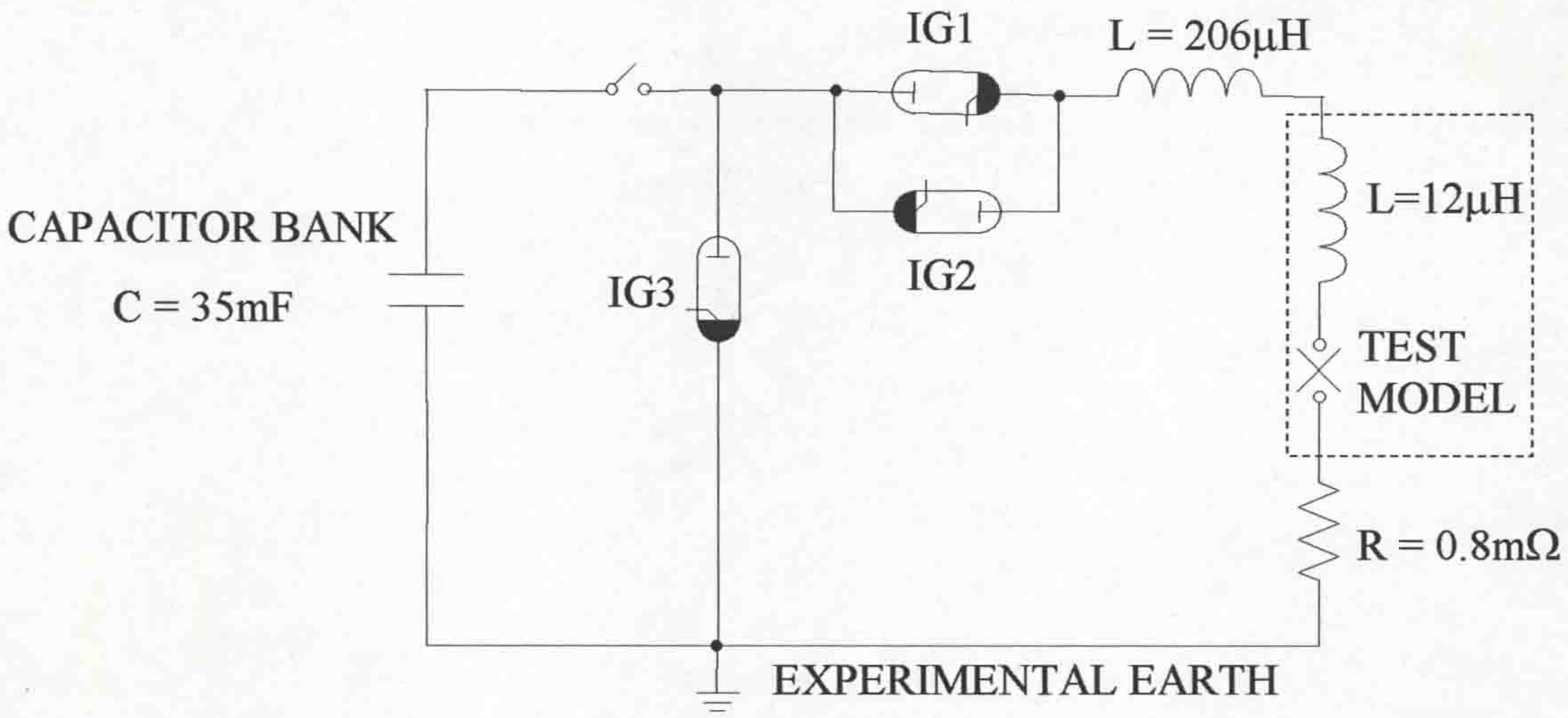

Figure 4.3 Experimental test circuit

The central control unit (CCU) controls the current and voltage magnitudes provided by the power supply to the test model via the ignitrons (IG1, IG2). It controls the test timing sequence during the experimental tests. In the case of the current interrupter model operation, only two half-cycles of current were necessary for the tests, since the breaker has a specified arc interruption time lying within this interval. The test model included the coil of 12μH (resistance of the coil is ~6mΩ) for the magnetic arc control, which was connected in series with the experimental test model and current shunt of 0.8mΩ (fig. 4.3). Experimental earth provided the earthing between the power supply system and the test model during the experimental test investigations.

4.1.4 Control and timing sequence

The operation of the experimental test facility was controlled by the CCU. The CCU provided trigger pulses for the different components of the high current circuit, including the diagnostic equipment with preset delays between pulses to achieve the correct timing sequence. The experimental timing sequence during the design development was different for each experimental test. Therefore, the tests sequence description for the each model (**chapter 3**) is described separately in **sections 4.1.6.2** for the arc control test head and in **section 4.1.6.3** for the current interruption test heads. **Section 4.1.6.1**, the design evaluation test head time sequence provided the experiment timing sequence for the preliminary arc tests (**section 5.2.1**) for design development (**chapter 3**).

4.1.5 Arc test head design geometries

The experimental facility for testing the models for the arc control and current interruption are introduced, including the design evaluation test head provided the preliminary arc tests for the arc test head design geometry. The diagnostic equipment arrangement test facility used for the investigations relevant for design and development of arc test head are described.

4.1.5.1 Design evaluation test head

An arrangement of PTFE materials in the circuit breakers is constantly evaluated for achieving the effective PTFE ablation (Telfer *et al*, 2002). Figure 4.4 demonstrates the PTFE arrangement (Kidman, 2003) in the non-rotary arc interrupter (reference breaker) that is evaluated on the basis of the previous design (Mori *et al*, 2002, 2005). The experimental device (fig. 4.4) provided an estimation of the PTFE arrangement into non-rotary arc interrupter for the design and modelling of a novel rotary arc interrupter geometry, which is presented in **chapter 3**. The power supply rod provided the electrical connection between the capacitor bank (producing quasi-dc and ac-arc current) and the ring electrode that is connected to the anode-contact. The inner PTFE rod, situated inside of the cylindrical copper cathode, is fixed in the

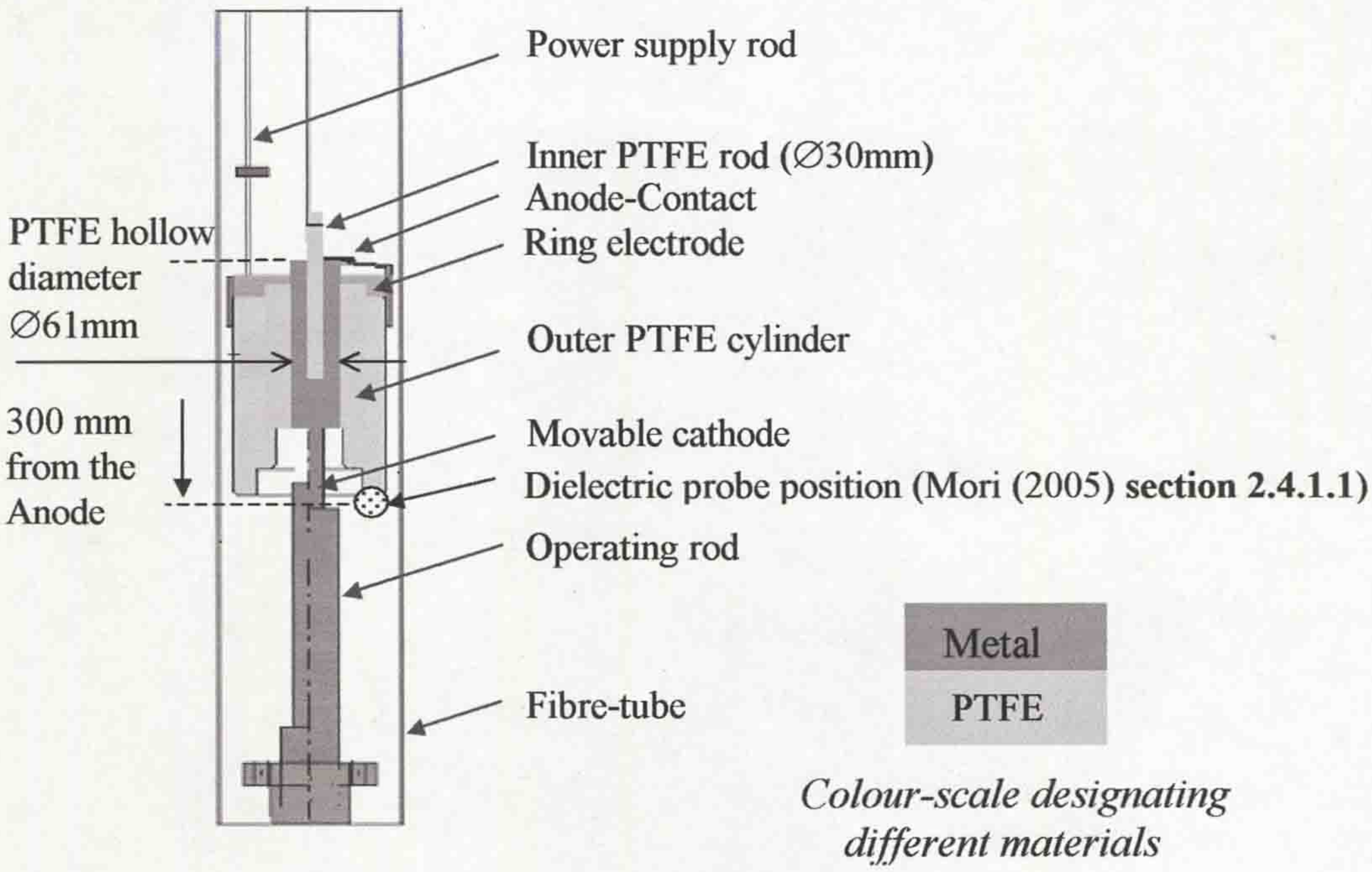

Figure 4.4 Non-rotary arc interrupter assembly

same position by the rod that is connected to the top part of the current interrupter. In the other words, when the movable cathode changes its position during retraction, the inner PTFE rod remains at the same position. The operating rod is connected with the movable cathode, operated by the hydraulic system. All parts are fixed inside of the fibre-tube within which the quenching gas (SF_6 or N_2) at different pressures (0-3bar) is contained, using a test circuit showing in figure 4.8.

4.1.5.2 Arc control test head

The electrical test circuit used in the experiments is shown in figures 4.5, 4.6. This consists of a capacitor bank for the main circuit including the arc and *B*-field producing coil which is situated inside of PTFE cylinder, (**section 3.1.1**, fig. 3.2).

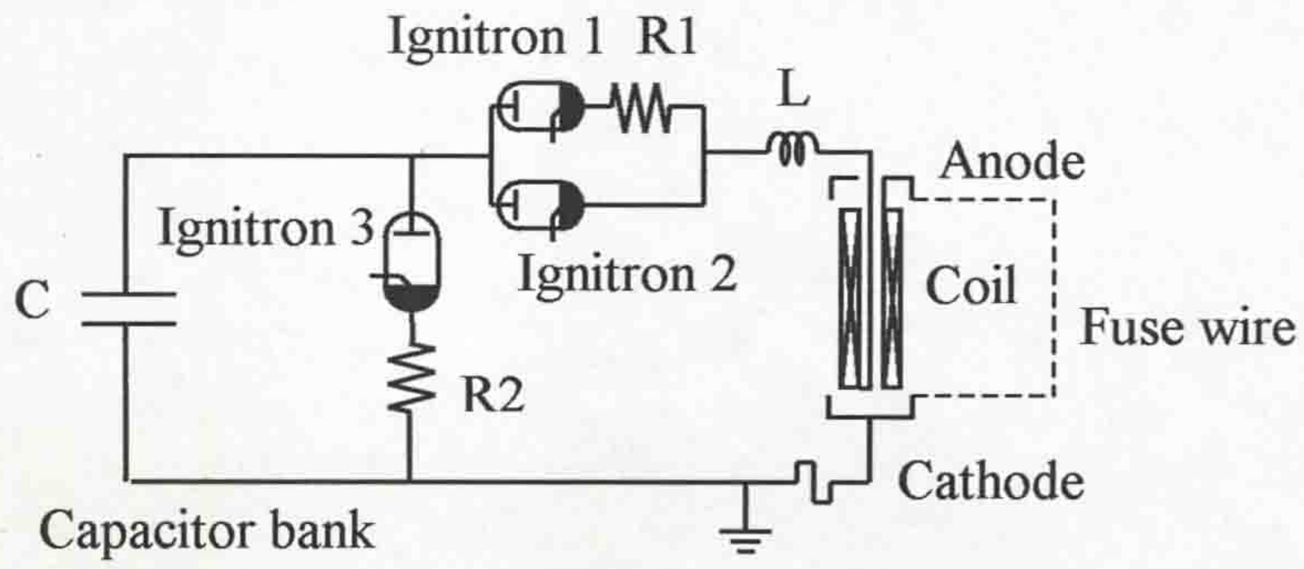

Figure 4.5 Test circuit

Ignitron 1 (Ign 1), connected in series with a resistor, is triggered to conduct a quasi-steady dc current through the coil and fuse wire. Ignitron 2 (Ign 2) is triggered to short circuit the current limiting resistor R1 and the first ignitron (fig. 4.5) and so produce a main half cycle sinusoidal current. The maximum duration of the electrical arc event is determined by triggering the dump ignitron 3 (Ign 3) at 30 ms after the switching of Ign 2 in order to dump the remaining energy from the capacitor bank through R2. The duration of the dc-arc discharge was set at 30ms, while the ac-arc was set at 10ms (one half cycle). For visual monitoring the electrical arc in real time, a high-speed camera and video recorder were used (figures 4.6, 4.7 and 4.10). The experimental investigations of the arc were divided into two parts. The first was the electrical arc measurements and the second was the visual arc observation before and after the current half cycle. Both the level of dc and ac arc current and voltage were recorded utilizing a digitizing oscilloscope (GW Instek GDS-830, **section 4.2.8.3**). A high voltage probe was used with a 1000:1 divider (Tektronix type P6015A, **section**

4.2.3) was used to measure the voltage and a current shunt, which had a resistance of 0.8 mΩ was used for the current measurement (**section 4.2.2**). High-speed photographs of the arc column were taken with a high-speed camera (**sections 4.2.7.2**, **4.2.7.3**). The exposure time for one frame was set at 6.6μs and a frame speed of 10000 frames per second was used for examining the dc-arc discharging period.

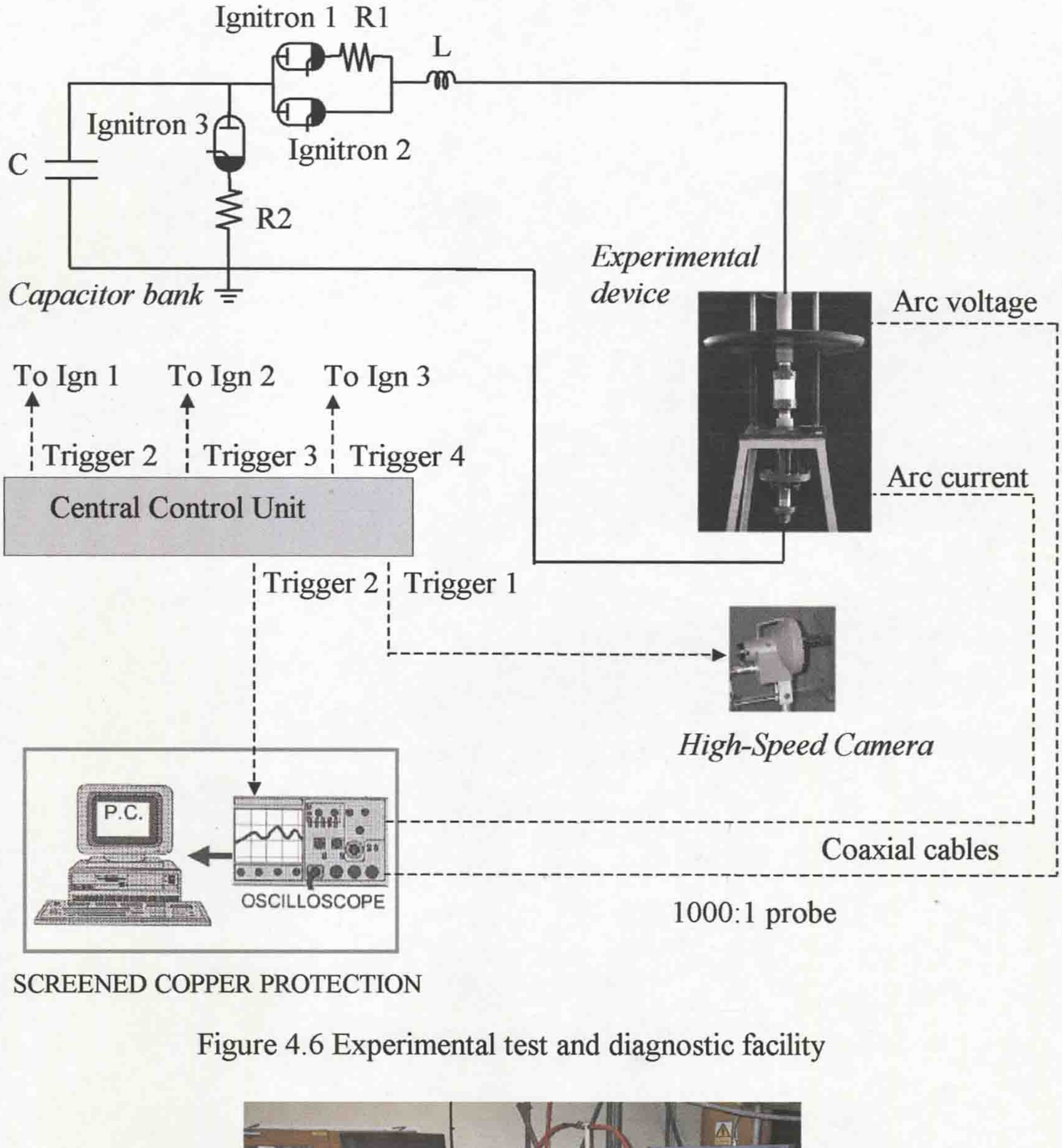

Figure 4.6 Experimental test and diagnostic facility

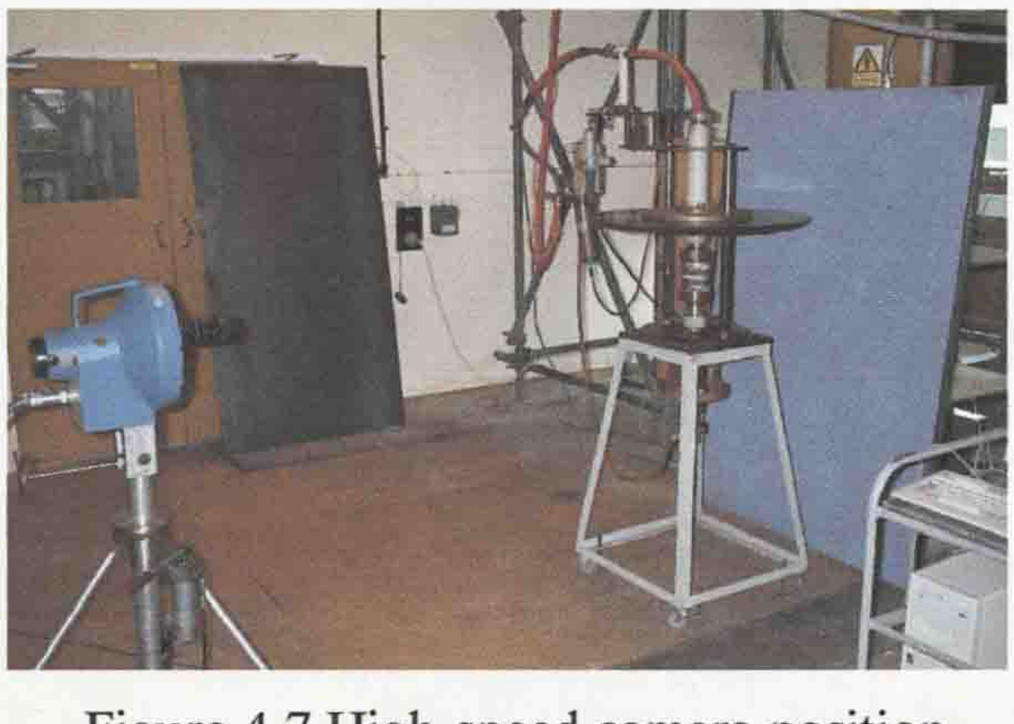

Figure 4.7 High-speed camera position

Black & white film (type XP2 SUPER 400) was used in the camera. A video camera was used to observe the rig after the dc and ac arcing with the frame duration set at 40ms per frame (**section 4.2.7.4**). A trigger pulse for the camera and recording oscilloscope were derived from the central control unit of the power supply system.

4.1.5.3 Current interruption test head

The test facility relevant to the interrupter design development (**sections 3.2** and **3.3**) is described, indicating the electrical, mechanical-drive, dielectric strength optical diagnostic equipment and test facility which are employed for the various experimental investigations. A range of experimental results relevant to the design evaluation test head (e.g. preliminary arc tests for design development, **section 4.1.5.1**) use the same test facility and diagnostic equipment and are presented in section (**section 5.2.1**). The timing sequences of experiments (**section 5.2.1**) are followed in the same manner as for the current interruption test head investigations (**section 4.1.6.3**). The test system including the diagnostic and power supply for the experimental test models is shown in figure 4.8. The test circuit has already been described in **section 4.1.5.2**. The power supply system and the central control unit organize the switching of the ignitrons that produce the quasi-dc and ac-arc currents, dumping the capacitor bank to the experimental earth at the end of tests. The equipment is screened from electromagnetic interference that can be produced by the burning arc. Electrical and optical probing are included ranging from the dielectric strength, arc speed/rotation, contact travel to optical monitoring etc. The optical sensors (situated close to the test model) were optical fibres rather than has been making from the electronically based. One of the advantages of the optical fibers in this kind of measurements is that the radio frequency radiation, propagating from the electrical arc cannot influence the measurement signal, because of its optical nature (Medlock, 1989). Moreover, the optical fiber provides good electrical insulation from high-voltages during the arcing time. The optical signal is detected and transformed into an electronic signal (**section 4.2.7.1**) that is recorded by an oscilloscope connected to a personal computer (PC). The high-speed cameras as well as the moving contact (cathode) mechanism have the same trigger operation (Trigger 1) as shown in figure 4.8. The initial arc discharge and rotation in the current interrupter head was found experimentally (fig. 4.9, e.g. off centre of the movable parts).

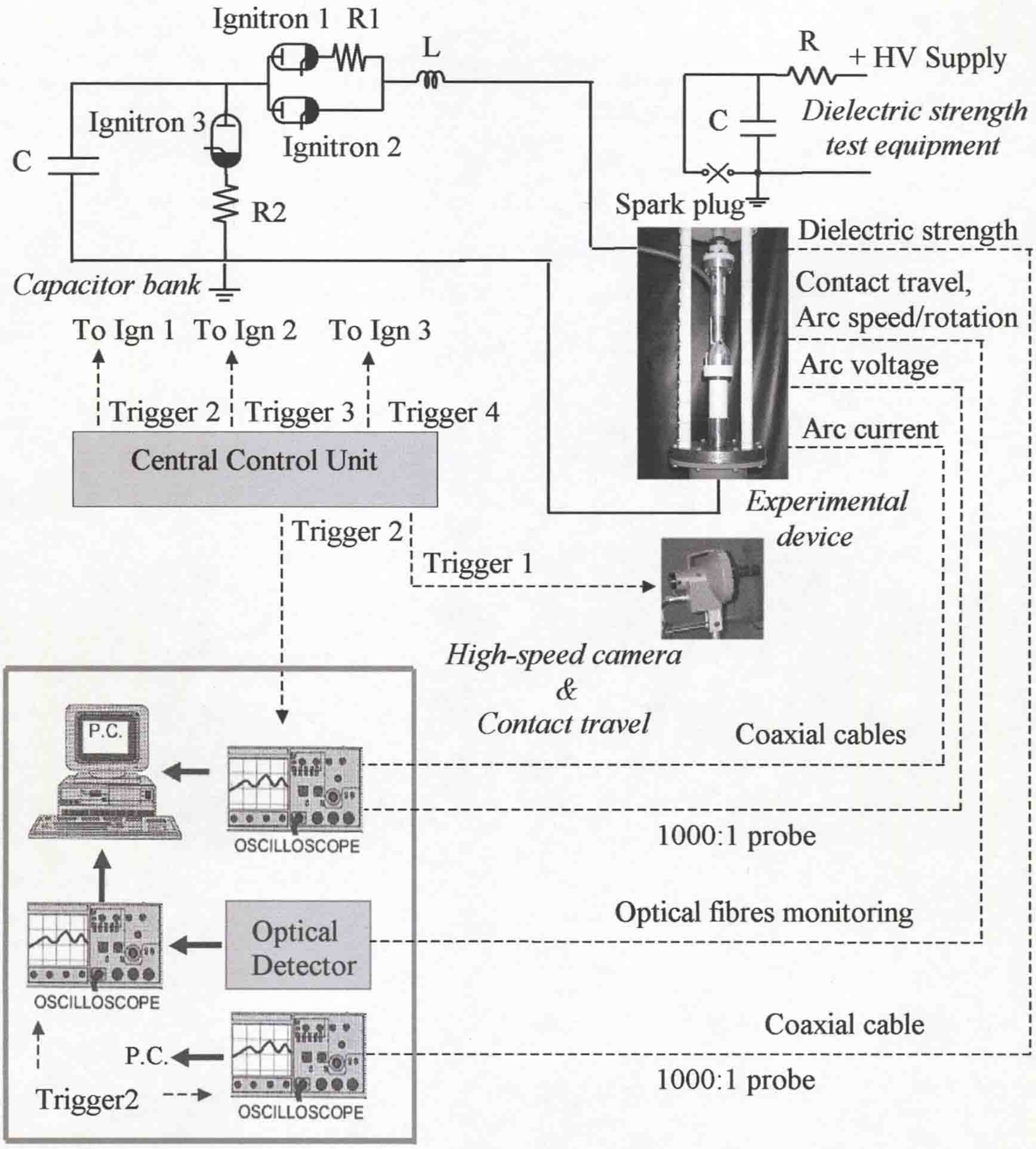

Figure 4.8 Test facility and diagnostic equipment

Theoretically, the arc motion should be followed from the right to the left sides around the model (fig. 3.7b), passing by the first and second high-speed cameras (fig. 4.9). The camera positions provide the full visual observation of the open rig. Their synchronization is not perfect because of the shutter delays of each camera (**section 4.2.7.3**). Therefore, one frame error of 0.15ms for a framing rate of 7500 frames per second is allowed between two cameras. Cameras 1 and 2 are situated at 120 degrees inclination from each other as shown in figure 4.9. A video camera (fig. 4.10) was used to observe the device after arcing with the frame duration set at 40ms per frame.

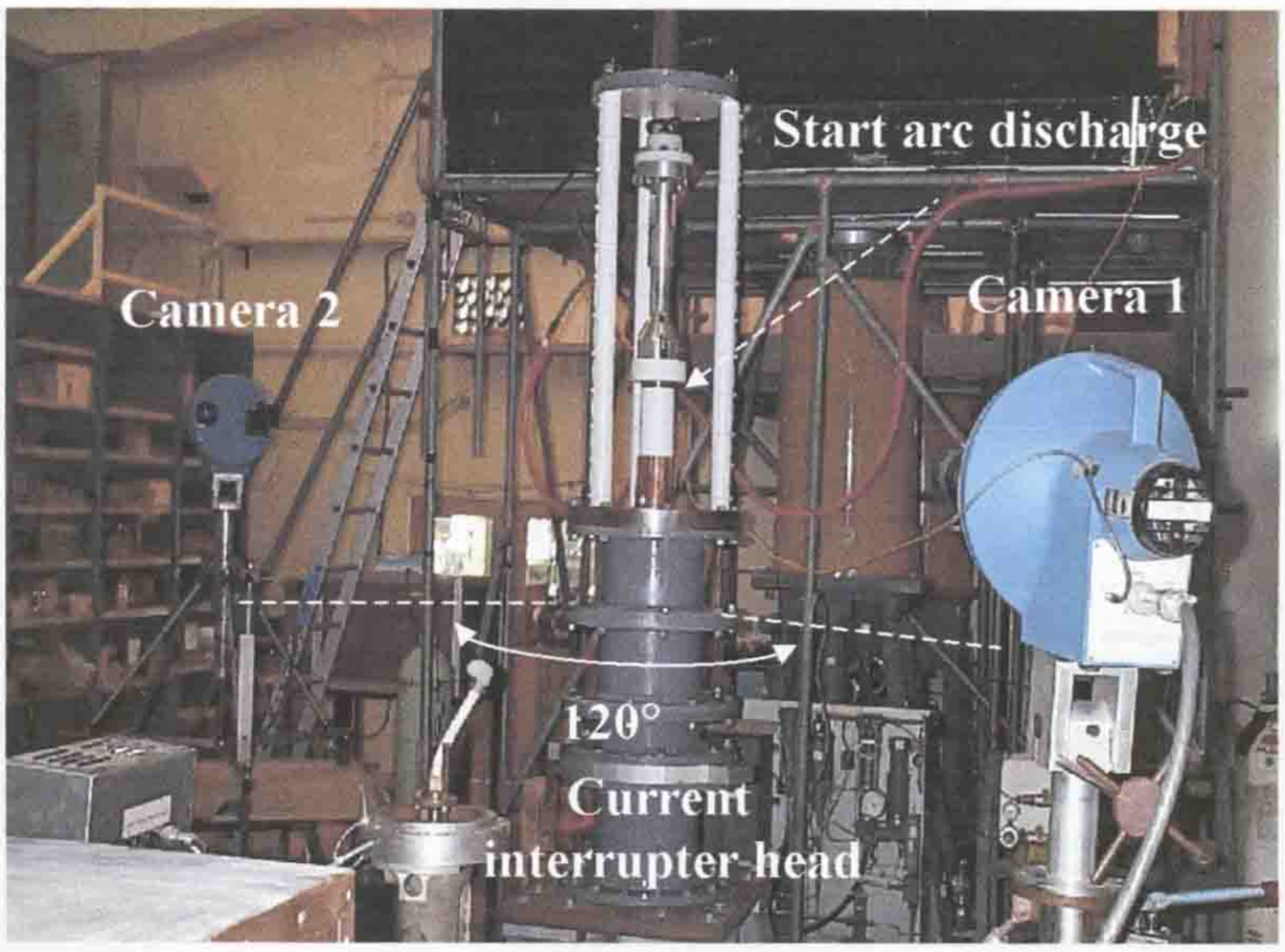

Figure 4.9 Positions of cameras

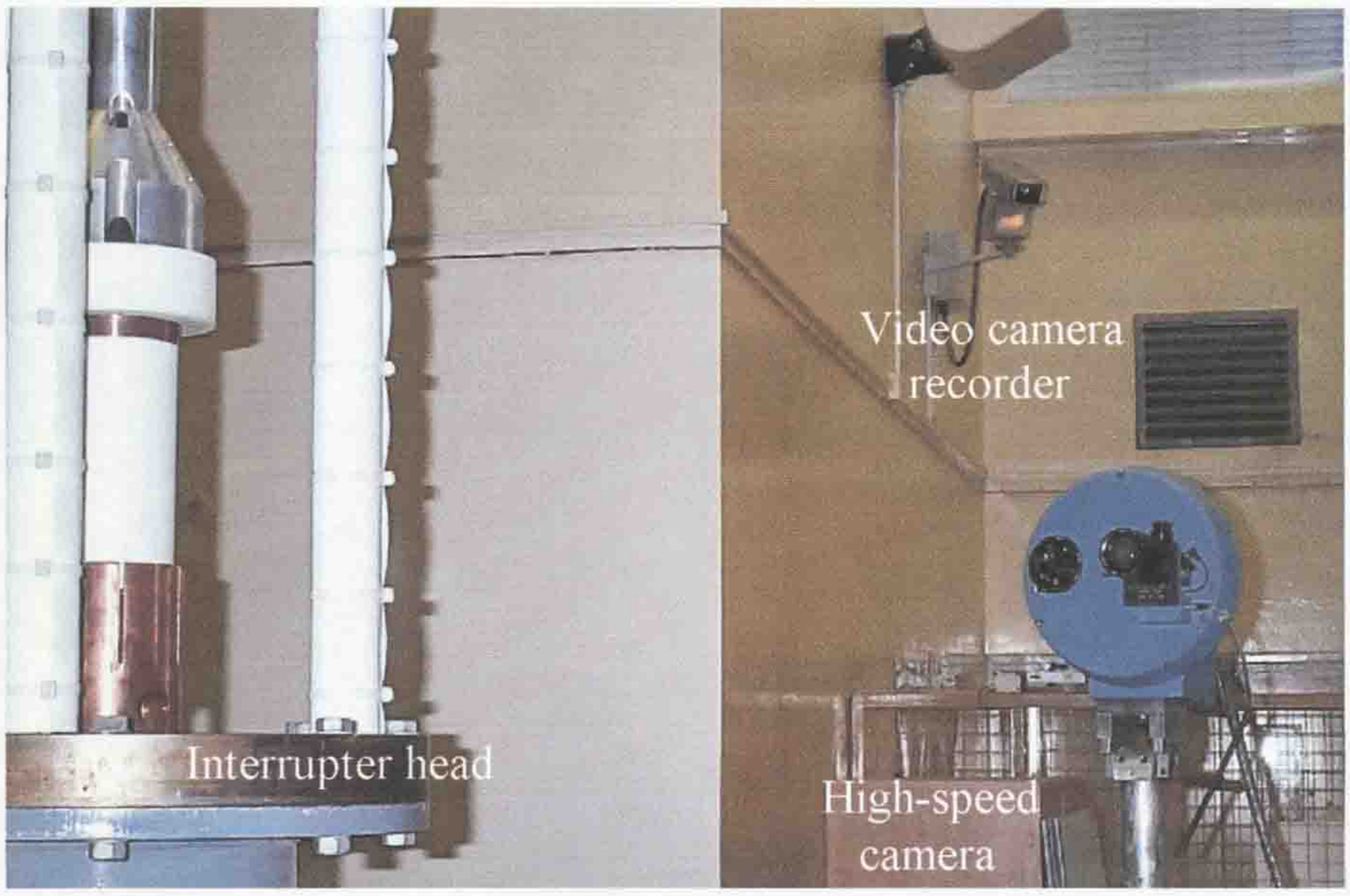

Figure 4.10 Optical test facility

4.1.6 Time control sequence

Description of the timing control sequence for the preliminary arc tests (design evaluation test head (**section 4.1.5.1**)), arc control (**section 4.1.5.2**) and current interruption (**section 4.1.5.3**) test heads are described.

4.1.6.1 Design evaluation test head time sequence

The time sequence of the arcing tests for monitoring the design evaluation test head is similar to the current interruption test head timing sequence of experiments (**section 4.1.6.3**) operating in the same manner.

4.1.6.2 Arc control timing sequence of experiments

The electrical and optical equipment for monitoring the experimental model needed to be synchronised to operate during the arcing tests. The test circuit operation (fig. 4.6) demonstrates the test facility for the experiments including the diagnostic equipment. This section describes the arc control test head timing sequence for dc and ac arcing tests, which is summarized in figure 4.11.

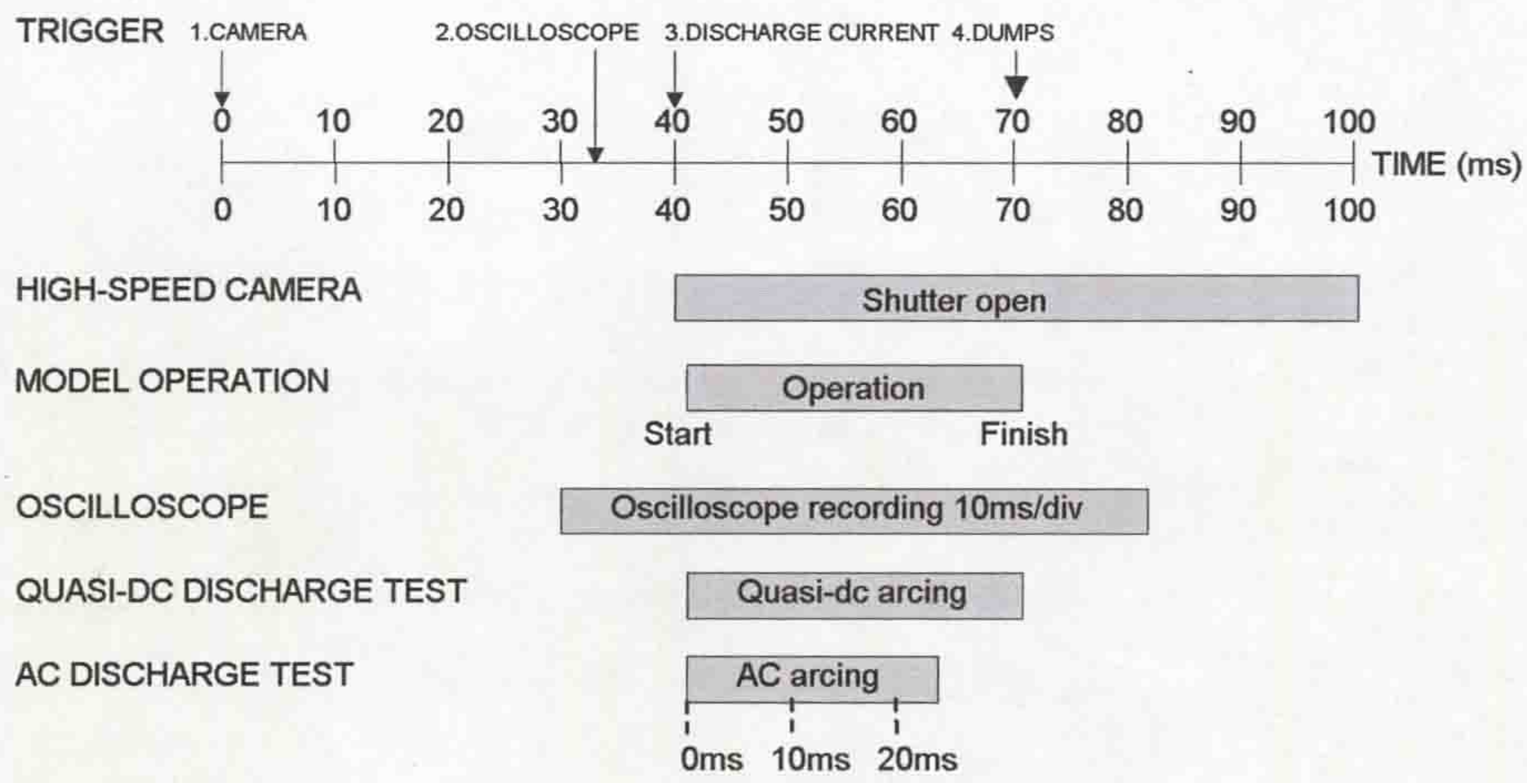

Figure 4.11 Experiments time sequence

The central control unit of the power supply system sends its first trigger pulse (Trigger 1) to the shutter of the high-speed camera, (fig 4.6). The time of the shutter operation is fluctuates because the mechanical delays. After 30ms, Trigger 2 synchronizes the oscilloscope and Ignitron 1 to induce the quasi-steady dc current follow through the model. This made of operation is used for the quasi-dc arcing tests. Trigger 3 is operated for producing a main half cycle sinusoidal current, and it is used for the ac arcing tests. At 40ms, the discharge current commences to follow through the experimental model igniting the electrical arc between the electrodes, while the shutter is fully opened. The high-speed camera operates for 60ms. The precise model operation depends upon the type of the arcing test. For the quasi-dc arcing tests, the model time operation is 30ms, while for the ac arcing tests it can

extend up to 20ms. After about 70ms, the dump is operated (Trigger 4) and the capacitor bank is fully discharged. The total oscilloscope recording time used in the tests is 50ms.

4.1.6.3 Timing sequence of the current interruption test head

The time sequence of the dc and ac arcing tests of the interrupter head has already been shown in figure 4.11. Where as **section 4.1.6.2**, described the timing sequence of the arc control test head, demonstrating a novel method of the arc control. This section describes the corresponding sequences for a long ac-arcing test up to 20ms (arc duration from the contact separation). The quasi-dc and ac-arc currents used in these tests operate during the arcing time with some timing shift, (fig. 4.11, quasi-dc and ac arcing discharge). In other words, in order to provide the larger arcing gap between the electrodes at current zero, the quasi-dc arc current is changed to the ac-arc during the arcing tests.

4.1.7 Experimental earth and isolation

A single earth point is important for any high current and high voltage test circuit. This is known as an experimental earth. It usually connected to a copper rod located in the foundations of the building. The earth connection in the research laboratory was situated close to the test system and had a short cable with low impedance capable of caring a current of several kilo-amperes (kA). Other equipment in the laboratory is connected to the normal 250V mains supply. This equipment was isolated from the experimental earth by 1:1 isolation transformers. This avoided duplicate earthing, which could lead to earth loop currents causing measurement errors etc. They also provide protection from the equipment in case of any fault development in the main experimental loop.

4.1.8 A common signal return path

The principle of the point earthing (that prevented any earth loops and induced voltage loop) required that all probe signals should return to the experimental earth via a single cable sheath. The return signals from the current

shunt flowed thought the outer sheath of the interconnecting cable. On the other side, through the same cable flowed a signal current from the voltage probe. These induce an E.M.F. in the current measuring loop due to the coupling between the core/sheath and the resistive voltage drop of the sheath (Spencer, 1987). Calculation of this type error (Taylor and Wang (1981)) can be achieved utilising the system parameters such as: an arc current of 0.1A, recovery voltage of 10kV, signal frequency of 0.1MHz, a five meters cable with impedance of 0.013 Ω/m. The calculated percentage error was 0.6%. A similar assessment of this error was made for the test system at test signal of 1MHz, cable length two metres and arc current of 0.5A by Spencer (1987). The calculated error was 0.8%. This arrangement was used in the present project where the value of error is acceptable for the experimental system. However, this parameter can be changed if a longer cable were to be used or if the frequency of the signals was high (i.e. more then 10MHz).

4.2 DIAGNOSTIC MEASUREMENTS

During the project, several diagnostic techniques for electrical, mechanical-drive, dielectric strength, magnetic and optical measurements etc. are employed. This section describes the diagnostic equipment and their calibration, which were used in the interrupter design development.

4.2.1 Diagnostic test parameters

The arrangement of diagnostic measurements involved in this project is shown in figure 4.12. The current, voltage and magnetic field measurements characterize the electrical parameters during the experimental tests. The mechanical-drive of the interrupter is related to the contact travel measurement, providing a good indication of the movable rod behaviour. The optical investigations include the optical fibre arc speed and arc rotation measurements including the high-speed and video photographs observations, providing good reference for the electrical measurements during the experiments with electrical arcs. The PTFE ablation diagnostic is used for material ablation calculation, providing information about the quantity (volume) of ablated material produced during the arcing time. Dielectric strength measurements determine the dielectric strength recovery conditions of the

quenching medium in the interrupter immediately after current zero. The gas pressure measurements characterize the aerodynamic parameters in the chamber of the current interrupter, which used in the preliminary arc tests for design development (**section 5.2.1**).

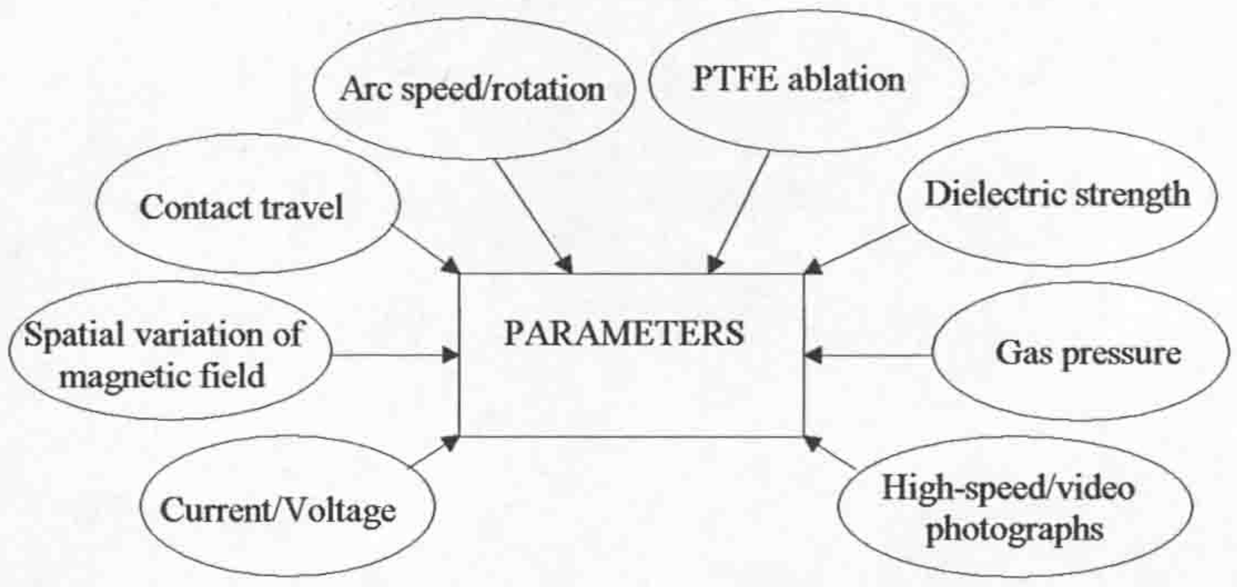

Figure 4.12 Measurable parameters

The measurement of the parameters mentioned above is described in detail in the following sections.

4.2.2 Current measurement

In high-voltage technology, plasma physics and power electronics low-ohmic resistors are often used to measure high, rapidly changing currents (Schwab, 1972). The arc alternating current value is constantly changing during one half cycle of arcing and varies from kilo-amperes to a few amperes at current zero. This section describes the current measurement regimes, which is divided into the two parts. The first part is devoted to the peak current measurement. The second one describes the current zero measurement. The position of the current shunt in the circuit is shown in figure 4.3. One terminal is connected direct to experimental earth. Second one, to the measurement point. This shunt chosen depended on the magnitude of the current and the time-period of current operation.

4.2.2.1 Peak current measurement

During the research period, heavy surge currents and quasi direct currents were measured with a coaxial current shunt of resistance 0.8mΩ, which was able to measure a pulse current rating of 100kA, bandwidth 500kH. The design of the shunt

is similar to that investigated by Grundy, 1977. The current shunt is considered as a four terminal device connected in series with the power circuit and has two connections across which is a resistive element for precision measurements. The coaxially constructed shunts with low ohmic value has a higher thermal capacity and could operate at higher levels of continuous current as the resistance element can be of larger cross section area. The potential difference between the measurement terminals of a low value ohmic shunt is,

$$v(t) = Ri(t) + L\frac{di}{dt} \pm M\frac{di}{dt} \tag{4.1}$$

Where, $v(t)$ - Instantaneous output voltage of shunt

$i(t)$- Instantaneous current

L - Internal inductance of the shunt resistance

M - Mutual inductance

t - Time

R - DC shunt resistance

The shunt used in this research has a low mutual inductance, sufficiently low self inductance as similar shunts used by other experimentalists (Park 1947, Schwab 1971). Consequently the second and third terms of the first-order filter (4.1) can be ignored and this equation after some approximation is,

$$v(t) = Ri(t) \tag{4.2}$$

The low ohmic value of this current shunt was required to limit heat dissipation and loading effects on the circuit under test, producing a good signal to noise ratio. Therefore, suitable resistors ideal for such investigations have values between 0.1mΩ and some 100mΩ, (Schwab, 1971). The BNS coaxial cable of 2-metre length connected the measuring terminal of the current shunt to the oscilloscope. When the low output impedance (0.8mΩ) is connected to the high input impedance (from 1 MΩ to 10MΩ) of the monitoring equipment, it is usual to insert a 50Ω termination onto the input of the oscilloscope. This impedance can prevent the formation of reflected waves in that cable.

4.2.2.2 Current zero measurement

The current zero investigations in this project were monitored by a 0.8mΩ current shunt, which was used for the peak current measurements. The period of the current zero including a post arc current were investigated utilizing the digitising oscilloscope "GW Instek GDS-830", providing an accuracy of current measurement up to 10A and a time resolution up to 0.5μs.

4.2.3 Voltage measurement

This section discusses the overall and local arc voltage regimes, which were measured during quasi-dc and one half alternating current cycle of arcing. In order to exclude any other circuit voltage drops differential measurements may make in case.

4.2.3.1 Overall arc voltage

The overall arc voltage monitored by the voltage probe on the circuit breaker (having magnetic coil) consisted of two components, arc and coil voltages. The summation of these components determines the total voltage across the breaker terminals.

$$v(t) = R_a(t)i(t) + L\frac{d(i)}{dt} + R_c(t)i(t) \qquad (4.3)$$

Arc voltage Coil voltage

Where, R_a - Resistance of arc

L - Inductance of coil

R_c - Resistance of coil

Equation (4.3) shown the relationship between the arc and coil voltages to the voltage *v(t)* across interrupter terminals. The coil voltage is proportional to the coil inductance magnitude (L) and its impedance. The overall voltage can be

approximated as localised if the voltage value across the coil is small. This can be ignored for a small coil inductance magnitude. The position of the voltage probe was chosen far from the arc interaction in order to avoid any damages the voltage probe during arcing tests in the interrupters. The interconnecting cable from the coil was attached to a high-voltage feed through the insulator of the breakers. The other side of the coil was connected to the electrode (cathode) in series with the experimental earth of the system. The high-voltage probe was connected to localised side of the breakers (anode) in relation to the experimental earth. The voltage probe was 1000 attenuation (Tektronix P6015A). It added high-voltage measurement capability to oscilloscopes and other measurement devices and had an input impedance of 1MΩ and input capacitance of 7pF to 49pF. The probe consisted of two major assemblies: the probe body and the compensation box. The probe body was made of high-impact thermoplastic that provided mechanical protection for the internal components of the probe and electrical protection for the user. The compensation box connected to an oscilloscope and had a cable that attached to the probe body. The compensation box contained an adjustment network to optimise the frequency response from DC up to 75MH with a maximum voltage peak pulse of 40kV.

4.2.4 Magnetic flux measurement

The magnetic flux density measurement technique introduced in this section. The test system for the magnetic field measurements is described, including the unit calibration intended for investigations of the spatial variation of magnetic fields produced by the coil fixed within the rotary arc interrupter (**chapter 3**). A search coil was wound around a Teflon former (magnetic permeability could be considered as for an air core) outer diameter of 8mm and length of 11mm was used for measurements of the spatial variation of magnetic field around the coil located within the PTFE cylinder (fig. 4.13). The dimensions of the search coil were such as to provide easy external accesses to the PTFE cylinder situated around the coil and which protect the coil from the electrical arc. The radial and axial peak values of the coil magnetic field around the model (PTFE cylinder) were measured and calculated in the same manner, and the total peak magnitudes (radial and axial components) of the magnetic fields around the experimental interrupter were obtained for an alternating current of 5.3kA flowing trough the coil (**section 5.2.3.1**).

4.2.4.1 Test circuit

This investigation was for the estimation the external *B* field distribution of the coil. The analytical solution of the magnetic field in free space is described in **section 3.4**. The *B* field around the model is difficult to estimate precisely because of the non-current distribution in the coil having turns of thin, wide strip with a rectangular cross-section. This is a reason of using the practical measurements of the external to the coil B field utilizing exiting alternating current. The *B* field measurement is based on the method utilized an initially calibrated search coil, under ac conditions within a long solenoid. The magnetic field generated by exited coil was measured using a search coil, where the B field lines passed through the search coil producing an instantaneous changing voltage across the search coil that was directly monitored using an oscilloscope. The test facility and a search coil assembly for the magnetic flux density measurement are shown in figure 4.13. One coil has been used for axial and radial magnetic field measurements, separately.

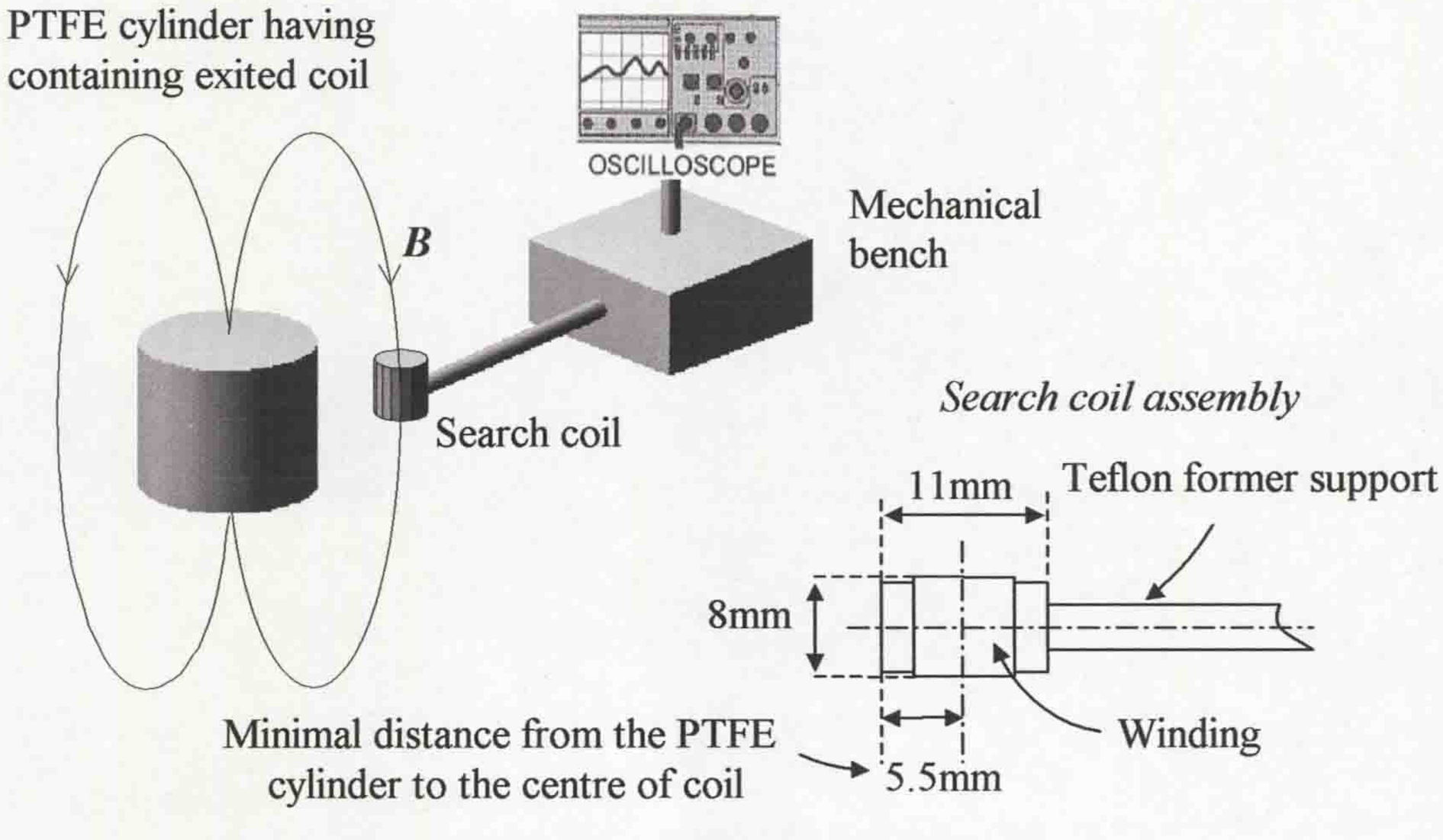

Figure 4.13 Test facility for measuring B field

The diameter of the search coil should be as small as possible, since the magnetic flux density is not spatially uniform and therefore the small diameter of the coil improves the accuracy of the measurement area. On the other hand, a small search coil can measure the outer magnetic field of the measurement coil situated close to it.

4.2.4.2 Calibration of magnetic flux measuring system

The search coil calibration system is shown in figure 4.14. The main part of the calibration system (experimental research laboratory at the University of Liverpool) is the long solenoid caring 1080 turns (N) and having a coil length ($l_{solenoid}$) 0.851m. The magnetic flux density at the centre of the long solenoid is (Cullwick, 1966):

$$B_{solenoid} = \frac{I \times N}{l_{solenoid}} \times \mu, \ [T] \tag{4.4}$$

Where: $\mu = 4\pi \times 10^{-7}, [H/m]$ - permeability in free space

I - current, $[A]$

The inner magnetic field distribution in the centre of the long solenoid is considered as uniform. Therefore, the accuracy of the measurement at this point will be maximal. The current through the solenoid was changed via a variable ac-transformer. Consequently, when the current through the long solenoid was increased a higher strong magnetic flux density was produced inside the solenoid.

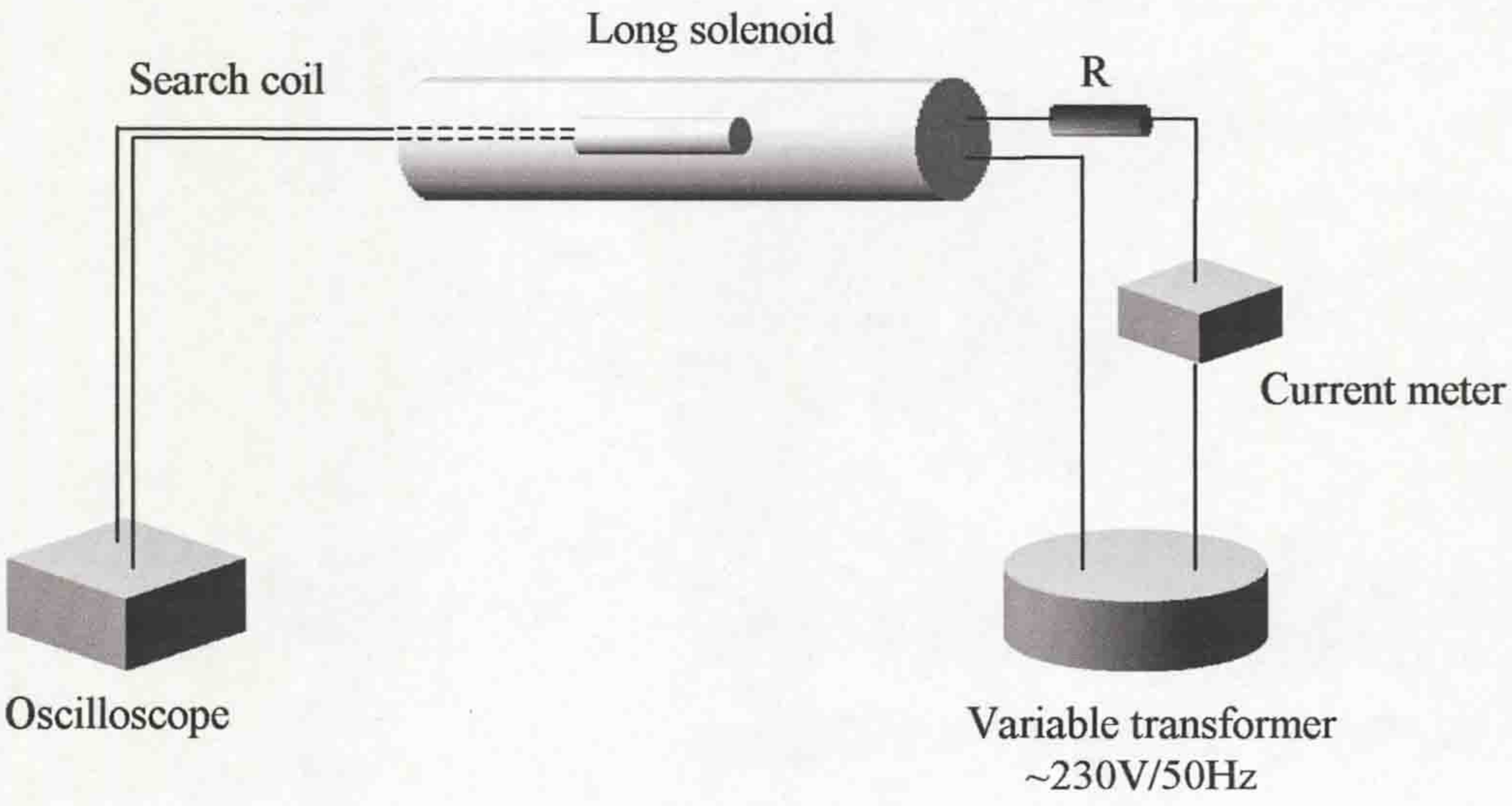

Figure 4.14 Calibration search coil setup

The search coil situated in the centre of the solenoid (inside) produced an instantaneous changed voltage due to the inner B field. This voltage was monitored using an oscilloscope. The current meter was used to measure the RMS current through the solenoid, which could be transformed to a peak value of the current.

$$\hat{I} = \sqrt{2} \times I_{RMS} \tag{4.5}$$

This transformation is needed because the current measurement for the interrupters is calculated from its peak value. The relationship between the peak magnetic flux density in the centre of the long solenoid and the reference voltage of the search coil is shown in figure 4.15. Figure 4.15 shows the practical and theoretical curves. The

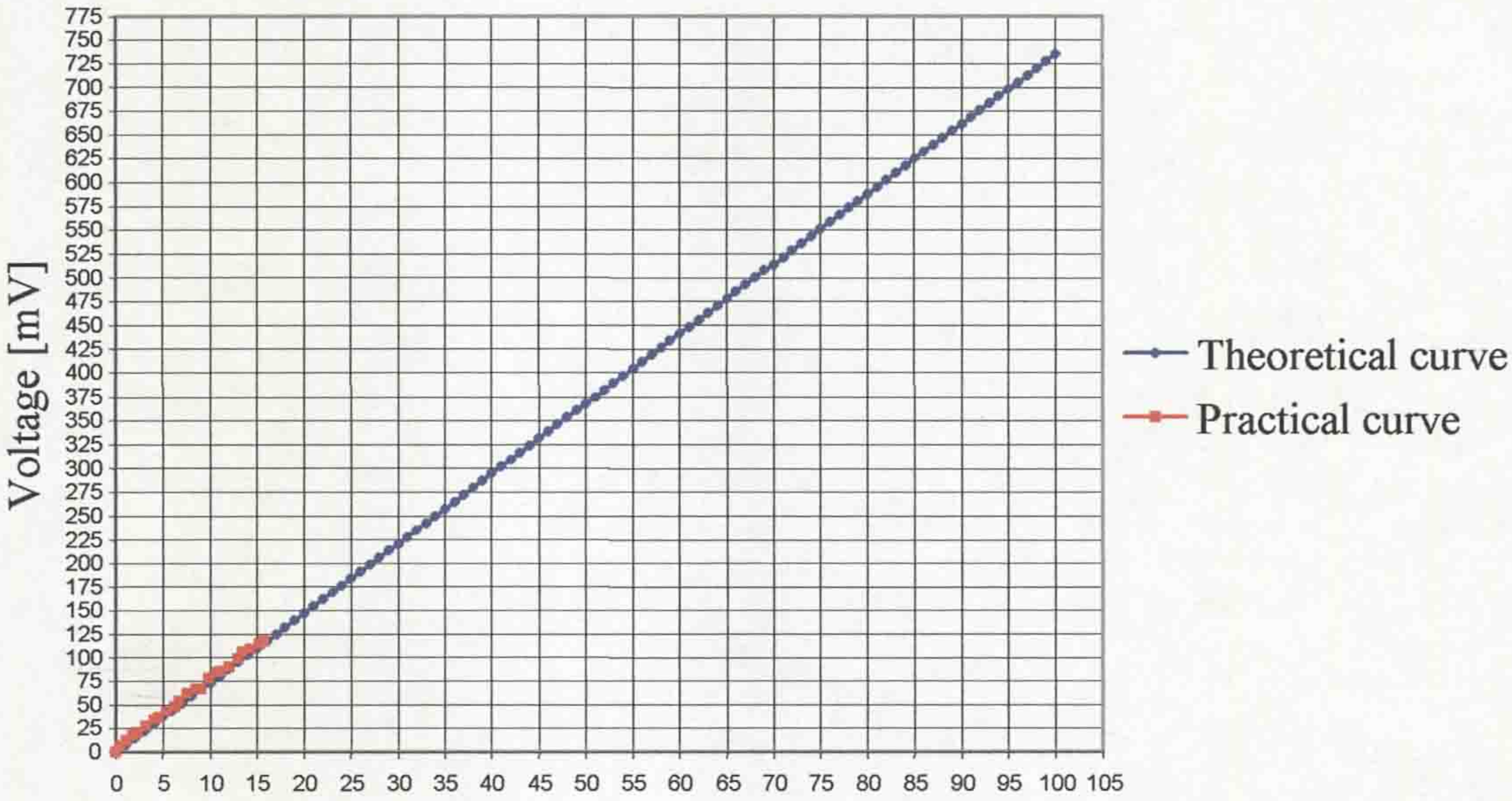

Figure 4.15 Search coil Voltage/Magnetic flux density calibration curves

practical curve was measured up to the solenoid current limit utilizing the calibration system. The theoretical curve (y=7.3519x) is continuation of the practical curve for the stronger magnetic field because the long solenoid has the air core (Microsoft EXCEL is used). When the search voltage on the oscilloscope is zero, the B field of the long solenoid is a maximum (fig. 4.16). The search voltage is integrated in order to yield the peak value of the B field ($\hat{B}$). For an ac current with a frequency of 50 Hz the coil magnetic field is determined as (Guru, 2004):

$$\mathrm{b} = \hat{B} \sin \omega t \;\text{ so that }\; \left.\frac{dB}{dt}\right|_{\max} = \omega \hat{B} \tag{4.6}$$

Where: $\omega = 2\pi f = 2\pi \times 50 = 100\pi$, $f = 50\,[Hz]$ ac current frequency

The search coil voltage v_{sc} is determined as: (Guru, 2004)

$$v_{sc} = N_{sc}\frac{d\phi}{dt} \quad \text{thus} \quad \hat{V}_{sc} = N_{sc}A\frac{dB}{dt}\Big|_{\max} = N_{sc}A\hat{B}\omega \tag{4.7}$$

Where N_{sc} is the number of turns for the search coil ,

$\hat{B}$ - peak value of the magnetic field

A – search coil cross sectional area

Assume that $N_{sc}A = k$

Then $$k = \frac{v_{sc}}{\hat{B}} \times \frac{1}{\omega} \tag{4.8}$$

From figure 4.15, the average k parameter is 0.026. If the magnetic field variation is non sinusoidal with time, then the value of magnetic field is obtained by the interpretation of the search voltage (Guru, 2004) i.e.:

$$\mathrm{b} = \frac{1}{k}\int_{t_0}^{t_1} v_{sc}\,dt \tag{4.9}$$

Where, t_1 is the time when the B field has a peak value. An example of the search coil voltage integration is shown in figure 4.16. At the point t_1, the peak magnetic field is a maximum as well as the ac current flowing through the measurement coil, (fig. 4.16). The phase difference between the exiting current and magnetic field is near zero because the inductance of the coil is small that confirms the assumption that there are no secondary currents induced in the weakly conducting materials situated around the measured coil (**section 3.4**). Microsoft EXCEL is used for the search coil voltage integration from t_0 to t_1. An integration of the search coil voltage determines the value of magnetic field at different time scale is: $b_n = \frac{1}{k}\sum_{i=0}^{i=n} v_{sc_i}\Delta t$.

Where, i is a sample number, Δt is a sample at time interval at 0.1ms. The peak value of the magnetic field is an integration of the all samples during a period of 4.3ms, (fig. 4.16). Equation (4.9) is used for the radial B_x and axial B_z magnetic fields calculations.

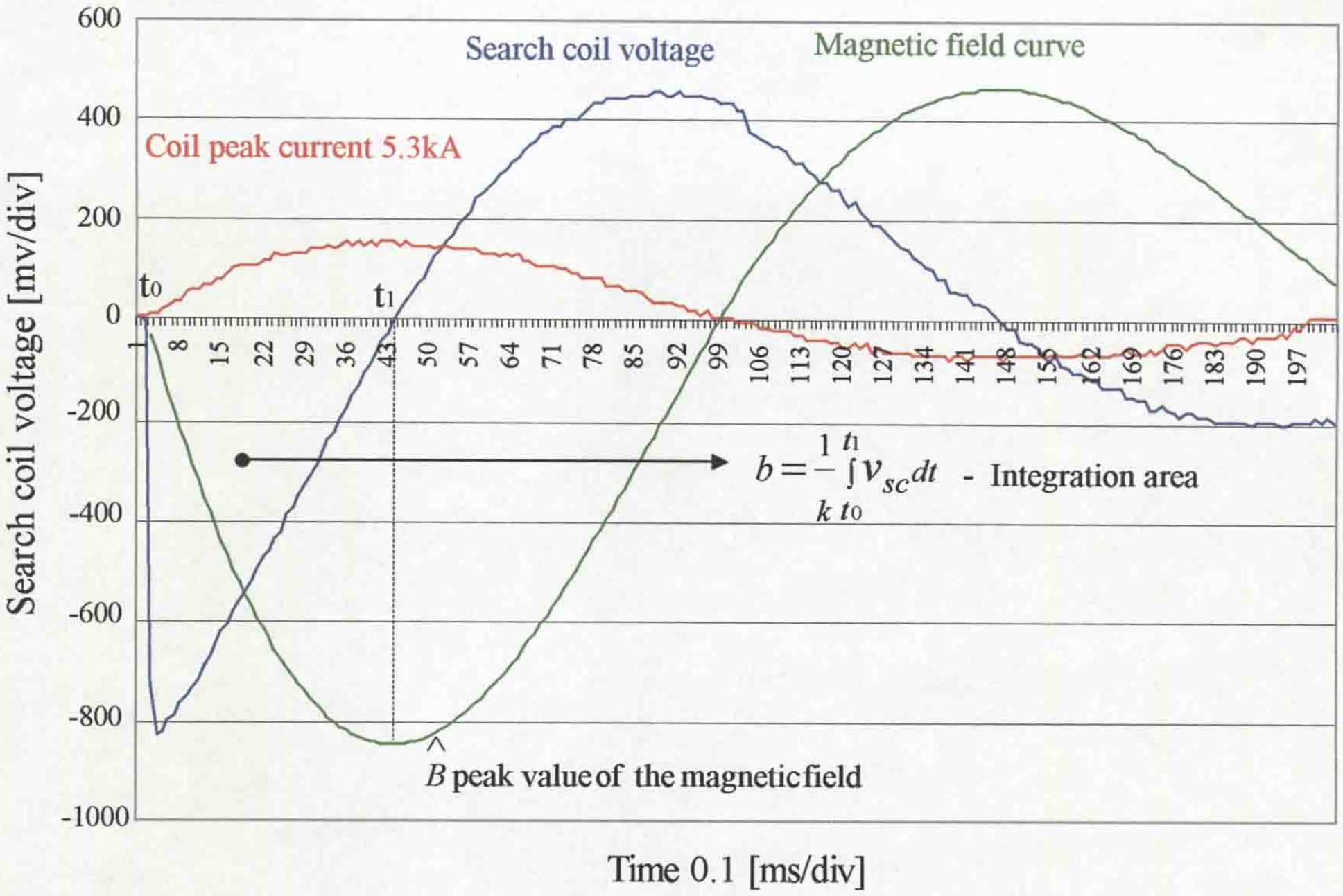

Figure 4.16 Example of the integration of search coil voltage

4.2.5 Contact travel measurement

In order to estimate the mechanical position of the movable contact of the interrupter, the optical fibre travel recorder system was used. The travel contact calibration of two interrupter heads (**sections 3.2**, **3.3** and **4.1.5.1**) were made in relation to the time, which were used during experimental tests.

4.2.5.1 Optical fibre travel recorder system

In general, two techniques for monitoring the travel contact are used. The first involves a displacement sensor. This method has a number of disadvantages. The first one is the large size of the sensor (device), which is situated remotely from the rod of the circuit breaker. As a result, this method is prove to errors for instance due to coupling uncertainties. The second method is based on an optical fibre travel recorder. The advantage of this method is in use of sensors, which measure the contact movement directly. In addition, because of their small size the sensors can be situated close to the movable rod. Such a device therefore reduces the chance of

errors. A schematic diagram of the optical fibre travel recorder system is shown in figure 4.17.

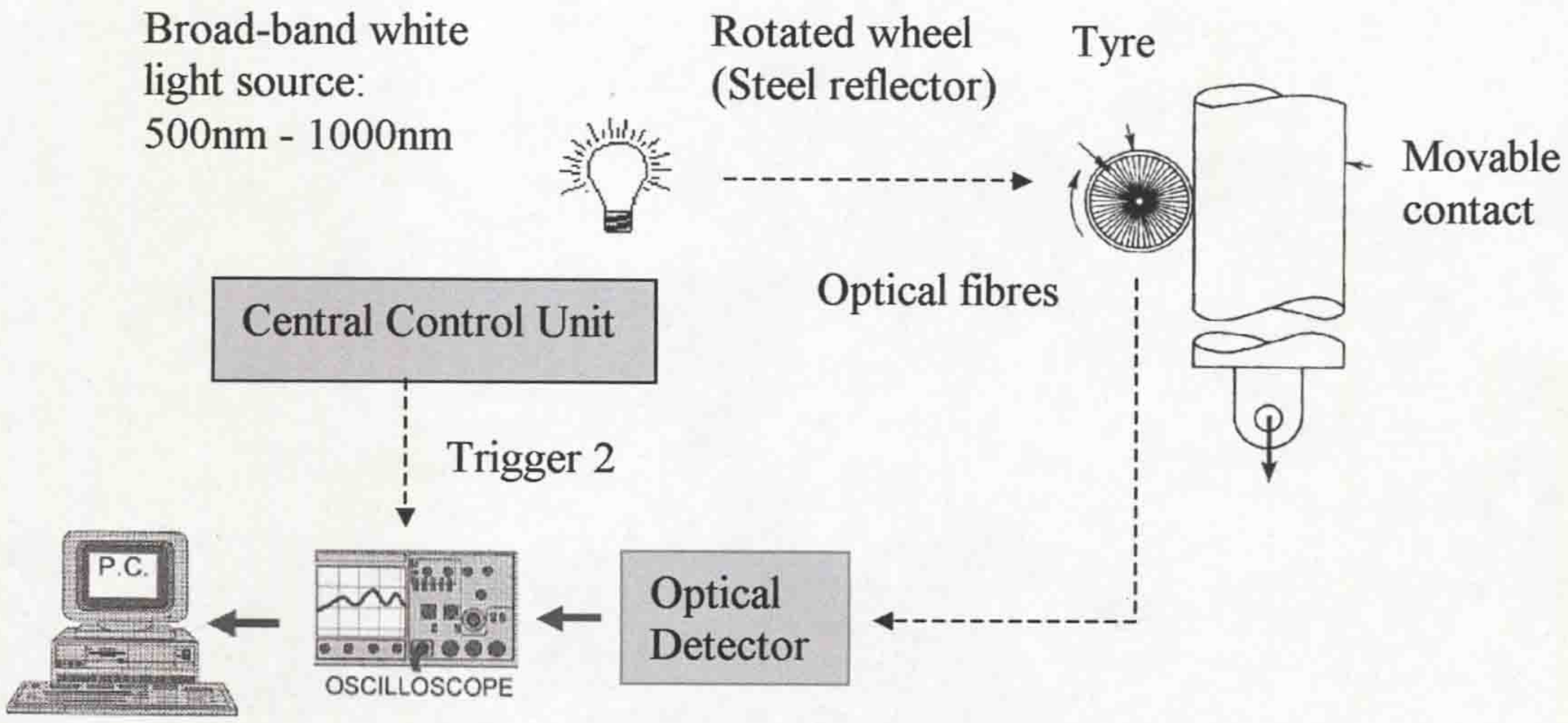

Figure 4.17 Optical fibre travel recorder system

The Optical fibre travel recorder system is based on light reflection from a steel rotating wheel (or a long foil ruler attached on the movable rod), which is situated directly in contact with the rod of the movable contact, (Shimmin, 1986).

A constant intensity broad-band white light source is connected to the rotating reflecting steel wheel (or long foil ruler) by an optical fibre. The optical detector receives the reflected light via a second fibre, transforming it to an electrical signal connected to an oscilloscope. The data from the oscilloscope is analysed by a PC. On the steel reflector wheel (foil ruler) white-black lines are marked, which reflect or absorb the white light from the source to the optical detector. The optical travel recorder system is synchronised by a trigger pulse from the Central Control Unit receiving this pulse when the movable contact starts to operate.

4.2.5.2 Travel contact calibration of the non-rotary arc interrupter

This section describes the determination of the electrode gap length as a function of time.

The contact travel and speed records for experimental non-rotary arc (reference) interrupter are shown in figure 4.18.

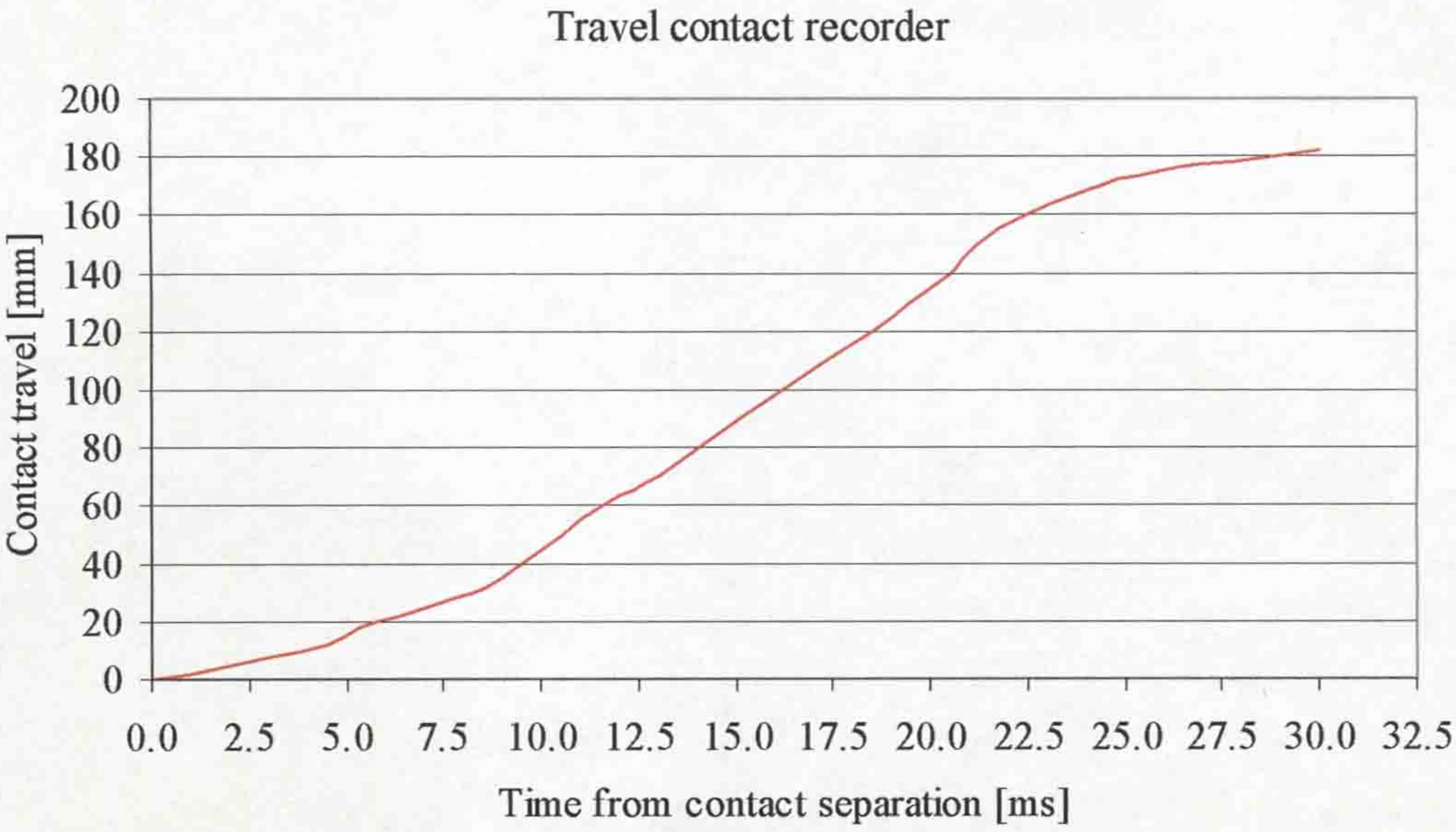

a) Contact travel of the movable electrode

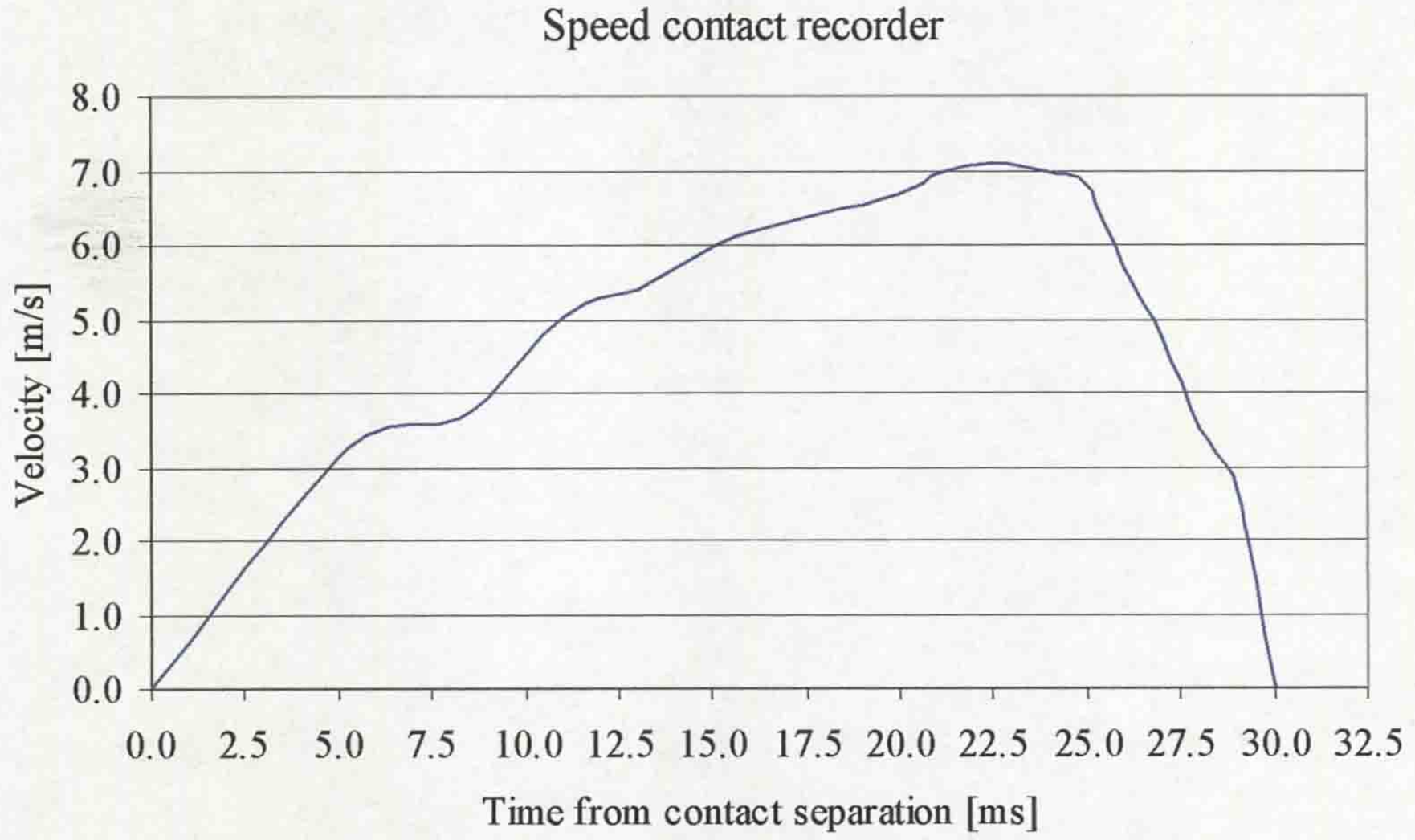

b) Contact speed of the movable electrode

Figure 4.18 Movable contact calibration of the non-rotary arc interrupter

The calibration curve record of figure 4.18 commences from the point of electrodes contact separation. It was found, that the movable rod reaches an electrode gap of 180mm in 30ms, (fig. 4.18a). In addition, the contact speed curve shows that at 22.5ms, the maximal cathode velocity was 7.1m/s, (fig. 4.18b). During the preliminary arc tests for design development (**section 5.2.1**), the contact travel calibrations were used in the same manner with the non-rotary arc interrupter head experiments. These results provided the components optimization in the design of a novel rotary arc interrupter (**chapter 3**).

4.2.5.3 Travel contact calibration of the rotary arc interrupter

In order to estimate the mechanical-drive characteristic of the novel rotary arc interrupter, the optical fiber travel recorder system (**section 4.2.5.1**) was used for travel contact calibration. An example of the contact travel calibration of the experimental interrupter is shown in figure 4.19. The size of the experimental bench, onto which the experimental breaker was fixed, limited the access to optical

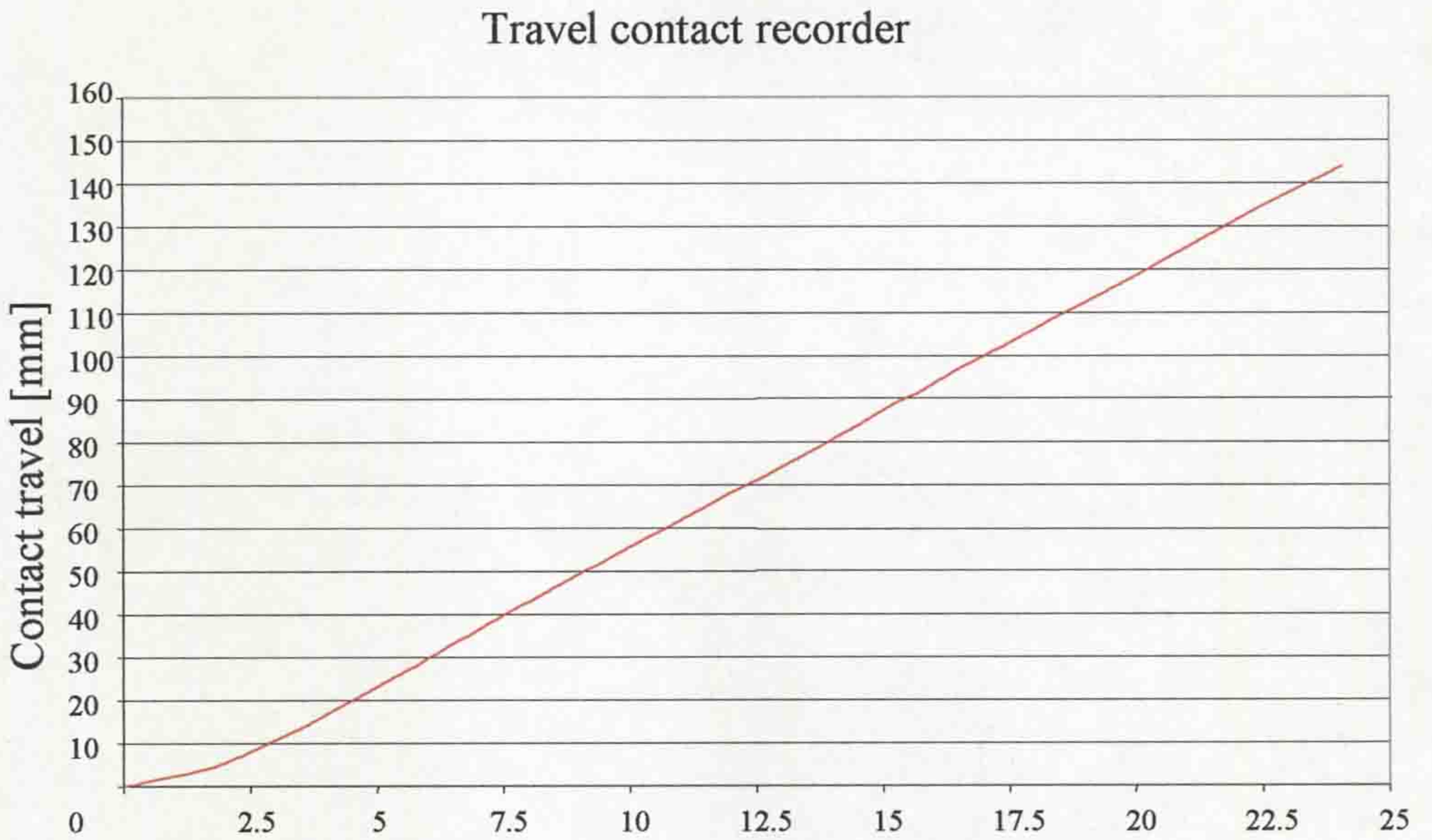

a) Contact travel record of the movable electrode

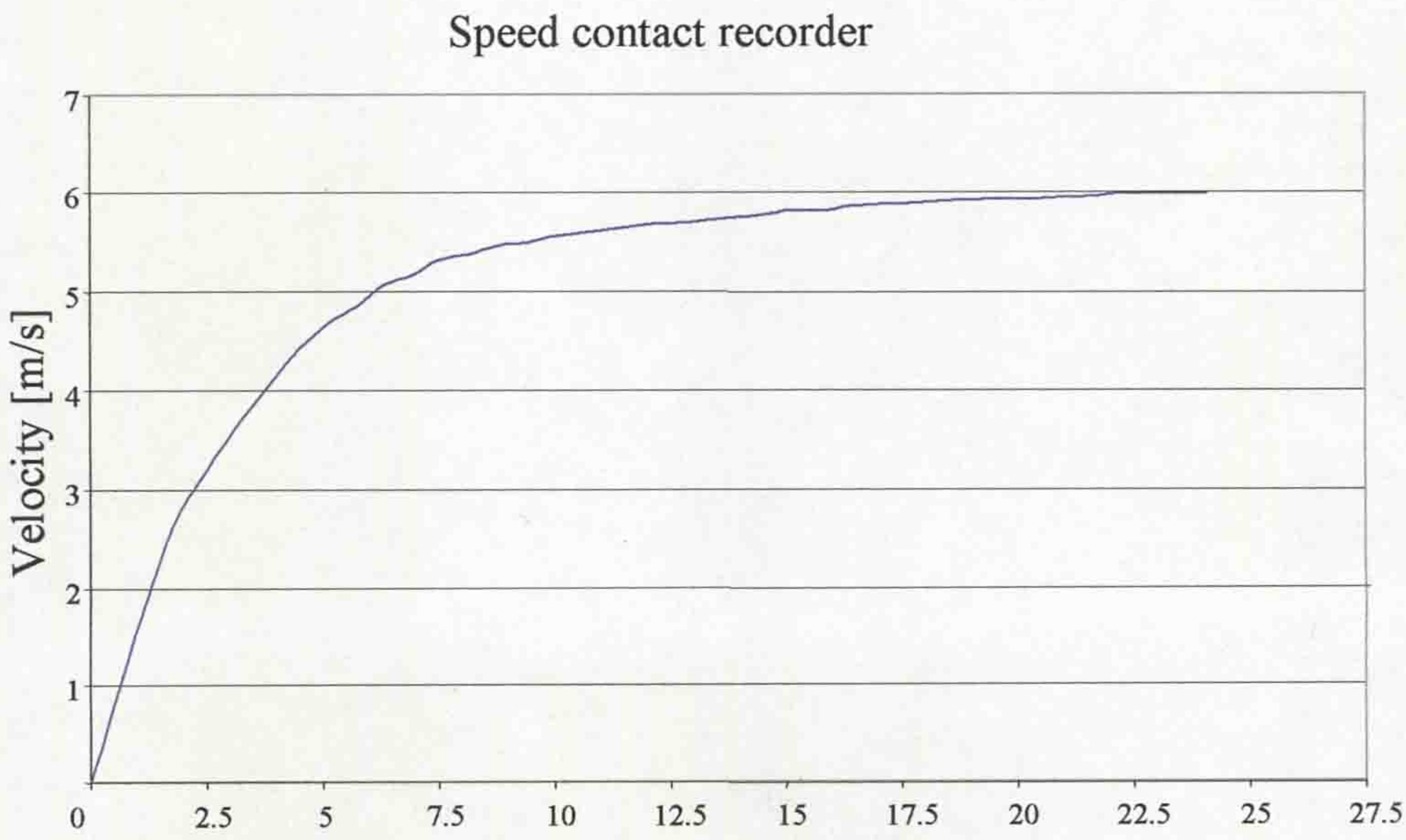

b) Contact speed record of the movable electrode

Figure 4.19 Mechanical-drive calibration of the novel rotary arc interrupter

sensor to monitor the contact travel gap. Therefore, the calibration of the maximal possible mechanical-drive gap of 145mm was investigated being adequate for arcing measurements in the experiments of this project. Figure 4.19a shows that the travel contact covered a gap of 145mm in 24.3ms. This distance is adequate for the dc-arcing experiments with test durations up to 24.3ms and ac-arcing tests of duration up to 20ms. The contact speed characteristic (fig. 4.19b) shows that at fist the travel contact moved, slowly. After 2ms, the contact accelerated more rapidly. At 22ms, the travel contact reached it maximal speed of 6m/s. In fact, the weight of the cathode influences the contact speed characteristic and should therefore be minimised. The travel contact investigations were employed under certain conditions (air, atmospheric pressure) and the calibration curve may be slightly changed with a different medium.

4.2.6 Gas dielectric strength measurement

4.2.6.1 Introduction

During the gas circuit breaker operation, the behaviour of the hot gas generated by arc is important for the current fault interruption investigations, including the post arc dielectric strength in gas breakers. Investigations of a gas blast circuit breaker (Okamoto *et al*, 1991) show that during the arcing time the dielectric strength of the hot gas is decreased.

This section describes the dielectric strength measurement equipment for monitoring the novel rotary arc interrupter (**chapter 3**). Calibration of the components of the equipment is described in air and at atmospheric pressure. The method is applied later for prototype interrupter dielectric strength investigations in the same manner (**section 5.2.3.4**).

4.2.6.2 Principle of system operation

The experimental test facility for the interrupter dielectric strength monitoring has been shown previously in figure 4.8. The dielectric strength measurement technique is based on investigations, which were previously applied in

rotary arc interrupter tests (Ennis, 1996). The principle of operation of the dielectric probe is based upon the circuit shown on figure 4.20.

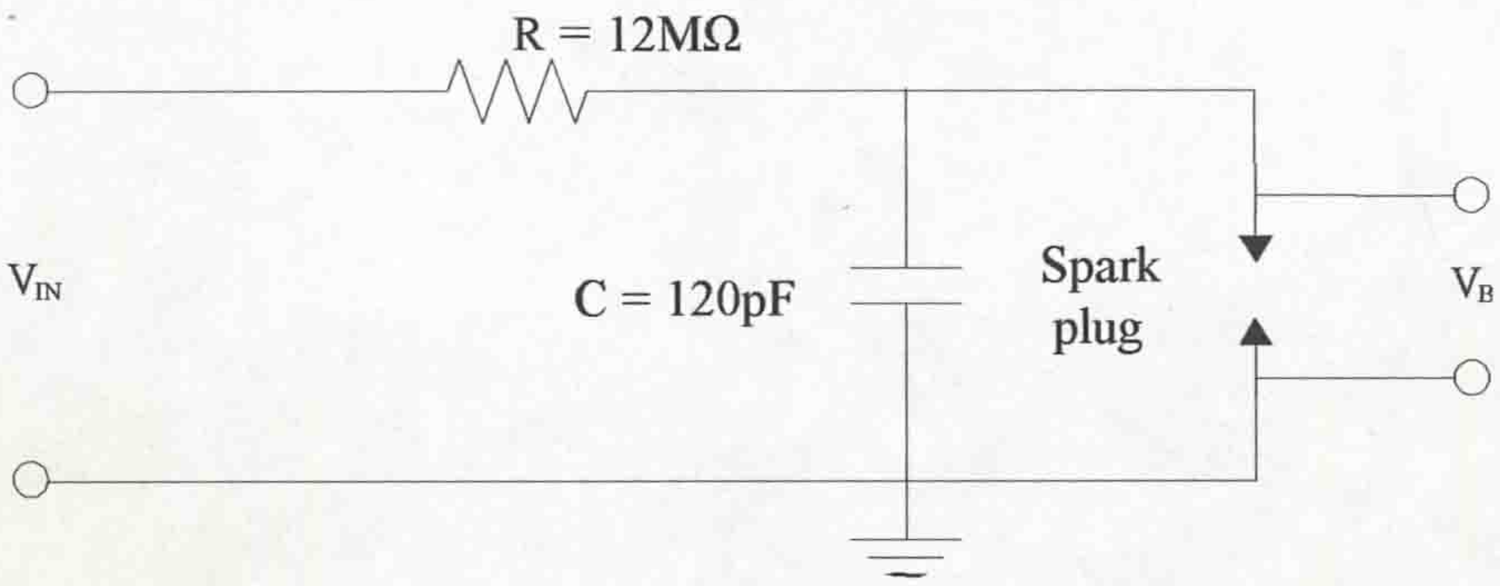

Figure 4.20 Dielectric probe schematic circuit

A high voltage (HV) source of 16kV (V_{IN}) charges up a sufficiently small capacitor C (capacitance of 120pF) through a resistor R (12MΩ). The dielectric strength at different media is monitored via the breakdown voltage (V_B). When the voltage across the capacitor C reaches the breakdown voltage of the gas, breakdown occurs (discharge through the spark plug contacts), leading to the capacitor C to be discharged to the experimental earth. After breakdown, the voltage across the capacitor begins to rise because of a charging current of 1mA flowing from the HV source. If the medium in which the breakdown occurred is sufficiently uniform, the total capacitor charging and breakdown periods (Δt) should be about the same. Diagrammatically the repetitive discharge waveform is shown in figure 4.21 from t_0 to t_1 (sufficiently uniform medium). The total period Δt (rise and breakdown voltages) for the RC-integrating circuit (fig. 4.20) is about 1.5ms. This provides a

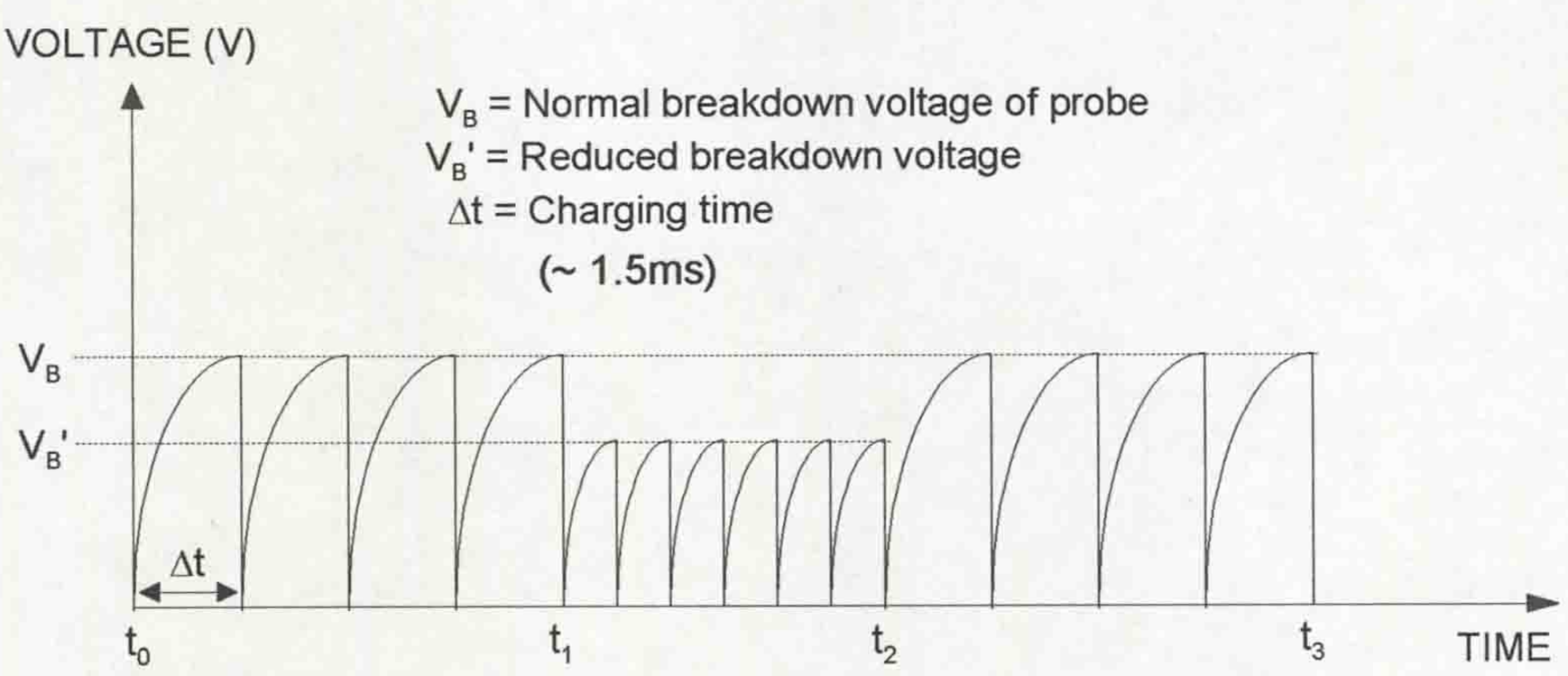

Figure 4.21 Breakdown discharge waveform

repetitive discharge of around 660Hz frequency in cool air (300K), at atmospheric pressure and provides a suitable sampling rate.

In the case of hot gas entering into the test gap of the spark plug, ionization of the gas increases, which leads to the breakdown voltage and amplitude of the discharge waveform being lower. Moreover, the total capacitor charging and breakdown periods (Δt) are reduced as is shown in figure 4.21 (time between t_1 and t_2). From t_2 to t_3 the waveform re-established itself to the previous level, indicating the full dielectric recovery. Two important pieces of information can be obtained using this dielectric strength monitoring method. The first is the extent of the dielectric loss. The second is the duration of the reduced dielectric strength.

The position of the spark plug in the rotary arc interrupter is shown in figures 4.22 and 5.4). Particular spark plug electrodes configuration was chosen for the

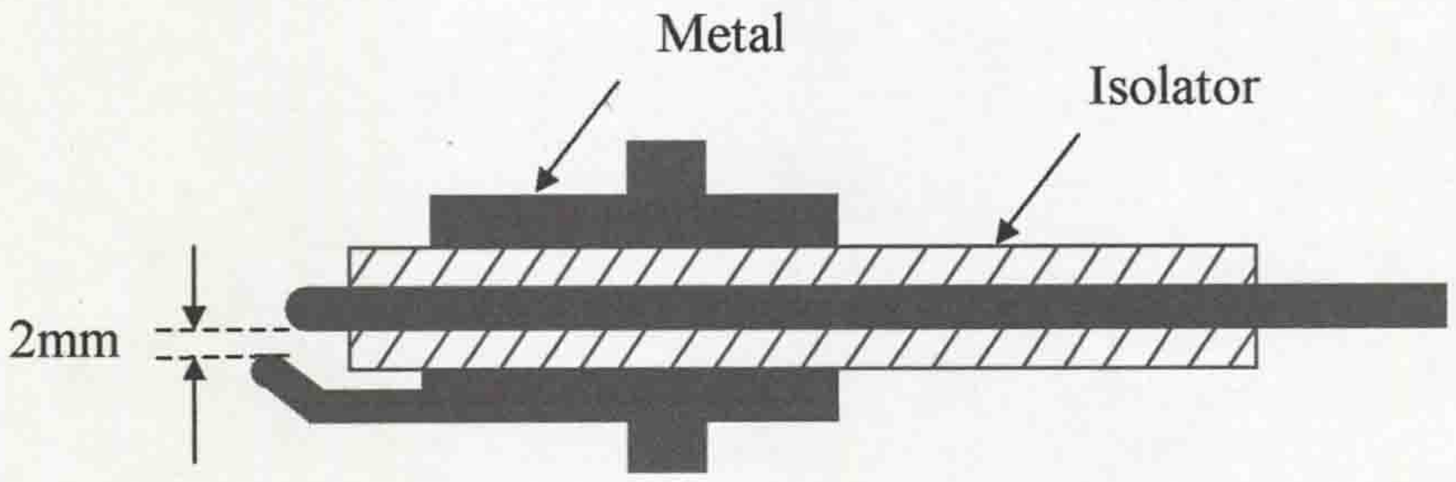

a) Spark plug configuration

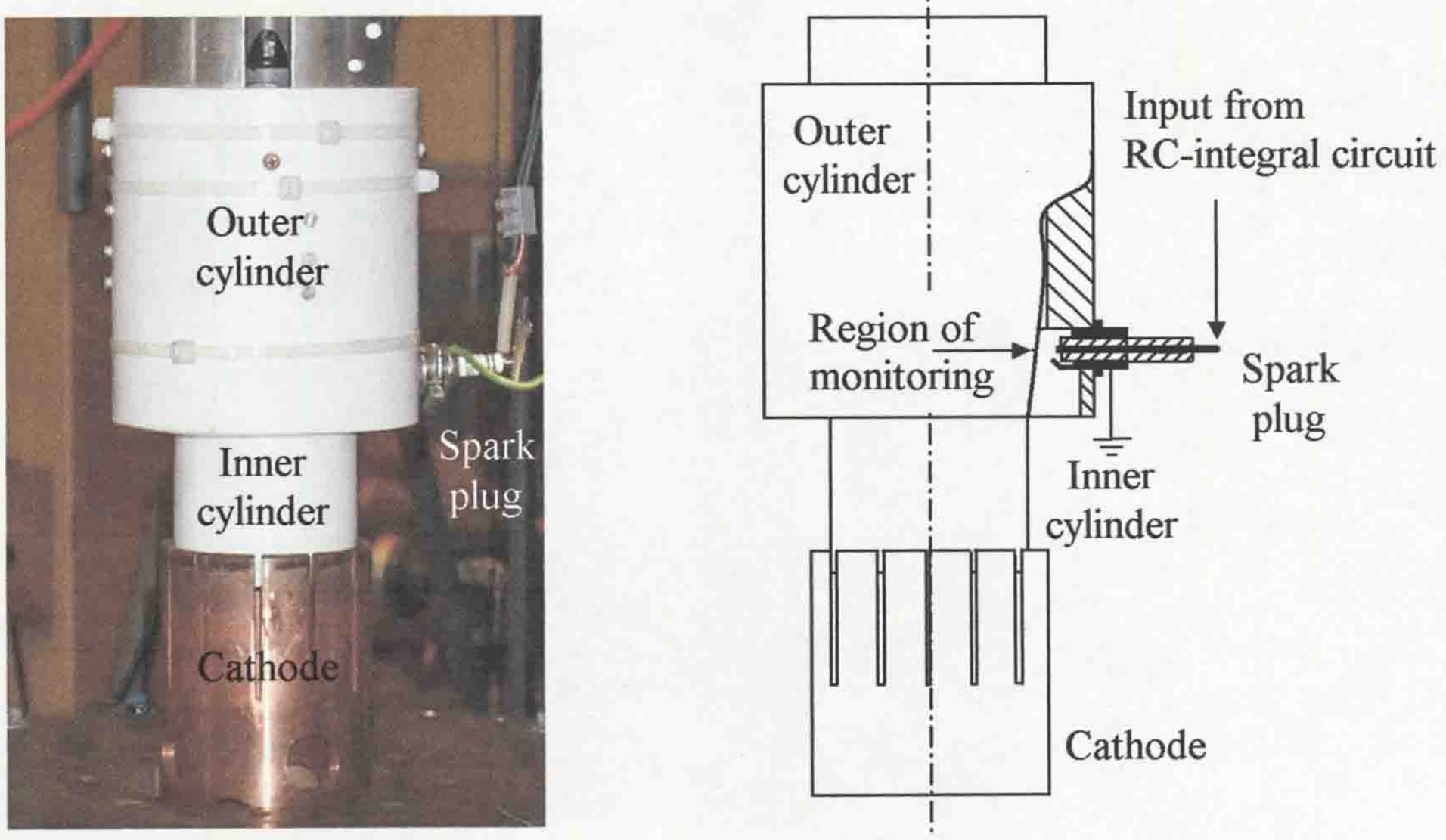

b) Identification of the spark plug position

Figure 4.22 Spark plug situation within the interrupter

experimental tests in air and at atmospheric pressure (fig. 4.22a). These conditions led to an increase in the spark plug gap up to 2mm, providing sufficiently stable repetitive pulsed discharge waveforms and with high amplitude voltage pulses. As a result, the lifetime of the spark plug (*NGK* type R, BPR 6ES) is increased, reducing the electrodes corrosion during the series of tests. The spark plug position identification within the interrupter is shown in figure 4.22b. The dielectric probe (4.20) together with the HV source produced repetitive discharge pulses through the spark plug (4.22a) situated inside the interrupter head between the outer and inner PTFE cylinders (Region of monitoring, fig. 4.22b).

4.2.6.3 Calibration of dielectric strength measurement system

The dielectric strength test equipment (fig. 4.8) was calibrated under the certain conditions mentioned above (**section 4.2.6.2**) in air, at atmospheric pressure. The interrupter ac current operation of 5kA was chosen as a reference current in which the result obtained could be compared with previous results Ennis (1996) and Mori (2005). During the calibration test, the dielectric strength diagnostic equipment (high-voltage probe of 1000:1 divider Tektronix type P6015A and oscilloscope) was operated. An example of the dielectric strength calibration curve (without the interrupter operation) with a sufficiently high time resolution is shown in figure 4.23.

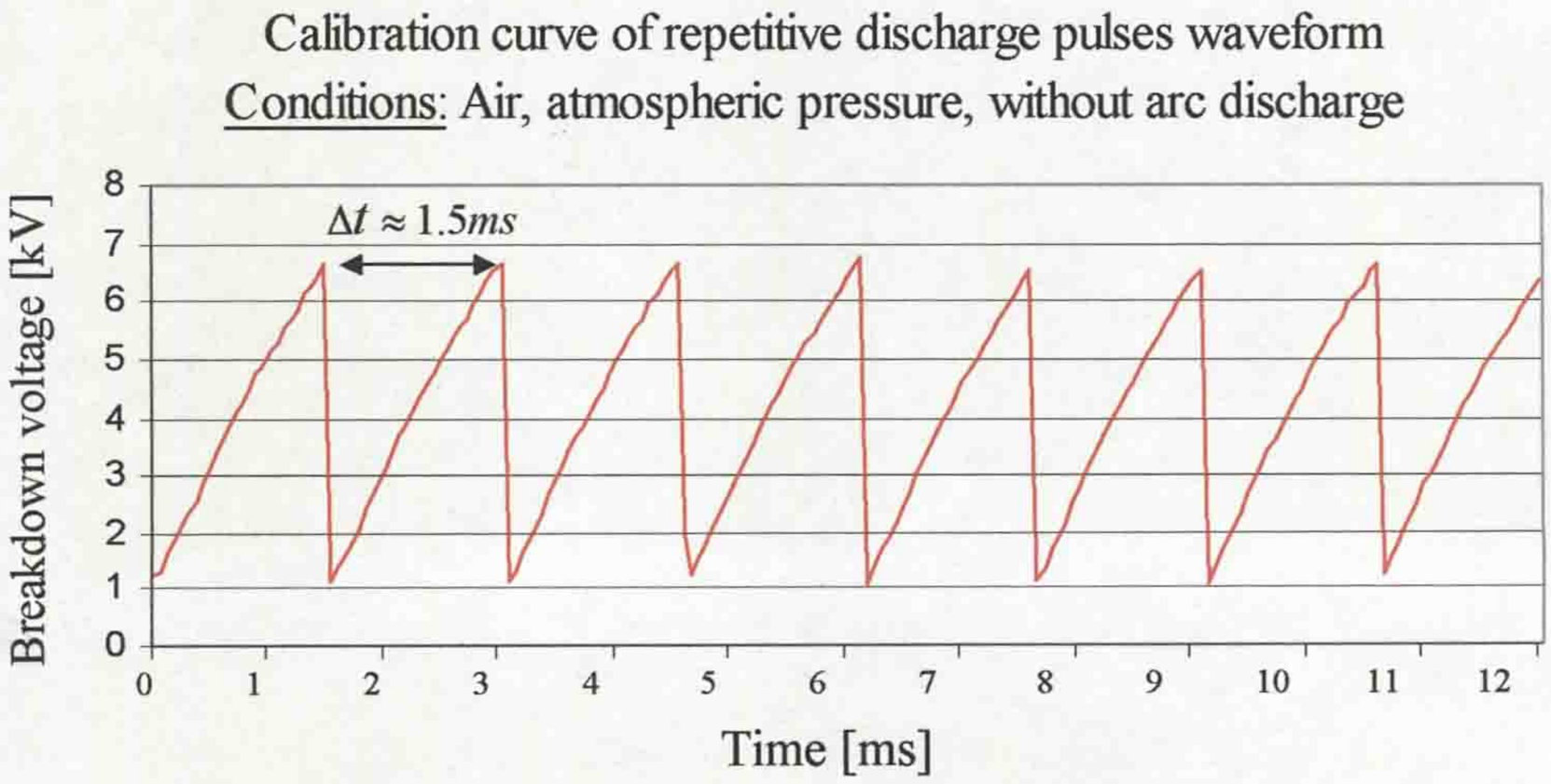

Figure 4.23 Example of the spark plug calibration

It was found that the dielectric probe's pulse breakdown voltage through the medium (air, atmospheric pressure) was around 6.5kV, producing quite stable repetitive

discharge pulses with a time duration of 1.5ms. An example of the timing sequence of the experiment is shown in figure 4.24.

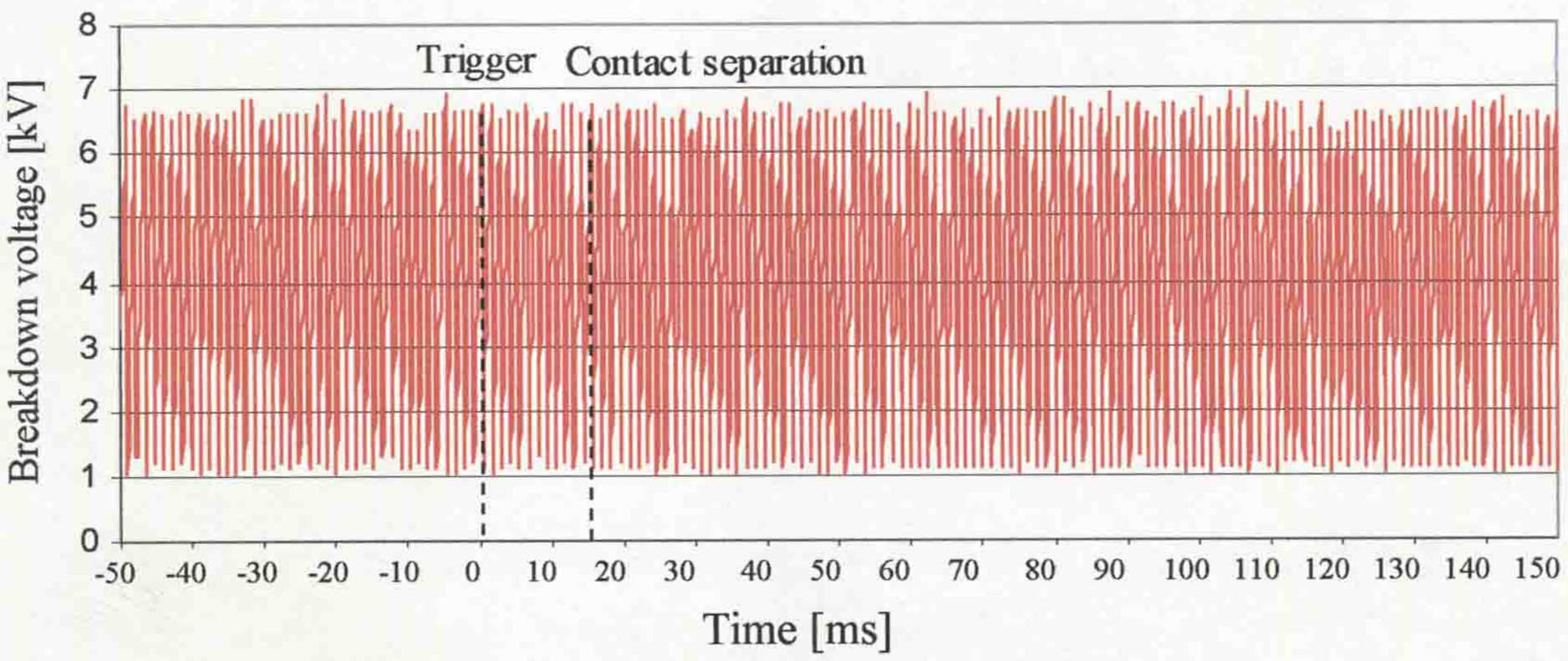

Figure 4.24 Test timing sequence for calibration

In order to monitor the extent of the dielectric loss within the interrupter during the arcing time, including the duration of the reduced dielectric strength (post arcing time) the time resolution in the oscilloscope was increased. The dielectric strength measurements presented in **section 5.2.3.4** used the timing sequence of the experiments (fig. 4.24) in the same manner.

4.2.7 Optical measurements

In this section, optical measurements techniques are described that have been applied in this project for design development and evaluation (**chapter 3**). These methods include optical fibre monitoring methods for arc speed (rotation) indication, high-speed and video photographic observations of the arc behavior during arcing and post arcing time. High-speed photographic monitoring of the test models and visual observation of the devices post arcing time determined the main strategy of the design development during the experimental works.

4.2.7.1 Optical fibre viewing system

The optical fibre sensing system is schematically presented in figure 4.8.

It consists of an optical fibre link (protected from the external strong light radiation), optical detector and signal processing system (oscilloscope and P.C.). The electric arc as a source transmits light radiation that was incident on the optical fibre (sensor) and which transmitted the light signal to the optical detector (10-channels optical detector). The optical detector is used as an interface, transforming the light signal to an electrical signal for connection to the signal processing system. Significant immunity of the optical fibres to electromagnetic interference (Medlock, 1989) and high electrical insulation from the arc enable the optical fibre viewing system to be situated sufficiently close to the development structure during the arcing time.

Arc rotation (speed) monitoring in the rotary arc interrupter used three optical fibre links connected to the 10-channels optical detector and to the additional signal processing systems in the same manner (fig. 4.8). The optical fibres position arrangement were different for each experiment and are described in **section 5.1.3.3** in detail.

4.2.7.2 High-speed photographic equipment and shutter system

The high-speed photographs of the arc column were obtained with a Cordin camera, Model 350 (Rotating Drum Framing Camera) located at a distance of 2 - 3 metres from the light source (Experimental device). The high-speed continuous writing camera is a portable research instrument designed for motion analysis and velocity studies. This camera contained both a rotating drum and a rotating mirror and offered a range of framing rates from 224 to 35000 frames per second. The octagonal rotating mirror relayed the image obtained from the objective lens (f/1.8 with coated optics) onto the film by a system of stationary mirrors. During this project, black and white (XP2 SUPER 400) and colour (35 SURVEI COLOR SUPERIA 400) films were used for the camera operation. A meter length film was rotated on the drum and all 224 pictures were taken at essentially the same framing rate because of the stable rotation speed on the camera's spinning drum. During the arcing tests, the exposure times were controlled by the framing rate and the type of stop used. At a top speed of 35000 frames per second, a frame was exposed every 28.5 microseconds at a selectable shuttering speed of 0.9, 1.9 and 3.8 microseconds per frame. The total writing time at top speed was 6.4 milliseconds. In practices a size of stop of 3/16 inch was used with a frame speed between 10000 - 20000 frames

per second that corresponded to the writing time between 22.4 - 11.2 milliseconds giving exposure times of 6.6 - 3.3 microseconds. This camera examined the arcing period for either one or two half cycles and the quasi-dc arcing period, providing sufficiently accurate photography during the arcing time.

Two distinct types of shuttering were used with the high-speed photographic camera (Model 350). One was provided by the capping shutter, which controlled the total writing time. The rotating mirror in conjunction with the stops provided the second type of shuttering. The light followed a fixed path through the camera optics until it encountered an octagonal rotating mirror, which reflected the beam. The direction of the beam was determined by the angle of the rotating mirror's face. The size and shape of this beam were determined by the entrance stop. Each individual frame of film was exposed only during the time when the sweeping light beam passed across the exit stop. Consequently, the duration of the exposure depended upon two factors: the speed of the mirror, and the size of the stops. With an increase in mirror speed, the reflected light beam passed more quickly across the exit stop. With an increase in the size of the stop, the light beam needed to swing farther to pass completely across the exit stop. Therefore, at any given camera speed, the stop determined each individual frame's exposure time. The capping shutter in the camera was released by a solenoid with a time response 1/500 to 1 second nominal. As a result, during the arcing test the time sequence of the camera commenced to operate before the arcing time in order to avoid any delay from the shutter operation.

4.2.7.3 Timing control sequence

The capping shutter operation depended on the solenoid response to the trigger pulse from the central control unit for shutter operation (fig.4.8). The shutter operation time was not constant because of the mechanical delay (**section 4.2.7.2**). Therefore, the first trigger pulse to the shutter operation was usually initiated 40 ms early before arcing commenced and it was fully open at the arcing time (fig. 4.11).

4.2.7.4 Video recorder system

The video recorder system, as a part of the experimental research laboratory

at the University of Liverpool was operated during the series tests for design development (**chapter 3**). A Panasonic CCTV video camera showing in figure 4.10 (Security camera) was able to observe the test rig after the dc and ac arcing with a frame duration set at 40ms (25Hz frame frequency). Video frames, obtained from the camera allowed the post arc processes occurring in the experimental devices (post arc plasma propagation) to be observed dynamically. However, the strong light radiation from the arc and electromagnetic wave propagation produced by the arc could disturb the camera operation post high arc currents. Therefore, the video camera monitoring was only used at low currents.

4.2.8 Other measurements

Auxiliary measurement methods utilised in this project are presented in this section. The pressure and PTFE ablation measurements, including oscilloscope-recording system have been used during the design development (**chapter 3**).

4.2.8.1 Pressure measurement

Pressure monitoring was used in the preliminary arc tests (**section 5.2.1**) for design development. The pressure gauge monitored the chamber pressure inside the interrupter (non-rotary arc reference interrupter) up to 3bar (pressure gauge).

4.2.8.2 PTFE ablation measurement

The use of PTFE ablation measurements in this project is described. The main aim of these measurements was to investigate a relationship between volumes of ablated PTFE material and the arc energy, which was needed for that ablation. The ablation monitoring method was based on visual observation of the volume of PTFE material in the interrupter head (**section 3.2**) by measuring the diameter of the PTFE cylinder after 40 tests, in air, at atmospheric pressure and at different ac current levels (**section 5.2.3.6**).

The design of the novel rotary arc interrupter was based on the results obtained from the PTFE ablation measurements, which determined the geometric shape of the prototype interrupter (**section 3.3**).

4.2.8.3 Oscilloscope recording unit

A digitising oscilloscope "GW Instek GDS-830" was used in the project for various parts of the investigations. It provided accurate measurements of the current, voltage, dielectric strength, arc rotation, contact travel and magnetic flux density during the arcing and post arcing time. The 100MSample per second resolution (bandwidth 100MHz) of the oscilloscope supported the high-resolution waveform monitoring with a time base of 2ns/div to 5s/div. The oscilloscope had an input impedance of 1MΩ, an input capacitance of 7pF to 49pF, and used the storage memory for saving the waveform traces. Therefore, these results were transferred to a Personal Computer (PC) utilising an RS-232 serial interface. All oscilloscopes were powered trough 1:1 isolation transformers and 1:1 probe transformer providing electrical isolation of the external triggers of the oscilloscopes from the control system.

4.3 CONCLUSIONS

The experimental systems (power supply, central control and optical unites, **section 4.1**) and diagnostic measurements (electrical, mechanical, optical, **section 4.2**), described in this chapter, are important for design development (**chapter 3**) providing an effective interrupter design, modelling and interrupter condition monitoring. The conventional diagnostic methods (current, voltage, high-speed and video photography, optical fibre probing, magnetic field probing and dielectric strength probing) mentioned above, provided an effective evaluation of the design development during the experimental work. The experimental tests and results (**chapter 5**) obtained during the project used the experimental systems and diagnostic measurements in the same manner.

CHAPTER 5 - EXPERIMENTAL TESTS AND RESULTS

This chapter is devoted to experimental tests with the devices that are designed for arc control and interruption (**chapter 3**) and to the test results obtained during this project. The experimental tests and results, presented in this chapter, are divided into three parts. The preliminary tests (**section 5.1.1**) for arc control design determined the subsequent design strategy of the arc control model, including the design and modelling of the novel rotary arc interrupter. The arc control test investigations (**section 5.1.2**) describe a second part of the experimental works. The tests relevant to a novel rotary arc interrupter design (**section 5.1.3**) are a third part of the experiments, describing the interrupter head tests and their evaluation. The experimental test facility and diagnostic measurements (**chapter 4**) used in these tests were in the same manner.

5.1 EXPERIMENTAL TESTS

This section presents the test strategy for each experiment involved in the experimental investigations. The purpose of each test is described and the test results (**section 5.2**) later are presented.

5.1.1 Preliminary investigations for design development

The preliminary arc tests in SF_6 and N_2 media are presented at different pressure (0-3bar). The PTFE arrangement into non-rotary arc interrupter (**section 4.1.5.1**) (reference breaker) was tested for the test head design geometry of a novel rotary arc interrupter (**chapter 3**) in order to estimate:

- Quasi-dc and ac arc behaviour in different media
- Electrode gap at current zero
- Optimal length of the magnetic coil for design development (**section 3.1.3**)

The experimental tests facility (fig. 4.8) and diagnostic measurements relevant to the quasi-dc (up to 9.3kA), ac (up to 18kA) currents, at different arc duration (up to around 38ms) and voltage tests were used in preliminary arc investigations in the same manner as for the rotary arc interrupter tests (**section 5.2.3.2**).

5.1.2 Arc control tests

A description of the experimental tests relevant to arc control model (**section 3.1**) is introduced. The electrical parameters tests and optical test investigations (high-speed and video photographs) provided the experimental proof (**section 5.2.2**) of the new concept of arc control in air, at atmospheric pressure, which may be used in the high-voltage circuit breakers.

5.1.2.1 Electrical parameter experiments

Electrical parameter experiments in the arc model test head included both current and voltage measurements, which are involved during the model tests. The current and voltage measurement techniques have been described in **sections 4.2.2**, **4.2.3** and the experimental results were obtained in the same manner as described in **section 5.2.2.1**. Low values of quasi-dc and ac arc currents were used in the model investigations, providing effective conditions for observation by the high-speed and video cameras in air, at atmospheric pressure.

5.1.2.2 Optical test

Optical investigations of the model for the arc control provide effective observation of the quasi-dc arc during the arc interaction and post arcing periods. The high-speed camera (**section 4.2.7.2**) was used in the optical tests, providing high-speed photographs of the arc column in detail. A frame speed of 10000 frames per second, with an exposure time of 6.6μs was used for examining the dc-arc discharging period. Black and white film (type XP2 SUPER 400) was used in the camera. The video recorder camera was used to observe the rig after the dc/ac arcing with a frame duration set at 40ms per frame, in air and at atmospheric pressure.

5.1.3 Novel rotary arc interrupter tests

The aim of the experimental tests with the interrupter heads was to measure the B-field distribution around the coil contained within the test head (**section 3.2**), test the interrupter head in air, at atmospheric pressure using the new concept for arc

control (**section 3.1**) and to evaluate its performance (**section 3.3**). The purpose of each test is described and the results are obtained in the same manner (**section 5.2.3**).

5.1.3.1 Magnetic field experimental test

Magnetic field measurements were made for determining the relationship between the ac-peak current of 5.3kA and the total *B*-peak field distribution produced by the coil (contained within the PTFE) around the PTFE cylinder as a function of the distance from the cylinder (fig. 5.1). The technique of magnetic field measurements using the search coil is described in **section 4.2.4**. The coil and the PTFE cylinder are of a symmetrical geometry. Section 4 of the geometry (fig. 5.1) was chosen for the B field measurements because of the comfortable access to the PTFE cylinder. As a result, 16 measurement points were chosen. The radial B_x and axial B_z components of magnetic fields were measured (Johnk, (1988) and Guru *et al*, (2004)) and the total *B*-field calculated. A linear relationship between the higher current and total magnetic field around the model was anticipated because of the air core of the coil. The positions of different sections shown on figure 5.1 are identified by a colour-scale.

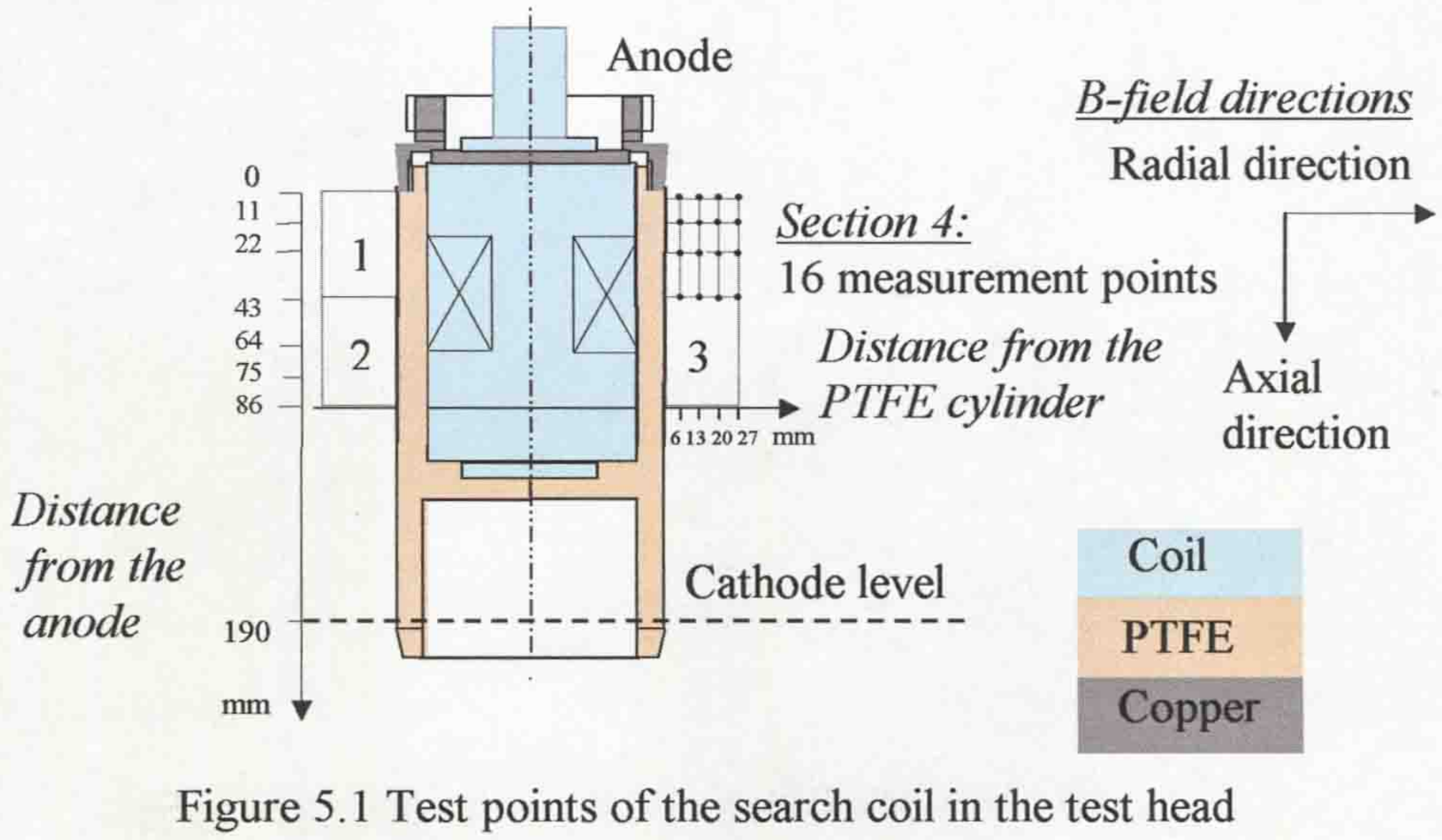

Figure 5.1 Test points of the search coil in the test head

5.1.3.2 Electrical tests

In thesis section electrical parameter tests for interrupter design development **sections 3.2** and **3.3** are introduced. Experimental investigations were

first undertaken with the current interrupter head. These tests involved inspecting the critical ability of the breaker head to interrupt (at current zero, in air and at atmospheric pressure) the maximal level of ac-arc current while the arcing time (hence contacts gap) was minimal. A detail investigation of the current zero area is presented for a critical gap and current where arc may be not interrupted properly. These tests show what happens in the period just after current zero. The restrike voltage across the interrupters test head was investigated for different contacts gaps and current levels. These experiments yield the post arc conductivity at the instant of arc extinction, accompanying various restriking voltage transients. The critical performance of the interrupter heads has been tested in relation to the arcing time and contact gap, and is compared to other interrupter performances. For the arc voltage monitoring, the coil voltage was not included (**section 4.2.3**) in order to obtain the absolute arc voltage measurements. Therefore, the total voltage across the interrupter terminals (including the coil voltage) should be slightly higher because the coil voltage is proportional to the coil inductance magnitude and it impedance (**section 4.2.3**).

5.1.3.3 Optical fibre tests

The optical fibre tests provided observations of the arc rotation and speed. The concept of the arc control for the new rotary arc interrupter was based on the results obtained in these investigations (**section 5.2.3.3**). The manner of observing the ac-arc rotation and speed is shown schematically in figure 5.2.

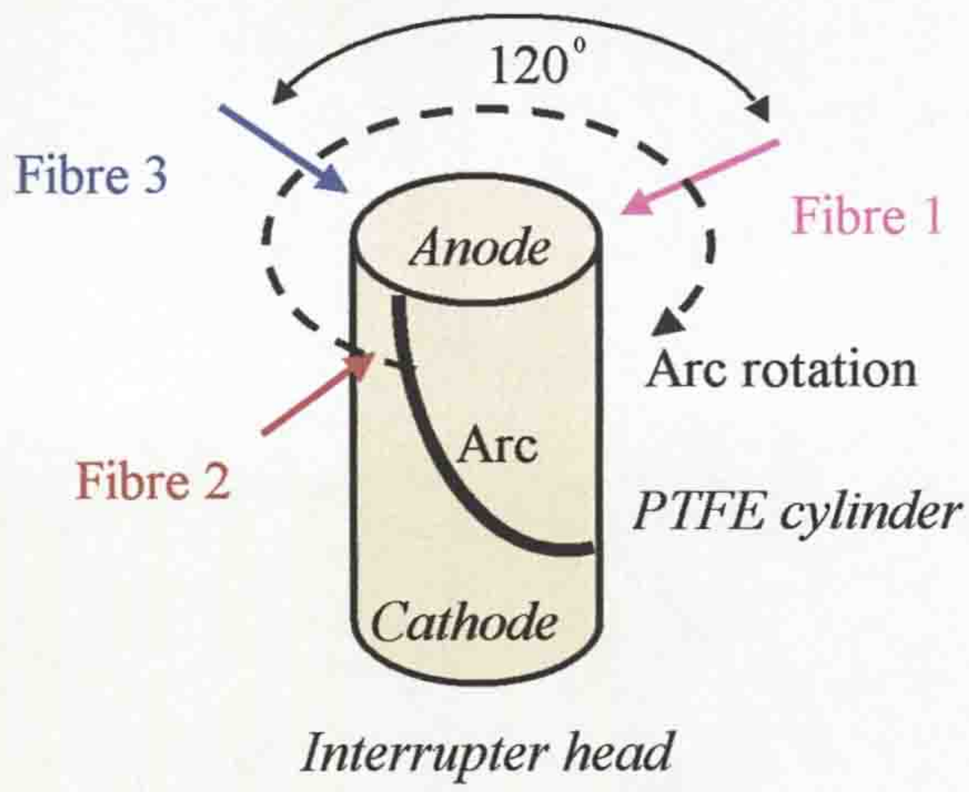

Figure 5.2 Horizontal positions of optical fibres

The optical fibers were fixed at the top of the interrupter head giving a horizontal view towards the PTFE cylinder. Three fibers were situated on the same plane 120 degrees from each other. The ac-arc 13.25kA was investigated in air, at atmospheric pressure, with an ac-arc duration of 14ms. The ac-arc rotation was followed around the PTFE cylinder. Figure 4.9 shows the arc discharge initiation area at the time of the electrodes disconnection. Fibre 1 was fixed close to this point and was considered as an initial point of the ac-arc rotation. The magnetic field around the PTFE cylinder was measured for a 5.3kA alternating current (**section 5.2.3.1**) and was calculated theoretically for a 13.25kA ac-arc (Tab. 6.1, current interrupter head).

The vertical optical fibre positions (fig. 5.3) provided observation of the ac-arc length at its rotation profile from the arc initiation until the arc extinction.

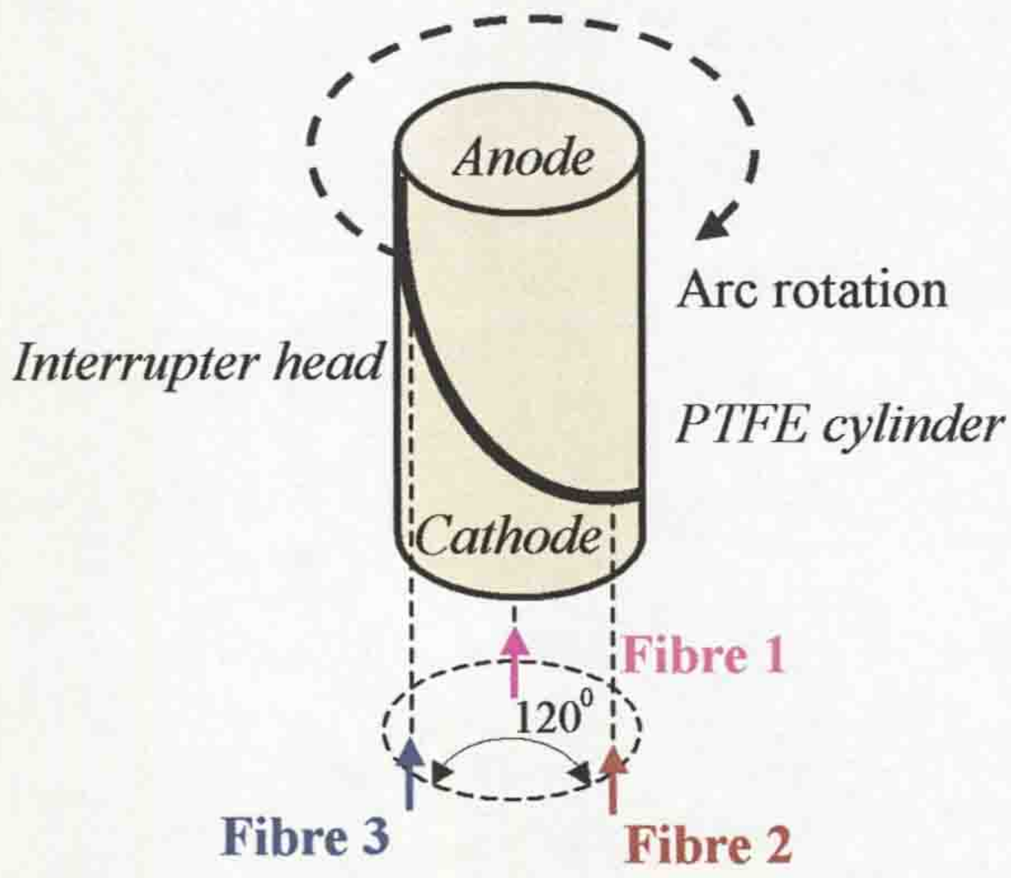

Figure 5.3 Positions of vertical mounted optical fibres

The arrangement of the optical fiber positions around the interrupter head gave a vertical view along the PTFE cylinder from the bottom upwards. The three optical fibres were fixed at 120 degrees to each other. Fibre 1 is fixed at the point of the ac-arc initiation, (fig. 5.3). The PTFE cylinder has diameter of approximately 100mm. From the known time of one turn of the rotary arc (period of pulse, fibre1) and the distance ($2\pi R$ - circumference length of the cylinder) of approximately 314mm, the arc speed at any arcing time point can be calculated as: (Speed = Distance / Time). Data (**section 5.2.3.3**) obtained during the rotary arc tests applied this calculation method for the arc speed estimation.

5.1.3.4 Dielectric strength experiments

Dielectric strength investigations were undertaken on the prototype rotary arc interrupter experiments in air, at atmospheric pressure. The aim of these experiments was to investigate the dielectric strength recovery characteristics, of the interrupter, from arc initiation to arc extinction including the post arcing time when the dielectric strength of the medium should become fully recovered. The technique used (**section 4.2.6.2**) was based on the investigations of Ennis (1996) and Mori (2005) presented in **section 2.4.1.1**.

Position of the spark plugs 1, 2 and 3 within the novel rotary arc interrupter is shown in figure 5.4.

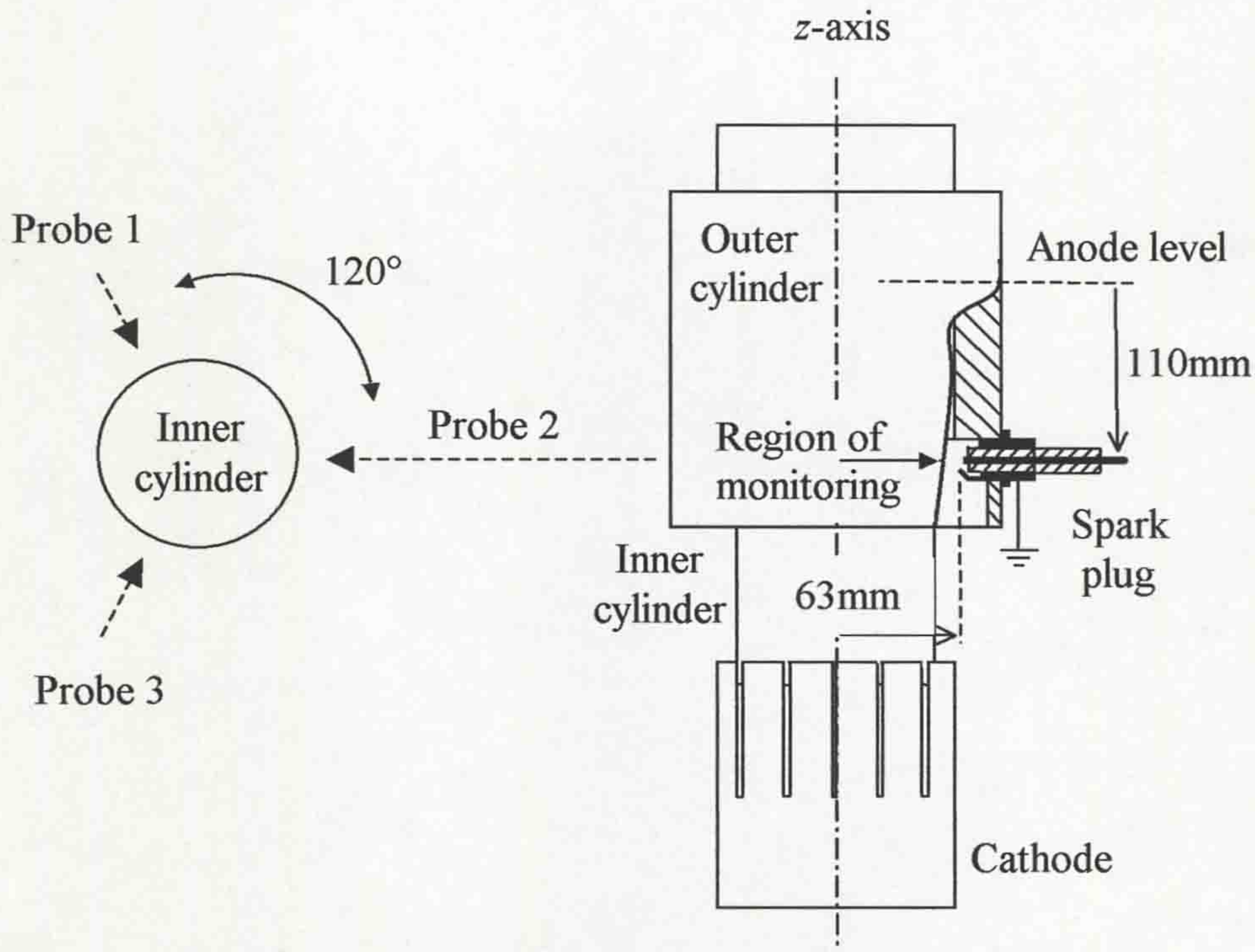

a) Top view b) Identification of the spark plug location

Figure 5.4 Spark plugs position within the interrupter

Figure 5.4b shows that the probes (spark plugs) position 1, 2 and 3 are situated around 63 mm from *z*-axis of a circular inner PTFE cylinder and around 110 mm from the anode to the region of monitoring levels. For the present investigations, the probes was inserted between the inner and outer PTFE cylinders (fig. 5.4b). The

dielectric strength (around the interrupter) between the two PTFE cylinders were tested using three test points, situated 120 degrees from each other (fig. 5.4a). A typical example of one test point is shown in figure 4.22. The purpose of these experiments was to investigate the distribution of dielectric strength around the novel interrupter. The test conditions for the atmospheric ac-arc of around 5kA, in air, arc duration of 12-20ms and 129.8mT magnetic field producing coil were chosen for the novel rotary arc interrupter as being close to the previous tests of the Ennis (1996) providing good comparison possibilities.

Experimental tests in the prototype interrupter were to investigate the relationship between the electrodes gap and response of the dielectric probe. The test results are presented in **section 5.2.3.4**.

5.1.3.5 Optical experimental tests

Optical methods for monitoring the interrupter head are described, in which high-speed, video photographs and visual observations were used. Investigations of the quasi-dc and ac arc columns have been made using two high-speed cameras (Cordin, model 350) each situated 120 degrees with respect to the other. This arrangement enabled the arc column to be observed from two positions at the same time. It means that the rotary arc can be monitored continuously at different positions around the current interrupter head (fig. 4.9). The high-speed camera was used at a frame speed of 7500 frames per second, exposure time of ~6.6 microseconds for examining the dc and ac arcs discharging period. Black & white film (type XP2 SUPER 400) and colour (35 SURVEI COLOR SUPERIA 400) films were used for the cameras. The video recorder camera was used to observe the interrupter head after the quasi-dc and ac arcing duration and set at 40ms per frame. During the arc interaction, discolouration of the PTFE cylinder of the interrupter head could occur. Therefore, the experimental breaker was visually inspected post arcing.

5.1.3.6 PTFE ablation experiments

The purpose of the PTFE ablation tests was to explore how the volume of ablated PTFE material depended on the electrical energy expended. The method is based on the visual observation of the volume of PTFE material in the interrupter

head by measuring the diameter of the PTFE cylinder after 40 tests, in air, at atmospheric pressure and at different ac current levels up to 16kA. An example of

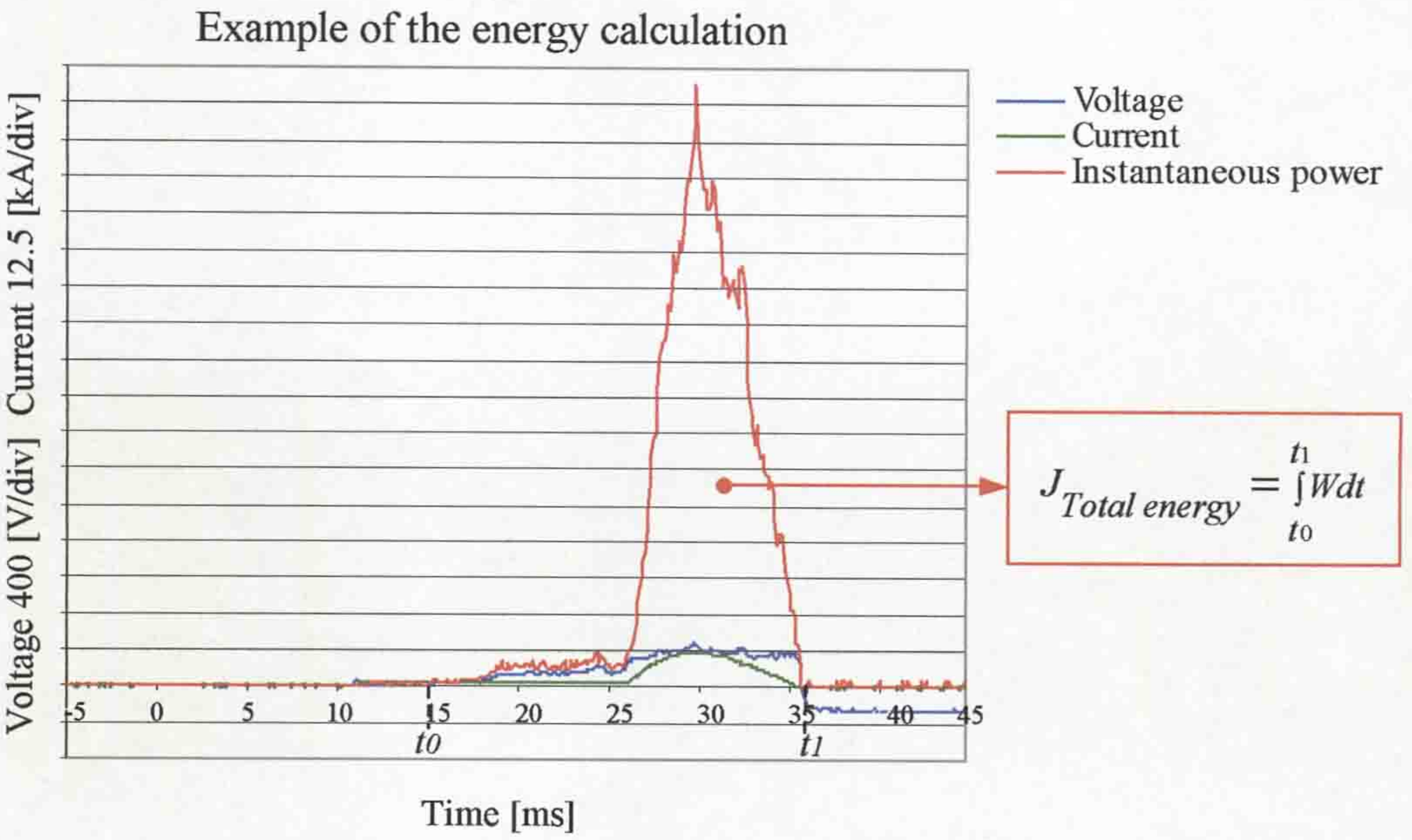

Figure 5.5 Total energy (1Joule = 1Watt x Second) during arcing (ac-peak 12.25kA)

the total energy calculation during arcing is shown in figure 5.5. The instantaneous power, which is expended, is calculated as the instantaneous arc voltage multiplied by the instantaneous arc current ($\Delta W = \Delta V \times \Delta I$). As a result, the total energy expended during arcing is presented as an integration of the instantaneous power with respect to time of the arc interaction $\sum \Delta W \Delta t$ (where $\Delta t = 0.1ms$ is one sample of the time scale).

The results obtained are not considered as absolute because of the difficulty in measuring accurately the PTFE diameter, which changed its shape after ablation.

5.2 TEST RESULTS

The experimental test results obtained are relevant to preliminary arc tests for design development (**chapter 3**), which has led to the design of two independent devices for arc control and interruption. Conclusions of the test results relevant to the experimental devises are described.

5.2.1 Preliminary arc tests for design development

5.2.1.1 DC arc investigations

The novel arrangement of the PTFE materials in the non-rotary arc interrupter (**chapter 4**, fig. 4.4) was tested in Nitrogen (N_2) and SF_6 gases, and at different pressures. Figure 5.6 shows the time variation of arc current and voltage for different quasi-dc arcs (N_2, 3bar pressure gauge) with maximum values in the range 0-9.3kA and also is indicated the peak recovery voltages for each quasi-dc arc with values in the ranges 450V (9.3kA) to 1250V (2.0kA). The results show a progressive shift to longer times of the peak arc voltage with a decrease in arc current (~25ms (9.3kA) to 38ms (2.0kA)).

Figure 5.7 shows the current and voltage variations with time for quasi-dc arcs in SF_6, at 3bar chamber pressure. The maximum current was in the range 0-9.3kA and the arc voltage in the range 590V to 1400V. There is a progressive shift in the time of the peak arc voltage with a decrease in arc current (22ms (9.3kA) to 35ms (2.0kA)).

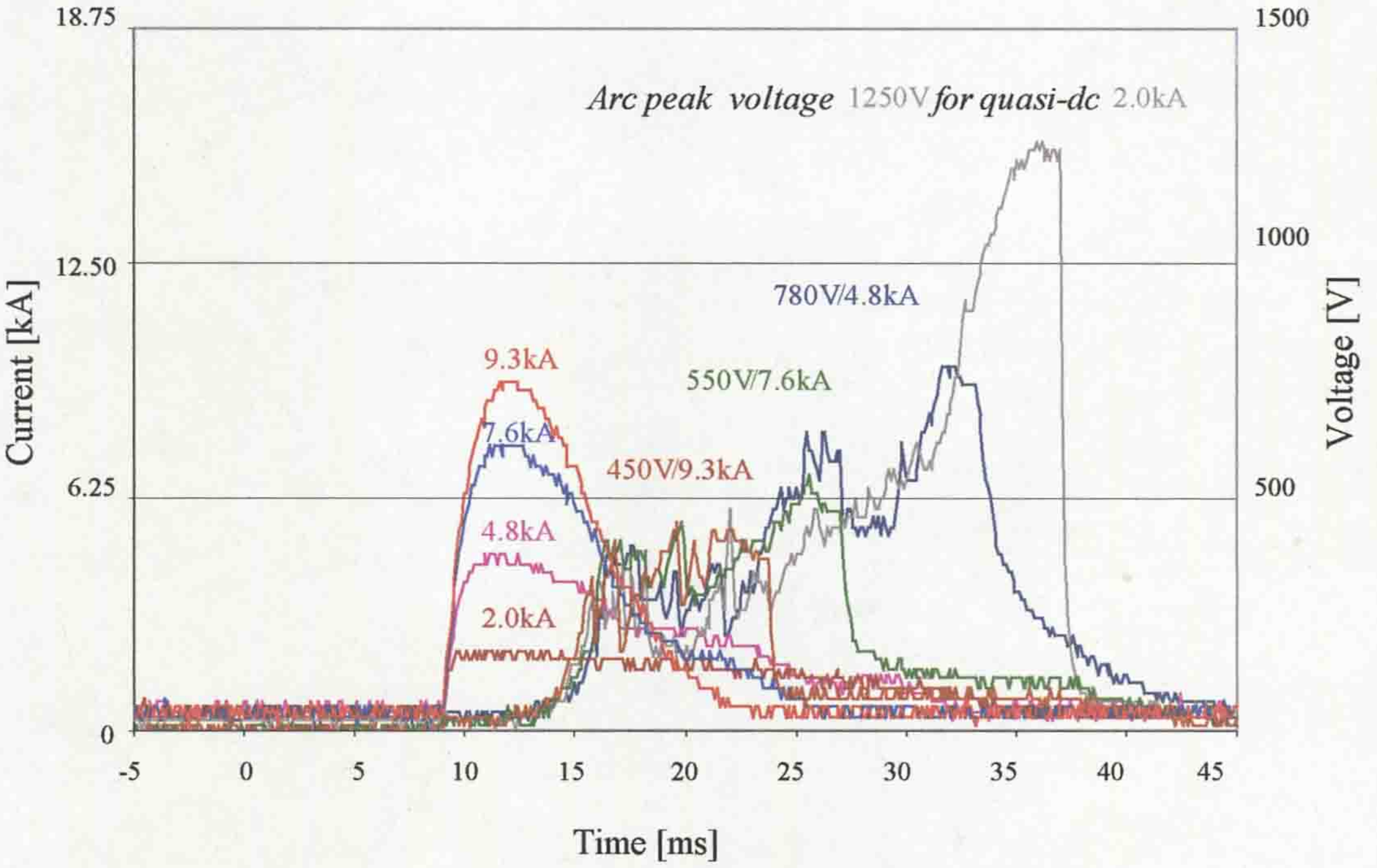

Figure 5.6 Quasi-dc arc currents and voltages as a function of time (N_2 gas, at 3bar chamber pressure)

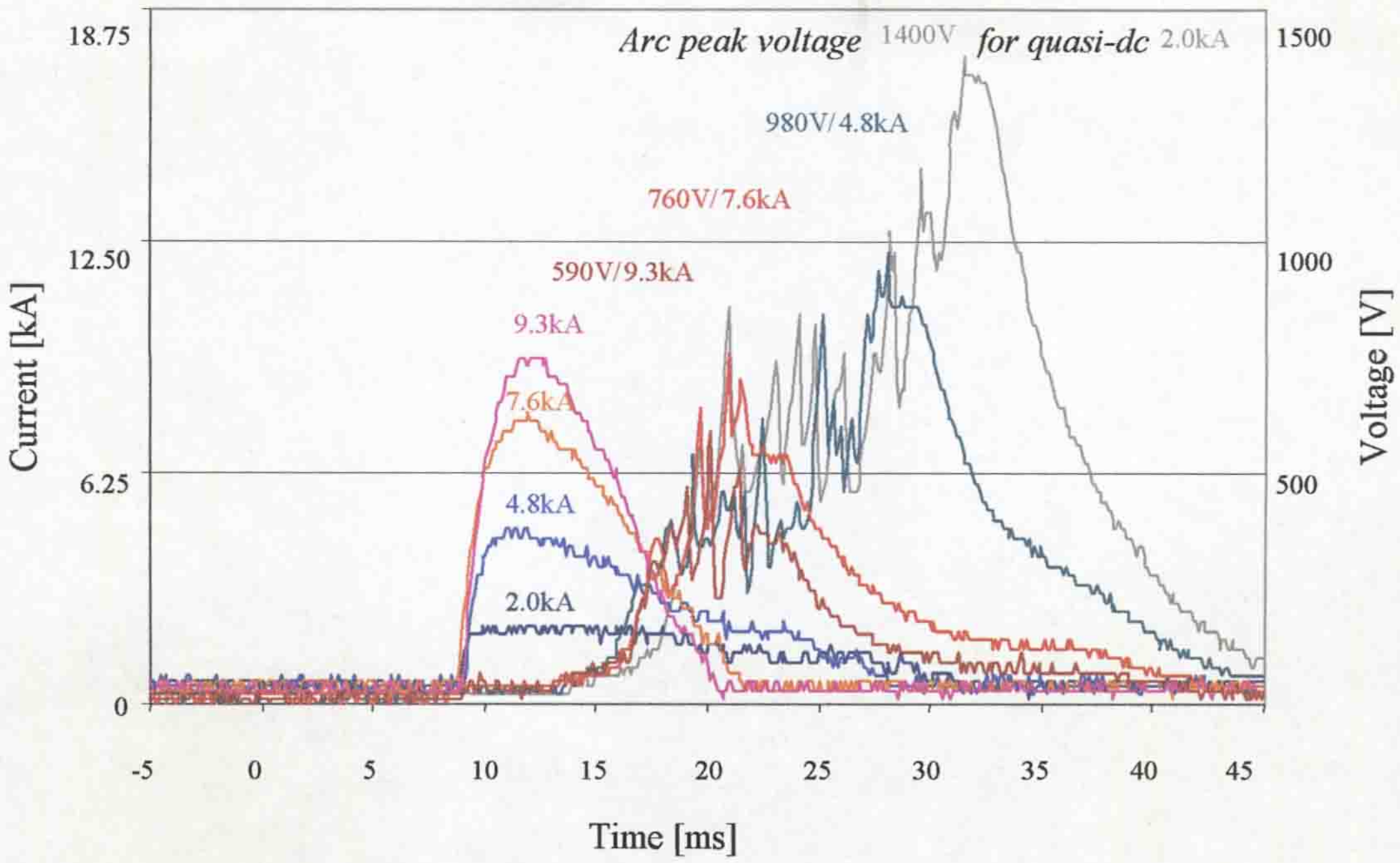

Figure 5.7 Quasi-dc arc current and voltage as a function of time (SF_6 gas, at 3bar chamber pressure)

Comparison of the time variation of arc voltage for N_2 and SF_6 (figures 5.6 and 5.7) indicates a move gradual increase in SF_6 before the peak value. Where as in N_2, the voltage after peak reduces to its half value less than for 1ms, in SF_6 it takes typically about 3ms.

The effect of gas pressure upon arcing was investigated by measuring the time variation of arc voltage for a quasi-dc arc of 2kA in both N_2 and SF_6. The results are shown on figures 5.8 (N_2) and 5.9 (SF_6).

The N_2 results (fig. 5.8) show an arc voltage gradually increasing with time, the different pressure effect becoming more pronounced at later time ($\geq$30ms).

The SF_6 results (fig. 5.9) show more pronounced voltage fluctuations than in N_2 (~400V) with higher voltage peaks at the two highest pressures (2, 3bar). Moreover, the arc voltage at the pressures of 0.5 and 1bar are approximately the same for both N_2 and SF_6.

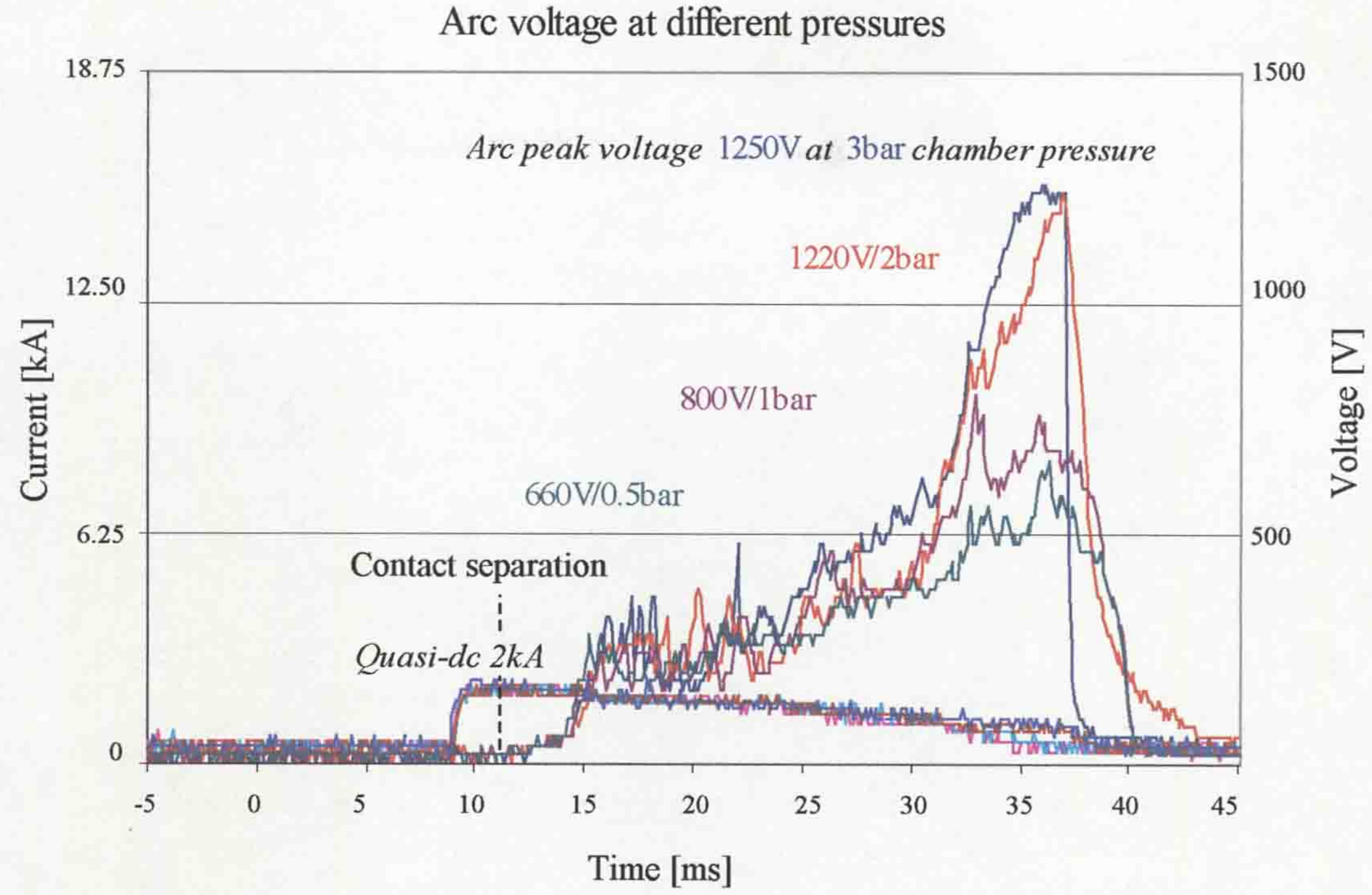

Figure 5.8 DC-arc investigations in N_2 gas, at different pressures

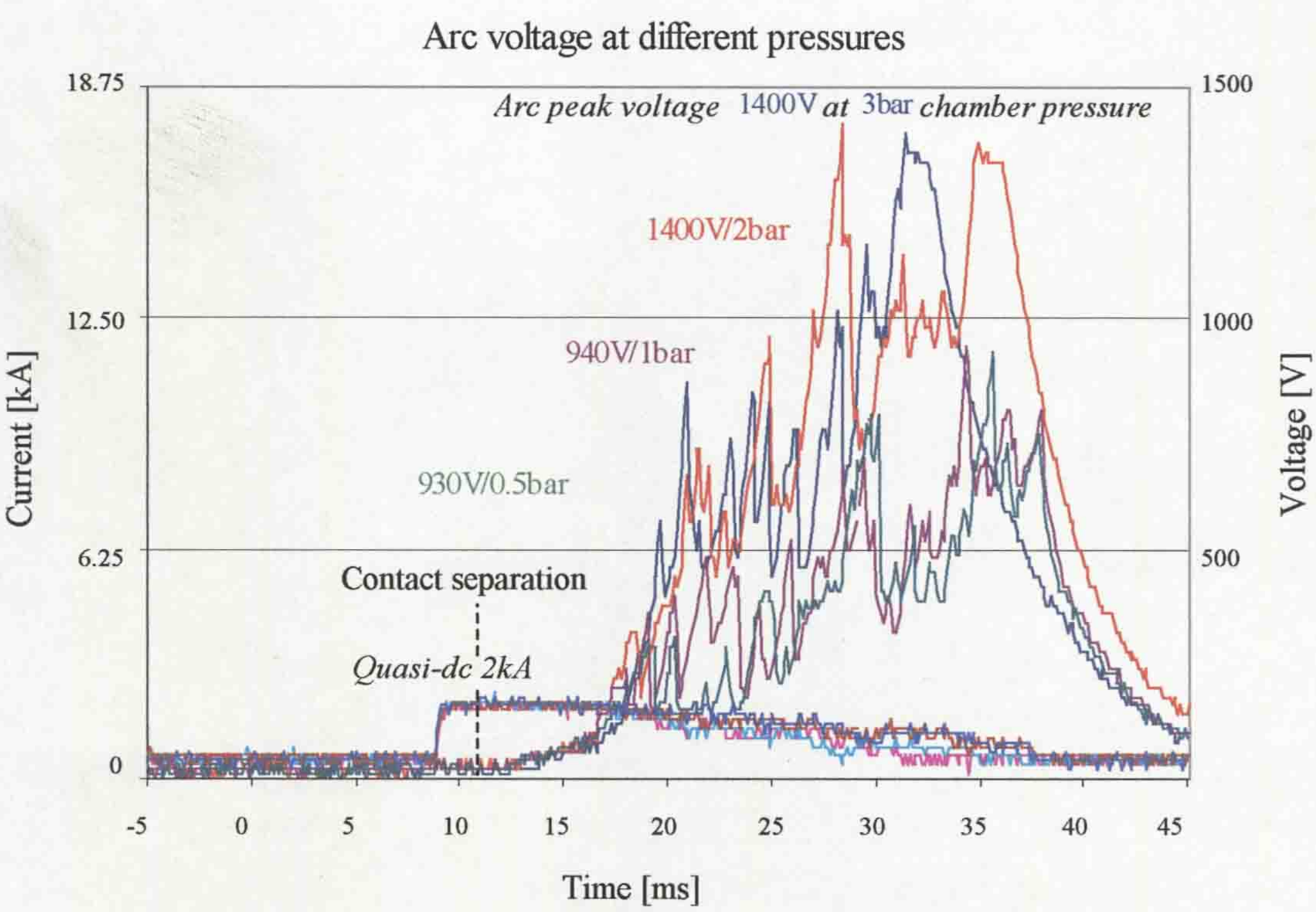

Figure 5.9 DC-arc investigations in SF_6 gas, at different pressures

5.2.1.2 AC arc investigations

The non-rotary arc interrupter (reference breaker, fig. 4.4) has been investigated at different ac-arc currents and durations in N_2 and SF_6 gases, with 3bar pressure gauge. During the experimental tests, a 2kA quasi-dc arc provided a flexible start time for the first ac-arc half cycle after contact separation.

The arc current and voltage waveforms for different ac currents in the range 12-18kA are shown on figure 5.10 for N_2 and figure 5.11 for SF_6. In addition, the ac waves at these current levels were applied at different times after contact separation so that the contact gaps corresponding to an instantaneous current were different.

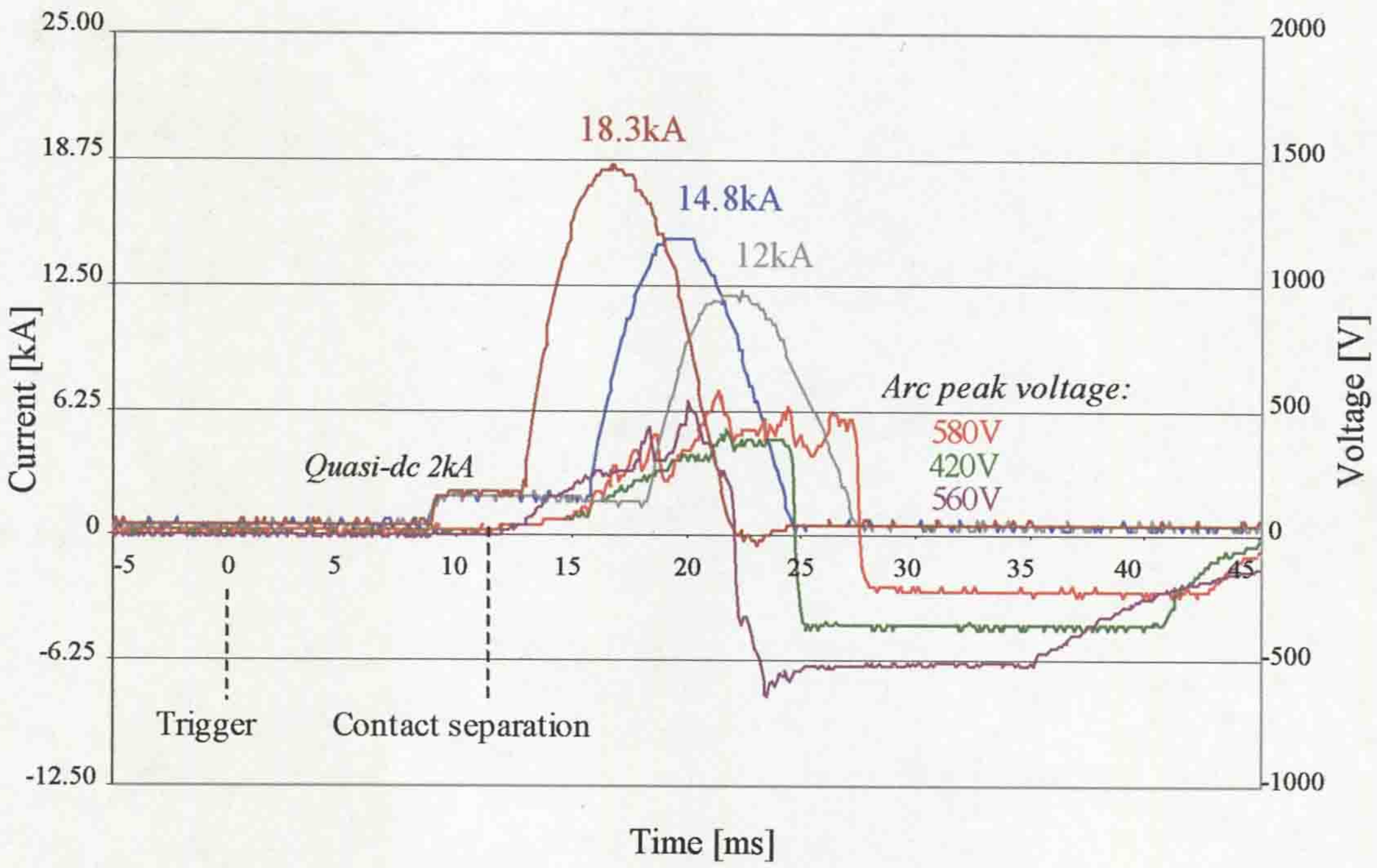

Figure 5.10 Arc current and voltage waveforms
(N_2 gas, 3bar chamber pressure)

The results for N_2 (fig. 5.10) show voltage values during the main ac wave almost independent of the peak ac current. The results for SF_6 (fig. 5.11) show a similar trend although there is evidence of the extinction peak being higher for the lowest current.

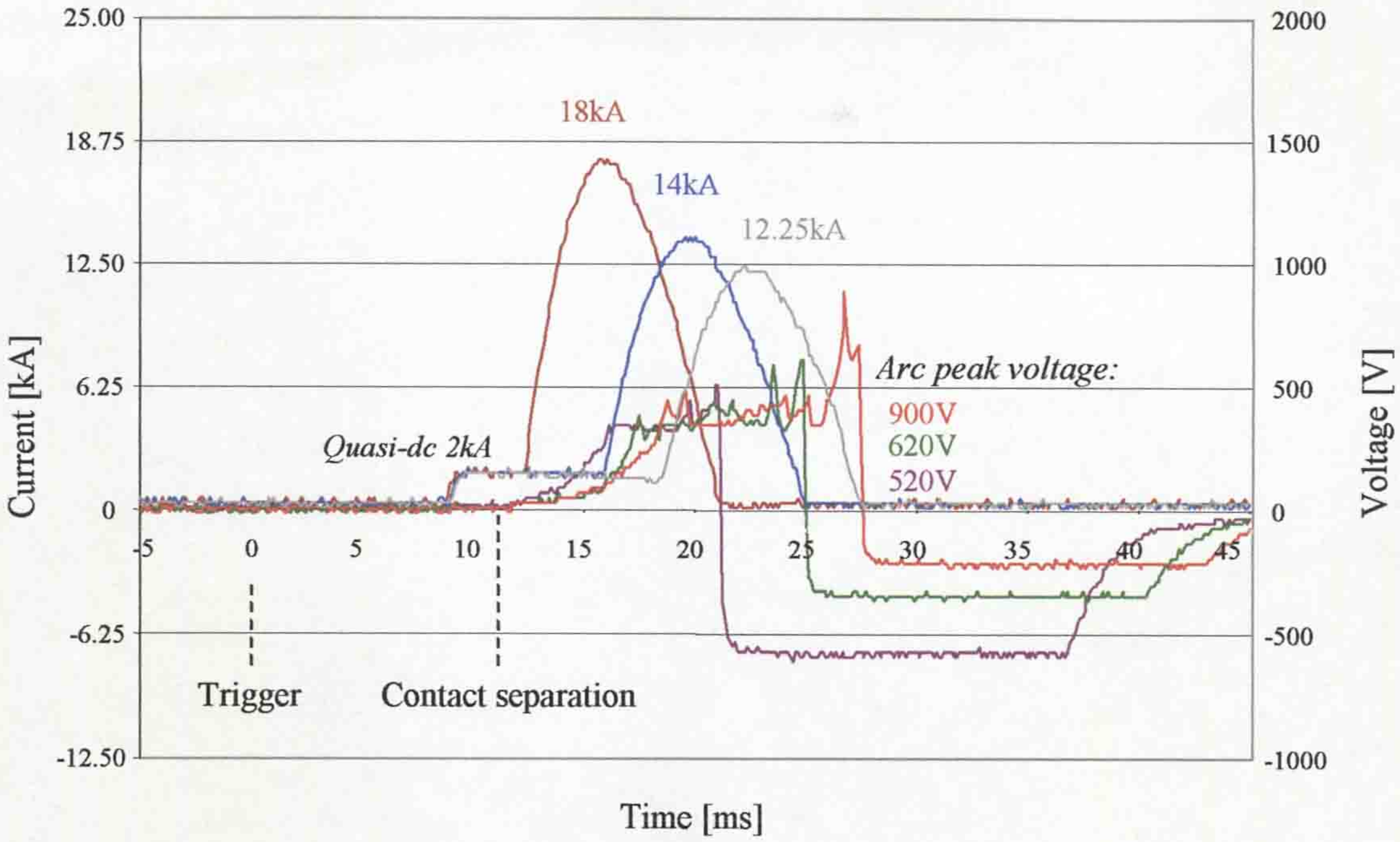

Figure 5.11 Arc current and voltage waveforms
(SF_6 gas, 3bar chamber pressure)

5.2.1.3 Contact gap length measurements

Contact gap measurements were made in order to estimate the ac-arc extinction gap at current zero for the non-rotary arc interrupter (fig. 4.4). These tests are important for choosing the optimal length of the coil producing the magnetic field in the novel rotary arc interrupter (**chapter 3**).

In order to determine a minimal electrode gap in the non-rotary arc interrupter, at which the ac-arc is interrupted at current zero, the ac-arc was tested under representative conditions: current operation 13.5kA to 18.5kA, 3bar pressure gauge, N_2 and SF_6. A travel recorder suitably calibrated has been used for monitoring the electrodes position at the time of the ac-arc interruption. An example of a travel record has been shown in figure 4.18. Figure 5.12 shows the relationship between the number of ac half cycles (1 or 2) of the ac-arc and the gap between the electrodes at the time of the arc interruption. Numbers 1 and 2 indicate the number of half cycles, which shows whatever the ac-arc was interrupted at the first (1) or second (2) current zero. The results show that for interruption at the first current zero a gap of 4.5cm was needed for SF_6 and 4.9cm for N_2. Such a first half cycle interruption occurred at around 18kA peak current.

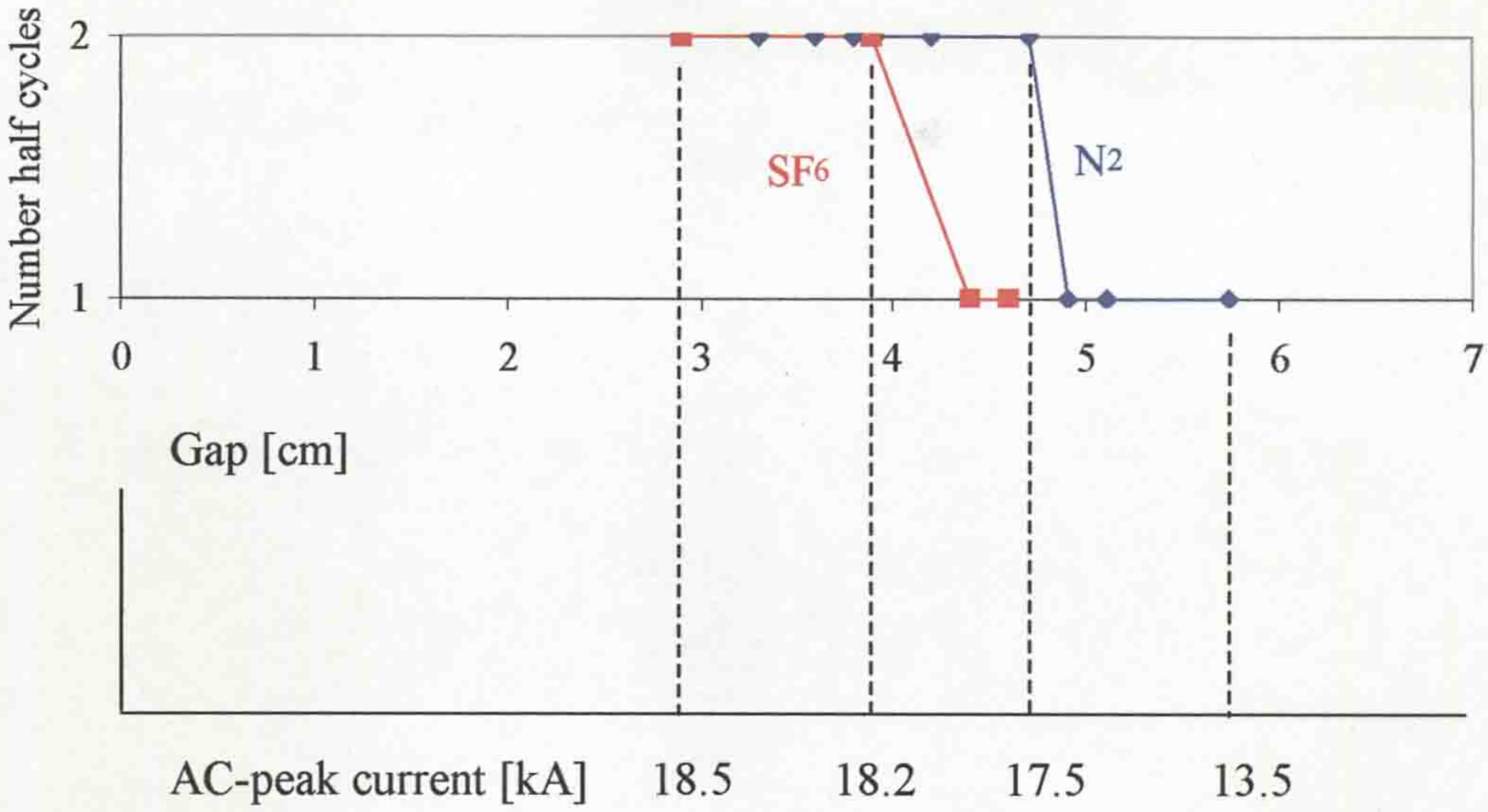

Figure 5.12 Relationship between peak alternating current and gap length at which current interruption occurred and also indicated in the number of half cycles over which the arc burned (N_2, SF_6, 3bar)

5.2.1.4 Conclusions

Analysing the experimental results previously mentioned a conclusion could be found that for dc arc in N_2, at 3bar pressure gauge the arc voltage behaviour gradually changed without so large voltage jumps in contrast to SF_6 where the voltage changes with big amplitude of oscillation. In addition, the arc voltage in N_2 (dc tests) drops rapidly at the time when the arc is interrupted, compare to SF_6 where the voltage is dropped quite slowly. Moreover, the experimental results with SF_6, using the same conditions, at different pressures showed that average arc voltages of the dc arc are dropped at current zero for around 350V (from 3bar pressure to 0.5bar) during the arc interaction. The same dc arcs behaviour observed at different pressure for N_2. This conclusion may be applied for the test results (at low pressure, up to 0.5bar) of the ac arc, where the chamber pressure has been set at 3bar, continually. The highest arc-peak voltage in SF_6 was observed at current zero in ac-arc tests (fig. 5.11) compare to N_2 where the voltage extinction peak was lower at 3bar pressure (fig. 5.10). The quenching media of SF_6 provides this kind of the ac-arc behavior at current zero.

Ac-arc test results obtained from the experimental tests of the non-rotary arc interrupter are compared and analyzed with the results obtained from the novel rotary arc interrupter test heads (**section 6.1.4**).

Tests results relevant to gap length measurements for design development (**chapter 3**) showed that the minimal contact gap was around 50mm, where the ac-arc was successfully interrupted in SF_6, N_2 and at 3bar pressure gauge. This dimension was applied as a length of the coil, producing magnetic field for arc control and interruption (**chapter 3**).

5.2.2 Results relevant to arc control

Experimental results for the arc control model (**section 5.1.2**) are presented. Current and voltage waveforms have also been obtained along with optical measurements from high-speed photographs and video records during the arcing and post arcing times.

5.2.2.1 Electrical parameters

Tests were first performed with a quasi-dc arc under the following condition: 1.3 kA/1.3 kV, quasi-dc time 30ms. A typical example of the dc current and voltage waveforms are shown in figure 5.13. On this figure, T is the oscilloscope trigger pulse from the central control unit. 9 ms later, the quasi-dc 1.3 kA/1.3 kV current is initiated igniting the electrical arc between the electrodes via a fuse-wire. After about 4.5 ms, the arc voltage increased before decreasing again and then forming a series of irregular oscillations. This voltage waveform is typical of those recorded under such quasi-dc arcing condition.

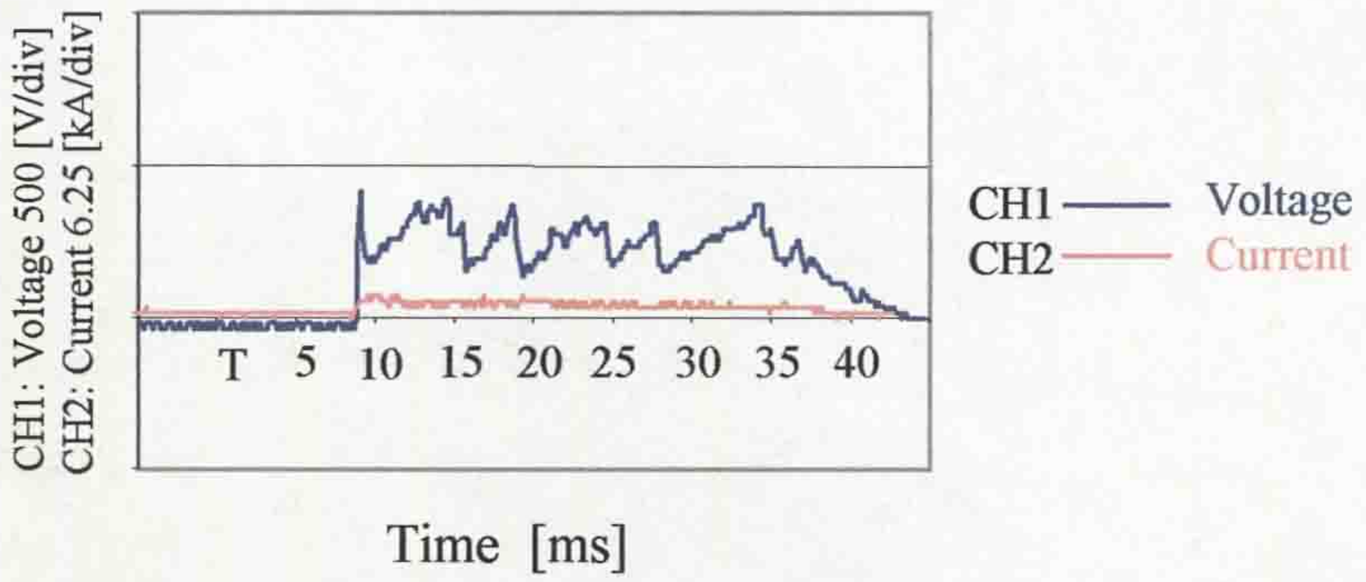

Figure 5.13 Current and voltage waveforms vs. time corresponding to the quasi-dc arcing condition

There were also performed experiments with a half- sinusoidal current of

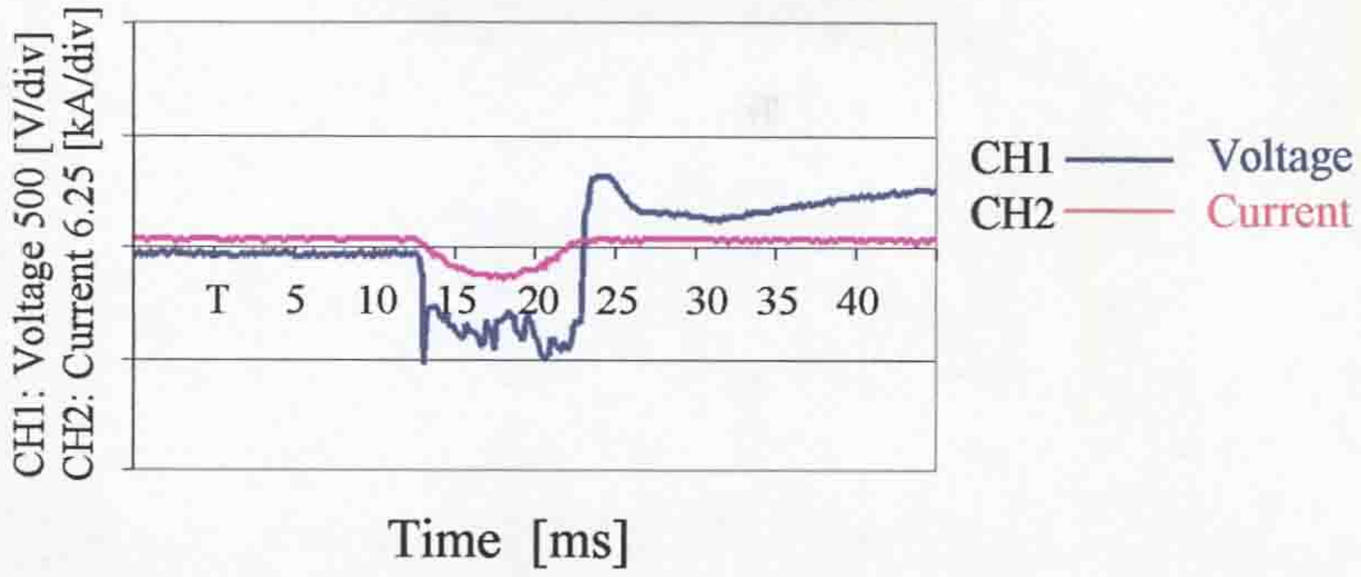

Figure 5.14 Current and voltage waveforms for a 50 Hz ac current

approximately 50Hz wave frequency. A typical time varying current and voltage record is shown in figure 5.14, corresponding to a peak current of 1.35kA. This record shows also a number of irregular voltage oscillations as in the quasi-steady dc case. The restrike voltage after current zero is also apparent on the voltage waveform.

5.2.2.2 Results of optical test

High-speed photographs and video recording of the device during arcing and post arcing time have been obtained. Figure 5.15 shows some examples of high-speed photographs that were taken under quasi-dc arcing conditions. These show an arc column initially formed vertically between the two contacts at 0.5ms following fusion of the fuse wire. At 1ms, the arc column becomes obliquely orientated under the influence of the magnetic fields. This distortion grows through frames at 1.5ms and 2ms until at 2.5ms the arc is orientated horizontally within the photographic fields of view. At 3ms, there is evidence of swirling plasma around the horizontal arc. At 3.5ms, the plasma swirl remains visible but the vertical column connecting to the top electrode also becomes visibly distorted to the right of the plasma. At 4ms, this distortion became so severe that the horizontal arc plasma ruptured.

Figure 5.16 shows some video frames (post arc observation) at 40, 80 and 120ms after arc initiation of a quasi-dc arc. They show the persistence of a plasma, but quite remotely driven away from the PTFE cylinder.

Figure 5.17 shows the corresponding video frames for an ac arc of peak current 1.35kA, demonstrating that the elements of plasma spread away from the model test head mostly in the horizontal direction.

The post quasi-dc and ac arc observations indicated that the persistence of plasma volumes was longer for the dc-arc compared to the ac-arc.

The arc model test head was investigated visually after the experimental tests.

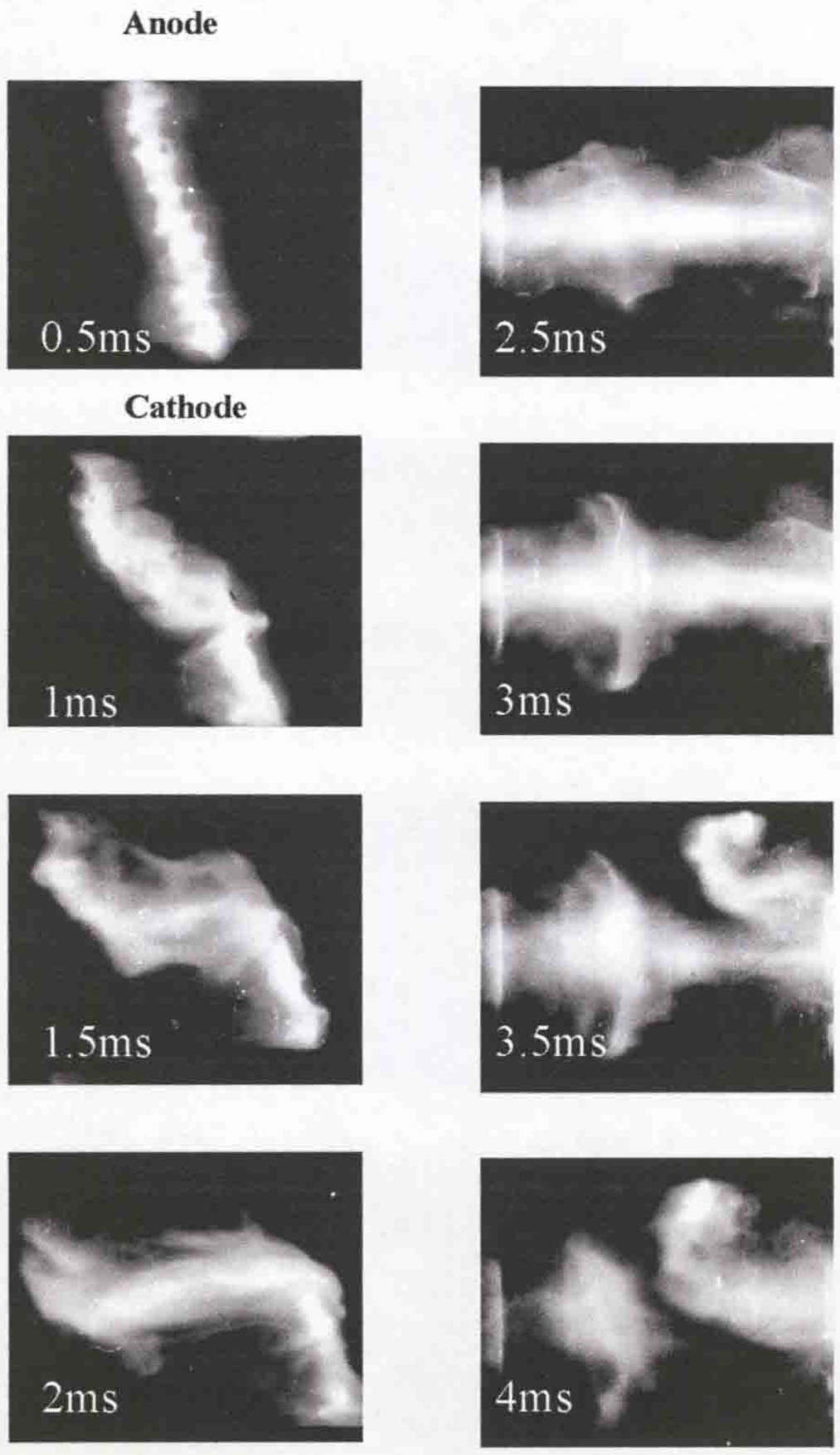

Figure 5.15 Example of high-speed photographs of arc in air, atmospheric pressure, quasi-dc 1.3kV/1.3kA, (framing rate 10000 frames per second)

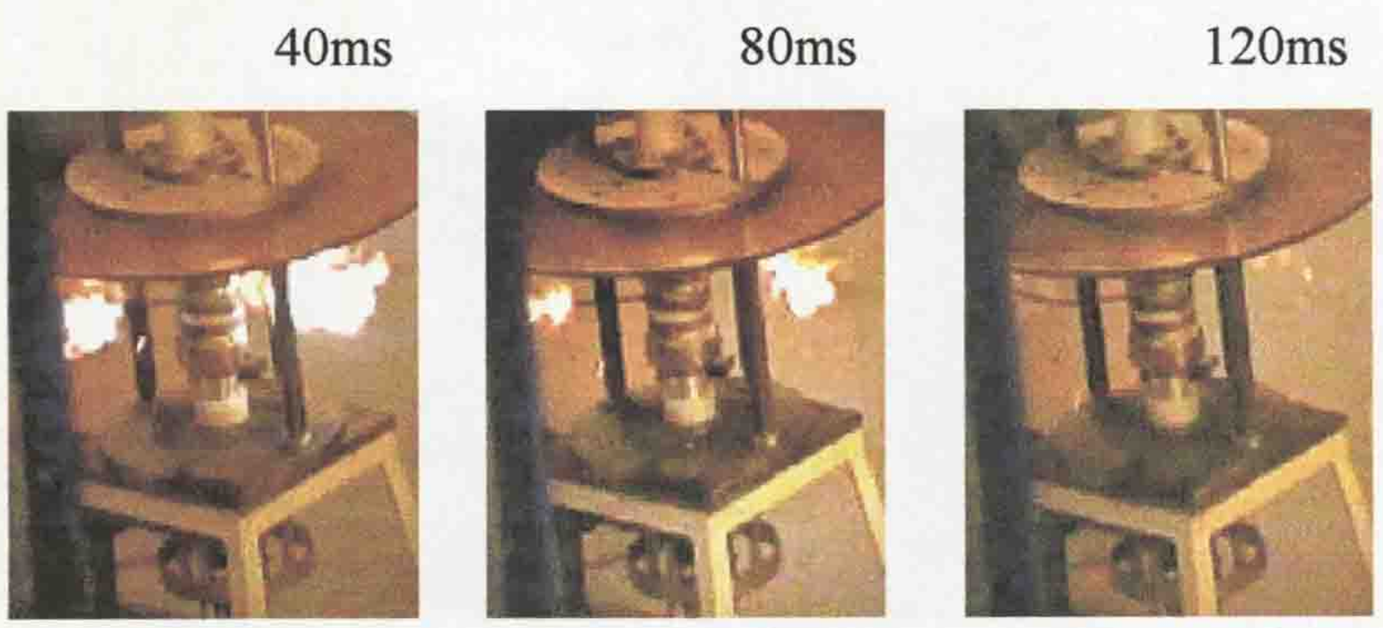

Figure 5.16 Video frames showing a post dc-arc repulsive effect (peak current 1.3kA)

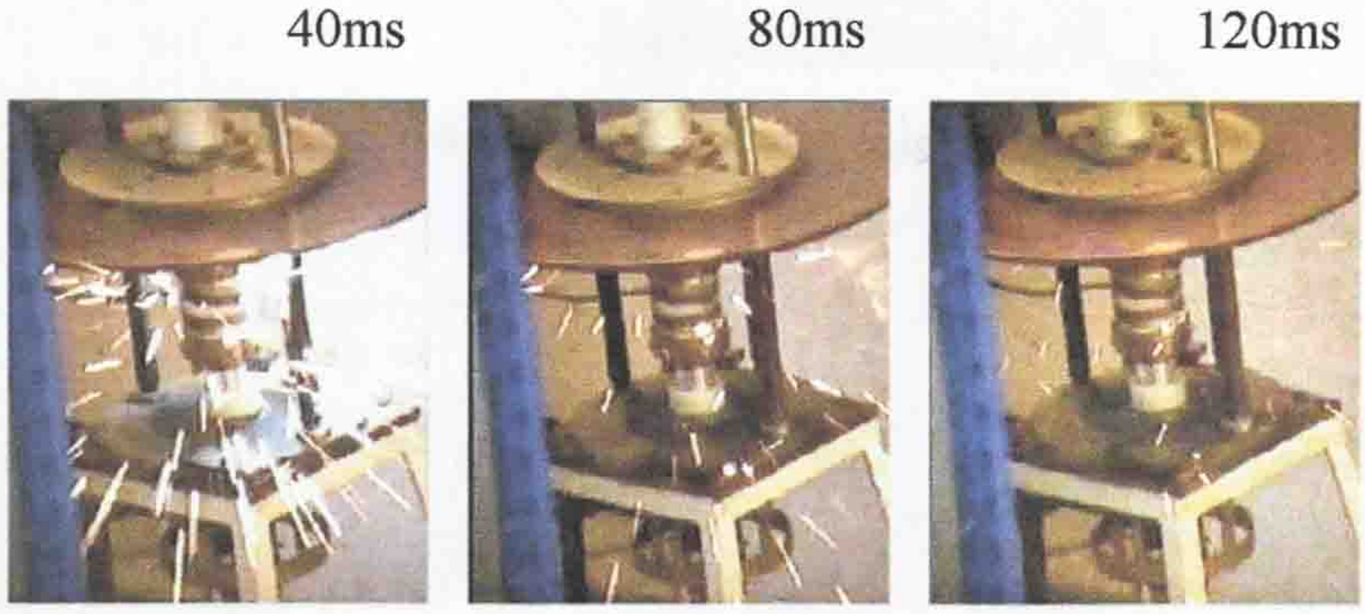

Figure 5.17 Video frames showing a post ac-arc repulsive effect (peak current 1.35kA)

For instant, inspection of the PTFE cylinder post arcing showed discolouration produced by the arc plasma in close proximity to the PTFE cylinder, (fig. 5.18).

Figure 5.18 Discolouration of the PTFE cylinder in the experimental interrupter

5.2.2.3 Conclusions

The results obtained from the model test head experiment may be summarised as follows:

- A comparison of the high-speed photographic frames of figure 5.15 with the voltage waveforms of figure 5.13 suggest that the periodic voltage fluctuations excursion of figure 5.13 correspond to the shorting and re-establishment of the electric arc turns. Inspection of frames of this kind also showed that the arc column was twisted around the PTFE cylinder

horizontally. This is confirmed by inspection of the PTFE cylinder post arcing, which shows discolouration produced by the arc plasma in close proximity of the PTFE (fig. 5.18).

- The electrodes positions in figure 5.18 shows that the anode and cathode are at a fixed distance from each other. As a result, the electrical arc is rapidly wrapped around the PTFE cylinder by the Lorenz forces in the opposite directions at the top and bottom of the coil (figure 5.15, frames 0.5ms-2ms). The duration of one turn of twisting arc is about 4.5ms, of a current 1.3kA (fig. 5.15, frame 4ms). As a result, the arc is twice re-established within 10 ms.

5.2.3 Results for novel rotary arc interrupter

Results obtained during experiments on the novel rotary arc interrupter (**section 5.1.3**) are described. Practical measurements of the spatial variation of B fields around the interrupter were obtained using the measurement method described in the **section 4.2.4**. Current and voltage waveforms, dielectric strength and optical fibre monitoring have also been obtained along with optical measurements from high-speed photographs and video records during the arcing and post arcing times.

5.2.3.1 Spatial variation of magnetic field

Test results for the magnetic field distribution around the model test head are described in this section. The results presented refer to the grid shown on figure 5.1 defining the positions at which measurements were made. Figures 5.19a (Tab. 5.1), b (Tab. 5.2) and c (Tab. 5.3) show the spatial variation of the B field radial, axial and total components at various axial (r) positions (0-43mm), radii (6-27mm).

Distance from the Anode, *r* *mm*	B, mT Distance from the cylinder *6mm*	B, mT Distance from the cylinder *13mm*	B, mT Distance from the cylinder *20mm*	B, mT Distance from the cylinder *27mm*
0	136.7	100.1	70.5	48.1
11	130.1	100.9	70.7	49.6
22	97.2	70.5	56.0	36.3
43	0	0	0	0

Table 5.1 Outer radial B_x field

Distance from the Anode, *r* *mm*	B, mT Distance from the cylinder *6mm*	B, mT Distance from the cylinder *13mm*	B, mT Distance from the cylinder *20mm*	B, mT Distance from the cylinder *27mm*
0	14.3	6.8	2.6	2.3
11	31.9	24.8	21.4	17.6
22	76.7	55.2	42.7	29.8
43	104.0	74.5	56.7	38.8

Table 5.2 Outer axial B_z field

Distance from the Anode, *r* *mm*	B, mT Distance from the cylinder *6mm*	B, mT Distance from the cylinder *13mm*	B, mT Distance from the cylinder *20mm*	B, mT Distance from the cylinder *27mm*
0	137.6	100.3	70.6	48.2
11	134.0	104.0	73.9	52.6
22	123.8	87.8	70.4	47.0
43	104.0	74.5	56.7	38.8

Table 5.3 Outer total B field

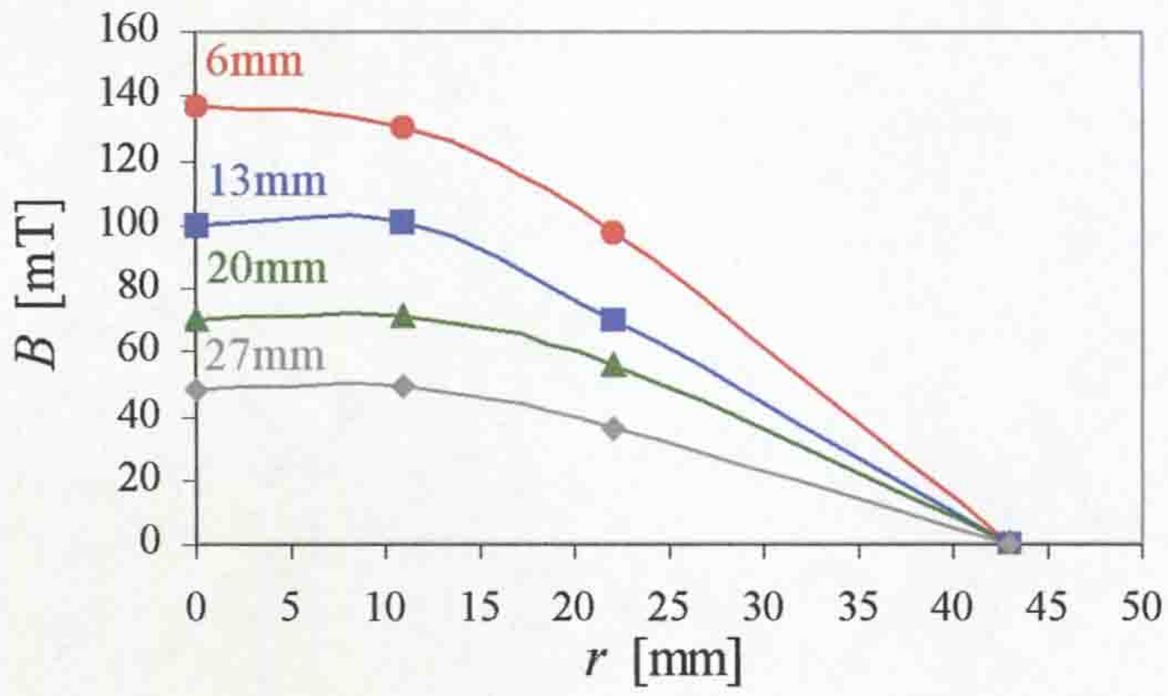

a) Radial B_x field component vs radius with axial (r) position as parameter (Tab.5.1)

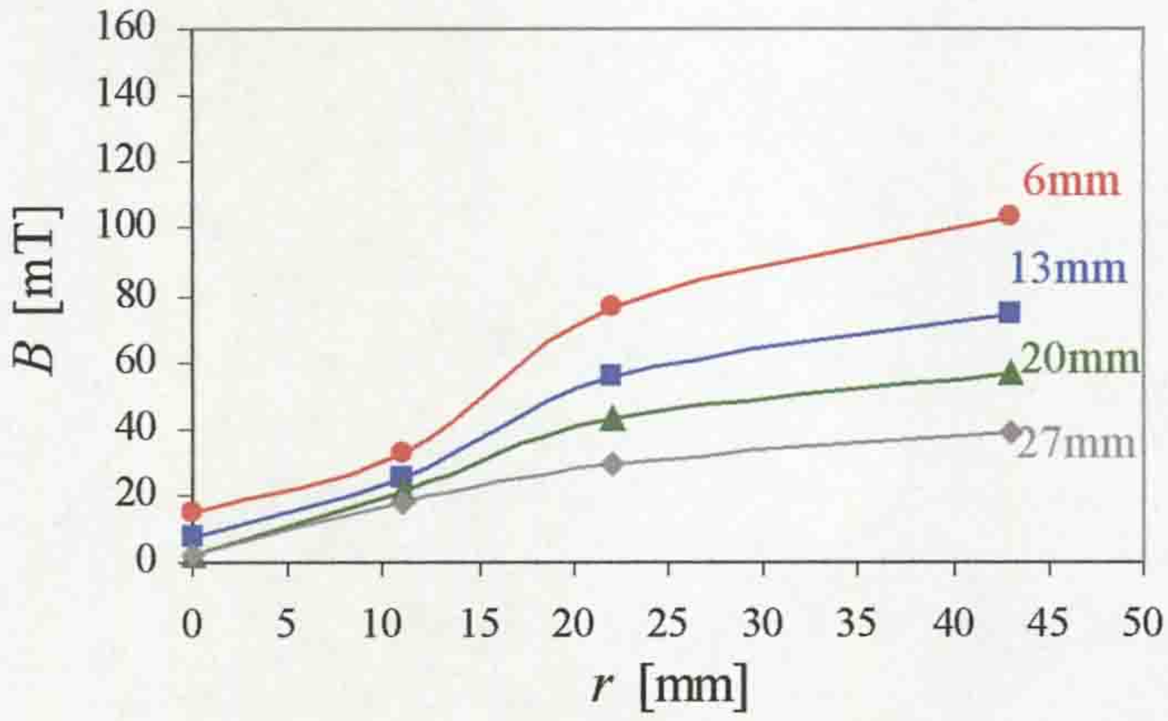

b) Axial B_z component vs radius with axial (r) position as parameter (Tab. 5.2)

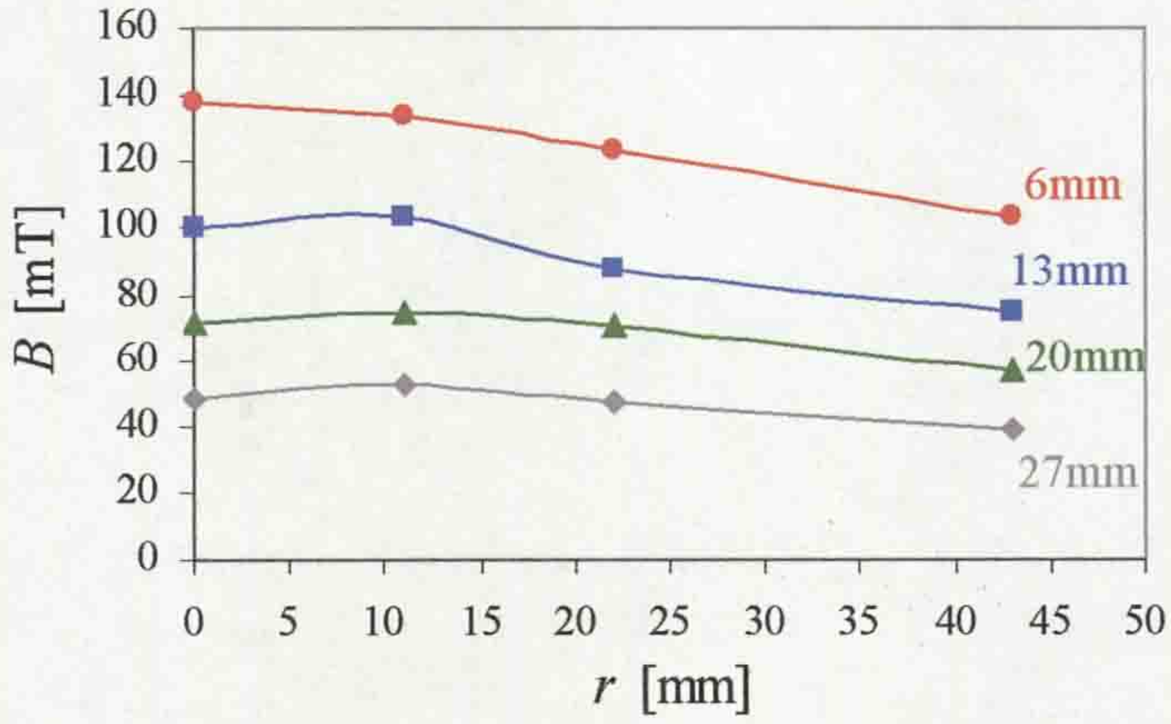

c) Total B field vs radius with axial position as parameter (Tab. 5.3)

Figure 5.19 Spatial variation of the B field components at various positions

Imagine in mind that the first measurement point ~0mm from the anode and ~6mm from the PTFE cylinder, (fig. 5.1). The B field is at a maximum value of 137.6mT at this point. The measurement was repeated on the point 43mm from the anode, at the same point from the cylinder (6mm). It was found that the maximum value of magnetic field of 104.0mT occurred at the midpoint of the coil. Peak values for outer total magnetic field at the ends of the coil are greater then those at the centre, since the current distribution flowing in the planar round coil is non-uniform with increasing current at the end of the coil and a reduced current in the middle of the coil. The error due the physical size of the search coil was ignored because the accuracy of the calibration method was limited (**section 4.2.4**). The directions of the radial and axial components of the magnetic field, producing coil, including the resulting total field are summarization for section 4 (fig. 5.1) shown on figure 5.20.

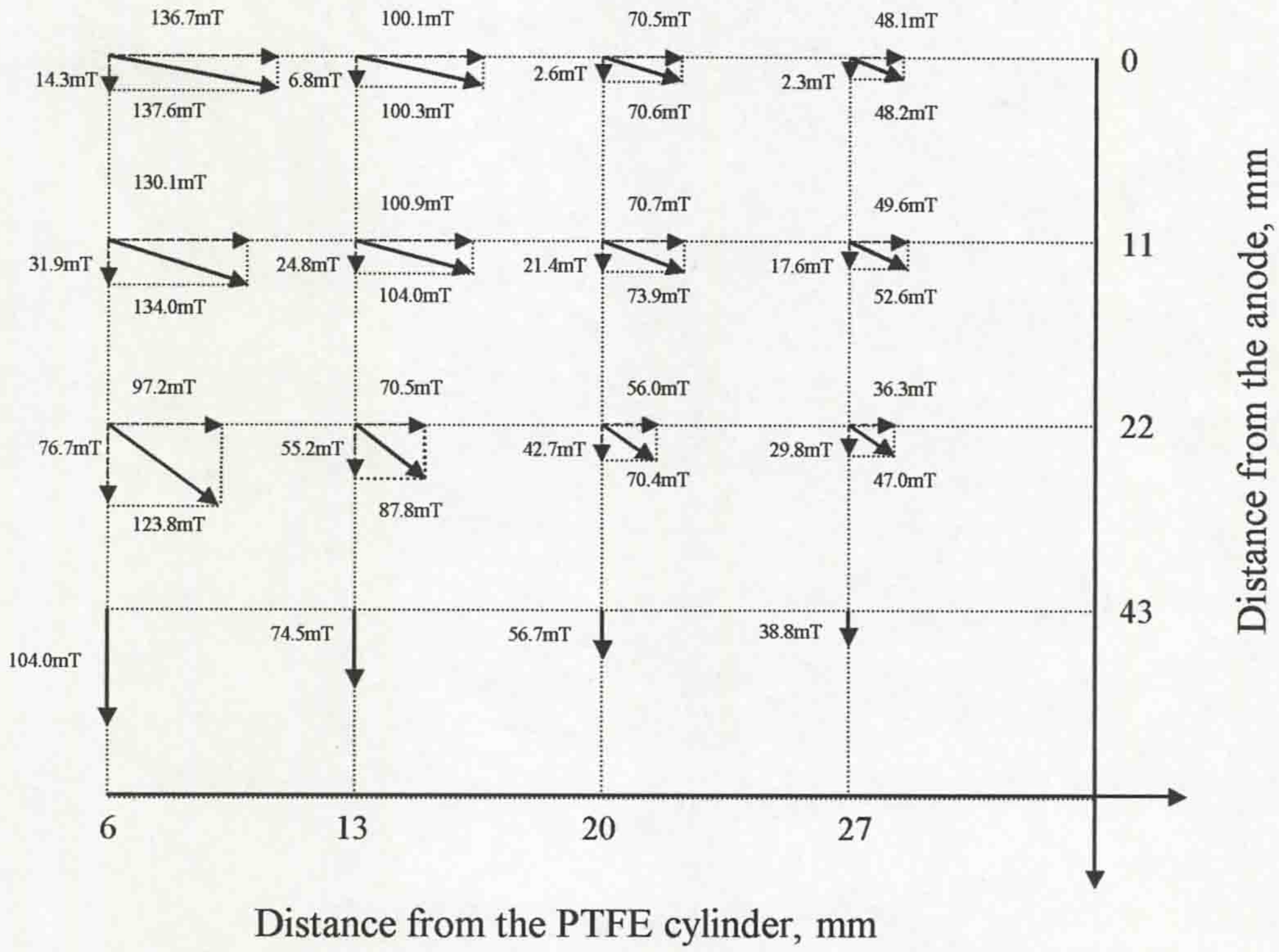

Figure 5.20 Orientation of the total magnetic field vector as a function of spatial dimension

Since the magnetic field of the cylindrical coil should be symmetrical about the vertical axis, the total spatial variation of the magnetic field may be extrapolated from the two dimensional distribution of figure 5.20 to the three dimensional distribution shown on figure 5.21.

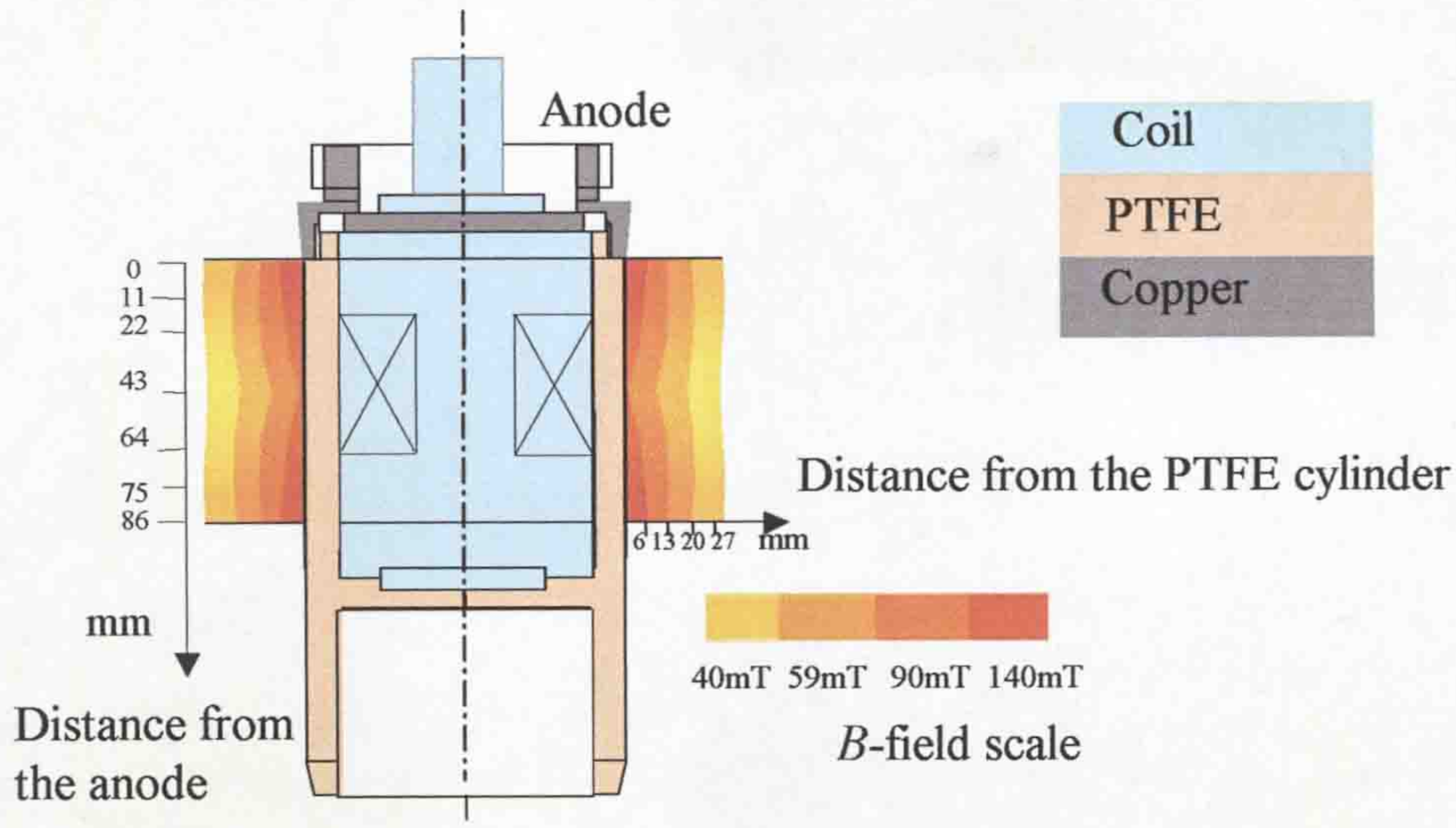

Figure 5.21 Total peak magnetic field distributions for a peak ac current 5.3kA (extrapolated from figure 5.20)

5.2.3.2 Electrical characteristics

Current and voltage waveforms for the rotary arc interrupter head (fig. 3.8) are presented in order to determine the ability of the interrupter head to interrupt the ac arc at current zero, at different peak current levels. Figure 5.22a shows relationship between the contact gap length, and arc current levels, at atmospheric pressure, in air and for current peak ac values in the range 11.8kA to 16.2kA (with a coil operation). The results of figure 5.22a show for air current and voltage variations with time as well as the contact gaps length at various times and the arc duration. The timing of the ac pulse has been made to increase the peak current increase so that the contact gap length at the first ac current zero becomes shorter. The voltage waveforms at each peak current are of a similar magnitude (~250V in meaning to the 400V for the longer gaps). Current interruption occurred at the first current zero for the longer gap (lower current was 11.8kA, 13.2kA, 14kA), but did not occur until the second current zero for the higher current (16.2kA), shorter arc gap (~70mm). For this current the negative current excursion produced a negative arc voltage whose magnitude (~400V) is similar to that of the other currents with nearest gap lengths. Figure 5.22b shows the arc interruption curve of 12.8kA, arc duration of 17.5ms (Gap 102mm) without the arc driving coil. The post arc current is presented (e.g. negative arc voltage fluctuations). Figure 5.23 shows time expanded current and voltage results for the current zero period of a 14.5kA ac arc in

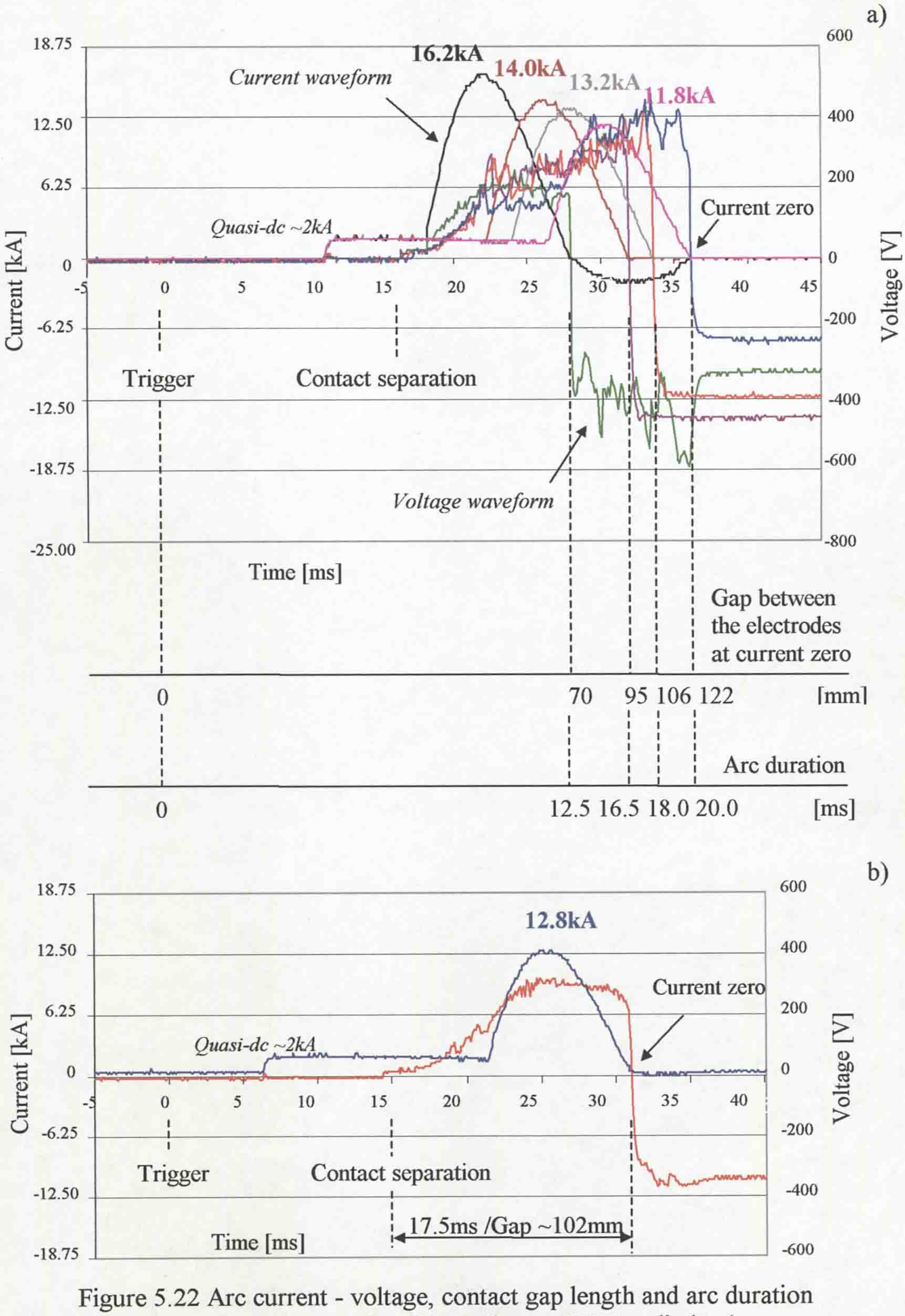

Figure 5.22 Arc current - voltage, contact gap length and arc duration in atmospheric pressure air with an inner PTFE cylinder (current interrupter head) with a) and without b) the arc driving coil

air, at different gap lengths corresponding to times in the range 14.8ms to 18.5ms. The post arc current investigation in the current interrupter head design is shown. The results show that an ac-arc duration of 18.5ms interrupted with a minimal value

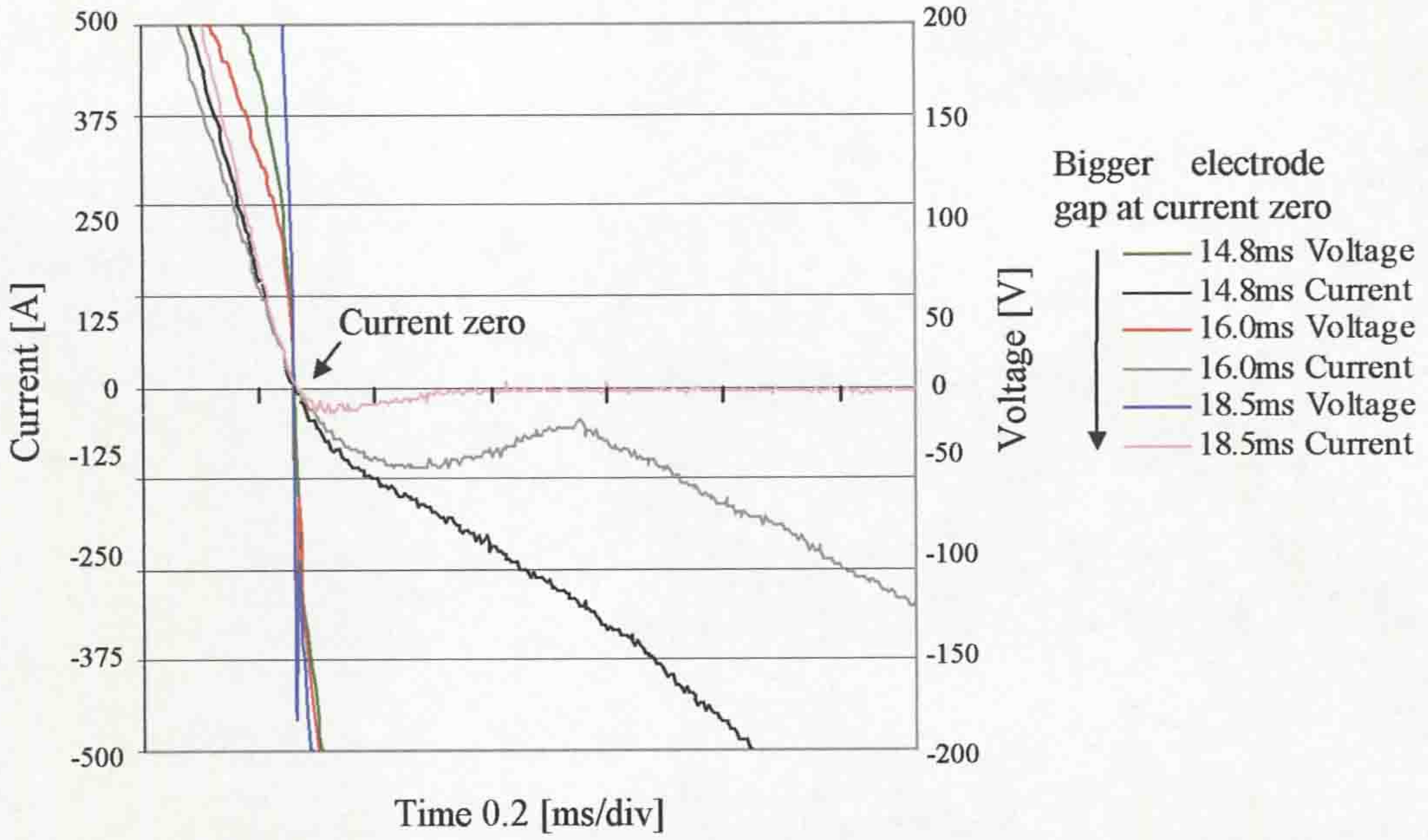

Figure 5.23 Current and Voltage variations during the current zero period for a 14.5kA, in air and different gap lengths

of post arc current of 30A after the current zero. At 16ms arc duration, this is considered as a critical interruption condition for the current interrupter head, atmospheric ac-arc attempts to interrupt the current during first 0.4ms after current zero with a minimal post arc current of 110A. After this period, the ac-arc is re-established increasing its value up to several hundreds ampere. An arc duration of 16ms correspond to electrode distances of 93mm from the arc initiation to the current zero, while for the arc duration of 18.5ms this distance is 108mm. Figure 5.23 shows that rotary ac-arc duration of 14.8ms is not interrupted at current zero which corresponds to the minimal electrodes distance of 87mm.

Figure 5.24 shows the restriking voltages for air arc, at different contact gaps and current levels, on a short time scale of 20μs/div. Figure 5.24a shows the restrike voltages for current zero at a gap length of 87mm following peak ac current of 12.5kA, 13.5kA, and 14.5kA. Figures 5.24b,c show the corresponding results at current zero gaps of 93mm and 108mm.

These results show that after current zero the recovery voltage overshoots during for first 7-8μs beyond which it increases monotonically. Comparisons of figures 5.24a,c show the electrode distances in the current interrupter of 87mm and 108mm show that although the restrike voltage waveforms are similar, the post arc currents for a 108mm gap is approximately one half of those for an 87mm gap.

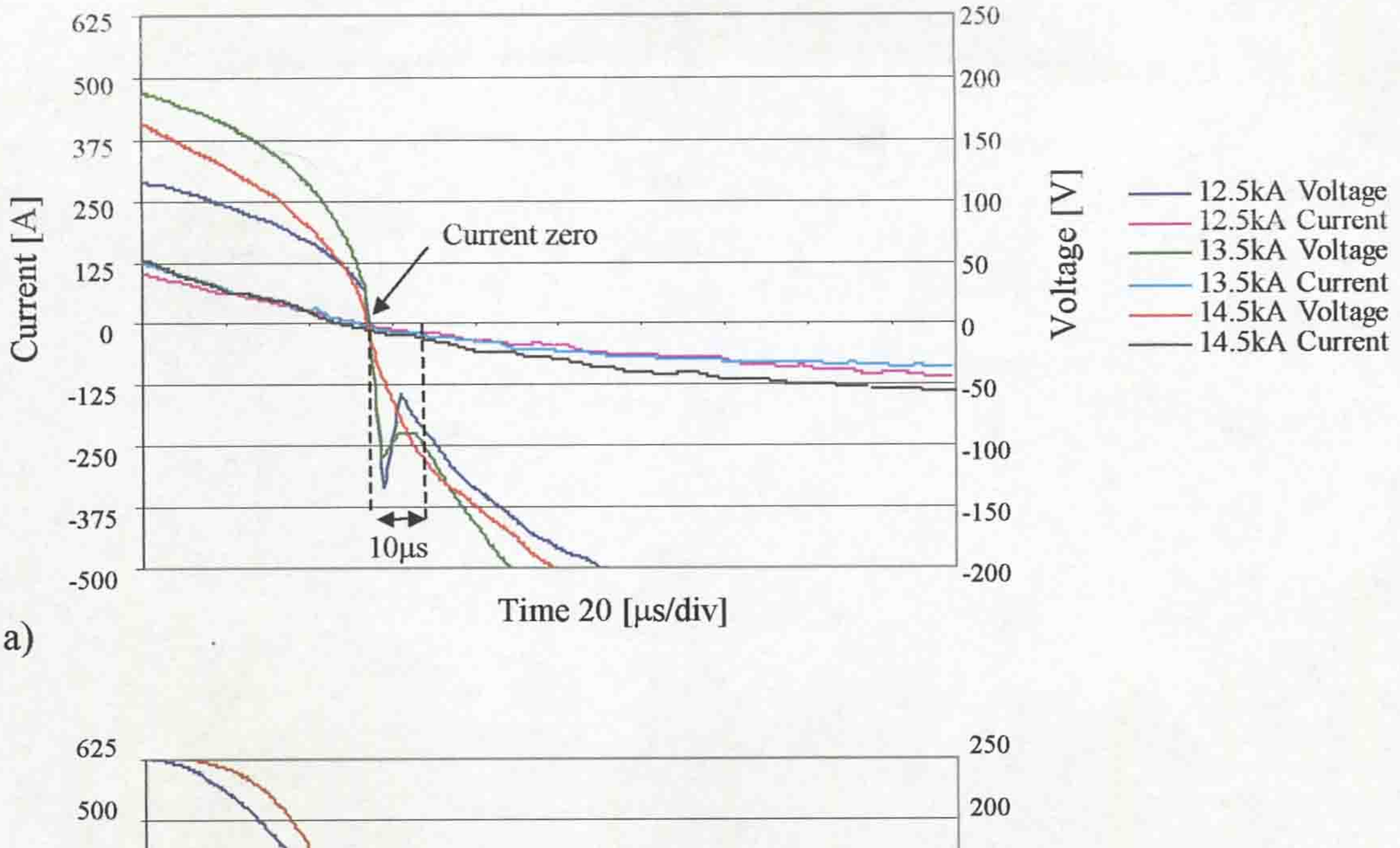

a)

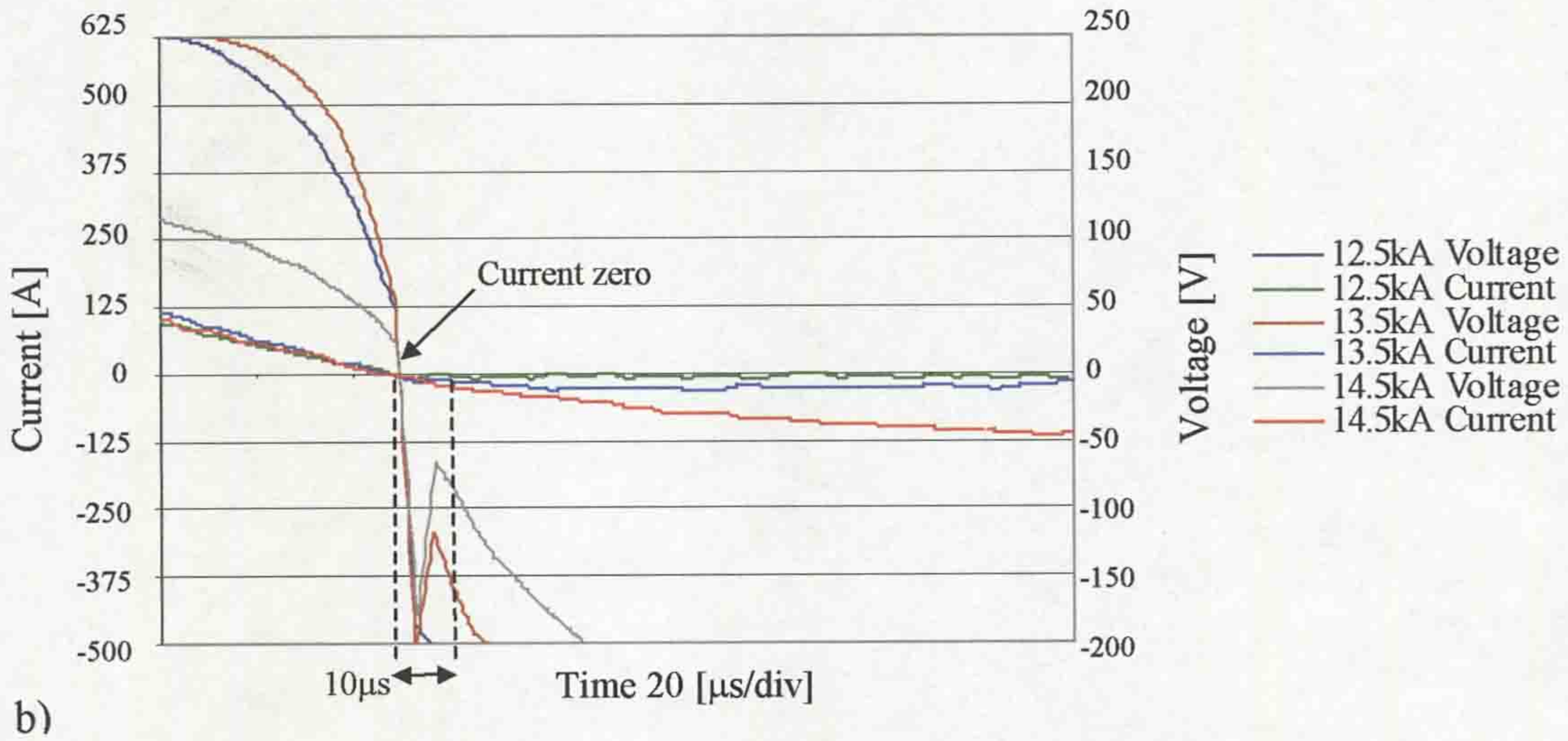

b)

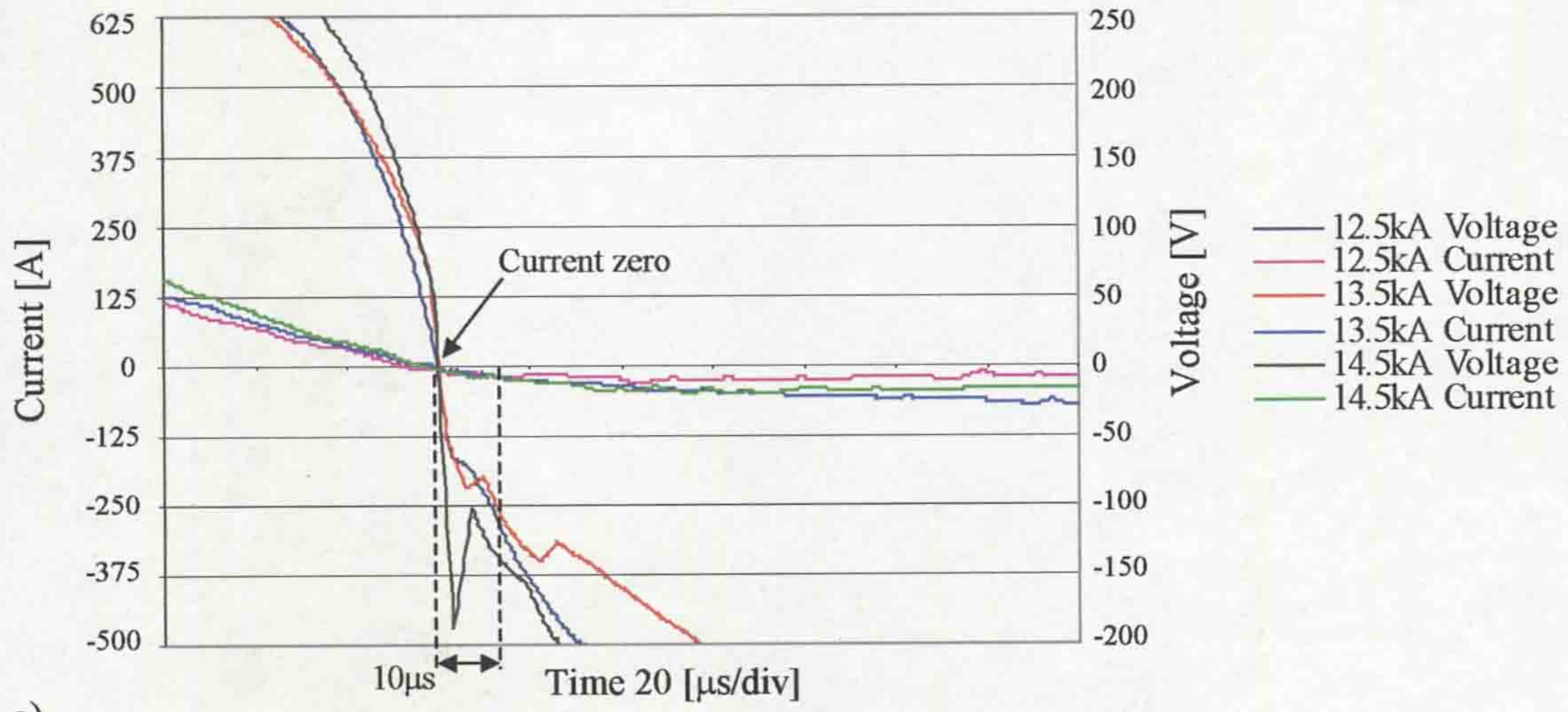

c)

Figure 5.24 Current and Voltage variations during the current zero period on the expanded time scale for 12.5kA, 13.5kA and 14.5kA peak ac current, in air

a) 87mm gap 14.8ms arc duration

b) 93mm gap 16.0ms arc duration

c) 108mm gap 18.5ms arc duration

The critical conditions of the current breaker head interruption for a current of 14.5kA, at 16ms arc duration (fig. 5.24b) demonstrates a large overshoot immediately after current zero during 7microseconds, which leads to an increase in the post arc current up to 110A and which was not interrupted at current zero (fig. 5.23).

Figure 5.25 shows the rate of change of recovery voltage with time as a function of the rate of change of current before current zero derived from figures 5.24a,b and c.

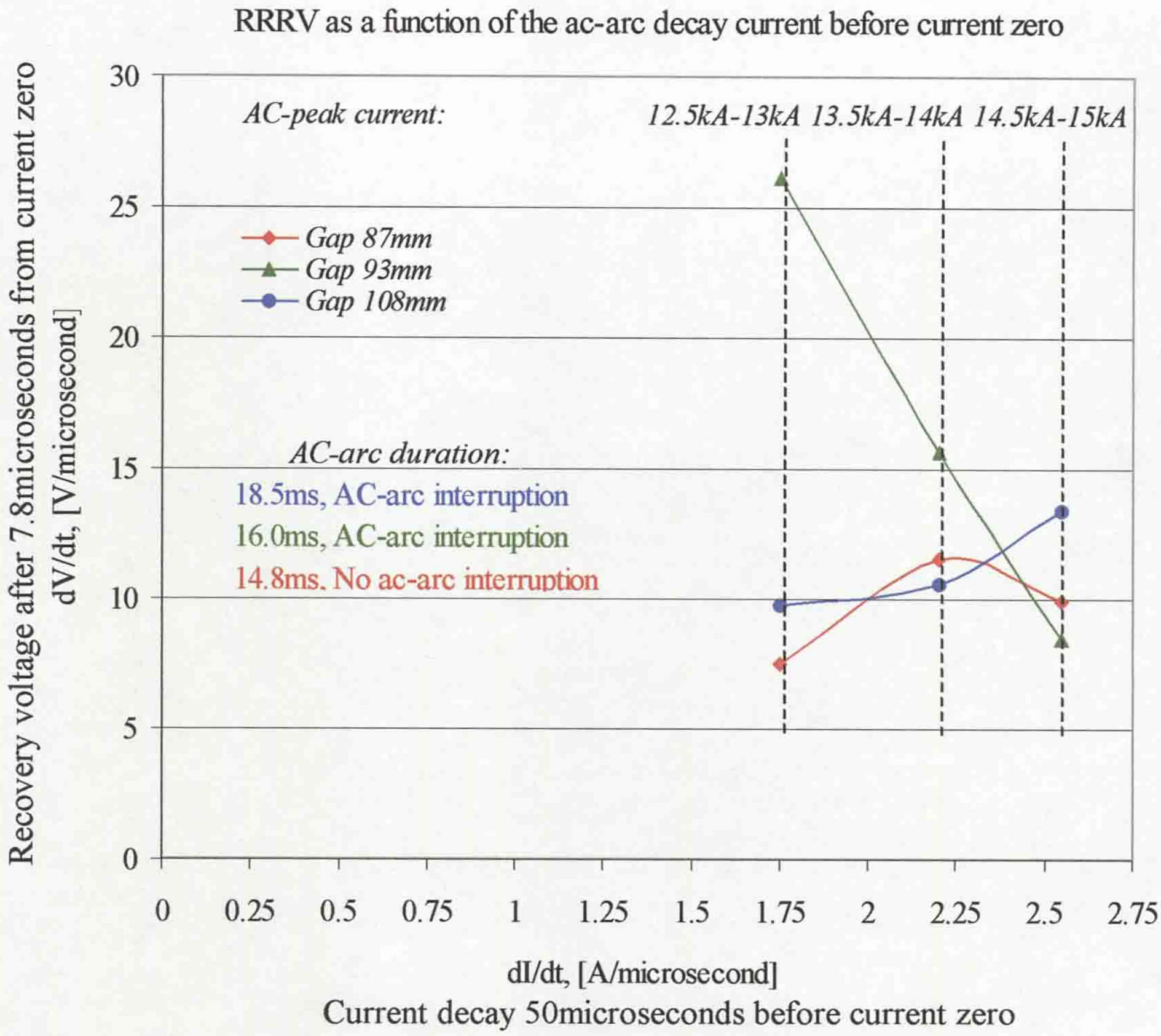

Figure 5.25 RRRV of the interrupter head as a function of decay current

The calculation of RRRV is made for the time window of 7.8miroseconds after current zero. The decay current measurement before current zero is for a time window of 50microseconds. The three curves in figure 5.25 demonstrate the ac-arc behaviour after 7.8microseconds from current zero for different electrodes gaps, and

at different ac-arc current interactions. It was found that at 16ms arc duration (electrodes gap 93mm) the RRRV is reduced from 26V/μs for the ac-peak current of 12.5-13kA to 8V/μs for the 14.5-15kA, while for 18.5ms arc duration (electrodes gap 108mm) the RRRV increased from 10V/μs to 13V/μs. In both cases, ac-arc interruption was observed. At 14.8ms, arc duration (electrodes gap 87mm) ac-arc interruption was not observed for any of the peak ac-arc currents investigated. These results simply show that the 13.5-14kA arcs of duration 16ms corresponding to an electrode gap of 93mm is a critical point at which the ac-arc may be not be successfully interrupted in air, at atmospheric pressure. Figure 5.26 show current and voltage variations with time for the novel prototype interrupter and for a range of peak ac currents (7-15kA) for fixed contact gap (106mm), at 18ms arc duration. These ac-arc interruption test results at different current levels demonstrate that the amplitude of the arc voltages increased close to current zero extinction peaks, which leads to an improvement in the condition of arc interruption.

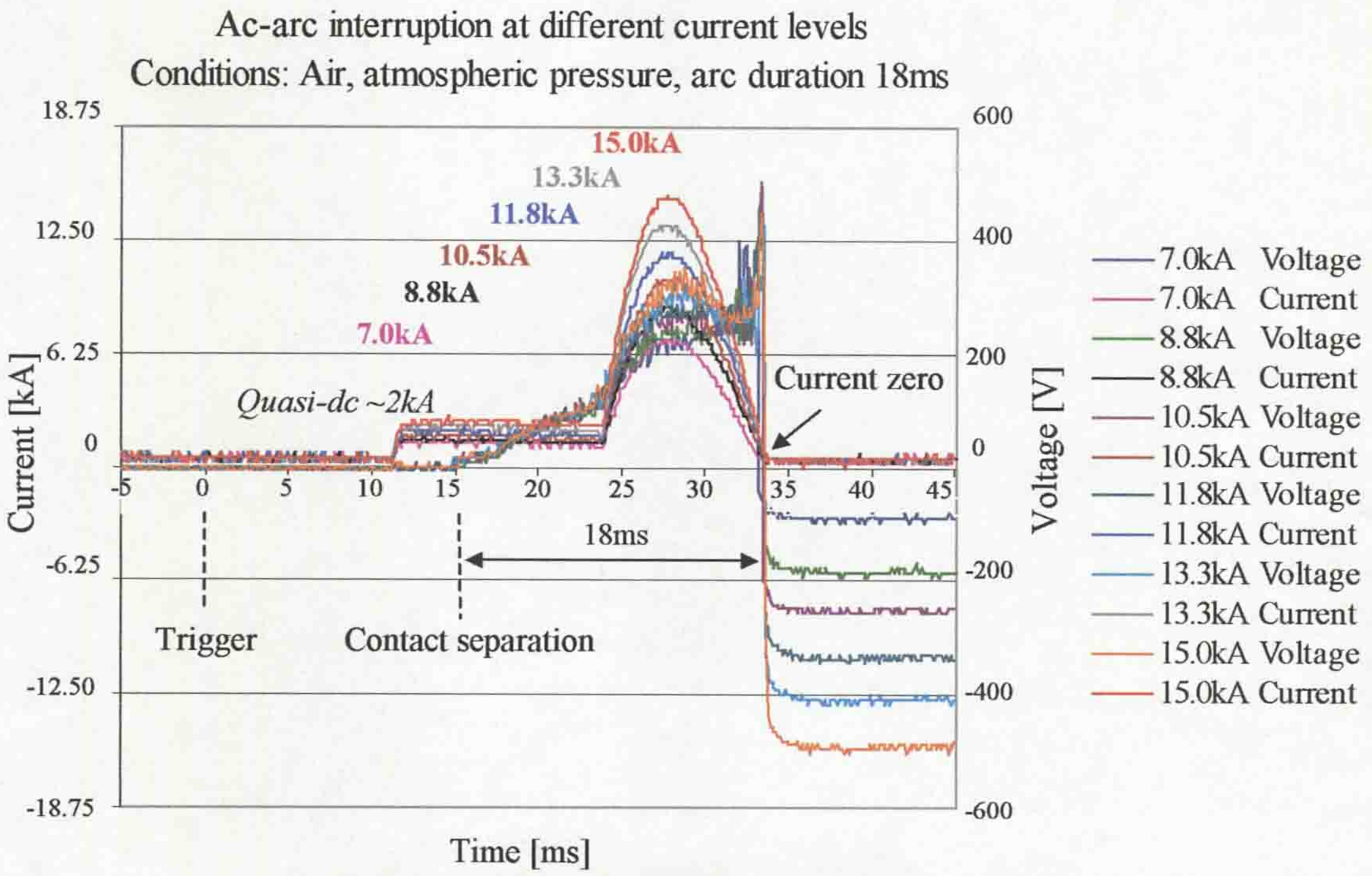

Figure 5.26 Prototype interrupter operation

Outer and inner PTFE cylinders have also been used in the prototype current interrupter (fig. 3.11). Experimental results for the prototype interrupter are presented in figure 5.27 in order to compare these results to the experimental results of the current interrupter head (without the outer PTFE cylinder operation, fig. 5.22a).

The experimental conditions in both experiments are otherwise identical. The arc voltage in the prototype interrupter drops rapidly at the time of arc extinction. The ac duration was found to be 12.5ms and arc extinction voltages up to about 500V at 11.8kA peak current were observed.

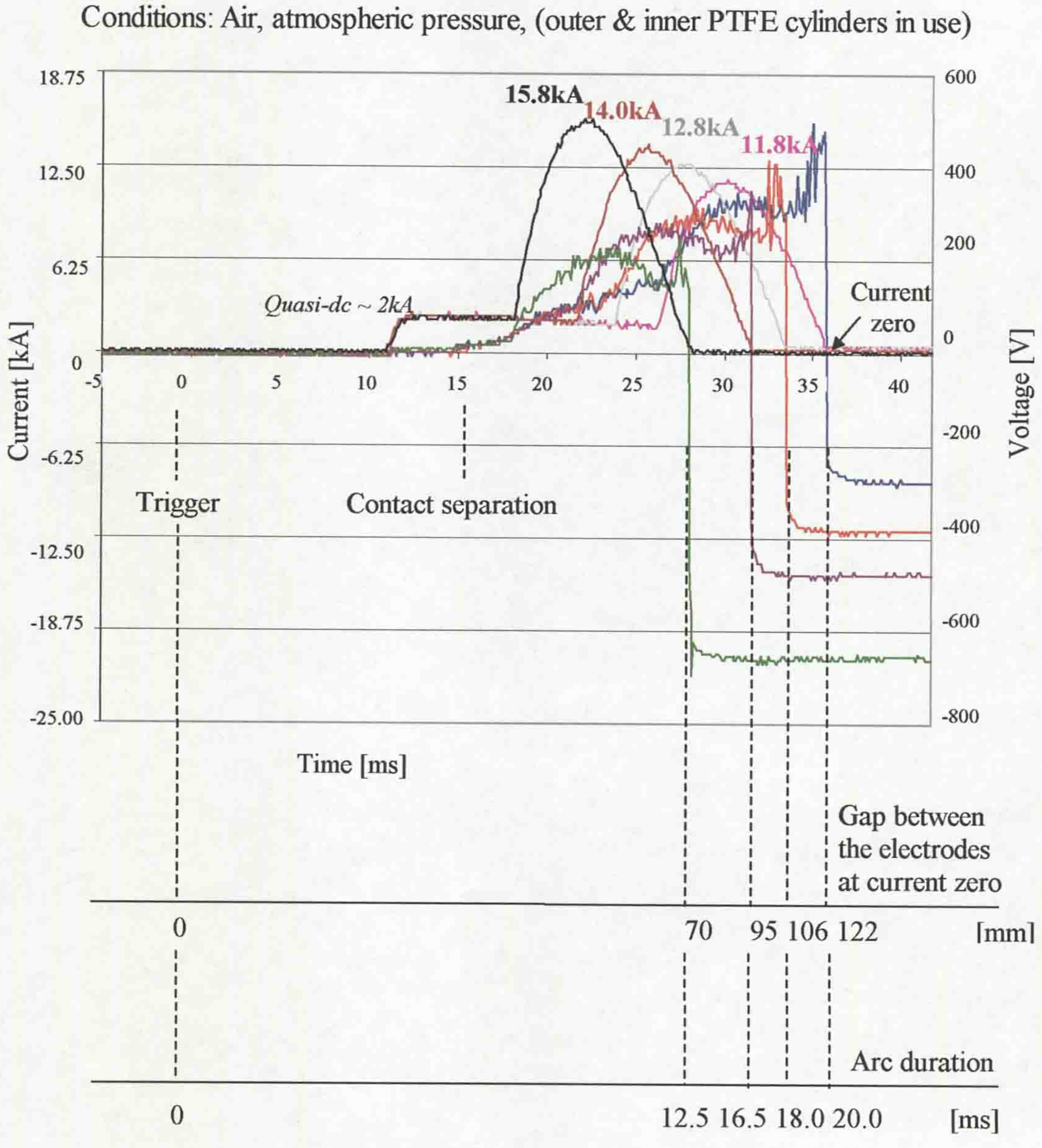

Figure 5.27 Prototype current interrupter investigations

5.2.3.3 Optical fibre monitoring results

Results relevant to arc rotation in the interrupter head are presented in this section. An ac-arc current of 13.25kA of arc duration 14ms was chosen for the

tests in air, at atmospheric pressure.

An example of results from the horizontal view optical fibre monitoring of the arc rotation is shown in figure 5.28. The results are for one half cycle of a sinusoidal current flowing through the coil producing magnetic field. The phase difference between the current and magnetic field is near zero (fig. 4.16) because the inductance of the coil is small. Also shown on figure 5.28 is the contact travel as a function of time, which can be related to the contact travel calibration curve of the interrupter (fig. 4.19). The optical fibre results are in the form of optical pulses, which correspond to the optically emitting arc passing part the fibre tip. Then the time for a single rotation of the arc corresponds to the time difference between two consecutive pulses recorded by a single fibre. More detailed rotational speed can be determined by detecting the time between pulses recorded by consecutive fibres since the angular disposition of the fibres is known. The speed of rotation determined from these sequences of pulses is shown as a function of time on figure 5.28a superimposed onto B field waveform. Results for two tests and their average are shown. The average speed of the rotary arc (13.25kA) increases as the magnetic field of the coil is increased, reaching the maximal value of 930 metres per second at around 7.5ms from arc initiation. At 7.5ms, the travel contact recorder curve of the movable cathode shows that cathode position is around 40mm from the anode, so located almost at the centre of the coil. From arc initiation to 8ms, the number of arc rotations is seven. At the arc extinction point, the average velocity of the arc is reduced to 161m/s and the number of arc rotations from the arc initiation reaches 14. However, the total number of the arc rotations during one ac half cycle is 13 (from 4ms to 14ms). Thus during quasi-dc arcing, which continues for 4ms, the arc passes one revolution. On the arc rotation curve, (fig. 5.28) the point "0" on three fibres curves indicates arc initiation. Fibre1 (fig. 5.28b) is located close to the arc initiation area (fig. 4.9). During the quasi-dc arcing time, fibre1 detects that the arc has rotated one revolution of around 2ms from the point "0". The point "1" indicates the start time for arc revolution during one ac half cycle. At arc extinction, corresponding to current zero, a post arc plasma phenomenon was observed by fibres 1 and 2. During the post arcing time (arc extinction state), the fibres 1 and 2 detect the post arc plasma (high-intensive light) for about 0.7ms, (fig.5.28b).

An example of stable arc rotation is shown in figure 5.29.

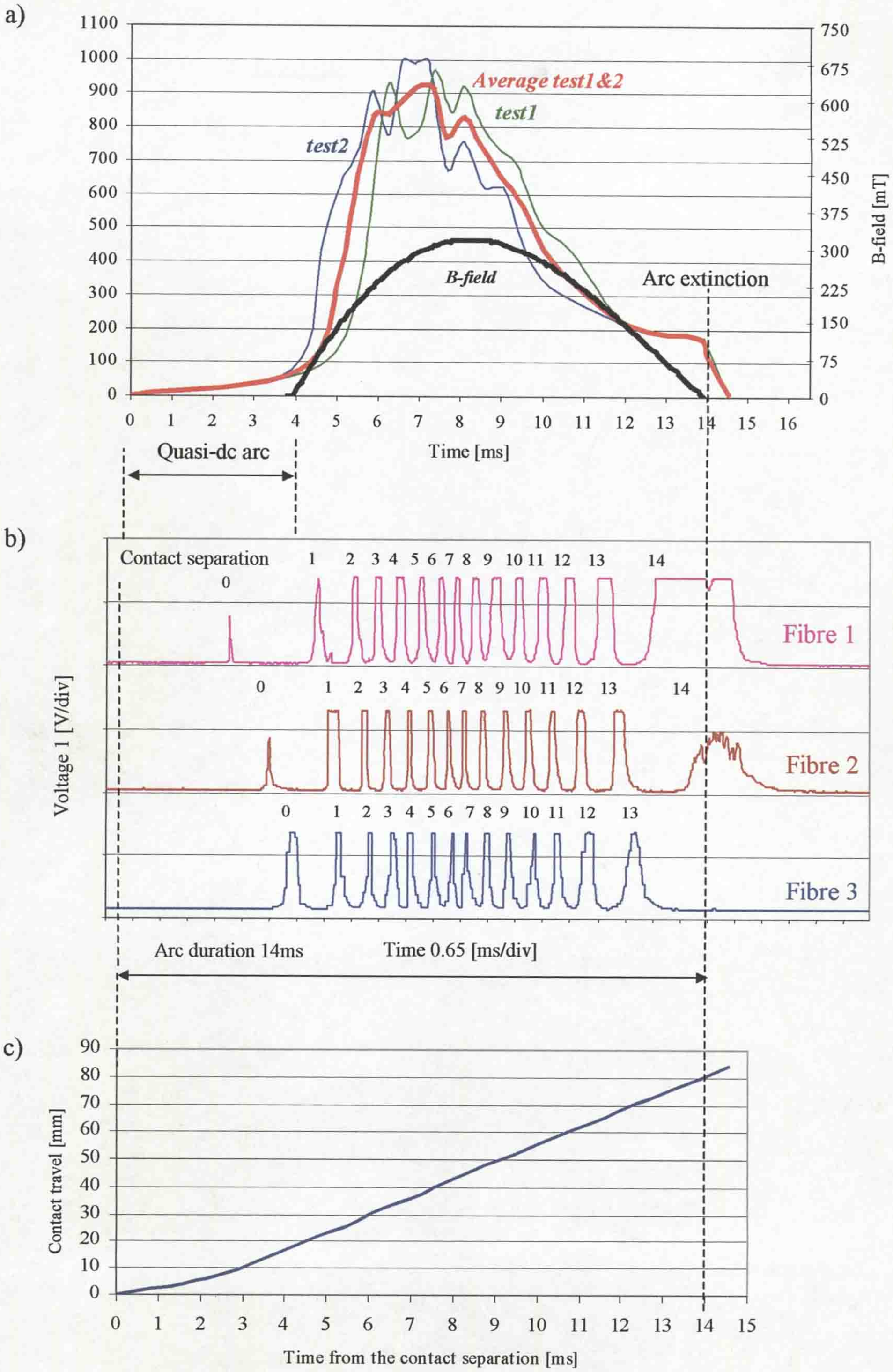

Figure 5.28 Arc rotation monitoring by the horizontal optical fibres
a) AC-arc (13.25kA) speed and magnetic field vs time
b) Signal from each of the three optical fibres
c) Contact travel

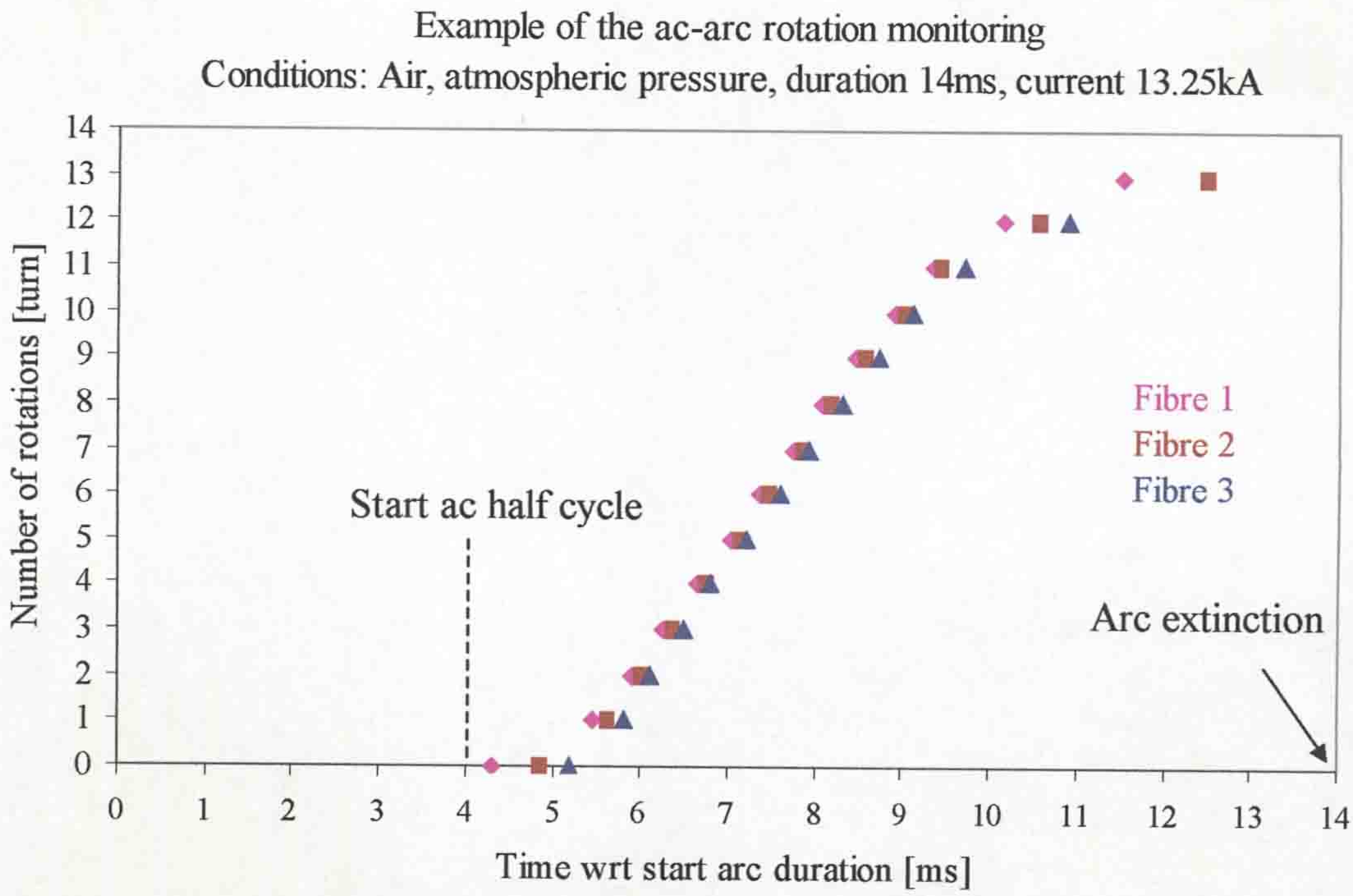

Figure 5.29 Example of ac-arc rotation viewed by horizontal optical fibres

It was found that the ac rotary arc slightly changes it stability during one ac half cycle of the current 13.25kA. The three fibres (fibre1, fibre2 and fibre 3) on figure 5.29 detect arc rotation with some time delay between each fibre. The pulse-time delay from the each fibre relates to the distances between the fibre positions, which remain the same during the experiments. From the start point of the ac half cycle, there is evidence that arc rotation increases becoming more stable from 4 ms until around 8ms of the arc duration and decreases, becoming less stable from 8ms until 14ms (arc extinction). The longitudinal extent of the arc was monitored with the vertical optical fibres as described in **section 5.1.3.3**. Typical results are given on figure 5.30 for which the operating conditions are the same as in the horizontal optical fibre monitoring tests. During the first 4ms from contacts separation a quasi-dc arc occurs. During that period, the dc-arc rotates once around the PTFE cylinder. From the ac-arc initiation point, it was found that the duration of the pulses (detected by three optical fibers, which reflect the ac-arc profile length) change. Overall a series of optical pulses of the form observed with the horizontal fibres are apparent. However, inspection of the each pulse time shows that the time at which this is observed by each fibre 1; 2 and 3 increased from about 8ms, trough 1ms to 4ms consistent with the contact moving axially and the arc plasma being visible via each optical frame.

The movable cathode of the interrupter head is situated at bottom edge of the coil at around 12ms from the electrodes contact separation. Once after that point, the ac-arc length begins to wrap around the PTFE cylinder. The pulses duration from the three fibres (fig. 5.30) are once increased during the last 2ms until current zero being observable on the pulses 13 (Fibre 3), 14 (Fibre 1) and 14 (Fibre 2). From the fibre position identification, (fig. 5.3) the duration and separation of these pulses during the last 2ms (fig. 5.30) may be concluded that the arc is wrapped around the PTFE cylinder close to current zero. For example, the resistance of luminousity from 11.5ms to 14.5ms of fibre 1 shows the arc plasma is stationary at that position.

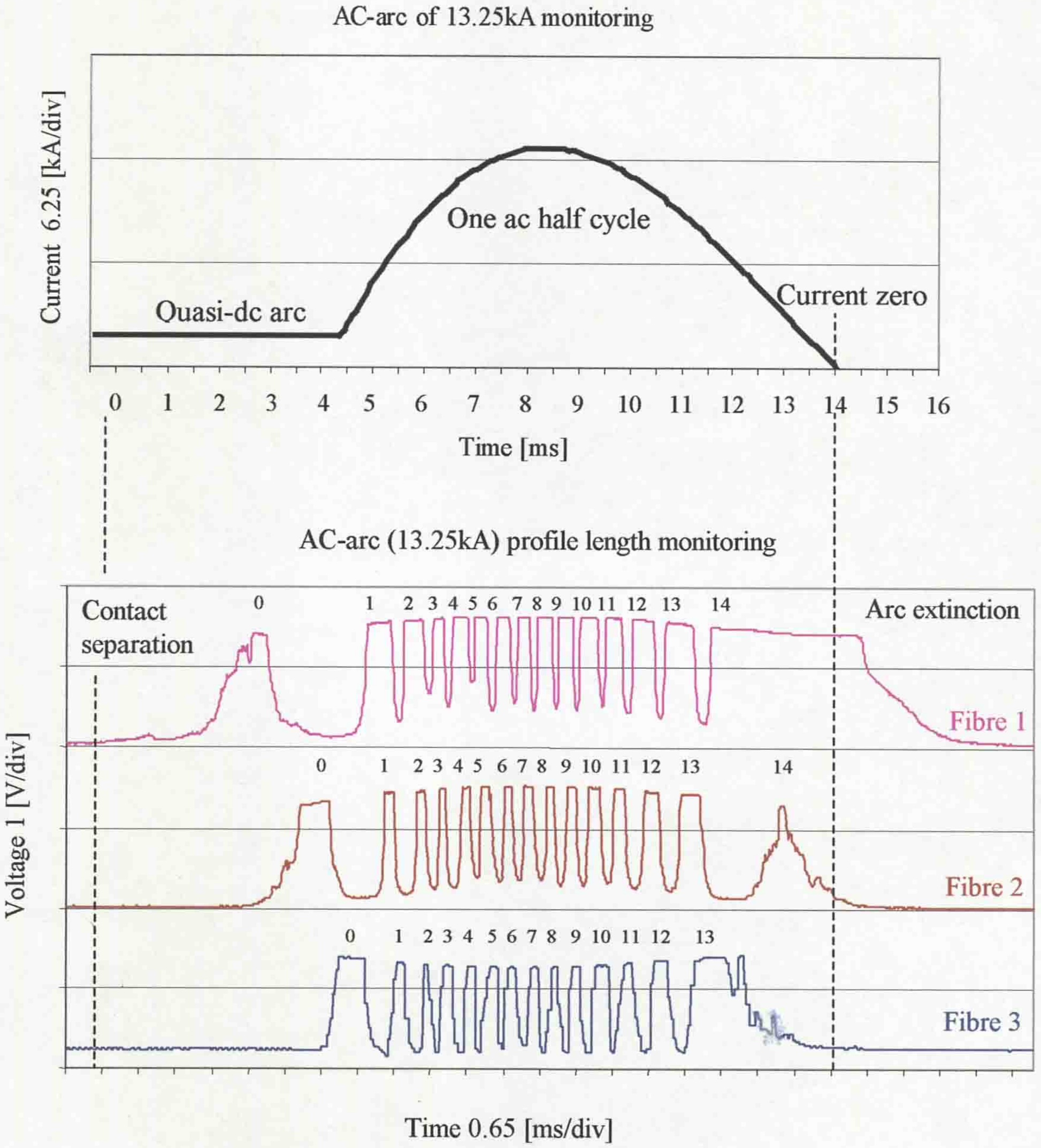

Figure 5.30 Example of the ac-arc length monitoring at its rotation profile viewed by the vertical optical fibres

However, for fibre 2 there is absence of luminousity between 11.5ms and 12.5ms implying that the arc plasma is behind the PTFE cylinder. Fibre 3 indicates an arc presence during this period but vanishes at 12.5ms when fibre 2 begins to record an arc presence. Again, a convoluted arc is indicated. The ac-arc position around the cylinder is difficult to observe at last milliseconds before current zero using at fibres 2 and 3. However, high-speed photography can be used for detailed ac-arc length investigations during the last milliseconds of arc existence (**section 5.2.3.5**).

5.2.3.4 Dielectric strength results for the novel rotary arc interrupter

Results from dielectric probes with the prototype rotary arc interrupter are presented which give the dielectric strength response at various locations within the prototype interrupter head during ac-arc interruption. Dielectric probe test points

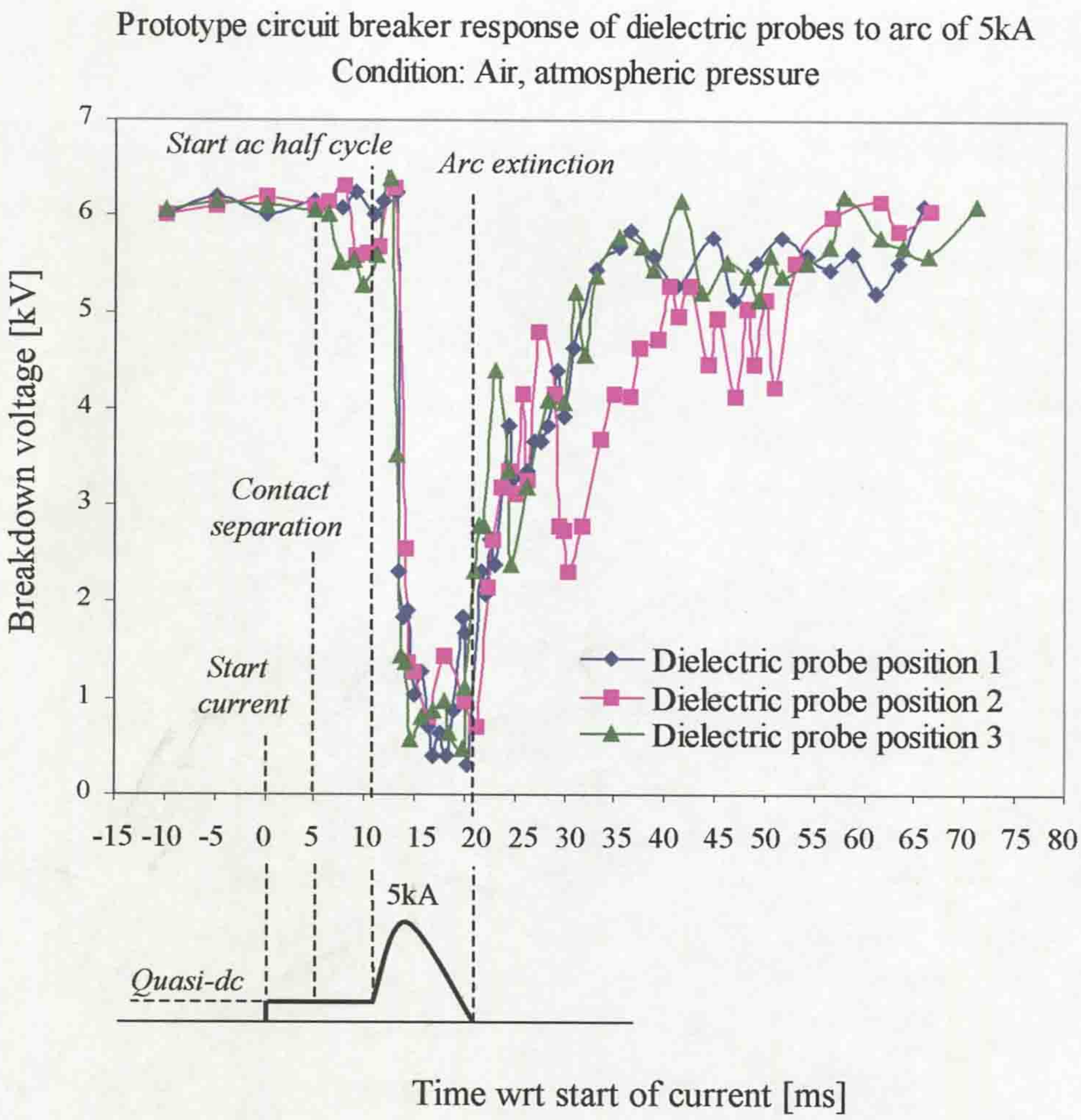

Figure 5.31 Comparison of dielectric probe results vs. time at different probe positions within the interrupter. (Position defined on figure 5.4)

within the prototype current interrupter have been previously indicated in **section 5.1.3.4**. Measurement at each point of the prototype interrupter is tested separately and the average result for the dielectric probe position 1, 2 and 3 is shown in figure 5.31.

Figure 5.31 shows the response of the dielectric probe to a 5kA arc, where the dielectric probes are fixed at the bottom part of the prototype interrupter head (fig. 5.4). The response of the dielectric probes to a 5kA arc (fig. 5.31) is not significantly changed for an applied force of 649N/m (5kA x 129.8mT) to produce the arc rotation by the coil B field of 129.8mT. At 5ms, after a quasi-dc arc of 0.8kA, the contact separation is operated that slightly changes the breakdown voltage monitored by the dielectric probes. At 11.5ms, when the ac-arc is present, the breakdown voltage is sharply reduced (~0.5kV), recovering to some intermediate value and after some time (45-50ms) recovering fully. The post arc breakdown voltage values (by the probes 1, 2 and 3) show that within the current interrupter there is a sufficiently high level of ionization giving a breakdown voltage of (~4-5kV) compared to a pre arc value of ~6kV. The breakdown voltages obtained with dielectric probe 2 exhibit high amplitude oscillations, in contrast to probes 1 and 3 and there is a clearer more abrupt indication of the dielectric recovery. Therefore,

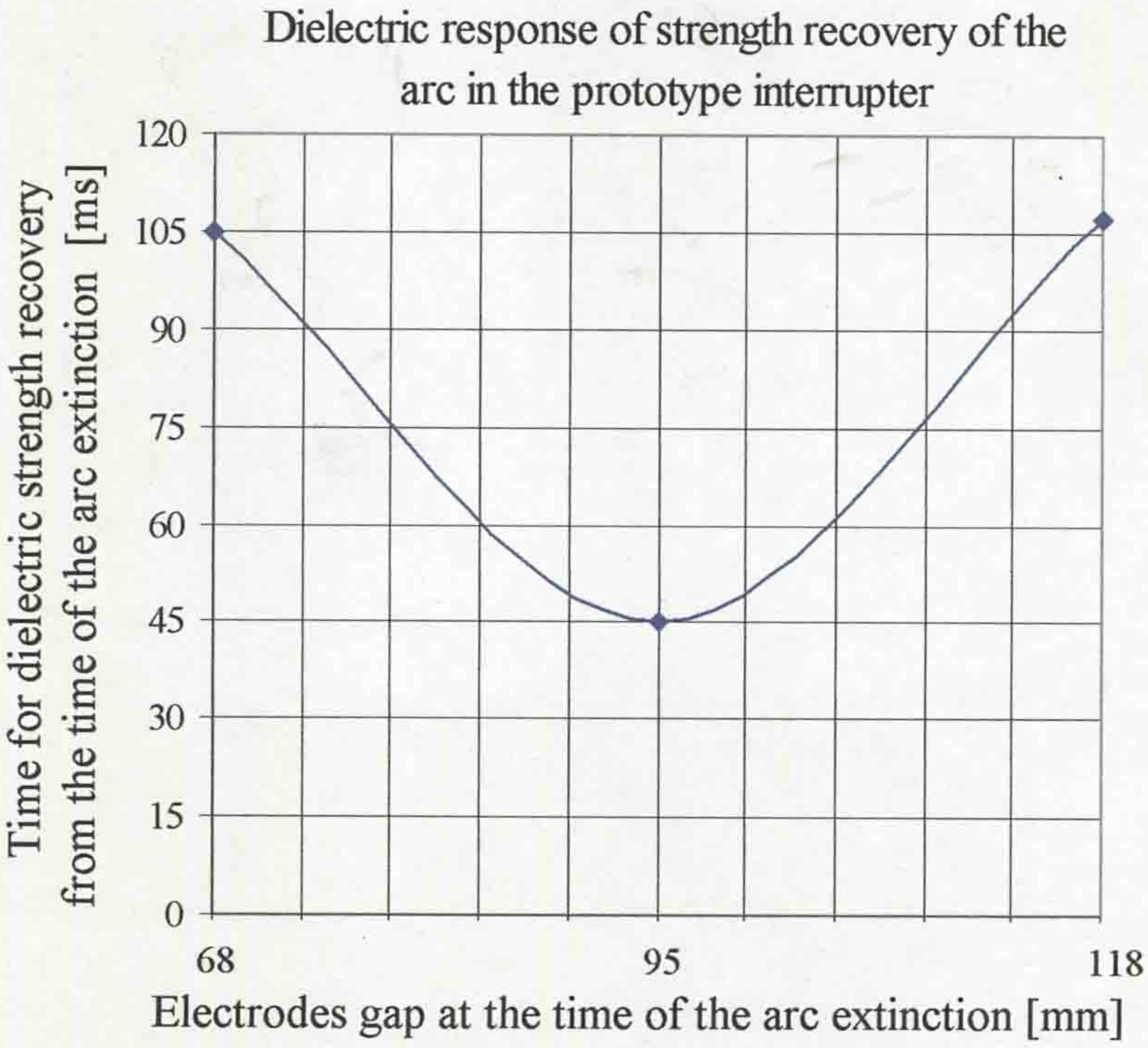

Figure 5.32 Dielectric recovery time vs. gap length at arc extinction (ac-arc 5kA, air, atmospheric pressure)

dielectric probe tests for different contact gaps of the ac-arc extinction (fig. 5.32) were conducted with the dielectric probe at position 2.

Figure 5.32 shows the dielectric probe response with the prototype rotary arc interrupter for an ac-arc of 5kA, in air, at atmospheric pressure and at different electrode gaps for tests when the arc was extinguished. During a number of repeat tests (3 tests), the average values of the dielectric recovery times for different electrode gaps (arc duration) were found. An example of a test results on which the averages of figure 5.32 are based is shown in figure 5.33. It was found that for the 20ms of arc duration (fig. 5.33a), the average recovery of dielectric integrity post arcing was slow, being about 105-107ms while the contacts gap at the arc extinction was around 118mm (fig. 5.32). Figure 5.33a shows that breakdown voltage slowly recovered to the pre arcing breakdown voltage. For an arc duration of 16.5ms (fig. 5.33b), the recovery of dielectric strength post arcing was more rapid, being about 30-45ms while the electrodes gap was 95mm at the time of arc extinction (fig. 5.32). At 12ms (fig. 5.33c), the initial dielectric strength recovery is more rapid than for the 20ms case (fig. 5.33a). However, the breakdown voltage remains at an intermediate value of 5.5kV for a prolonged period only fully recovered after 105ms while the contacts gap at the arc extinction was around 68mm (fig. 5.32).

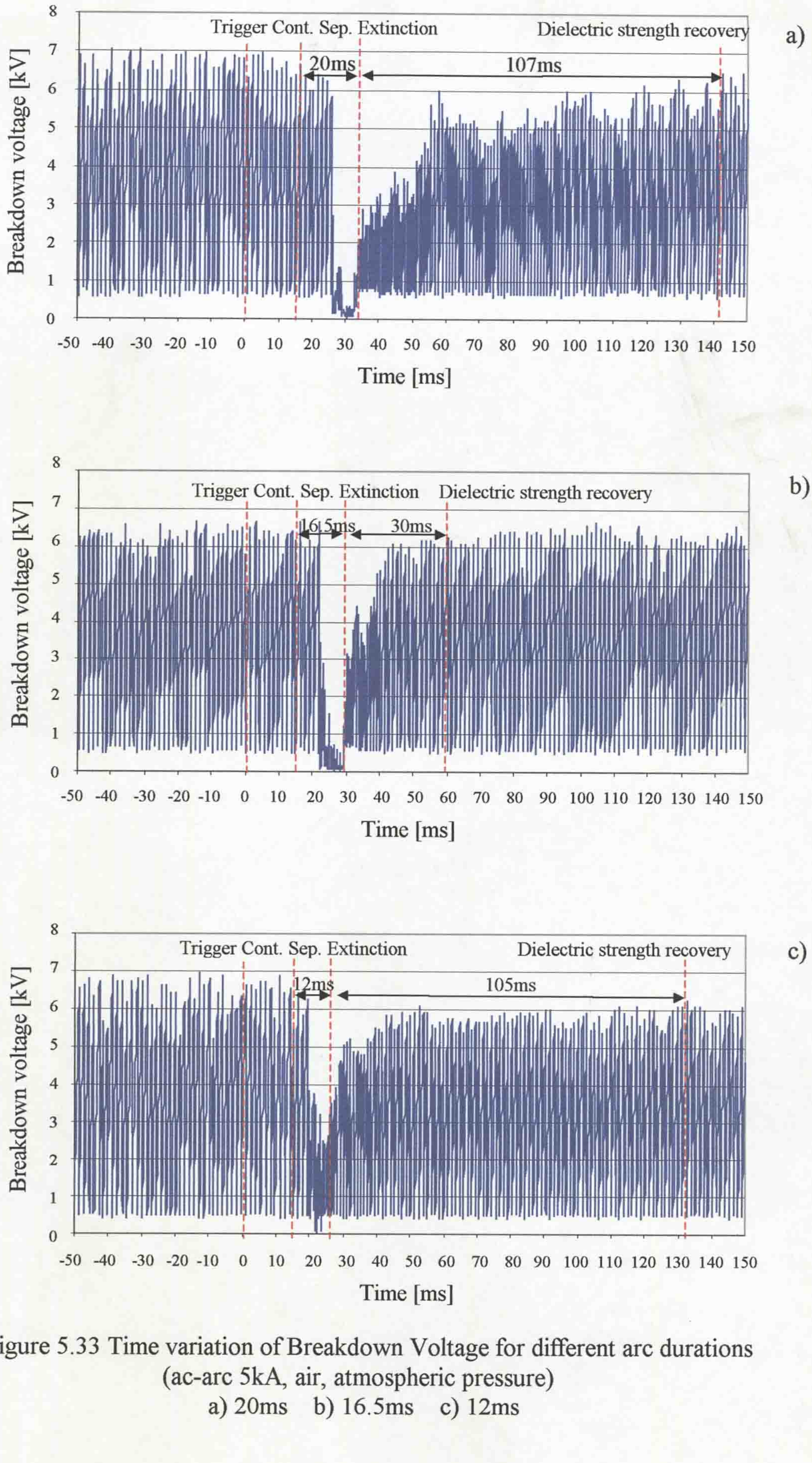

Figure 5.33 Time variation of Breakdown Voltage for different arc durations (ac-arc 5kA, air, atmospheric pressure)
a) 20ms b) 16.5ms c) 12ms

5.2.3.5 Optical imaging tests

High-speed photographs and video recorder observations of the dc and ac arcs are presented describing the arc behaviour in the current interrupter head (fig. 3.8) and prototype interrupter (evaluation of the interrupter head, fig. 3.12).

The dc-arc interaction monitoring is very important for prediction the ac-arc behaviour close to current zero. From the experimental point of view the minimum level of Lorenz force required to produce arc motion seems to be between 6 and 10N/m. For the series coil used, it would theoretically require to produce magnetic field of 20-25mT to generate such a force. This expectation is in good agreement with the experimental results, (Ennis, 1994). For the series coil used in the rotary arc interrupter head, it would theoretically require an arc current of 1.5kA to generate a magnetic field of 35-40mT, producing level of Lorenz force around 55-60N/m.

Optical observations, for the dc-arc of 1.5kA (arc duration ~23ms) have been made in air, at atmospheric pressure utilizing the test facility and diagnostic equipment described in **chapter 4**. A typical example of optical observations of the quasi-dc arc is shown in figure 5.34. The position of the coil in relation to the electrodes location at the time of the arc interaction give an insight into the arc behaviour during the arcing time (fig. 5.34). From the electrical (**section 5.2.3.2**) and dielectric strength (**section 5.2.3.4**) test results of the prototype interrupter it was found that ac-arc is successfully extinguished when the contact gap is around 95mm. As a result, the high-speed photographs observation of the quasi-dc arc is focused in the area of electrodes gap where the interrupter potentially has good conditions for the arc interruption. Identification of the PTFE cylinder, coil, electrodes positions on the high-speed photographic frame is indicated in the view of the scale (fig. 5.34). The scale of the photographic image is related to the diameter of the PTFE cylinder, which is about 100mm. The electrode gap position was calculated using the travel contact recorder curve of the rotary arc interrupter (fig. 4.19). A low current is chosen to provide clear observation of the dc-arc in the area of current zero, including the post arcing time. The camera 1 (fig. 4.9) was operated for observing the arc interaction, using a framing rate of 7500 frames per second. The high-speed photographs (fig. 5.34) of the quasi-dc arc interaction in the interrupter head (fig. 3.8) exhibit slow arc motion from 12.6ms (after contact separation) while the gap

between the anode (A) and cathode (C) is 74mm. At 16.2ms, the arc column becomes obliquely orientated under the influence of the magnetic fields. The electrodes gap at the same time was around 94mm. This interaction grows until at 20.7ms the arc was orientated horizontally, around the PTFE cylinder containing the coil, within the photographic fields of view. The gap between the electrodes was about 125mm. Frames 19.8ms and 20.7ms demonstrate this arc phenomenon, showing that the arc plasma is concentrate more in the middle of coil orientated

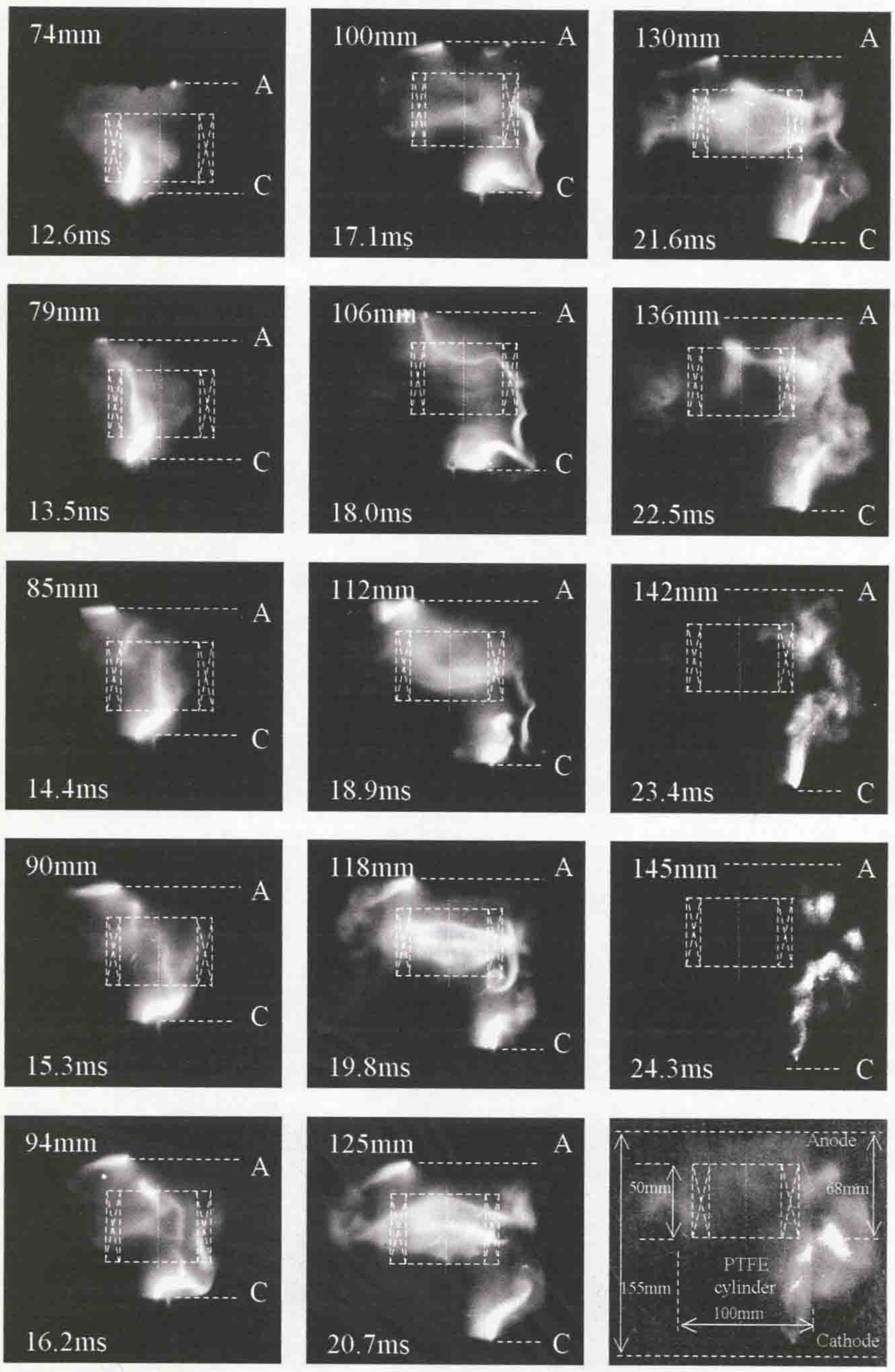

Figure 5.34 Example of high-speed photographs of an arc in air, atmospheric pressure, quasi-dc 1.5kA, (framing rate 7500 frames per second)

horizontally. The arc radius at 20.7ms was about 65mm. At 21.6ms, the horizontal part of arc remained at the same level from the anode. At 22.5ms, the horizontal arc plasma has become ruptured and it was extinguished at around 23.4ms while the distance between the electrodes was about 142mm and the arc plasma radius was about 80mm. The reason of the long arc time interruption is in the dc-arc current, which only gradually reduced to zero. High-speed photographs have been taken with two high-speed cameras operated at the same time but at the different positions (fig. 4.9). The experimental conditions for the ac-arc control and interruption was chosen to be the same as in the optical fibre tests (**section 5.1.3.3**). An ac-arc current of 13.25kA (arc duration 14ms) was chosen in order to compare the results obtained with the high-speed camera with the results obtained in the optical fibre tests. A colour film was used for detailed observation of the burning arc, PTFE cylinder and contacts interaction (fig. 3.8).

An example of the ac-arc rotation (13.25kA) in the current interruption head using high-speed camera 1 (fig. 5.35) and camera 2 (fig. 5.36) shows the ac-arc rotation during one ac half cycle, including the post arcing time of about 0.7ms. The ac-arc starts to operate at around 3.9ms after arc initiation, persisting about 10ms and is extinguished during the period 13.8-14.1ms.

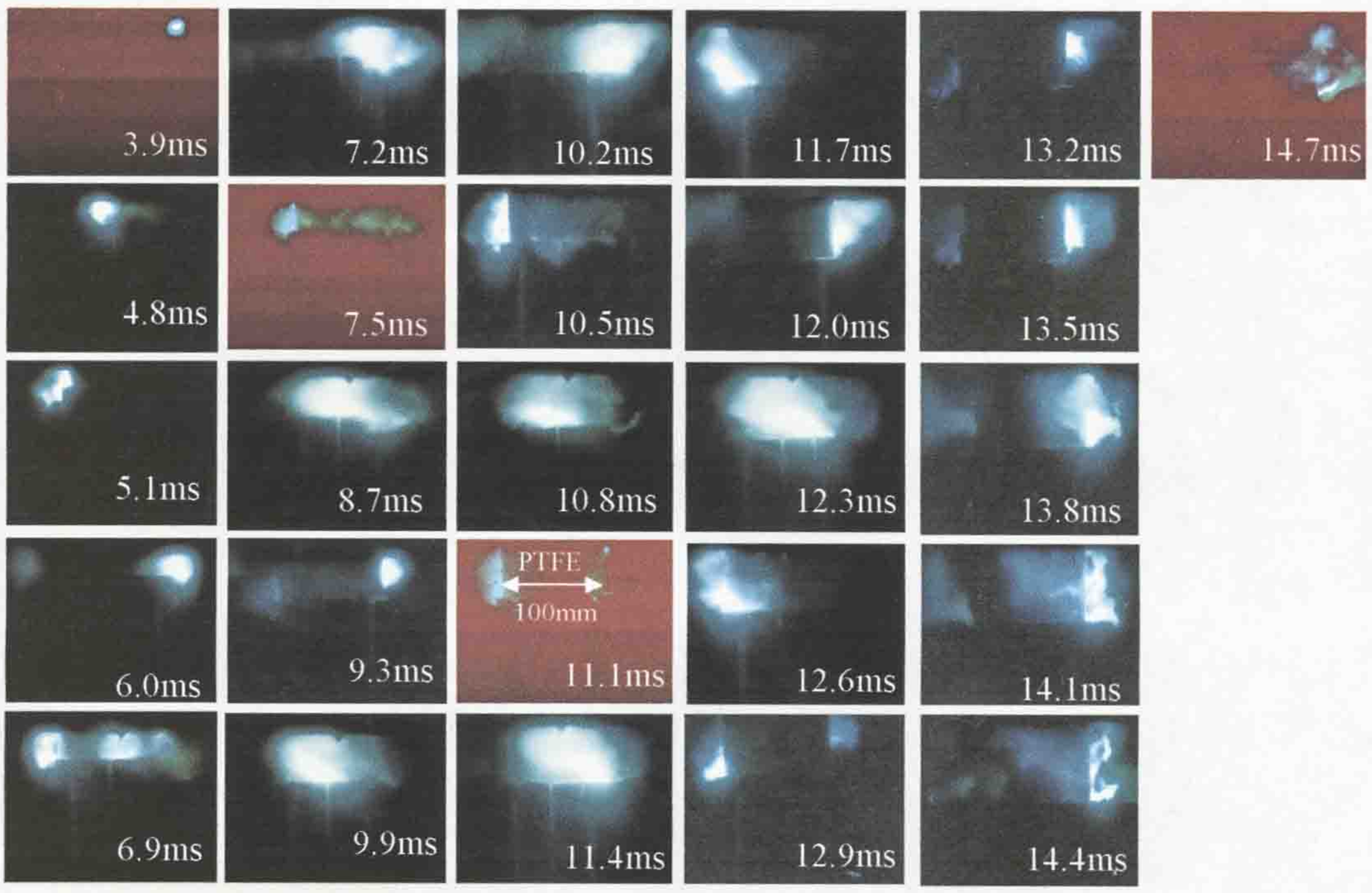

Figure 5.35 Example of high-speed photographs (camera 1) of ac-arc in air, atmospheric pressure, ac-arc of 13.25kA, (framing rate 7500 frames per second)

From 3.9ms to 5.1ms (camera 1) the ac-arc is observed to move from the right side, within the photographic fields of view, to the left (fig. 5.35). This is confirmed by camera 2 from 4.3ms to 5.5ms (fig. 5.36), while the contact gap between the electrodes is around 20-25mm (fig. 5.28).

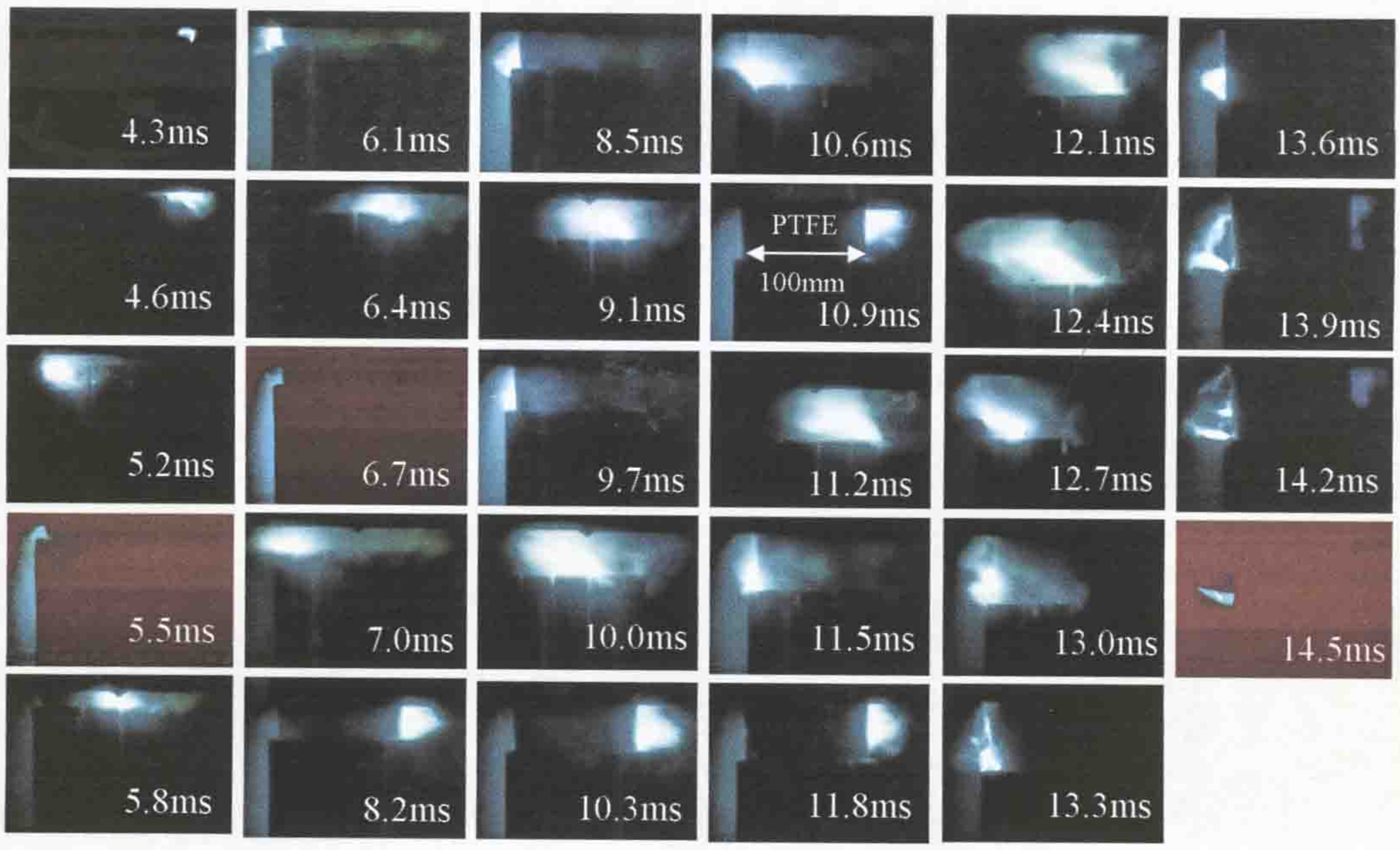

Figure 5.36 Example of high-speed photographs (camera 2) of ac-arc in air, atmospheric pressure, ac-arc of 13.25kA, (framing rate 7500 frames per second)

After 5.5ms, the ac-arc rotational velocity incresed under the influence of the magnetic fields. This is evident on traces of the rotary arc at 6.9ms, at 7.5ms of the camera 1 (fig. 5.35) and at 6.1ms, at 7.0ms of the camera 2 (fig. 5.36). The velocity of the rotary arc is shown by both cameras to be close to the maximal speed from 7.0ms to around 8.5ms. The framing rate of both high-speed cameras was fixed at 7500 frames per second, corresponding 0.15ms frame duration. From the optical fibre monitoring results (fig. 5.28), during the period of 7-8ms from arc initiation, the pulse duration detected by fibres 1, 2 and 3 was around 0.3-0.35ms. As a result, the rotary arc creates effect that arc is rotated in the opposite direction within the photographic fields of view, (at 7.5ms, 8.7ms) camera 1 and (at 8.5ms, 9.1ms) camera 2. The electrodes gap at the same time was around 46-50mm from the contact separation. After around 9ms, the velocity of the rotary arc begins to reduce, changing its orientation horizontally. This is observed by camera 1 (at 9.9ms, 10.8ms, 11.4ms) and by camera 2 (at 9.1ms, 10.0ms, 11.2ms). The electrodes gap at 11.2ms was around 62mm. After the 12ms of arc duration, the arc length is increased

significantly, orientated horizontally within the photographic fields of view of both cameras 1 (at 12.3ms) and 2 (at 12.4ms). The arc, orientated horizontally, rotated until current zero as observed by cameras 1 and 2 (at 13.8-14.1ms). At 13.9ms and 14.2ms (camera 2) there is evidence that arc is forced away from the PTFE cylinder. This observation is supported by camera 1 (at 13.5ms, 13.8ms and 14.1ms) while the gap between the electrodes was around 80mm. Within the post-arcing time (around 0.7ms after current zero), the hot gas (plasma) is observed mostly by camera 1 (at 14.4ms, 14.7ms) and this observation is in good agreement with the optical fibre tests after current zero (fig. 5.28), where fibres 1 and 2, locating close to that area, detected the hot gas in the view of the bright light. The frame 14.7ms (camera 1) and 14.5ms (camera 2) show the post-arc images after the ac-arc repulsive effect. The arc radius during first 13ms (cameras 1 and 2) coresponded to the PTFE cylinder radius (~50mm). Beyand 13ms, there is evidence that the arc radius is increased (~70mm) close to current zero (at 13.8ms and 13.9ms). The increase of the arc plasma radius continued after current zero (at 14.5ms and 14.7ms, radius ~80mm).

Figure 5.37 shows an estimate of the arc length defined from the images of figures 5.35 and 5.36 at various times presented as a percentage of a maximum arc length recorded. The arc length has been estimated relative to the diameter of the PTFE cylinder (~100mm) as recoreded on the images. Also shown on figure 5.37 is contact position as a function of time. Two independed observations (camera1 and camera 2) were used for arc length estimate and the average is also shown on figure 5.37. It was found that during first 12 ms the arc length gradualy incresed until the contact travel reached around 70mm (fig. 5.37b). After 12ms from arc initiation, the arc length is rapidly increased (fig. 5.37a) and continues to increase during the final 2ms until current zero (14ms). This observation is in good agrement with the optical fibre length monitoring (fig. 5.30), where duration of the pulses (fibre 1, fibre 2 and fibre 3) are rapidly increased after 12ms from arc initiation. Arc location close to current zero in figure 5.38 showing in relation to the PTFE cylinder images (containing coil) are given. These frames are from the some tests figure 5.35 ((camera 1, figure 5.38a) and figure 5.36 ((camera 2, fig. 5.38b) showing ditails of the last 3ms of the arcing, including some post arcing. It was found that ac-arc column became obliquely orientated under the influence of the magnetic fields having an oblique orientation when the cathode (C) is level with the bottom of the

coil (camera 1, at 11.4ms and camera 2, at 11.5ms). This oblique orientaton continues until the arc becomes horizontal (camera 1, at 12.3ms and camera 2, at 12.4ms). The arc core is concentrated at the middle of the coil during its motion around the PTFE cylinder. Immediately prior to current zero, the arc is mostly wound around the cylinder forcing it away from the PTFE (camera 1, at 13.8ms and camera 2, at 13.9ms). During the ac-arc interruption a loud acoustical signal is occurred, which was probably produced by the rapid outward expansion of the arc (camera 1, at 14.4ms and camera 2, at 14.2ms). Inspection of the electrodes and PTFE cylinder in the interrupted head (fig. 5.39) post arcing showed little electrode wear and some discouloration of the surface of the PTFE where arc had been located.

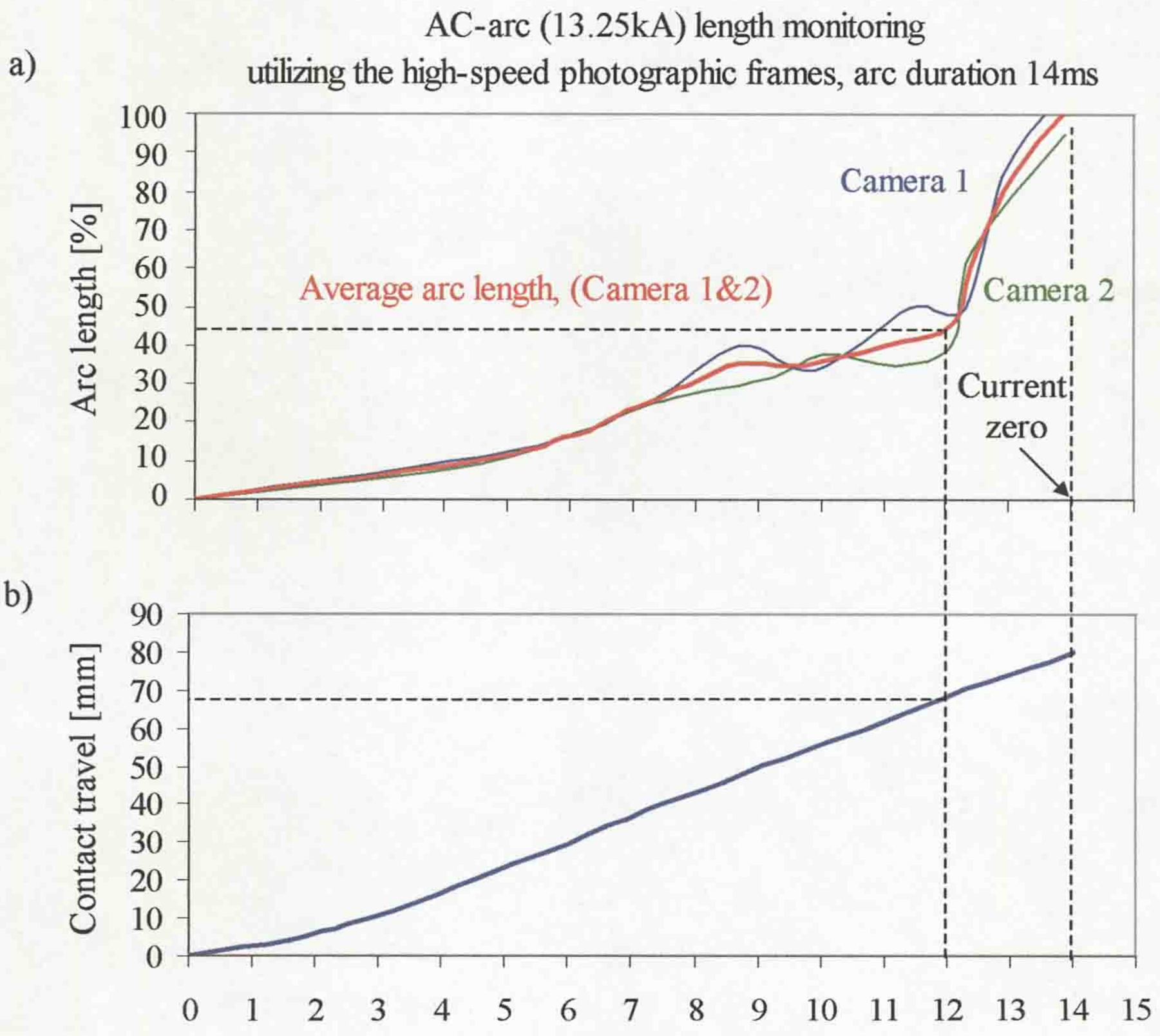

Figure 5.37 AC arc length and contact position as a function of time
(Arc length determined from photographic images figures 5.35, 5.36)
a) Arc length b) Contact position

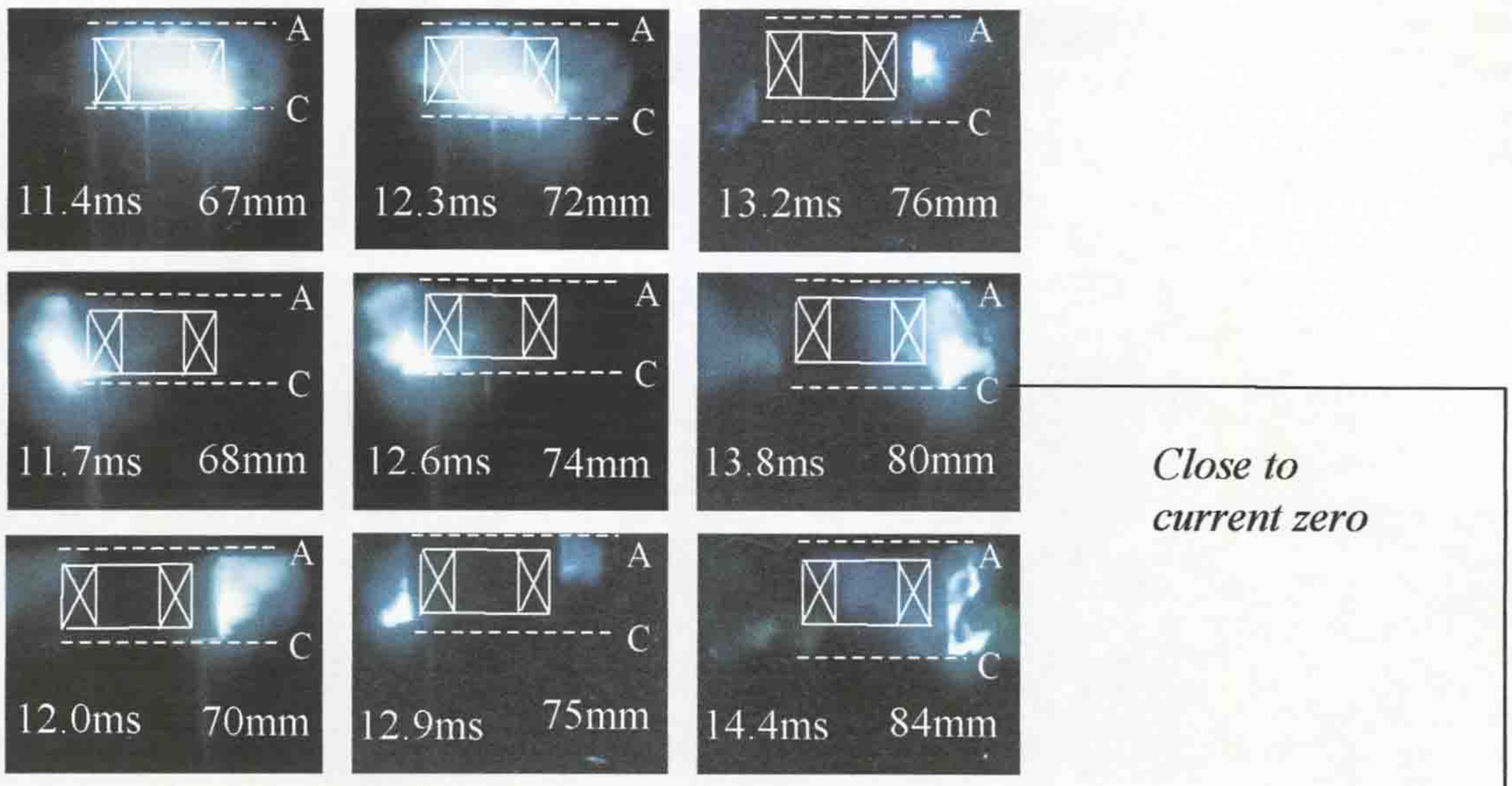

a) High-speed photographs of the camera 1

b) High-speed photographs of the camera 2

Figure 5.38 Position of the ac-arc at current zero

In parallel to these tests, a video camera (fig. 4.10) was used to observe the rig after the ac arcing with the frame duration set at 40ms per frame. Figure 5.40 shows one example of such a video frame coresponding to 40ms after ac-arc initiation. The video frame shows that the post ac-arc plasma displaced from the PTFE cylinder at 40ms after ac-arc initiation. This implies that the post ac-arc plasma (hot gas) continues deviate radilly from the PTFE cylinder after current zero.

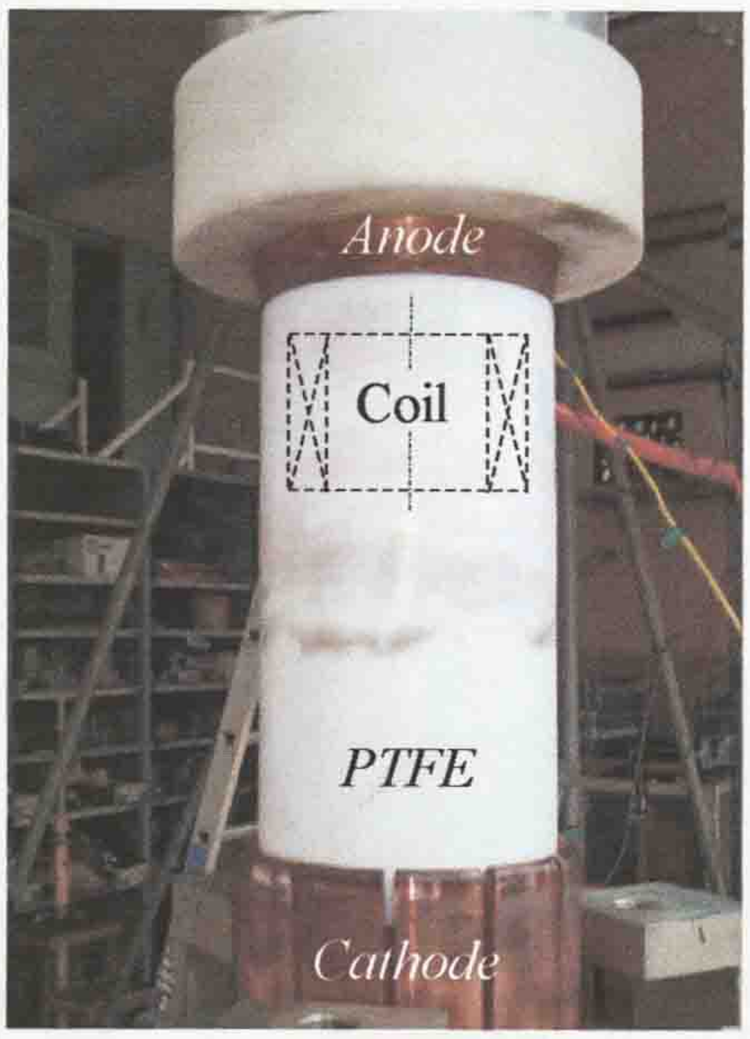

Figure 5.39 PTFE discolouration
in the current interrupter head
following arcing

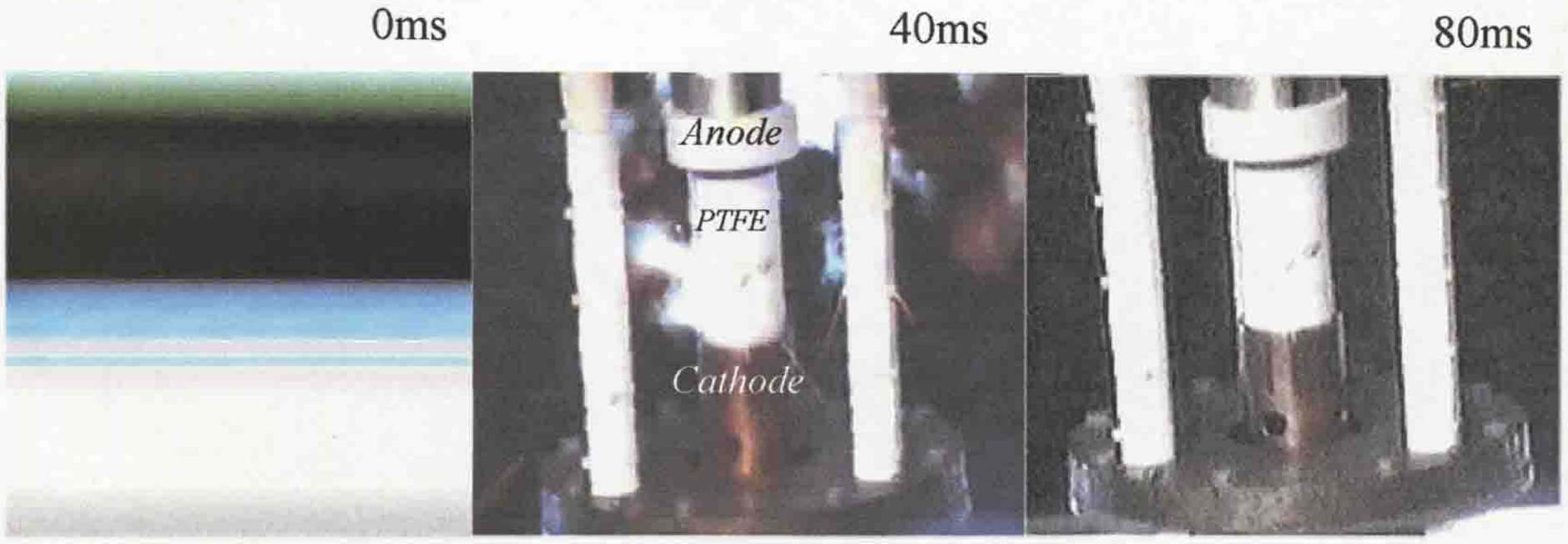

a) Arc initiation b) Post-arc repulsive effect c) Post repulsive period

Figure 5.40 Video frame showing the post ac-arc repulsive effect

Inspection of the current interrupter head post arcing not only showed the PTFE cylinder to be discoloured (fig. 5.39) but also that the PTFE cylinder was ablated by the arc burning close to the PTFE such that the shape of the cylinder changed to

become conical. The condition of the electrodes after 100 tests at 12.5kA to 16.5kA ac-arc current (arc duration of 12.5ms to 20.0ms) remained and could have been operated for a further long duration (fig. 5.39). To demonstrate the advantage in this respect figure 5.41 shows an image of the PTFE cylinder after an ac-arc current of 12.8kA (arc duration of 17.5ms) without the arc driving coil. After a single test (fig. 5.22b), electrode destruction is observed, (fig. 5.41). The vertical discolouration region on the PTFE cylinder and two lardge dots (electrodes damage) on the electrodes prove that ac-arc burned without any rotary motion.

Some additional post arc observations of the prototype rotary arc interrupter are apparent from figure 5.42. During arc interruption the breaker operation forces the ac-arc to be wound around the inner PTFE cylinder close to current zero (fig. 5.38). The repulsive effect on the arc which is observed in the area of current zero shows the arc is induced to expand radially in the horizontal direction from the inner

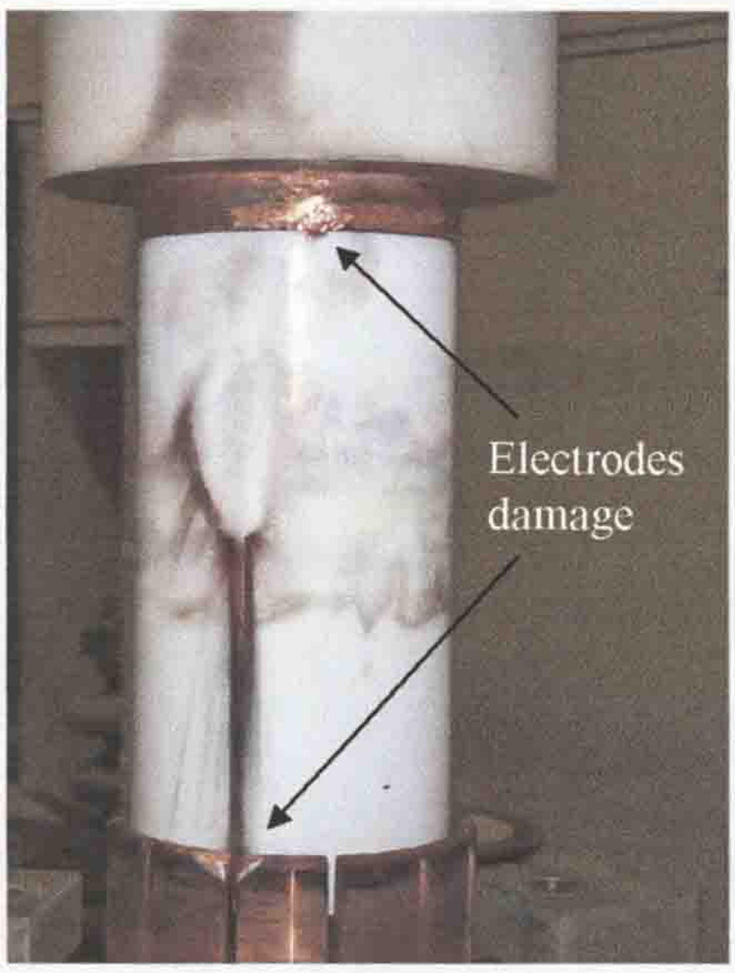

Figure 5.41 Circuit breaker head observation after one ac-arc (12.8kA) test without the coil operation, arc duration of 17.5ms

PTFE cylinder. This is confirmed by the video frame (fig. 5.40) showing that post arc plasma (hot gas) is radially expanding. The outer PTFE cylinder of the prototype interrupter constrains this action and leads to the ac-arc producing a self-blast repulsive effect after current zero. In addition, the outer cylinder directs the post arc plasma to be driven away from the contact gap. This is confirmed by the video frame (40ms after the arc initiation, peak current around 10.5kA) demonstrating that post arc plasma, in the shape of a ring, is located at the bottom part of supports around

the cathode (fig. 5.42c) . Discolouration of the inner and outer PTFE cylinders show that arc is located between the two PTFE cylinders when the arc repulsive effect occurred (fig. 5.42a,b). Moreover, during the ac-arc extinction a loud acoustical signal is occurred (same to current interrupter head tests) probably by the rapid outward expansion of the arc.

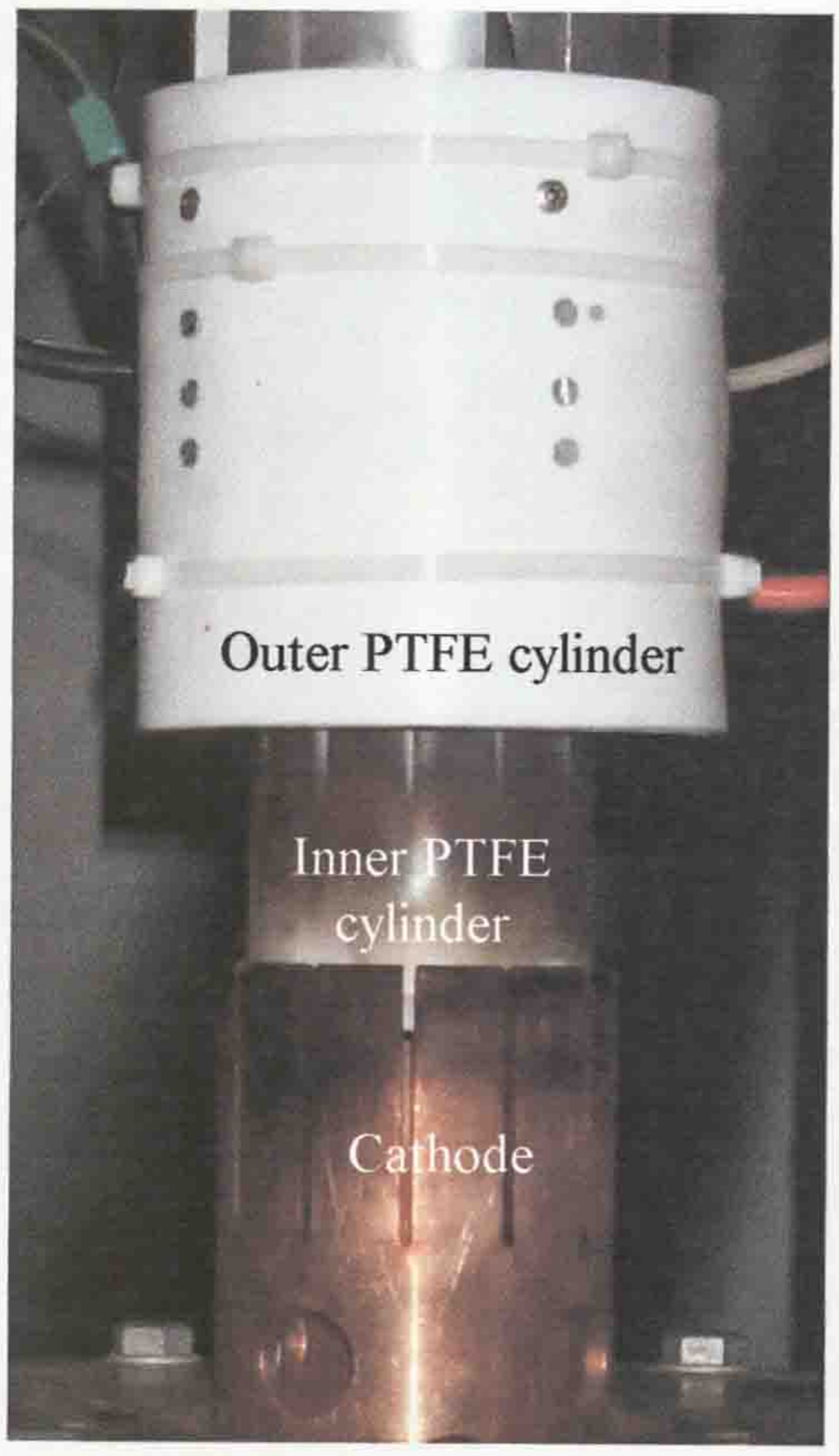

a) Discolouration of the inner PTFE cylinder

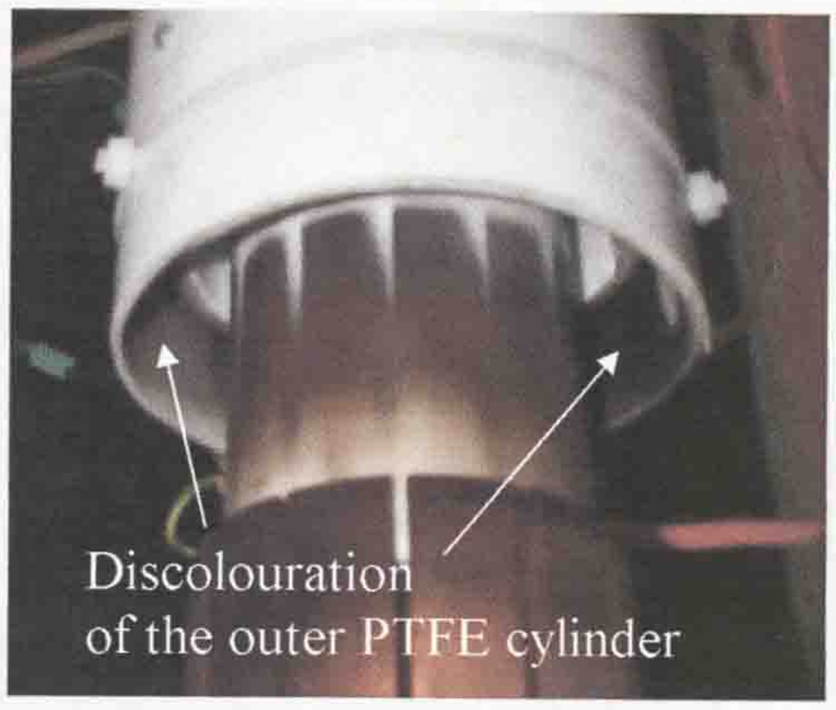

b) View of the prototype interrupter from the bottom side of the breaker

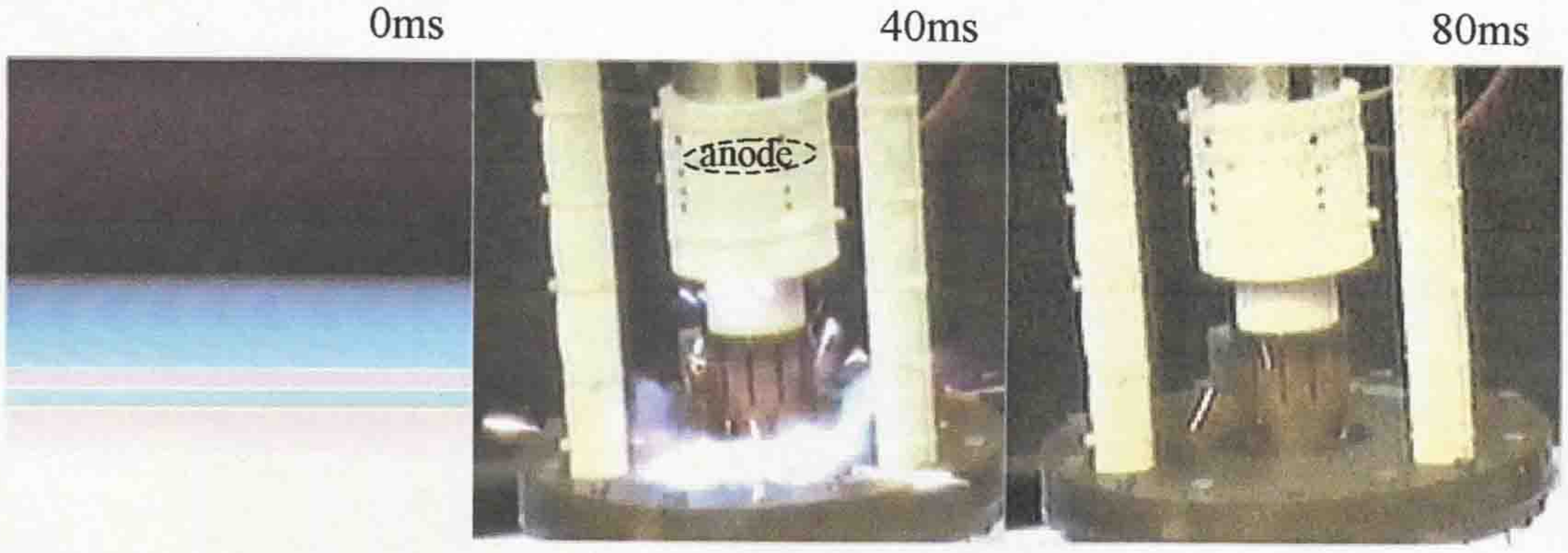

c) Video frame showing the post ac-arc self-blast effect

Figure 5.42 Post arc observation of the prototype interrupter

5.2.3.6 PTFE ablation results of the current interrupter head

The test results relevant to the PTFE ablation monitoring of the current interrupter head are presented in this section. The current interrupter head (fig. 3.8) was inspected after 40 tests at different current levels. The dimensions of the PTFE cylinder at various axial locations measured are shown in figure 5.43.

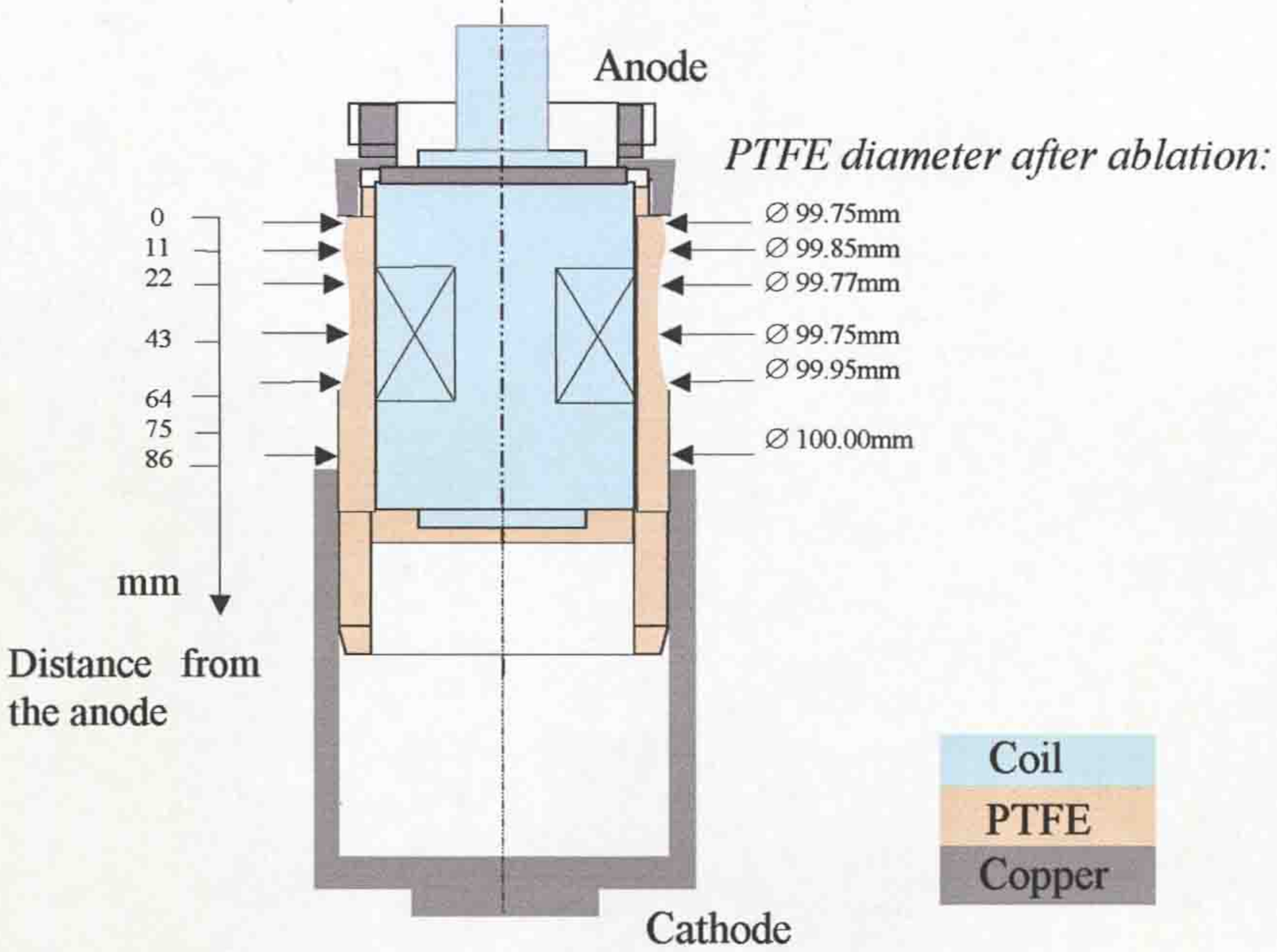

Figure 5.43 Measured diameters of the PTFE cylinder at various axial locations

The shape of the PTFE cylinder was substantially changed after the series tests. The volume of PTFE material, which removed by ablation during the 40 tests, to a first approximation was V=2118 mm^3 composed to the initial volume of the PTFE cylinder of 383080 mm^3 (where a maximum experimental length of the cylinder was 122mm (20ms arc duration), deep 10mm and a circumference length of the cylinder around 314mm).

Using the calculation technique previously mentioned (**section 5.1.3.6**) the total power of 40 ac-arc tests is W=168.097, [MW x Second]. As a result, the total energy, which was spent for the PTFE ablation material of 1 mm^3, is:

$$J = \frac{W}{V_{ablation}} = \frac{168.097 \times 10^6}{2118} \approx 79.365 \left[\frac{\text{kW Second}}{\text{mm}^3} \right] \approx 79.365 \left[\frac{\text{kJ}}{\text{mm}^3} \right] \qquad (5.1)$$

It was found that ablation distribution around the PTFE cylinder was related to the magnetic field distribution around the coil situating inside the PTFE cylinder. As a

result, the PTFE ablation observed at the centre of the coil where the ac-arc core was positioned azimuthally around the PTFE cylinder and the arc was electromagnetically attracted to the coil (fig. 5.38). Furthermore, the length of the arc was increased providing a mechanism for greater interaction between the rotary arc and the PTFE cylinder.

The ablation distribution of the outer PTFE cylinder of the prototype interrupter was observed visually where the trend of ablation was similar to the inner PTFE cylinder.

5.3 DISCUSSION

Chapter 5 has presented results obtained from the preliminary arc tests for design development (**section 5.2.1**), test results relevant to arc control (**section 5.2.2**) and results on a novel rotary arc interrupter (**section 5.2.3**). Three separate sets of experiments have been undertaken, using quasi-dc and ac arcs.

The arc behaviour in SF_6 and N_2 gases has been investigated using the PTFE arrangement in the non-rotary arc interrupter (**section 5.2.1**). It was found that the arc voltage of quasi-dc arc (2kA-9.3kA), in N_2 is varied gradually with time where as in contrast the SF_6 voltage changes occurred with high amplitude of oscillations superimposed. In addition, the arc voltage in N_2 gas reduced rapidly at the time of arc interruption compared to SF_6 where the voltage is reduced more slowly. Moreover, the arc voltages in SF_6 and N_2 gases are similar when the quasi direct current is increased up to 9.3kA. However, the peak voltages in SF_6 are higher compared to N_2, because of the high amplitude dc-arc voltage oscillations. Results for quasi-dc arcs in SF_6 and N_2 at different pressures (0.5bar-3bar) were obtained using a current of 2kA. It was found that the arc voltages in SF_6 and N_2 gases were significantly reduced as the pressure changed from 3bar to 1bar. At 0.5bar and 1bar, the peak arc voltages in both media were similar (e.g. it was observed that arc voltages in each gas converged to similar values). Ac-arc investigations in SF_6 and N_2 showed that arc behaviour was similar to the quasi-dc arc. However, with SF_6 the arc peak was increased at current zero when the duration of the ac-arc was prolonged.

Gap measurements in the non-rotary arc interrupter (**section 5.2.1**) showed that in both gases the average distance between the electrodes, when the arc was successfully extinguished at current zero, was about 50mm. Thus, since the length of

the magnetic coil for design development (**chapter 3**) should be the length of the electrode gap and it should not be more than 50mm.

The arc control test results (**section 5.2.2**) demonstrate that it is possible to force the 1.3kA arc to be wound around the PTFE cylinder in air, at atmospheric pressure. Moreover, the mechanism whereby the arc was forced also contributed to the arc being forced during the post-arc time.

Finally, results obtained from the novel rotary arc interrupter (**section 5.2.3**) indicated that the maximum magnitude of the magnetic field (external to the coil) at the edge of the anode is about 137.6mT with a minimum at the centre of the coil of 104.0 mT at a distance of 6mm from the PTFE cylinder (fig. 5.21). In addition, the magnitude and shape of the magnetic field (**section 5.2.3.1**) is not spatially uniform and changes with distance. For instance, at a distance of 27mm from the PTFE cylinder the B-field value is about 3 times less than for 6mm. However, the field is symmetrical about the vertical axis up to the measurement limit at 27mm. The interrupter is able to control and to interrupt a 15kA ac-arc in air, at atmospheric pressure (**section 5.2.3.2**). The time of the ac-arc interruption for this arc current is about 18.0ms. The interrupter head investigations show that a rotary ac-arc of 13.25kA (arc duration of 14ms) is rapidly rotated at a velocity of around 930 m/s (**section 5.2.3.3**). The number of ac-arc rotations during a 10ms window is 13. The recovery characteristics of dielectric strength for the prototype rotary arc interrupter in air, at atmospheric pressure, with a current of 5kA produce a sufficiently rapid dielectric recovery at gap around 95mm (**section 5.2.3.4**).

The high-speed and video recorder observations (**section 5.2.3.5**) demonstrate that the ac-arc is wound around the PTFE cylinder and repulsed away from the PTFE cylinder close to current zero. This effect is accompanied by a high amplitude acoustic signal indicative of an aerodynamic self-blast repulsive effect. During the arc rotation (arc duration of 14ms) the ac-arc length is substantially increased after 12ms following the contact separation, while the electrodes gap is around 70mm. This process continued until current zero. The life of the electrodes is significantly increased using the model of the arc interruption, in air, at atmospheric pressure.

The ablation of the PTFE cylinder has been observed visually (**section 5.2.3.6**). The shape of the cylinder in the current interrupter head changed from being cylindrical to conical after 40 tests and the energy spending for PTFE

material loss through ablation was $79.365\,kJ/mm^3$. The same trend of the PTFE ablation (shape of the outer PTFE cylinder) was observed in the prototype interrupter visually.

CHAPTER 6 - ANALYSIS OF RESULTS

The behaviour of the arc in the various devices designed in this project allows an understanding to be gained of processes occurring during and post arcing. The implications of the results relating to current interruption are discussed in this chapter.

The range of test heads used and operating conditions (Tab. 6.1) were as follows:

A. Contact gap with inner PTFE rod and outer PTFE cylinder, no coil (fig. 4.4)

B. Contact gap with inner PTFE cylinder, with coil (fig. 3.3, 3.6)

C. Contact gap with inner PTFE cylinder, no coil (fig. 3.8, 3.11)

D. Contact gap with inner PTFE cylinder, with coil (fig. 3.8, 3.11)

E. Contact gap with inner and outer PTFE cylinders, with coil (fig. 3.11, 3.12)

A summary of measurements made (Tab. 6.2) is as follows:

A(i) - Non-rotary arc interrupter (A) (Reference interrupter Tab. 6.1)

B(i) - Arc control unit (model) (B) (Tab 6.1)

C(i) - Current interrupter head without the arc driving coil (C) (Tab. 6.1)

D(i) - Current interrupter with the arc driving coil (D) (Tab. 6.1)

E(i) – Prototype interrupter (E) (Tab.6.1)

and *i* - current level used.

Experiment	*I peak* AC/DC	*B peak field*	*F*	*Gap*	*V extinction*	*H.S. Photo*	*Video*	*Optic. Fibre*	*Dielect. Strength*
A. Non-rotary arc reference interrupter: (preliminary arc tests)	kA	mT	N/m	m	Figure	Figure	Figure	Figure	Figure
	2.0 DC				5.6 5.7 5.8 5.9				
	4.8 DC				5.6 5.7				
	7.6 DC				5.6 5.7				
	9.3 DC				5.6 5.7				
	12.0 AC 12.2 AC			0.110	5.10 5.11				
	14.8 AC 14.0 AC			0.093	5.10 5.11				
	18.3 AC 18.0 AC			0.068	5.10 5.11				
B. Arc control model: (with the arc driving coil)	1.3 DC				5.13	5.15 7.3	5.16		
	1.3 AC	33.75	43.9	0.093	5.14		5.17		
C. Current interrupter head: (without the arc driving coil)	12.8 AC			0.102	5.22				
D. Current interrupter head: (with the arc driving coil)	1.5 DC					5.34			
	5.3 AC	*B-field measurements*			*4.16*				
	11.8 AC	306.35	3615	0.122	5.22, 5.24 5.25				
	13.2 AC	342.70	4524	0.106	5.22 5.24 5.25	5.35 5.36 5.38	5.40	5.28 5.29 5.30 6.20	
	14.0 AC	363.47	5088	0.095	5.22 5.23 5.24 5.25				
	16.2 AC	420.59	6813	0.070	5.22				
E. Prototype interrupter: (with the arc driving coil)	5.0 AC	129.81	649						5.31 5.32 5.33 6.15 6.17
	10.5 AC	272.60	2862	0.106	5.26		5.42 6.13		
	11.8 AC	306.35	3615	0.122	5.26, 5.27				
	13.3 AC	345.30	4592	0.106	5.26, 5.27				
	14.0 AC	363.47	5088	0.095	5.27				
	15.0 AC	389.43	5841	0.106	5.26				
	15.8 AC	410.20	6481	0.070	5.27				

Table 6.1 Range of experimental arc units and conditions used

Current		*Voltage*						*High-speed photos*				*Optic fibres*		*Video* *(Post arc)*	*Dielect. probe*	*B-field probe*	*Geometry*
		Power	**Rotation**	**Azim. arc**	**Ext. peak**	***RRRV***	***V max***	**Arc length**	**Arc speed**	**Radial expan-sion**	**Arc radius**	**Arc speed**	**Arc position**	**Plasma position**	**V break-down**	**Bx, Bz**	**PTFE erosion**
Quasi -DC	**Main**	D(×)	D(±)	D(±)	A(*) B(−)		A(*) B(−)		D(±)		D(±)	D(±)	D(±)		E(+)		B(−) D(×)
	Current zero				A(*)		A(*)				D(−)						
	Dielectr. recovery				A(*)		A(*)							B(−)			
1/2 cycle AC	**Main**	D(×)	D(±)	D(±)	A(×) B(−) C(Δ) D(×) E(□)	D(#)	A(×) B(−) C(Δ) D(×) E(□)	D(±)	D(±)		D(±)	D(±)	D(±)		E(+)	D(∇)	B(−) D(×) E(×)
	Current zero	D(×)	D(±)	D(±)	A(×) B(−) C(Δ) D(×) E(□)	D(#)	A(×) B(−) C(Δ) D(×) E(□)	D(±)	D(±)	D(±)	D(±)	D(±)	D(±)		E(+)	D(∇)	
	Dielectr. recovery		D(±)	D(±)	A(×) B(−) C(Δ) D(×) E(□)	D(#)	A(×) B(−) C(Δ) D(×) E(□)	D(±)	D(±)	D(±)	D(±)	D(±)	D(±)	B(−) D(±) E(•)	E(+)		
2x1/2 cycle AC	**Main**	D(×)															D(×)
	Current zero	D(×)															D(×)

Table 6.2 Measurement methods used for different current waveforms and various testing (A-E, Tab. 6.1)
(where: (*) = 2→9.3kA, (−) = 1.3→1.5kA, (+) =5.0kA, (±) = 13.2kA, (□) = 7→15.8kA, (∇) =5.3kA, (×) = 12→17kA, (#) = 12.5→15kA, (•) = 10.5kA, (Δ) = 12.8kA)

6.1 ARC PHENOMENA

6.1.1 Arc shape

It is simpler to study a rotary arc discharge in an open rig (figures 3.3 and 3.8) in air, at atmospheric pressure since it is easier to join visual access to monitor the arc interaction processes. However, the air and PTFE material in which the arc burns form a mixture of gases along with vaporized compounds produced by the air reacting with the incandescent electrodes. Because of the high arc temperatures, both cathode and anode are incandescent, the mixture of gases is turbulently agitated, and the electrodes are gradually eroded. These conditions complicate the visual observation of the arc shape observation and therefore the low quasi-dc and alternating currents operation was required for reducing these various effects for initial investigations. This section is devoted to arc shape survey in the devices that are designed for arc control and interruption.

6.1.1.1 Arc shape in arc control model

An arc current operation of 1.3kA was chosen to demonstrate the extent of arc control in the model test head (fig. 3.3).

The interaction of the current flow in the arc channel can interact with the magnetic forces leading to a possible overpressure within the arc channel give a reference, i.e. there is a mechanical force at each point of the column which is directed toward the axis (**section 2.2.3.1**). However, when the magnetic field becomes sufficiently strong, the pressurization is aerodynamically moderated by the radial flow of gas becoming aerodynamically unsustainable and leading to a helical flow of gas around the arc axis (Shishkin and Jones, 1985).

The photographic results of arc shape presented in **section 5.2.2.2** are considered with respect to such effects. Two examples of high-speed photographs of quasi-dc arc of 1.3kA in air, atmospheric pressure, framing rate 10000 frames per second are shown in figure 6.1 corresponding to two distinctly different arc shapes in the arc control model (fig. 3.3).

Figure 6.1a shows an arc column formed vertically between two contacts (anode and cathode) 0.5ms following arc initiation.

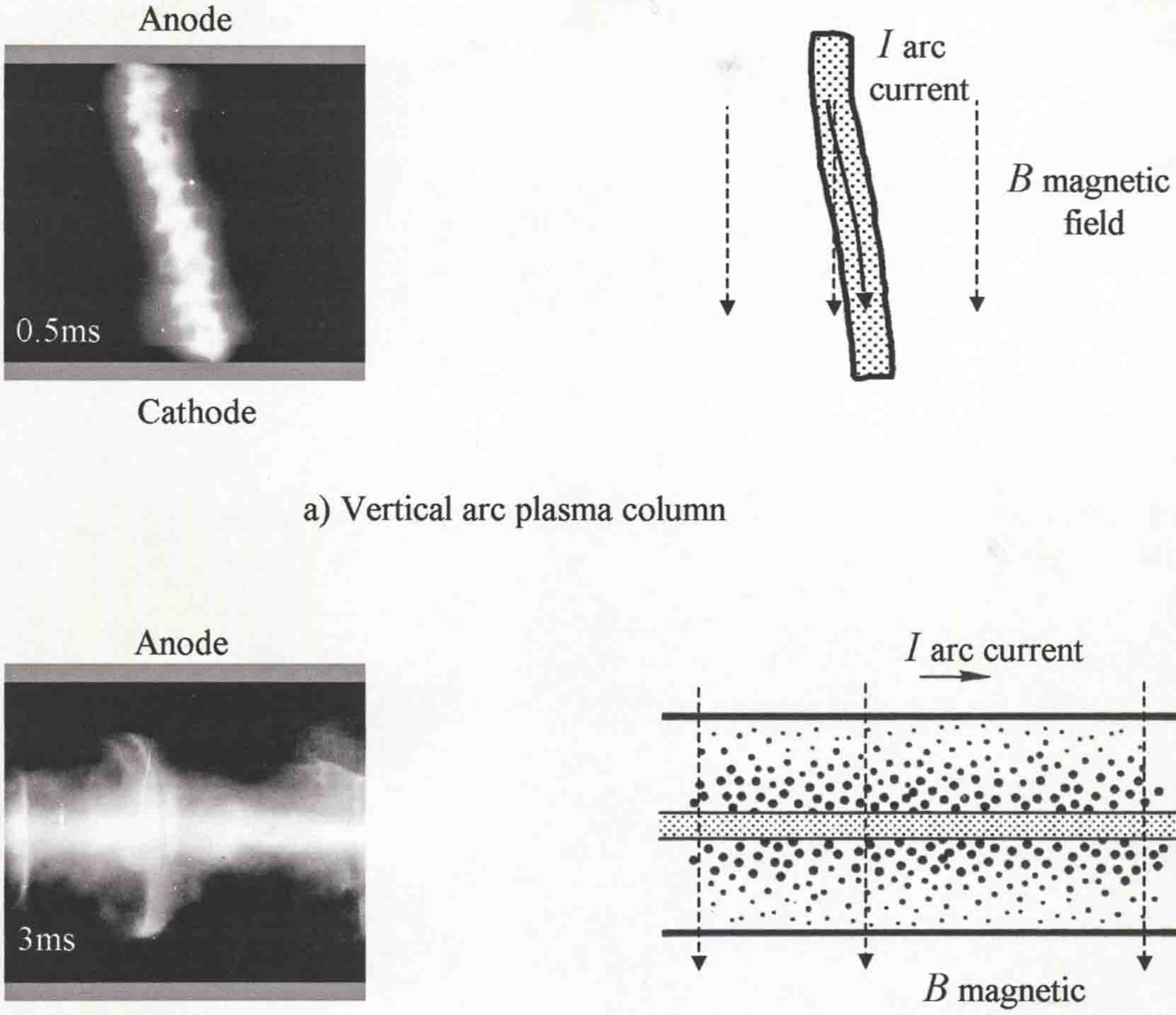

a) Vertical arc plasma column

b) Horizontal circular arc plasma column

Figure 6.1 Photographic evidence showing the existence of two different arc shapes
a) Vertical b) Horizontal circular

During the subsequent 2.5ms, interaction between vertical asymmetry of the arc column and the applied B field leads the Lorenz forces at the top (anode) and bottom (cathode) to operate in opposite directions and force the arc to be orientated horizontally.

At 3ms (fig. 6.1b), there is evidence of swirling plasma around the horizontal arc. During the last 1.5ms, the plasma swirl remains visible but becomes visibly distorted, and leads to the horizontal arc plasma becoming ruptured (fig. 5.15). The duration of the existence of one turn of the arc is about 4.5ms for a quasi-dc current of 1.3kA. After 4.5ms, there is evidence of shorting and re-establishment of the arc (fig. 7.3). The horizontal nature of the arc is confirmed by inspection of the PTFE cylinder post arc time showing horizontal discolouration produced by the arc plasma

in close proximately with the PTFE (fig. 5.18).

A number of shorting and re-establishment of the arc maybe depended on the energy contained in the capacitor bank of the power supply system, supporting this arc discharge (fig. 5.13). A typical example of expansion the post dc arc plasma (fig. 5.16) shows that a plasma remotely driven away from the test head.

6.1.1.2 Arc shape in current interrupter head

The arc shape is transformed in case of the rotary ac-arc of 13.25kA, arc duration of 14ms operating in the current interrupter head (fig. 3.8). The high-speed photographs confirmed the arc column shape change during the arc rotation (fig. 5.35 and fig. 5.36). Figure 6.2 shows a typical example of these photographic results (framing rate 7500 frames per second) at 12.4ms arcing (fig. 5.36) corresponding to distinctly different arc shape. After current zero, the radial arc plasma deviate radilly from the current interrupter test head (14.2ms, fig. 5.38b).

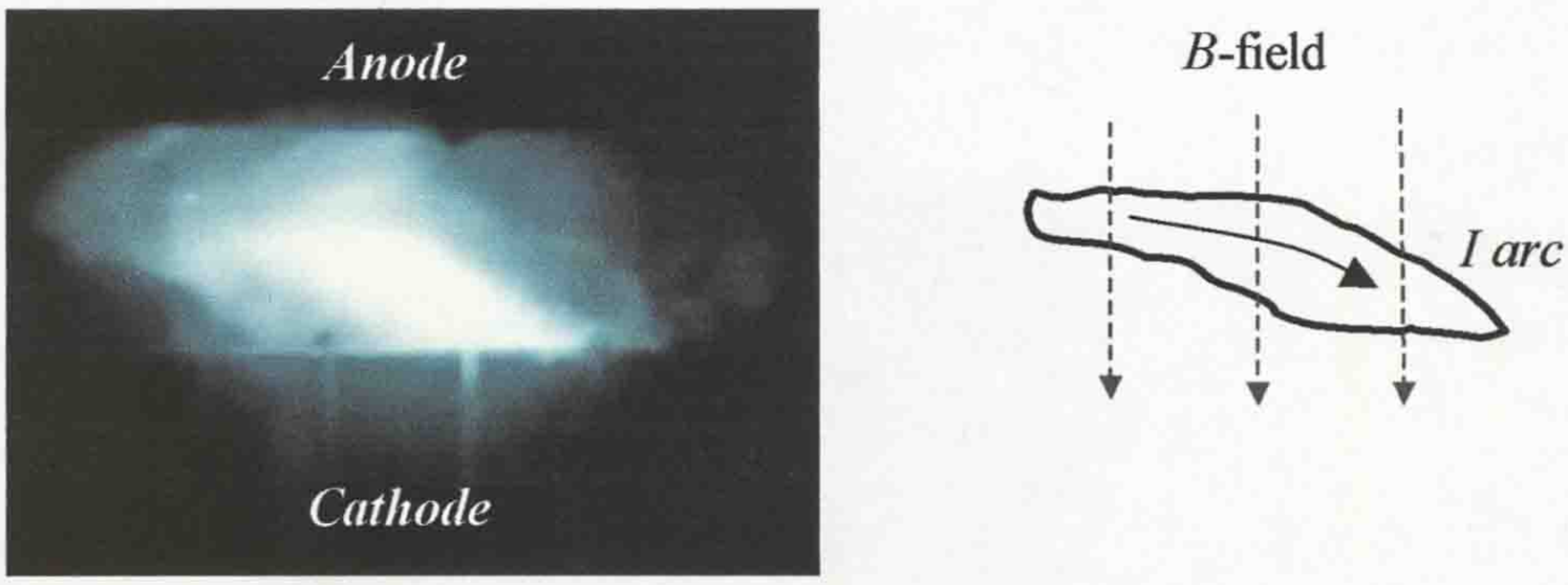

Figure 6.2 Photographic evidence demonstrating the existence of horizontal circular arc shape in the rotary arc current interrupter head (at 12.4ms, fig. 5.38b)

Inspection of the rotary arc shape in the interrupter using optical fibre measurements on the azimuthal gap (**section 5.2.3.3**) were made. The optical fibers were fixed at the bottom of the interrupter head giving vertical view along the interrupter head from the bottom upwards (**section 5.1.3.3**). Three fibers were situated on the same plane 120 degrees from each other. The ac-arc 13.25kA was investigated in air, at atmospheric pressure, with an ac-arc duration of 14ms. The ac-arc rotation was followed around the test head. It was found that during the first ~12ms (Gap ~68mm) from contacts separation the arc rotation was occurred. When the movable rod (cathode) of the interrupter head is located at bottom edge of the coil (Gap 68mm) the pulses duration (representing the arc length) from the three fibres (fig. 5.30) were

once increased (i.e. the arc length began to wrap around the interrupter head during the last 2ms, rapidly). The high-speed photography can be used for detailed ac-arc length investigations during the last milliseconds of arc existence because of the problems mentioned in **section 5.2.3.3**.

6.1.2 Aerodynamic post arc effect

Survey of the results concerning repulsive post arc effects is presented for each of the three arc test rigs investigated: arc control, current interrupter and prototype breaker heads, which is an evaluation of the current interrupter head. Sample images for each of these different arrangements are presented in figure 6.3. Figure 6.3a,b correspond to the dc arc (fig. 5.16) and ac arc (fig. 5.17) controlling. Figure 6.3c corresponds to the rotary arc breaker (fig. 5.40) and figure 6.3d the new model breaker (fig. 5.42c). Comparison of the video images shows evidence that the post arc plasma continues to expand after current zero for each test head even at 40ms. For the arc control model (**section 3.1**) the arc appears to be wrapped around the PTFE cylinder azimuthally without any arc rotation superimposed. Identification of the PTFE cylinder and electrodes positions on the video frames is indicated in the view of the scale (fig. 6.3). The scale of the video images is related to the diameter of the PTFE cylinder, which is about 100mm. The position of the hot gas or particles (trace) with relation to the PTFE diameter can give the velocity of expansion. As a result, during the post arcing time the plasma volumes move radially outwards without any evidence of azimuthal displacement (fig 6.3a,b). The speed of expansion of the plasma volumes from a number of images inspected (figures 5.16, 5.17) was around $v_r \approx$ 2-5m/s for both AC/DC arcs. There is an implication that it is slow because no arc rotation superimposed. In contrast, for the current interrupter head (**section 3.2**) there is evidence of both radial repulsion ($v_r \approx 75$m/s and later (fig. 6.3c) as 12m/s when the loop distance is 0.3m from the test head) and azimuthal rotation (fig. 6.3c). In the current interrupter head the radial repulsion velocity is sufficiently high. As a result, the post arc plasma repulsion speed is difficult to measure using video frames (fig. 6.3c, fig. 5.40) because exposure of each video frame is 40ms. Therefore, the velocity of the radial repulsion of the post-arc plasma was estimated using a high-speed photography immediately

after current zero (fig. 5.38,b at 13.6ms, 13.9ms and 14.2ms). The rotation is evident in that the hot gas (plasma) assumed rather than isolated volumes form and spreads mostly in the horizontal direction. Optimization of the current interrupter test head leads to design the prototype rotary arc interrupter (**section 3.3**). In the case of the

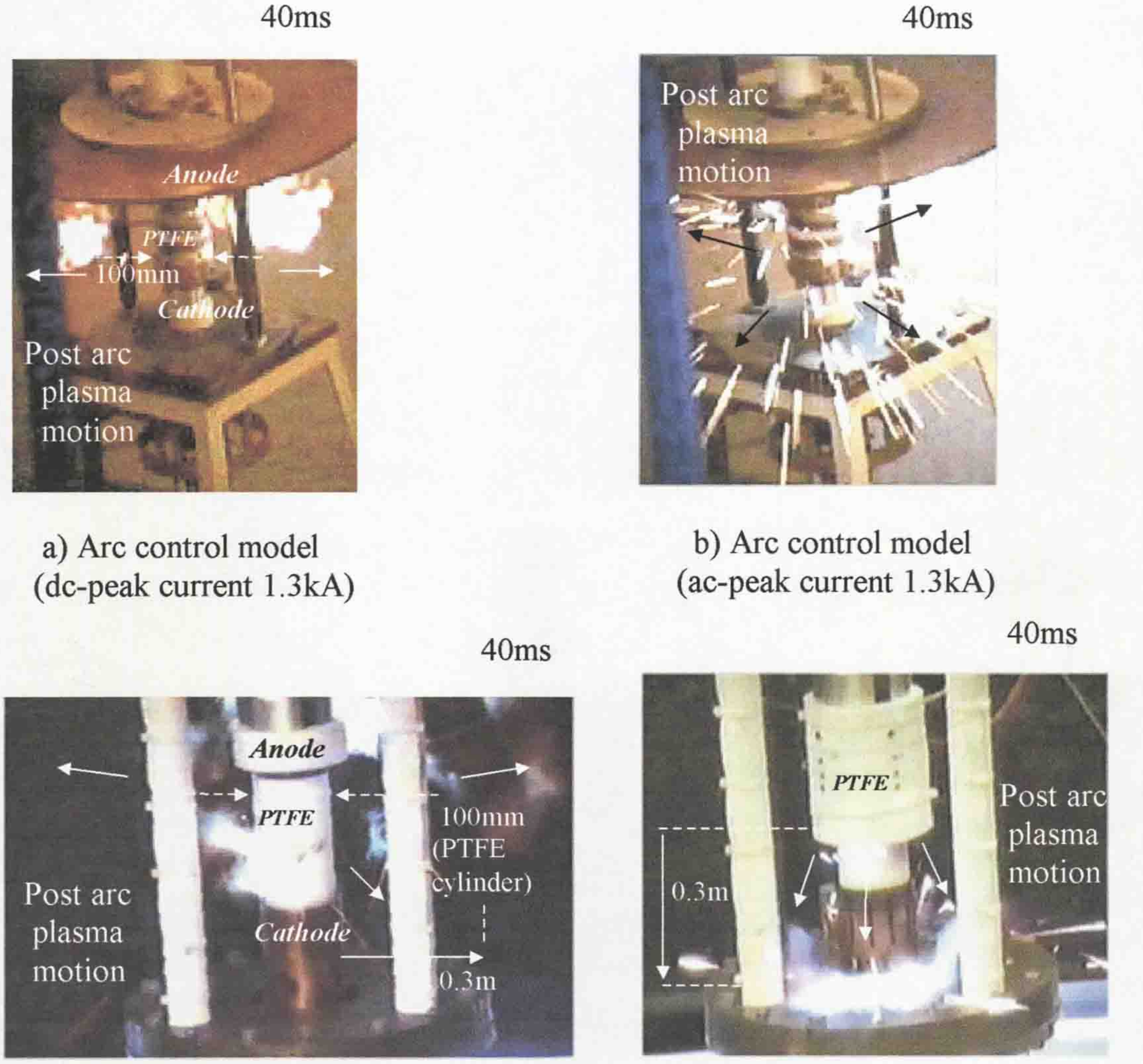

a) Arc control model (dc-peak current 1.3kA)

b) Arc control model (ac-peak current 1.3kA)

c) Current interrupter head (ac-peak current 13.25kA)

d) Prototype interrupter (ac-peak current 10.5kA)

Figure 6.3 Examples of video frames showing the post arc azimuthal expansion for the different test rigs

prototype interrupter, images show that the post arc plasma assumes the shape of ring (fig. 6.3d, 5.42). These images suggest that the arc was forced from the vertical (start of arc rotation) to the horizontal (end of arc rotation) orientation. Position of the post arc plasma at the bottom part of stands shows that plasma is pushed away from the prototype interrupter head at the same time. The rate of axial displacement of the loop is 17m/s being 0.3m from the test head, (fig. 6.3d).

6.1.3 Analysis of magnetic field distribution around the interrupter

The spatial variation of magnetic field around the PTFE cylinder containing the coil have been presented in **section 5.2.3.1** and theoretical analysis method given in **section 3.4**. The experimental results obtained using an ac peak current of 5.3kA following through the coil lead to the following conclusions:

- The maximum value for the total *B*-field is at the tips of the electrodes (137.6mT) with a minimum value at the centre of the coil (104.0mT) at a radial distance from the axis of the coil of 0.056m (6mm from the PTFE cylinder, **section 5.2.3.1**, Tab. 5.3).

- The total magnetic field is not spatially uniform. For instance, at a radial distance of 27mm from the PTFE cylinder (Tab 5.3) the total *B*-field value was about 3 times less than for a distance of 6mm. However, the field is almost radially symmetrical about the vertical axis up to the measurement limit at 27mm.

- The relationship between the coil current and total *B*-field is linear at the high levels of the ac current because of the air-core of the coil.

The radial separation of the inner and outer PTFE cylinders in the prototype rotary arc interrupter (**section 3.3**) is around 20mm. However, after ablation of the inner and outer PTFE cylinders this separation may increase. Therefore, the magnetic field measurements and theoretical calculation of the B field produced by the coil at 27mm were employed as the possible distance between inner and outer PTFE cylinders (fig. 3.16).

The analytical solutions for the magnetic field of a circular cylindrical solenoid in free space can yield the total B field at any point external to the solenoid (**section 3.4**). However, this solution considers a line current density distribution in the conductor as a thin filament of negligible cross section where the current density is considered as uniform. The current density in the foil conductor of the solenoid

used in the arc control model and interrupters is not uniform (**Appendix III**). As a result, a non-uniform current density distribution within the round planar coil (**section 3.1.3**) with rectangular cross section (close to the foil) leads to a non-uniform magnetic field distribution external to the circle cylindrical coil. In addition, the radius of the coil *a* in the theoretical calculation of the magnetic field (**section 3.4**) should be much less than *r* (distance from the Z-axis of the coil to the point external to the coil). According to **section 3.4**, this difference is sufficiently small which could produce approximation in the theoretical calculations of the B field.

Comparisons of the total theoretical (**section 3.4.2**) and measured (**section 5.2.3.1**) magnetic B-fields calculation along the axis of a cylindrical coil at different radial distances from the axis of the coil are presented in figure 6.4. These results show B field as a function of axial position for four radial positions (56, 63, 70, 77mm on figures 6.4a,b,c and d respectively). The values of magnetic field B_o external to and half way along the coil length (Z = 0mm) show good agreement between the measured and calculated values at all radii. However, at the ends of the coil (length 50mm) the theoretical and measured magnetic fields are different.

Figure 6.4a shows that the measured B field from the centre of the coil (0mm) to the 43mm (distance to the anode) is 137.6mT compared to the theoretical value of 89.5mT at 56mm from the Z-axis of the coil (6mm from the inner PTFE cylinder). At 63mm (fig. 6.4b) from the Z-axis of the coil (13mm from the inner cylinder), the theoretical field at 43mm is 67.7mT compared to the measured value of 100.3mT. At 70mm (fig. 6.4c) from the Z-axis of the coil (20mm from the inner cylinder) the theoretical field at 43mm is 52.2mT compared to a measured value of 70.6mT. Finally, at 77mm (fig. 6.4d) (corresponding to 27mm from the inner cylinder) the theoretical field at 43mm is around 41.1mT compared to a measured value of 48.2mT.

In addition, the values of theoretical and measured total B fields show good agreement under condition ($r>>a$) e.g. these results are close when the radius of the coil *a* is much less than *r*.

These calculations were made rather then using software packages such as "Opera-2d" because the non-uniform distribution of current (**Appendix III**) in the coil winding is difficult to accommodate in such software packages.

Comparison of the theoretical and practical magnetic field estimations lead

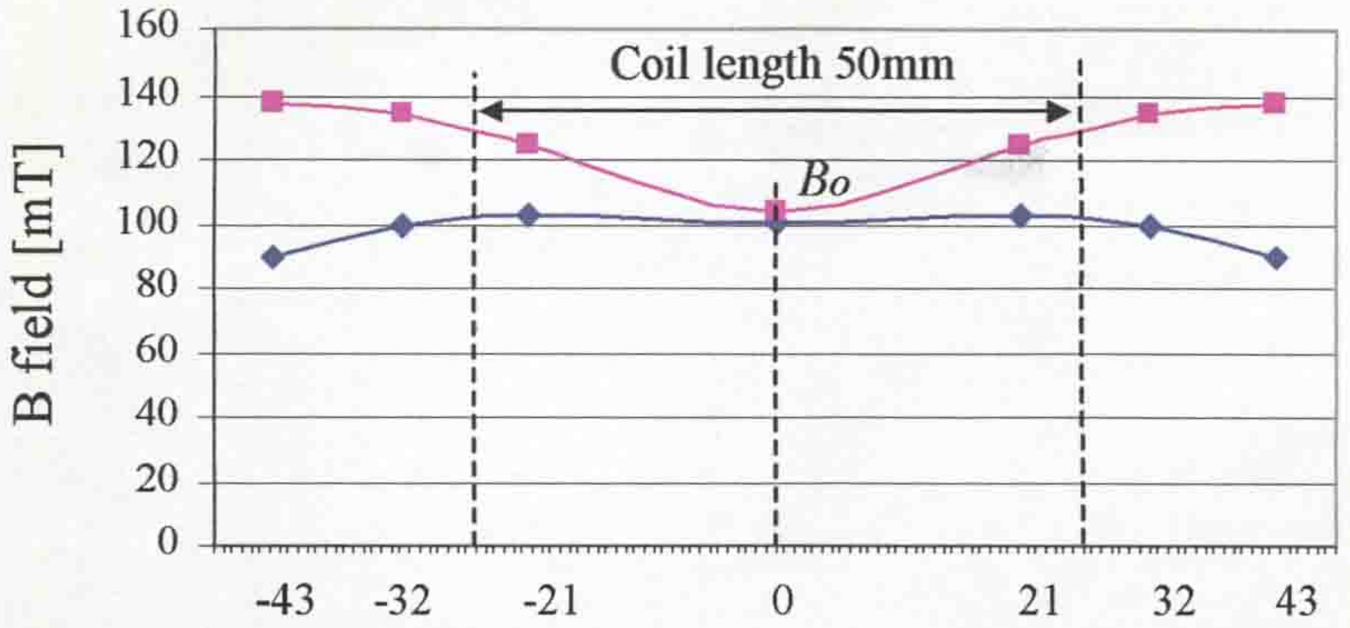

a)

56mm from Z-axis of the coil

Practical

Theoretical

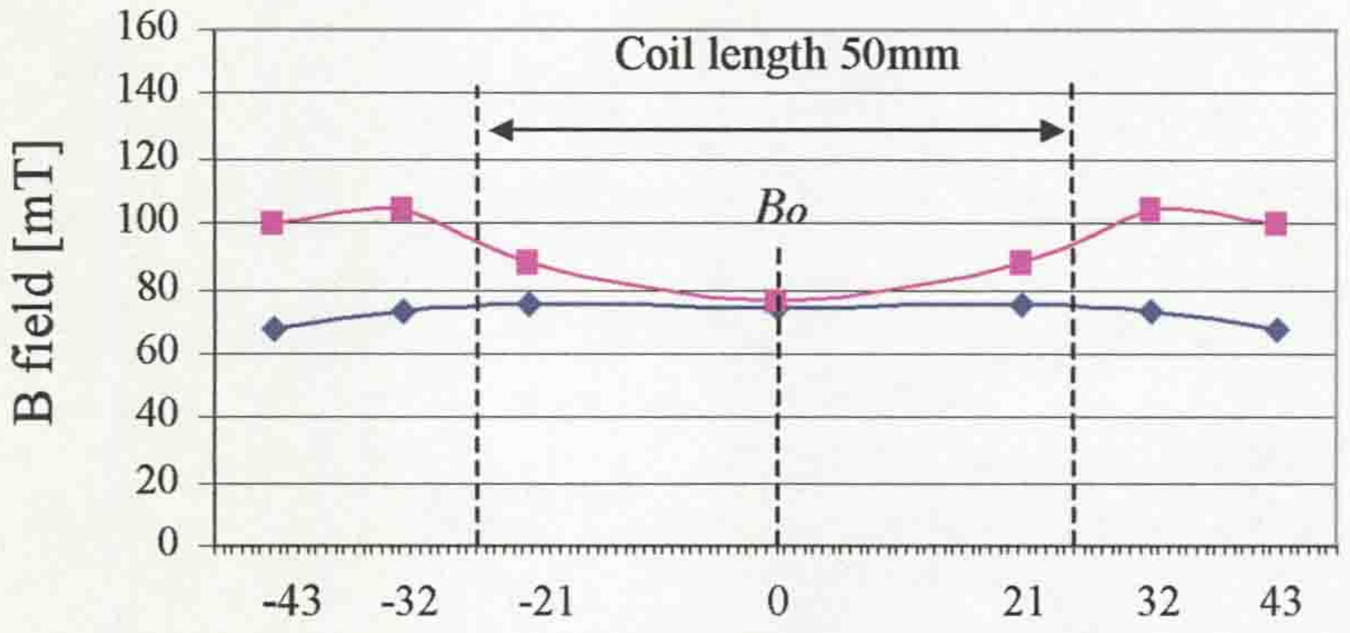

b)

63mm from Z-axis of the coil

Practical

Theoretical

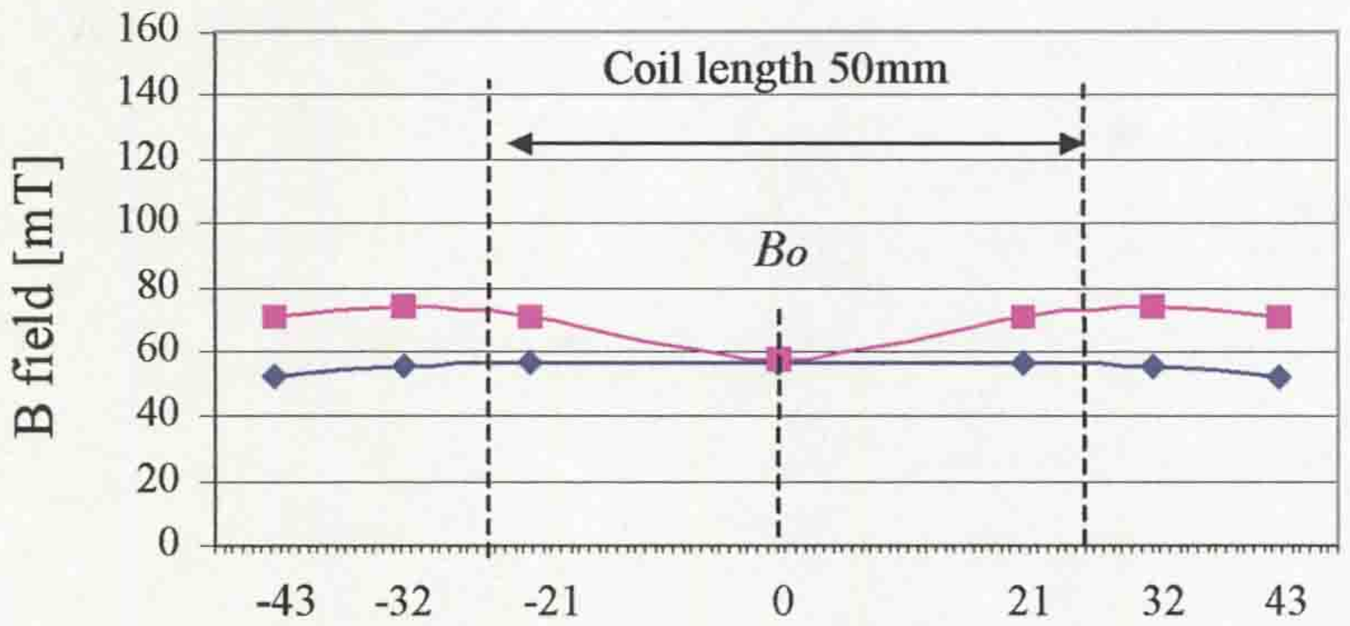

c)

70mm from Z-axis of the coil

Practical

Theoretical

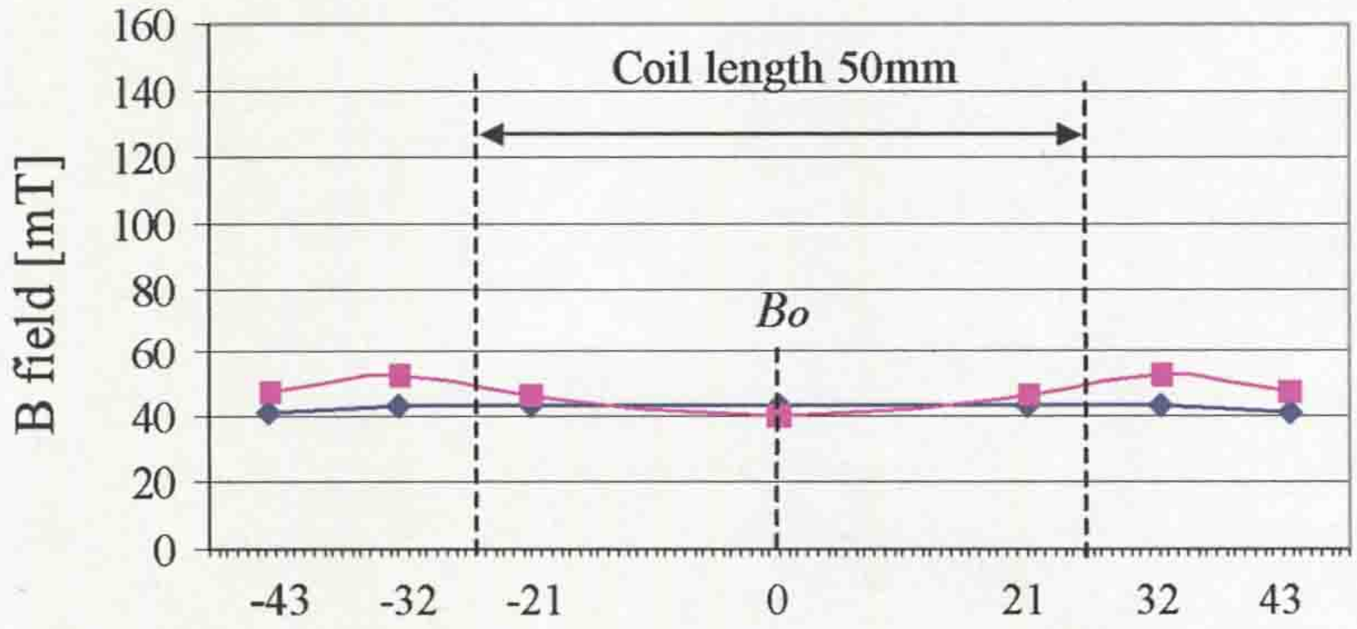

d)

77mm from Z-axis of the coil

Practical

Theoretical

Fig. 6.4 Comparison of total theoretical and measured B field values along the axis of a circular cylindrical coil at difference radial distances (ac peak current of 5.3kA)

to the conclusion that the analytical solution (**section 3.4**) may be used for the preliminary theoretical magnetic field calculations for future design developments (**chapter 3**).

6.1.4 Current interruption analysis of different interrupters

6.1.4.1 Comparison of reference and prototype interrupters over current zero

Analysis of the ac-arc interruption conditions (**sections 5.2.1**, **5.2.3**) is considered and experimental results with different interrupter configurations and media compared. Figure 6.5 compares results of the non-rotary arc interrupter head (reference breaker, **section 4.1.5.1**) in N_2, at different pressures (0.5, 3bar) with the novel prototype rotary arc interrupter (prototype breaker, **section 3.3**) in Air, at atmospheric pressure.

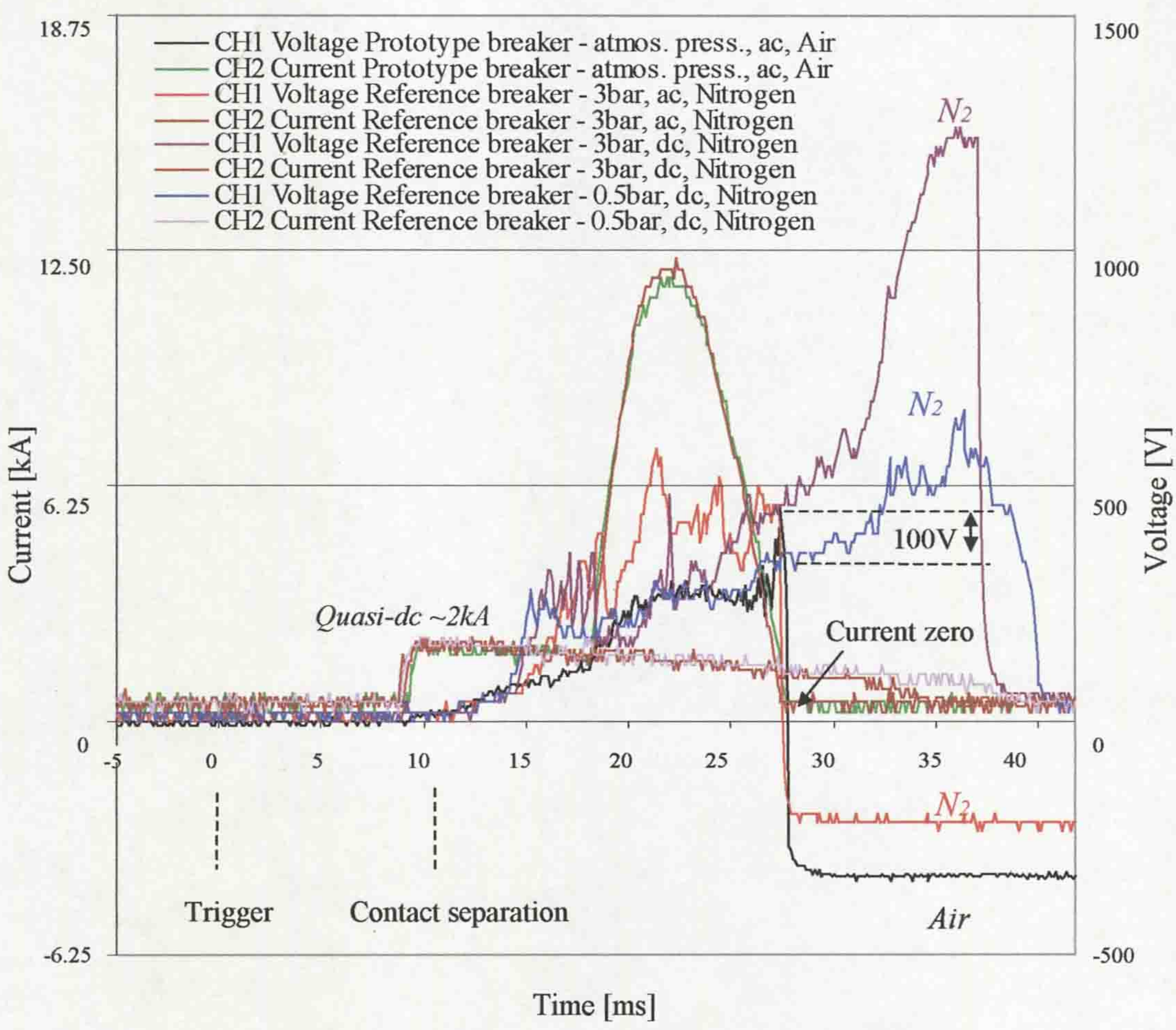

Figure 6.5 Comparison of the current and voltage: time variations for the reference and prototype interrupters operating in Nitrogen (N_2) at different pressures and in Air

Both a quasi-dc 2kA arc and a 12kA ac-arc results are shown for the reference (non-rotary arc breaker) and only the ac-arc (12kA) results are shown for the prototype rotary arc interrupter. The dc-arc results show that up to 28ms (fig. 6.5) the 3bar voltages progressively deviate above the 0.5bar results so that at 28ms (from the trigger) there is a 100V difference (20%). For the ac reference breaker results the arc voltage is generally higher than corresponding dc results until close to current zero at 28ms when they are of similar values. With the prototype breaker the arc voltage is similar to the 0.5bar dc case until very close to current zero when it rapidly increases to the same value as the 3bar reference breaker result. Thus, the prototype breaker has an operating pressure advantage (atmospheric pressure) compared to the reference breaker (0.5 and 3bar pressure gauge). Moreover, the ΔV fluctuations (ac-arc case) for the prototype interrupter (~20V) are much less than for the reference breaker (~100V).

Figure 6.6 compares the experimental results of the non-rotary arc breaker (reference breaker) in SF_6, at different pressures to the prototype rotary arc interrupter in Air, at atmospheric pressure. The results show that for a 12.4kA ac-arc the peak-voltage with the reference breaker in SF_6, at 3bar gauge pressure is much higher (~250V) just before current zero compared to the prototype breaker operated in Air, at atmospheric pressure. However, inspection of the dc-arc (~2kA) in the reference circuit breaker with SF_6 shows that the arc voltage is reduced by about 330V when the gauge pressure was reduced from 3bar to 0.5bar. This arc behaviour is observed around current zero (i.e. arc duration of 18ms from contact separation (fig. 6.6)). This implies that the magnitude of the ac-arc peak voltage just before current zero could be the same for both interrupters at 0.5bar pressure gauge, the reference one with SF_6 but the prototype one with air (fig. 6.6).

Analysis of the results presented in figures 6.5 and 6.6 leads to suggests that an optimal arc duration, for the arc peak-voltage to be significantly increased at current zero, is between 16ms to 20ms for the prototype interrupter in N_2 or Air, at a pressure gauge close to atmospheric. Although the ac-arc can be interrupted after shorter arc duration lower peak-voltages just before current zero are observed (fig. 5.27). It also seems that the use gases such as N_2, Air could form alternatives to SF_6 by utilizing the prototype arc interrupter technology (**chapter 3**).

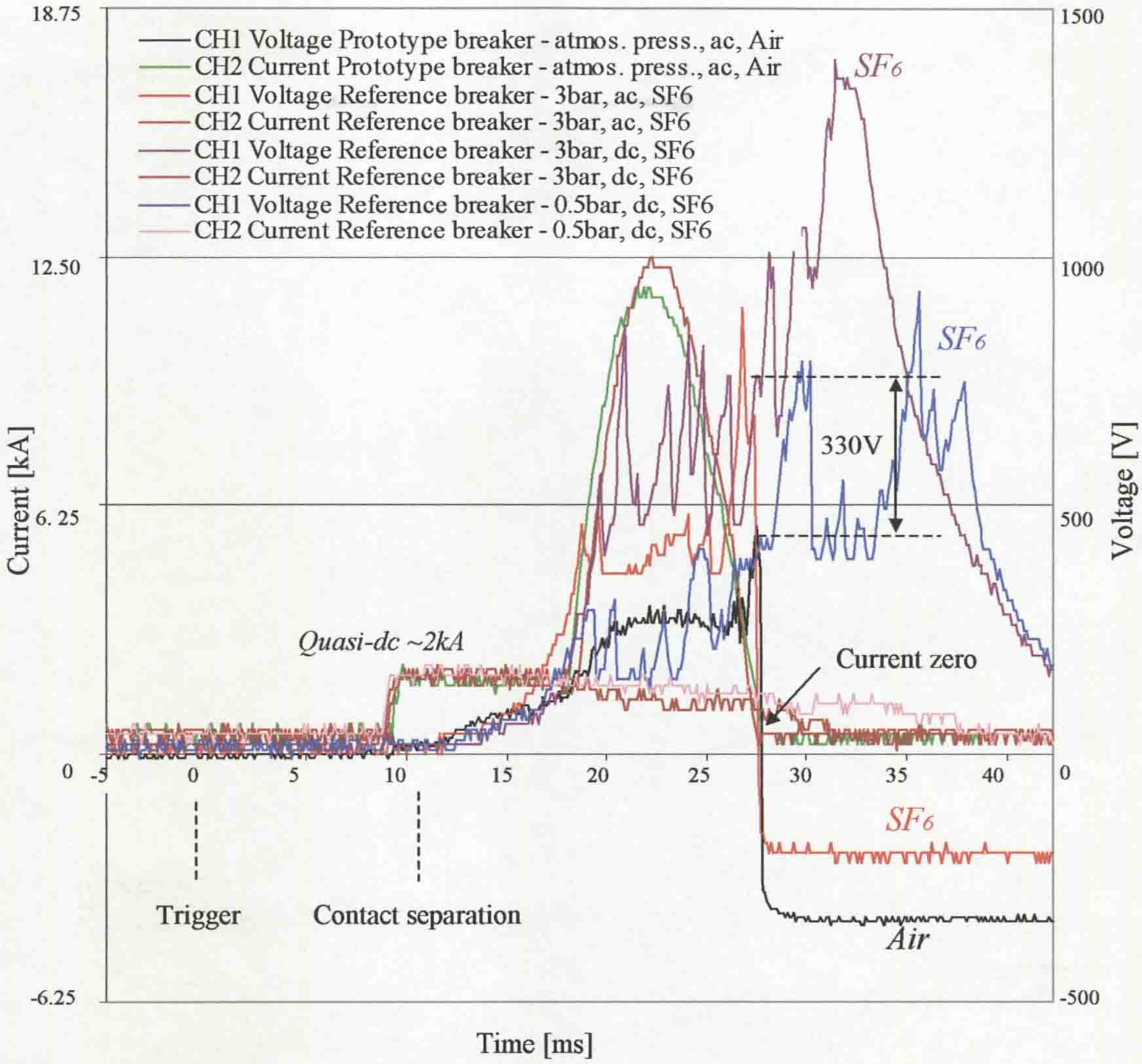

Figure 6.6 Comparison voltage: time characteristics of the reference (SF_6) at different pressures and Air for the prototype interrupters

6.1.4.2 Design evaluation test head

Analysis of the results (**section 5.2.1**) relevant to the design evaluation test head (reference breaker, **section 4.1.5.1**) is described.

The extinction peak on the arc voltage prior to current zero is one of the significant parameters for indicating current interruption ability (Jones, 1988 and Flurscheim, 1982). Therefore, the magnitude of the arc voltage extinction peaks were plotted against current peak values and are shown on figure 6.7 for N_2 and SF_6. This shows the variation of the arc voltage extinction peaks with quasi-dc current (maximum value) in N_2 and SF_6, at 3bar pressure gauge . It is apparent that the arc voltage peaks for both N_2 and SF_6 decrease with current, the N_2 values being about 200V lower than in SF_6 (figures 5.6 and 5.7).

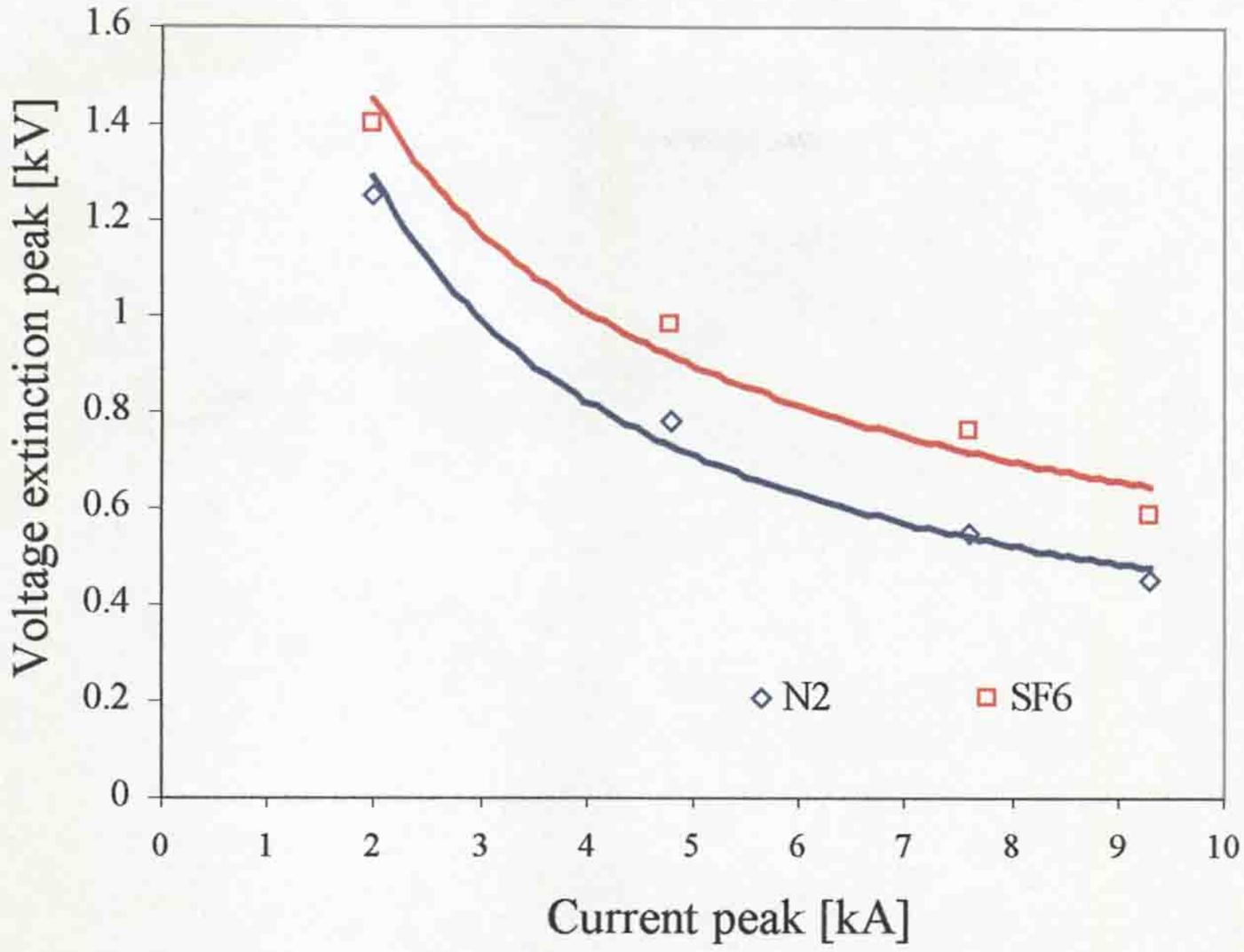

Figure 6.7 Comparison of voltage extinction peaks as a function of dc-arc currents for N_2 and SF_6 (3bar, reference interrupter)

Results showing the dependence of extinction voltage as a function of pressure (0.5-3bar) for the quasi-dc arc of 2kA are shown on figure 6.8. These show

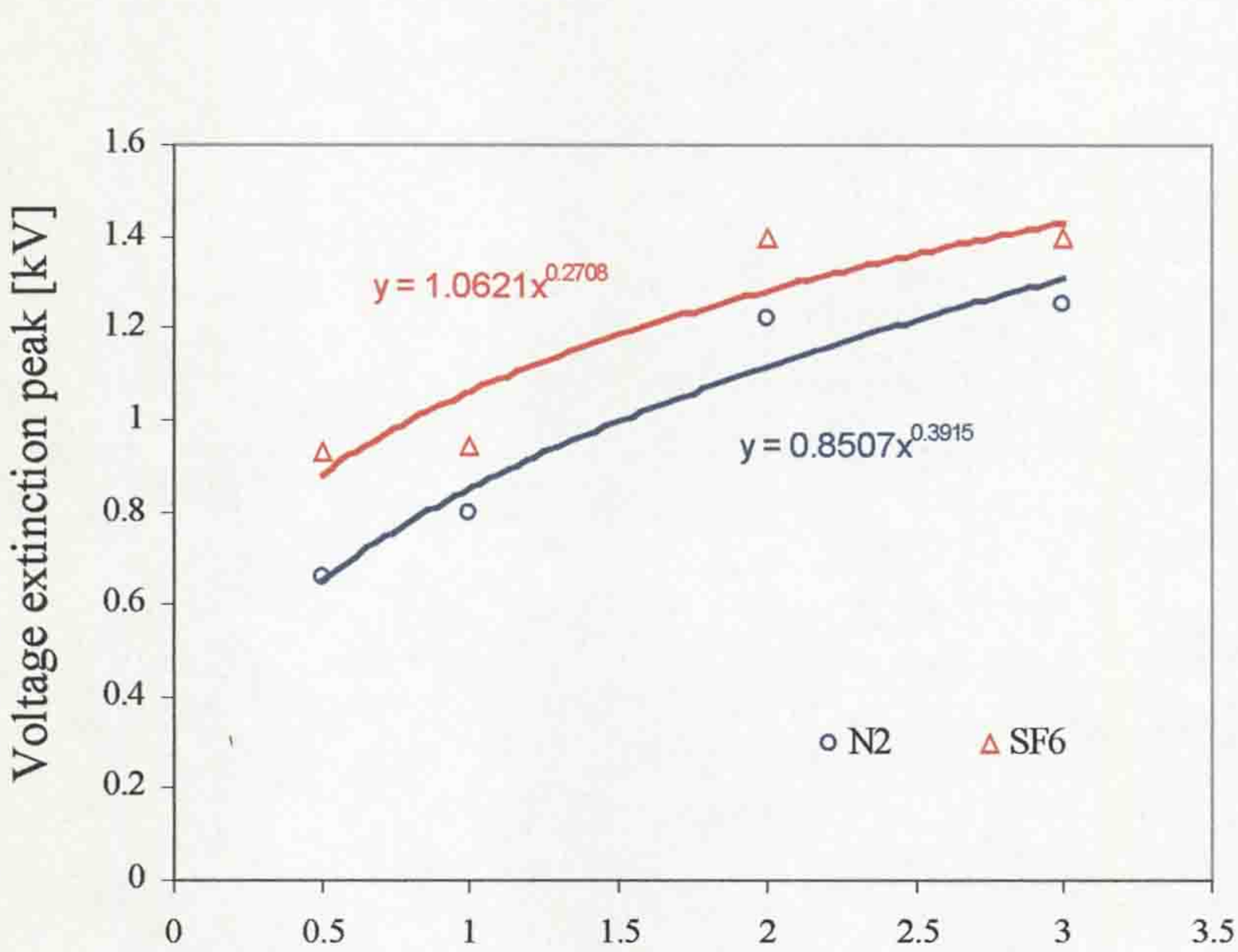

Figure 6.8 Comparison of voltage extinction peaks as a function of pressure (2kA dc-arc) for N_2 and SF_6

a difference of about 200V between N_2 and SF_6, except at 0.5bar when the SF_6 value is 250V greater than the N_2 value. In the pressure rang 1-2bar there is a substantial

increase in the extinction peak level (~500V) in both gases (figures 5.8 and 5.9). Results for the extinction peak variation with peak current and contact gap length under ac-arc conditions (3bar pressure) in both N_2 and SF_6 are shown on figure 6.9.

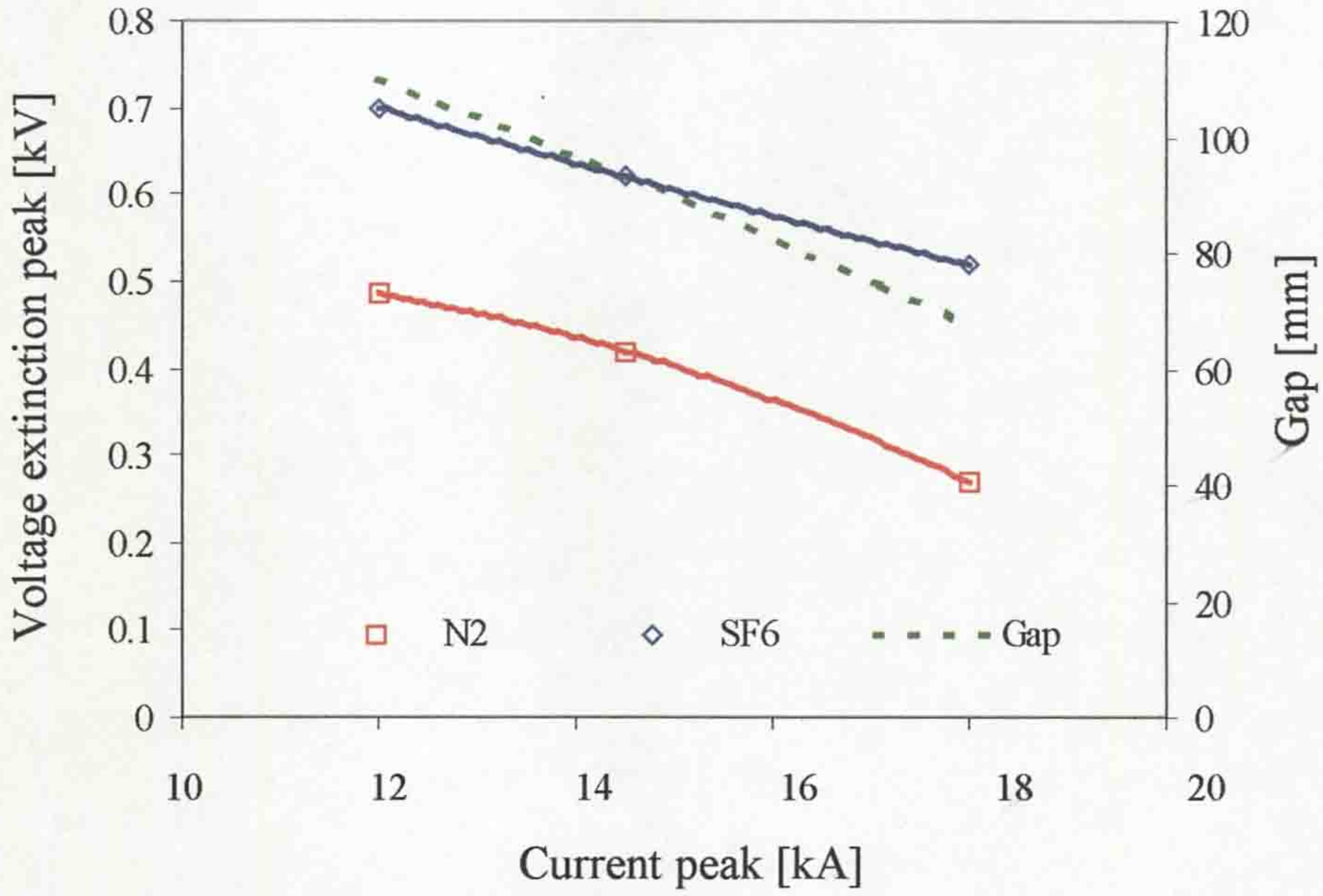

Figure 6.9 Voltage extinction peak and contact gap length as a function of ac-arc peak current (N_2, SF_6, 3bar pressure); (dashed curve – contact gap)

The arc voltage extinction peaks in both N_2 and SF_6 reduce as the current peak increases and when the gap between the electrodes is reduced. However, in both cases the contact gap has also reduced as the current increased (dashed curve, fig. 6.9). The difference between the voltage extinction peaks for N_2 and SF_6 is about 200V for the alternating currents investigated (figures 5.10 and 5.11).

6.1.4.3 Current interruption test heads

Results of the analysis of experiments (**section 5.2.3.2**) with the two current interruption test heads (current interrupter and prototype interrupter heads) are presented. Values of the extinction peaks on the arc voltage prior to current zero of the ac-arc were determined as in **section 6.1.4.2** for the evaluation test head as an indication of the interruption ability of the test head. Figure 6.10 shows the extinction peak voltage as a function of the peak ac current for the breaker head with (prototype) and without (current interrupter head) the outer PTFE cylinder (figures 5.22 and 5.27). These results show that the extinction peak values for both

interrupters are identical apart from the 11.8kA result. Also shown on figure 6.10 is the contact gap as a function of peak current.

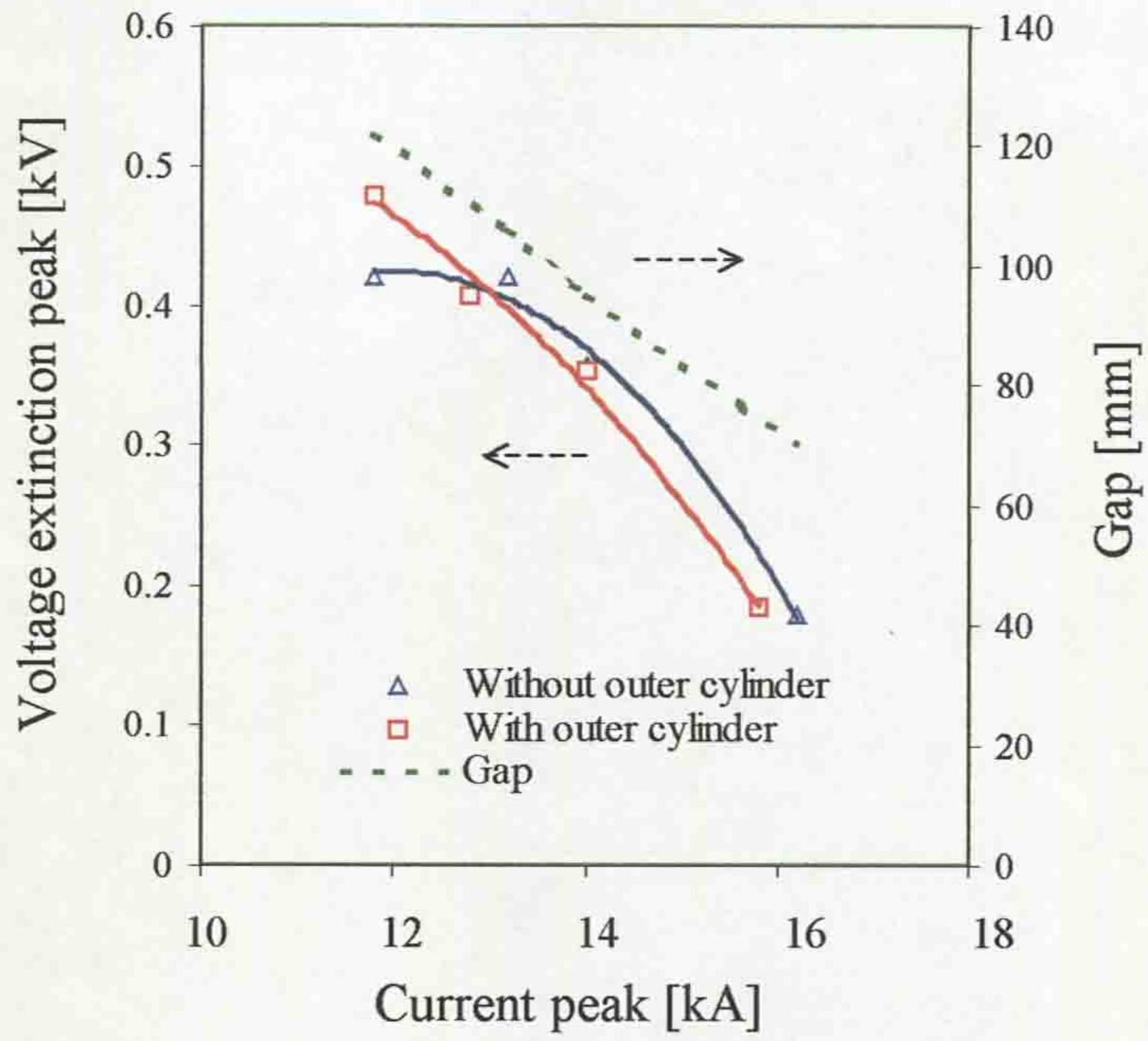

Figure 6.10 Voltage extinction peaks and contact gap as a function of peak ac-arc current for the current and prototype interrupter heads in air, at atmospheric pressure (dashed curve – contact gap)

The contact gap change corresponds to the different arcing duration in both interrupters. The implication is that the effect of the outer PTFE cylinder is only manifest for gaps above 106mm. Figure 6.11 shows the variation of the peak B

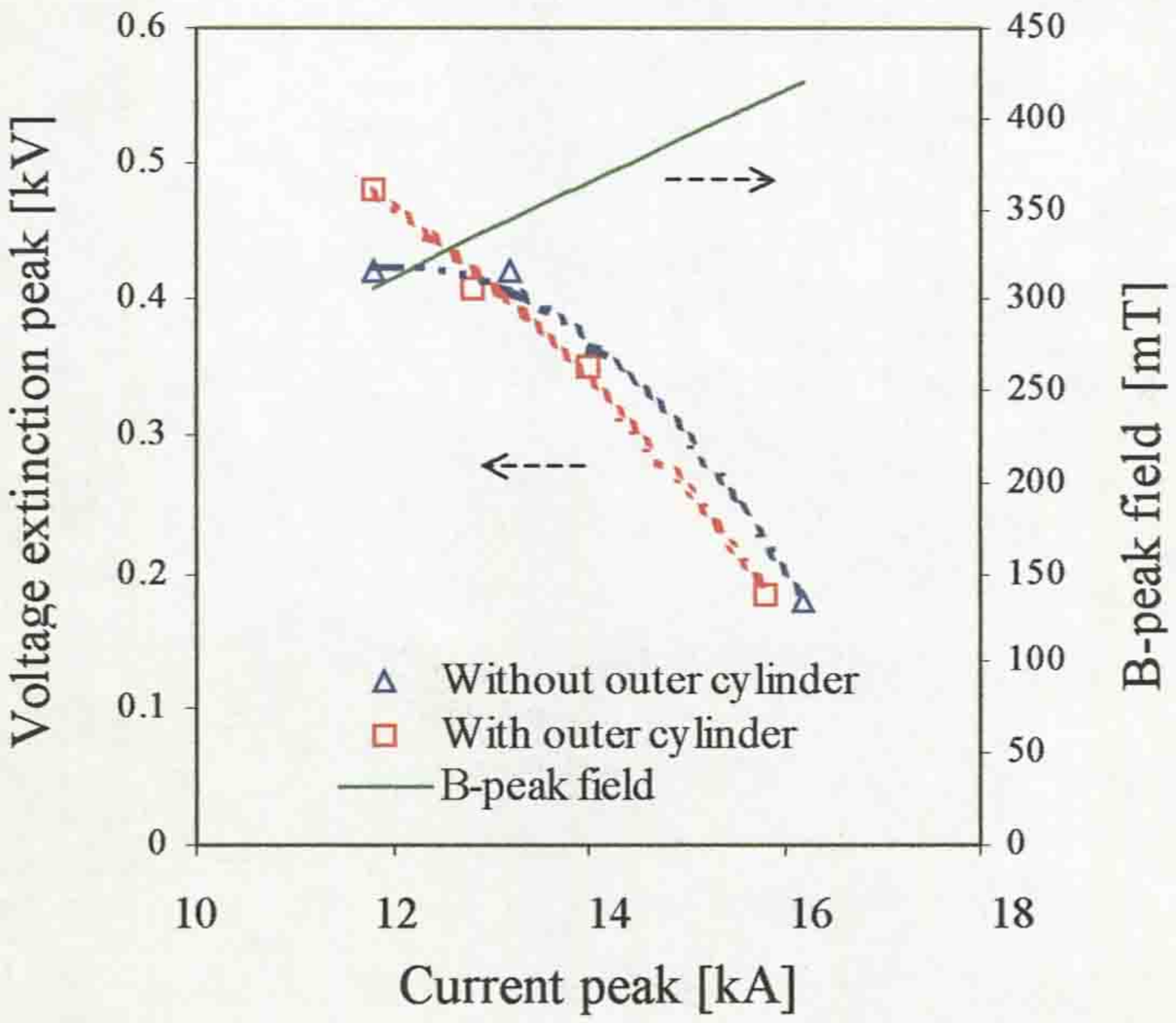

Figure 6.11 Voltage extinction peaks and peak magnetic field in air, at atmospheric pressure as a function of peak ac current (Interrupter with and without outer cylinder)

field produced by the interrupter coil as a function of peak arc current. These results show that the voltage extinction peak for both interrupter configurations reduced at higher magnetic fields (fig. 6.11), which coincided with the gap between the electrodes being reduced (fig. 6.10). Figure 6.12 shows the variation of the voltage extinction peak with peak ac-arc current (8.8-18kA for current, prototype and reference interrupters, at different pressures and gases) and coil B-field for two gap conditions:

- A fixed contact gap of 106mm obtained from figure 5.26 (ac-arc duration 18ms) and designated by square symbols

- Different gaps (current and prototype interrupters) of 122mm, 95mm and 70mm corresponding to peak currents 11.8kA, 14kA and around 16-18kA (figures 6.10, 6.11) and 110mm, 93mm and 68mm (reference interrupter, fig. 6.9) respectively

Thus, the effect of the gap varying simultaneous to the arc current can be discriminated. The results shown on figure 6.12 yield the following approximate empirical relationship, which may predict the voltage extinction peak and may be accommodated at different environmental conditions such as pressure and gas:

$$V_{EXT} \cong K(1+\alpha B_p^m) l^g i_p^{-n} \left[\frac{P}{P_{REF}}\right]^e d^{\left[\frac{l}{L}\right]}, \text{ [kV]} \qquad (6.1)$$

Where the parameters B_p, i_p, l and P (P_{REF}) are the peak magnetic field [T], peak current [A], contact gap [m] and pressure (reference pressure) [bar] respectively. Coefficients K (for Air), α, m, g and n are constants determined from figure 6.12 having the values 90.0, 1.8, 1.0, 1.64 and 0.23 respectively, for our operating conditions. Alternately, constant K for N_2 and SF_6 are 96 and 172 respectively determined from figure 6.12b. The curves (1, 2, 3 and 4) corresponding to these constants are compared with the experimental data in air, at atmospheric pressure on figure 6.10, 6.11 and 6.12. The constant e is determined from the design evaluation test head (fig. 6.8 section **6.1.4.2**) and represents the curve for the voltage extinction

peak as a function of pressure and current for different gases being 0.27 (SF_6) and 0.39 (N_2). The constant e= 0.39 may be applied for air because the N_2 and Air properties are similar. d represents relative coefficient of the arc chamber volume (with d=1.0 and without d=0.9 outer PTFE cylinder) as a function of gap in the current interruption test heads obtained from figures 6.10 and 6.12. L, the gap constant of 106×10^{-3}, [m] represents the threshold gap beyond which the effect of outer cylinder should be observed in the current interruption heads (fig.6.10).

The effect of the arc chamber diameter was not included since it was unchanged during the test. However, the experiments of the previous authors (Mori *et al*, 2005) on atmospheric rotary arcs in SF_6, in hollow polymeric cylinders showed that the extinction peaks for higher peak currents were lower in the small bore chamber. Moreover, the extinction peaks for the larger bore chamber were higher then those for the small one (Mori *et al*, 2005). Therefore, these investigations may be used for the preliminary voltage extinction peak estimation for different arc chamber diameters after solving equation 6.1.

The empirical relationship may be used for designs (A, B, C, D, E) presented in Table 6.1.

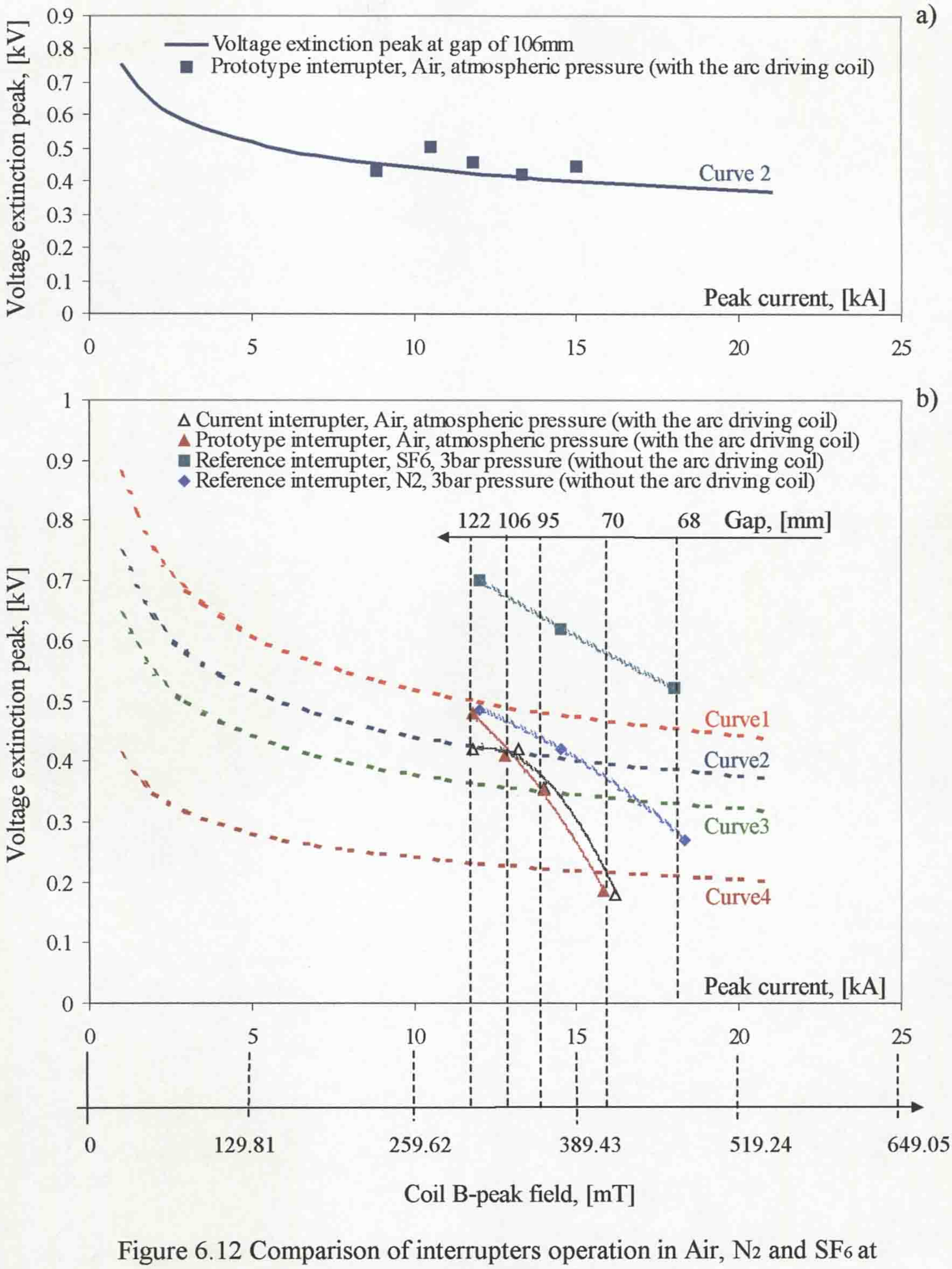

Figure 6.12 Comparison of interrupters operation in Air, N_2 and SF_6 at different pressures and gaps

a) Prototype interrupter operation at constant gap of 106mm,

b) Voltage extinction peak in air (atmospheric arc) as a function of current, B-field and different gaps for the current and prototype interrupters (Curve 1: coil current 11.8kA and B-field 306.35mT, gap 122mm; Curve 2: coil current 13.2kA and B-field 342.7mT, gap 106mm; Curve 3: coil current 14kA and B-field 363.47mT, gap 95mm; Curve 4: coil current 16.2kA and B-field 420.59mT, gap 70mm) and reference interrupter (no B-field, N_2 and SF_6, 3bar pressure).

6.1.5 Investigation of gas dielectric strength in the prototype interrupter

Analysis of the experimental results (**section 5.2.3.4**) relevant to the recovery of dielectric strength of the prototype rotary arc interrupter (**section 3.3**) is presented, with regard to the dielectric probe values after arc extinction in air, at atmospheric pressure.

The experimental conditions considered are an ac-arc of 5kA with the current flowing through the coil, to produce a magnetic field of 129.8mT and a Lorenz force of 649N/m for the arc rotation in the prototype interrupter (**section 5.1.3.4**). Dielectric probes situated around the prototype breaker at 120° from each other (fig. 6.13) show that the dielectric strength was fully recovered approximately 45-50ms after the arc extinction (fig. 5.31). The dielectric probe at position 2 indicated that in that area the dielectric strength behaviour was unstable compared to positions 1 and 3 (fig. 5.31).

A video frame at 40ms after arc initiation (fig. 6.13) shows that there is more post arc plasma at that angular position.

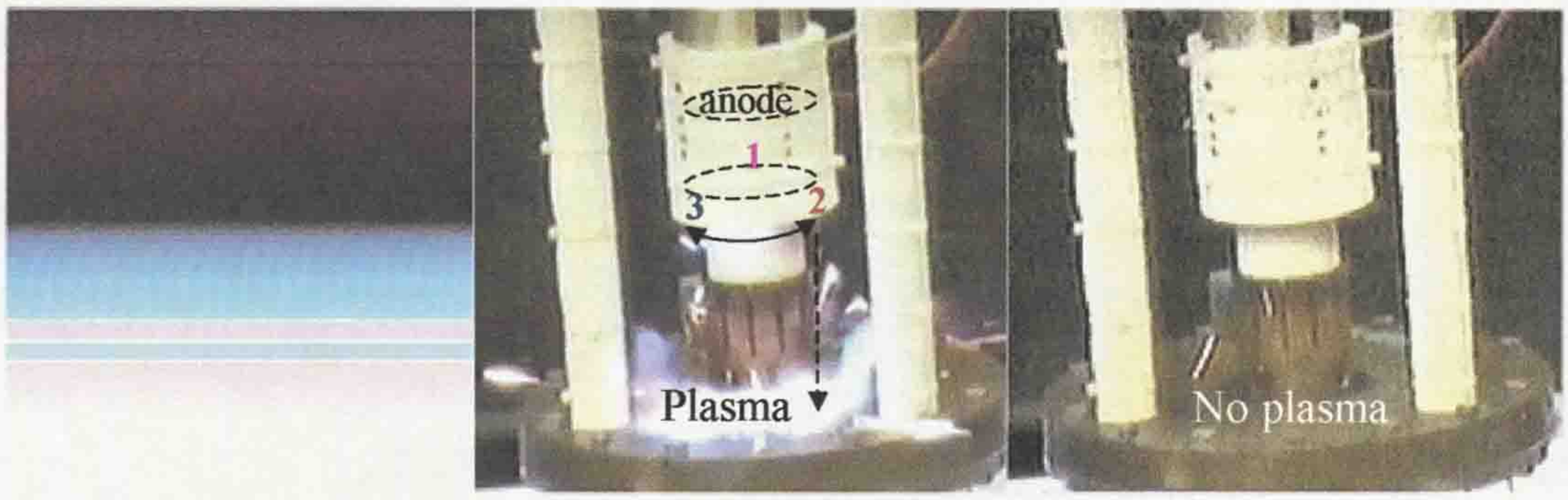

a) 0ms b) 40ms c) 80ms

Figure 6.13 Position of dielectric probes (1, 2, 3, fig. 5.4) around the prototype interrupter relative to the external post arc plasma location

In addition, more discolouration of the inner PTFE cylinder is observed at locations between probes 1 to 2 and 2 to 3, while less discolouration is observed between probes 1 to 3 (fig. 6.14). This is consistent with the dielectric observation that the lowest dielectric strength is close to probe 2. Consequently, dielectric probe 2 was chosen for other investigations as most unstable dielectric strength area within the prototype interrupter.

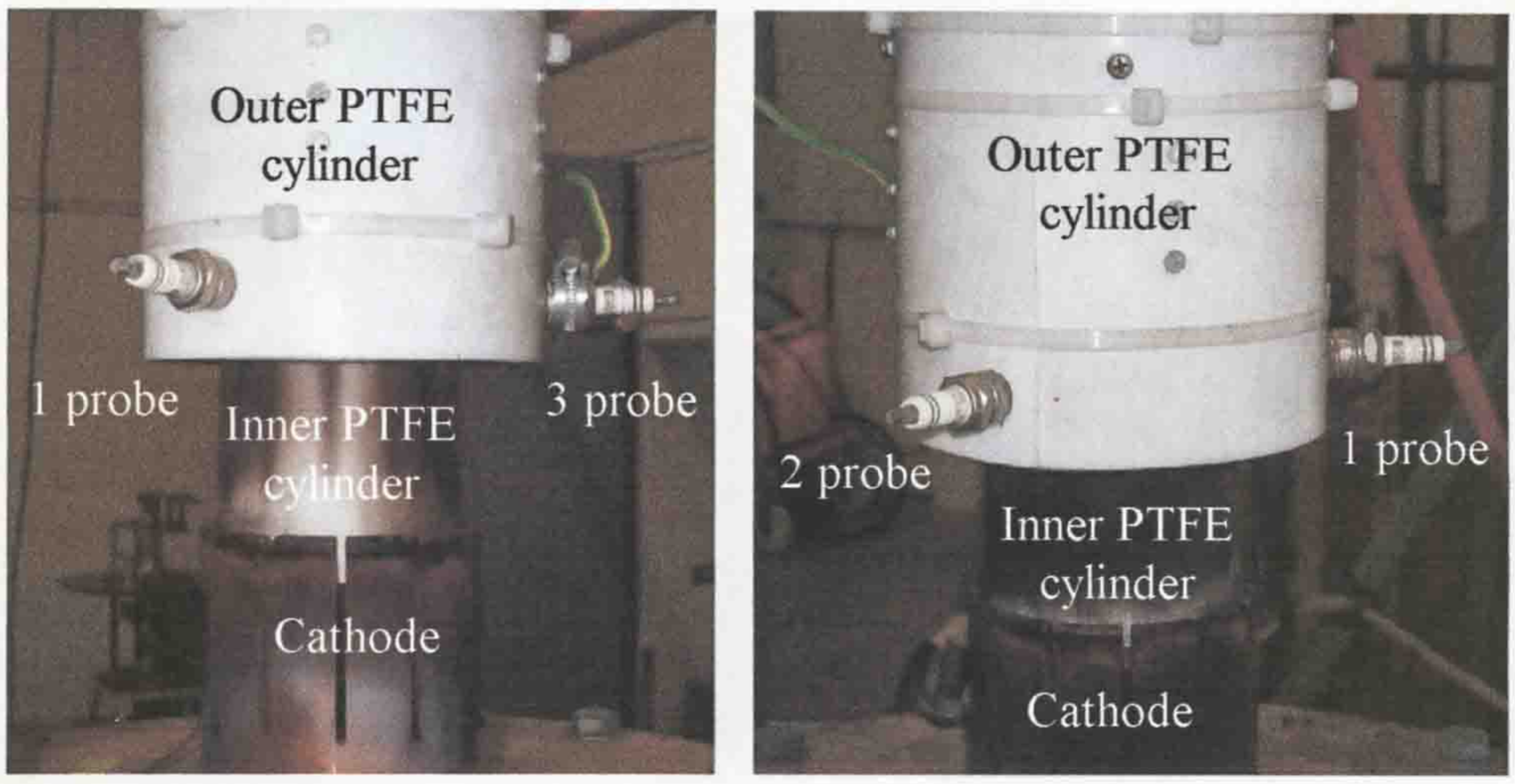

Figure 6.14 Discolouration of the inner PTFE cylinder of the prototype interrupter in relation to the 1, 2 and 3 dielectric probe positions

The dielectric probe breakdown voltage as a function of time with arc duration as parameter is shown on figure 6.15. The ac duration corresponds to different contact gaps at current zero, these ranging from 68mm for an arc duration

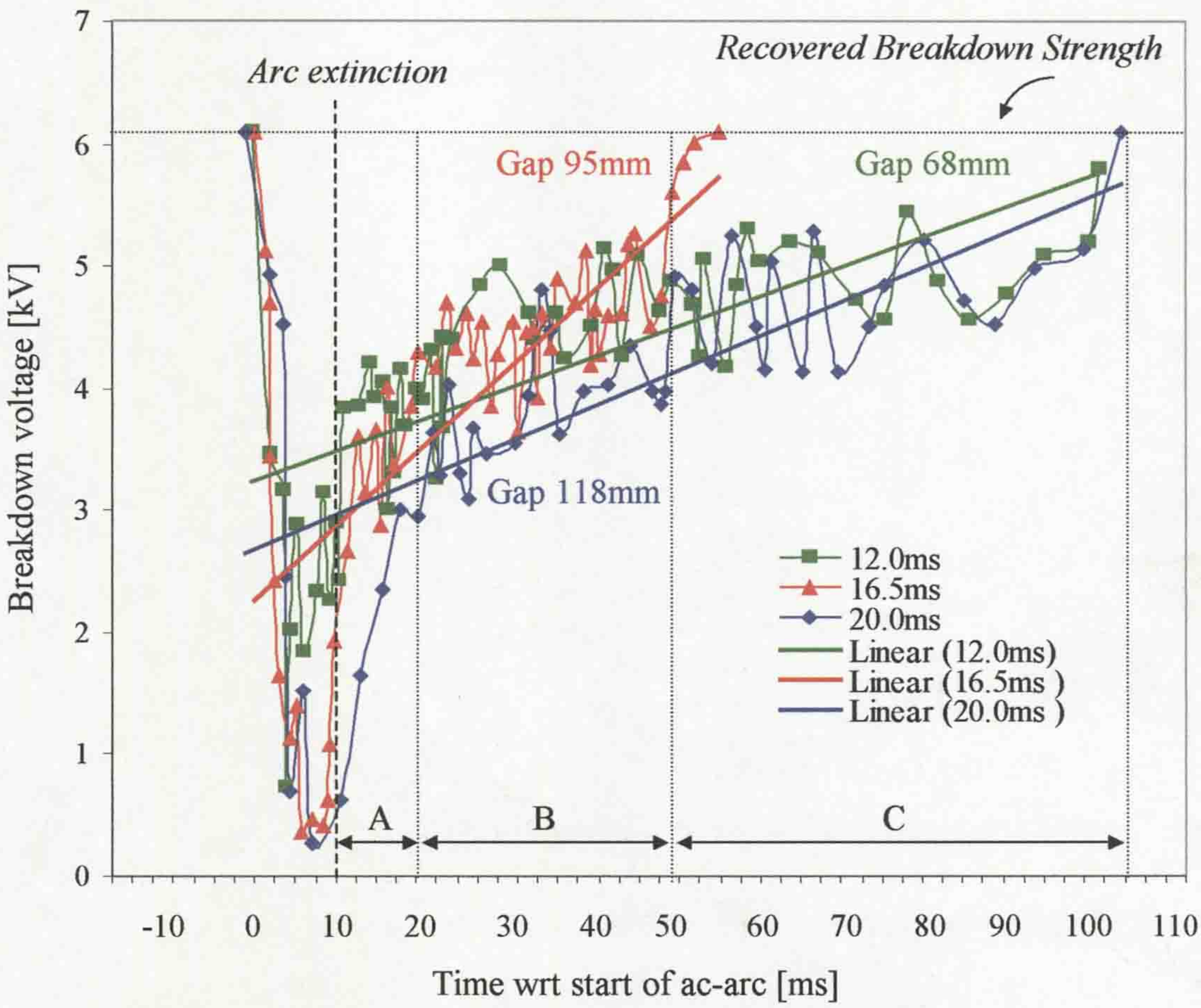

Figure 6.15 Three dielectric recovery zones (A, B, C) for various contact gaps with the prototype rotary arc interrupter

of 12ms to 118mm at about 20ms. These results show that the early dielectric recovery (t≤20ms) becomes slower as the contact gap increases (fig. 6.15, zone A). Between 20 and 52ms (zone B), the dielectric recovery seems independent of gap length within the fluctuations, which occur. Beyond 52ms (zone C), the 95mm gap recovers rapidly from about 5 to 6kV within about 5ms. The 68mm and 118mm gaps continue their slower recovery being fully recovered at about 107ms.

Figure 6.16 shows the position of the cathode when the ac-arc was extinguished at current zero for the three different arc durations (12, 16.5, 20ms).

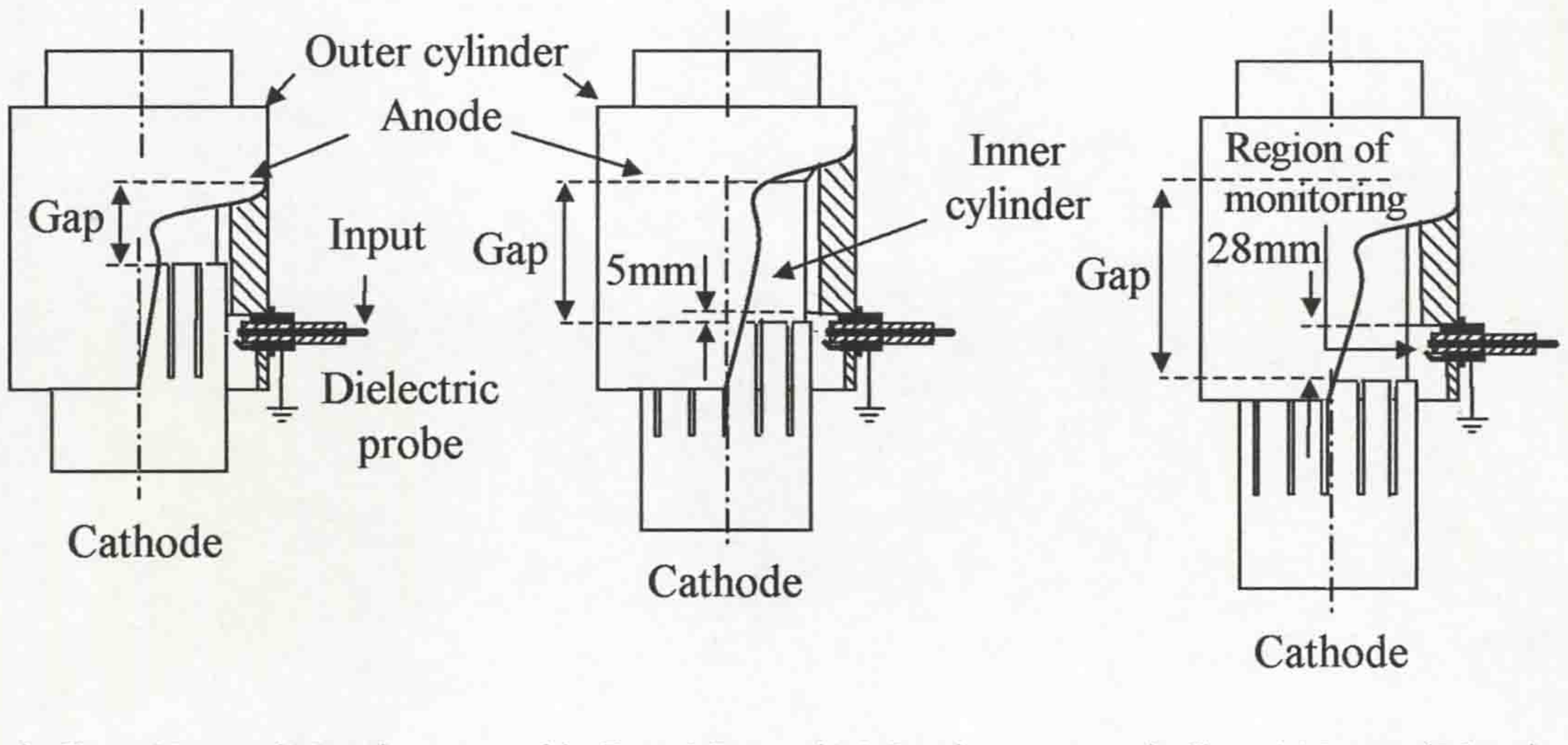

a) Gap 68mm (12ms) b) Gap 95mm (16.5ms) c) Gap 118mm (20ms)

Figure 6.16 Contact zero position of the contacts between the inner and outer PTFE cylinders of the prototype rotary arc interrupter for different arc durations

Figure 6.16a (12ms) shows that the cathode was located within the gap between the inner and outer PTFE cylinder (around 22mm depth) at current zero. As a result, the cathode blocks the region where the post arc plasma might emerge due to a self-blast effect so explaining why the breakdown voltage recovery is more rapid during the first 10ms (from the arc extinction) compared to the 16.5ms and 20ms arc duration results (fig. 6.15). However, after 10ms from the arc extinction the breakdown voltage recovers more slowly until fully recovered at 105ms. This behaviour would be consistent with the cathode having moved about 17ms to expose the dielectric probe fully to remnants of the arc heated gas remaining within the inner and outer PTFE cylinder. For the 16.5ms arc duration, the ac-arc was extinguished while the electrodes gap was 95mm (fig. 6.16b). In this case, the cathode was almost 5mm lower than the outer PTFE cylinder (the inner surface of cylinder), providing

the maximal post arc plasma repulsive effect from the area between inner and outer PTFE cylinders. As a result, a substantial amount of arc-heated gas was detected by the dielectric probe, leading to a breakdown voltage, which was low around 0.3kV, few milliseconds before arc extinction (fig. 6.15, Gap 95mm). The dielectric strength then rapidly recovers to the same level as the 12ms arc duration results showing consistent dielectric conditions to occur in both cases. However, after 45ms from arc extinction the breakdown voltage fully recovered to the pre-arc breakdown voltage level (fig. 6.15), showing that weak dielectric gas was removed from the monitoring region. The lowest dielectric strength persisted largest after current zero for a contact gap of 118mm (arc duration 20ms) (fig. 6.16c). In this case, the cathode location was 28mm lower than the outer PTFE cylinder. Figure 6.15 shows that for a gap of 118mm the breakdown voltage recovery thereafter reached similar levels to the 12 and 16.5ms results recovering fully after 107ms. This again shows a consistent behaviour regarding the dielectric strength of the remaining hot gas, which is similar to the other cases. The present dielectric recovery results may be compared with those reported by Ennis (1996) for SF_6 at 3bar pressure using a conventional rotating arc interrupter (**chapter 2**, **section 2.4.1.1**) and Mori (2005) for SF_6, at atmospheric pressure. The results of figure 6.15 show that the relative recovery voltages (fig. 6.17) obtained with the prototype interrupter in air, at atmospheric pressure are similar to those reported by Ennis (1996) in SF_6, 3bar and (Mori, 2005) in SF_6, atmospheric pressure (fig. 4.4, reference interrupter with arc driving coil and without inner PTFE rod). The most rapid dielectric strength recovery for the present prototype rotary arc interrupter was around 45ms (16.5ms arc duration, figures 6.15 and 6.16b) compared with 58ms (fig. 6.17) reported by Ennis (1996) and Mori (2005) in SF_6 (fig. 2.22). It may therefore be concluded that the proposed interrupter provides similar relative dielectric recovery conditions in air, at atmospheric pressure as the conventional rotary arc interrupters, which used SF_6, at 3bar pressure (Ennis, 1996) and SF_6, at atmospheric pressure (Mori, 2005). Moreover, the empirical relationship derived by Mori (2005) (equation (2.15) **section 2.4.1.1**) may be applied to the prototype interrupter for the dielectric recovery estimation (e.g. similar behaviour of the interrupters response of dielectric probe to arc, fig. 6.17). In the present case, the diameter of the cylinder (equation 2.15) was not varied. It becomes constant depending on design (e.g. larger or smaller arc chamber or the inner diameter of the cylinder, fig. 6.16).

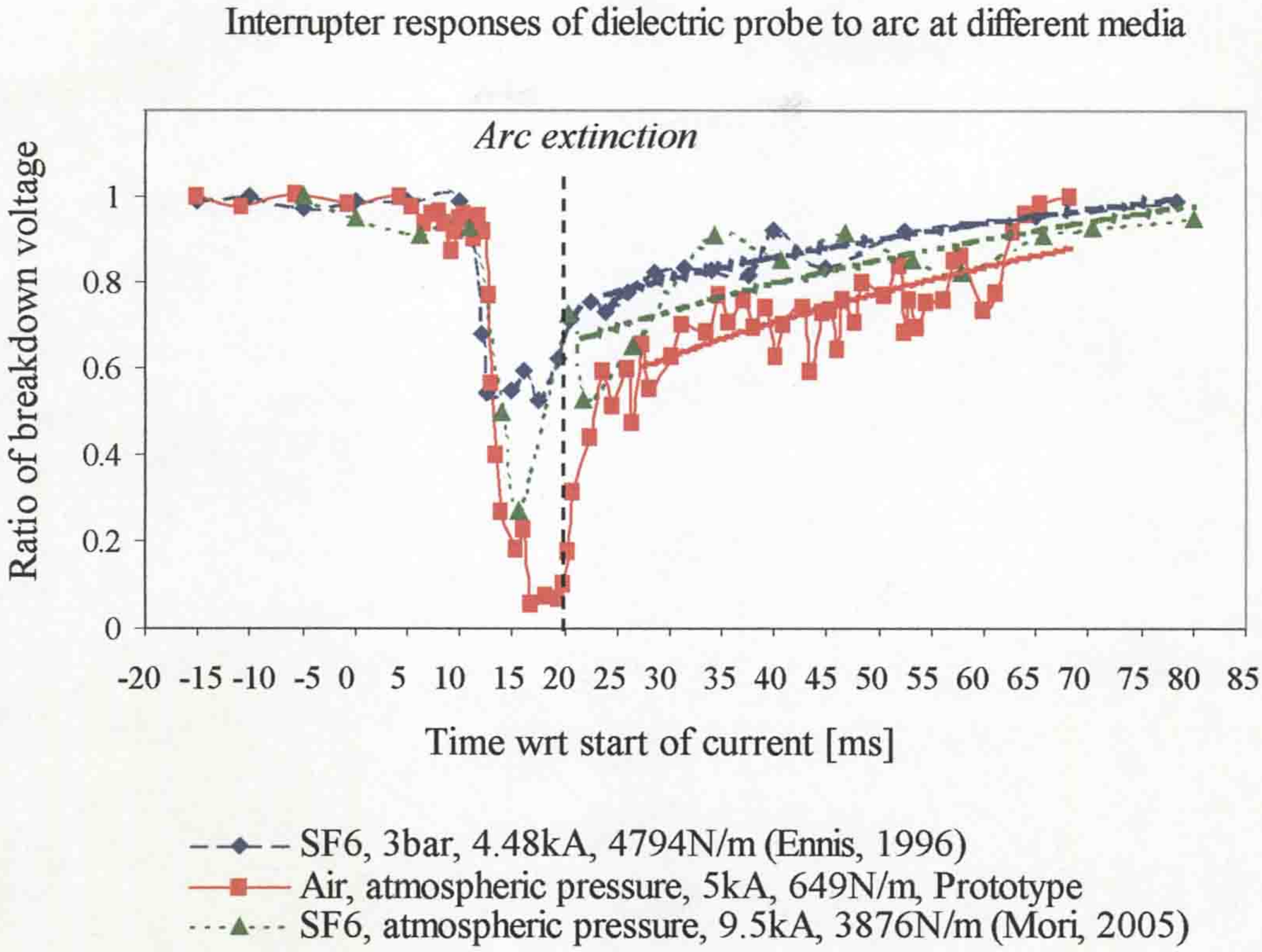

Figure 6.17 Response of dielectric probe for arc duration of 16.5ms (present prototype interrupter) compared with the other interrupters of Ennis (1996) and Mori (2005)

6.1.6 PTFE ablation distribution

This section explores the role of rotary arc in producing PTFE ablation in the prototype interrupter designed in **chapter 3**.

An assessment of the amount of PTFE ablation has been in terms of reductions made by arcing in the inner radius of the PTFE cylinder and amount of arc energy to which it has been exposed. Figure 6.18 shows the radius of the PTFE cylinder as a function of axial distance (origin at the centre). After 40 arcing tests at currents up to 16kA, the profile of the PTFE surface was modified as shown indicating loss of material around the origin. The change in profile was estimated to correspond to a total of $1\,\mathrm{mm}^3$ of PTFE having been ablated. The total energy expected in producing this ablation was estimated as about $79\,\mathrm{kJ/mm}^3$. The change in radius distribution due to ablation is almost symmetrical about the vertical Z-axis of the cylinder (fig. 6.18). The PTFE cylinder also carried the B field-producing coil within it as indicated on figure 6.11 (See also chapter 3, fig. 3.7).

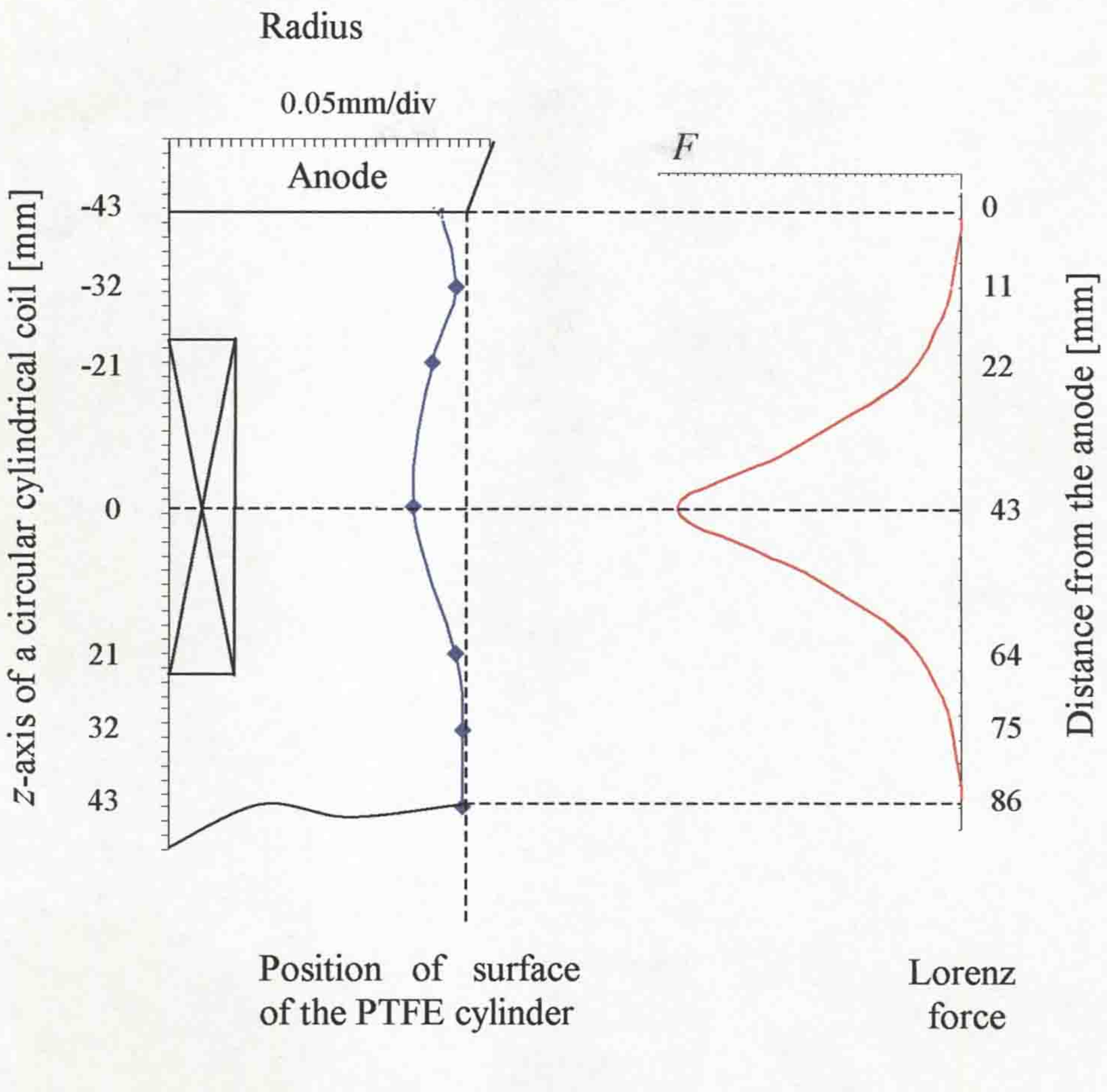

Figure 6.18 Axial variation in PTFE cylinder radius due to ablation and the axial distribution of the Lorenz force

The vertical scale (Z-axis) of the coil is identified with the magnetic field distribution around the PTFE cylinder, which shown on figure 6.4. The radius in figure 6.18 represents the scale of the ablation surface of the PTFE cylinder in relation to the coil and anode. A maximal Lorenz force (F) occurs when the ac-arc is located circumferentially. This force acts inwards radially. Figure 6.19 shows the location of the arc around the PTFE cylinder in relation to the magnetic field direction, produced

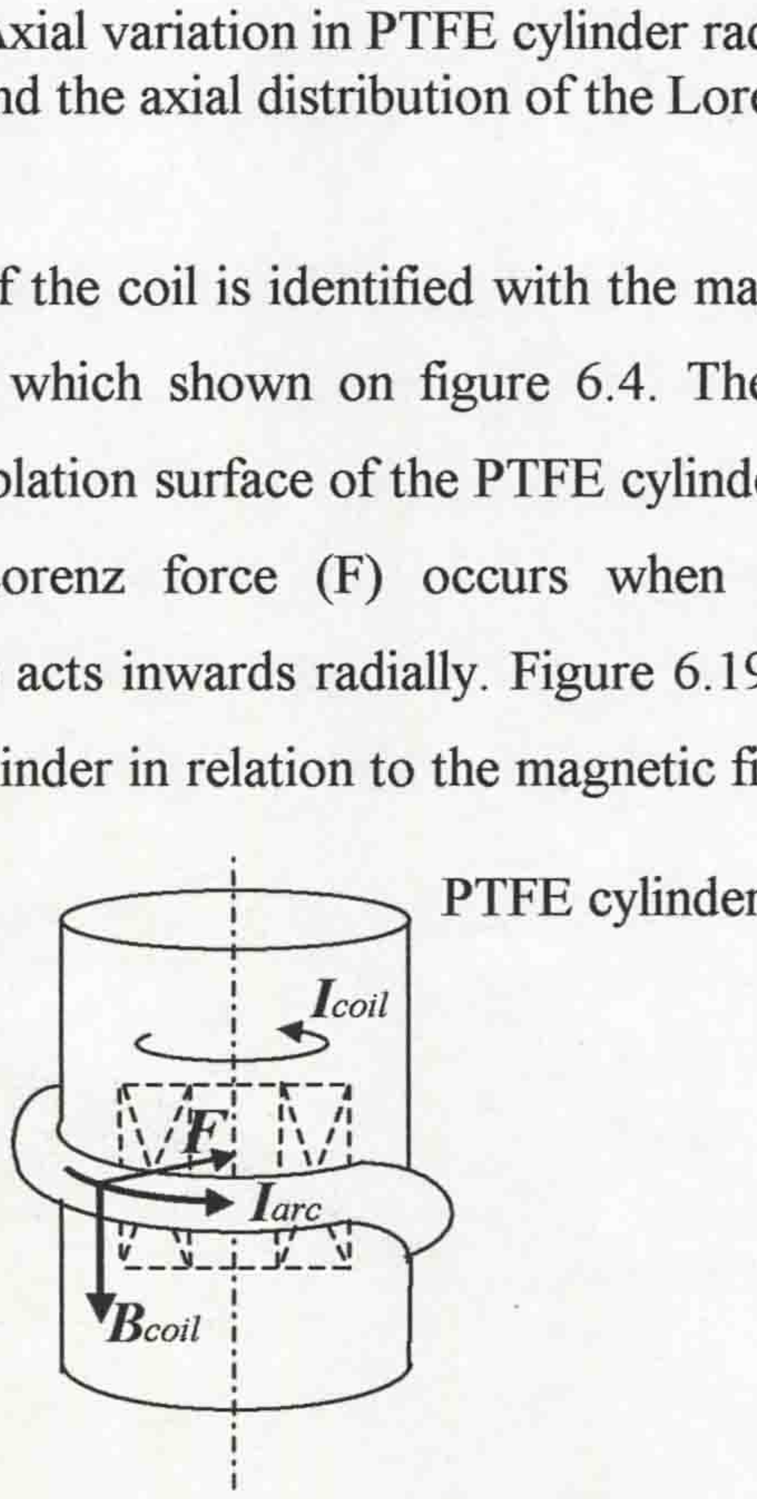

Figure 6.19 Lorenz force (F) operating at the centre of the coil in relation to the PTFE cylinder containing the coil

by the coil. This behaviour of the arc is confirmed by the photographic image shown on figure 6.2.

The magnetic field distribution around the PTFE cylinder, along the Z-axis of the coil (fig. 6.4), shows that the external B field at the centre of the coil (43mm from the anode) is less than at 0mm from the anode (fig. 6.18). As a result, and because of the contact separation exposing the PTFE material initially closest to the anode. The PTFE ablation is more pronounced from 0mm to 68mm from anode and less from 68mm to 86mm (fig. 6.18). The rotary arc initially rotates around the PTFE cylinder positioned vertically along contact gap. The Lorenz forces operating parallel to the surface of the PTFE cylinder force the arc to around the cylinder. The interaction between the vertical arc and the PTFE cylinder is minimal. Consequently, the ablation surface of the PTFE cylinder from 0mm to 11mm from the anode (fig. 6. 18) is not significant compared to the area from 11mm to 68mm. When the movable cathode is positioned half way along the coil, the Lorenz forces begin to act on the arc in such a manner as to draw it towards the PTFE cylinder radially. As a result, the electric arc is positioned azimuthally around the PTFE cylinder increasing its length and is electromagnetically attracted to the PTFE cylinder containing the coil. Moreover, the arc core is concentrated at the middle of the coil azimuthally around the cylinder (fig. 6.2). Such mechanism provides greater interaction between the rotating arc and the PTFE cylinder increasing ablation from surface of the cylinder close to the coil (fig. 6.19).

The similar trend of PTFE ablation (outer PTFE cylinder) was observed visually in the prototype interrupter where such mechanism provides ablation of surface close to the coil. The experimental bench, onto which the experimental interrupter was fixed, required significant time to disconnect and re-connect mechanical parts of the interrupter. Therefore, the outer PTFE cylinder was observed externally (fig. 5.42a,b). Discolouration of the inner and outer PTFE cylinders show that arc is located between the two PTFE cylinders. Furthermore, the azimuthally positioned arc may produce greater evaporation of the PTFE material increasing the volume of quenching gas around the PTFE cylinder.

6.1.7 Arc velocity as a function of arc length

The results presented in figure 5.28 for arc velocity and the results given on

figure 5.37 may be analysed to provide information about the relationship between the rotary arc length and speed. Such results are shown in figure 6.20 for a current of 13.25kA and arc duration of 14ms, in air, at atmospheric pressure.

Figure 6.20a shows the time variation of the arc velocity along with the time variation of the B field. During the first 4ms, the arc was sustained by a low-level quasi-dc current, which produced little B field. Following inspection of the alternating current (4-14ms) the B field increases as does the arc velocity, which reaches about 930m/s at the peak B field. Thereafter the arc velocity fluctuates in the range 760-830m/s as the B field progressively reduced so did the arc velocity (7.5-12ms). Between 12 and 14ms, the arc velocity remained fairly stable around a value of 160m/s before arc was extinguished.

Figure 6.20b shows the change in arc length as a function of time corresponding to the same conditions as figure 6.20a and which have been derived from high-speed photographs (fig. 5.35) and (fig. 5.36). The result shows the arc length progressively increasing with time up to the peaks in the B field and velocity (~8ms). Thereafter (8-12ms), the arc length slightly increases marginally (~38-45%). However, beyond 12ms the arc length increase rapidly up to 100% in 2ms, corresponding to the period of relatively constant 160m/s velocity on figure 6.20a.

Figure 6.20c shows the contact travel as a function of time. This result show that the steady arc rotation and rapid arc-lengthening period (12-14ms) corresponded to arc contact gap increasing from 68 to 80mm.

Figure 6.20d shows the current and voltage arc waveforms as a function of time. The arc voltage waveform change corresponded to the period from 4 to 14ms (gap ~80mm) during the rotary and azimuthal arc periods. The voltage extinction peak is significantly reduced because the arc gap reduced to 80mm. The implications are that early in the ac half-cycle arc acceleration dominates over lengthening whilst later in the half cycle the converse is true. It should be recognized that for a contact gap greater than 68mm the B field at each end of the gap produce B fields and hence Lorenz forces in opposite directions, and creates the conditions whereby the azimuthal arc is formed. These features are indicative of the different nature of the azimuthal arc compared to the rotary arc and the manner in which the latter transforms to the former.

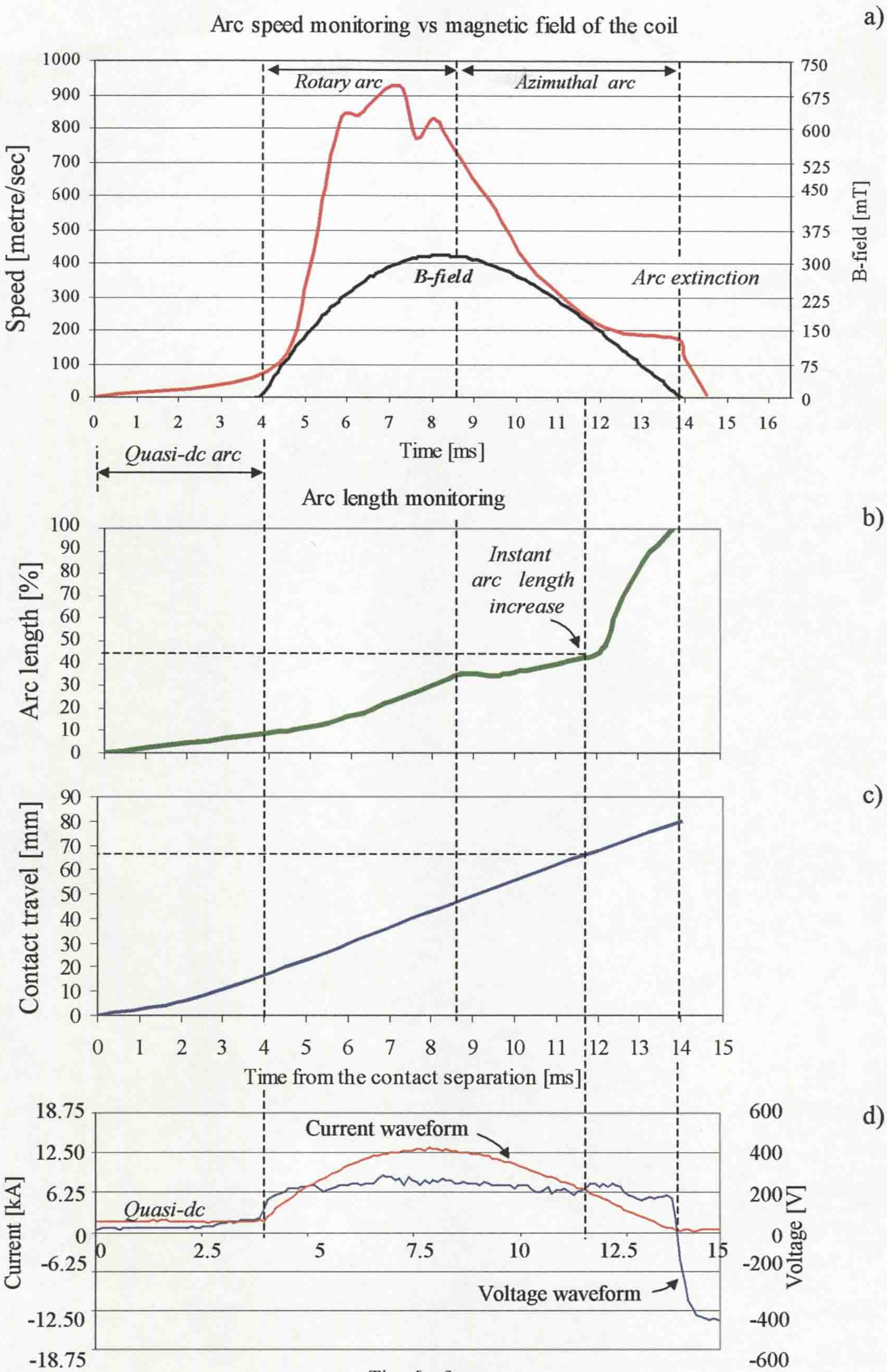

Figure 6.20 Behaviour of the electromagnetically driven arc
(air, atmospheric pressure, ac-arc 13.2kA)
a) Arc velocity and B field vs time b) Arc length vs time
c) Contact travel vs time d) Current/Voltage vs time

6.2 SUMMARY

An analysis has been presented of results given in **chapter 6** which relate to the time variation of arc voltage in the various interrupter units investigated and in different arc atmospheres (SF_6, N_2 and Air). The role of the magnetic field distribution has been shown to induce high ablation of PTFE close to central regions of the coil.

Photographic evidence with the current interrupter head has enabled the shape and movement of the arc to be quantified. Dielectric strength measurements have also been analysed. Arc velocity variations have been compared with arc lengthening, contact travel and voltage variation. There is photographic evidence post arcing for the remnant plasma to be expelled radially from the contact gap with the open current interrupter head and for plasma to be expelled axially, probably do to self-pressurization effects in the annular PTFE gap, prototype interrupter.

Comparison of the prototype interrupter results in air with those in the reference interrupter and a basic helical arc interrupter leads to the following conclusions:

- The prototype interrupter appears to generate arc extinction peaks in air which are of a similar magnitude to those in SF_6 (close to atmospheric pressure) and in N_2 at $\times 3$ higher pressure

- The prototype interrupter in air produces similar dielectric recovery trends to a helical arc SF_6 interrupter given by Ennis (1996) and Mori (2005)

CHAPTER 7 - GENERAL DISCUSSION

7.1 TECHNOLOGICAL APPLICATIONS OF THE NEW METHOD OF THE ARC CONTROL

The recently designed method of the arc control may be applied in the current-limiting switches, low or middle voltage rotary arc circuit breakers etc. There are preliminary indications that arc quenching (in the prototype interrupter) similar to SF_6 maybe obtained with the use of air within the azimuthal arc unit and that dielectric recovery strengths similar to those (**section 6.1.5**) achieved with rotary arc interrupters are achievable. Technological application of the new method may lead to remove SF_6 from the circuit beaker use, using a gas such as Air or Nitrogen.

From the ecological point of view, pure SF_6 has a grater ability to absorb infrared radiation (**section 2.3.2.4**) and these properties make SF_6 a potent global warming gas that can affect directly the Global Warming Potential. Therefore, a new technological solution of the arc control can lead to improve the ecology on the planet by limiting the use of SF_6 (a greenhouse gas) in high-voltage switchgear industry worldwide.

Aerodynamic self-blast effect observed in different interrupter units presents many technological challenges and has important implication commercially. Finally, containing and controlling such arc plasma using the new method of arc control presents research interest in the area of plasma physics where the open rig can provide external access for monitoring and observation the arc properties at the time of arc interaction.

Several facets affecting arc control have been investigated:

- Electromagnetic manipulation to form an azimuthal dc-arc during 2.5-3ms in the arc control model (**section 5.2.2**, fig. 5.15) and ac-arc for 11.5-12.5ms in the current interrupter head (figures 5.35, 5.36).

- Production of PTFE ablation by squeezing the arc onto the surface (current interrupter head, fig. 5.39)

- Use of expansion of azimuthal arc for quenching in the current interruption head in air, at atmospheric pressure (fig. 5.22)

- Use of azimuthal arc within an annular gap between two PTFE cylinders to produce self-pressurization in the prototype interrupter (fig. 5.42)

7.2 APPROACH FOR ARC INTERRUPTION

The investigations reported in this thesis have demonstrated a number of significant aspects relating to the following:

- An azimuthal arc can be formed through the deployment of a new form of electromagnetic arc control

- The azimuthal arc can be made to self-extinguish

- The azimuthal arc can be used for ablating PTFE material

- The azimuthal arc and ablation can be used for self-pressurization

- The behaviour of the azimuthal arc in air compares favourably with a rotary arc in SF_6

The behaviour of the azimuthal arc has been shown experimentally from high-speed photography (**chapter 5**, figures 5.15, 5.34, 5.35, 5.36 and **chapter 6**, figures 6.1, 6.2, and **chapter** 7, fig. 7.3) and from optical fibre probes (**section 5.2.3.3**) including dielectric strength (**section 5.2.3.4**) to behave in the modes shown schematically on figure 7.1. The arc is initially formed vertically between the anode and cathode on contact separation and is immediately rotated due to the Lorenz force produced with a B-field coil being suitably orientated at this short gap location (fig. 7.1a). In other words, an electromagnetic force is drown from the coil (depended on the arc current) for driving the arc. As the contact gap increases, the arc column extends axial into regions of different magnetic field orientations (**chapter 3**, fig.3.7c and

chapter 5, figures 5.20, 5.21). The spatial B field distribution is such that it distorts the arc column by the contrary rotation of the anode and cathode regions of the arc so that it assumes the azimuthal form shown on figure 7.1b and which persist until current zero of the ac half cycle (**chapter 6**, fig. 6.20). In this mode electromagnetic force is drown from the coil to maintain the azimuthal arc shape. At current zero, the B field coil loses its influence on the arc control (since i =0 and B≈0, fig. 4.16). The electromagnetically compressed plasma is then related so that the arc helix repels itself azimuthally in so doing the arc column self-disrupts (fig. 7.1c).

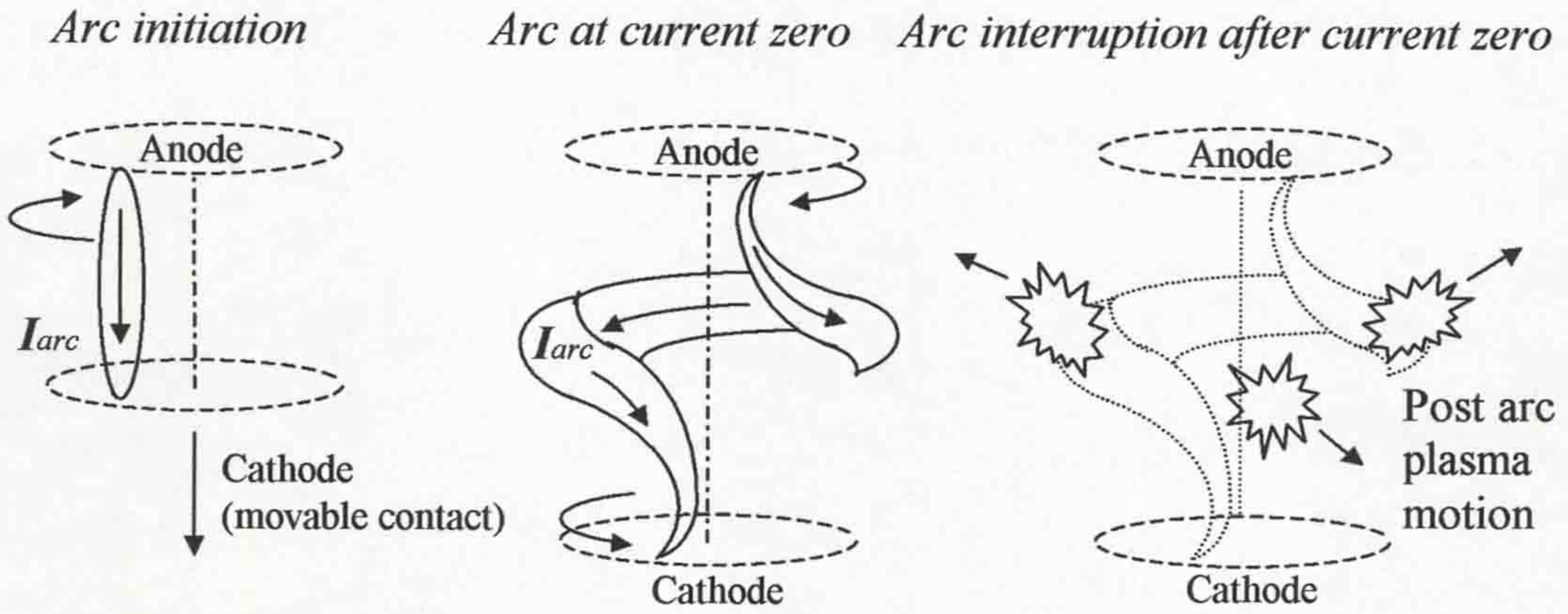

a) Electromagnetic (e.m.) and rotation phase (e.m. drives the arc)

b) Formation & maintenance of azimuthal arc, e.m. compressed arc orientation and rotation phase

c) Arc disruption (compressed arc conversion)

Figure 7.1 Transformation of the arc during the arc interruption

7.3 ADVANTAGES OF THE NEW ROTARY ARC INTERRUPTER TECHNOLOGY

7.3.1 Interrupter geometric shape

One aspect of the present work has been to confine the arc plasma column within an annular gap between the coil having PTFE (inner) and an outer PTFE cylinder (fig. 7.2).

It has been necessary to base the dimensions of this gap as well as the axial length of the arc constraining PTFE cylinders from the preliminary tests concluded with the other arc test head (fig. 5.12). This refers to the need for

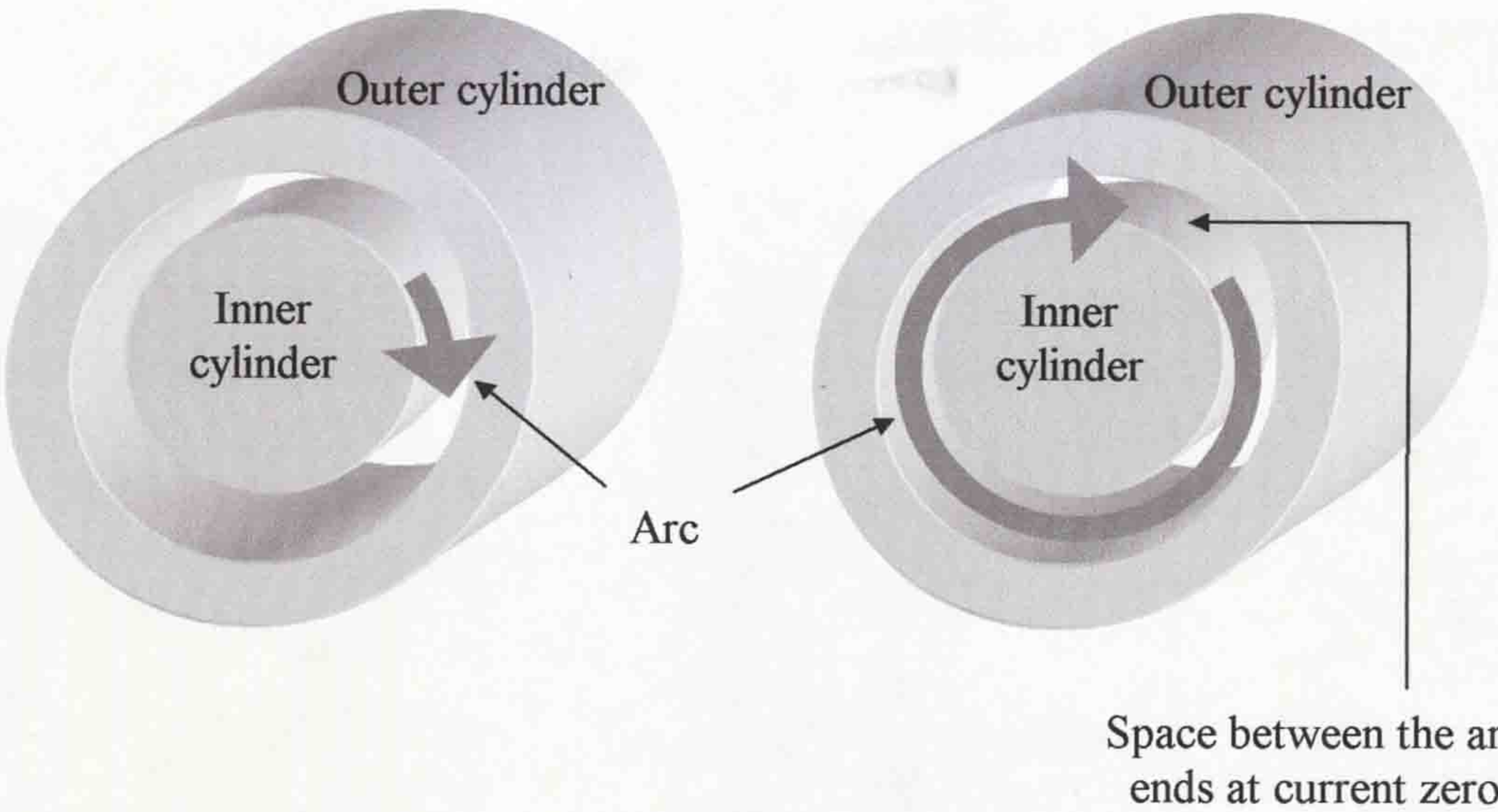

a) Arc initiation

b) Arc extinction (fig. 6.14)

Figure 7.2 Position of the rotary arc between inner and outer PTFE cylinders in the prototype breaker chamber

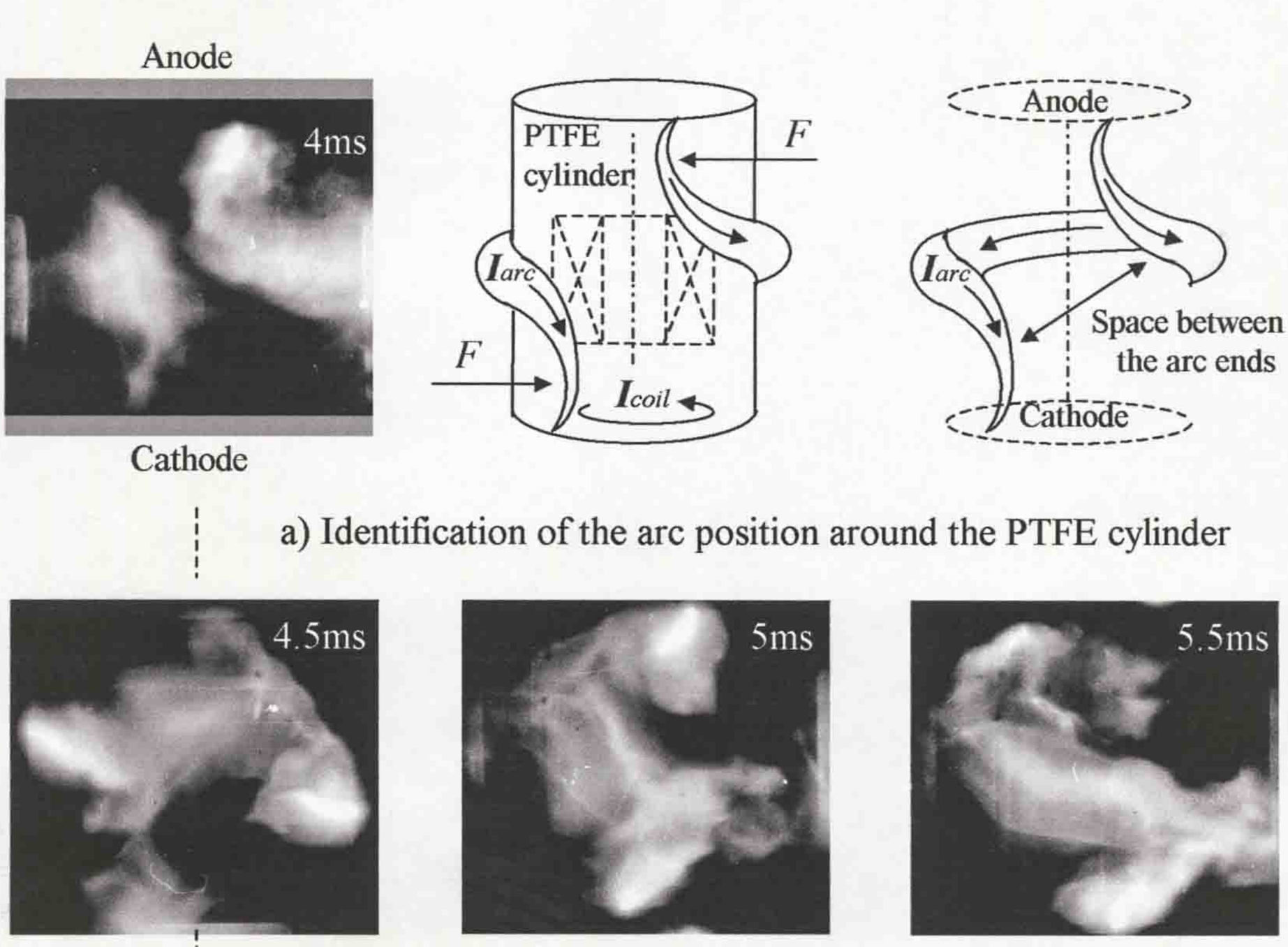

a) Identification of the arc position around the PTFE cylinder

b) Process of arc itself shorting and reestablishment

Figure 7.3 Example of high-speed photographs of arc in air, atmospheric pressure, quasi-dc 1.3kA, (framing rate 10000 frames per second) demonstrating the arc shorting and reestablishment in the arc control model

adequate (fully opened contact gap) B field producing coil, length and typical arc column radial dimensions etc. The values chosen for these variations parameters have already been given (**chapter 3**, **section 3.1.3**, **3.4.2**, **Appendices IV** and **V**).

Experimental tests (**chapter 5**, **section 5.1.1**, **5.1.2**, **5.1.3**) have shown that these dimensions are at least adequate in that the indicators are that the arc appears to behave as anticipated. There is a reasonable level of PTFE ablation (**chapter 5**, **section 5.2.3.6**), the arc can be extinguished (**section 5.2.3.2**) and good dielectric recovery achieved (**sections 5.2.3.4** and **6.1.5**). Central to good operation of the prototype interrupter is the need to maintain the azimuthal form of the arc column during the high current arcing phase.

Figure 7.3 shows that the electromagnetic system supports such an arc form in a stable manner. The figure shows a series of frames 0.5ms apart commencing at 4ms. The first frame shows well the anode and cathode arc column are separated by the arc being azimuthal. In the 5ms frame the arc short-circuits but commences to reform the helical shape in the 5.5ms frame.

Duration of the azimuthal arc depends on a number of aspects such as the geometric shape of the test units (diameter and height of the PTFE cylinder), media where the azimuthal arc is formed etc.

Experimental results with the arc control unit showed the azimuthal quasi-dc arc shorting and reestablishment formed during 5-5.5ms after arc initiation (figures 5.15 and 7.3). This trend occurred when the gap between the electrodes was already large from the arc initiation. In contrast, the current interrupter head investigations showed that azimuthal ac-arc could be formed after about 12ms (figures 5.35 and 5.36). Its duration is depended on the arc current duration, geometric shape of the coil situating within the interrupter test head and its axial position along the gap.

Comparison of the post arc current investigations of the current interrupter head (fig. 3.8) and prototype interrupter (fig. 3.12) showed that former was extinguished by the loop arc expansion (fig. 6.3c) whilst the later was extinguished by self-pressurization (fig. 6.3d).

The most effective technique of both interrupters is a compromise between the need for their use. The voltage characteristics of the current interrupter head (fig. 5.22) and prototype interrupter (figures 5.26 and 5.27) suggest that the current interrupter head may be used for current limiting (high voltage) when the prototype interrupter may be used in the current interruption (high extinction voltage peak).

Moreover, a number of units (prototype interrupters) may be used in series to increase voltage capabilities.

7.3.2 Contact wear

Statistics show that over 80% of in-service problems of the circuit breaker are due to mechanical failures (Browne, 1984). It is therefore essential to design it with the concept that once installed, it will be forgotten.

A large number of mechanical operations were conducted with the same pare of contacts in the current interrupter test heads (figures 3.8, 3.12) during this experimental work. This number was about 400 closing and separation operation in total with arc currents. This behaviour may be attributed to the arc column and roots an both anode and cathode being continually moved by the electromagnetic force so reducing contact erosion.

7.3.3 PTFE ablation

The controlled PTFE ablation is considered as one of the significant advantages of proposed technique for arc manipulation.

The experimental results for the location of the maximum erosion of the PTFE (**section 6.1.6**, fig. 6.18), the images showing the location of the azimuthal arc (fig. 5.38) and the estimated location of the highest Lorenz force (fig. 6.18) indicate collectively that the PTFE ablation is strongly influenced by the magnetic field. Such controlling magnetic field produces the formation of the azimuthal arc as well as attracting the arc loop to make close contact with the inner PTFE cylinder. Visual inspection of the outer PTFE cylinder (prototype interrupter) showed the same trend of PTFE ablation as in the current interrupter head tests in which more ablation observed in the regions (close to the coil) where the azimuthal arc was formed.

The optimum thickness of the PTFE cylinder is a compromise between the need for minimum thickness in order to increase the magnetic flux acting on the arc and having sufficient PTFE volume available for ablation over a large number of interrupter operations without the threat of thermally or electrically damaging the coil. Further fork would be needed to optimize the PTFE dimensions.

In order to avoid the arc self-shorting, the diameter of the inner PTFE cylinder must be larger than the length of the azimuthal arc column wrapped around this cylinder (figures 7.2 and 7.3). This effect may be useful in developing a model for arc instant deformation based on conditions described above and to incorporate it within the new arc interruption model (**chapter 3**) since this provides the basis of a useful design tool for arc interruption at current zero.

7.3.4 Recovery of dielectric strength

The experimental tests with the prototype interrupter showed that the dielectric strength recovery after current zero is approximately uniform azimuthally within the annular space. Three dielectric probes situated between the two cylinders (prototype interrupter) at azimuthal locations from the coil 120° intervals showed this regularity. However, it seems that different positions of the cathode at current zero, in relation to the two PTFE cylinders, may produce slightly different dielectric strength recovery post arcing.

7.3.5 Empirical model

The experimental results obtained in this project under a range of different conditions have enabled empirical model (**section 6.1.4**) to be derived for quantifying trend of the voltage extinction peak (V_{EXT}) with operating conditions i_p, B_p, l, d, P and at different gases (Air, N_2 and SF_6). Two gap conditions:

- A fixed contact gap (fig. 6.12a)
- Different gaps (fig. 6.12b)

have been tested in the reference, current and prototype interrupters at different conditions yielding the approximate empirical relationship of V_{EXT} (**section 6.1.4.3**). The empirical expression (equation 6.1, **section 6.1.4.3**) may be used for designs (A, B, C, D, E) presented in Table 6.1 and therefore allows some approximate predications to be made prior to experimental investigations.

In the case of the dielectric recovery tests, the results may be compared with those of Ennis (1996) and Mori *et al* (2005) for two other types of

electromagnetic arc control conditions. The results, which are given on figure 6.17 (**section 6.1.5**) in the form of relative breakdown voltage also applies to the present results.

7.4 GENERAL CONCLUSIONS AND FUTURE WORK

The investigations reported in this thesis demonstrated a number of significant aspects relating to the following:

An azimuthal arc can be formed through the deployment of a new form of electromagnetic arc control.

A new technique for ac current interruption is based on the concept of arc expansion to produce extinction.

The annular arc column can be automatically formed and the resulting plasma ring, after current zero, may be expelled either radially or axially.

Preliminary indications are that the arc quenching in air, at atmospheric pressure with the new interrupter is similar to quenching in SF_6 with other rotary arc devices.

The azimuthal arc can be contracted around a PTFE cylinder to produce ablation.

The combination of the new form of the azimuthal arc with ablation production in atmospheric air to produce highly effective arc self-extinction is novel.

The experimental investigations of the behaviour of the prototype interrupter (**chapter 5**) are limited to tests only in air and in the open atmosphere. Future work is necessary to deploy the interrupter within a closed chamber to provide a wider range of operating conditions (e.g. initial gas pressure).

Future work in the following aspects is suggested:

- Further exploration of the effect of geometry upon the formation and expansion of the azimuthal arc without the outer cylinder (e.g. larger diameter coil to produce larger helix).

- Further exploration of the azimuthally constrained arc to investigate effect of different annular gap (e.g. gap length and arc chamber diameter) sizes etc. Use of pressure measurements to confirm hypothesis of pressurization with and without azimuthal arc production.

- Possible use of mixtures of units - azimuthal interrupter without and with outer PTFE cylinders in series to explore current limiting and interruption effects together in one assembly.

- Possible deployment of " Ribs" on inner PTFE cylinder to prevent short circuiting and produce multiple loops.

Further investigation is required to examine the model under a fast rising recovery voltage.

APPENDIX I

Papers related to work presented in this thesis

The following pages show reprint of conference paper related to work presented in this report:

THE INTERACTION OF HIGH CURRENT ELECTRIC ARCS WITH SPATIALLY VARYING CROSS MAGNETIC FIELDS.

L.M. Shpanin, M.C. Kidman, J.E. Humphries, J.W. Spencer, G.R. Jones

(To be presented at) XV International Conference on Gas Discharges and their Applications /GD 2004/, Toulouse, France, Sept 5-10, 2004, pp183-186.

Two papers have been accepted for publication in the proceeding of the XVI International Conference on Gas Discharges and their Applications /GD 2006/ Xi 'an, China, Sept 2006 related to work addressed in the present thesis:

THE USE OF SPATIALLY DISTRIBUTED MAGNETIC FIELDS FOR ARC CONTROL AND CURRENT INTERRUPTION AT ATMOSPHERIC PRESSURE.

L.M. Shpanin, J.E. Humphries, J.W. Spencer, G.R. Jones, D.R. Turner

and

FORMATION AND PROPULSION OF AN ATMOSPHERIC PRESSURE PLASMA RING.

L.M. Shpanin, D.R. Turner, J.E. Humphries, J.W. Spencer, G.R. Jones, B.E. Djakov

THE INTERACTION OF HIGH CURRENT ELECTRIC ARCS WITH SPATIALLY VARYING CROSS MAGNETIC FIELDS

L.M. Shpanin, M.C. Kidman, J.E. Humphries, J.W. Spencer, G.R. Jones

Centre for Intelligent Monitoring Systems, Dept of Electrical Engineering and Electronics,
University of Liverpool, Brownlow Hill, Liverpool L69 3GJ UK
e-mail: joe@liverpool.ac.uk

ABSTRACT

This contribution examines a different deployment of magnetic fields for controlling electrical arcs. It utilises a current carrying coil outside of which an atmospheric pressure electric arc is formed. Experimental results are presented including high speed photographs and current and voltage waveforms. These results show that the arc column can be substantially convoluted with evidence of an azimuthal plasma flow around the arc column itself.

INTRODUCTION

The control of electric arcs at atmospheric pressures is important for the operation of many devices such as plasma torches, arc heaters etc. Some equipment utilise a combination of electromagnetic fields and high temperature insulation materials in order to provide suitable conditions for long duration arc control. Most of these use the same arc-rotating technique utilising different gases to increase their effectiveness. A new design principle for controlling the electric arc is introduced which is different from previous designs. The basis of previous methods is to produce passive electrical arc rotation inside a coil producing magnetic field for control. In contrast to these previous techniques the arc is wrapped around the outside of the coil and is electromagnetically attracted to it. The coil produces a strong magnetic field which interacts with the convoluted arc creating Lorenz forces for producing arc movement. This design also uses a polymeric material for enhancing this interaction.

EXPERIMENTAL DEVICE

The experimental test rig for producing the magnetic field and arc is shown on Figure 1 and was built to demonstrate the feasibility for arc control via this arrangement. An open rig is chosen for monitoring the behaviour of the arc rotation in detail under the following conditions: air, atmospheric pressure. Ring-electrodes are situated at a fixed distance from each other. The coil is connected in series with the electrodes and situated inside a white PTFE cylinder. A fuse wire is linearly connected between the two electrodes enabling the electric arc to be ignited between them. The concept for controlling the arc is shown in Figure 2. The inner coil produces an outer strong magnetic field around the PTFE cylinder. As a result, different Lorenz force directions are created producing two main field components for controlling the arc.

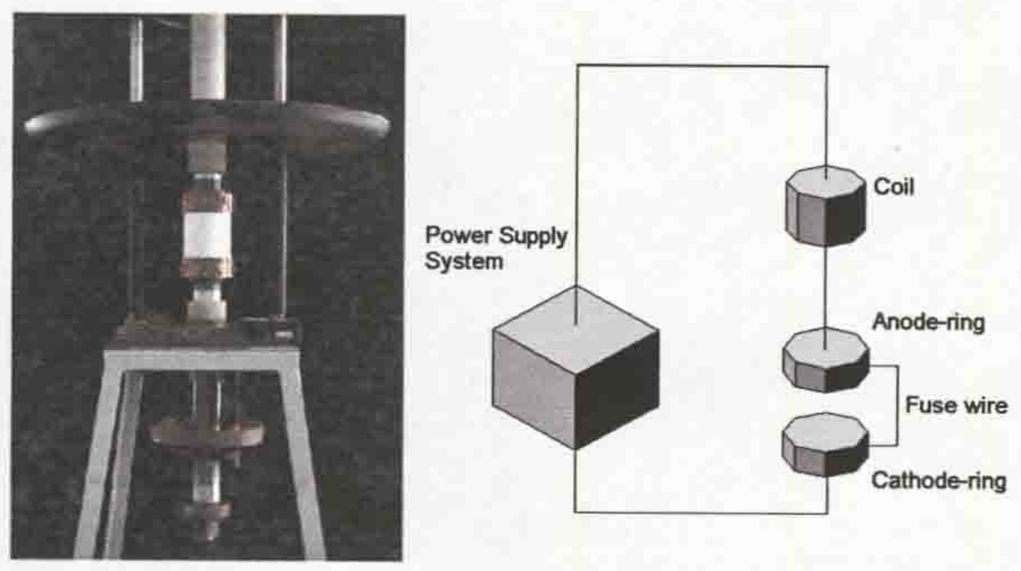

Figure 1. Experimental apparatus assembly

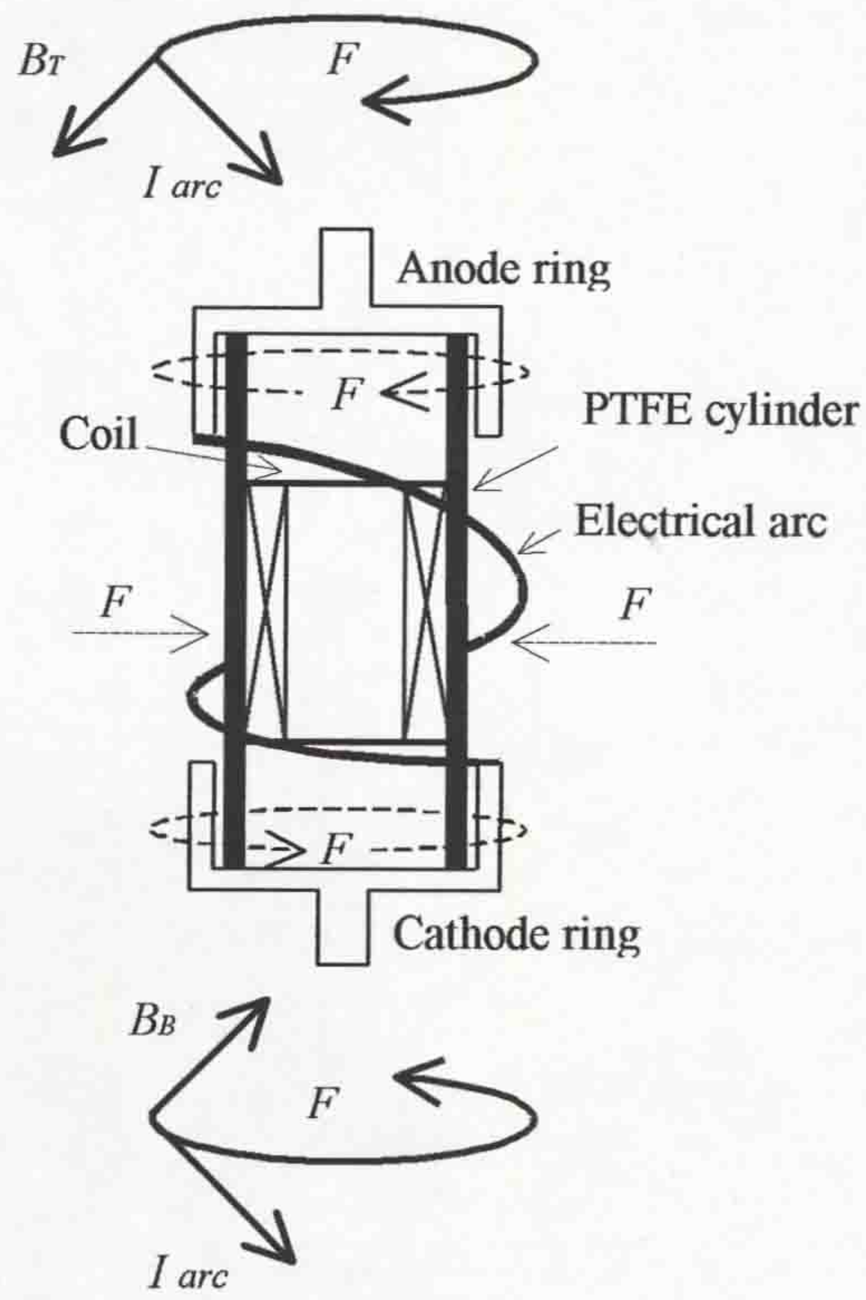

Figure 2. Technique of controlling the arc

1 to 4

The first is the radial component of the magnetic field producing two opposite directions of the Lorenz forces F at the top and bottom of the coil, (B_T, B_B, Figure 2). This direction of rotation will be maintained even when the current changes direction because the phase difference between the current and magnetic field is near zero. This advantage gives a good opportunity for choosing a specific time to control the arc. The second is the axial magnetic field producing a Lorenz force perpendicular to the PTFE cylinder, when the electric arc is positioned azimuthally around the PTFE cylinder. As a result, the arc is electromagnetically attracted to the coil. As the arc is also rotating, the length of the arc is increased. Both these magnetic fields provide a mechanism for greater interaction between the rotating arc and the PTFE cylinder. Furthermore, through ablation the thermal energy of the arc is reduced and as a consequence the duration of the arc may also be reduced. Figure 1 and Figure 2 show the electrodes fully extended with the coil situated inside the PTFE cylinder at the same distance from each of the electrodes.

EXPERIMENTAL TEST CIRCUIT

The electrical test circuit used in the experiments is shown in Figure 3.

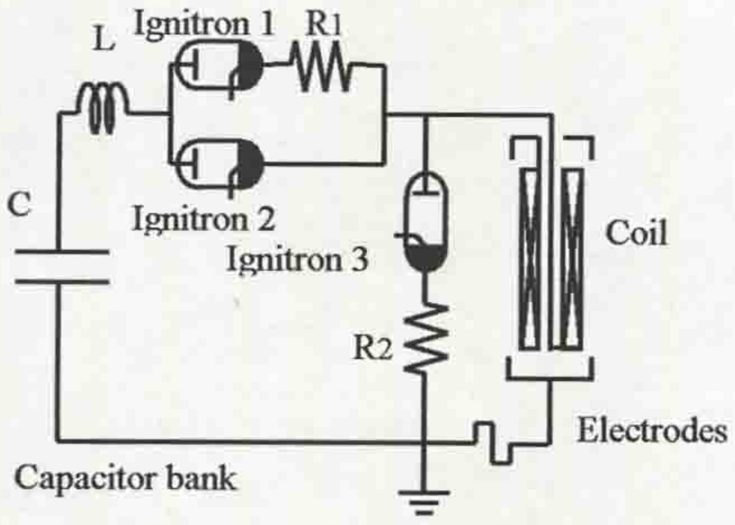

Figure 3. Test circuit

This consists of a capacitor bank for the main circuit including the arc and *B*-field producing coil which is situated inside of the PTFE cylinder (Figure 2). Ignitron 1, connected in series with a resistor, is triggered to conduct a quasi-steady dc current through the coil and fuse wire. Ignitron 2 is triggered to short circuit the current limiting resistor R1 and the first ignitron (Figure 3) and so produce a main half cycle sinusoidal current. The maximum duration of the electrical arc event is determined by triggering the dump ignitron 3 at 30 ms after the switching of ignitron 2 in order to dump the remaining energy from the capacitor bank through R2. The duration of the dc-arc discharge was set at 30ms, while the ac-arc was set at 10ms (one half cycle). For visual monitoring the electrical arc in real time a high speed camera and video recorder were used.

EXPERIMENTAL MEASUREMENTS

The experimental investigations of the arc were divided into two parts. The first was the electrical arc measurements and the second was the visual arc observation before and after the current half cycle. Both the level of dc and ac arc current and voltage were recorded utilising a digitising oscilloscope (GW Instek GDS-830). A high voltage probe was used with a 1000 divider (Tektronix type P6015A) was used to measure the voltage and a current shunt which had a resistance of 0.807 mΩ used for the current. High-speed photographs of the arc column were taken with a Cordin high-speed camera (model 350). Black & white film (type XP2 SUPER 400) was used in the camera. The exposure time for one frame was set at 0.1ms and a frame speed of 10000 frames per second was used for examining the dc-arc discharging period. A video camera was used to observe the rig after the dc and ac arcing with the frame duration set at 40ms per frame. A trigger pulse for the camera and recording oscilloscope were derived from the power supply system.

EXPERIMENTAL RESULTS

The first tests performed were with a quasi-dc arc under the following condition: 1.3 kA-1.3 kV, quasi-dc time 30ms. A typical example of current and voltage waveforms are shown in Figure 4. On this figure T is the trigger pulse from the central control unit. 9 ms later the quasi-dc 1.3 kA-1.3 kV current is initiated igniting the electrical arc between the electrodes. After about 4.5 ms the arc voltage increases before decreasing again and then forming a series irregular oscillations. This voltage waveform is typical of those recorded under such quasi dc arcing condition. There were also performed experiments with a half-sinusoidal approximately 50Hz current wave. A typical time varying current and voltage

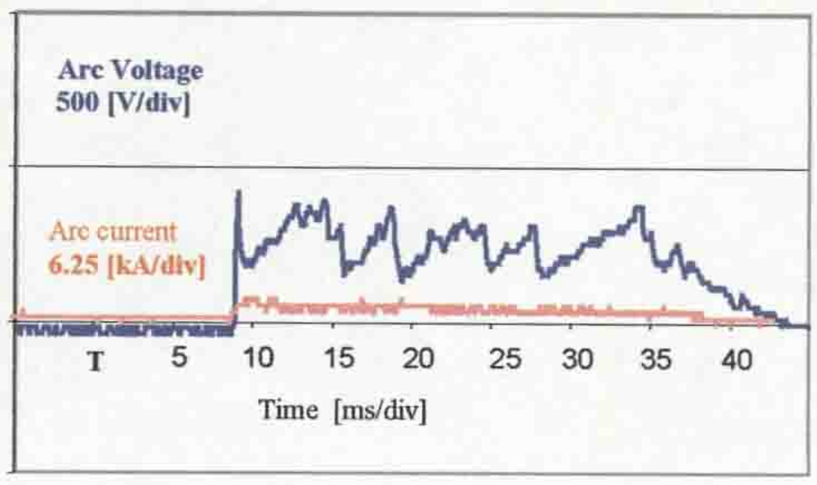

Figure 4. Current and voltage waveforms corresponding to the quasi steady arcing condition

record is shown in Figure 5, corresponding to a peak current of 1.35kA. This record shows also a number of irregular voltage oscillations as in the quasi-steady dc case.

Figure 7 shows some examples of high-speed photographs that were taken under quasi dc arcing conditions. These show an arc column formed

vertically between two contacts at 0.5ms following fusion of the fuse wire. At 1ms the arc column becomes obliquely orientated under the influence of the magnetic fields. This distortion grows through frames at 1.5ms and 2ms until at 2.5ms the arc is orientated horizontally within the photographic fields of view. At 3ms there is evidence of swirling plasma around the horizontal arc. At 3.5ms the plasma swirl remains visible but the vertical column connecting to the top electrode also becomes visibly distorted to the right of the plasma. At 4ms this distortion has become so severe that that the horizontal arc plasma has become ruptured. Figure 8 shows some video frames at 40, 80 and 120ms after arc initiation of a quasi-dc arc. They show the persistence of plasma, but quite remote driven away from the PTFE cylinder. Figure 9 shows corresponding video frames for an ac arc of peak current 1.35kA.

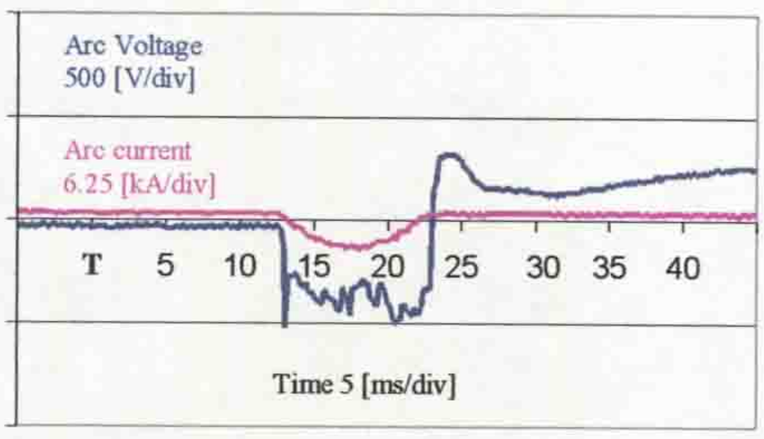

Figure 5. Current and voltage waveforms for a 50 Hz current waveform (peak current 1.35kA)

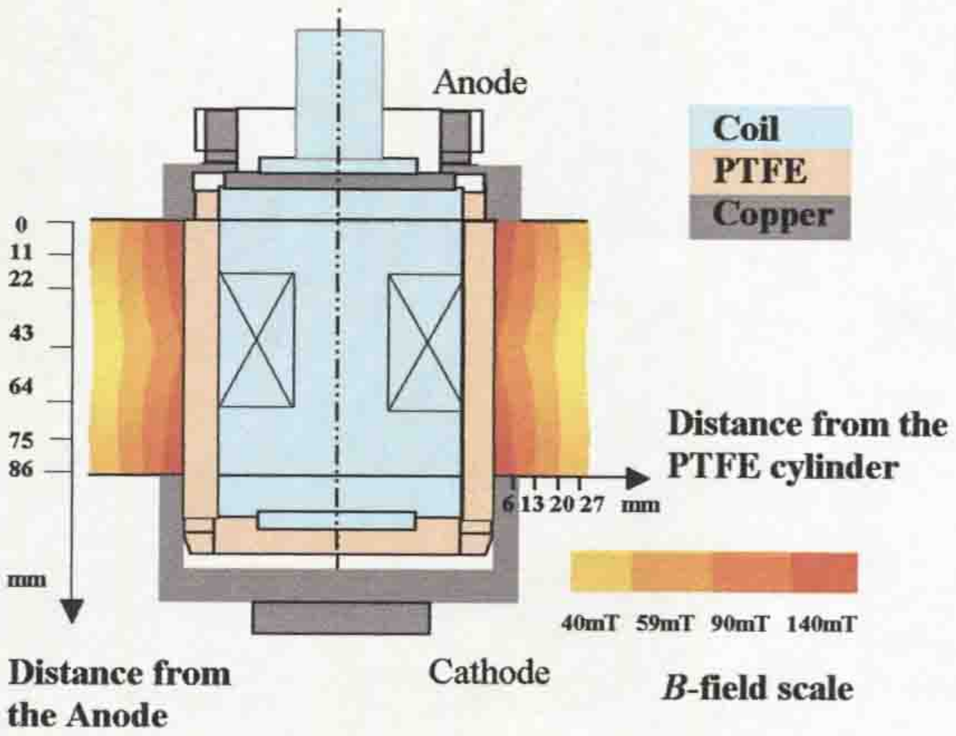

Figure 6. Outer B-peak magnetic field distribution for a peak ac current 5.3kA

Magnetic field measurements were made for the determination of the relationship between the ac peak current of 50Hz and *B*-peak field distribution produced by the coil around the PTFE cylinder as a function of the distance from the cylinder. The radial and axial magnetic fields were measured [1-2] and the resulting *B*-field calculated. Figure 6 shows an example of the B-field distribution around the coil for an ac peak current of 5.3kA flowing through the coil. The maximum value for the *B*-field is at the end of the electrodes (137mT) with a minimum at the centre of the coil (104mT) at a distance of 6mm from the PTFE cylinder. The magnitude and shape of the magnetic field is not spatially uniform and changes with distance. For instance, at a distance of 27mm from the PTFE cylinder the B-field value is about 3 times less than for 6mm. However, the field is symmetrical about the vertical axis up to the measurement limit at 27mm (Figure 6).

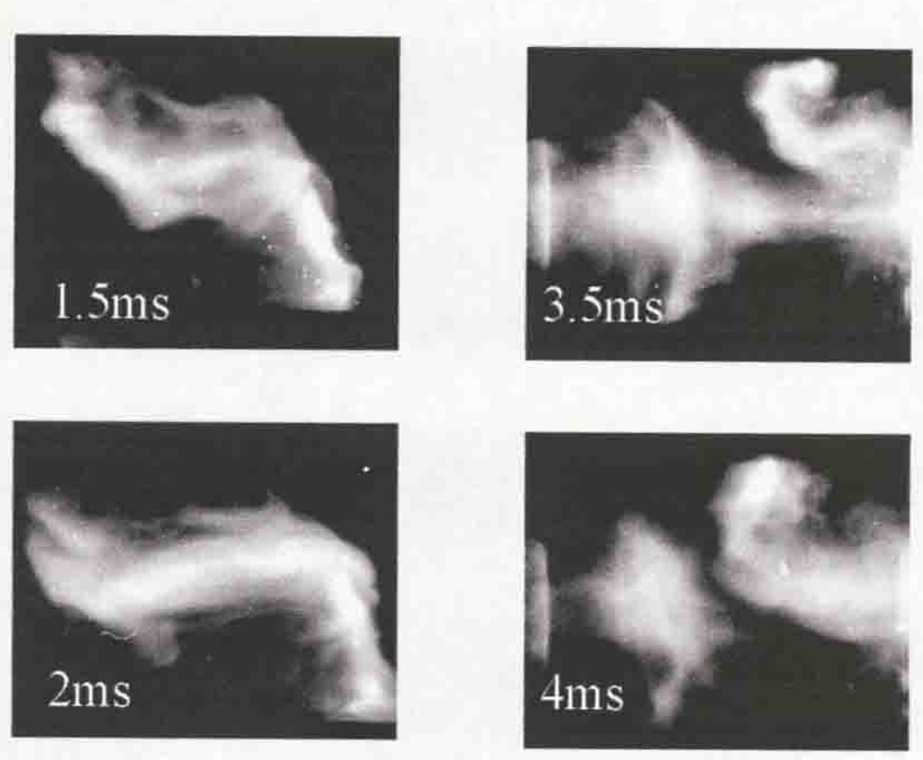

Figure 7. Example of high-speed photographs of arc in air, atmospheric pressure, quasi-dc 1.3kV/1.3kA, (framing rate 10000 frames/Sec, exposure 6.6μs)

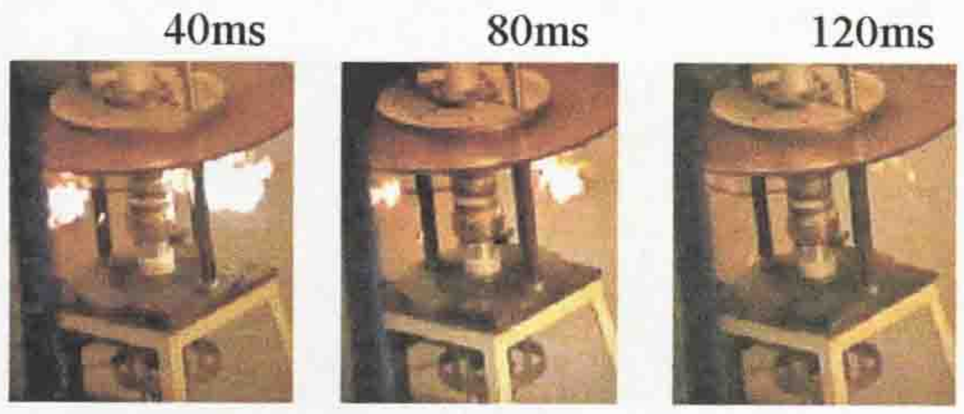

Figure 8. Video frames showing a post dc-arc repulsive effect (peak current 1.3kA)

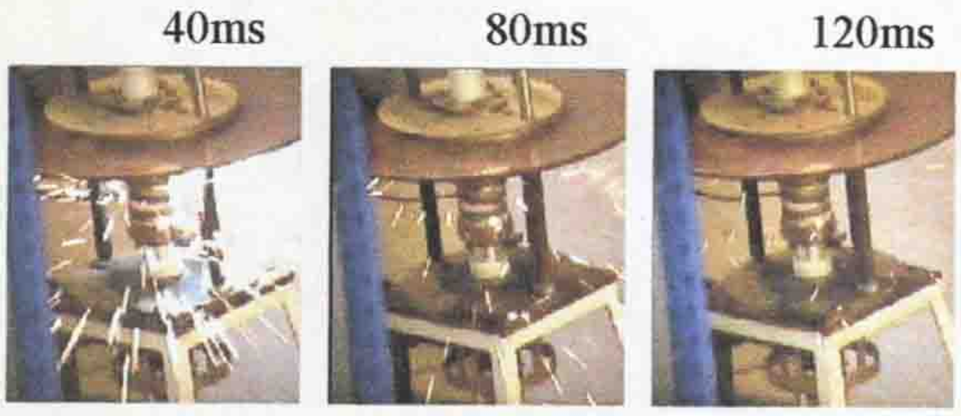

Figure 9. Video frames showing a post ac-arc repulsive effect (peak current 1.35kA)

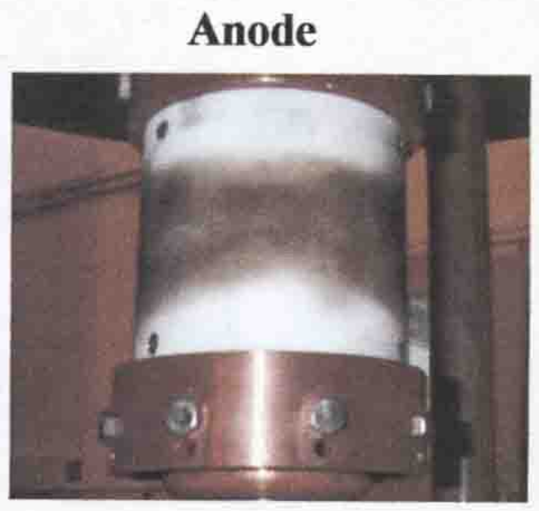

Figure 10. Discolouration of the PTFE cylinder in the experimental interrupter

DISCUSSION OF RESULTS

A comparison of the high-speed photographic frames of Figure 7 with the voltage waveforms of figure 4 shows that the periodic voltage excursion of figure 4 correspond to the shorting and reestablishment of the electric arc turns. Inspection of frames of this kind also shows that the arc column is twisted around the PTFE cylinder horizontally. This is confirmed by inspection of the PTFE cylinder post arcing, which shows discolouration produced by the arc plasma in close proximately with the PTFE (Figure 10). The electrodes positions in figure 10 shows that the anode and cathode are at a fixed distance from each other. As a result, the electrical arc is rapidly twisted around the PTFE cylinder by Lorenz forces in opposite directions at the top and bottom of the coil (Figure 7, frames 0.5ms-2ms). The duration of one turn twisting arc is about 4.5ms, current 1.3kA (Figure 7, frame 4ms). This is the reason that the arc is twice re-established within 10 ms.

ACKNOWLEDGEMENTS

The authors express their gratitude to Mr. D.R. Turner, for his valuable assistance in this project. Special thanks to Ms. N.R. Telfer and Mr. R.M. Forde for their help with the machining of the device and to Dr. A. G. Deakin for his help and advice.

REFERENCES

[1] Carl T.A. Johnk, "Engineering electromagnetic fields and waves" 2nd edition, Wiley International Edition, pp. 270-275, 1988.

[2] Web Site: UniS Electronics and Physical Sciences, http://www.ee.surrey.ac.uk/Workshop/advice/coils/terms.html#flux

The use of spatially distributed magnetic fields for arc control and current interruption at atmospheric pressure

L.M. Shpanin, J.E. Humphries, J.W. Spencer, G.R. Jones and D. R. Turner

Centre for Intelligent Monitoring Systems, Dept of Electrical Engineering and Electronics,
University of Liverpool, Brownlow Hill, Liverpool L69 3GJ UK
E-mail: joe@liverpool.ac.uk

ABSTRACT

This contribution describes a new means of controlling electric arcs in air, at atmospheric pressure using spatially varying complex magnetic fields. Photographic evidence for the arc behaviour is presented along with results for the time variation of arc current and voltage. Dielectric recovery after the current zero has also been measured and compared with results obtained by other authors from different devices.

1. INTRODUCTION

A number of high current interruption devices using atmospheric pressure electric arcs with complex magnetic field have been produced for arc control and extinction. These include high current limiting switches, linear drives in low voltage switches and arc rotation for control of gas heating in higher voltage switches [1]. A new technique for ac current interruption is based on the concept of arc expansion to produce extinction [2]. With this method the ac-arc is wound around a coil during the main current phase and expands outwards during the approach to current zero. A strong magnetic field produced by the coil electromagnetically attracts the convoluted rotary arc to the coil whilst also creating Lorenz forces for rotating and lengthening the arc. This contribution describes various arc voltage waveforms produced during the operation of the interrupter along with some results for the dielectric strength of the arc-heated gas.

2. PRINCIPLE OF OPERATION

A schematic of the experimental test head for producing the magnetic field and high-current atmospheric arc in air is presented in figure 1. This consists of a B field-producing coil within a PTFE (Inner) cylinder around which a moveable cylindrical cathode fits. A further PTFE cylinder surrounds this cylindrical cathode. Figure 1a shows the interrupter head in the closed position with the anode and cathode in contact. The coil, anode and cathode are all connected in series. Figure 1b shows the anode and

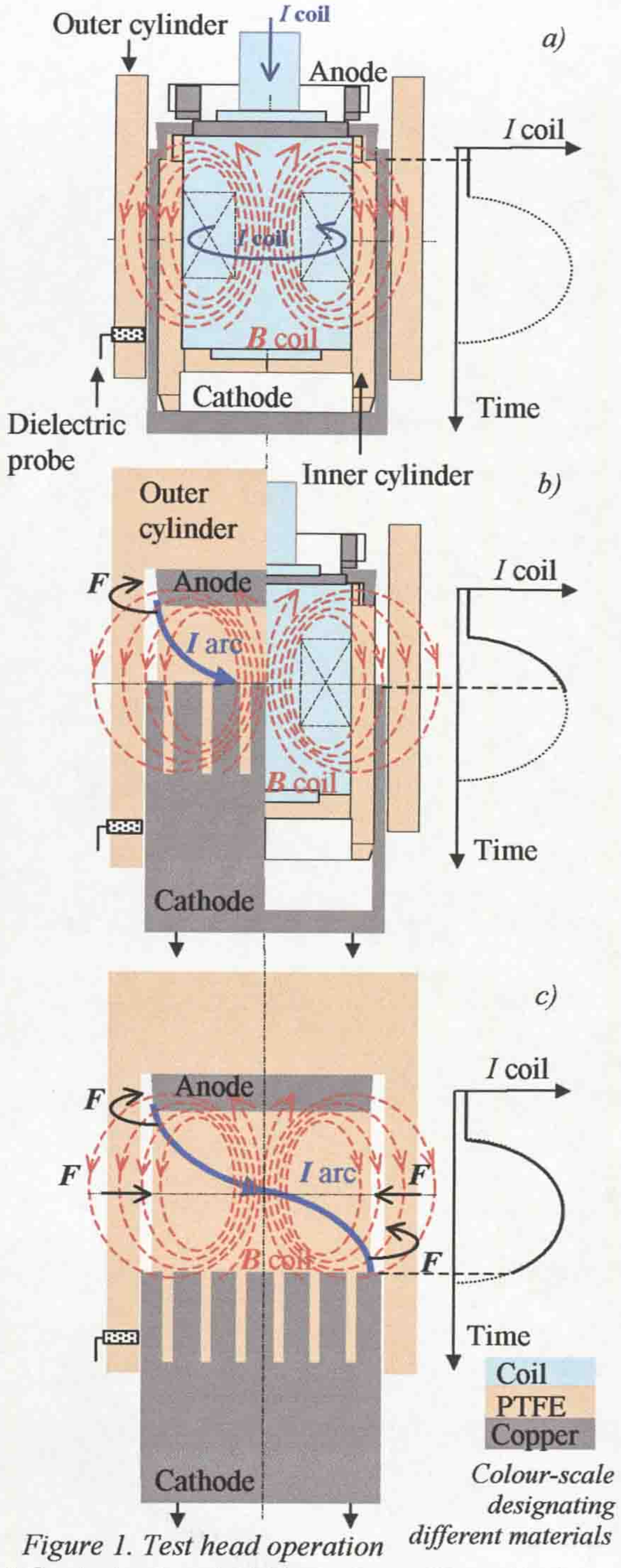

Figure 1. Test head operation
a) Contacts closed, b) Contact gap 68mm (Arcing), c) Contact gap 95mm (Interruption)

cathode parting and an electric arc being formed within the B field produced by the coil. The time variation of the current thought the coil is shown on the insertions to figures 1a and b. The Lorenz forces act upon the arc forcing it around the PTFE cylinder. The arc length increases gradually until the movable cathode is level with the centre of the coil, when the Lorenz forces begin to act on the arc in such a way as to draw it towards the PTFE cylinder radially. This is because the radial *B* field of the coil is low outside the coil (especially at the centre of the coil), while the axial coil *B* field is higher at the same point. Since the current direction in the coil and the arc is the same, the arc is electromagnetically attracted to the coil. As a result, the electric arc is rapidly wound around the PTFE cylinder increasing its length. When the electrode positions is as shown in figure 1c the arc experiences a different Lorenz force direction at the top and bottom of the coil, which enhances the arc winding process. By driving the arc plasma against the PTFE cylinder surface, ablation of the PTFE is encouraged. When the cathode moves further, the annular gap between the inner and outer PTFE cylinders is opened enabling the arc-heated gas to escape. This enhances the arc interruption and dielectric recovery process. For the present experiments, a dielectric probe [3] was situated in the wall of the outer PTFE cylinder as shown on figure 1.

3. EXPERIMENTAL TESTS

A number of tests and measurements have been made on the model interrupter. AC currents in the range 8.8 to 15kA have been studied with a total arc duration of 18ms. The time variation of both current and voltage have been measured along with the dielectric strength of the arc heated gas [3]. High-speed photographs of the arc discharge were also taken with the outer PTFE cylinder removed in order to visualise the arc movement. Video images were also obtained with the outer PTFE cylinder in place.

4. EXPERIMENTAL RESULTS

4.1 ARC PHOTOGRAPHY

The high-speed photographs were taken with two high-speed cameras operated at the same time but at different azimuthal positions situated 120 degrees with respect to the other. Some typical high-speed photographs are shown on figure 2 for the period leading to current zero (12.3 to 14.4ms) of a 13.2kA peak current arc (14ms duration). Column (a) figure 2 shows frames from the first camera and column (b) from the second camera. These frames show that the ac-arc column became obliquely orientated under the influence of the magnetic field. This oblique orientaton continued until the arc became horizontal (fig. 2: (a) camera 1, at 12.3ms and (b) camera 2, at 12.4ms). The arc core is concentrated at the middle of the coil during its motion around the PTFE cylinder. Immediately prior to current zero, the arc is mostly wound around the cylinder forcing it away from the PTFE (camera 1, at 13.8ms and camera 2, at 13.9ms). During the ac-arc interruption a loud acoustical signal occurs probably produced by the rapid outward expansion of the arc (camera 1, at 14.4ms and camera 2, at 14.2ms).

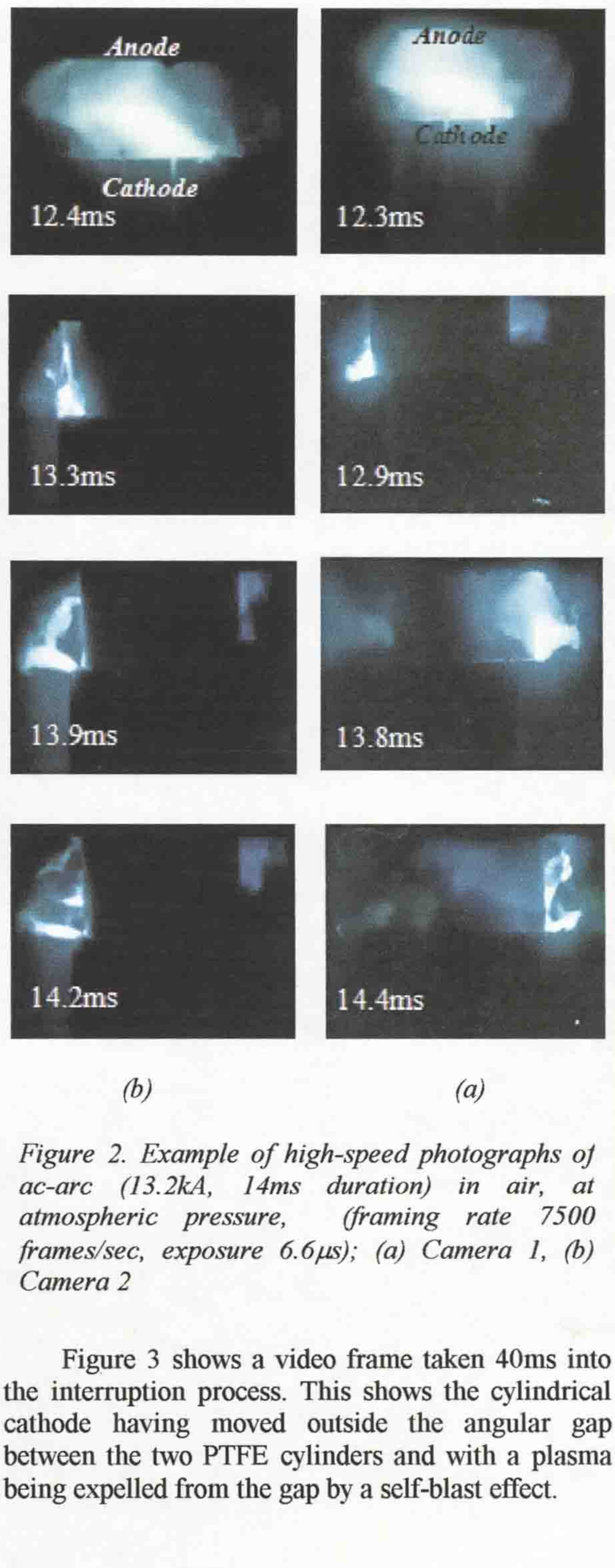

Figure 2. Example of high-speed photographs of ac-arc (13.2kA, 14ms duration) in air, at atmospheric pressure, (framing rate 7500 frames/sec, exposure 6.6μs); (a) Camera 1, (b) Camera 2

Figure 3 shows a video frame taken 40ms into the interruption process. This shows the cylindrical cathode having moved outside the angular gap between the two PTFE cylinders and with a plasma being expelled from the gap by a self-blast effect.

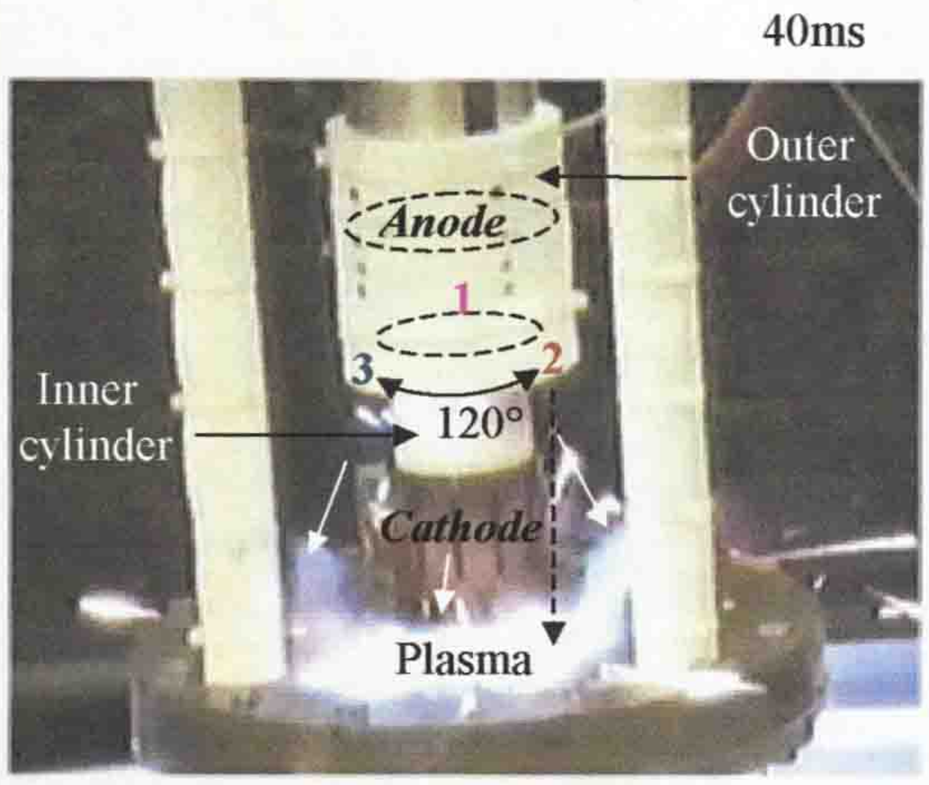

Figure 3. Expulsion of arc plasma from the open annular gap between the two PTFE cylinders at 40ms (Ipeak 10kA), (1,2 and 3 - dielectric probes)

4.2 ARC VOLTAGES

Figure 4 shows the time variation of arc voltage and current for one half cycle of current preceded by a quasi-steady 2kA current for peak current levels of 8.8, 11.8 and 15.0kA.

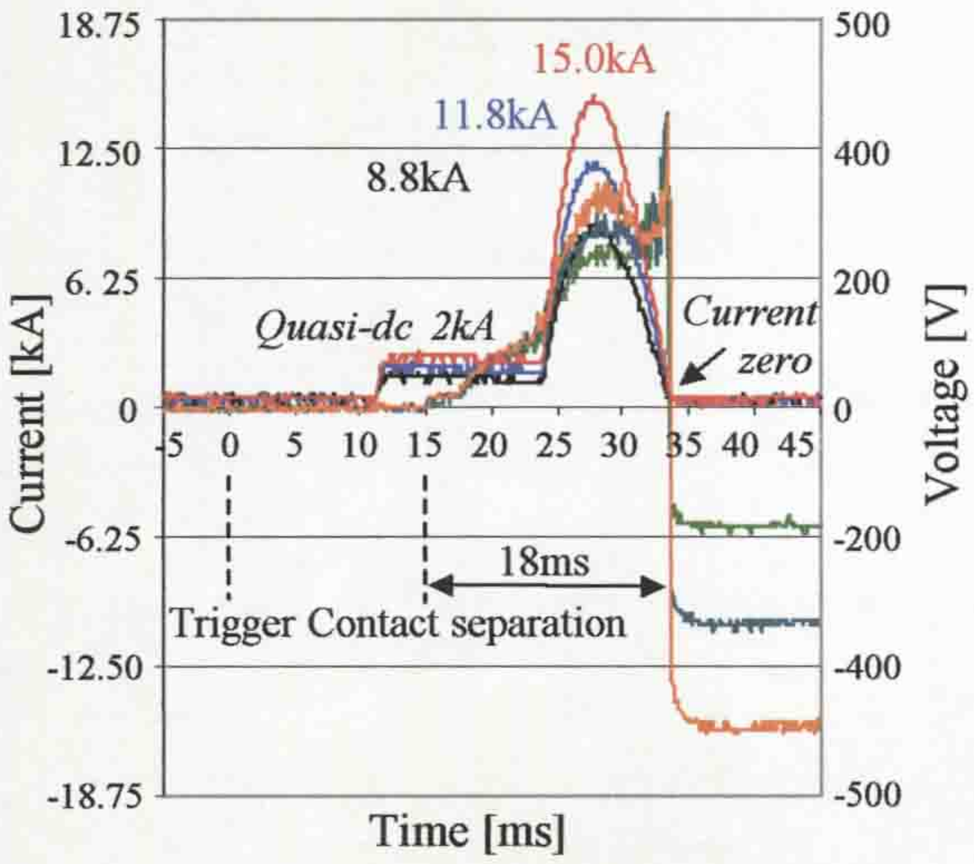

Figure 4. Interrupter operation at different currents, arc duration 18ms in air, at atmospheric pressure

The results show the arc voltage close to current peak increases with arc current. In each case, an extinction peak is apparent. Following current interruption the post arc voltage increases from 200 to 450Vas the arc current increases due to the nature of the test circuit used (L-C system) [3]. In each case, the current was successfully interrupted.

4.3 DIELECTRIC STRENGTH

Results obtained with the dielectric probe (fig. 1) are shown on figure 5 for a 5kA ac-arc.

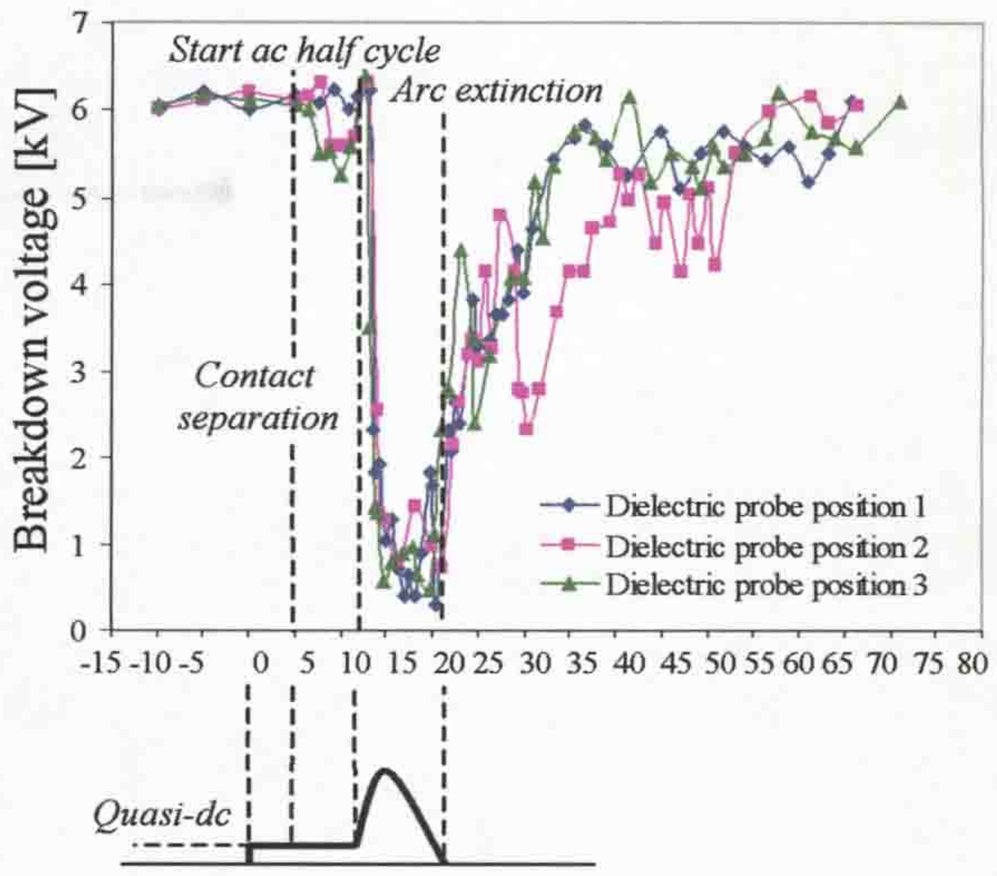

Figure 5. Comparison of dielectric probe results vs. time at different probe positions within the circuit interruption (5kA peak)

The results are for the different azimuthal positions each 120° different around the test head at the axial location sown on figures 1 and 3. These show the following effects:

- 5ms after contact separation with a 2kA dc holding arc there is evidence of a small reduction in dielectric strength (ΔV≈0.75kV).
- At 11.5ms, when the ac-arc is present, the breakdown voltage is sharply reduced (~0.5kV).
- At arc extinction, the breakdown voltage recovers rapidly to about 2.5kV
- Between 20 and 30ms after arc extinction the breakdown voltage has increased to about 5kV compared to 6kV for the pre arc conditions.

The breakdown voltages obtained with dielectric probe 2 exhibit high amplitude oscillations compared to probes 1 and 3 and there is a clearer more abrupt indication of the dielectric recovery. Therefore, this probe 2 was used for measurements with various contact gaps the results being shown on figure 6.

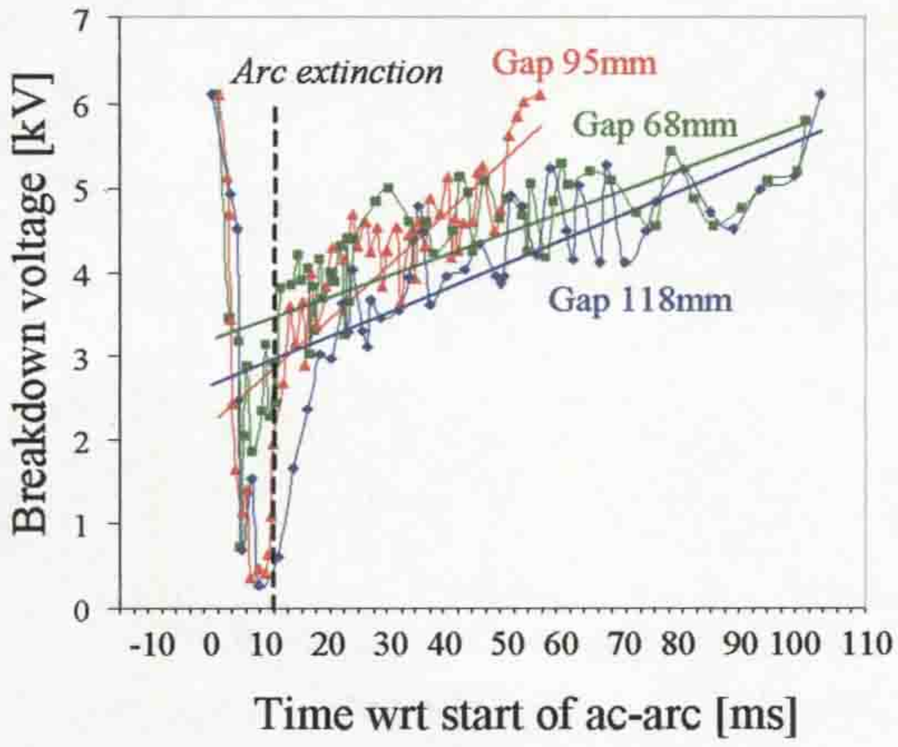

Figure 6. Breakdown voltage as a function of time for different arc gaps

These show that the 118mm gap produces the slowest initial dielectric recovery. Thereafter in the time period 20 to 50ms the dielectric recovery of each gap proceeds at the same rate. The 95mm gap then recovers rapidly to the pre arc value. The 118mm and 68mm gaps recover to the pre arc value by about 107ms.

5. EMPIRICAL RELATIONSHIPS

Experimental results of the form shown on figure 4 enable empirical relationships to be derived.

In the case of the dielectric recovery tests, the results may be compared with those of Ennis (1996) [3] and Mori *et al* (2005) [4] for two other types of electromagnetic arc control conditions. The results, which are given on figure 7 in the form of relative breakdown voltage also applies to the present results.

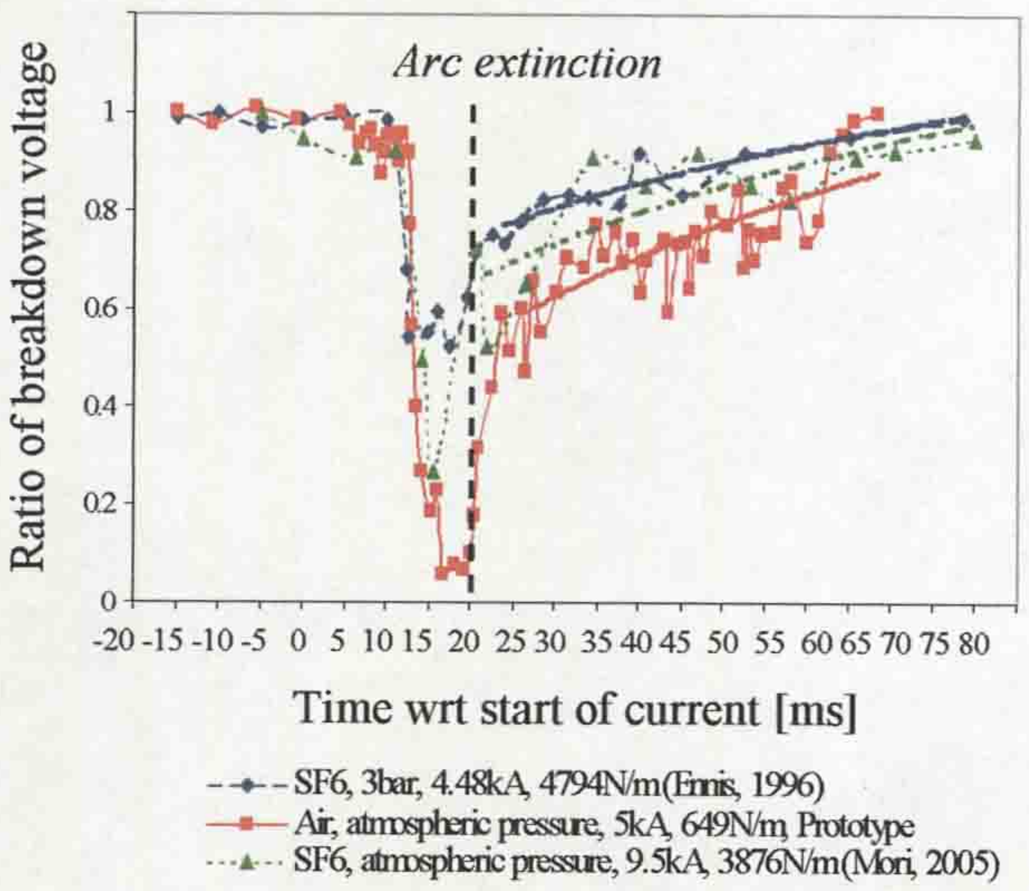

Figure 7. Response of dielectric probe for arc duration of 16.5ms (prototype interrupter) compared with the other interrupters of Ennis (1996) and Mori (2005)

For the case of the arc voltage results of figure 4, values of extinction peak voltages prior to current zero can also be empirically related to operating conditions. The relationship derived for this case is of the following form:

$$V_{EXT} \cong K(1+\alpha B_p^m) l^g i_p^{-n} d^{\left[\frac{l}{L}\right]}, \text{ [kV]} \qquad (5.1)$$

Where the parameters B_p, i_p, l the peak magnetic field [T], contact gap [m], peak current [A] respectively. Coefficients K, α, m, g and n are constants determined from the tests (fig. 4) having the values 90.0, 1.8, 1.0, 1.64 and 0.23 respectively, for our operating conditions. d represents relative coefficient of the arc chamber volume (with d=1.0 and without d=0.9 outer PTFE cylinder) as a function of gap in the current interruption test head. L, the gap constant of 0.106, [m] represents the threshold gap beyond which the effect of outer cylinder (larger voltage extinction peak) should be observed in the current interruption head (fig. 1). The effect of the arc chamber diameter was not included since it was unchanged during the test. However, the experiments of the previous authors [4] on atmospheric rotary arcs in SF_6, in hollow polymeric cylinders showed that the extinction peaks for higher peak currents were lower in the small bore chamber. Moreover, the extinction peaks for the larger bore chamber were higher than those for the small one [4]. Therefore, equation 5.1 may be used for the preliminary voltage extinction peak estimation at different arc gaps in air and at atmospheric pressure taking into account the experimental results of the previous authors [4].

6. CONCLUSIONS

Experimental evidence has been provided to show that a high current arc at atmospheric pressure may be rapidly convoluted into a spiral using appropriate B field configurations. It has been shown that such arcs can be formed up to at least 15kA in a confined volume and that they may be rapidly extinguished when the alternating current reduces to zero. The arc control and extinction appears to be due to a combination of electromagnetic drive, aerodynamic pressurisation and possibly material ablation. Photographic evidence and electric measurements have been presented to define some of the arc properties. Empirical relationships for the breakdown voltage [4] and voltage extinction peak (equation 5.1) have also been considered.

REFERENCES

[1] Flurscheim C.H., "Power circuit breaker theory and design", IEE, New York, Peter Peregrinus, 1982

[2] Shpanin L.M., Kidman M.C., Humphries J.W., Spencer J.W., Jones G.J., " The interaction of high current electric arcs with spatially varying cross magnetic fields", Proc. of XVth Int. Conf. on Gas Discharges and their Applications, Toulouse, France, pp183-186, 2004

[3] Ennis M.G. "Investigation of fundamental processes affecting the behaviour of electric arcs in electromagnetic interrupters" PhD thesis, Univ. of Liverpool, 1996

[4] Mori T., Spencer J.W., Humphries J.E., Jones G.R., "Diagnostic measurements on rotary arcs in hollow polymeric cylinders", IEEE Trans. Power Deliv., Vol.20, No. 2, pp765-771, Apr. 2005

Formation and propulsion of an atmospheric pressure plasma ring

L.M. Shpanin [1], D.R. Turner [1], J.E. Humphries [1], J.W. Spencer [1], G.R. Jones [1], B.E. Djakov [2]

[1] Centre for Intelligent Monitoring Systems, Dept of Electrical Engineering and Electronics, University of Liverpool, Brownlow Hill, Liverpool L69 3GJ UK, E-mail: joe@liverpool.ac.uk
[2] Institute of Electronics, Bulgarian Academy of Science, E-mail: bdjakov@aubg.bg

ABSTRACT

This contribution addresses the problem of producing directed plasma propulsion at atmospheric pressure using spatially varying complex magnetic fields. The approach is based upon electromagnetically restricting an annular atmospheric arc plasma column during heavy current flow and releasing the plasma restriction when the sustaining current ceases to flow. Photographic results are presented to show that such an annular plasma column can be automatically formed and that the resulting plasma ring may be expelled either radially or axially.

INTRODUCTION

There are many potential applications for atmospheric pressure plasmas, which could be produced simply and conveniently e.g. thrusters for atmospheric/space use, electric current limitation and switching, materials processing etc. In this contribution, we examine the possibility of producing such a plasma from a magnetically manipulated electric arc loop without the restrictive need for fuse arc initiation used previously [1].

Experimental investigations are reported on the form of electromagnetic arc control suggested by Shpanin *et al* [2] for current interruption to further explore the method for producing an annular arc plasma column conveniently and flexibly for various plasma applications. The investigations have focussed upon a device, which can rapidly form and maintain a plasma loop in a controlled manner before releasing the electromagnetically compressed plasma thus propelling the plasma either radially or axially at atmospheric type pressures. Details are given of the unit designed to achieve this along with some preliminary results.

EXPERIMENTAL UNIT

The experimental unit used in the investigations is shown schematically in figure 1. It consisted of a fixed anode, a movable cathode, an inner PTFE cylinder (containing a coil) and an outer PTFE cylinder. An electric arc was formed between the anode and cathode and the current flowing through it also passed through the coil to produce a magnetic field (B field), which interacted with the arc.

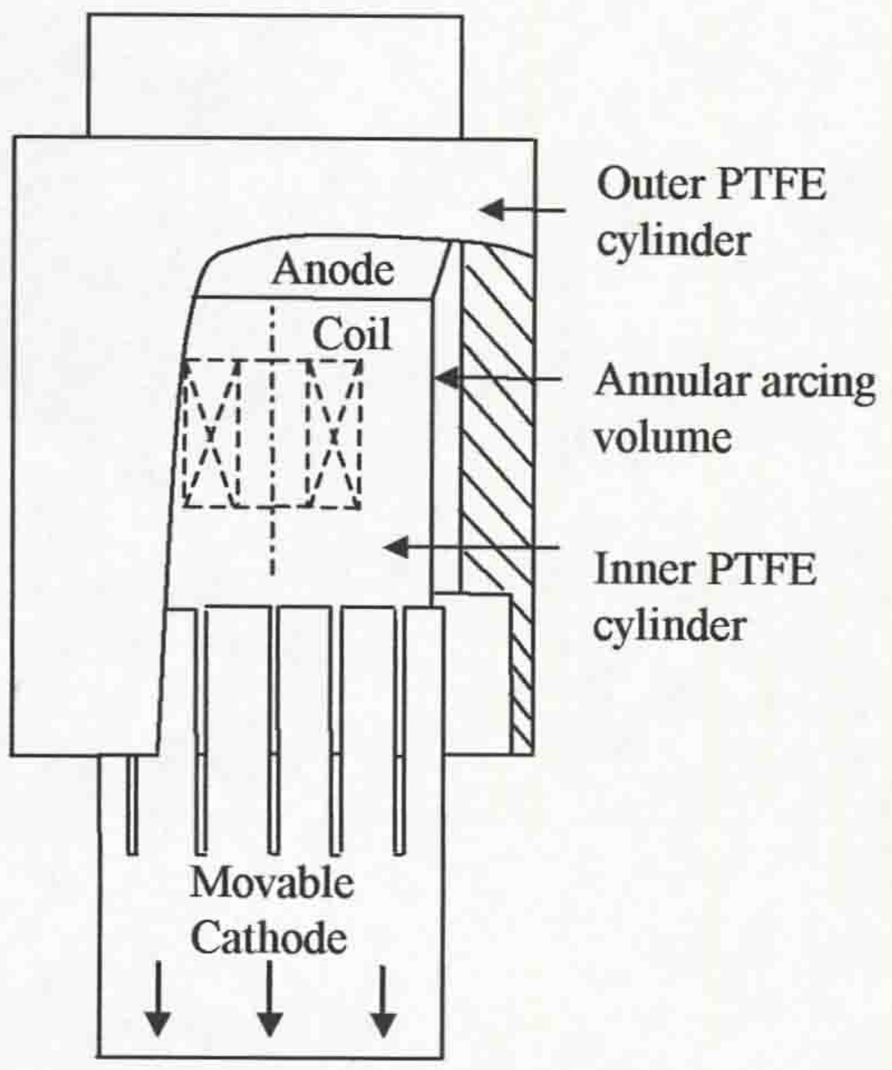

Figure 1. Schematic of experimental unit

The electric arc was formed by separating the anode and cathode connected across a capacitive source producing a quasi-steady current. At a predetermined time after contact separation when the contact gap was sufficiently long an alternating current (50Hz) was switched through the arc and coil. Tests were performed with arc/coil currents of 10-15kA at a frequency of 50Hz.

B FIELD DISTRIBUTION

Central to the present investigation was a need to appreciate the magnitude and form of the B field produced by the embedded coil to which the arc plasma was exposed. This B field was therefore calculated theoretically (Appendix I) and the results confirmed by a few measurements. Examples of radial and axial components (Bx, Bz) of the B field calculated in this manner are given on figures 2b,c as a function of axial distance z and with radial position as parameter.

1 to 4

The results show that the maximum value of Bx occurs at the coil ends (x=56mm, z≈15mm) whilst the maximum value of Bz occurs half way along the coil axis (x=56mm, z≈43mm). The minimum value of Bx occur at z≈43mm, respectively. Thus, there is a spatial shift between the maximum values of Bx, Bz.

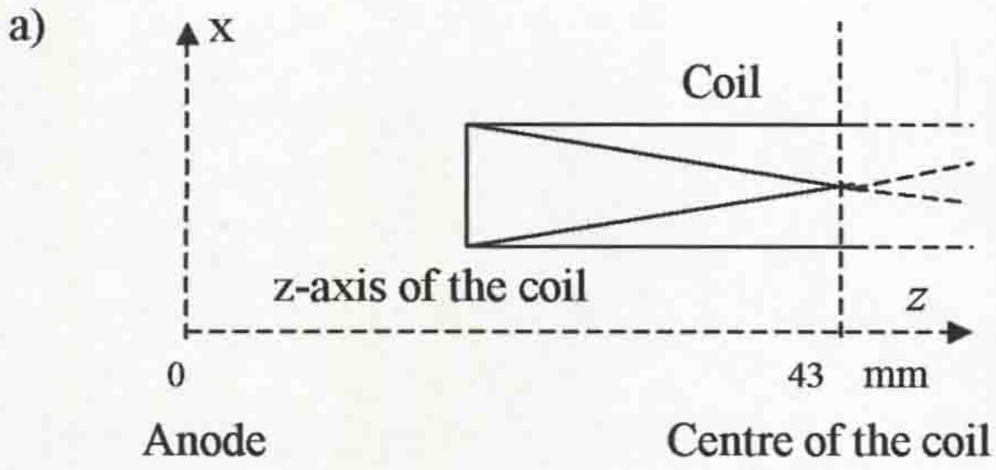

Figure 2. Calculated magnetic field components (values) produced by the coil at various axial (z) and radial (x) positions. a) Coil geometry, b) Radial Bx: axial position with radius as parameter, c) Axial Bz: axial position with radius as parameter, (I=5.3kA, N=16, h=0.05m, a_1=0.02m, a_2=0.038m, Appendix I).

ARC TESTS

The experimental tests were performed with a ~13.2kA ac-arc, of duration 14ms. The electrode gap at arc extinction was ~83mm. The total calculated *B* peak field external to the coil (radius of 56mm, z≈15mm) was 251.35mT, and the resulting Ampere force acting on the arc was 3318N/m. A typical time varying current and voltage record for such a test is shown in figure 3. The operational procedure was to produce initially a quasi-steady current (~2kA) during the flow of which the two contacts (figure 1) were separated and an electric arc formed. After a further period to allow the contact gap to lengthen sufficiently the main alternating current (13.2kA peak) was triggered. This was accompanied by an increased voltage across the arc (figure 3). The current and voltage reduced to zero 14ms after arc initiation following which the voltage across the arc gap reversed to a value determined by the residual charge on the supply capacitor bank.

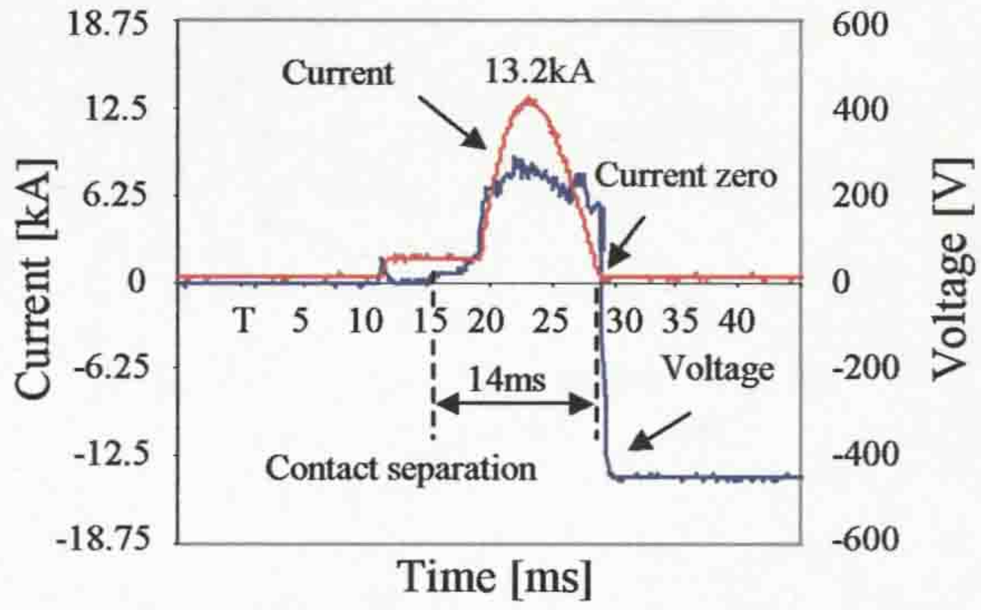

Figure 3. Current and voltage waveforms corresponding to the ac-arc (13.2kA) condition

ARC PLASMA PHOTOGRAPHY

The behaviour of the arc plasma when exposed to the B field produced by the current flowing through the coil (figure1) after contact separation (figure 3) has been explored with high-speed photography [3]. Tests were first performed without the outer PTFE cylinder in order to examine the disposition of the arc plasma column during and after current flow in the presence of the B field. Some typical examples of the high-speed images (7500 fps. 6.6μs exposure) are shown on figure 4. Eight frames are shown during the time interval 12.3-14.4 ms after arc initiation (figure 4), which are taken with two high-speed cameras operated at the same time but at different azimuthal positions situated 120 degrees with respect to the other. Figures 4a,b correspond to about 1.6ms before the current reached zero and when the inter electrode gap was about 70mm (e.g. figure 1 with the main part of the arc exposed to the central part of the B field producing coil, z≈43mm – figure 2). The frames show the arc plasma column inclined almost horizontally between the two electrodes. Figures 4c,d show the arc column ~0.8ms later orientated behind the inner PTFE cylinder. At ~0.8ms later (figure 4e,f), close to the zero of current the arc column appears to be still partially convoluted around the inner PTFE cylinder but is also expanding radially outward. Immediately after current zero (figure 4g,h), the arc plasma appears to have been radially ruptured. Figure 5 shows a frame from a video recording of the arcing event (40ms after current initiation). This confirms the

convoluted nature of the arc column as well as its tendency to expand radially away from the inner PTFE cylinder on the cessation of current flow. The second series of tests were conducted with the outer PTFE cylinder (figure 1) in position.

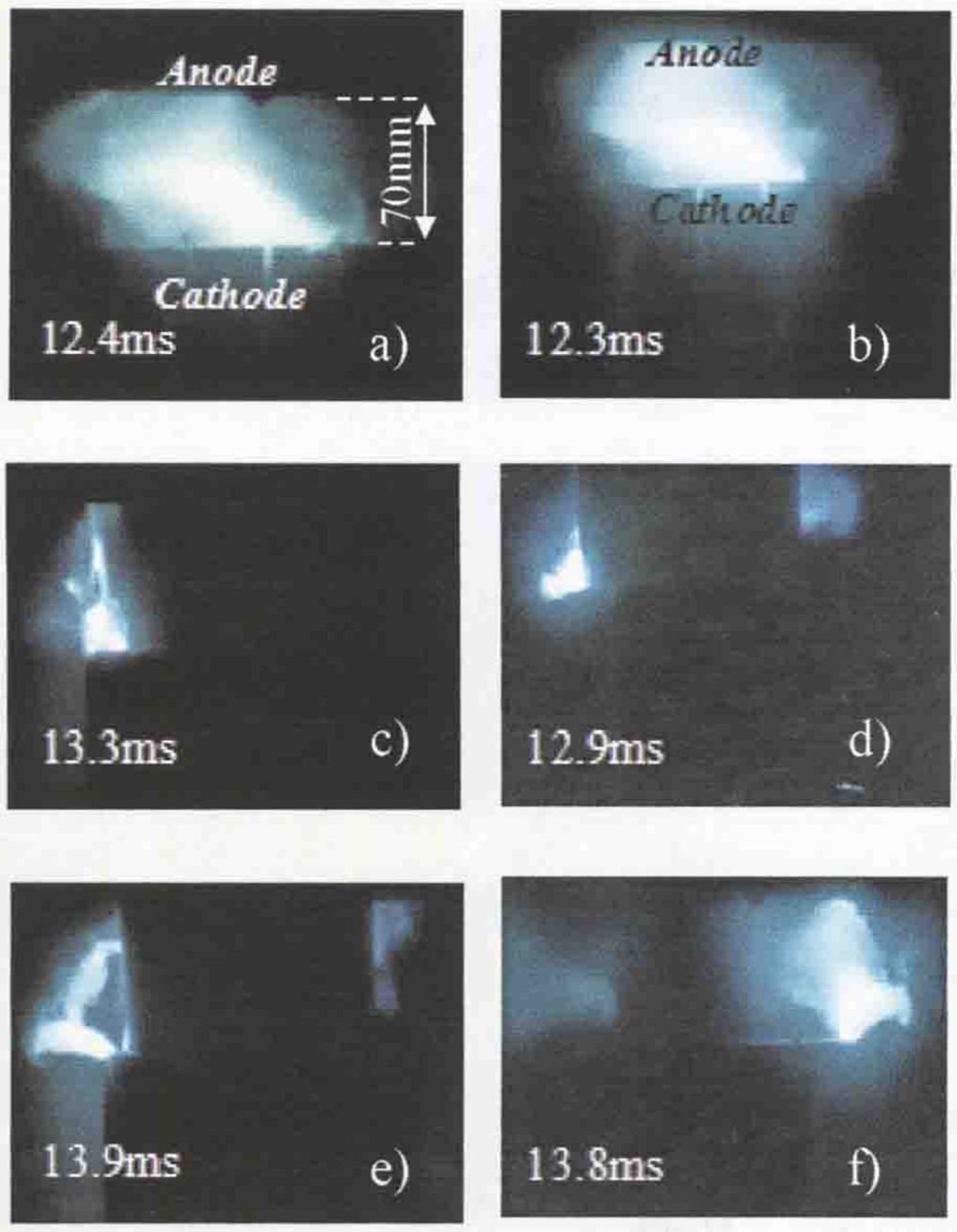

(II) *(I)*

Figure 4. Examples of high-speed photographs of arc in air, at atmospheric pressure, ac 13.2kA, duration of 14ms (framing rate 7500 frames/sec, exposure 6.6μs); (I) Camera 1, (II) Camera 2

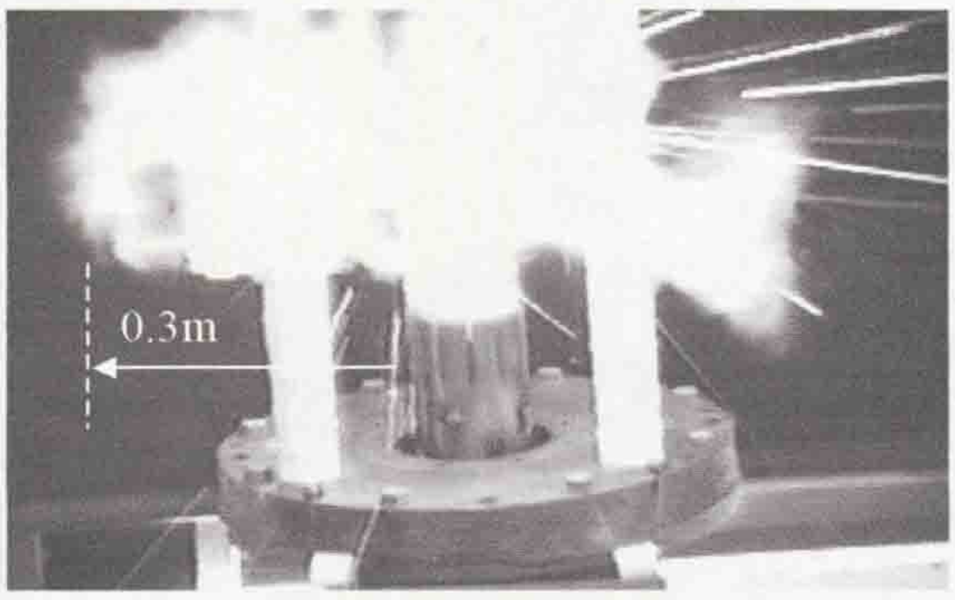

Figure 5. Video frame showing the post arc plasma ring expanding radially after a 10kA peak alternating current: successive frame 40ms from arc initiation (streaks – trajectories of luminous particles)

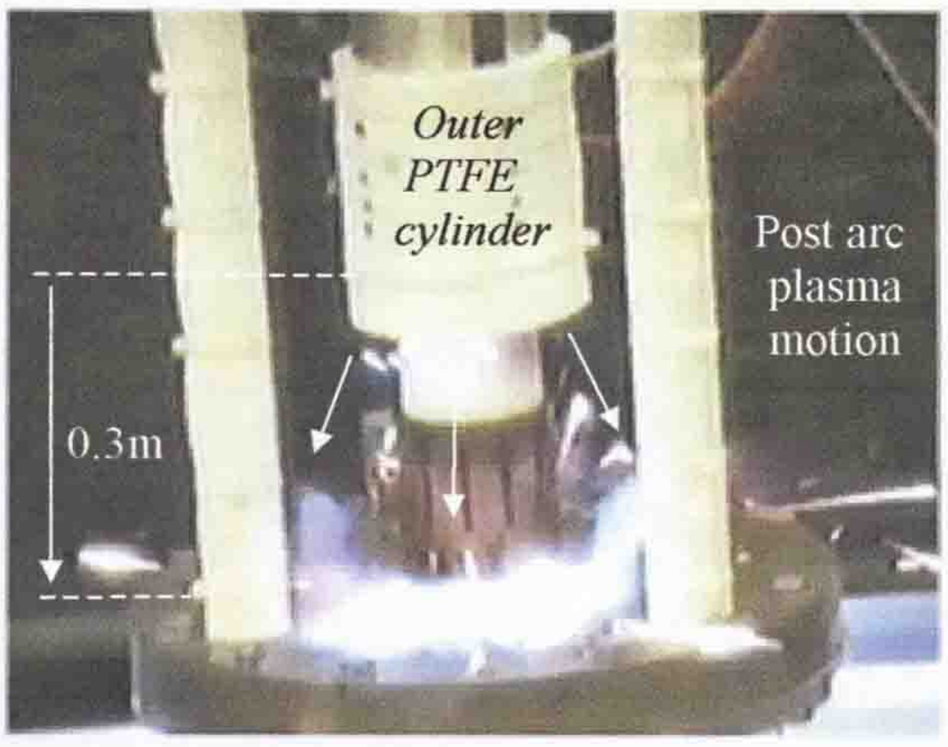

Figure 6. Axial plasma propulsion (40ms after arc initiation)

Video frames (figure 6) were taken after a 10kA alternating current arc from which can be seen an annular plasma ring displaced well away from the exit of the outer cylinder and convoluted around the cylindrical base of the cathode. This is indicative of the extent to which the plasma annulus has been driven axially from the original arcing volume. The arc plasma in this case was not visible until the movable cathode had cleared the end of the outer PTFE cylinder.

DISCUSSION

The arc plasma behaviour (figures 4, 5, 6) may be explained qualitatively in terms of the B field configurations of figure 2. B_x being a maximum at the coil end leads to the longitudinal arc formed on contact separation rotating due to the azimuthal Ampere force ($I_z \times B_x$), (figure 7). As the contact gap lengthens, the arc column extends into the mid coil region where B_x tends to zero but B_z is a maximum. The rotation of the axial arc constitutes an azimuthal current component (I_o), which interacts with B_z to produce a radial Ampere force ($I_o \times B_z$) thus confining the arc around the inner PTFE cylinder (figure 7). A further lengthening of the contact gap leads to the added arc length extending into the high Bx region at the other extremity of the coil where Bx is maximal but in the opposite sense to the first coil end. Consequently, the azimuthal Ampere force in this region ($I_z \times B_x$) rotates the arc section exposed to it in the opposite sense to the first arc section so distorting the central section of the arc column into a convolute, tightly wound onto the inner PTFE, (fig. 7). Following the cessation of current flow and in the absence of an outer PTFE cylinder, the relaxation of the radial Ampere force leads to a rapid, outward expansion radially of the arc loop (figures 4 and 5). This may be regarded as being caused by the excessive plasma pressure which is no longer balanced by the electromagnetic forces that have been acting during the arc loop formation (but becoming smaller as the current reduces).

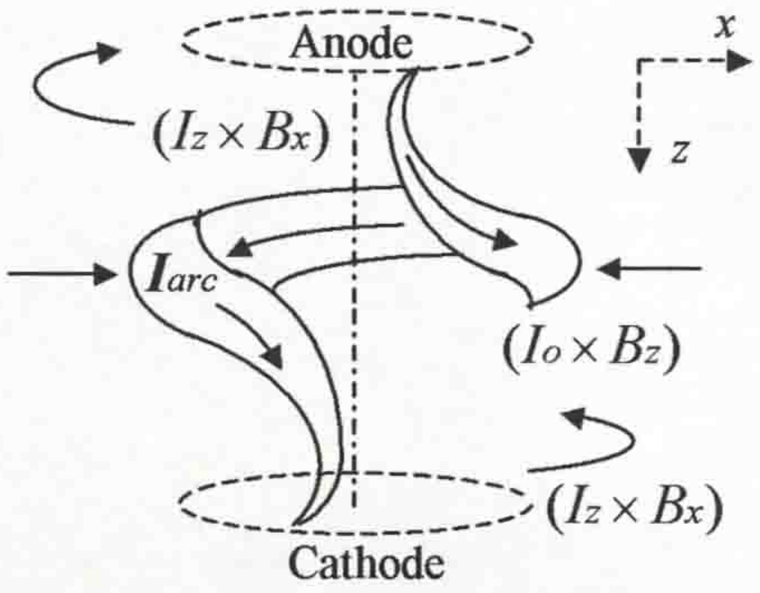

Figure 7. Schematic of annular arc formation by B field distribution

Estimates of the rate at which the plasma loop initially expands radially from the frames of figure 4 yields an approximate value of 75m/s and later (figure 5) as 12m/s when the loop radial distance is 0.3m from the test head. In the presence of an outer PTFE cylinder the rapid radial expansion of the plasma loop is constrained by the inner wall of the outer PTFE cylinder, so trapping the energy within the annular volume between the inner and outer PTFE cylinders. Subsequently, when the moving cathode exits from this annular gap the trapped plasma loop expands axially, being driven along the cathode stem as observed experimentally on figure 6. The rate of axial displacement of the loop is 17m/s being 0.3m from the test head, (figure 6). These two manifestations - with and without the outer PTFE cylinder produce respectively a means of propelling plasma either axially or radially providing a good degree of flexibility for future possible applications.

APPENDIX I
B FIELD COMPUTATIONS

Figure A.1 shows a schematic of an annular section across the B field-producing coil of the arc plasma device. The inner and outer radii of the coil are a_1 and a_2 respectively, and its length is h. The radial and axial B field components (Bx, Bz) produced by the entire coil at a point x_0, z_0 may be calculated by integrating the fields from annular elements, each of thickness dz over the coil length h using equations (1) – radial B field, (2) – axial B field and (3) – total B field [3]. The geometry is azimuthally symmetrical.

$$B_x = \frac{\mu NI(a_2^2 + a_1 a_2 + a_1^2)}{4h} \times \times \int_0^h \left\{ \frac{x_0 (z_0 - z)}{\left[z_0^2 - 2z_0 z + z^2 + {x_0}^2 \right]^{\frac{5}{2}}} \right\} dz \qquad (1)$$

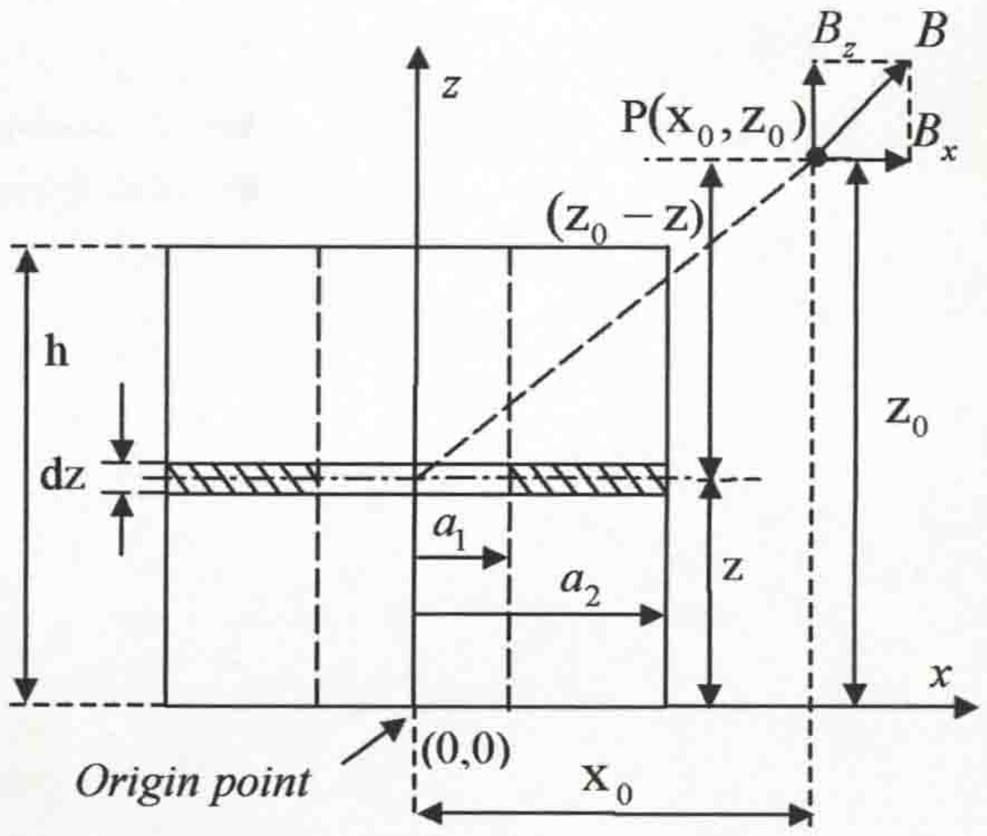

Figure A.1 Schematic of a radial element across the B field-producing coil

$$B_z = \frac{\mu NI(a_2^2 + a_1 a_2 + a_1^2)}{6h} \times \times \int_0^h \left\{ \frac{(z_0^2 - 2z_0 z + z^2)}{\left[z_0^2 - 2z_0 z + z^2 + {x_0}^2 \right]^{\frac{5}{2}}} - \frac{x_0^2}{2\left[z_0^2 - 2z_0 z + z^2 + {x_0}^2 \right]^{\frac{5}{2}}} \right\} dz \qquad (2)$$

$$B = \sqrt{\left(B_x^2 + B_z^2 \right)} \qquad (3)$$

Where, μ=permeability of free space (1.7×10^{-7} H/m), N=number of coil turns, I=coil current, z= height of an individual layer (e.g. from 0 to h).

REFERENCES

[1] Ennis M.G., Wood J.K., Spencer J.W., Turner D.R., Jones G.R, Coventry P, "Current limiting properties of an expanding helical arc", IEE, Proc.-Sci. Meas. Technol., Vol. 142, No 3, pp201-204 1995.

[2] Shpanin L.M., Kidman M.C., Humphries J.W., Spencer J.W., Jones G.J., " The interaction of high current electric arcs with spatially varying cross magnetic fields", Proc. of XVth Int. Conf. on Gas Discharges and their Applications, pp183-186, 2004.

[3] Shpanin L.M., "Electromagnetic arc control for current interruption" PhD thesis, Univ. of Liverpool, 2006.

APPENDIX II

Derivation of expressions for magnetic field (in term of Cartesian coordinates)

Relationship between the radial (B'_x) and axial (B'_z) magnetic fields components (rectangular coordinate) and B_r and B_θ field components (spherical coordinate) is presented on figure II.1 for the complete solenoid at point ***P(xo, zo)***.

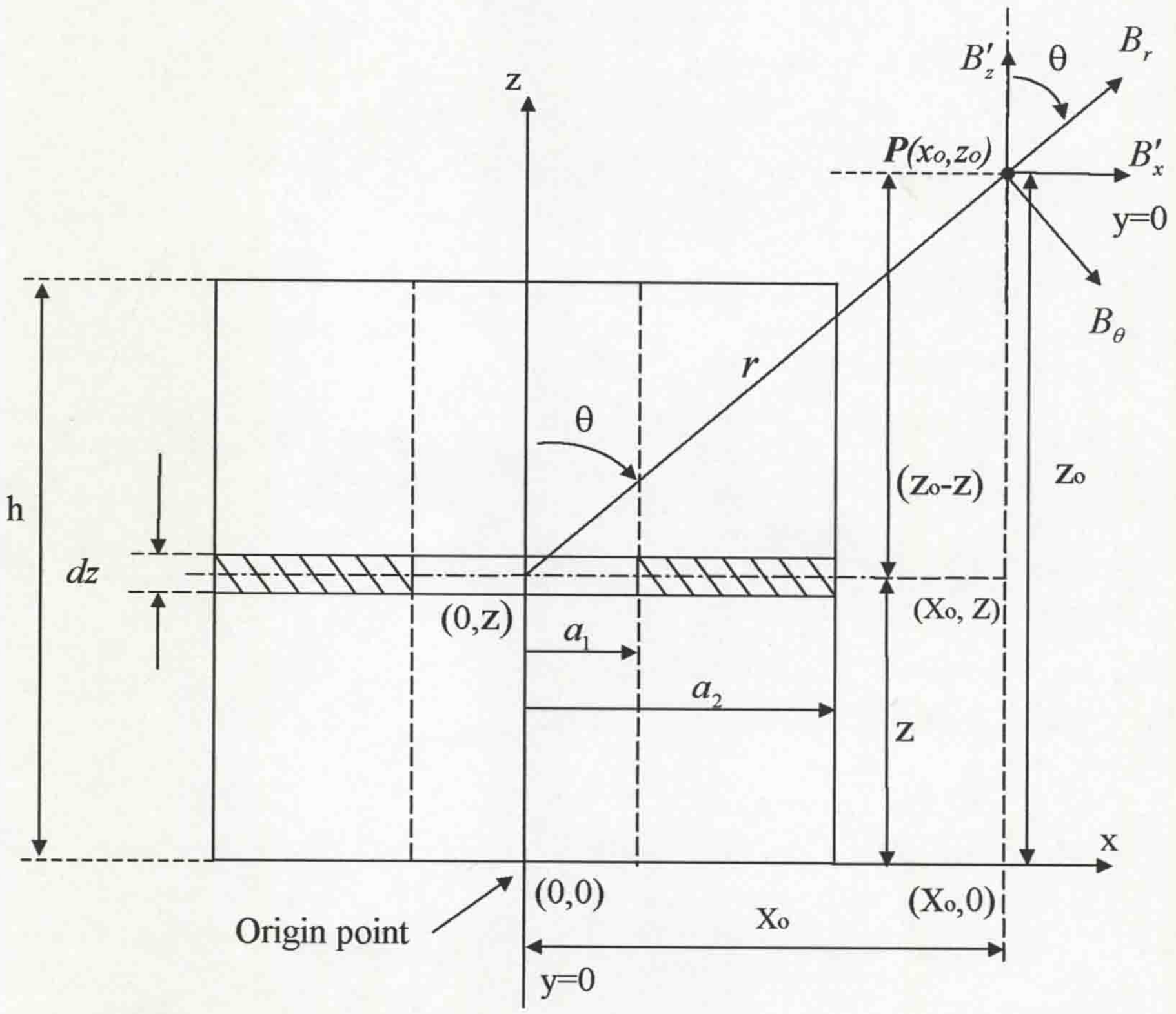

Figure II.1 Magnetic field due to a radial element of thickness *dz* of a solenoid of length h, inner a_1 and outer a_2 radiuses (Cartesian coordinates)

Let z be height of the layer with coordinate (0,z) and the (0,0) coordinate is an origin point at bottom of the solenoid.

For the point ***P(xo,zo)***:

$$r^2 = x_0^2 + (z_0 - z)^2 \tag{II.1}$$

and

$$\sin\theta = \frac{x_0}{r} \tag{II.2}$$

$$\cos\theta = \frac{(z_0 - z)}{r} \tag{II.3}$$

Consider the elemental layer at Z, resolving B_r and B_θ components in the rectangular directions gives the components of the total B field due to the layer as

$$\Delta B'_z = B_r \cos\theta - B_\theta \sin\theta \tag{II.4}$$

$$\Delta B'_x = B_r \sin\theta + B_\theta \cos\theta \tag{II.5}$$

Where B_r and B_θ are given by equations (3.17) and (3.18) respectively (**chapter 3, section 3.4.1**)

Then

$$\begin{aligned}
B'_z &= \frac{\mu NI(a_2^2 + a_1 a_2 + a_1^2)}{6r^3 h} dz \cos\theta \times \cos\theta - \\
&- \frac{\mu NI(a_2^2 + a_1 a_2 + a_1^2)}{12r^3 h} dz \sin\theta \times \sin\theta = \\
&= \frac{\mu NI(a_2^2 + a_1 a_2 + a_1^2)}{6h} dz \times \frac{1}{r^3}\left(\cos^2\theta - \frac{\sin^2\theta}{2}\right) = \\
&= \frac{\mu NI(a_2^2 + a_1 a_2 + a_1^2)}{6h} dz \times \left(\frac{(z_0 - z)^2}{r^5} - \frac{x_0^2}{2r^5}\right) = \\
&= \frac{\mu NI(a_2^2 + a_1 a_2 + a_1^2)}{6h} dz \times \left\{\frac{(z_0 - z)^2}{\left[(z_0 - z)^2 + {x_0}^2\right]^{\frac{5}{2}}} - \frac{x_0^2}{2\left[(z_0 - z)^2 + {x_0}^2\right]^{\frac{5}{2}}}\right\}
\end{aligned} \tag{II.6}$$

Integrating over the length of the coil (h), the total value of B_z in Tesla at point $P(x_o,z_o)$ on figure II.1 is:

$$\begin{aligned}
B_z &= \frac{\mu NI(a_2^2 + a_1 a_2 + a_1^2)}{6h} \times \\
&\times \int_0^h \left\{\frac{(z_0^2 - 2z_0 z + z^2)}{\left[z_0^2 - 2z_0 z + z^2 + {x_0}^2\right]^{\frac{5}{2}}} - \frac{x_0^2}{2\left[z_0^2 - 2z_0 z + z^2 + {x_0}^2\right]^{\frac{5}{2}}}\right\} dz
\end{aligned} \tag{II.7}$$

and

$$B'_x = \frac{\mu NI(a_2^2 + a_1 a_2 + a_1^2)}{6r^3 h} dz \cos\theta \times \sin\theta +$$

$$+ \frac{\mu NI(a_2^2 + a_1 a_2 + a_1^2)}{12r^3 h} dz \sin\theta \times \cos\theta =$$

$$= \frac{\mu NI(a_2^2 + a_1 a_2 + a_1^2)}{6h} dz \times \frac{1}{r^3}\left(\cos\theta \sin\theta + \frac{\sin\theta\cos\theta}{2}\right) = \qquad \text{(II.8)}$$

$$= \frac{\mu NI(a_2^2 + a_1 a_2 + a_1^2)}{4h} dz \times \left(\frac{x_0(z_0 - z)}{r^5}\right) =$$

$$= \frac{\mu NI(a_2^2 + a_1 a_2 + a_1^2)}{4h} dz \times \left\{\frac{x_0(z_0 - z)}{\left[(z_0 - z)^2 + {x_0}^2\right]^{\frac{5}{2}}}\right\}$$

Thus the total value of B_x in Tesla at point ***P(xo,zo)*** on figure II.1 is:

$$B_x = \frac{\mu NI(a_2^2 + a_1 a_2 + a_1^2)}{4h} \times$$

$$\times \int_0^h \left\{\frac{x_0(z_0 - z)}{\left[z_0^2 - 2z_0 z + z^2 + {x_0}^2\right]^{\frac{5}{2}}}\right\} dz \qquad \text{(II.9)}$$

APPENDIX III

General shape of magnetic field distribution due to a coil

The general shape of magnetic field distribution due to a coil is sketched in figure III.1 (**section 2.4.1.1**, magnetic field measurements).

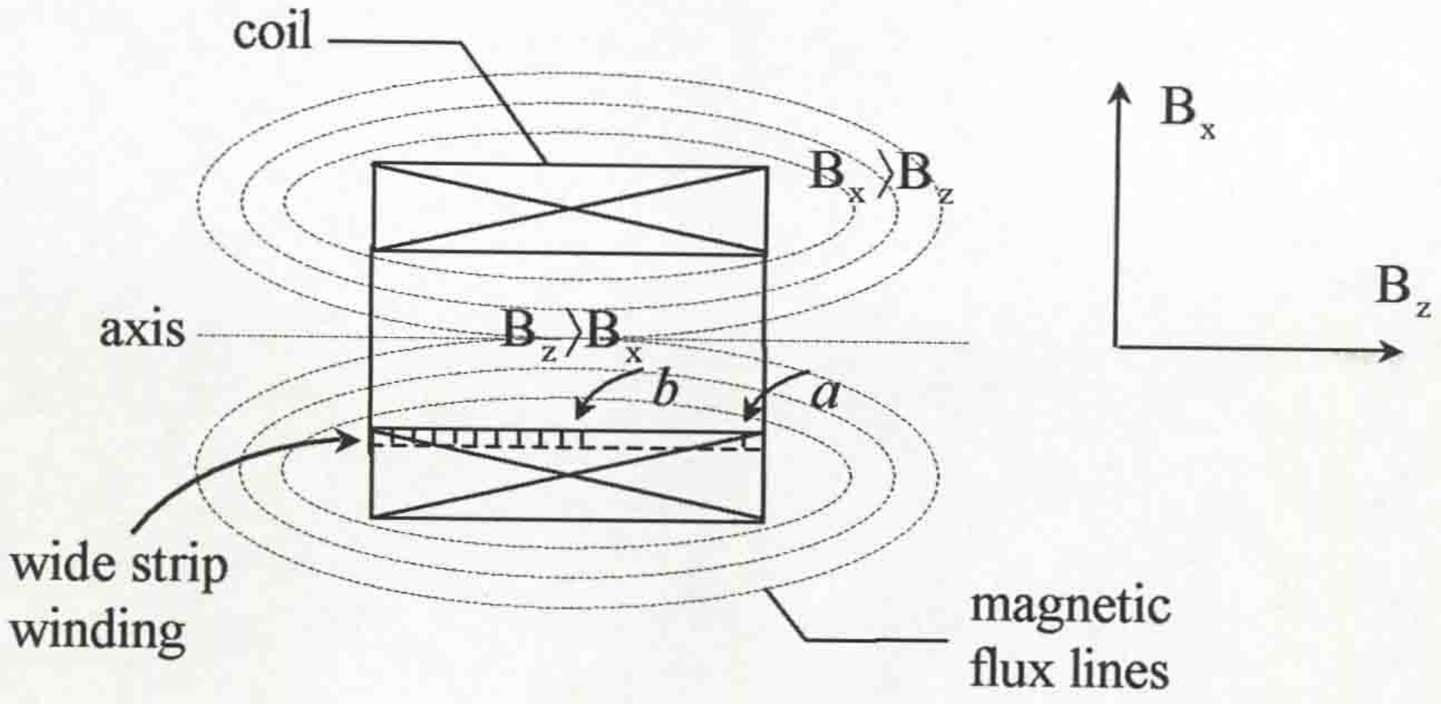

Figure III.1 General magnetic field distribution within a short coil

The magnetic field of the coil has an axial B_z and a radial B_x components which are produced by the coil. Their distributions are not uniform within and around the coil. The magnetic field of the coil has no component in the circumferential direction since the coil is cylindrically symmetrical along the axis of the coil.

The non-uniform distribution of the current flowing trough the foil coil influences the magnetic field shape of the coil using a wide strip (foil) having a cylindrical shape of winding (fig. III.1). A typical example sketched above (fig. III.1) demonstrates a short planar cylindrical coil having a wide strip (rectangular cross-section) winding. The B_z field components are much greater then B_x components within the coil (in the centre). In addition, B_z components external to a coil are still greater then B_x components at the middle of the coil, but they are much weaker then inside of the coil. At the ends of the coil the radial components of the B field is higher then axial field components. The wide strip may be presented as a number of elemental coils contained inside this strip. Two elemental coils of the strip ("a" and "b") showing in figure III.1 are situated within the coil at the end of the coil (elemental coil "a") and at the middle of the coil (elemental coil "b"). The important point is that an elemental coil "b" has a greater flux linkage than elemental coil "a"

because of non-uniform B field distribution (fig. III.1). Thus the inductance of "b" is greater than that of "a" (straight relation between the inductance and magnetic field, (Cullwick, 1966)). The elemental coils "a" and "b" (and all other elemental coils in the wide strip turn, fig. III.1) are in parallel in which the equivalent circuit is thus as

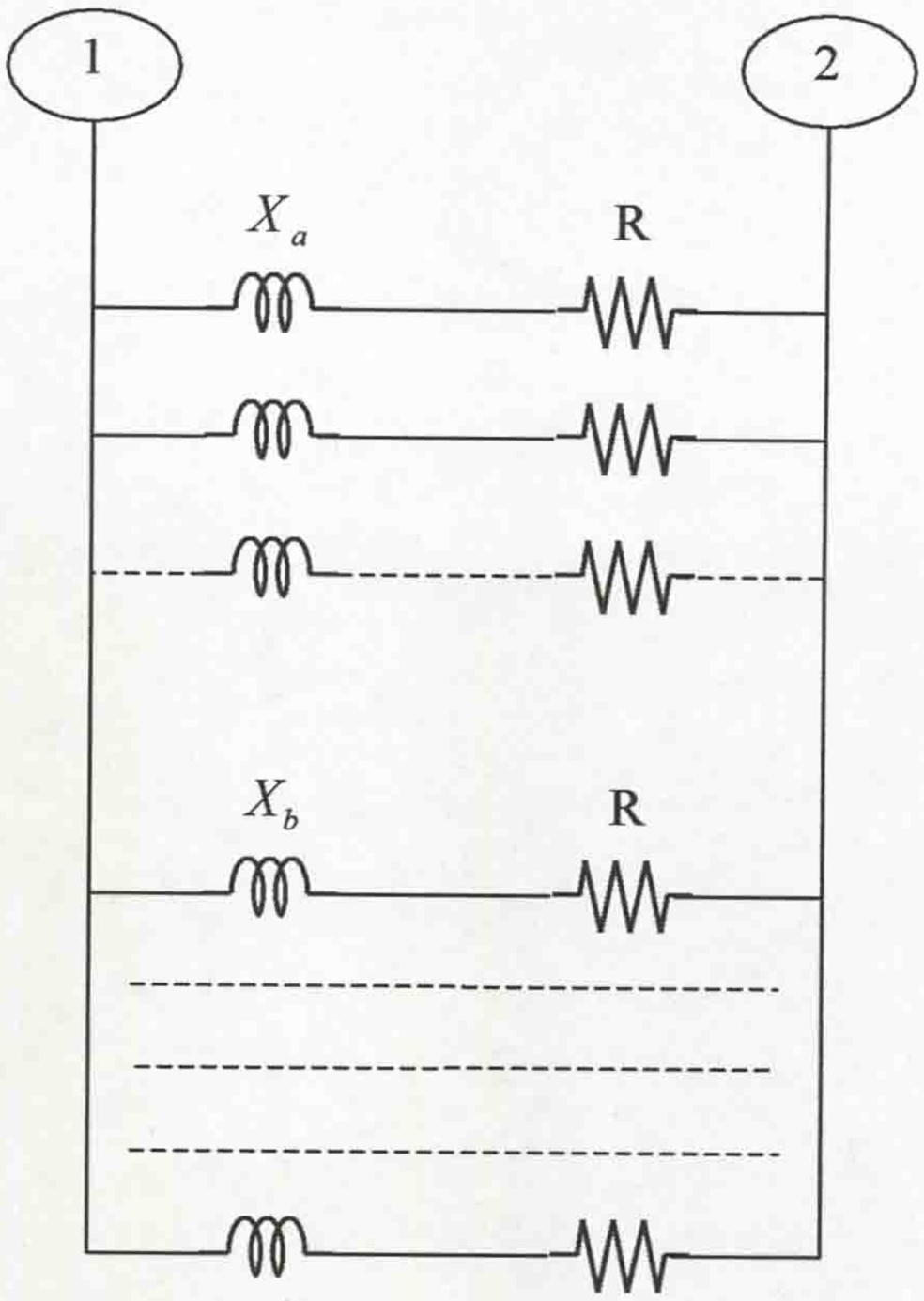

Figure III.2 Equivalent circuit of the elemental coils within a wide strip turn

presented in figure III.2.

The active resistance R of the coil is the same for each elemental coil. However, the reactive resistances X for each branch (fig. III.2) are different $X_b \rangle X_a$. With the voltage between points 1 and 2 to each of the coil (the same for each parallel branch) the current $I_a \rangle I_b$ (opposite relation between the inductance (resistance) and current, (Cullwick, 1966)). Therefore, the magnetic fields at the ends of the coil are increased due to the non-uniform current distribution in the coil (straight relation between the current in the coil and B field, producing coil (Cullwick, 1966)). Furthermore, there will also be a phase difference between the current and magnetic field, which is dependent on the inductance of the coil.

APPENDIX IV

Sketches of mechanical details of the arc control test head

The following pages show the sketches of mechanical details of the arc control test head related to work presented in this report:

1. Arc control test head assembly
2. Frame of the coil
3. Cap of the coil
4. Insulating Cylinder
5. Electrode Support
6. Ring-electrode (Anode & Cathode)

Centre for Intelligent Monitoring Systems

THE UNIVERSITY *of* LIVERPOOL

Department of Electrical Engineering and Electronics

Brownlow Hill
Liverpool
L69 3GJ

Telephone 794 4547

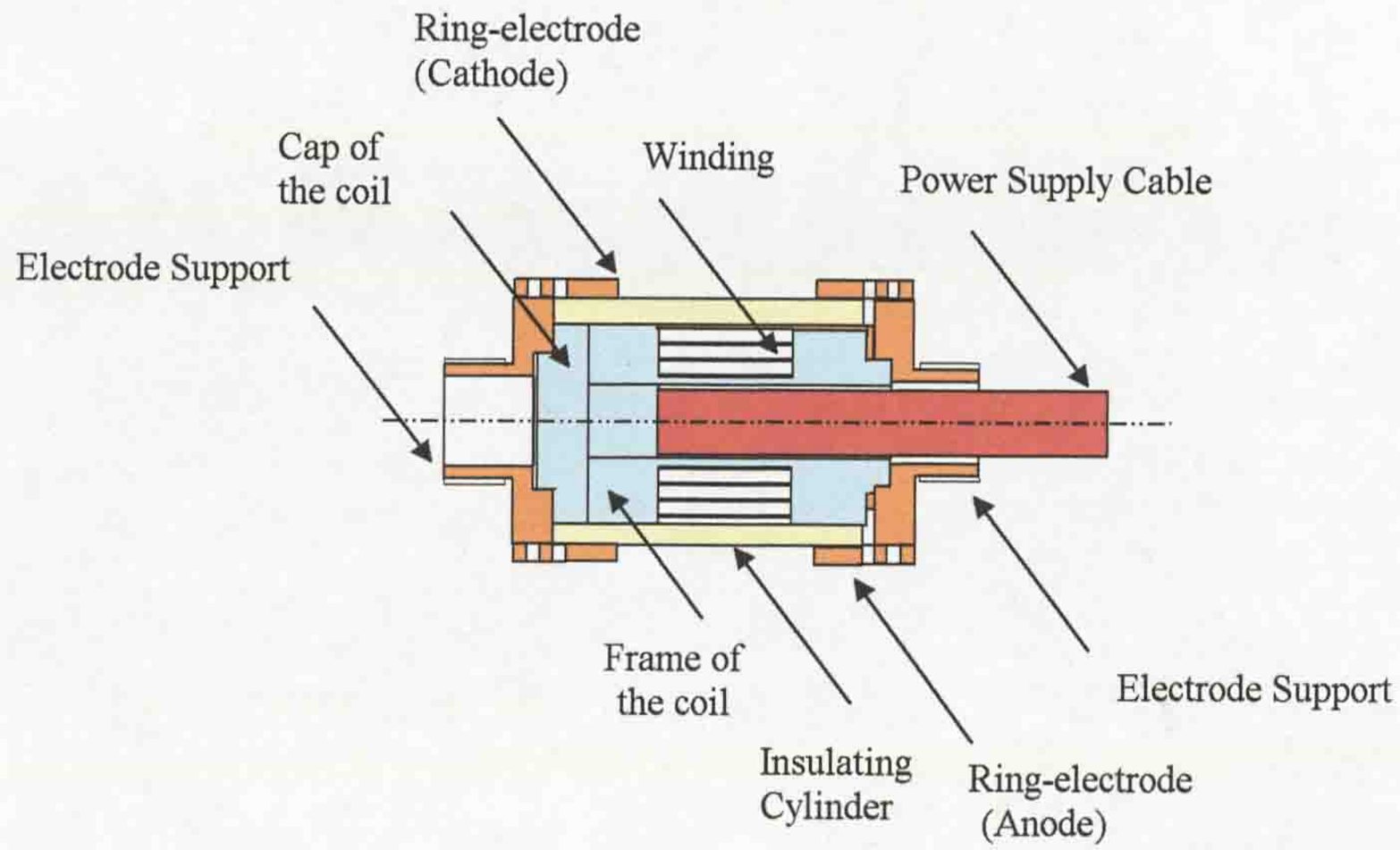

Grey PTFE (Coil)

Copper

White PTFE

Colour-scale designating different materials

NOTE

ALL DIMENSIONS IN MILLIMETRES
REMOVE ALL BURRS AND SHARP EDGES

SCALE	GENERAL TOLERANCES	TITLE	MATERIAL	PROJECTION	DRAWN	DATE	QTY
1- 4	± .2mm	Arc control test head	Various	3rd Angle	L. Shpanin	Aug 05	1

Centre for Intelligent Monitoring Systems

THE UNIVERSITY
of LIVERPOOL

Department of Electrical Engineering and Electronics

Brownlow Hill
Liverpool
L69 3GJ

Telephone 794 4547

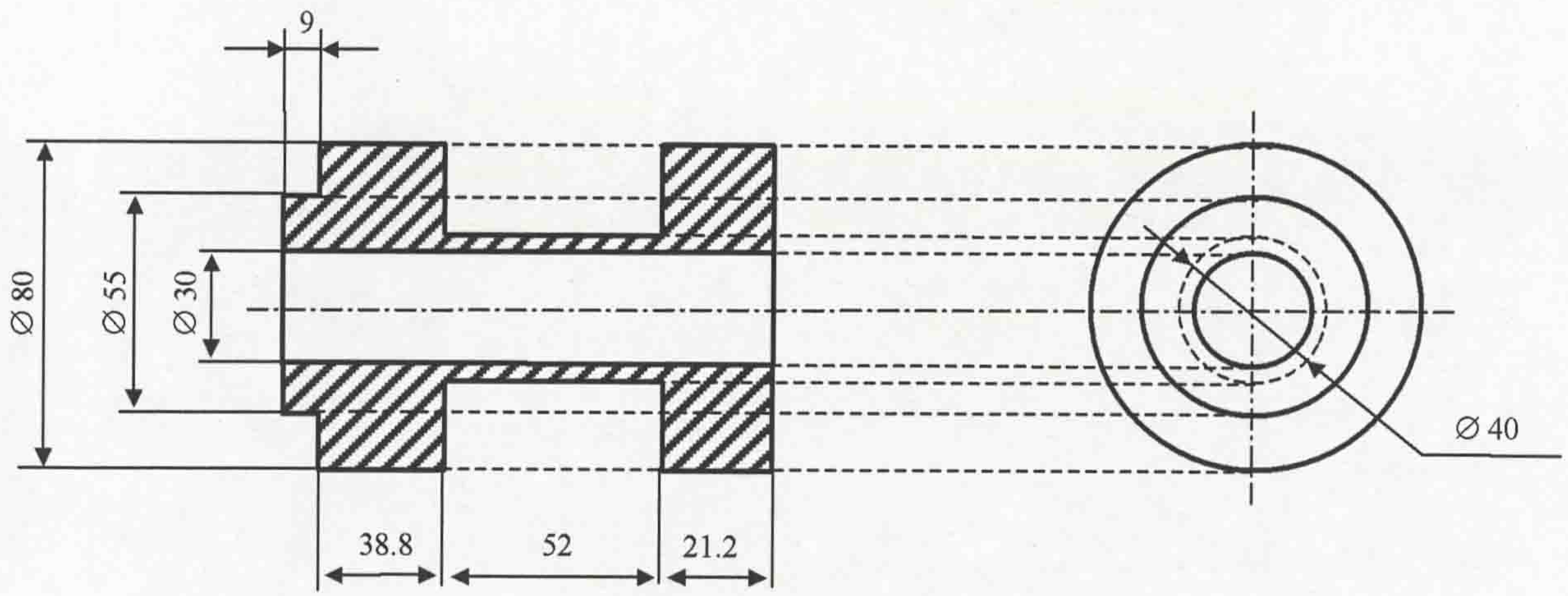

NOTE

ALL DIMENSIONS IN MILLIMETRES
REMOVE ALL BURRS AND SHARP EDGES

SCALE	GENERAL TOLERANCES	TITLE	MATERIAL	PROJECTION	DRAWN	DATE	QTY
1- 2	± .2mm	Frame of the coil	PTFE	3rd Angle	N. Telfer	Aug 05	1

Centre for Intelligent Monitoring Systems

THE UNIVERSITY
of LIVERPOOL

Department of Electrical Engineering and Electronics

Brownlow Hill
Liverpool
L69 3GJ

Telephone 794 4547

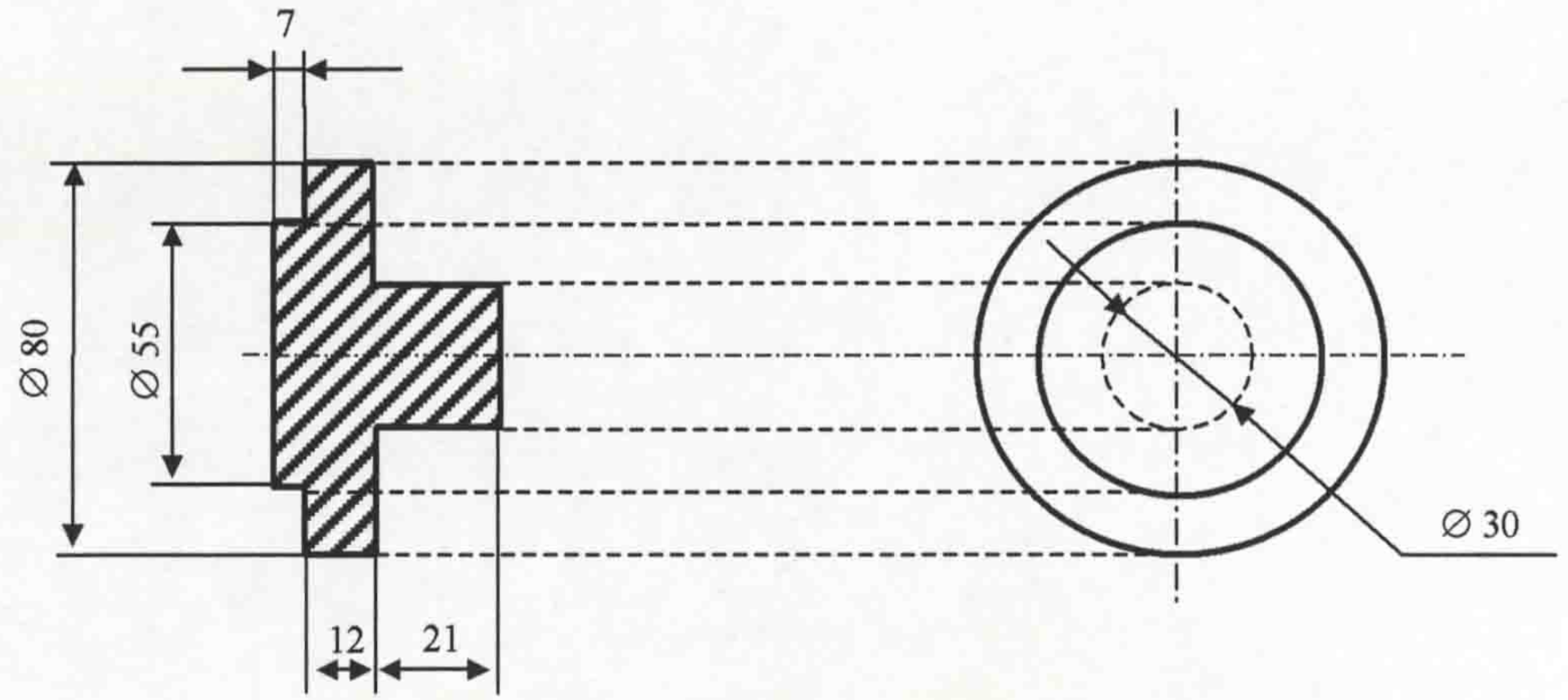

NOTE

ALL DIMENSIONS IN MILLIMETRES
REMOVE ALL BURRS AND SHARP EDGES

SCALE	GENERAL TOLERANCES	TITLE	MATERIAL	PROJECTION	DRAWN	DATE	QTY
1- 2	± .2mm	Cap of the coil	PTFE	3rd Angle	N. Telfer	Aug 05	1

Centre for Intelligent Monitoring Systems

THE UNIVERSITY *of* LIVERPOOL

Department of Electrical Engineering and Electronics

Brownlow Hill
Liverpool
L69 3GJ

Telephone 794 4547

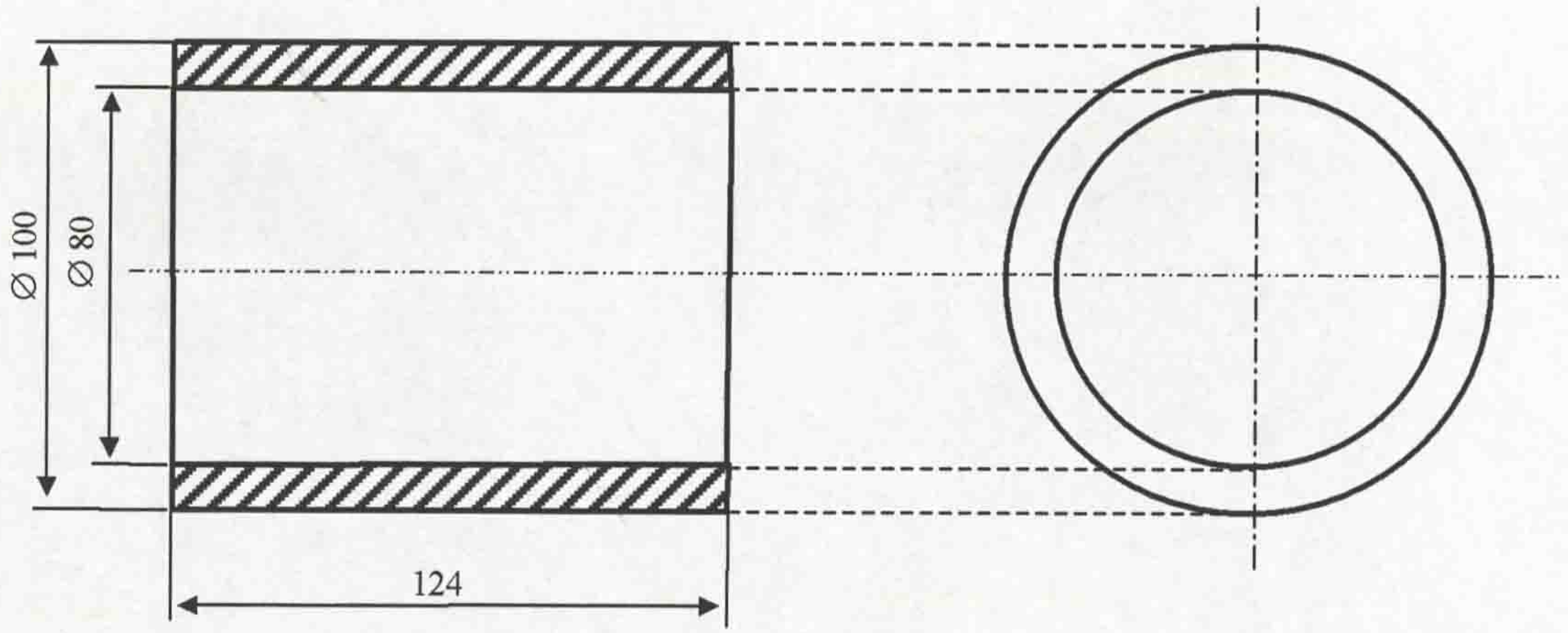

NOTE

ALL DIMENSIONS IN MILLIMETRES
REMOVE ALL BURRS AND SHARP EDGES

SCALE	GENERAL TOLERANCES	TITLE	MATERIAL	PROJECTION	DRAWN	DATE	QTY
1-2	± .2mm	Insulating Cylinder	PTFE	3rd Angle	N. Telfer	Aug 05	1

Centre for Intelligent Monitoring Systems

THE UNIVERSITY *of* LIVERPOOL

Department of Electrical Engineering and Electronics

Brownlow Hill
Liverpool
L69 3GJ

Telephone 794 4547

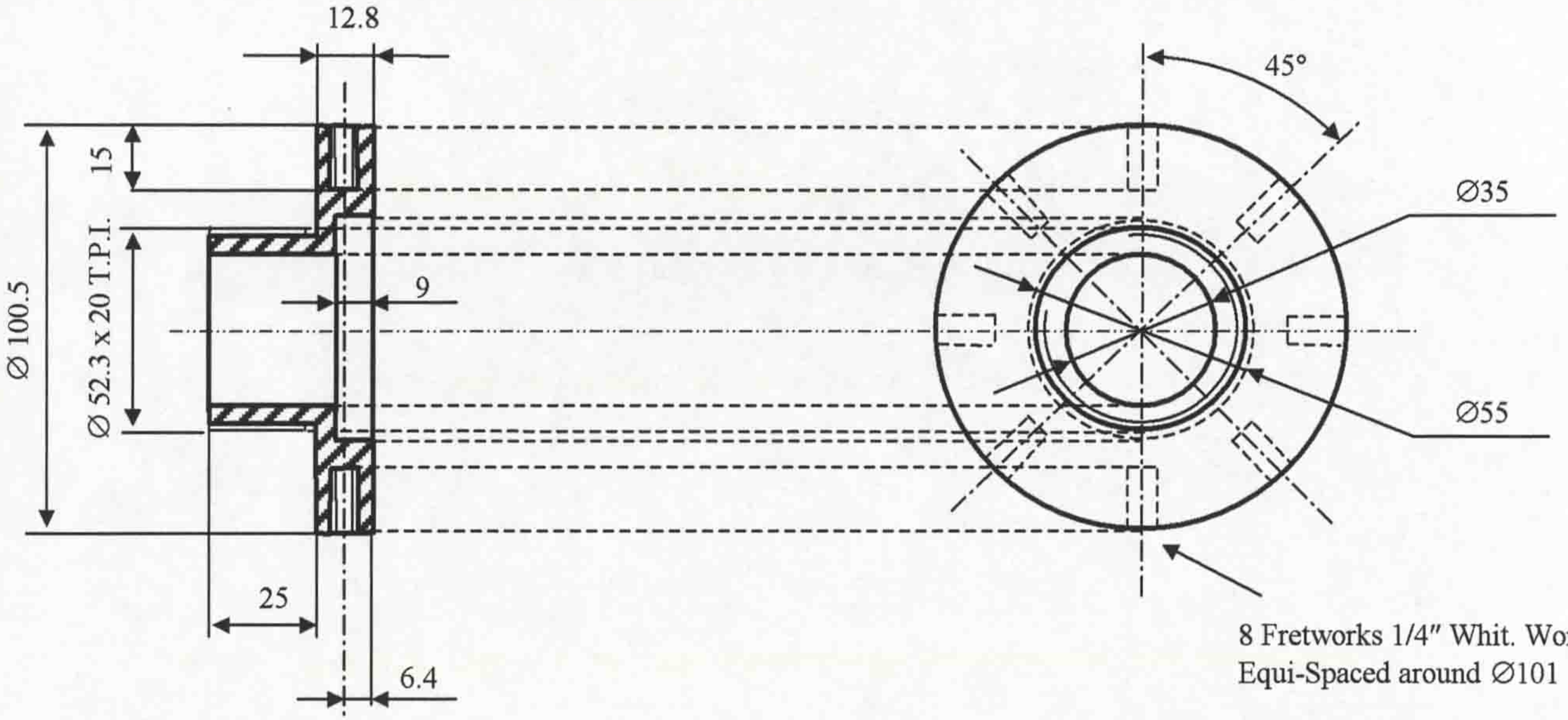

NOTE

ALL DIMENSIONS IN MILLIMETRES
REMOVE ALL BURRS AND SHARP EDGES

SCALE	GENERAL TOLERANCES	TITLE	MATERIAL	PROJECTION	DRAWN	DATE	QTY
1- 2	± .2mm	Electrode support	Copper	3rd Angle	N. Telfer	Aug 05	2

Centre for Intelligent Monitoring Systems

THE UNIVERSITY *of* LIVERPOOL

Department of Electrical Engineering and Electronics

Brownlow Hill
Liverpool
L69 3GJ

Telephone 794 4547

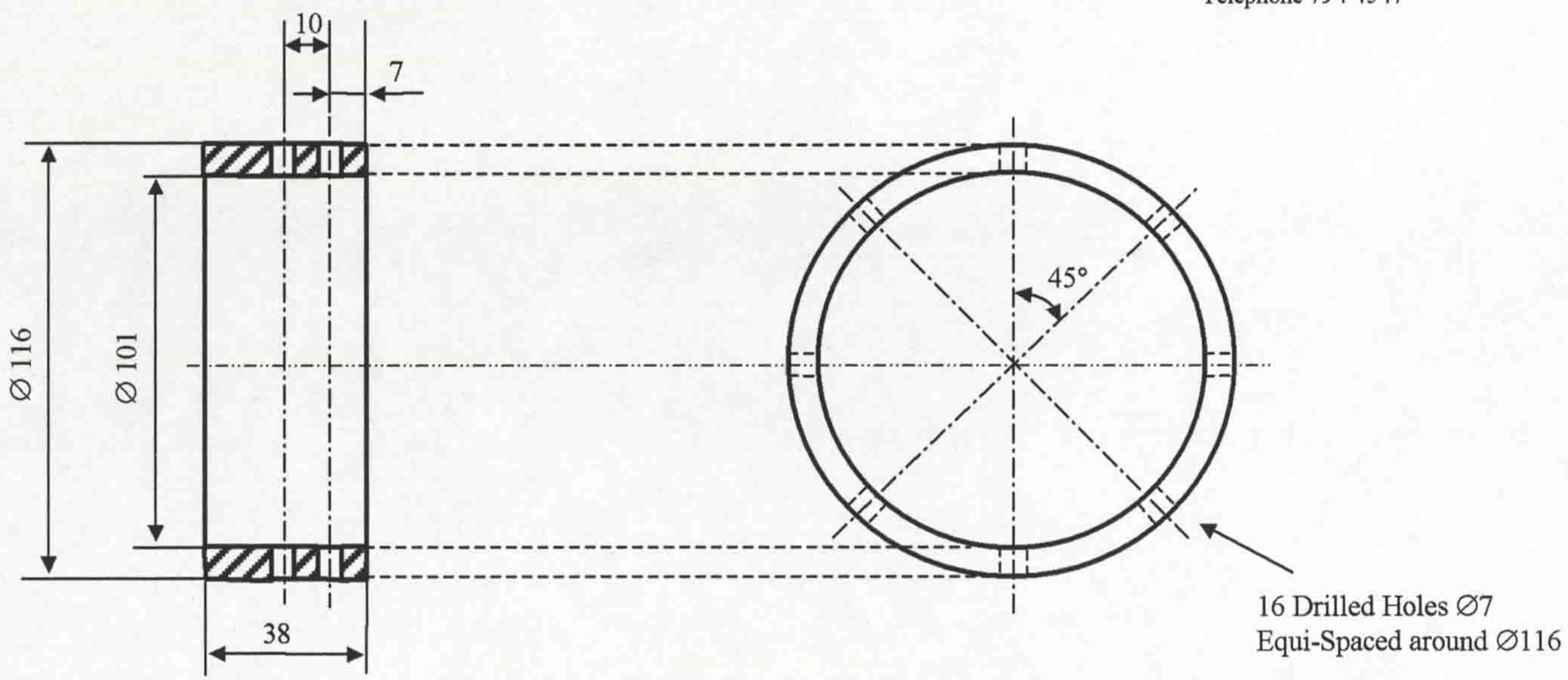

NOTE

ALL DIMENSIONS IN MILLIMETRES
REMOVE ALL BURRS AND SHARP EDGES

SCALE	GENERAL TOLERANCES	TITLE	MATERIAL	PROJECTION	DRAWN	DATE	QTY
1-2	± .2mm	Ring-electrode	Copper	3rd Angle	N. Telfer	Aug 05	2

APPENDIX V

List of sketches following mechanical details of current interrupters

The list of sketches following mechanical details of the prototype rotary arc interrupter (current interruption test head) related to work described in this report is presented:

1. Prototype interrupter test head assembly
2. Electrode Support Strut (movable rod)
3. Electrode Spring (Cathode)
4. Insulating Cylinder 1
5. Cap of the coil
6. Insulating Collar
7. Electrode-Anode (Locking contact ring)
8. Frame of the coil
9. Insulating Cylinder 2

Additional details designed for the test head operation:

1. Column Strut (Support)
2. Locking Nut (Support)
3. Collar (Interface tube adjustment)
4. Insulator Sleeve (Insulated section)
5. Spacer (Insulated section)
6. Insulator Cap (Insulated section)

Centre for Intelligent Monitoring Systems

THE UNIVERSITY *of* LIVERPOOL

Department of Electrical Engineering and Electronics

Brownlow Hill
Liverpool
L69 3GJ

Telephone 794 4547

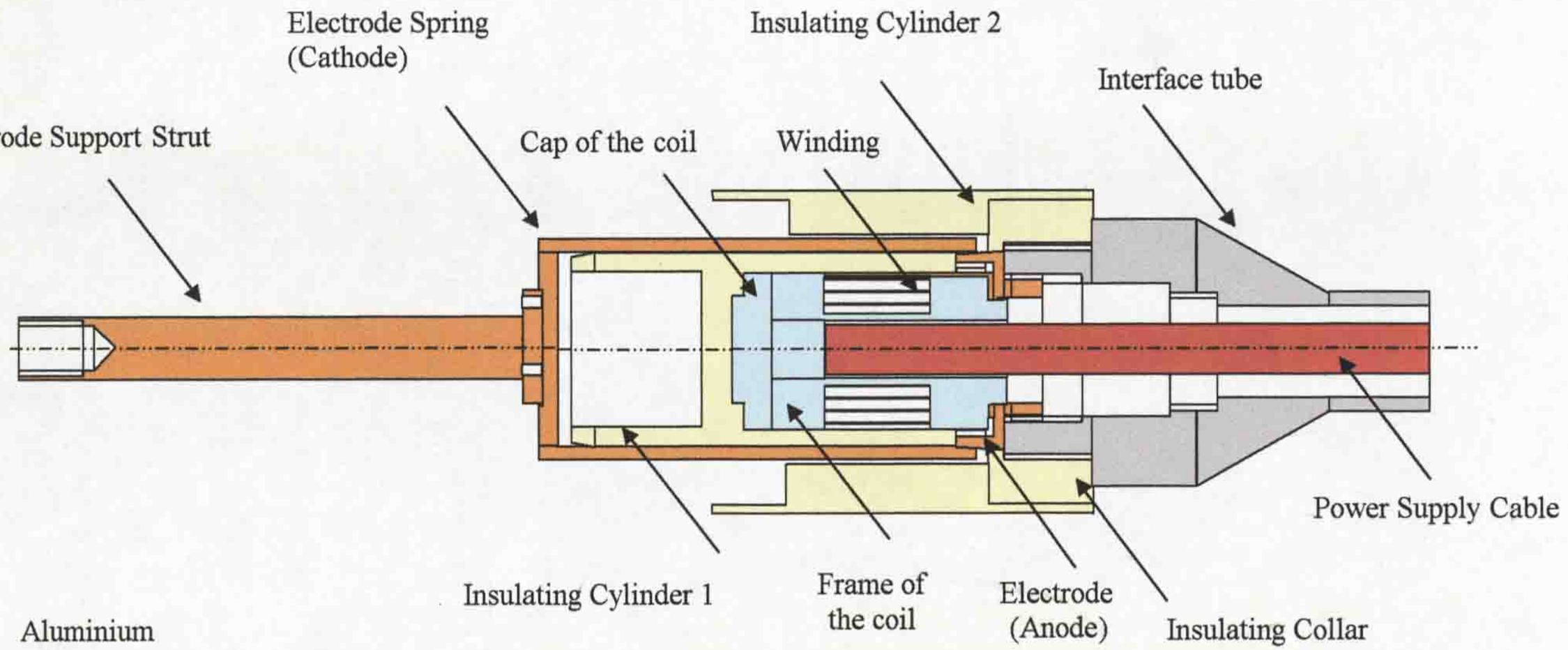

Aluminium

Grey PTFE (Coil)

Copper

White PTFE

Colour-scale designating different materials

NOTE

ALL DIMENSIONS IN MILLIMETRES
REMOVE ALL BURRS AND SHARP EDGES

SCALE	GENERAL TOLERANCES	TITLE	MATERIAL	PROJECTION	DRAWN	DATE	QTY
1-4	± .2mm	Prototype interrupter test head	Various	3rd Angle	L. Shpanin	Aug 05	1

CIMS
Centre for Intelligent Monitoring Systems

THE UNIVERSITY *of* LIVERPOOL

Department of Electrical Engineering and Electronics

Brownlow Hill
Liverpool
L69 3GJ

Telephone 794 4547

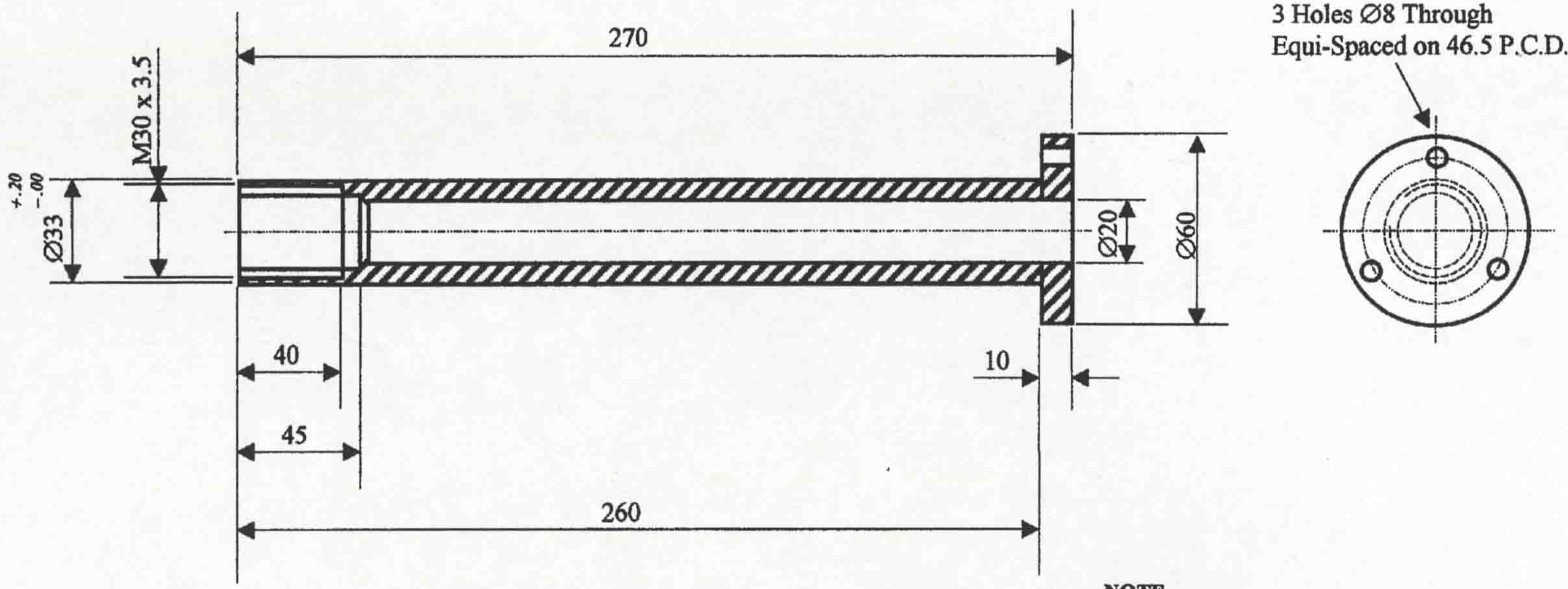

NOTE

ALL DIMENSIONS IN MILLIMETRES
REMOVE ALL BURRS AND SHARP EDGES

SCALE	GENERAL TOLERANCES	TITLE	MATERIAL	PROJECTION	DRAWN	DATE	QTY
1-2	± .2mm	Electrode Support Strut	Copper	3rd Angle	R.Forde	Aug 03	1

CIMS
Centre for Intelligent Monitoring Systems

THE UNIVERSITY *of* LIVERPOOL

Department of Electrical Engineering and Electronics

Brownlow Hill
Liverpool
L69 3GJ

Telephone 794 4547

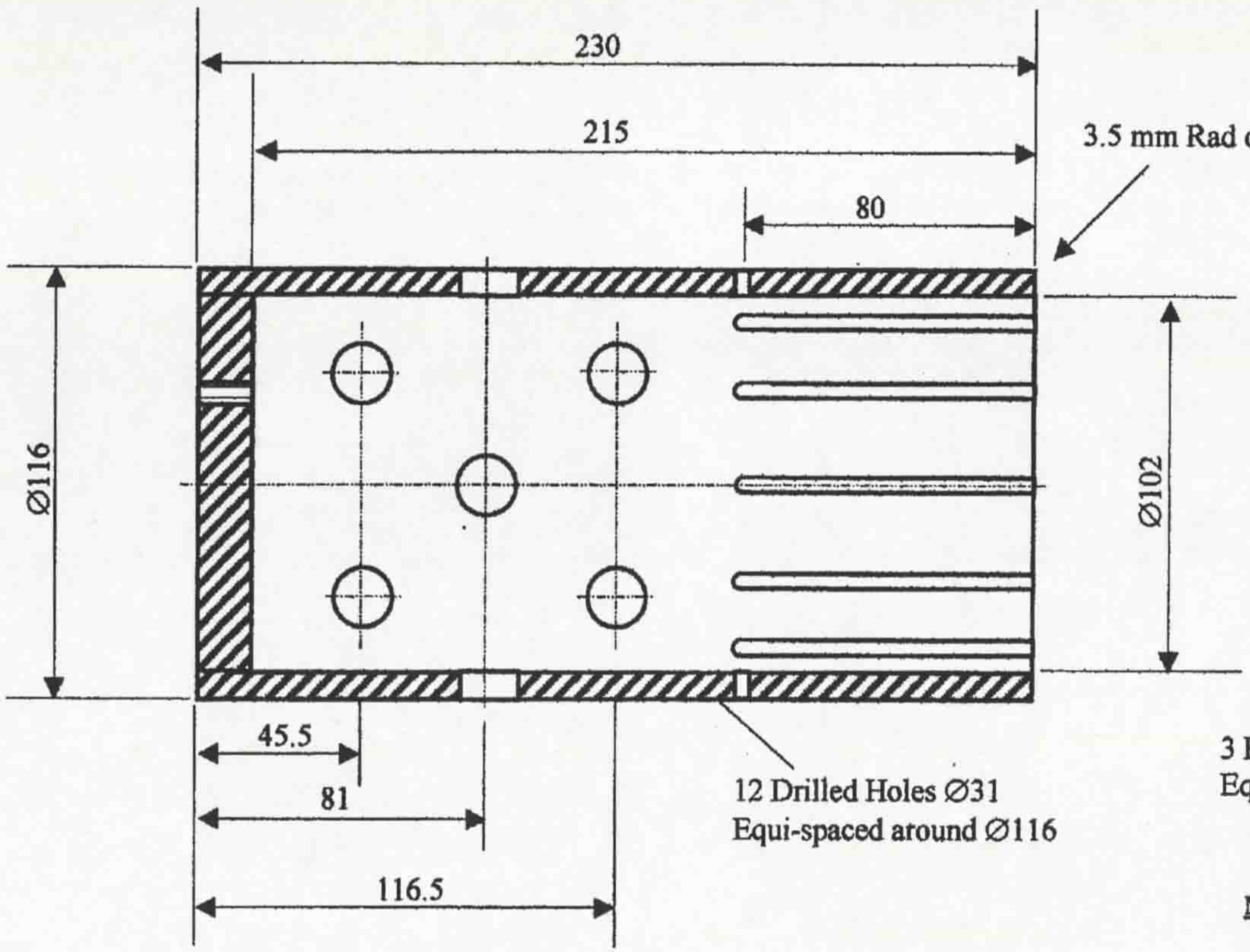

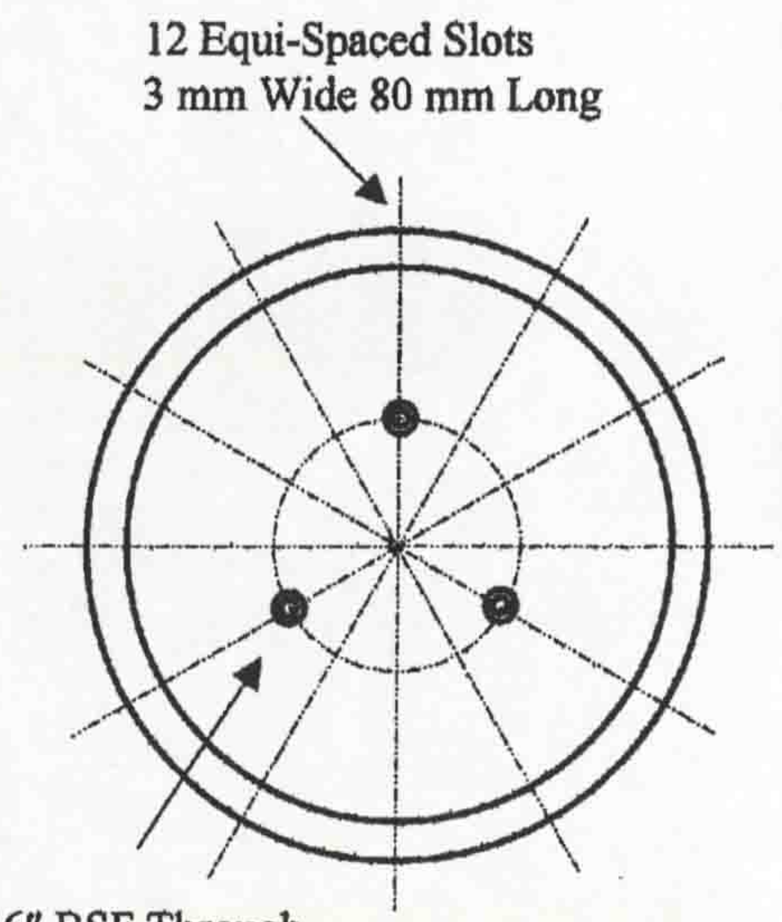

NOTE

ALL DIMENSIONS IN MILLIMETRES
REMOVE ALL BURRS AND SHARP EDGES

SCALE	GENERAL TOLERANCES	TITLE	MATERIAL	PROJECTION	DRAWN	DATE	QTY
1-2	± .2mm	Electrode Spring	Copper	3rd Angle	R.Forde	Aug 03	1

Centre for Intelligent Monitoring Systems

THE UNIVERSITY *of* LIVERPOOL

Department of Electrical Engineering and Electronics

Brownlow Hill
Liverpool
L69 3GJ

Telephone 794 4547

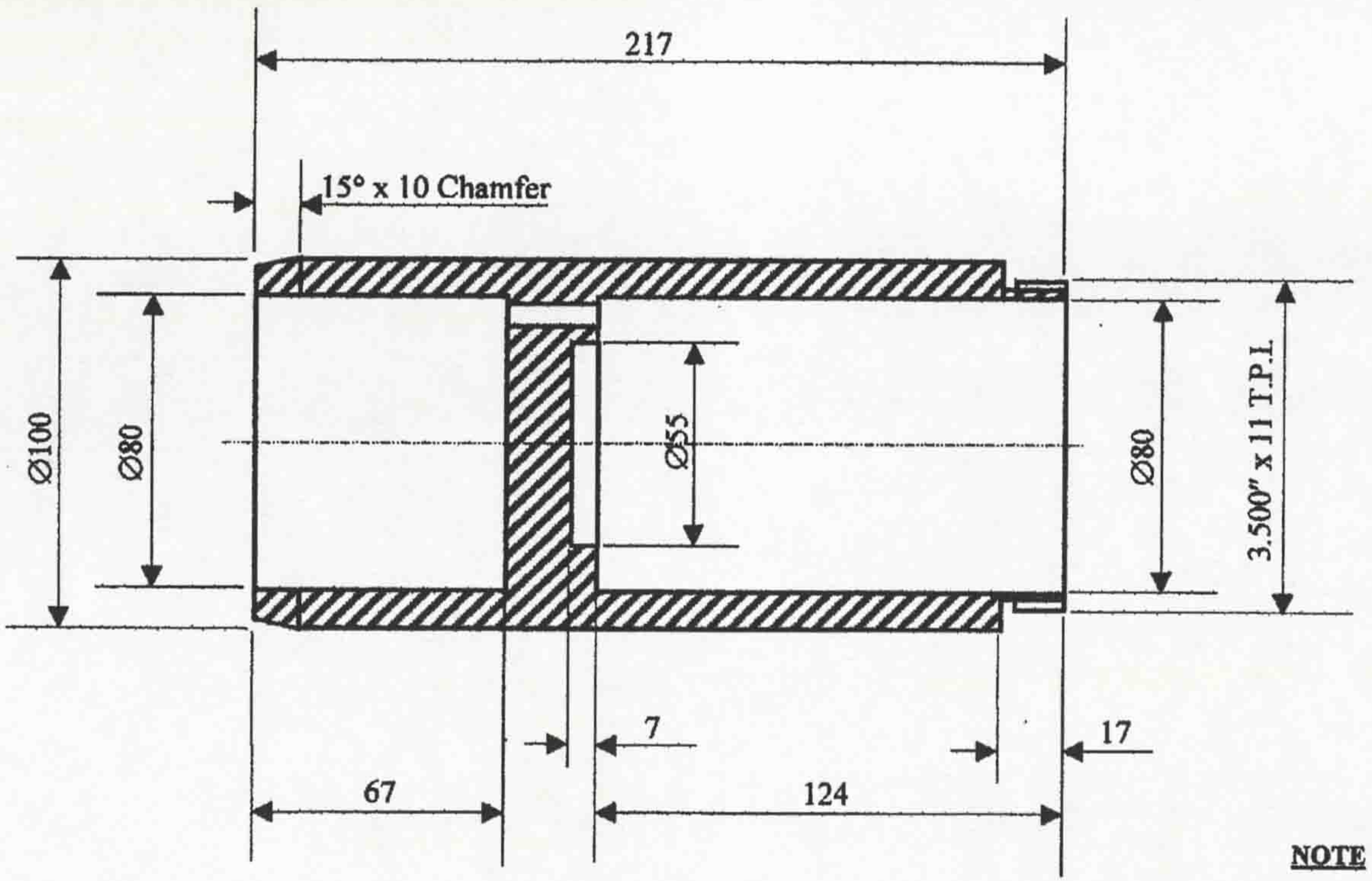

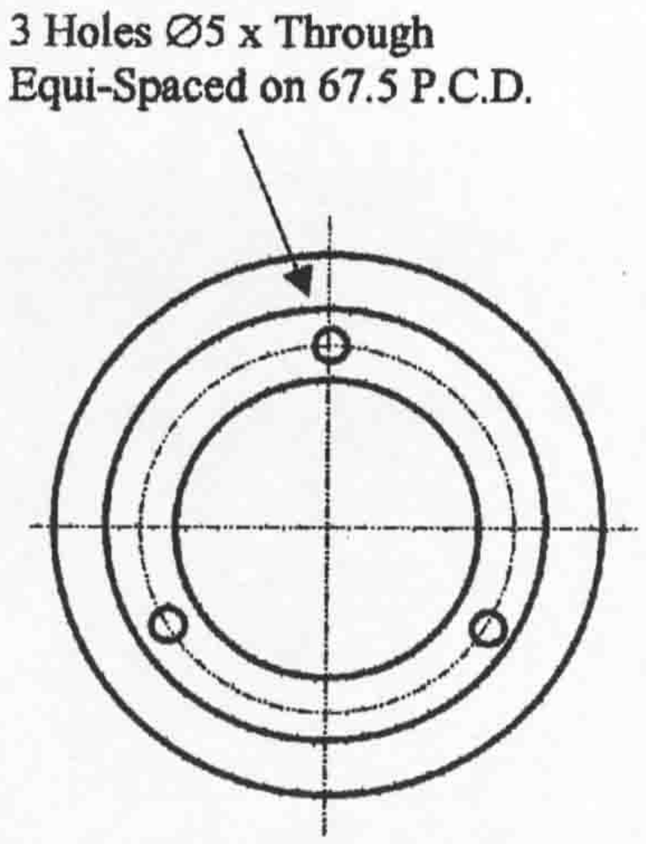

NOTE

ALL DIMENSIONS IN MILLIMETRES
REMOVE ALL BURRS AND SHARP EDGES

SCALE	GENERAL TOLERANCES	TITLE	MATERIAL	PROJECTION	DRAWN	DATE	QTY
1-2	± .2mm	Insulating Cylinder	PTFE	3rd Angle	R.Forde	Aug 03	1

Centre for Intelligent Monitoring Systems

THE UNIVERSITY *of* LIVERPOOL

Department of Electrical Engineering and Electronics

Brownlow Hill
Liverpool
L69 3GJ

Telephone 794 4547

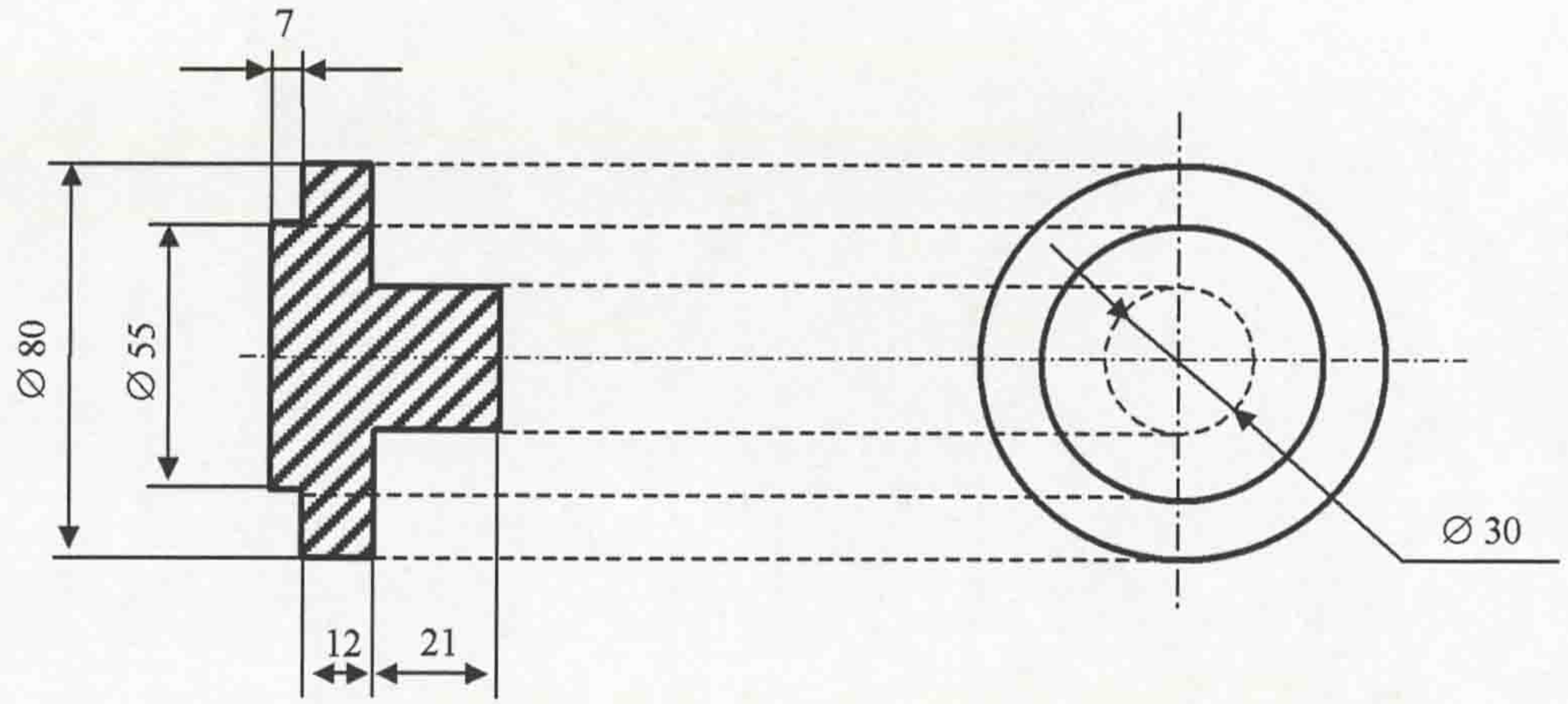

NOTE

ALL DIMENSIONS IN MILLIMETRES
REMOVE ALL BURRS AND SHARP EDGES

SCALE	GENERAL TOLERANCES	TITLE	MATERIAL	PROJECTION	DRAWN	DATE	OTY
1- 2	± .2mm	Cap of the coil	PTFE	3rd Angle	N. Telfer	Aug 05	1

CIMS

Centre for Intelligent Monitoring Systems

THE UNIVERSITY *of* LIVERPOOL

Department of Electrical Engineering and Electronics

Brownlow Hill
Liverpool
L69 3GJ

Telephone 794 4547

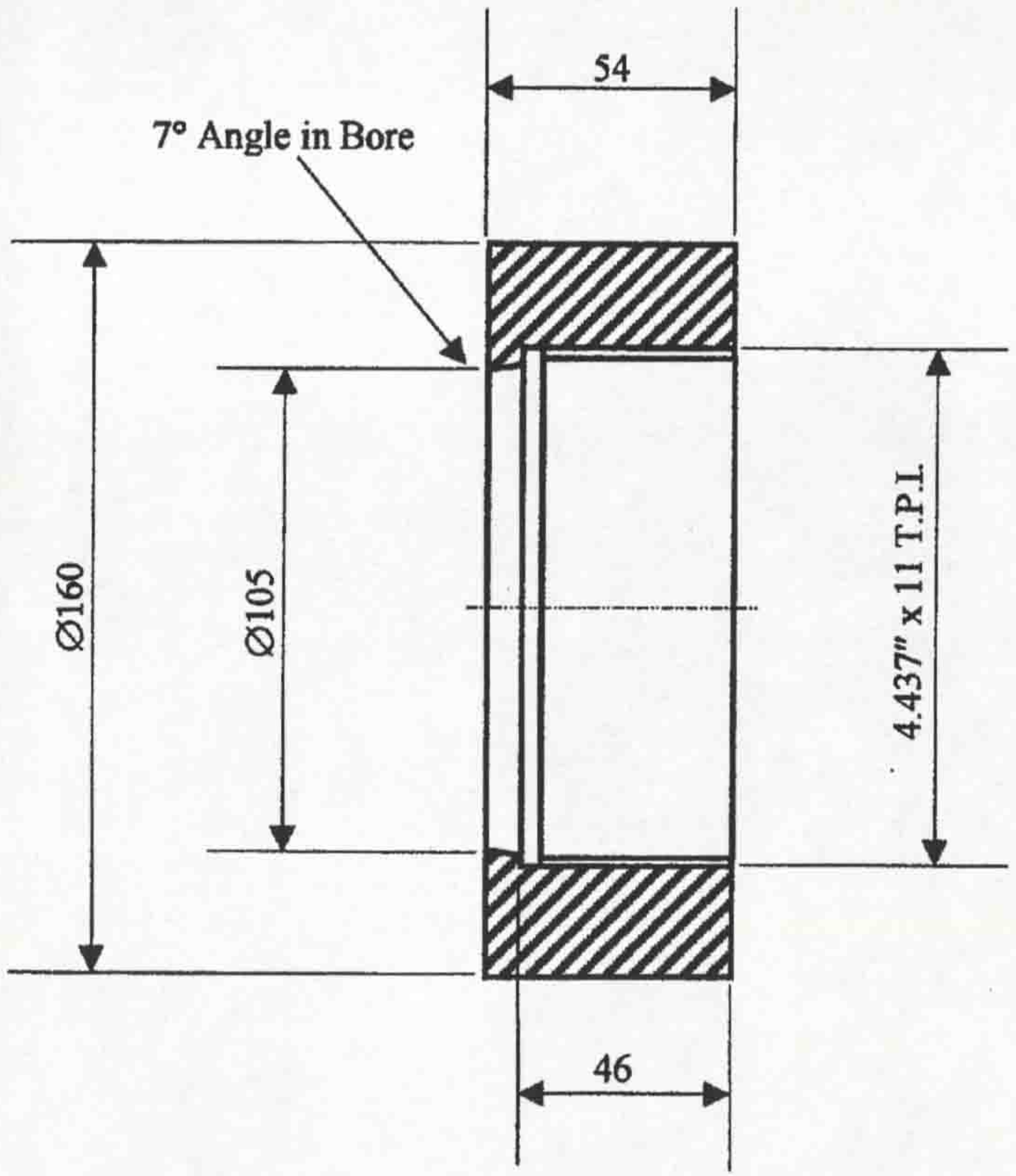

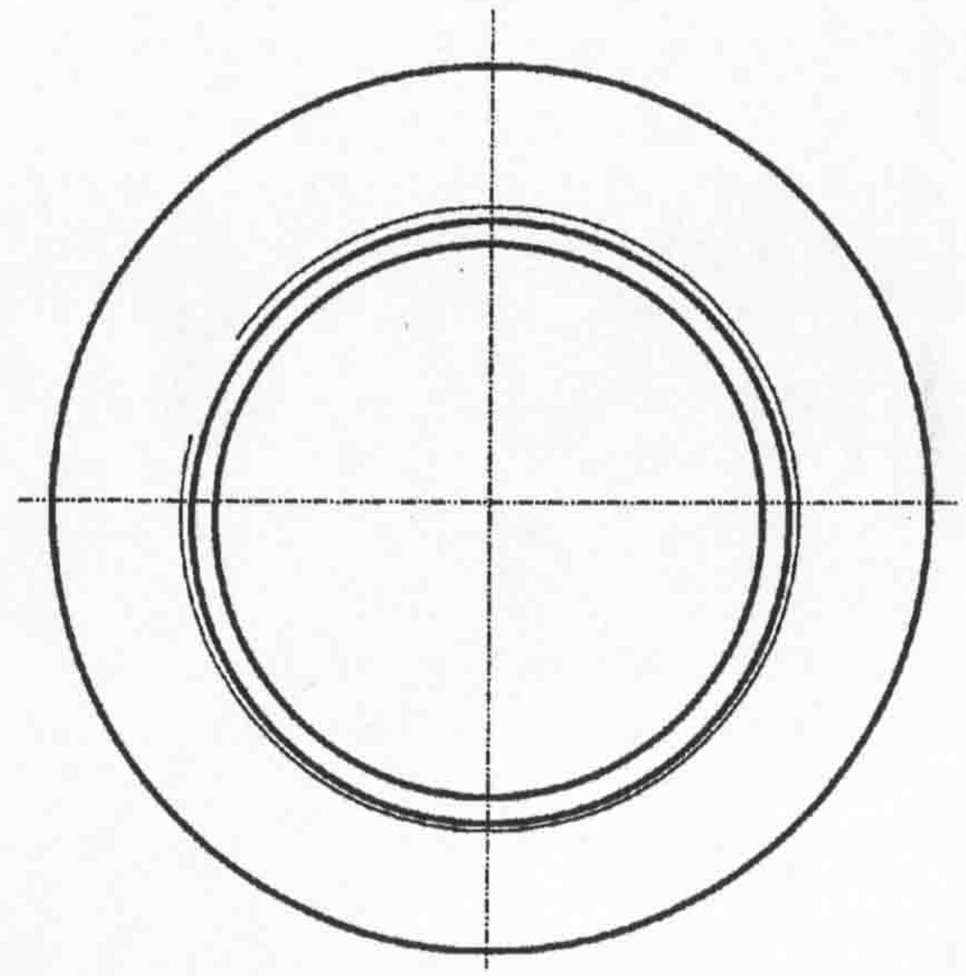

NOTE

ALL DIMENSIONS IN MILLIMETRES
REMOVE ALL BURRS AND SHARP EDGES

SCALE	GENERAL TOLERANCES	TITLE	MATERIAL	PROJECTION	DRAWN	DATE	QTY
1-2	± .2mm	Insulating Collar	PTFE	3rd Angle	R.Forde	Aug 03	1

CIMS
Centre for Intelligent Monitoring Systems

THE UNIVERSITY *of* LIVERPOOL

Department of Electrical Engineering and Electronics

Brownlow Hill
Liverpool
L69 3GJ

Telephone 794 4547

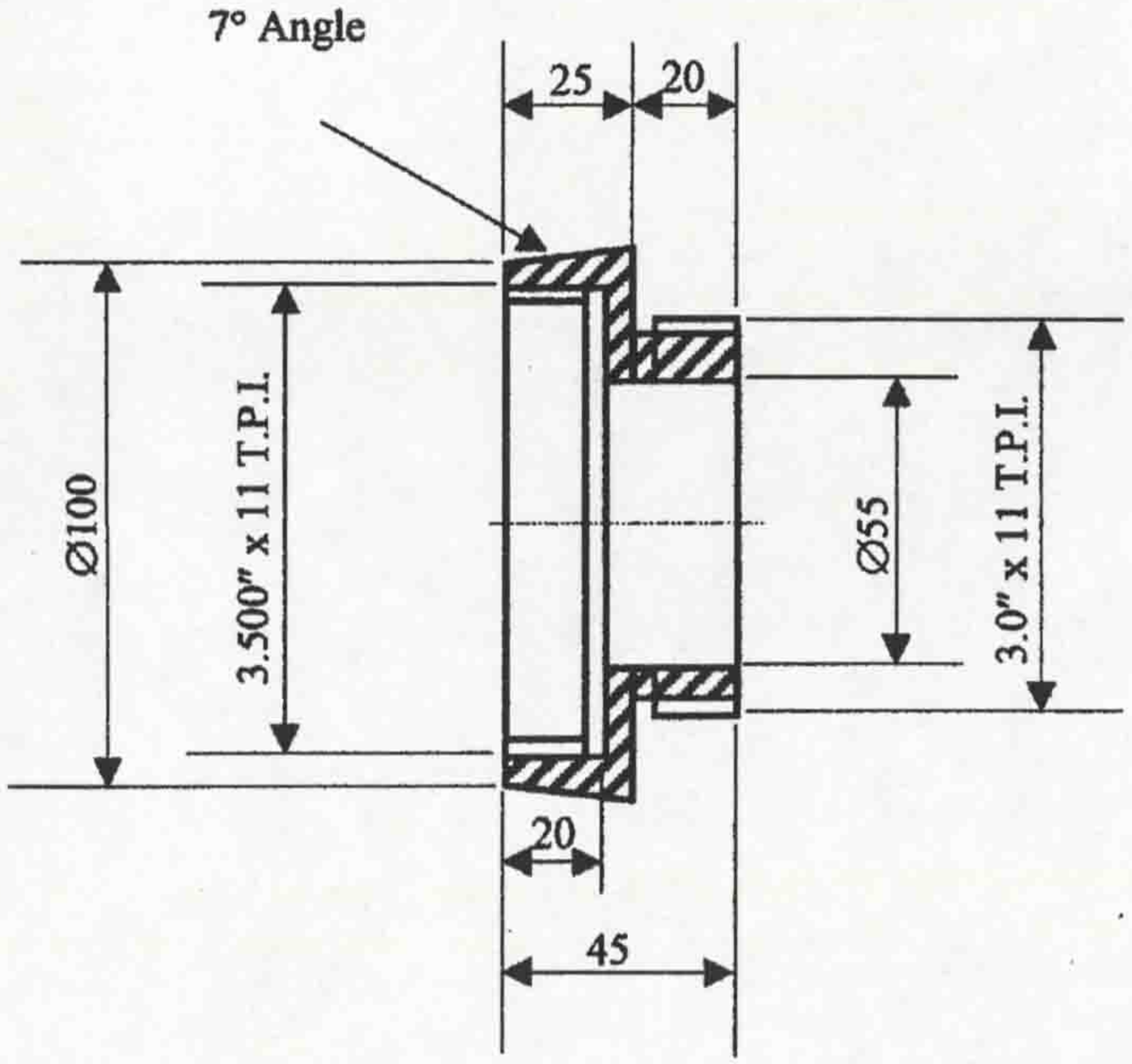

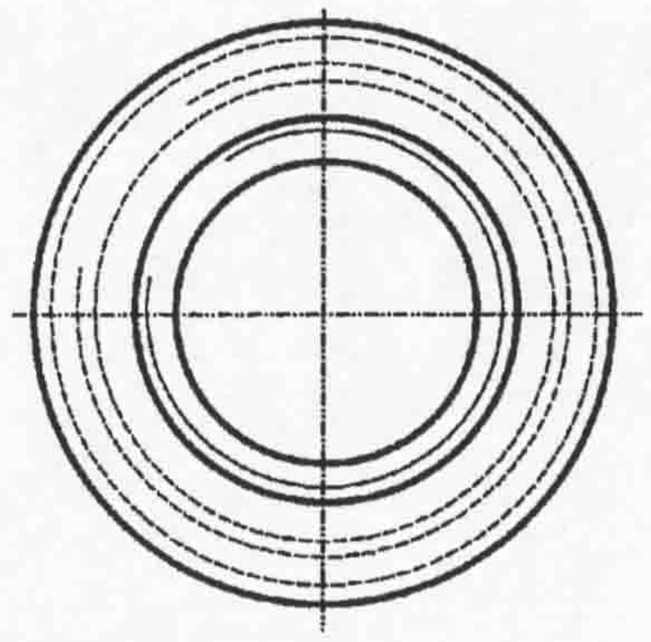

NOTE

ALL DIMENSIONS IN MILLIMETRES
REMOVE ALL BURRS AND SHARP EDGES

SCALE	GENERAL TOLERANCES	TITLE	MATERIAL	PROJECTION	DRAWN	DATE	QTY
1-2	± .2mm	Locking Contact Ring	Copper	3rd Angle	R.Forde	Aug 03	1

Centre for Intelligent Monitoring Systems

THE UNIVERSITY
of LIVERPOOL

Department of Electrical Engineering and Electronics

Brownlow Hill
Liverpool
L69 3GJ

Telephone 794 4547

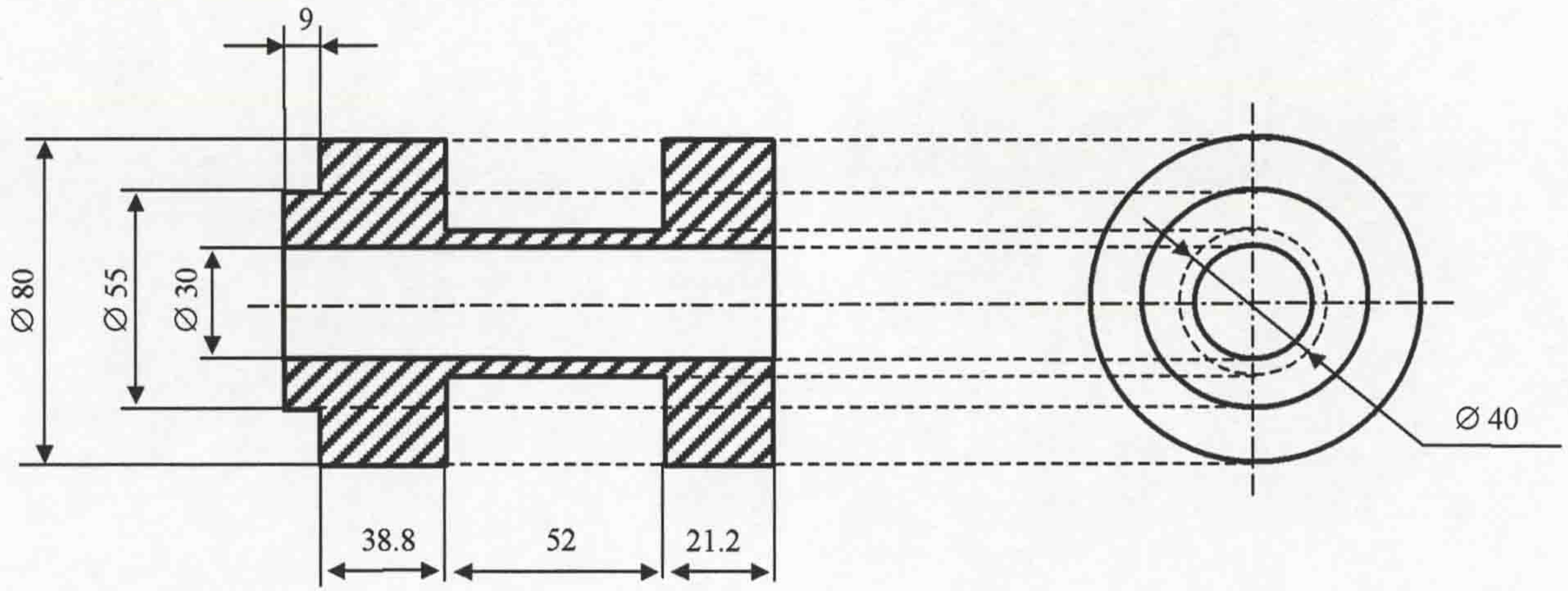

NOTE

ALL DIMENSIONS IN MILLIMETRES
REMOVE ALL BURRS AND SHARP EDGES

SCALE	GENERAL TOLERANCES	TITLE	MATERIAL	PROJECTION	DRAWN	DATE	QTY
1- 2	± .2mm	Frame of the coil	PTFE	3rd Angle	N. Telfer	Aug 05	1

Centre for Intelligent Monitoring Systems

THE UNIVERSITY *of* LIVERPOOL

Department of Electrical Engineering and Electronics

Brownlow Hill
Liverpool
L69 3GJ

Telephone 794 4547

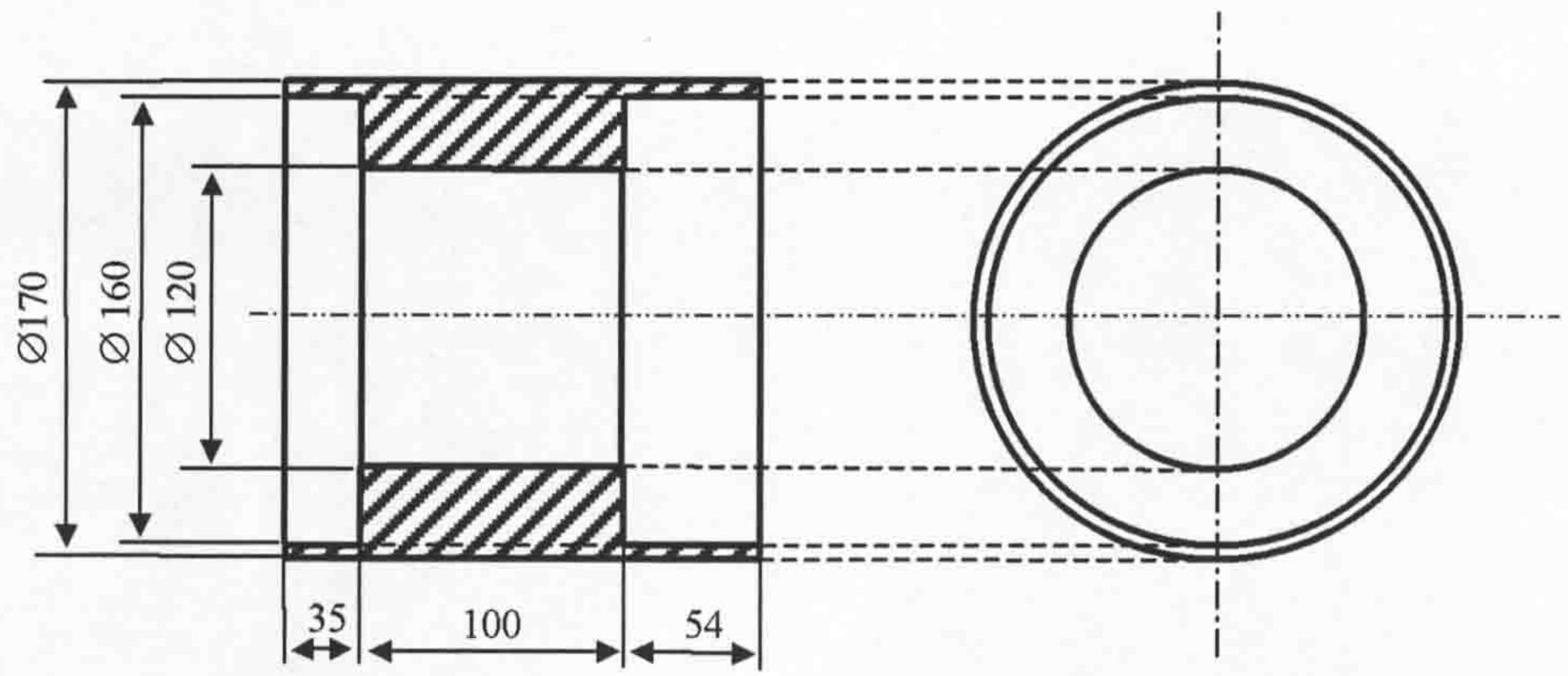

NOTE

ALL DIMENSIONS IN MILLIMETRES
REMOVE ALL BURRS AND SHARP EDGES

SCALE	GENERAL TOLERANCES	TITLE	MATERIAL	PROJECTION	DRAWN	DATE	QTY
1-4	± .2mm	Insulating Cylinder 2	PTFE	3rd Angle	L. Shpanin	Aug 05	1

Centre for Intelligent Monitoring Systems

THE UNIVERSITY *of* LIVERPOOL

Department of Electrical Engineering and Electronics

Brownlow Hill
Liverpool
L69 3GJ

Telephone 794 4547

NOTE
¾" BSP Thread Both Ends With a
Ø24 x 4 Wide Under Cut

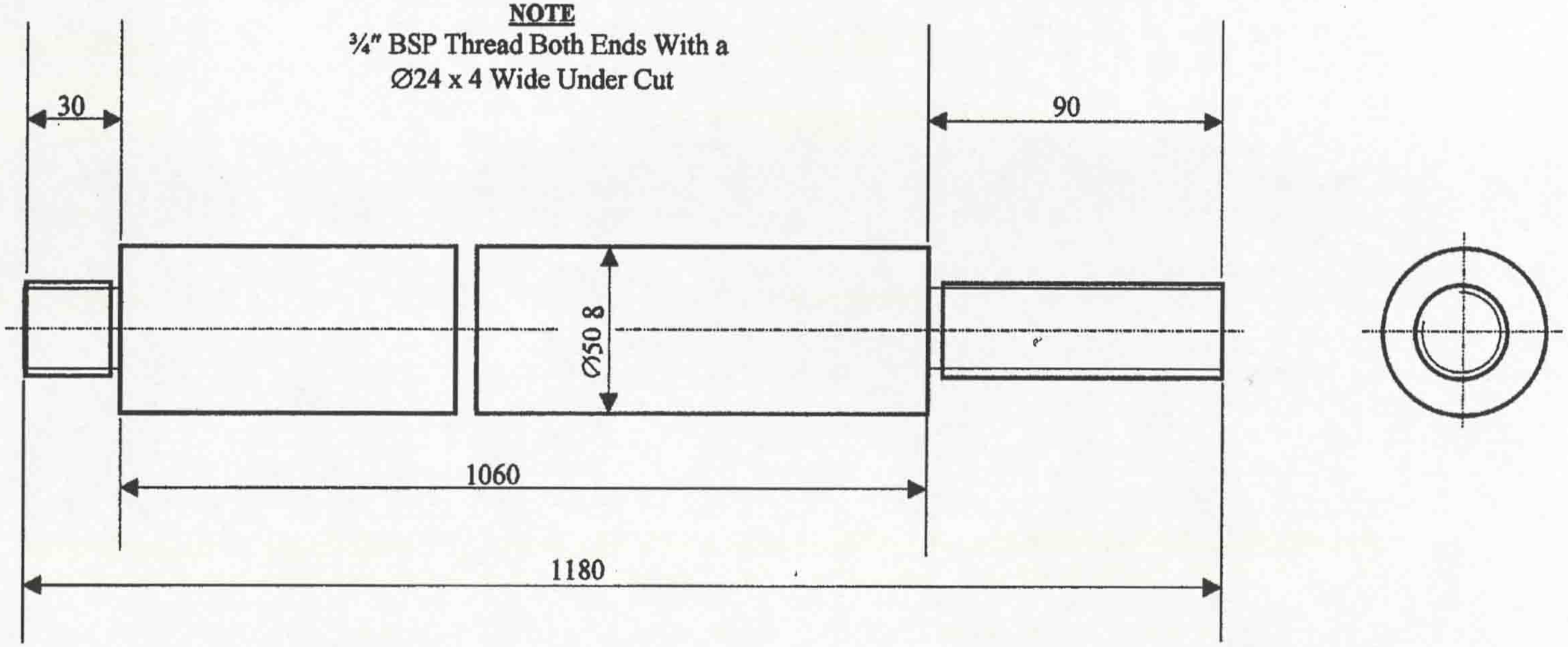

NOTE

ALL DIMENSIONS IN MILLIMETRES
REMOVE ALL BURRS AND SHARP EDGES

SCALE	GENERAL TOLERANCES	TITLE	MATERIAL	PROJECTION	DRAWN	DATE	QTY
1-2	± .2mm	Column Strut	Ø2" EN 24T Steel Bar	3rd Angle	R.Forde	July 03	3

Centre for Intelligent Monitoring Systems

THE UNIVERSITY
of LIVERPOOL

Department of Electrical Engineering and Electronics

Brownlow Hill
Liverpool
L69 3GJ

Telephone 794 4547

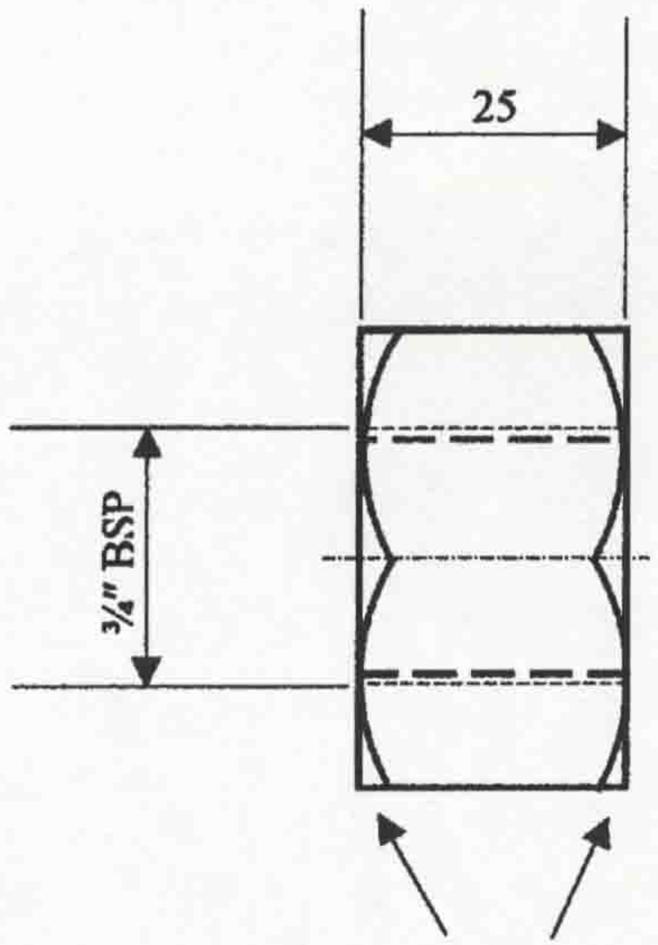

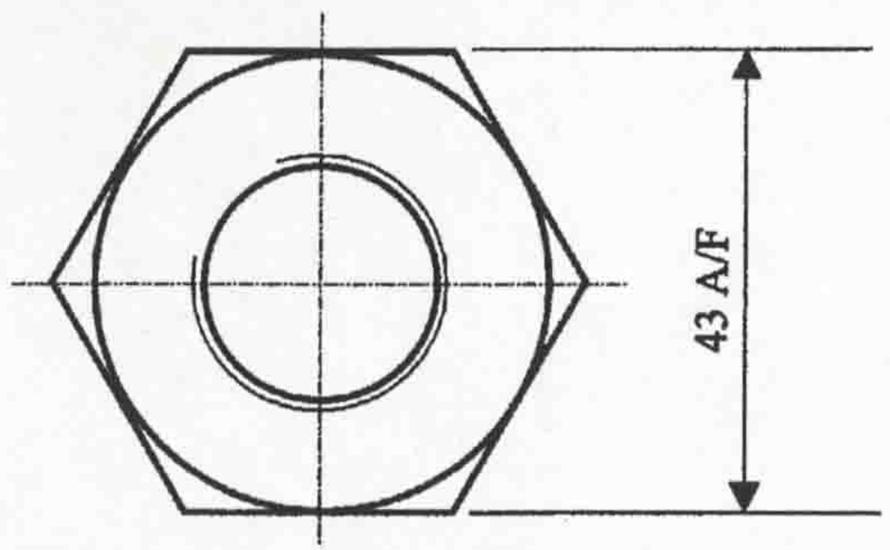

NOTE

ALL DIMENSIONS IN MILLIMETRES
REMOVE ALL BURRS AND SHARP EDGES

SCALE	GENERAL TOLERANCES	TITLE	MATERIAL	PROJECTION	DRAWN	DATE	QTY
1-1	± .2mm	Locking Nut	Ø2" EN 24T Steel Bar	3rd Angle	R.Forde	July 03	3

Centre for Intelligent Monitoring Systems

THE UNIVERSITY
of LIVERPOOL

Department of Electrical Engineering and Electronics

Brownlow Hill
Liverpool
L69 3GJ

Telephone 794 4547

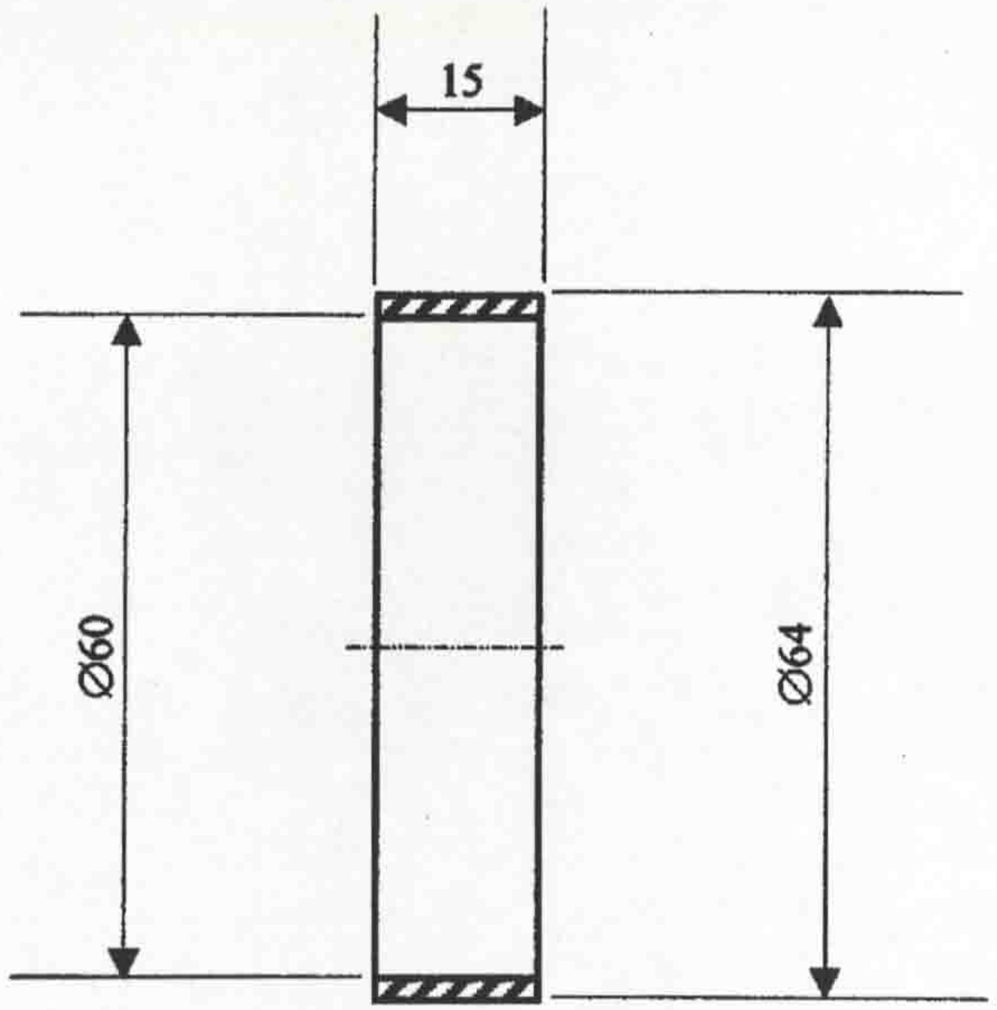

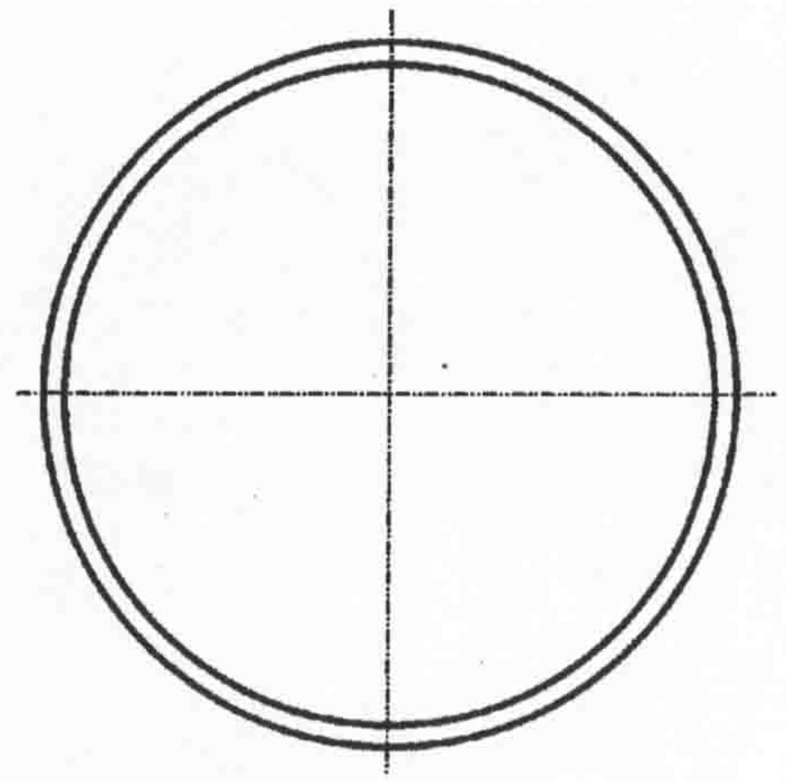

NOTE

ALL DIMENSIONS IN MILLIMETRES
REMOVE ALL BURRS AND SHARP EDGES

SCALE	GENERAL TOLERANCES	TITLE	MATERIAL	PROJECTION	DRAWN	DATE	QTY
1-1	± .1mm	Collar	Aluminium	3rd Angle	R.Forde	Aug 03	1

CIMS
Centre for Intelligent Monitoring Systems

THE UNIVERSITY *of* LIVERPOOL

Department of Electrical Engineering and Electronics

Brownlow Hill
Liverpool
L69 3GJ

Telephone 794 4547

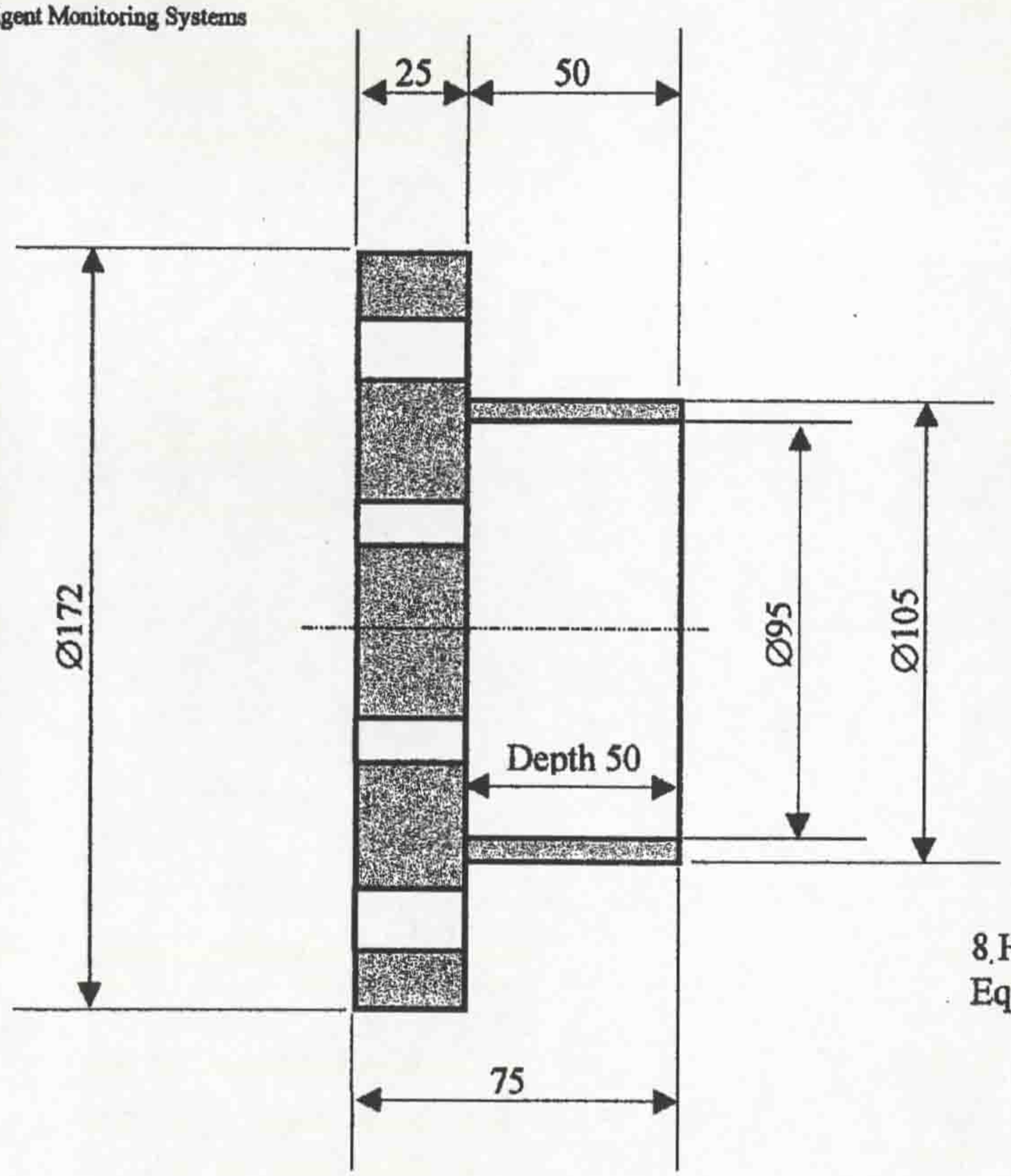

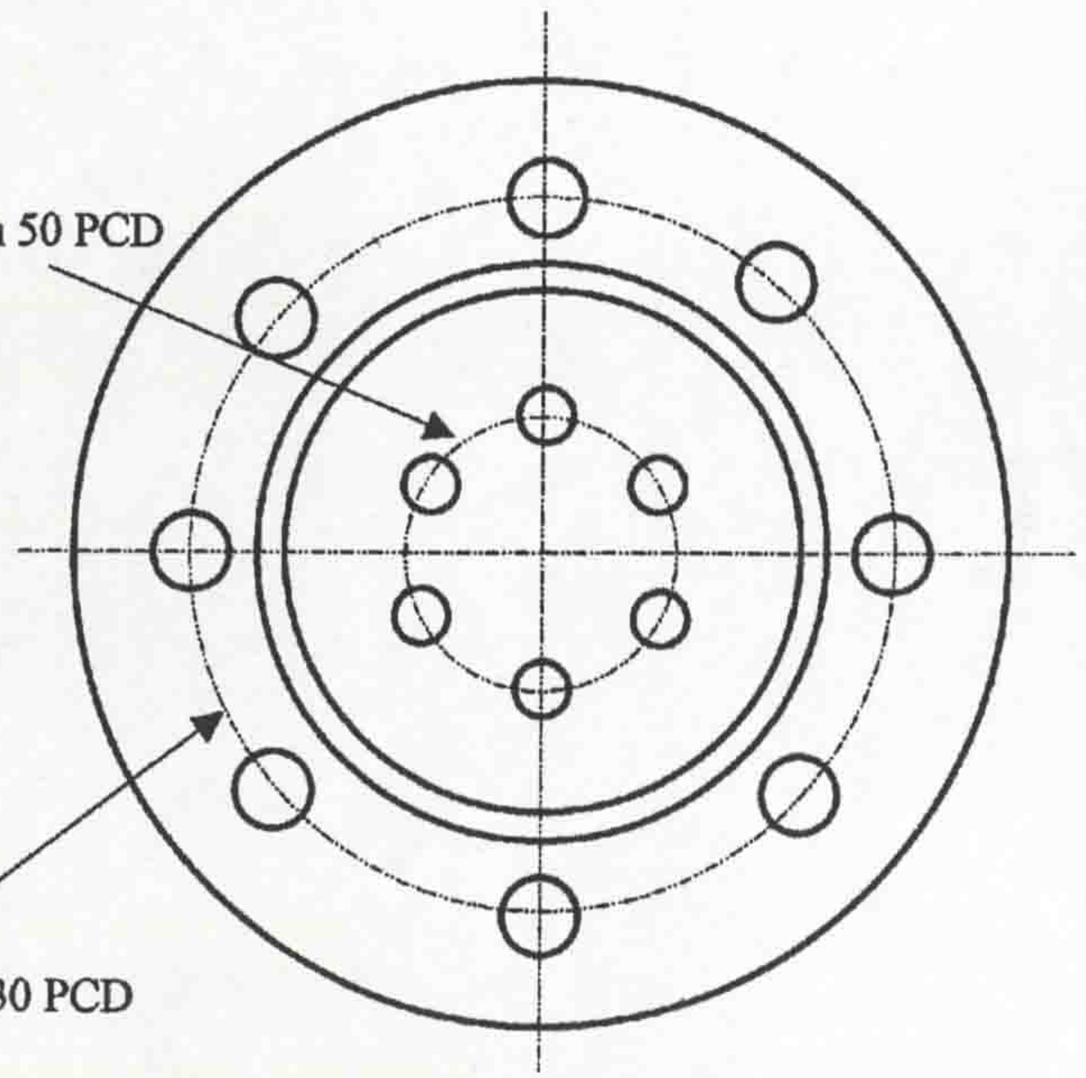

NOTE

ALL DIMENSIONS IN MILLIMETRES
REMOVE ALL BURRS AND SHARP EDGES

SCALE	GENERAL TOLERANCES	TITLE	MATERIAL	PROJECTION	DRAWN	DATE	QTY
1-2	± .1mm	Insulator Sleeve	Nylon	3rd Angle	R.Forde	July 03	1

Centre for Intelligent Monitoring Systems

THE UNIVERSITY
of LIVERPOOL

Department of Electrical Engineering and Electronics

Brownlow Hill
Liverpool
L69 3GJ

Telephone 794 4547

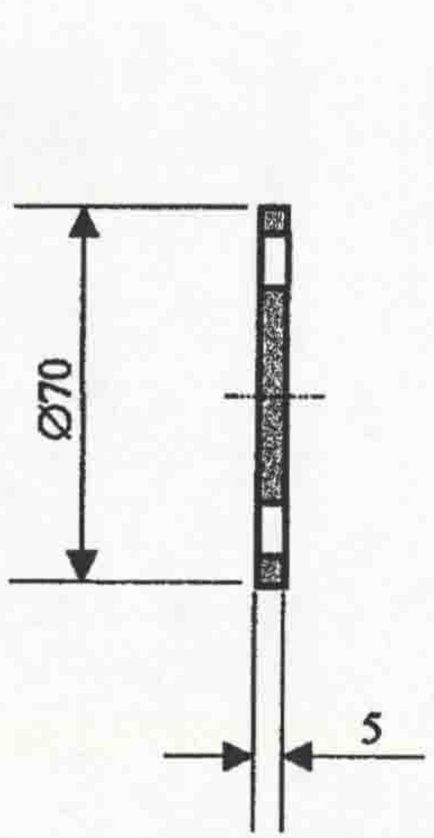

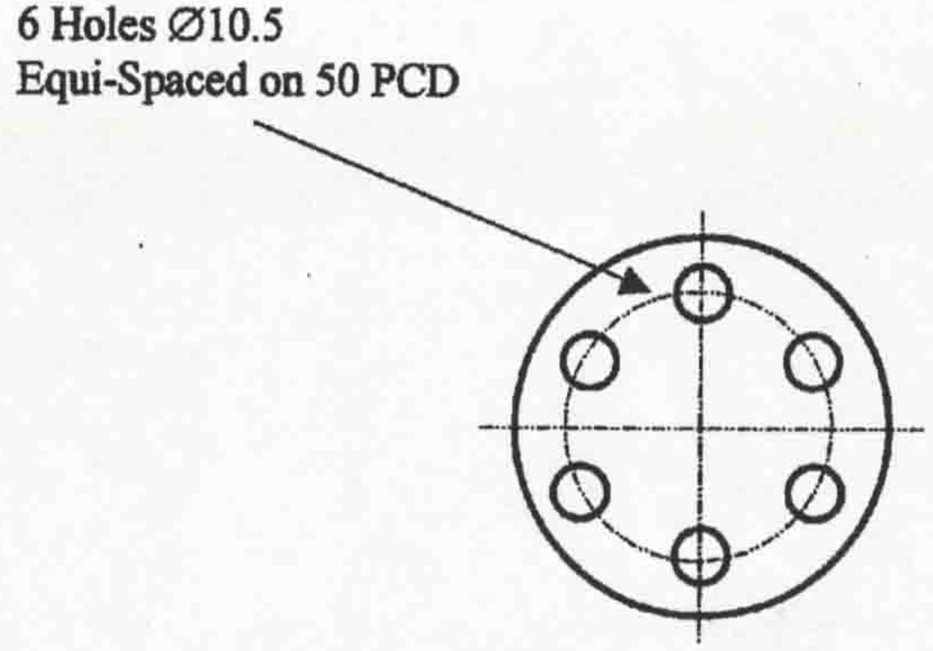

NOTE

ALL DIMENSIONS IN MILLIMETRES
REMOVE ALL BURRS AND SHARP EDGES

SCALE	GENERAL TOLERANCES	TITLE	MATERIAL	PROJECTION	DRAWN	DATE	QTY
1-2	± .1mm	Spacer	Mild Steel	3rd Angle	R.Forde	July 03	1

Centre for Intelligent Monitoring Systems

THE UNIVERSITY
of LIVERPOOL

Department of Electrical Engineering and Electronics

Brownlow Hill
Liverpool
L69 3GJ

Telephone 794 4547

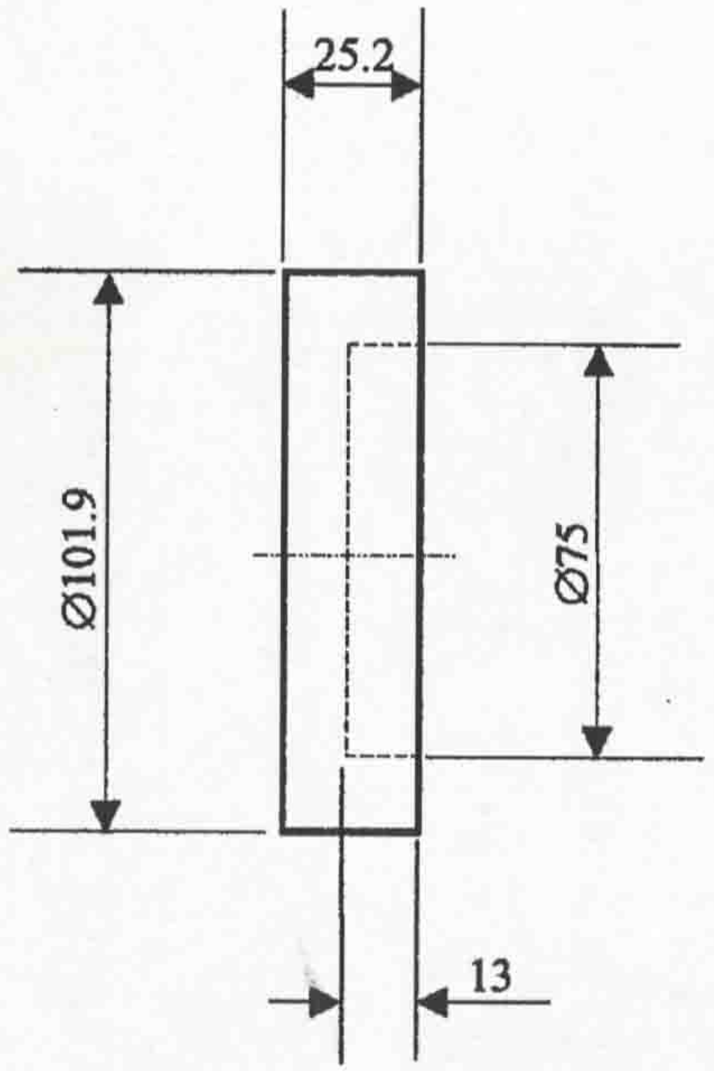

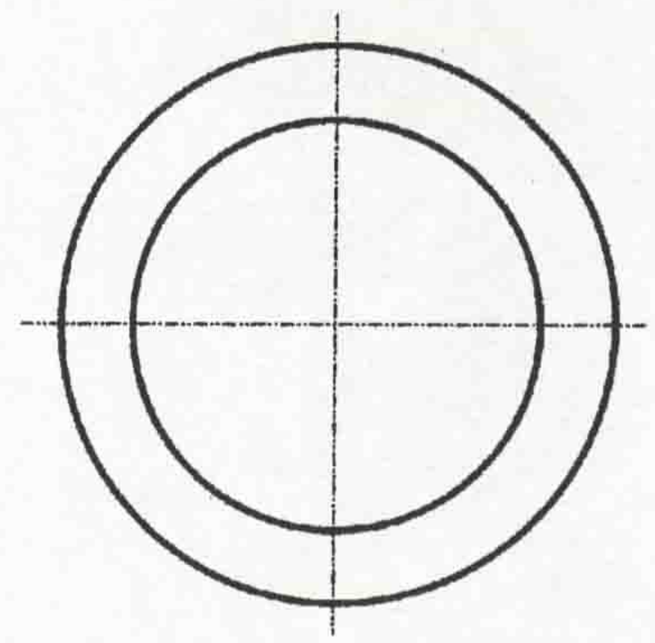

NOTE

ALL DIMENSIONS IN MILLIMETRES
REMOVE ALL BURRS AND SHARP EDGES

SCALE	GENERAL TOLERANCES	TITLE	MATERIAL	PROJECTION	DRAWN	DATE	QTY
1-2	± .1mm	Insulator Cap	Nylon	3rd Angle	R.Forde	July 03	1

REFERENCES

ADAMS V.W. (Sept. 1963)
Technical Note Aero. 2915

ALI S.M.G., RYAN H.M., LIGHTLE D, SHIMMIN D.W., TAYLOR S and JONES G.R. (1985)
High power short circuit studies on a commercial 420kV;63kA puffer circuit breaker.
Trans. IEEE, PAS-104, No.2, February, pp459-467.

ALI S.M.G (1-6 July 2001)
Switchgear design, development and service.
High Voltage Engineering and Testing, University of Northumbria at Newcastle, Ninth International School, pp286-318.

ALI S.M.G (1-6 July 2001)
Difference in performance between SF_6 and vacuum circuit breakers at distribution voltage levels.
High Voltage Engineering and Testing, University of Northumbria at Newcastle, Ninth International School, pp376-388.

BACON E.K. (1976)
Irving Langmuir.
W.D. Miles, ed., American Chemists and Engineers, Washington, D.C., pp. 288-289.

BELMADINI B., CASANOVAS J., CASANOVAS A.M., GROB R. and MATHIEU J. (1991)
SF_6 Decomposition under Power Arcs - Physical aspects.
IEEE Trans. on Elect. Insul., Vol.26, No.6, December, pp1163-1182.

BROWNE (Jr.) T.E. (1948)
A study of arc behaviour near current zero by means of mathematical models.
Trans. Am. Inst. Electr. Eng., 67, Pt.I, pp141-153.

BROWNE (Jr.) T.E. (1984)
Circuit interruption, Theory and Techniques.
Marcel Dekker Inc., New York, pp135-156, 404-408.

BIERMANNS J. (1938)
The AEG air-blast breaker.
AEG Progress Report 1938-2.

CASSIE A.M. (1939)
A new theory of arc rupture and circuit-breaking.
CIGRE, **10,** pp102.

CHAPMAN A. (1977)
Electrical conductance of gas blast arcs.
PhD thesis, Univ. of Liverpool.

CHEN, F. F. (1984)
Plasma physics and controlled fusion.
2nd edition, University of California, USA, Vol.1, pp1-4, 177-181.

CHRISTOPHOROU, L.G., OLTHOFF, J.K., GREEN, D.S. (Nov. 1997)
Technical Note 1425 - Gas for electrical insulation and Arc interruption.
NIST (National Institute of Standards and Technology), USA, pp1-9, 16, 37.

COBINE J. D. (1958)
Gaseous conductors.
2nd edition, New York, Dover Publications, pp143-144, 343-348, 352-370, 372-382.

COOPER F.S. (1940)
Gas dielectric media, US Pat. 2221671.

COWLEY M.D. (1974)
Integral methods of analysing electric arcs.
J. Phys. D: Appl. Phys., Vol.7, pp2218-2245.

CULLWICK E.G. (1966)
Fundamentals of electro-magnetism.
3rd edition, Cambridge University press, pp144-162, 166-167

DAVY J. (1840)
The collected works of Sir Humphry Davy.
Vol. IV, Smith Elder and Co. Cornhill, London, pp110-112.

DHAR P.K., BARRAULT M.R. and JONES G.R. (1979)
A multiring radio frequency technique for measuring arc boundary variations at high currents and close to current zero.
Univ. of Liverpool, Arc Research Report, ULAP-T64.

DUNSHEATH P. (1962)
A history of electrical power engineering.
The M.I.T. Press, UK, LOC TK15. D8

DUPLAY C. and HENNEBERT J. (1983)
The breaking process with Fluarc SF_6 puffer and rotating arc circuit breakers and Rollarc contactors.
Merlin-Gerin Service Information E/CT 122.

ENNIS M.G., TURNER D.R., WOOD J.K., SPENCER J.W., JONES G.R., (1994)
Low current and reactive switching behaviour of rotating arc switchgear.
Trends in Distribution Switchgear, 4th Int. Conf., Publication No.400, IEE, pp.13-17.

ENNIS M.G., TURNER D.R., SPENCER J.W. and JONES G.R., (1996)
Rotating arc interrupter with independent field excitation.
IEE Proc.-Sci. Meas. Technol. Vol. 143, No. 2, pp.113-118.

ENNIS M.G. (1996)

Investigation of fundamental processes affecting the behaviour of electric arcs in electromagnetic interrupters.
PhD thesis, Univ. of Liverpool.

FANG M.T.C. (1983)
A review of gas blast circuit breaker arc modelling.
Liverpool University, Arc Reasearch Report, ULAP-T69.

FLURSCHEIM C.H. (1982)
Power circuit breaker theory and design.
2nd edition, IEE Power Engineering Series 1, New York, Peter Peregrinus.

FRANCISCO G. PENA-LECONA, JUAN F. MOSINO, VALERY N. FILIPPOV, R. A. MARTINEZ-CELORIO and ORACIO C. BARBOSA-GARCIA (2004)
An electro-optic fibre sensor with double pass configuration for measuring high ac voltage.
Centro de Investigaciones en Optica, Leon, Gto, CP 37150, Mexico,
University of Southampton, High field, Southampton, SO17 1BJ, UK,
Meas. Sci. Technol. **15** No. 6, pp1129-1132.

GROVER F.W. (1946)
Inductance calculations: Working formulas and Tables.
Dover Publications, Inc., New York, pp105-113.

GRUNDY J.A. (1977)
Sinusoidal response of coaxial current shunt.
Proc. IEE, Vol.124, N"5, pp499-504.

GURU B.S. and HIZIROGLU H.R. (2004)
Electromagnetic field theory fundamentals.
2nd edition, Kettering University, Cambridge University Press, pp143, 284-299

HEBERLEIN J.V.R, KIMBLIN C.W. and LEE A. (1984)
Nature of the electric arc. (In circuit interruption - Browne (Ed.)).
Marcel Dekker, Inc.

HENDERSON P.J., SPENCER J. and JONES G.R. (1993)
Pressure sensing using a chromatically addressed diaphragm.
Meas. Sci. Technol. 4, pp88-94.

JAKOB T., SCHADE E., and SCHAUMANN R. (1985)
Self-extinction and economic new principle for SF_6 circuit breakers.
Brown Bovery Publication, CH-A 194 280E

JOHNK CARL T.A. (1988)
Engineering electromagnetic fields and waves.
2nd edition, Wiley International Edition, pp270-275.

JONES G.R. and FANG M.T.C. (1980)
The physics of high power arcs.

Rep. Prog. Phys. 1980 **43**, pp1415-1465.

JONES G.R. (1984)
Predicting pressure transients due to arcing in two pressure, puffer and rotary arc interrupters.
Proc. IEE Symp. on Trends in modern switchgear design 3.3-150kV,
Newcastle, pp8.1-8.5.

JONES G.R., SHAMMAS N.Y. and PRASAD A.N. (1986)
Radiatively induced nozzle ablation in high-power circuit interrupters.
IEEE Trans. **PS-14**, pp413-422.

JONES, G.R., SHAMMAS, N.Y. and PRASAD, A.N. (1986)
University of Liverpool, Research Report ULAP-T84.

JONES G.R., KWAN S., BEAVAN C., HENDERSON P., and LEWIS E. (1987)
Optical fibre based sensing using chromatic modulation.
Opt. Laser Technol. 9 pp297-303.

JONES G.R. (1988)
High pressure arcs in industrial devices - Diagnostic and monitoring techniques.
Cambridge, U.K., Cambridge University Press.

JONES G.R. (1-6 July 2001)
Gas filled interrupters – fundamentals.
High Voltage Engineering and Testing, University of Northumbria at Newcastle,
Ninth International School, pp259-285.

KIDMAN M.C. (2003)
Private communication

KWEON K.Y. (2004)
Computer simulation of SF_6 arcs in a hybrid circuit breaker.
PhD thesis, Univ. of Liverpool.

LECLERC J.L., SMITH M.R., and JONES G.R. (1980)
Pressure transients in a model gas blast circuit breaker operating at extra high current levels.
IEEE, Trans. **PS-8**, pp376-384.

LEE, GREENWOOD, CROUCH and TITUS (1962)
Development of power vacuum interrupters.
Trans. Am Inst. Electr. Eng. 81, Pt.III, pp629-639.

LEWIS E., SHAMMAS N.Y. and JONES, G.R. (1985)
The current zero SF_6 blast arc at high di/dt.
Proc. Int. Conf. on Gas Discharges and their Applications, Oxford, pp35-38.

LYTHALL R.T. (1972)
J&P Switchgear book.

England, The Butterworth Group, pp 23-44, pp466-497.

MAYR O. (1943)
On the theory of the electric arc and its extinction.
ETZ, 64, pp645-652.

MEDLOCK R. (1989)
Fibre optics in process control.
Control Instrum. (UK) **21** pp105-108.

MENDIS S.R, BISHOP M.T. and WITTE J.F. (1996)
Investigations of voltage flicker in electric arc furnace power systems.
Industry Applications Magazine, IEEE, Vol. 2, Issue 1, pp28 – 34.

MORI T., SPENCER J.W., HUMPHRIES J.E., JONES G.R. (Sep. 2002)
SF_6 rotary arcs in hollow polymeric cylinders.
14th Int. Conf. Gas Discharges and their application, (UK), Vol.1, pp115-118.

MORI T., SPENCER J.W., HUMPHRIES J.E., JONES G.R. (Apr. 2005)
Diagnostic measurements on rotary arcs in hollow polymeric cylinders.
IEEE Trans. Power Deliv., Vol.20, No. 2, pp765-771.

NAKAO H., NAKAGOSHI Y., HATANO M., KOSHIZUKA T., NISHIWAKI S., KOBAYASHI A., MURAO T., YANABU S. (Oct. 2001)
DC current interruption in HVDC SF6 gas MRTB (Metallic Return Transfer Breaker) by means of self-excited oscillation superimposition.
Kansai Electr. Power Co. Inc., Osaka, Japan, Power Delivery, IEEE Transaction on, Vol.16, Issue: 4, pp687-693.

NOESKE H.O, BENENSON D.M., FRIND G., HIRASAWA K., KINSINGER R.E., NAGAMATSU H.T., SHEER R.E. and YOSHIOKA Y. (1983)
Applications of arc-interruption fundamentals to nozzles for puffer interrupters.
EPRI Report EL-3293, Project 246-2, pp1.1-1.9.

NONKEN G.C. (1941)
High pressure gas as a dielectric.
IEEE Trans. 60, pp1017-1020.

OKAMOTO M., ISHIKAWA M., SUZUKI K. and IKEDA H. (1991)
Computer simulation of phenomena associated with hot gas in puffer-type gas circuit breaker.
IEEE Trans. Power Deliv., Vol.6, No.2, April, pp833-839.

PANSINI A.J. and SMALLING K.D. (1992)
High voltage power equipment engineering.
Library of Congress Cataloging, USA, The Fairmont Press, Inc., pp41-63, 77-96.

PARRY J. (1984)
Future developments in SF6 switchgear for distribution systems incorporating a rotating arc circuit-breaking device.

Proc. IEE Symp. on trends in modern switchgear design 3.3-150kV, Newcastle, pp2.1-2.6.

PARK J.H. (1947)
Shunts and Inductors for surge-current measurements.
USA National Bureau of Standards, Research Paper RP1823, Vol.39, pp191-204.

PORTIS A.M. (1978)
Electromagnetic fields: Sources and Media.
John Wiley & Sons, University of California, Berkeley, pp632-637.

RUEGSEGGER W., MEIER R. and KNEUBUHL F.K. (1985)
Mass spectrometry of arcs in SF_6 circuit breakers.
Appl. Phys. B 37, pp115-135.

RYAN H.M. and JONES G.R. (1989)
SF_6 switchgear.
IEE power Engineering Series 10, UK, Peter Peregrinus Ltd., pp14-22, 167-177.

SAUERS I., ELLIS H.W., CHRISTOPHOROU L.G., GRIFFIN G.D. and EASTERLY C.E. (1984);
Spark decomposition of SF_6; toxicity of by-products.
Oak Ridge National Laboratory Report ORN/TM-9062.

SCHRADE H.O. (Sept. 1973)
Stable configuration of electric arcs in transverse magnetic field.
IEEE, Trans. Vol. PS-1, pp47-54

SCHWAB A.J. (1971)
Low-resistance shunts for impulse currents.
IEEE, Trans. of power apparatus and systems, PAS-90, pp2251-2257.

SCHWAB A.J. (1972)
High-voltage measurement *techniques.*
M.I.T. Press, Cambridge, Massachusetts, and London, England, pp48-53, 164-180.

SCHUPP J., FISCHER W., MECKE, H. (2000)
Welding arc control with power electronics.
Power Electronics and Variable Speed Drives,
8th Int. Conf. on (IEE Conf. Publ. No. 475), pp443-450.

SHIMMIN D.W. (1986)
High power short circuit studies on an SF_6 puffer circuit breaker.
PhD thesis, Univ. of Liverpool.

SHISHKIN G.G. and JONES J.R. (1985)
Electromagnetic emission from high current, convection controlled arcs.
Proc. VIII Int. Conf. on Gas discharge and their applications,
Oxford (Leeds University Press).

SILLARS R.W. (1973)
Electrical insulating materials and their application.
IEE Monograph Series 14, UK, Billing & Sons Ltd., pp137-179.

SORENSON R.W. and MENDENHALL H.E. (1926)
Vacuum switching experiments.
Trans. Am. Inst. Electric. Eng., 45, pp1102-1105.

SPENCER J.W. (1987)
Some investigations of the behaviour of a rotating arc discharge.
PhD thesis, Univ. of Liverpool.

TAYLOR S., WANG B. (1981)
ULAP Internal Report

TELFER D.J., T., HUMPHRIES J.E., SPENCER J.W. and JONES G.R. (Sep. 2002)
Influence of PTFE on arc quenching in an experimental self-pressurized circuit breaker.
14th Int. Conf. Gas Discharges and their application, (UK), Vol.1, pp91-94.

TODOROVIC P.S. and JONES G.R. (1985)
Time resolved laser Doppler measurements in the underexpanded jet of a model gas blast circuit breaker under arcing conditions.
IEEE Trans., **PS-13**, pp153-62

TOMINAGA S., KUWAHARA H., YOSHINAGA K. and SAKUMA, S. (1980)
Investigation on gas flow of puffer type gas circuit breaker based on observation of arc and pressure measurement.
Trans. IEEE, PAS-99, No.6, Nov/Dec, pp2040-2048.

TOMINAGA S., KUWAHARA H., YOSHINAGA K. and SAKUMA, S. (1981)
SF_6 gas analysis technique and its application for evaluation of internal conditions in SF_6 gas equipment.
IEEE Trans., PAS-100, pp4196-4206.

TUMA D.T. (1980)
A comparison of the behaviour of SF_6 and N_2 blast arcs around current zero.
IEEE Trans., PAS-99, pp2129-2137.

TURNER D.R. (2005)
Private communication

VON ENGEL, A. (1983)
Electric Plasmas: Their Nature and Uses.
Department of Engineering, University of Oxford, pp105-106.

WHITHEY W.B. and WEDMORE E.B. (1927)
Improvements in or relating to electric circuit breakers.
British Pat. 278764

YAN J.D. (1997)
Investigation of electric arcs in self-generated flow.
PhD thesis, Univ. of Liverpool.

INDEX OF SYMBOLS USED IN THE DESIGN DEVELOPMENT

INDEX OF PARAMETERS USED IN THE THEORETICAL MODELLING OF THE MAGNETIC FIELD PRODUCING COIL		
z_0	Cartesian coordinate of the point (in z-axis) at which the field is B_x, B_z	m
x_0	Cartesian coordinate of the point (in x-axis) at which the field is B_x, B_z	m
z	Height of an individual layer from the bottom of the coil and as such is the basic variable for the integration, which is done from z=0 to z=h, (where h is the length of the coil)	m
a_1	Inner radius of the coil	m
a_2	Outer radius of the coil	m
N	number of turns	
I	peak ac current	A
h	length of the coil	m
μ	permeability in free space (vacuum)	$=4\pi\times10^{-7}$ H/m
B_x	peak magnetic field component in x-axis	T
B_z	peak magnetic field component in z-axis	T
B	total value of the peak magnetic field $B=\sqrt{\left(B_x^2+B_z^2\right)}$	T
ϕ	Angle showing the orientation of the total B field with relation to the B_x and B_z field components	degree

INDEX OF PARAMETERS USED IN THE MAGNETIC FIELD MEASUREMENTS OF A COIL		
$\hat{V}_{sc}$	search coil peak voltage	V
v_{sc}	time changing search coil voltage	V
f	frequency	Hz
b	time changing magnetic field	T
μ	permeability in free space	H/m
$\hat{I}$	peak ac current	A
$\hat{B}$	peak magnetic flux density	T
I_{RMS}	RMS (root mean square) current	$=\hat{I}/\sqrt{2}$ A
ω	angular frequency	Radian
t	time	s

INDEX OF PARAMETERS USED IN THE CALCULATION OF A COIL		
L	inductance	H
a	mean coil radius	m
b	length of the coil	m
c	thickness of the coil	m
ρ_{copper}	copper resistivity	$=1.7\times10^{-8}\,\Omega$m
R	resistance of the coil	Ω
l	length of the strip	m
N	number of turns	
d	thickness of a strip	m